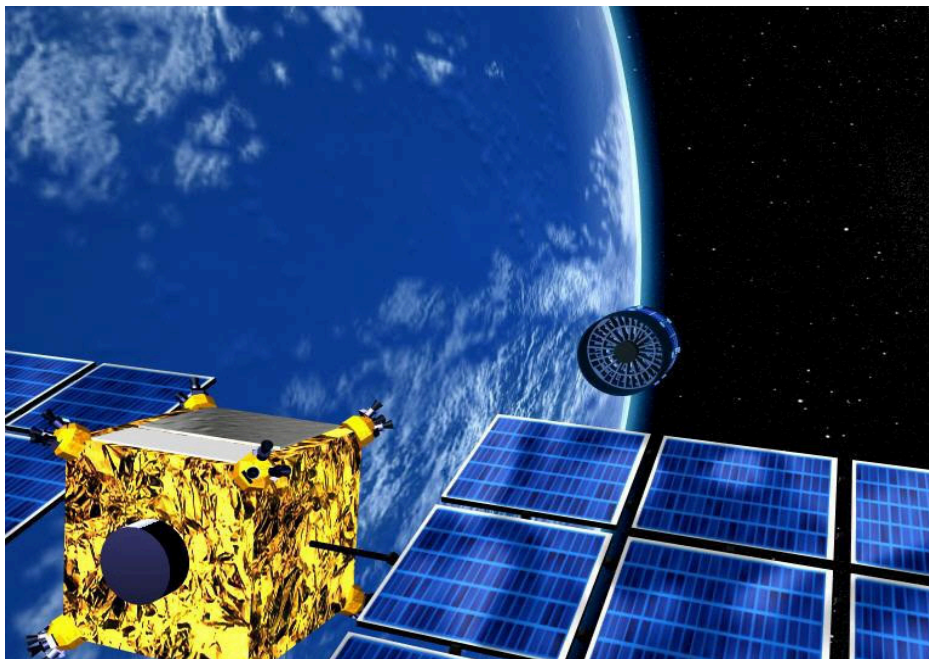


MAX-PLANCK-INSTITUT FÜR
EXTRATERRESTRISCHE PHYSIK

MPE Report 281

**Proceedings of the International Workshop
XEUS - studying the evolution
of the hot Universe**

**March 11-13, 2002
MPE Garching**



ISSN 0178-0719

85748 GARCHING · GERMANY

PROCEEDINGS OF THE INTERNATIONAL WORKSHOP
XEUS – STUDYING THE EVOLUTION
OF THE HOT UNIVERSE

HELD AT MPE GARCHING
March 11-13, 2002

edited by

G. HASINGER
Th. BOLLER
A.N. PARMAR

Proceedings of the Workshop "XEUS - studying the evolution of the hot Universe"
held in Garching, Germany, March 11-13, 2002

edited by

G. Hasinger, Th. Boller and A. Parmar

Table of Contents

Preface	
Conference Photographs	
The first stars and QSOs	1
<i>T. Abel</i>	
X-ray observations of the first QSOS	7
<i>G. Hasinger</i>	
Beyond the X-ray background with XEUS	19
<i>A. Comastri, P. Ranalli, M. Brusa</i>	
The X-ray Evolution of Galaxies: Implications for XEUS	25
<i>N. E. White</i>	
Chandra Observations of Narrow Line Galaxies	35
<i>I. Georgantopoulos, T. Shanks, M. Vallbe, A. Zezas, M.J. Ward, G.C. Stewart, B.J. Boyle, R.E. Griffiths</i>	
The growth of structures - Building clusters	39
<i>M. Arnaud</i>	
High redshift Sunyaev-Zel'dovich clusters and XEUS	49
<i>R. Kneissl</i>	
X-ray Absorption and Emission Spectroscopy of the Intergalactic Medium at Small Redshift	57
<i>F. Paerels, A. Rasmussen, S. Kahn, J.W. Herder, C. Vries</i>	
The Local Group WHIM Filament	65
<i>F. Nicastro</i>	
Detection of resonance absorption lines from the Intergalactic Medium by XEUS	77
<i>X. Barcons</i>	
Resonant scattering of X-rays by the warm intergalactic medium	85
<i>E. Churazov</i>	
The XEUS Mission	95
<i>A.N. Parmar</i>	
Metrology for the XEUS mirror plates	113
<i>R. Willingale</i>	
Alternative mirror technologies	119
<i>O. Citterio, M. Ghigo, F. Mazzoleni, G. Pareschi, B. Aschenbach, H. Bräuningner</i>	
Cryogenic Detectors (Narrow Field Instruments)	127
<i>H. Hoovers, P. Verhoeve</i>	
The Wide Field Imager for XEUS	135
<i>L. Strüder, P. Lechner</i>	
XEUS observations of hard X-ray sources	165
<i>H. Inoue</i>	
The neutron star equation of state from fast timing of X-ray bursts	173
<i>M. C. Miller</i>	
Highly Resolved X-ray Spectra with Chandra: Dynamics of Neutral and Ionized Matter	181
<i>N. S. Schulz</i>	
AGN iron lines: the complex picture from XMM-Newton and Chandra	191
<i>P. O'Brien, J. Reeves, K. Pounds, K. Page, M. Turner</i>	
High resolution spectroscopy of nearby AGN	199
<i>J.S. Kaastra</i>	
Reverberation revisited	207
<i>A.C. Fabian</i>	
A fast X-ray timing capability on XEUS	211

<i>D. Barret, G. K. Skinner, E. Kendziorra, R. Staubert, P. Lechner, L. Strüder, L. Stella, C. Miller</i>	
The importance of soft X-ray spectroscopy in the 0.1–0.5 keV range with XEUS	219
<i>Th. Boller, D. Breitschwerdt, L. Strüder, P. Predehl</i>	
Scientific and technical aspects of a low energy imaging spectrometer for XEUS	227
<i>R. Lieu</i>	
X-ray Astronomical Polarimetry in the XEUS Era	235
<i>E. Costa, P. Soffitta, G. Di Persio, M. Feroci, L. Pacciani, A. Rubini, R. Bellazzini, A. Brez, L. Baldini, L. Latronico, N. Omodei, G. Spandre</i>	
LMXRB in Elliptical Galaxies	243
<i>L. Angelini, S. Snowden, M. Loewenstein, R. Mushotzky</i>	
XMM-Newton observation of the first B[e] X-ray binary	247
<i>L. Boirin, A. N. Parmar</i>	
Investigating galactic halos with XEUS	251
<i>D. Breitschwerdt, M.J. Freyberg, W. Pietsch</i>	
Investigating the “missing baryon problem” with XEUS	255
<i>M.J. Freyberg, D. Breitschwerdt</i>	
X-ray polarimetry of AGN with XEUS	259
<i>D. Grupe, B.J. Wills</i>	
The Compton-thick AGN in the GPS radio source OQ+208	261
<i>M. Guainazzi, C. Stanghellini, P. Grandi</i>	
Light-weight X-ray optics for XEUS: alternative technologies	265
<i>R. Hudec, L. Pína, Inneman, V. Brožek, P. Chráska, K. Neufuss M., Zentková, Zentko</i>	
Large X-ray Optics: Lobster alternative	271
<i>R. Hudec, L. Pína, A., Inneman</i>	
Theory of Compact Stars	277
<i>M. Hanauske, D. Zschiesche, U. Eichmann, L.M. Satarov, I.N. Mishustin, J. Schaffner-Bielich, H. Stöcker, W. Greiner</i>	
The population of X-ray binaries and background AGN in the field of the Large Magellanic Cloud	281
<i>P. Kahabka</i>	
The X-ray evolving universe: (ionized) absorption and dust, from nearby Seyfert galaxies to high-redshift quasars	285
<i>S. Komossa, G. Hasinger</i>	
XMM-Newton Deep Survey in the Lockman Hole & the population of type-2 QSO	293
<i>I. Lehmann, G. Hasinger, V. Mainieri and the Lockman Hole team</i>	
Transition-edge microcalorimeters in Corbino disk geometry for XEUS NFI	295
<i>A. Luukanen, J. Huovelin, P. Keinänen, K. Kinnunen, A. Nuottajärvi, Pekola, J. Schultz, O. Vilhu</i>	
Submillimetre evidence for the coeval growth of X-ray absorbed QSOs and galaxy bulges	299
<i>M.J. Page, J.A. Stevens, F.J. Carrera</i>	
X-Ray Survey with High Spectral Resolution Microcalorimeters	303
<i>L. Piro, L. Colasanti, E. Costa et al.</i>	
The mass temperature relation for clusters of galaxies	307
<i>A. Del Popolo</i>	
Constellation-X Mirror Development: Lessons Learned Relevant to XEUS	317
<i>R. Petre and the Constellation-X SXT Team</i>	
The XEUS View of Nearby Clusters of Galaxies	327
<i>J. Schultz, J. Huovelin, O. Vilhu, P. Muhli, L. Alha, A. Luukanen, J. Pekola, H. Sipilä, S. Vaijärvi</i>	
The physics of shocks in the proto-stellar environment: Herbig-Haro objects observed with XEUS	331
<i>S. Sciortino, F. Favata, G. Micela, A. Parmar</i>	
The shape of the K_{α} line as the evidence for the black hole existence	339
<i>A.F. Zakharov, S.V. Repin</i>	
X-ray spectroscopy of GRB’s: Present Results and Future Perspectives for XEUS	343
<i>L. Piro</i>	
General relativity from neutron stars and stellar-mass black holes	354
<i>M. van der Klis</i>	
Rapporteur talk	363
<i>J. Bleeker</i>	

XEUS - Studying the Evolution of the Hot Universe

G. Hasinger¹, Th. Boller¹, A. Parmar²

¹Max-Planck-Institut für extraterrestrische Physik, Postfach 1312, 85741 Garching

²Space Science Department of ESA, ESTEC, NL

Abstract. XEUS, the *X-ray Evolving Universe Spectroscopy* mission is currently under study as a joint ESA-ISAS initiative in response to the ESA Horizon 2000+ recommendation to study the utilization of the International Space Station ISS for a major high-energy astrophysics mission. At an international workshop "The Next Generation of X-ray Observatories", held in July 1996 at Leicester University, science drivers and possible implementations of a major next generation X-ray mission following the current NASA Great Observatory *Chandra* and the ESA Cornerstone mission *XMM-Newton* were discussed [1].

The European and Japanese response to this challenge are cosmological studies of the early and evolving Universe and the unique role that X-ray astrophysics can play in unravelling the formation and evolution of the hot Universe, which is complementary to the major new initiatives for the cold and dusty Universe in the Infrared and Submillimeter domains. The XEUS mission science case and implementation plan have been prepared before the launch of *Chandra* and *XMM-Newton* [2, 3].

After the very successful launch and operation of both *Chandra* and *XMM-Newton* it became necessary to review and update the XEUS science case in light of the exciting and partly unexpected XMM-Newton and Chandra results as well as to inform and involve the wider astrophysical community. To this end we organised the workshop "XEUS - Studying the Evolution of the Hot Universe", held in March 11-13, 2002 at the Max-Planck-Institute for extraterrestrial Physics in Garching, Germany.

The scientific topics, among others, were: First stars and QSOs, Gamma Ray Bursts, the X-ray background, the evolution of AGN and galaxies, X-ray source populations in nearby galaxies, the formation and evolution of clusters, the warm-hot intergalactic medium and relativistic effects on matter under strong gravity. The workshop also provided an overview of the overall ESA Science and International Space Station programmes presented by the ESA Directors of Science and Manned Space Flight, as well as the instrumentation and telescope implementation planned for the XEUS baseline mission. Several new scientific proposals and their required instrumental capabilities were discussed, like a fast timing capability, a wide-field option, X-ray polarimetry and very high spectral resolution.

This workshop constituted an important step in the development of the XEUS project. On one hand it helped consolidating the science case and strengthening the community support for XEUS, on the other hand it outlined important possible additions to the XEUS capabilities, which could open completely new and interesting science areas and should be included in further studies of the XEUS system.

Acknowledgements. We thank the members of the Scientific Organising Committee: M. Arnaud, X. Barcons, R. Griffiths, G. Hasinger (Chair), H. Inoue, S. Kahn, K. Mason, M. Mendez, A. Parmar, L. Piro, L. Strder, M. Turner, and D. Willingale, and the and Local Organisation Committee: Th. Boller (Chair), B. Aschenbach, D. Grupe, R. Keil, N. Meidinger, F. Pfefferkorn. The conference photographs have been taken by D. Grupe. We thank Birgit Meyne for the professional support in organising the conference and editing these proceedings. We gratefully acknowledge the permission by the Springer Verlag to use their A&A L^AT_EX document class macro.

References

- [1] Turner M.J.L. & Watson M.G., The Next Generation of X-ray Observatories, Leicester University Report XRA 97/02, 1997
- [2] X-ray evolving-universe spectroscopy : the XEUS mission summary [Prepared by the XEUS Steering Committee]. ESA SP 1242, 2000
- [3] X-ray evolving-universe spectroscopy : the XEUS science case [Prepared by the XEUS Astrophysics Working Group]. ESA SP 1238, 2000



The First Black Holes

Tom Abel

Department of Astronomy and Astrophysics, Pennsylvania State University, University Park, 16802, PA, US

Abstract. Recently we have been able to ab initio simulate the formation of the very first stars in the universe in three dimensions using Eulerian adaptive mesh refinement. Starting from initial conditions drawn from a cosmological model for structure formation that is consistent with all observational data and a knowledge of primordial gas physics no free parameters remain in these models. Our simulations have covered 12 orders of magnitude in length and time scales and follow the formation of a protostar up to the point where it becomes optically thick to its own cooling radiation. At this time the proto star has one solar mass and accretes about 1 solar mass per century. This large accretion rate is a direct consequence of the higher gas temperature in primordial gas which are only allowed to cool down to ~ 200 K via molecular hydrogen. Fragmentation has not been found. This result has been found to be independent of numerical resolution, time step and refinement criteria or even and the hydrodynamic methods employed. Since the rapidly accreting protostar has little time to act back on the accretion flow we argue that a massive star must form. The UV output of this star destroys all molecular coolants in the host halo inhibiting the formation of any other stars in the $10^6 M_{\odot}$ dark matter halo in which it formed. The typical mass scales of the proto-stars, its accreting envelope, the "molecular cloud" within which it formed as well as the total mass of the systems can be understood analytically from chemical time scales and the properties of molecular hydrogen alone.

Interestingly our accretion profiles indicate that within the lifetime of a massive primordial star of three million years at most about 600 solar masses may be accreted onto the protostar. Also within the first 10,000 years already about 70 solar masses will be accreted. This is much faster than the Kelvin Helmholtz contraction time of the star indicating a robust lower limit to the initial mass of the first star. Within this wide range of possible initial masses the death of these star will lead very different remnants (Heger and Woosley 2001). In the case of stars with masses larger than 260 solar mass no metals may be released in black holes are the natural outcome. This may be an interesting possibility to form intermediate mass black holes which are attractive seeds to be nurtured to the super-massive black holes observed in the centers of nearby galaxies. However, no metals would be released and it would prove difficult to understand the transition to the formation of low mass metal enriched population II stars. Stars with masses below 140 solar masses¹ would enrich the intergalactic medium as well as form massive black holes. The coincidence of the Kelvin Helmholtz time with our computed accretion times at about 120 solar masses may argue in favor of such smaller masses. These first black holes may well leave the halos in which they formed for even rather modest kick velocities $\gtrsim 10$ km/s. Nevertheless, up to about one hundred thousand of these first black holes may remain in the Milky Way.

The realization that structure formation began within one hundred million years after big bang makes it difficult to study observationally these first crucial steps. Future observatories have hence to focus on larger collecting areas and wavelengths for which the universe is transparent up to redshifts of 30. XEUS offers the chance to open a new window to these so far dark ages.

Acknowledgements. I am grateful to my collaborators Greg Bryan and Mike Norman for the continuing work on this subject.

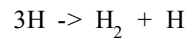
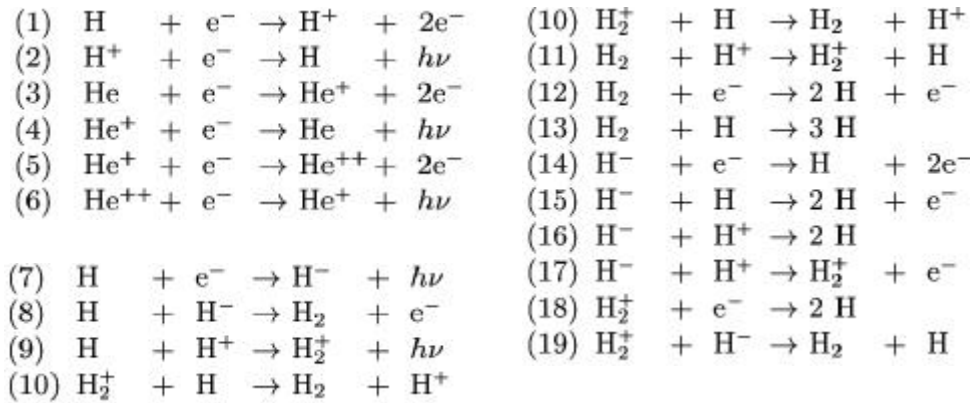
References

- Abel, T., Bryan, G.L., Norman, M.L. 2002, *Science*, 259, 93A.
Heger, A. & Woosley, S. E. 2002, *ApJ*, 567, 532

¹ The limiting masses quoted here rely on stellar models of primordial stars that do not include rotation, magnetic fields or mass loss and hence are somewhat uncertain.

Primordial Gas Chemistry

-Cold Intergalactic Gas falls into DM potential wells
 -associated adiabatic heating allows for chemistry



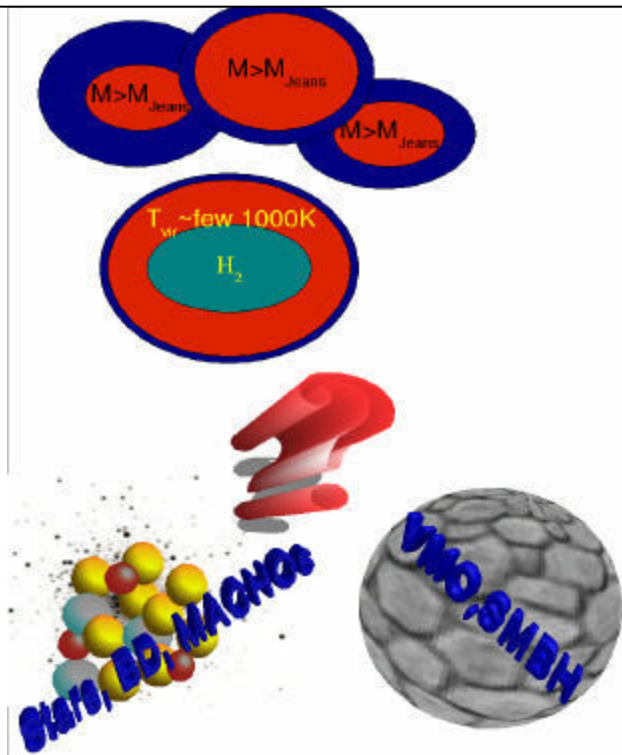
Tom Abel
 Penn State University

Abel, Anninos, Zhang, & Norman 1997, NewA

What then ?

Jeans Mass $T^{1.5}/n^{0.5}$

Thirty years of different
 "predictions" despite the same
 initial conditions.



Tom Abel
 Penn State University

Code

Adaptive Mesh Refinement code: **enzo** Bryan & Norman 1998,
Bryan, Abel & Norman 2001

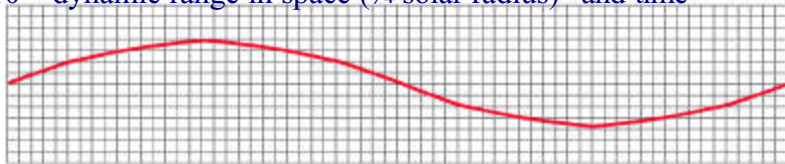
Gas dynamics (PPM), dark matter dynamics (APM), 9 species non-equilibrium chemistry and cooling (Abel et al 1997, Anninos et al 1997)

3 Conditions:

- DM (gas) mass exceeds 8 (4) times initial mass
- local Jeans length resolved at least by 64 zones !

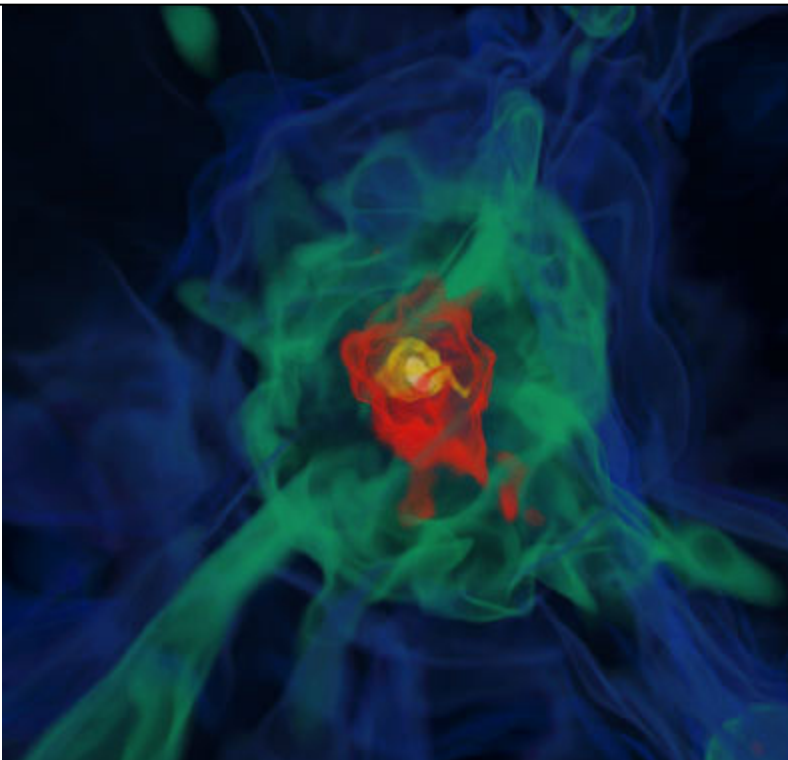
1 solar mass dark matter resolution

34 levels $\rightarrow 10^{12}$ dynamic range in space ($1/4$ solar radius) and time

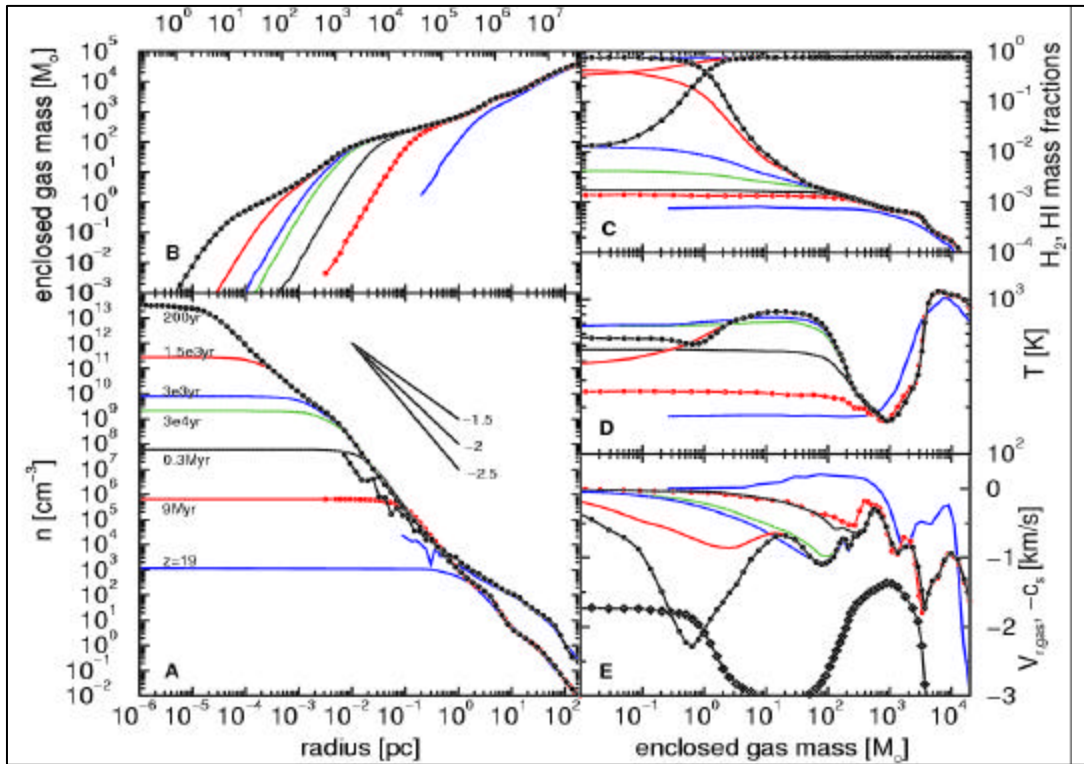


Tom Abel
Penn State University

Gas Density



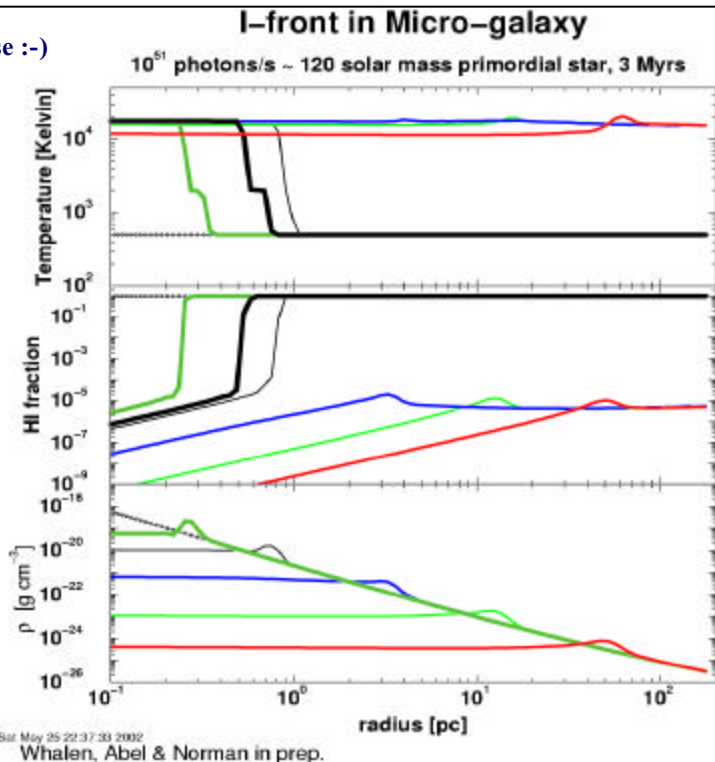
Tom Abel
Penn State University

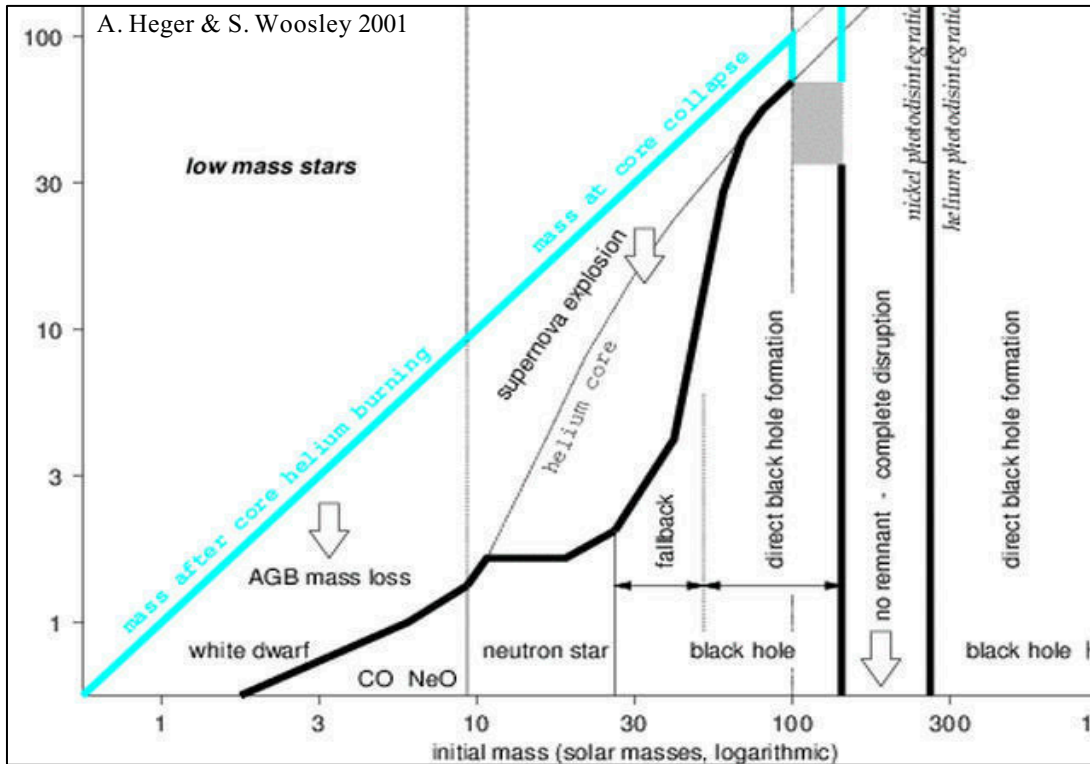


First HII region in the Universe :-)

With Dan Whalen & M. Norman
first preliminary results

ZEUS-MP:
parallel, 3D code,
can do hydro (MHD) in
3D spherical coordinates
including transfer from
point source & diffuse radiation
9 species primordial chemistry





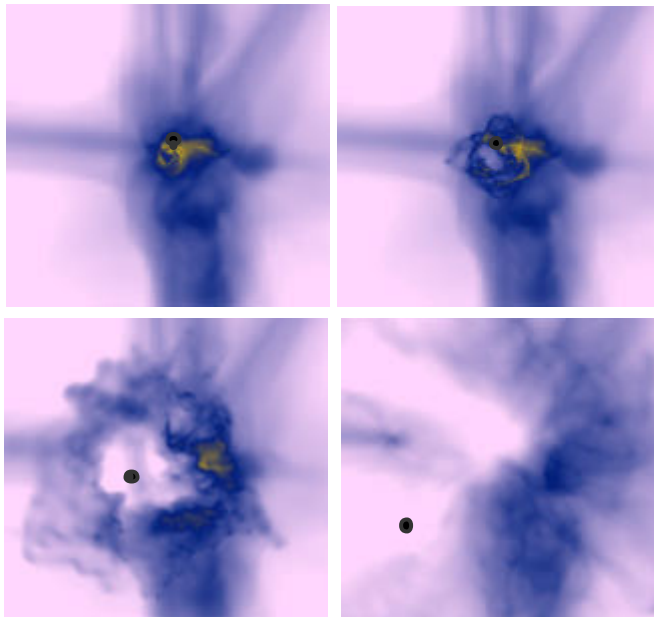
The First Black Holes?

In the preferred range of masses for the first stars the ones with $M_{\text{FS}} < 140 M_{\odot}$ and $M_{\text{FS}} > 260 M_{\odot}$ make black holes.

Even small kicks $\sim 10 \text{ km/s}$ \rightarrow leave the halo
 may be these are not the holes you want to nurture into quasars.

Perhaps there are none...

If $M_{\text{FS}} > 260 M_{\odot}$ no metals released !



First Structure Formation

Redshift 20,

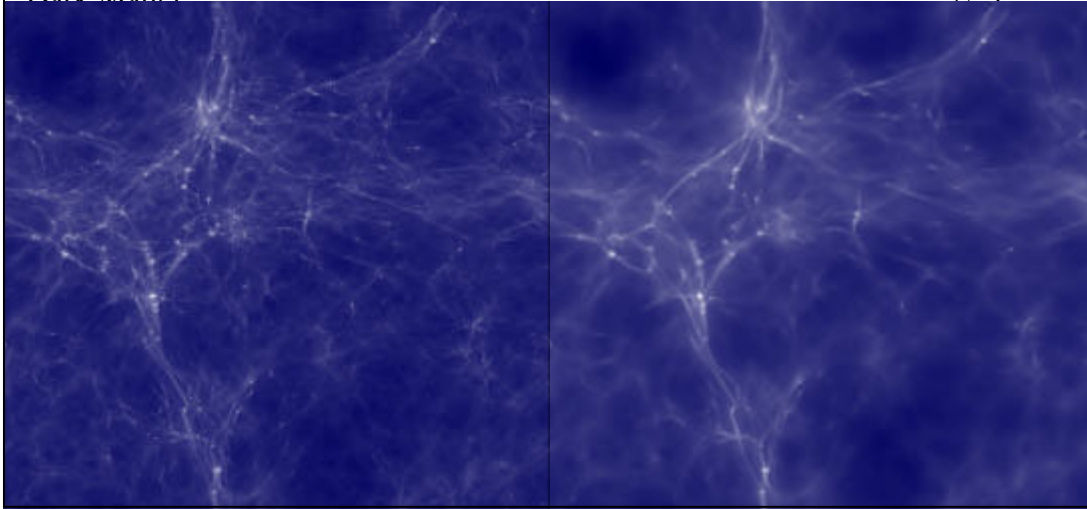
10,000 such cubes will eventually make up Milky Way -> approximately

100,000 remnants of truly primordial stars may be in the Milky Way.

Dark Matter:

Gas

128 comoving kpc



X-ray observations of the first QSOs

G. Hasinger

Max-Planck-Institut für extraterrestrische Physik, Postfach 1312, 85741 Garching

Abstract. Deep X-ray surveys have shown that the cosmic X-ray background (XRB) is largely due to accretion onto supermassive black holes, integrated over cosmic time. The characteristic hard spectrum of the XRB can be explained if about 80-90% of the light produced by accretion and black hole growth is absorbed by gas and dust. The total AGN light inferred from the XRB is consistent with the total mass in dark remnant black holes in nearby galaxies, assuming a standard accretion efficiency.

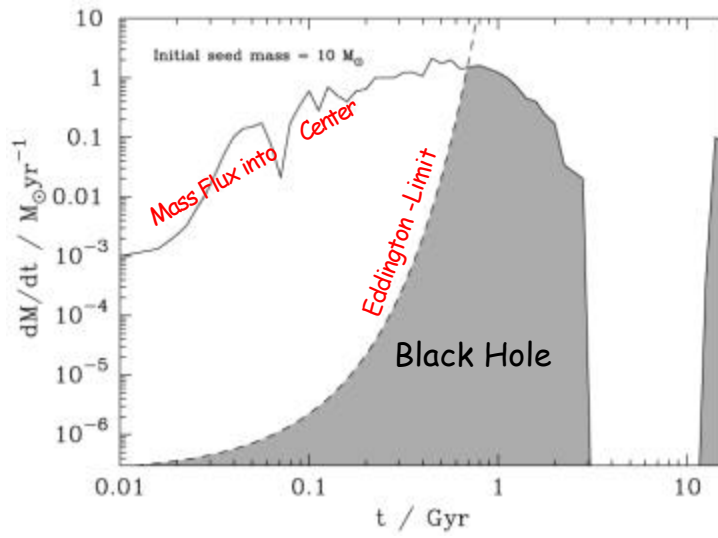
Chandra and XMM-Newton deep surveys are for the first time probing the space density and evolution of high redshift Seyfert galaxies. Spectroscopic identifications with 8-10m class telescopes leading to the conclusion that the cosmic history of Seyferts has a peak at redshifts ~ 0.7 , significantly lower than that of QSOs at $z=1.5-2$. At the faintest fluxes a population of normal galaxies at intermediate redshifts ($z < 1$) is detected.

The 1-2 Msec Chandra surveys can also be used to constrain formation of QSO at high redshifts ($z > 4$), where the space density of optically selected QSOs shows a pronounced decline, while the deepest X-ray surveys so far were still consistent with a constant space density for $z < 5$. Theoretical cosmological models predicted more than 100 $z > 5$ QSOs in any deep Chandra field, which can be definitely ruled out from the current data. The observed redshift distribution shows a weak indication of a QSO cut-off beyond a redshift of 4.

For the high priority XEUS science goal to study the first black holes at $z > 10$ this means, that the expected number of high redshift QSOs in a typical XEUS field of view is substantially smaller than for the optimistic expectations. To find the rare high luminosity, high redshift objects the XEUS field of view should be as large as possible. In addition, rare high redshift objects could be selected from sensitive wide angle surveys in several different wavebands (IR, X-ray).

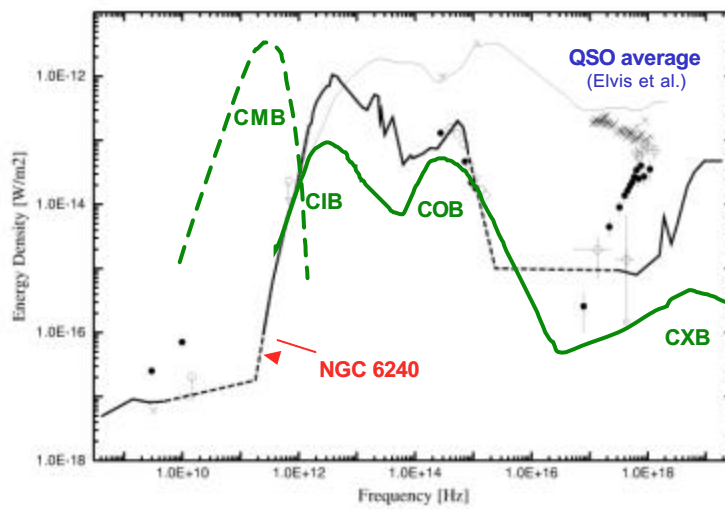
Acknowledgements. I thank my colleagues in the Chandra Deep Field South and XMM-Newton Lockman Hole teams for a very fruitful collaboration. We gratefully acknowledge the permission by the Springer Verlag to use their A&A L^AT_EX document class macro.

Formation of Quasars



Archibald et al., 2001

Absorbed AGN

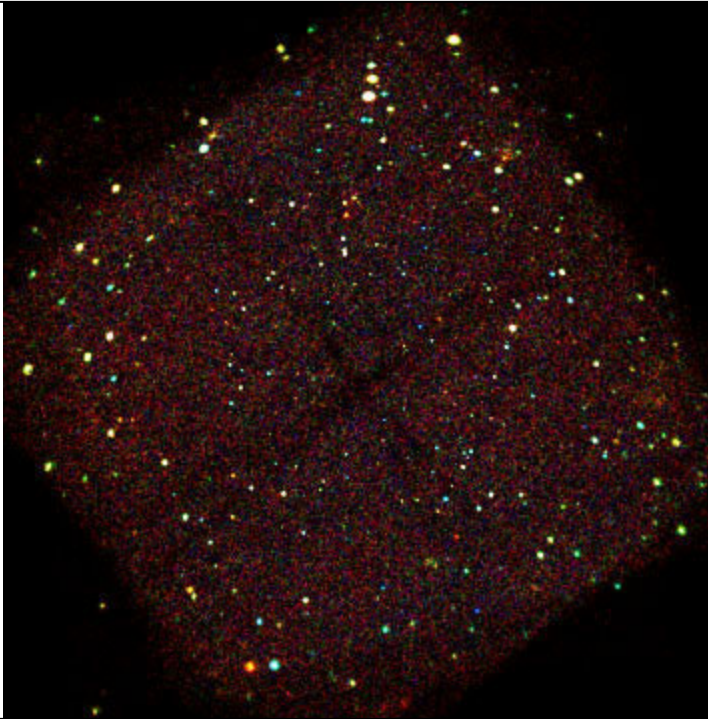


**Chandra Deep
Field South
(CDFS)**

940 ksec exposure
ACIS-I 64 arcmin²

$$S_{\min} = 6 \times 10^{-17}$$

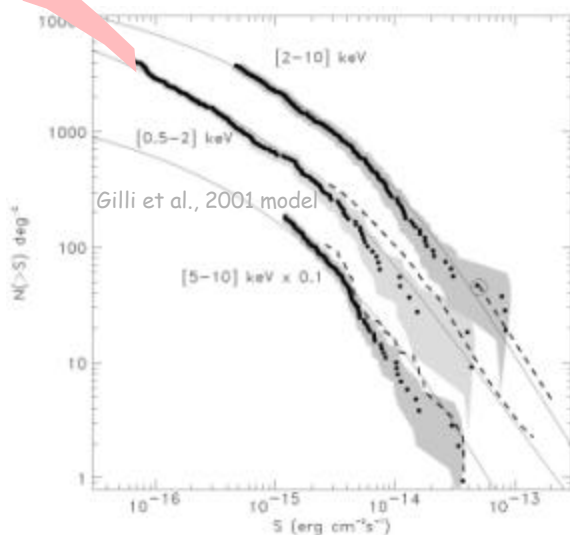
0.3-1 keV, 1-2 keV, 2-7 keV
Giacconi et al., 2001, ApJ



Brandt et al., 2002, ApJ

CDF Fluctuations
Miyaji&Griffiths 2002

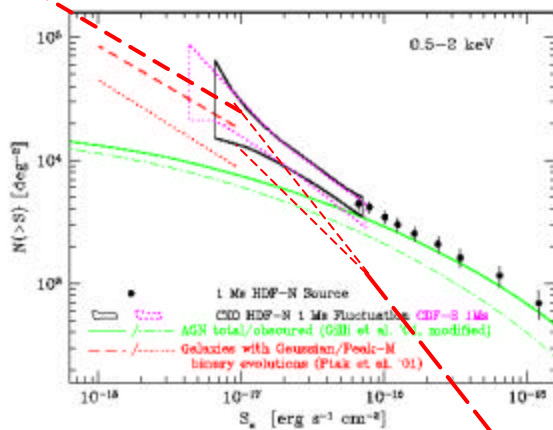
logN-logS



Chandra Deep
Field South
(940 ksec)

Rosati et al., 2001
astro-ph/0110452

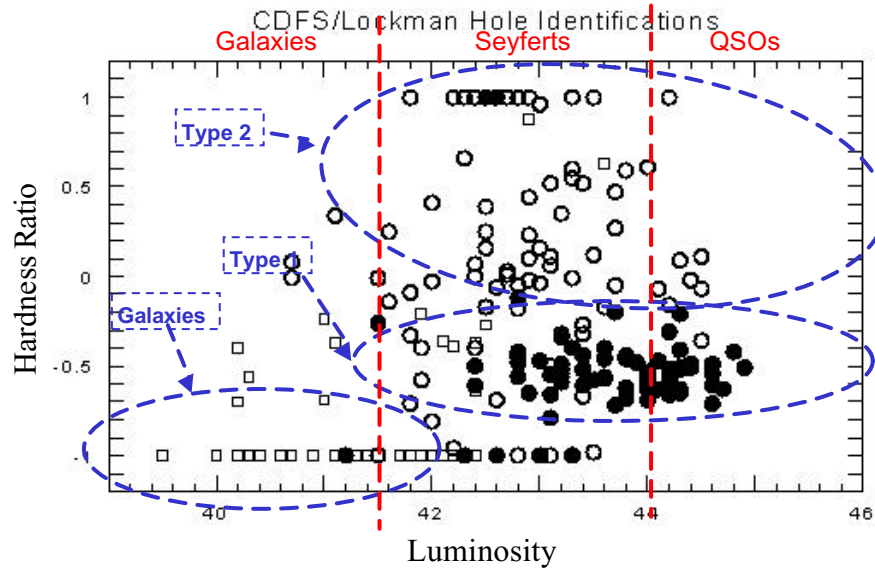
Contribution of Galaxies



Miyaji+Griffiths 2002

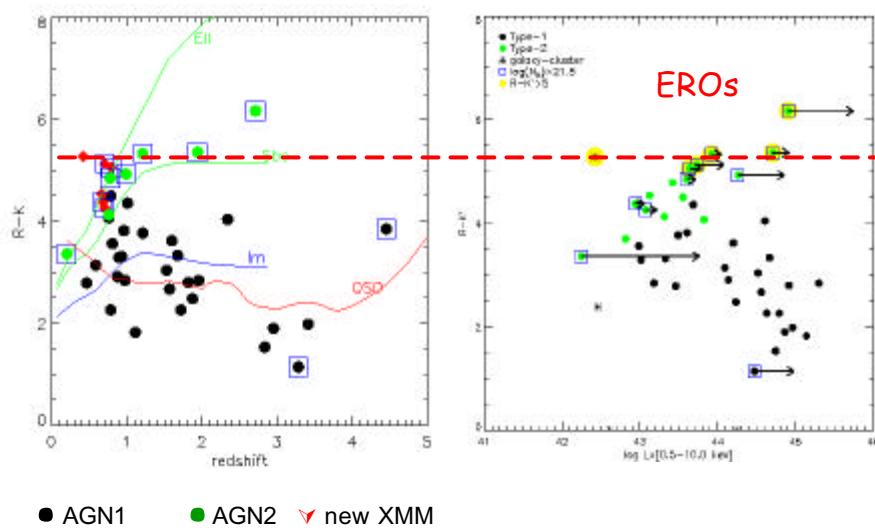
Normal Galaxies
(LH+CDFS)

X-ray Diagnostics



Chandra (CDFS) and XMM-Newton (Lockman Hole) sources, 222 Redshifts ~65% complete

Optical/NIR Colours

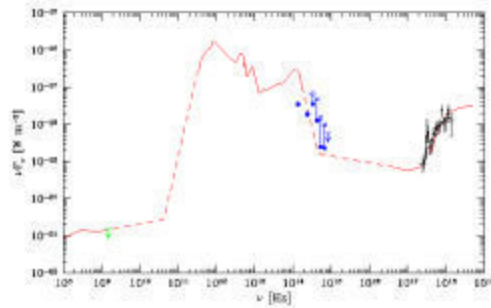
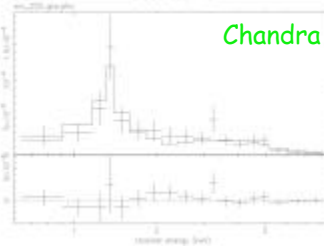
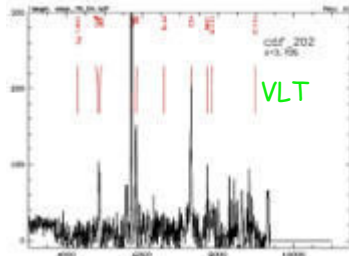


Mainieri , Bergeron et al. 2002

Highest-redshift Fe-line ?

CDFS #202: type-2 QSO, $z=3.705$
 narrow high-excitation lines

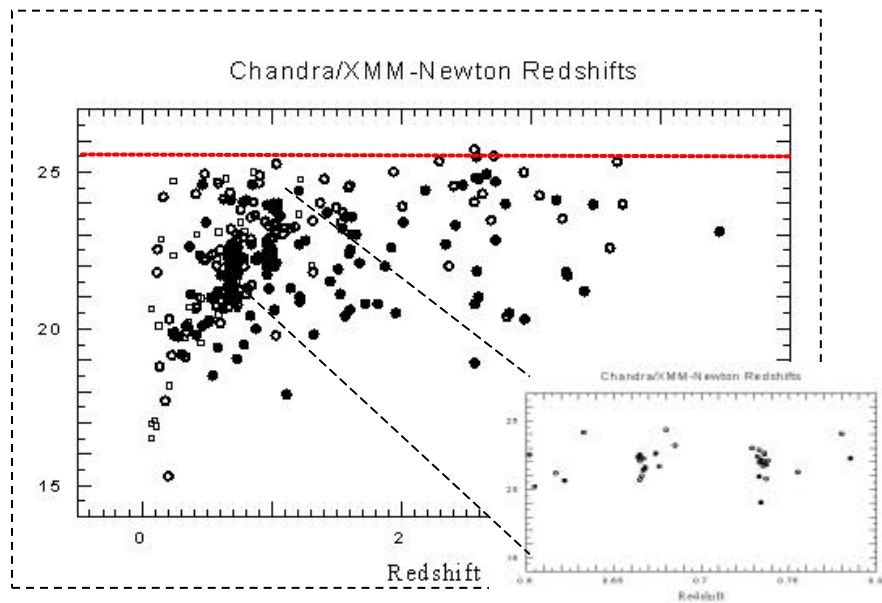
$L_x \bullet 10^{45}$ erg/s, $N_H \bullet 10^{24}$ cm $^{-2}$
 Fe-line @ 6.4 keV



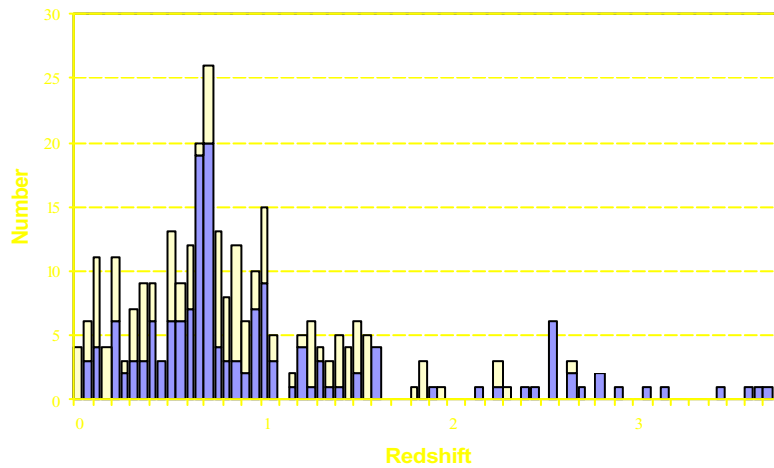
⇒ Rosetta-Stone
 for X-ray
 Background !!!

Norman et al., 2001

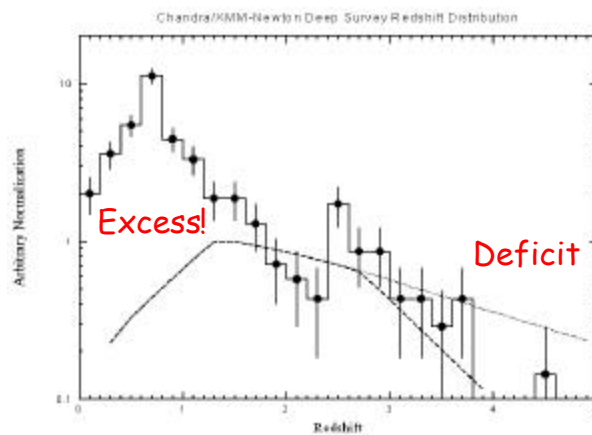
Redshift Distribution



CDFS Redshift Distribution



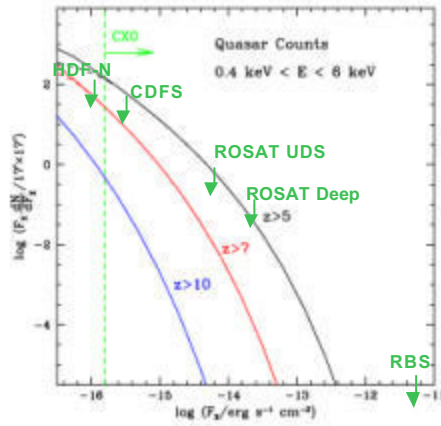
Redshift Distribution



Summing 296 spectroscopic redshifts from CDFS, Lockman Hole, HDF-N, Hawaii 12hr and A370 fields (Szokoly et al., 2002; Lehmann et al., 2002, Barger et al., 2001a+b)
Prediction by Gilli, Salvati&Hasinger, 2001

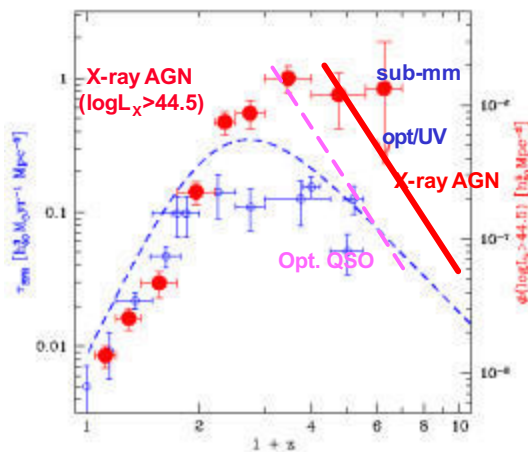
Predicted AGN Counts

Haiman & Loeb, 2000



=> few $z > 5$ QSO in every Chandra/Newton FOV ??

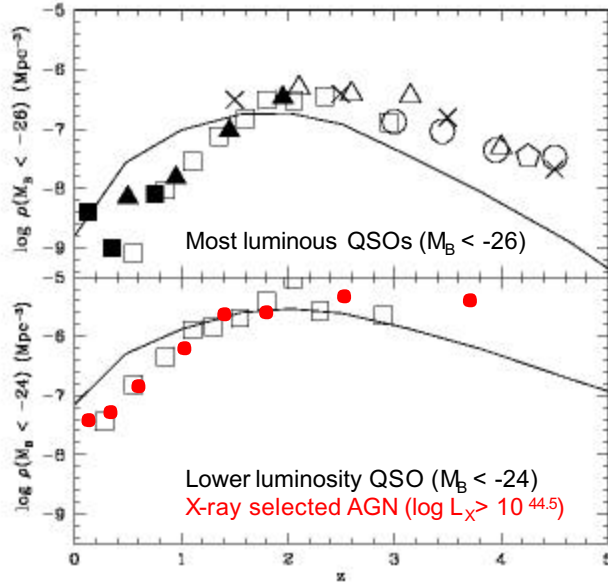
AGN activity vs. star formation rate



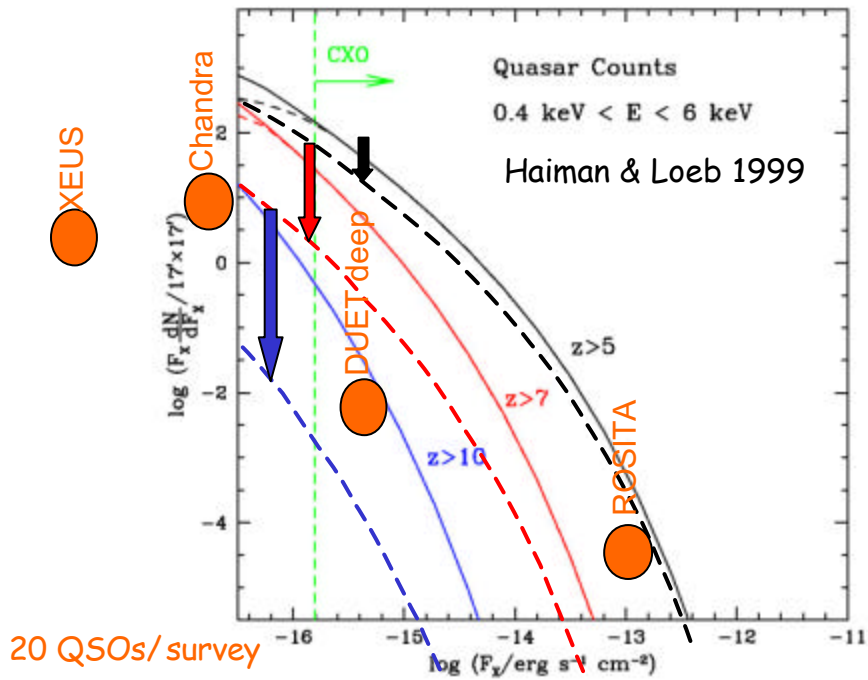
This work
 Schmidt, Schneider & Gunn 1995
 Fan et al., 2001
 Steidel et al., 1999
 Miyaji, Hasinger & Schmidt 2000

Who was there first?: **Black Holes** or **Stars** ?

CDM Models vs. Observations



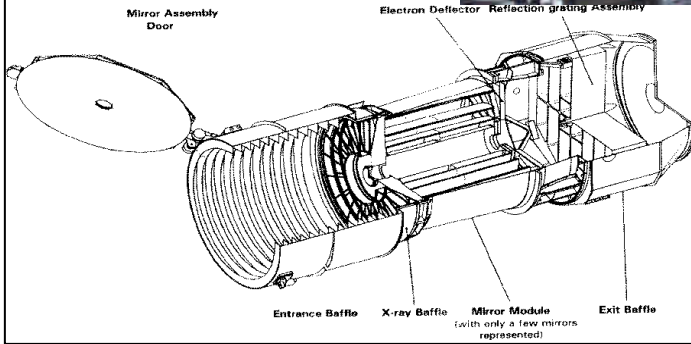
Kauffmann & Haehnelt 2000



DUET

(Dark Universe Exploration Telescope)

Utilize XMM FM5 (ESA)
Wide-Field CCD (MIT)
MIDEX Proposal
(PI R. Petre)

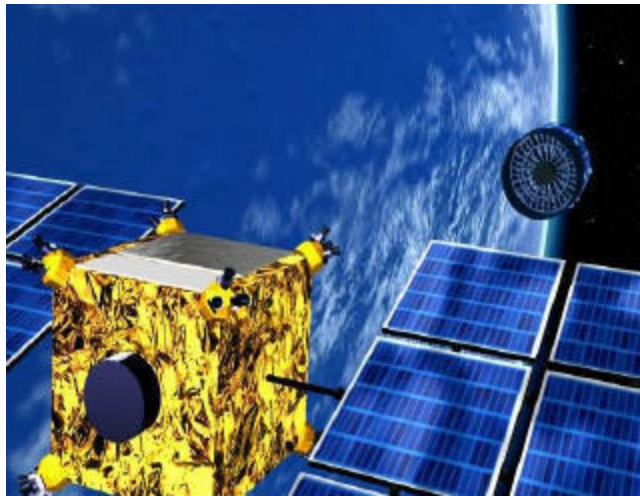


SLOAN Area
(2 yrs, 10^{-14} cgs, US lead)

150deg² Survey
(1 yr, 10^{-15} cgs, Europe lead)

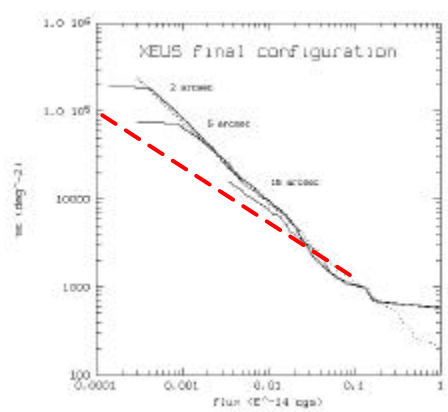
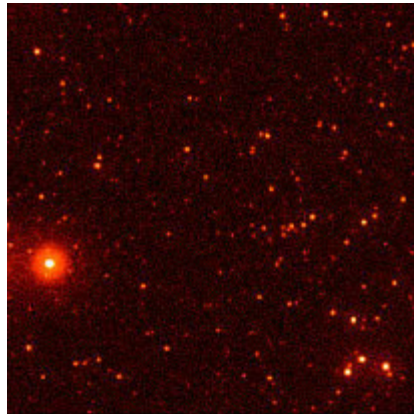
XEUS

(X-ray Evolving Universe Spectroscopy Mission)



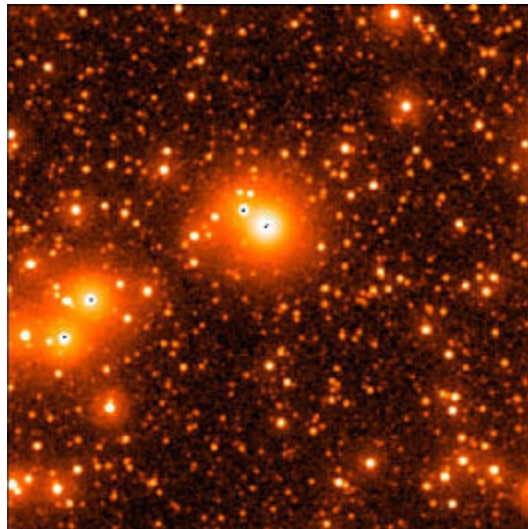
Original XEUS Simulations

XEUS 2



100 ksec, 0.5-2 keV, $S_{\min} = 3 \times 10^{-18}$ cgs

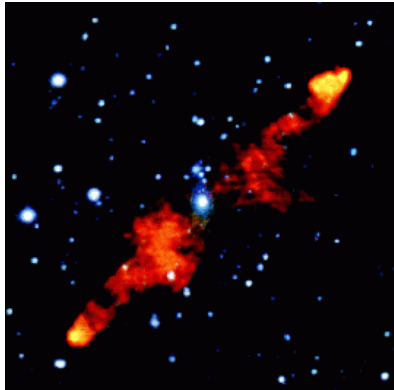
XEUS-II 1 Msec



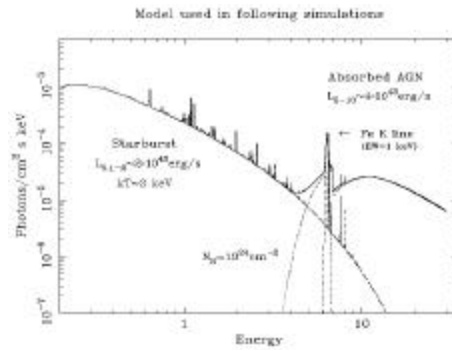
log scale

0.5-2 keV, $S_{\min} = 5 \times 10^{-19}$ cgs

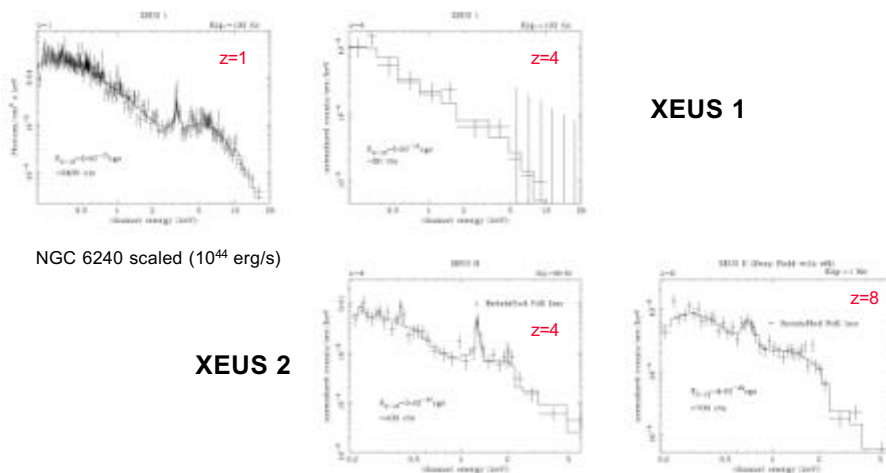
AGN and the obscured Universe



Model spectrum of NGC6240, a classical starburst/AGN hybrid, used in the following simulations.



XEUS spectra of AGN at high redshift



XEUS 1

XEUS 2

Cappi et al.

Beyond the X–ray background with XEUS

A. Comastri¹, P. Ranalli² and M. Brusa²

¹ INAF – Osservatorio Astronomico di Bologna via Ranzani 1, 40127 Bologna, Italy

² Dipartimento di Astronomia, Università di Bologna via Ranzani 1, 40127 Bologna, Italy

Abstract. We briefly discuss the perspectives of sensitive hard X–ray observations with the large collecting area X–ray telescopes of XEUS.

1. Introduction

Thanks to the excellent performances of the new generation of X–ray satellites both in terms of spatial resolution (*Chandra*) and high energy throughput (*XMM–Newton*) it has been possible to perform the deepest X–ray observations and almost completely resolve the 0.5–8 keV X–ray background (XRB) into single sources (Brandt et al. 2001; Giacconi et al. 2002). Although at the flux limits reached by deep *Chandra* surveys a large variety of sources has been detected, Active Galactic Nuclei (AGN) provide the most important contribution to the overall energy budget of the hard XRB. The increasing observational evidence of a large population of obscured sources support the prediction of AGN synthesis models for the X–ray background (Setti & Woltjer 1989; Comastri et al. 1995; Gilli et al. 2001). At this stage it seems obvious to conclude that there would be no other deep X–ray surveys if the origin of the XRB is considered a closed issue.

In the following we try to outline a few topics which would greatly benefit from further observations with a large collecting area X–ray facility such as XEUS.

2. The content of hard X–ray surveys

The overall status of optical follow–up observations of X–ray sources is usually summarized by plots of the R–band magnitude versus the 2–10 keV X–ray flux (Figure 1). The range of X–ray to optical flux ratios of spectroscopically identified AGN is marked with the shaded area within $-1 < \log(f_X/f_{opt}) < 1$ (Maccacaro et al. 1988). This trend holds for a large number of sources over a broad range of fluxes. Attention should be paid to those sources which deviate from $\log(f_X/f_{opt}) = 0 \pm 1$. The objects characterized by high values of f_X/f_{opt} are optically faint, sometimes below the limits of deep optical images. The spectroscopic identification of these objects is already challenging the capabilities of 8–10 m ground based telescopes. Although obscured accretion seems to provide the most likely explanation for their X–ray to optical flux ratios distribution (Comastri, Brusa & Mignoli 2002) the observed properties are also consistent with those expected for high redshift (possibly even $z > 6$) quasars and cluster of galaxies at $z > 1$.

A not negligible number of X–ray sources have optical counterparts which are brighter than expected for AGN and lie below $\log(f_X/f_{opt}) = -1$. The identification breakdown suggests that these objects are fairly normal galaxies and the X–ray emission is powered by processes associated with star formation, even though obscured accretion might be responsible of the peculiar broad band properties of a few of them (Comastri et al. 2002a).

3. Selected outliers in the f_X/f_{opt} plane

For the purposes of the present discussion we have selected three different classes of hard X–ray selected sources which, in our opinion, deserve further investigation and would greatly benefit from deeper X–ray observations. An expanded view of their X–ray and optical fluxes is reported in Figure 2. The red asterisks in the upper part of the diagram correspond to extremely red objects (EROs), the cyan squares around $\log f_X/f_{opt} \simeq -1$ are X–ray Bright Optically Normal Galaxies (aka XBONG; Comastri et al. 2002b), while the black circles in the lower left part are spectroscopically confirmed starburst galaxies.

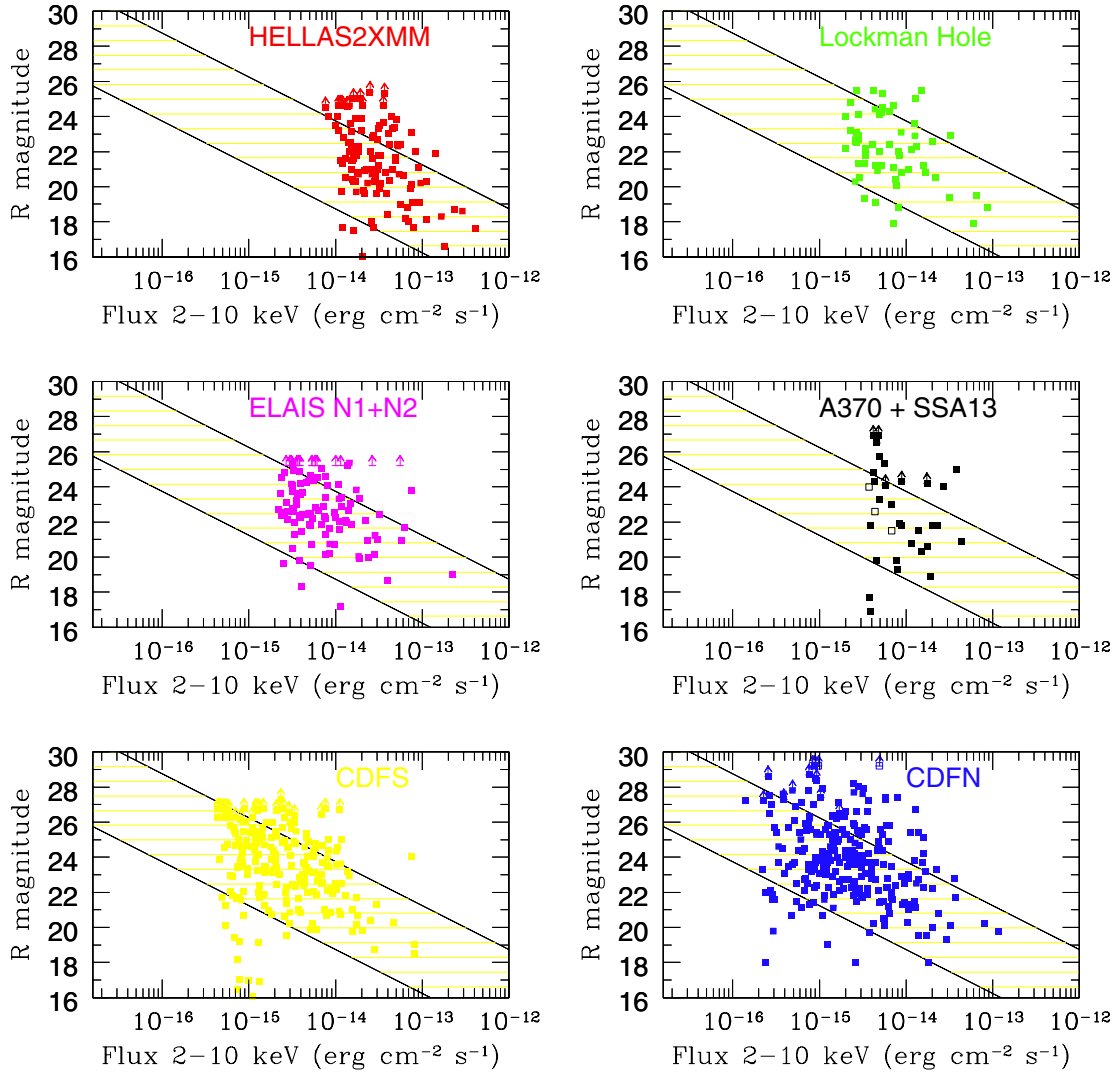


Fig. 1. The 2–10 keV flux versus the R band magnitude for six different surveys as labeled. From top left: the HELLAS2XMM survey (Baldi et al. 2002), the XMM survey in the Lockman Hole (Mainieri et al. 2002); the ELAIS deep *Chandra* survey (Manners et al. 2002), the combination of a few medium deep *Chandra* surveys (Barger et al. 2001), The *Chandra* Deep Field South (Giacconi et al. 2002) and the *Chandra* Hubble Deep Field North (Brandt et al. 2001). The upper (lower) solid line corresponds to $\log f_X/f_{opt}=1$ (-1). The shaded area represents the region occupied by conventional AGN (e.g. quasars, Seyferts, emission line galaxies).

3.1. Extremely Red Objects

The bulk of the overall energy output of Extremely Red Objects ($R-K > 5$ or $I-K > 4$) is, almost by definition, in the near-infrared band. The red colors are consistent with those expected for passively evolving galaxies, dust-enshrouded starburst galaxies or reddened AGN at $z \simeq 1$. Recent *Chandra* and XMM-*Newton* hard X-ray observations (Alexander et al. 2002a, Brusa et al. 2002a, Vignali et al. 2002) have proven to be very powerful in disentangling the various possibilities. The properties of X-ray detected EROs are consistent with those of high redshift, luminous, obscured AGN. Therefore, hard X-ray selected EROs have the properties of the so far elusive population of type 2 quasars predicted by the synthesis models and responsible for the energetically dominant component of the XRB. Stacking analysis of those objects which are not individually detected suggests that, on average, star-forming systems are more luminous X-ray sources than passively evolving galaxies (Brusa et al. 2002b).

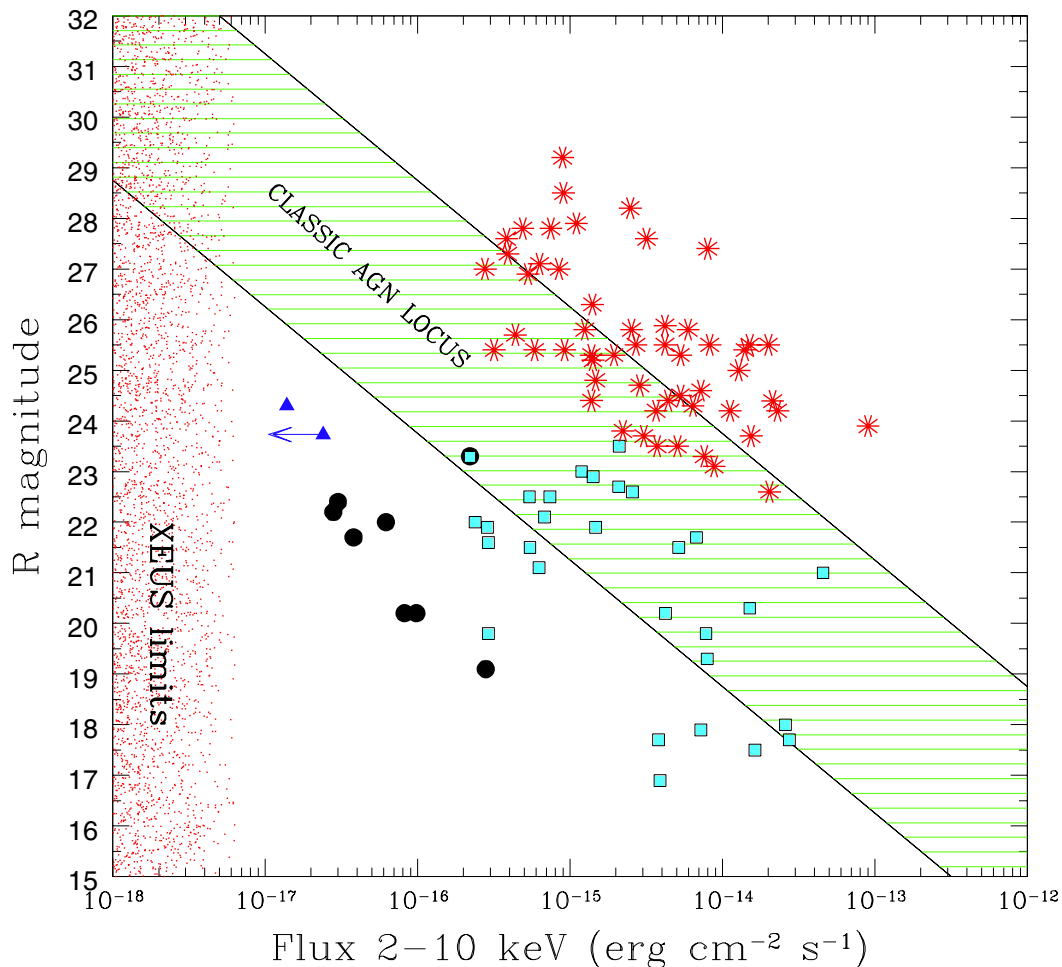


Fig. 2. The same plot of Fig. 1 for a few selected examples of recently discovered X-ray sources: EROs (red asterisks), XBONG (cyan squares), and individually detected star-forming galaxies (black circles) in the 2 Ms *Chandra* Deep Field North (Ranalli 2002). The blue triangles represent the results of stacking analysis of those EROs associated with dusty star-forming system (the detection) and passively evolving old galaxies (the upper limit).

3.2. X-ray bright optically normal galaxies

The excellent spatial resolution of the *Chandra* detectors allowed to unambiguously identify an intriguing new class of X-ray sources (Hornschemeier et al. 2001, Barger et al. 2002). They are found at moderately low redshift ($z < 1$) and are characterized by an absorption dominated optical spectrum and AGN-like hard X-ray luminosities ($L_{2-10} \simeq 10^{42-43}$ erg s $^{-1}$). The average value of their $\log(f_X/f_{opt})$ distribution is around -1 with a large dispersion (Fig. 2). An attempt to investigate their nature through a multiwavelength approach suggests that the putative AGN responsible for the hard X-ray emission is completely hidden at longer wavelengths (Comastri et al. 2002b). It has been also suggested that the observed broad band properties can be explained by the presence of an heavily obscured ($N_H > 10^{25}$ cm $^{-2}$) Compton thick AGN (Comastri, Brusa and Mignoli 2002).

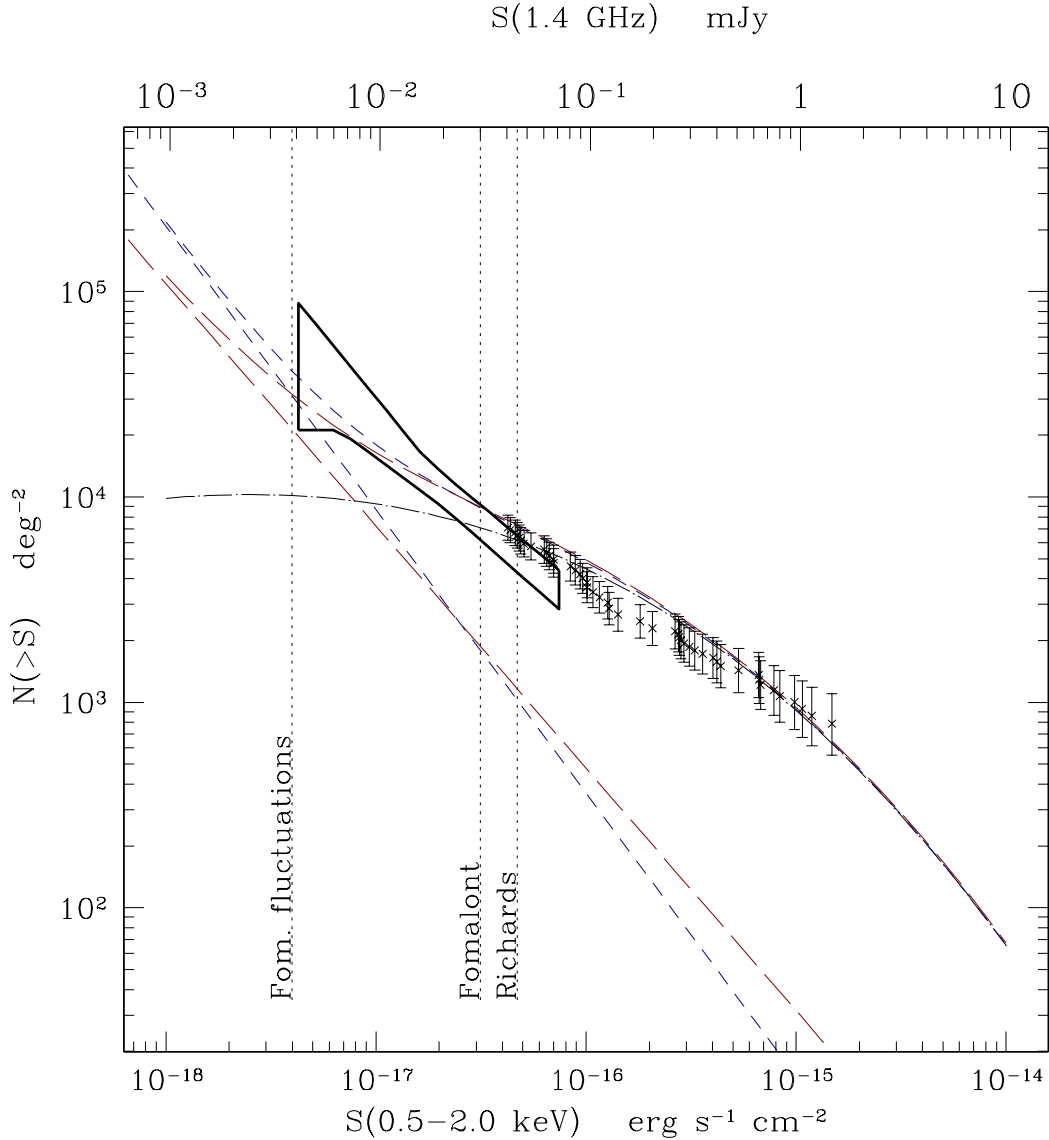


Fig. 3. X-ray counts derived from deep radio $\text{Log } N\text{-Log } S$. The blue short-dashed and red long-dashed straight lines represent X-ray counts derived from the 1.4 GHz (Richards 2000) and 5 GHz (Fomalont et al. 1991) $\text{Log } N\text{-Log } S$ respectively. Dots: observed X-ray number counts in the 1 Ms *Chandra* HDFN survey (Brandt et al. 2001) Horn-shaped symbols: results from X-ray fluctuation analysis (Miyaji & Griffiths 2002). Dot-dashed line: number counts from AGN synthesis models (Comastri et al. 1995). Vertical dotted lines: limiting sensitivities for the radio surveys. The sum of galaxies and AGN counts is also shown.

3.3. The hard X-ray luminosity and the star formation rate

It is well known that the radio and far-infrared luminosities of star-forming galaxies follow a tight linear relation. Making use of a sample of nearby star-forming galaxies observed by ASCA and BeppoSAX it has been shown that a linear relation holds also between the X-ray and both the radio and far-infrared bands (Ranalli, Comastri & Setti 2002). Such a relation has been extended to $z \simeq 1$ combining the 1 Ms *Chandra* Deep Field North exposures with deep $15\mu\text{m}$ ISOCAM (Alexander et al. 2002b) and 1.4 GHz VLA observations (Bauer et al. 2002) and up to $z \simeq 3$ via stacking analysis of Lyman break galaxies (Nandra et al. 2002). These results imply that the hard X-ray emission can be used as an absorption independent indicator of the star formation rate.

Moreover it is possible to compute the expected X-ray counts of star-forming galaxies from the $\text{Log } N\text{-Log } S$ measured in deep radio surveys (Fig. 3). The number counts of star-forming galaxies begin to overcome AGN counts at fluxes of the order of $10^{-17} \text{ erg s}^{-1} \text{ cm}^{-2}$. Interesting enough the predictions are fully consistent with the constraints from

fluctuation analysis in deep *Chandra* fields (Miyaji & Griffiths 2002) and with the number counts expected by the X-ray binaries resulting from the peak in the cosmic star formation rate at $z > 1$ (Ptak et al. 2001).

4. Perspectives for XEUS deep fields

The foreseen XEUS capabilities in terms of collecting area will allow to obtain (with exposure times ranging from 100 ks to 1 Ms) good quality X-ray spectra for almost all the X-ray sources discovered in the deepest *Chandra* and XMM-*Newton* surveys. Given that most of these sources are likely to be the obscured AGN responsible for the bulk of the hard X-ray background, it will be possible to completely characterize the cosmic history of accretion powered sources. It is also worth noticing that the detection of iron $K\alpha$ features could provide the only method (besides spectroscopy with 30–100 m optical telescopes and the photometric technique) to obtain a redshift estimate for those sources with extremely faint optical counterparts. The detection of X-ray sources will be pushed down to limiting fluxes of the order of a few 10^{-18} erg s $^{-1}$ cm $^{-2}$. At this level starburst galaxies will be detected in the X-ray band to at least $z \simeq 3$, allowing to obtain an independent constraint on the cosmic star formation history to be compared with those obtained at longer wavelengths, and to investigate the connection with the onset and fueling of massive black holes.

Acknowledgements. This research has been partially supported by ASI contracts I/R/113/01; I/R/073/01 and by the MIUR grant Cofin-00-02-36. We thank G.G.C. Palumbo for useful comments.

References

- Alexander, D.M., Vignali, C., Bauer, F.E., et al., 2002a, AJ, 123, 1149
 Alexander, D.M., Aussel, H., Bauer, F.E., et al., 2002b, ApJ, 568, L85
 Baldi, A., Molendi, S., Comastri, A., et al., 2002, ApJ 564, 190
 Barger, A.J., et al., 2001, AJ, 121, 662
 Barger, A.J., Cowie, L.L., Brandt, W.N., et al., 2002, AJ 124, 1839
 Bauer, F.E., Alexander, D.M., Hornschemeier A.E., et al. 2002, AJ in press (astro-ph/0207433)
 Brandt, W.N., et al., 2001, AJ, 122, 2810
 Brusa, M., Comastri, A., Daddi, E., Cimatti, A., & Vignali, C. 2002a, in “X-ray spectroscopy of AGN with *Chandra* and XMM-*Newton*”, eds. Boller T., Komossa S., Kahn S., Kunieda H. (astro-ph/0204251)
 Brusa, M., Comastri, A., Daddi, E., Cimatti, A., Mignoli, M., & Pozzetti, L., 2002b, submitted to ApJ
 Comastri, A., Setti, G., Zamorani, G., & Hasinger, G., 1995, A&A 296, 1
 Comastri, A., Mignoli, M., Ciliegi, P., et al., 2002a, ApJ 571, 771
 Comastri, A., Brusa, M., Ciliegi, P., et al., 2002b, in proceedings of “New Visions of the X-ray Universe in the XMM-Newton and Chandra Era”, 26-30 November 2001, ESTEC, The Netherlands (astro-ph/0203019)
 Comastri, A., Brusa, M., & Mignoli, M., 2002, proceeding of the workshop “X-ray surveys, on the light of the new observatories” Santander, September 2002, AN 324, in press
 Fomalont, E.B., et al., 1991, AJ, 102, 1258
 Giacconi, R., et al., 2002, ApJS, 139, 369
 Gilli, R., Salvati, M., & Hasinger, G., 2001, A&A, 366, 407
 Hornschemeier, A.E., Brandt, W.N., Garmire, G.P., et al., 2001, ApJ, 554, 742
 Maccacaro, T., Gioia, I.M., Wolter, A., Zamorani, G., Stocke, J.T.: 1988, ApJ 326, 680
 Mainieri, V., et al. 2002, A&A, 393, 425
 Manners, J.C., et al., 2002, MNRAS submitted (astro-ph/0207622)
 Miyaji, T., & Griffiths, R.E., 2002, ApJ, 564, L5
 Nandra, K., et al., 2002, ApJ, 576, 625
 Ptak, A., Griffiths, R., White, N., Ghosh, P., ApJ 559, L91
 Ranalli, P., Comastri, A., & Setti, G.C., 2002, A&A, in press
 Ranalli, P., 2002, proceeding of the workshop “X-ray surveys, on the light of the new observatories” Santander, September 2002, AN 324, in press
 Richards, E.A., 2000, ApJ, 533, 611
 Setti, G., & Woltjer, L., 1989, A&A, 224, L21
 Vignali, C., et al., 2002, proceedings of the 5th Italian AGN Meeting “Inflows, Outflows and Reprocessing around black holes”, astro-ph/0209415



Proceedings of the Workshop: "XEUS - studying the evolution of the hot universe"
held in Garching, March 11-13, 2002 eds. G. Hasinger, Th. Boller and A. Parmar, MPE Report 281

The X-ray Evolution of Galaxies: Implications for XEUS

N. E. White

GSFC, USA

Abstract. The X-ray evolution of the luminosity of normal galaxies is primarily driven by the evolution of their X-ray binary populations. The imprints left by a cosmological evolution of the star formation rate (SFR) will cause the average X-ray luminosity of galaxies to appear higher in the redshift range 1-3. As reported by White and Ghosh (1998) the profile of L_x with redshift can both serve as a diagnostic probe of the SFR profile and constrain evolutionary models for X-ray binaries. In order to achieve the science goal for XEUS of detecting the first black holes, it is necessary to avoid confusion from field galaxies. We report on the predictions from these models of the X-ray flux expected from galaxies and the implications for the telescope parameters of future deep universe missions such as XEUS.

Acknowledgements. We gratefully acknowledge the permission by the Springer Verlag to use their A&A L^AT_EX document class macro.

The X-ray Evolution of Galaxies: Implications for XEUS

Nicholas White
Laboratory for High Energy Astrophysics
NASA's GSFC

With contributions from
Pranab Ghosh, Andy Ptak, Richard Griffiths,
Paul Nandra, Steve Snowden, Will Zhang, Richard Mushotzky

X-ray Observations of Galaxies

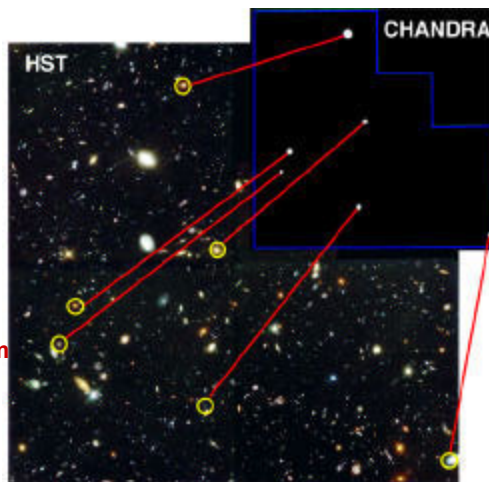
The Chandra deep fields show that the X-ray sky is dark and dominated by accreting supermassive black holes in the nucleus of a few percent of galaxies

Chandra is not yet detecting the X-ray counterparts to the majority of galaxies seen in the Hubble Deep Fields

Questions to be addressed:

**What is the expected X-ray emission from
? normal? galaxies at high redshift?**

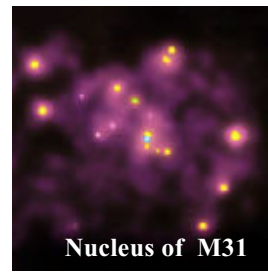
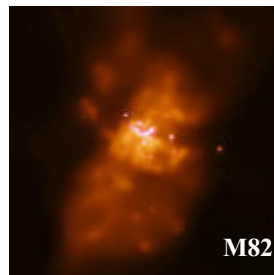
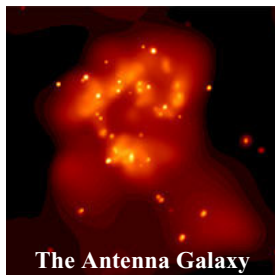
**How does this impact the XEUS science
requirements and mission design?**



Chandra Observations of Nearby Galaxies

The non-nuclear galaxy X-ray emission is dominated by X-ray binaries, with additional contributions from hot gas and supernova remnants

Integrated X-ray Luminosity of 10^{39} to 10^{41} erg/s



At redshift 1 the X-ray flux of these galaxies would be 10^{-17} to 10^{-19} erg $\text{cm}^{-2}\text{s}^{-1}$

- ? 5-500 times below the Chandra 1 Ms deep survey detection threshold
- ? Chandra can ultimately reach 3×10^{-18} erg $\text{cm}^{-2}\text{s}^{-1}$ in 10 Ms and so the higher luminosity high redshift galaxies should be directly detected
- ? Evolution of underlying source populations is an important factor

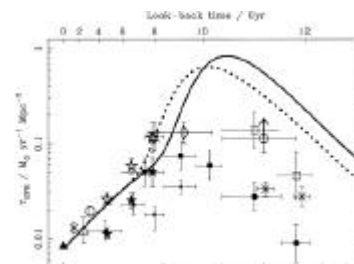
X-ray Evolution of Galaxies

X-ray luminosity of *normal* galaxies is dominated by their X-ray binary populations

- ? Typical luminosity of 10^{39} - 10^{41} erg/s that is proportional to galaxy L_B and L_{IR}

The star formation rate (SFR) has undergone a strong cosmological evolution

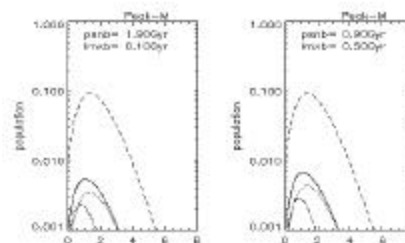
- ? 10-100 times higher at $z \sim 1$ to 3.5
- ? Details uncertain because of dust obscuration



Blain et al (1999)

An evolving SFR will increase the X-ray binary populations of galaxies and their overall X-ray luminosity (White & Ghosh 1998)

- ? HMXB have short lifetimes and track the instantaneous SFR
- ? LMXB will turn on when normal star comes into contact with Roche Lobe, 0.5 to 1 billion years after star formation burst
- ? LMXB are very long lived and are a fossil record of past star formation
- ? Prediction depends on models of LMXB evolution



Ghosh & White (2001)

Predicting the X-ray Evolution of Galaxies

X-ray luminosity evolution of galaxies predicted by Ghosh & White (2001)

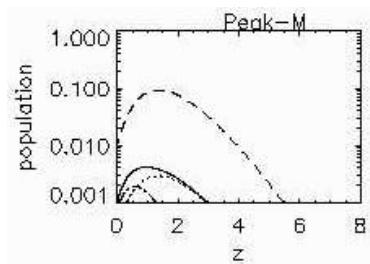
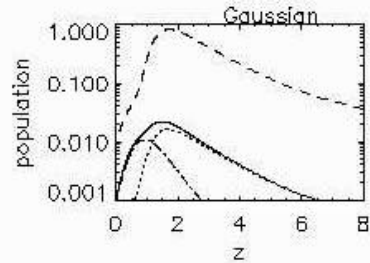
- ? Latest Star Formation Rate vs. redshift models
- ? Show here *peak-M* (Madau) and *Gaussian* (Blain et al) models represent two extremes

Predicts for typical spiral galaxy an increased X-ray luminosity with redshift

- ? 3 to 8 times at $z \sim 0.5$
- ? 4 to 16 times at $z \sim 1.0$
- ? Lag in LMXB turn on translates to an increase in L_x/L_B in redshift range 0.5 to 1.5

Seems consistent with X-ray flux of spiral galaxies in HDF-N Chandra observation:

- ? Brandt et al (2001) find no more than a factor of 2 increase in L_x/L_B at $z \sim 0.5$
- ? Hornschemeier et al (2002) find for a larger sample between $z \sim 0.4$ and 1.5 evidence for increase in L_x/L_B by factor of 2-3



Predicting the X-ray Evolution of Galaxies

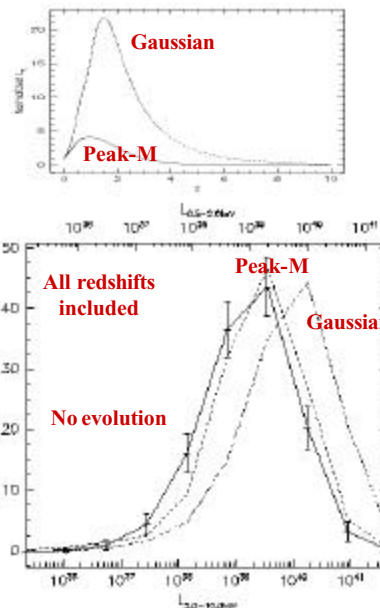
Ptak et al (2001) calculated the observable consequences for HDF-N X-ray observations using the Ghosh & White (2001) models:

- ? 125 galaxies in Cohen et al (2000) with measured redshifts
- ? Use L_x proportionality to L_B
- ? Evolve L_x to L_B ratio based on GW01 models
- ? Predict X-ray flux using redshift information
- ? Concentrate on *peak-M* (Madau) and *Gaussian* (Blain et al) which represents two extremes

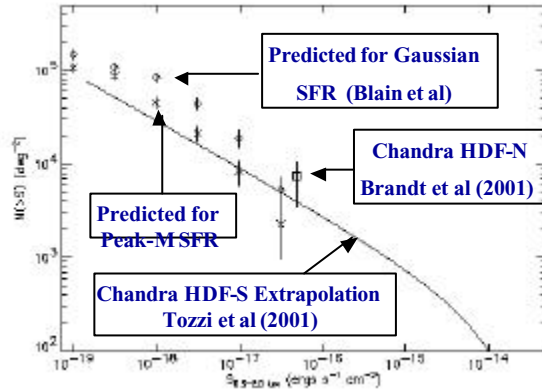
Between redshift 0.5 and 1.0 the average X-ray luminosity of galaxies increases

- ? *Peak-M*: 2×10^{39} erg/s to 6×10^{39} erg/s
- ? *Gaussian*: 2×10^{39} erg/s to 2×10^{40} erg/s

In the Gaussian model in particular there is a strong increase in L_x/L_B between 0.5 and 2.0



Predicted Galaxy X-ray Source Counts

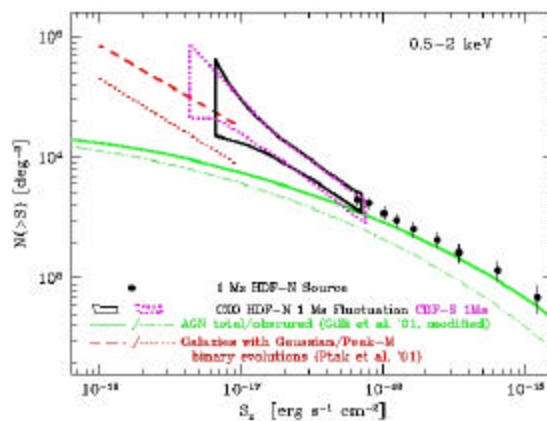


The predicted Log N - Log S distribution from Ptak et al (2001) using the predicted galaxy X-ray luminosity evolution from Ghosh and White (2001)

Predicts a population of star forming galaxies emerges at $F_X < 10^{-17}$ erg $\text{cm}^{-2} \text{s}^{-1}$

Chandra HDF Fluctuation Analysis

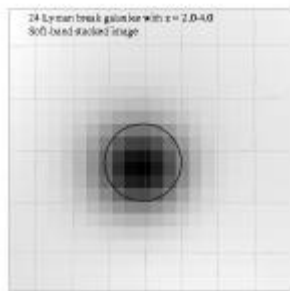
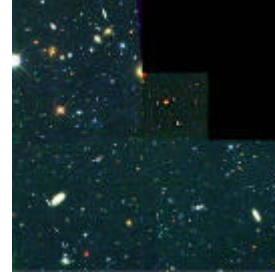
Miyaji & Griffiths (2002) have used a fluctuation analysis of the Chandra HDF fields to probe the source counts below the current deep survey limit



Consistent with the Ptak et al (2001), Ghosh & White (2001) predictions
Suggests that star forming galaxies dominate the X-ray sky at $F_X < 10^{-17}$ erg $\text{cm}^{-2} \text{s}^{-1}$

Chandra Observations of High Redshift Galaxies

- o Individual high redshift ($z \sim 2-4$) starburst galaxies in the Hubble deep field are too faint to be detected by Chandra - even in an 11 day (1 Ms) deep exposure
- o Brandt et al (2001) overlaid the Chandra images of 24 Lyman break galaxies in the HDF at $z \sim 3$
- o **This ? stacking analysis ? creates the equivalent of a 260 day (22 Ms) super deep Chandra exposure**



- o **This results in the detection of non-AGN X-ray emission from high redshift galaxies**
- o **The flux level is 3.10^{-18} erg/s/cm² giving a luminosity of 3.10^{41} erg/s, about the same as that of nearby starburst galaxies**
- o **To obtain a 1000 count spectrum of one of these galaxies with the final XEUS configuration will require a 1 million second exposure!**

Stacking Lyman/Balmer Break Galaxies

Nandra et al (2002) used galaxy stacking to probe galaxy emission at redshift 1 & 3

- ? **144 Lyman break galaxies (LBGs) at $z \sim 3$**
- ? **6 sigma detection at 3.3×10^{-18} erg cm⁻² s⁻¹**
- ? **3.5×10^{41} erg s⁻¹**

- ? **95 Balmer break galaxies (BBG) at $z \sim 1$**
- ? **9 sigma detection at 6.4×10^{-18} erg cm⁻² s⁻¹**
- ? **3.3×10^{40} erg s⁻¹ (or 6.6×10^{40} erg s⁻¹ using same L_x threshold for both BBG & LBG)**

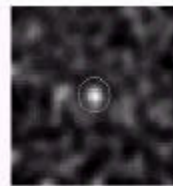
Indicates strong evolution of galaxy L_x with z

- ? **Scales with UV luminosity**
- ? **Probably not due to AGN activity**

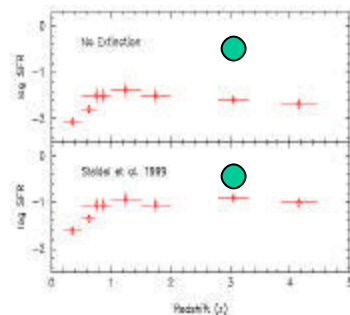
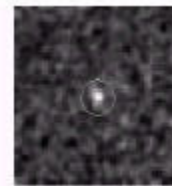
X-ray luminosity to IR scaling gives a star formation rate estimate consistent with extinction corrected uv estimates

- ? **a new important probe of star formation**
- ? **See poster by Paul Nandra**

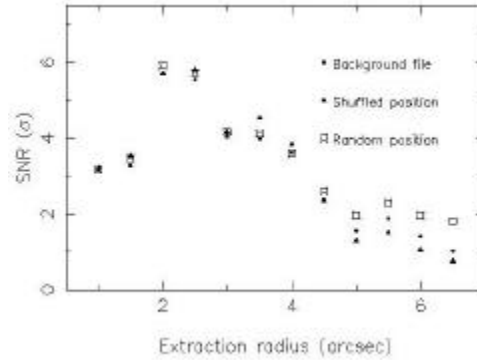
z=3



z=1



Angular Resolution Considerations from Stacking Analysis

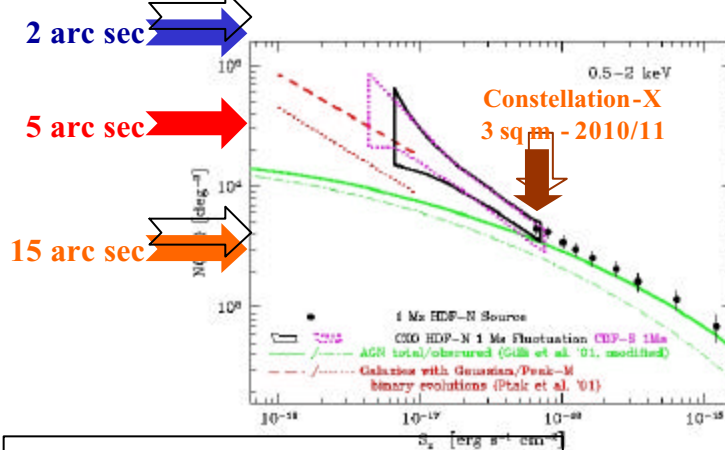


Nandra et al (2002) stacking analysis of Lyman and Balmer break galaxies demonstrates that peak signal to noise is at 2 arc sec extraction radius

- ? Avoid confusion from overlapping galaxies and optimal background
- ? Important that point spread function includes large fraction of power within 2 arc sec radius (equivalent to ~ 2 arc sec HPD)

Source Confusion Limits

Miyaji & Griffiths (2002) fluctuation analysis and Ptak et al (2002), Ghosh & White (2002) Galaxy X-ray evolution models can be used to estimate confusion limits



There are two confusion limits in X-ray astronomy
 AGN limit of $\sim 4,000 \text{ deg}^2$ at $10^{-16} \text{ erg cm}^{-2} \text{ s}^{-1}$
 Galaxies with $\sim 100,000 \text{ deg}^2$ at $10^{-18} \text{ erg cm}^{-2} \text{ s}^{-1}$

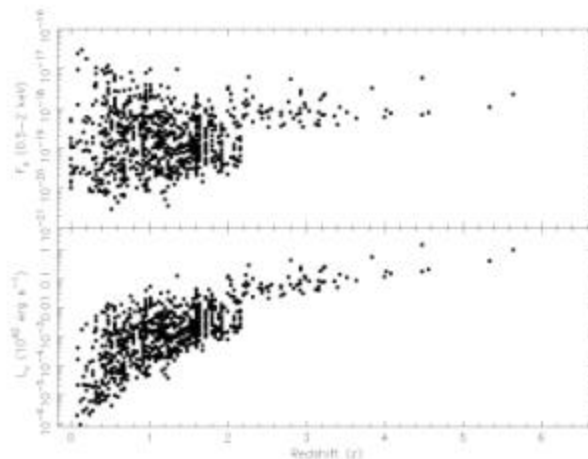
Simulating a XEUS Observation of HDF-N

Simulations of a 1 million second XEUS HDF observation with different angular resolution: 5 (XEUS requirement), 2 (XEUS goal) & 1 arc sec

- o 1067 Photometric redshifts and multi-band fluxes (U,B,V,I,J,H,K) taken from Fernandez-Soto *et al.* (1999)
- o Assume the rest-frame U-band (3000Å) flux traces star formation
- o Estimate in each case which observed band is closest to rest frame U
- o Calibrate rest-frame U versus F_x (0.5-2 keV) using known Lyman break and Balmer break galaxies in HDF-N (~10 of each in the field)
 - ? The mean F_x of the BBGs is about twice the LBGs
 - ? Use this ratio to predict 0.5-2 keV F_x from rest frame U for other galaxies.
 - ? Predicted flux ranges from 10^{-20} to 10^{-17} erg cm⁻² s⁻¹
 - ? Simulate image using XMM-Newton QuickSIM for pn CCD
 - ? 250 times area
 - ? 10 times background to account for longer focal length & open optical bench
 - ? Divided XMM-Newton PSF by factor of 3, 7.5 and 15

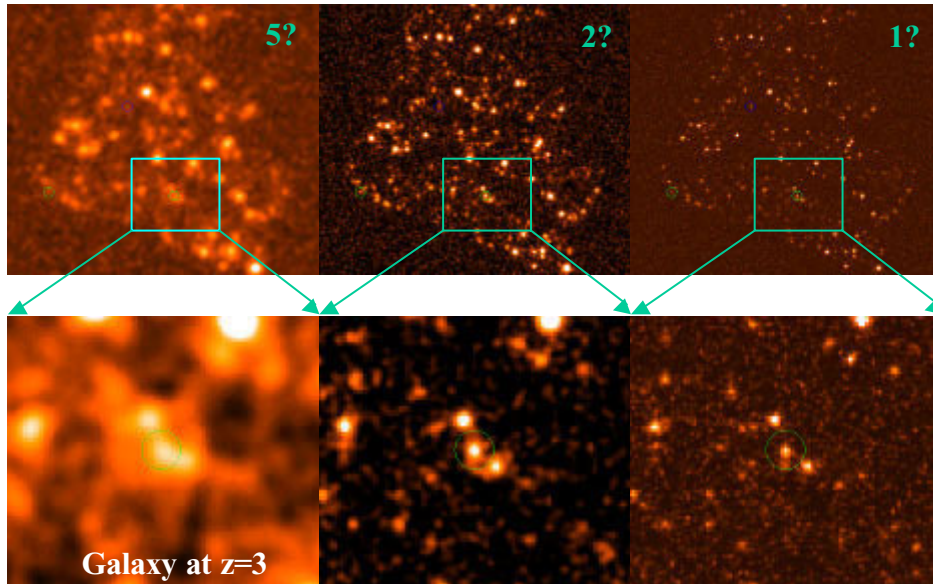
Thanks to Paul Nandra, Steve Snowden, et al

Predicted Galaxy Flux & L_x vs. Redshift

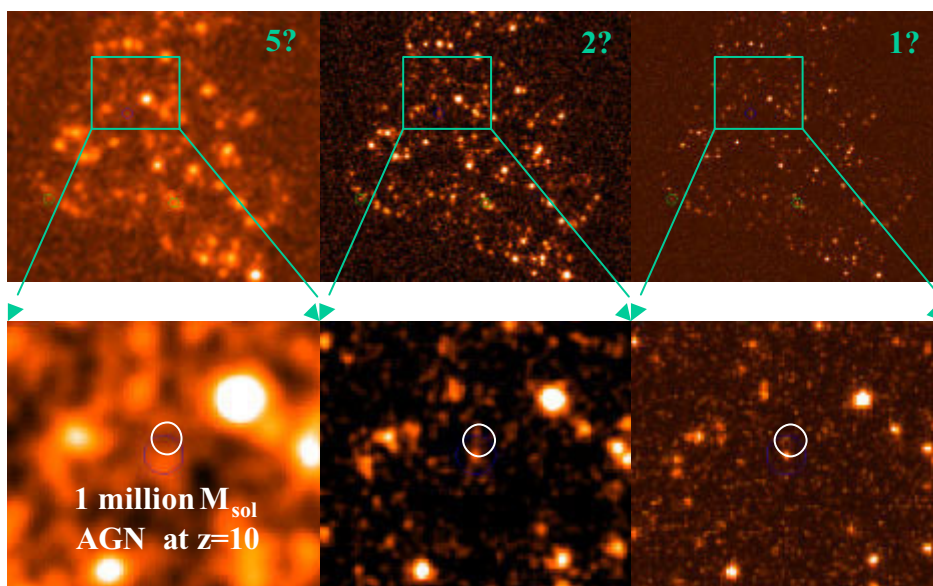


Many of the galaxies at $z < 2$ have fluxes of 10^{-20} to 10^{-17} erg cm⁻² s⁻¹

Simulations of XEUS HDF 1 million sec observation at different angular resolutions



Simulations of XEUS HDF 1 million sec observation at different angular resolutions (5, 2 and 1 arc sec)



The High-z Universe of Galaxies & Black

Holes

Useful things to keep in mind? .

At $z \sim 10$ a 1 million M_{sol} micro-AGN accreting at 10% of Eddington limit has a 0.5-2 keV flux of $\sim 2 \times 10^{-18} \text{ erg cm}^{-2} \text{ s}^{-1}$

? Same as Lyman Break Galaxies at $z \sim 3$ detected by Chandra

At $z \sim 10$ a 10^{41} erg/s galaxy or an accreting (10% Eddington) $\sim 10,000$

M_{sol} black hole have a flux of $\sim 5 \times 10^{-20} \text{ erg cm}^{-2} \text{ s}^{-1}$

? 100 times deeper than Chandra ultimate deep survey and the advertised XEUS deep survey limit

For a luminosity $< 10^{42} \text{ erg/s}$ the challenge will be to distinguish low luminosity AGN, from galaxy emission of many X-ray binaries

- O Spectra of Galaxies (sum of LMXB) and AGN are very similar
 - O Galaxy size of 0.5-1 arc sec requires 0.1 arc sec to resolve AGN
 - : Utilize other wavebands e.g. radio emission to differentiate, which requires arc sec or better positional accuracy
-

Summary - Implications for XEUS

Galaxies emerge as the dominant X-ray population at a 0.5-2.0 keV flux of $< 10^{-17} \text{ erg cm}^{-2} \text{ s}^{-1}$

With 30 m^2 collecting area it is inevitable that XEUS will study the X-ray properties of both galaxies and black holes at $z > 1$

The X-ray galaxy density is $> 50,000 \text{ deg}^2$ at $10^{-18} \text{ erg cm}^{-2} \text{ s}^{-1}$ and to avoid galaxy confusion requires 2 arc sec half power diameter

Consider optimizing the focal length, angular resolution and background to achieve a limiting sensitivity 100 times better than Chandra ($\sim 5 \times 10^{-20} \text{ erg cm}^{-2} \text{ s}^{-1}$) to reach $\sim 10^4 M_{\text{sol}}$ black holes and $\sim 10^{41} \text{ erg/s}$ starburst galaxies at $z \sim 10$ (see Will Zhang's poster)

With these parameters XEUS will light up the HDF in X-rays & be well matched to study the first black holes and galaxies to $z \sim 10$

Chandra Observations of Narrow Line Galaxies

I. Georgantopoulos¹, T. Shanks², M. Vallbe², A. Zezas³, M.J. Ward⁴, G.C. Stewart⁴, B.J. Boyle⁶, and R.E. Griffiths⁷

¹ Institute of Astronomy & Astrophysics, National Observatory of Athens, Greece

² Physics Department, University of Durham, UK

³ Harvard-Smithsonian Center for Astrophysics, Boston, MA, USA

⁴ University of Leicester, Leicester, UK

⁵ Anglo-Australian Observatory, Epping, Australia

⁶ Carnegie Mellon University, Pittsburgh, USA

Abstract. We present Chandra observations of 10 ROSAT sources which are associated with Narrow Line Galaxies (NLXGs). The goal is to accurately locate the position of the optical counterpart using Chandra's superb spatial resolution. In 3 out of 10 sources, the optical counterpart is confirmed to be the NLXG. This rate (3/10) is consistent with the cross-correlation analysis of Roche et al. (1995). These 3 sources represent a mixed bag of objects. One is a highly obscured (type-1.9) QSO at a redshift of $z=2.35$. The other two objects have 'normal' galaxy spectra. However, from their X-ray luminosity and hardness ratio we can infer that one is probably an obscured AGN while the other one may be a normal galaxy. Our work confirms that a small fraction of sources in deep ROSAT surveys is indeed associated with objects which have 'normal' galaxy optical spectra. However, a large fraction of these must be associated with Low Luminosity AGN. The implications for exploring the astrophysics of luminous galaxies and low luminosity AGN with X_{EU}S are discussed.

1. Introduction

The bulk of the sources detected in deep ROSAT surveys are associated with QSOs (Shanks et al. 1991, Hasinger et al. 1998). A small fraction of sources is associated with galaxies on optical CCDs (Boyle et al. 1995, Griffiths et al. 1995, McHardy et al. 1998). However, it has often been argued (eg Hasinger et al. 1998) that these galaxies may be just spurious identifications due to the high sky density of optical galaxies combined with the large positional error box of PSPC. Roche et al. (1995) and Almaini et al. (1997) performed cross-correlation studies of ROSAT sources and fluctuations with galaxies on Anglo-Australian telescope deep photographic plates. They detected a strong signal suggesting that a number of X-ray sources is indeed associated with optical galaxies. Of course it is unclear whether some of these optical 'galaxies' contain an active nucleus. Furthermore, this cross-correlation shows that these galaxies are real only on a statistical basis. That is we do not know which of the galaxies are the true counterparts and which are the chance coincidences, hampering us from examining their properties.

The deep Chandra surveys again find a large number of X-ray sources which are associated with galaxies (eg Mushotzky et al. 2000). Some sources at very faint fluxes (10^{-17} cgs) and relatively low luminosities ($L_x \sim 10^{41}$ cgs) are unambiguously star-forming galaxies. However, a large fraction of hard sources with high X-ray luminosities 10^{41-43} cgs are associated with galaxies with early-type spectra (ie absent or weak emission lines). It is often postulated that these objects are highly obscured AGN (eg Comastri et al. 2002) similar to NGC6240 (Vignati et al. 1999).

Here, we present snapshot (10 ksec) Chandra observations of 10 NLXGs detected in our deep ROSAT survey (Griffiths et al. 1995). The superb spatial resolution of Chandra and thus its very small positional error box (< 1 arcsec) allows us to check how many sources are indeed associated with NLXGs.

2. The Chandra Data

We have obtained snapshot exposures (10 ksec) of 10 ROSAT NLXGs with ACIS-S onboard Chandra. Chandra confirms the positions of the optical counterparts for 3 out of the 10 sources. These sources are listed in table 1.

RXJ13434+0001 is an obscured (type-1.9) QSO at a redshift of $z=2.35$ (Georgantopoulos et al. 1999). This Ultra-violet excess source presents only narrow lines in its optical spectrum. However, UKIRT observations reveal a broad

Name	Redshift	L_x (0.3-8 keV)
RXJ13434+0001	2.35	10^{45}
gsgp4x:69	0.2	10^{43}
gsp4x:109	0.1	5×10^{41}

H_α line suggesting that this object is an obscured AGN, similar to Seyfert-1.9 in the local Universe. Again, the ASCA X-ray spectrum reveals large amounts of obscuration ($N_H \sim 10^{23} \text{cm}^{-2}$).

GSGP4X:69 at a redshift of $z=0.2$ presents no broad emission lines in its spectrum obtained from the AAT 3.9-m telescope (see Griffiths et al. 1995 for details on the optical spectrum). Its 0.5-2 keV X-ray luminosity derived from the ROSAT observation is $\sim 10^{42}$ cgs, consistent with the luminosity of the most luminous star-forming galaxies (eg Zezas, Georgantopoulos & Ward 1998). However, the Chandra observations clearly demonstrate that we are dealing with an obscured AGN. The 0.3-2/2-8 keV hardness ratio translates to an obscuring column density of $> 10^{22} \text{cm}^{-2}$.

Again there are no signs of activity in the optical spectrum of GSGP4X:109 ($z=0.1$). The spectrum is that of a 'passive' early-type galaxy. The luminosity is consistent with that of a normal galaxy ($L_x \sim 10^{41}$ cgs) while the Chandra hardness ratio is very soft. Hence, most probably this X-ray source is associated with a normal galaxy.

Interestingly, the confirmation rate improves if we confine our sample to NLXGs with a) detection above the 5σ significance threshold and b) small separation between the ROSAT X-ray position and the optical counterpart ($\Delta_{ox} < 10$ arcsec). In this case we obtain a confirmation rate of at least 3 out of 7 NLXGs; 2 out of 7 are not confirmed by Chandra while 2 have not been observed. The above results are in good agreement with the cross-correlation analysis of Almaini et al. (1997). They find that about 4 out of 10 galaxies (with $B < 21$) should be real counterparts.

3. Discussion

The snapshot (10 ksec) Chandra observations of 10 NLXGs detected in our deep ROSAT survey confirm that a number of sources are indeed associated with galaxies and are not chance coincidences. These findings are in full agreement with the cross-correlation analysis of Roche et al. (1995) and Almaini et al. (1997). These appear to be a mixed bag of objects consisting of obscured AGN and possibly normal galaxies. Deep Chandra surveys are also detecting the same classes of galaxies (Mushotzky et al. 2000, Hornschemeier et al. 2002). Indeed, these galaxies can be roughly divided into two groups: a) those at faint fluxes 10^{-16-17} cgs with luminosities typically $L_x \sim 10^{41}$ cgs and soft X-ray spectra. b) 'passive' early-type galaxies with high X-ray luminosities ($L_x \sim 10^{42}$ cgs) and hard X-ray spectra (typically with $\Gamma < 1.4$). This class of objects presents great interest as the AGN characteristics are not obvious on the optical spectra. Large amounts of obscuration in the form of spherical coverage can account for this behaviour (eg Comastri et al. 2002).

Interestingly, the galaxies detected in deep ROSAT and Chandra surveys present some similarities with the 'composite' galaxies found in the ROSAT All-Sky Survey by Moran et al. (1996). These objects have high X-ray luminosities ($L_x > 10^{42}$ cgs) but the AGN features are very subtle or absent in their optical spectra. Instead, it is the star-forming component which dominates the spectrum. Chandra observations of these objects show clearly that the X-ray emission is dominated by an AGN (Georgantopoulos et al. 2002). A strong extended X-ray component is also present. The nuclear spectrum is soft ($\Gamma \approx 1.9$) typical of unobscured Low Luminosity AGN. The 'composite' objects are very similar to the galaxies detected in ROSAT or Chandra in the sense that the AGN remains undetected in the optical. However, the reasons for this behaviour are different in the two cases. In the case of the Chandra or the ROSAT NLXGs it is the obscuration while in the case of the composites it is the strong star-forming component which masks the AGN characteristics.

Regardless of the true nature of these Low Luminosity AGN detected in the ROSAT and Chandra surveys, it becomes evident that the classification based on the optical spectra is not always reliable. Instead X-ray diagnostics such as the Luminosity, the Hardness Ratios and variability play a major role in classifying these sources. Chandra observations of the Hubble Deep Field detect only 12 sources, (Brandt et al. 2001) out of a few thousand found in the optical image. Although the majority of these sources are probably AGN, this is not evident from the optical spectra alone (only two objects present clearcut QSO spectra). XEUS is expected to detect all sources in the Hubble Deep Field, provided that the spatial resolution is < 2 arcsec. The majority of these objects are very faint ($R > 24$) and thus only photometric information exists in the optical. A few hundred of these are expected to be AGN in analogy with the local Universe (Ho, Filippenko & Sargent 1997). The XEUS observations will be invaluable in determining the nature and astrophysics of faint sources in the deep Universe which so far remains largely unknown.

Acknowledgements. We would like to thank the organisers of this timely and interesting conference for their excellent work.

References

- Almaini et al. 1997, MNRAS, 291, 372
Boyle, B.J., McMahon, R.G., Wilkes, B.J., Elvis, M., 1995, MNRAS, 276, 315
Brandt, W.N., et al., 2001, AJ, 122, 1
Comastri, A., et al. 2002, ApJ, 571, 771
Hasinger, G., Burg, R., Giacconi, R., Schmidt, M., Trumper, J., Zamorani G., 1998, A&A, 329, 482
Ho, L.C., Filippenko, A.V., Sargent, W., 1997, ApJ, 487, 568
Hornschemeier, A. et al. 2002, ApJ, 568, 82
Georgantopoulos, I. et al. 1999, MNRAS, 305, 125
Georgantopoulos, I. Zezas, A., Ward, M.J., 2002, ApJ, in press, astro-ph/0210390
Griffiths, R.E., Georgantopoulos, I., Boyle, B.J., Stewart, G.C., Shanks, T., della Ceca, R., 1995, 275, 77
McHardy et al. 1998, MNRAS, 295, 641
Mushotzky, R.F., Cowie, L.L., Barger, A.J., Arnaud, K.A., 2000, Nature, 404, 459
Moran, E.C., Helfand, D.J., Halpern, J.P., 1996, ApJS, 106, 341
Roche, N., Shanks, T., Georgantopoulos, I., Stewart, G.C., Boyle, B.J., Griffiths, R.E., 1995, MNRAS, 273, L15
Shanks, T., Georgantopoulos, I., Stewart, G.C., Pounds, K.A., Boyle, B.J., Griffiths, R.E., 1991, Nature, 353, 315
Vignati, P., 1999, 353, 315 A&A
Zezas, A., Georgantopoulos, I., Ward, M.J., 1998, MNRAS, 301, 915 MNRAS,



The growth of structures - Building clusters

M. Arnaud

CEA/DSM/DAPNIA/SAP Saclay, 91191 Gif-sur-Yvette, France

Abstract. Clusters of galaxies are the largest and most massive collapsed objects in the Universe. In the standard cosmological scenario, they form from the collapse of initial density fluctuations that grow under the influence of gravity, following recurrent merging events. Clusters of galaxies are still forming at the present epoch and the observation of this evolving population provides unique constraints on the physics that governs large scale structure formation and evolution.

The presence of substructure in present epoch clusters give clear support to the hierarchical scenario. More recently, detailed gas temperature maps obtained with XMM and Chandra, and the discovery of cold fronts, provide unambiguous evidence of ongoing mergers. The substructures in clusters contain of fossil record of the merger history. Thus, statistical studies of the cluster morphology can provide important test of cosmological models of structure formation. However, data from a single epoch cannot unambiguously disentangle the merging history of clusters. The available data clearly show that the physics of merger events is a particularly complex process, which remains poorly understood, in particular the survival time of merger substructures.

In the hierarchical merging scenario, clusters are expected to constitute a homologous family. We do see regularity in the local cluster population - strong correlations between the various properties, like the luminosity, mass, temperature, velocity dispersion, evidence for universal density and temperature profile for hot clusters. However, it is now well established that a purely gravitational scenario fails to explain all the observed properties of clusters. For instance, the luminosity-temperature relation is steeper than expected and an entropy excess is observed in the core of cool systems. Recent XMM data suggest that this entropy floor has been established at high redshift. However, the physical origin of this break of self-similarity remains unknown. Various non-gravitational processes have been invoked, like pre-heating by early galactic winds or radiative cooling. Such departures from the simplest model could also be due to variation of the galaxy formation efficiency with the mass of the object or even some fundamental flaws in our modeling of the gravitational collapse of the dark matter.

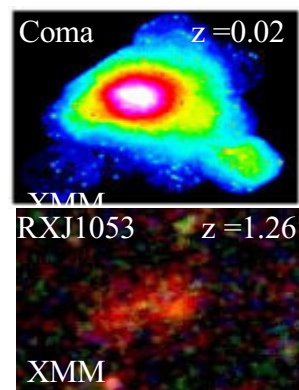
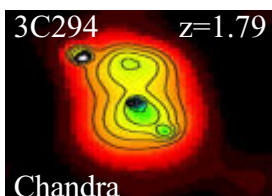
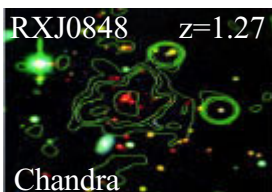
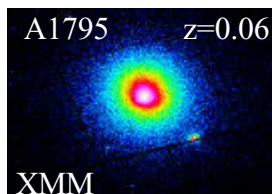
Although significant progresses are currently made with XMM and Chandra, in particular on the evolution of cluster properties with redshift, essential information will still be missing. We cannot measure the velocity structure of the gas, a key information to understand the complex physics of merger events. This information can only be provided by bolometer (or STJ) array type instruments, as planned for future missions like Astro-E II, Constellation X and XEUS. Equally important is the associated gain in sensitivity for line detection, allowing to probe the evolution of metallicity with redshift, an independent constraint on galaxy feedback. Finally a very high throughput mission, like XEUS, is the only way to observe directly the history of cluster formation, i.e. the merging activity and evolution of subclustering up to z at least ~ 2 and the physical properties of very high redshift groups, the progenitors of present day clusters.

Acknowledgements. We gratefully acknowledge the permission by the Springer Verlag to use their A&A L^AT_EX document class macro.

The growth of structures

Building clusters

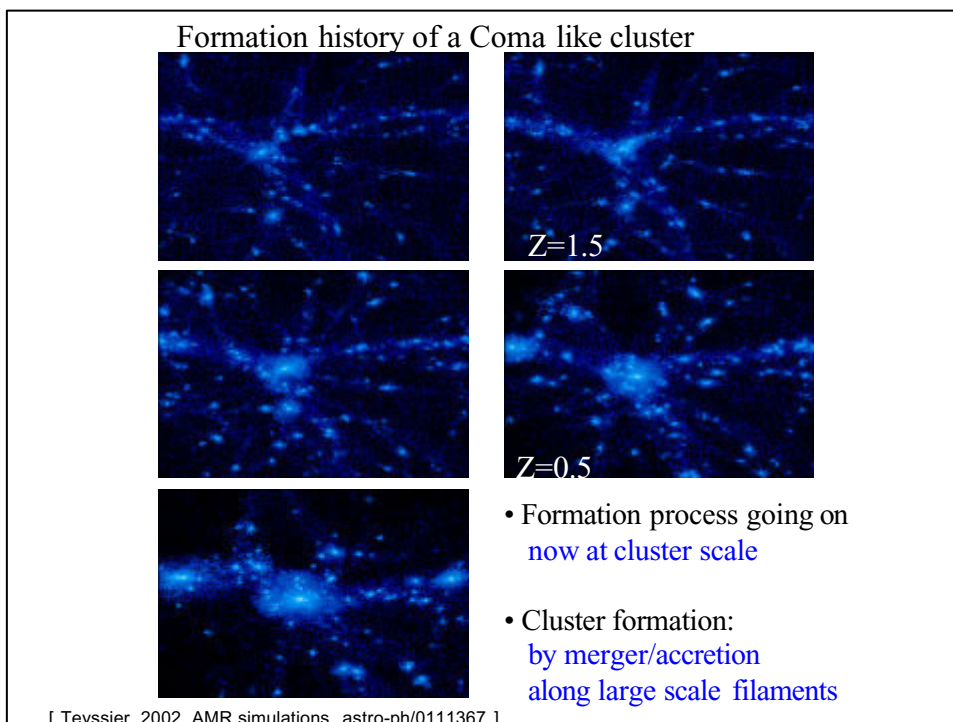
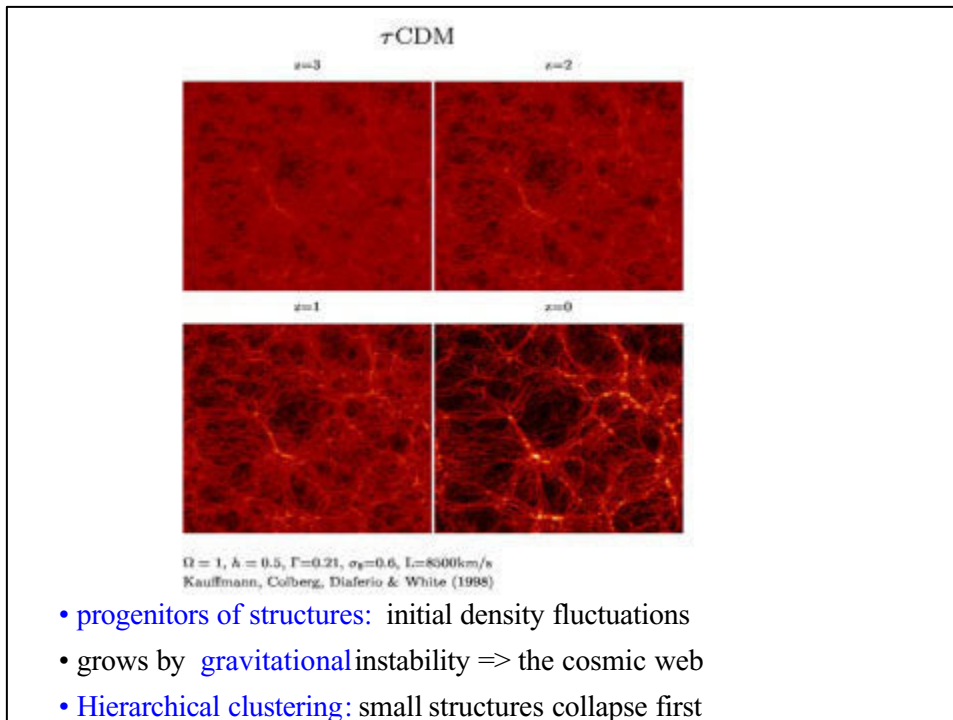
M.Arnaud (Sap Saclay)

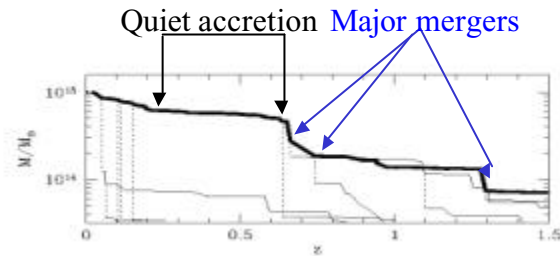


- Clusters exist up to high z
- Variety of dynamical state at all z

How cluster form?

[References : Briel et al, 2001; Arnaud et al 2001; Stanford et al 2001; Hashimoto et al, 2002; Fabian et al, 2001]





[Cavaliere et al, 1999]

Example of formation history of $10^{15} M_{\odot}$ cluster.

Hierarchical mass growth by

- **Merger of subclusters previously formed**
Major events: rare events
More merger with smaller groups
- **Quiet matter accretion**
between merger events

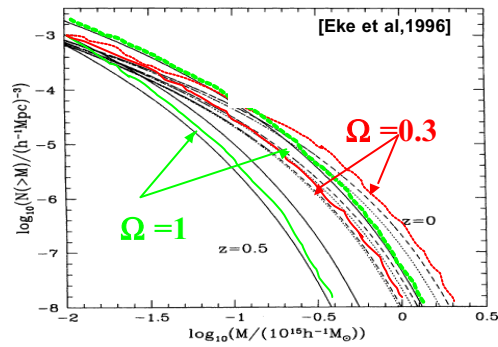
The cluster population is an evolving population

==> provide powerful test of structure formation:

Current tests:

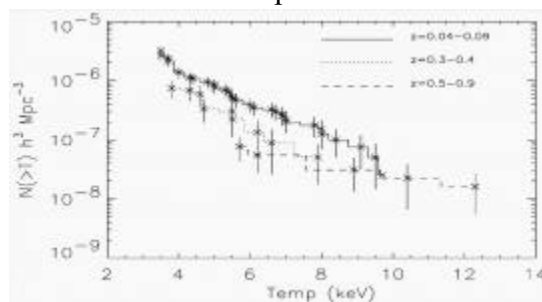
- Evolution of the mass function ($N(m)$)
- Study of dynamical state of nearby clusters
- Correlations between (relaxed) cluster properties

The evolution of cluster number density



- Less massive clusters at high z
- Amount of evolution depends on cosmological parameters

Observed temperature function

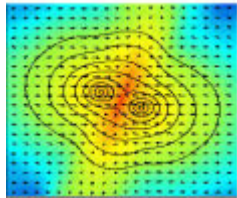


[Donahue et al, 1999, ApJ, 527, 525]

- We do see evolution
- Till now used to constrain Ω , assuming standard M-T relation
Need
- Ω and $P(k)$ determined independantly
- Better $N(T,z)$ high z and calibration of M-T relation
 - Progress expected with XMM follow-up
 - More massive clusters (All Sky Survey)

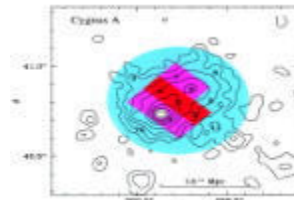
Dynamical state of nearby clusters

- Presence of sub-structures
- direct evidence of merging activities



[Ritchie & Thomas, 2002]

Numerical simulation (shock)



[Markevith et al, 1999]

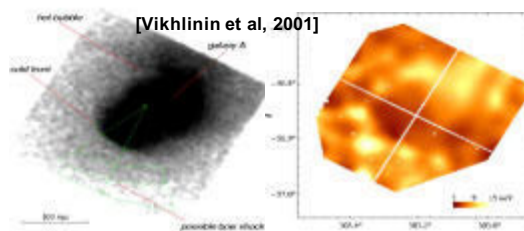
ASCA kT map

Clear support to hierarchical scenario

- Substructures: a fossil record of merging history

BUT

- Physics of merger events and relaxation time poorly understood



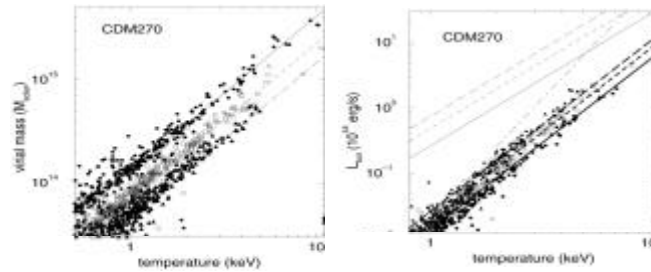
[Vikhlinin et al, 2001]

Chandra

Cold front (not shock) -> survival of dense subcluster core?

- statistical analysis of substructures in $z \sim 0$ clusters
--> Ambiguous test of formation scenario
(NB which also depends on Ω)

Correlations of (relaxed) cluster properties The self-similar model



Simple scaling laws:

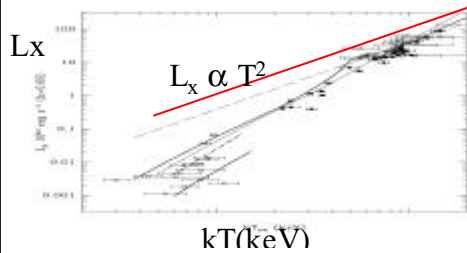
$$GM/R_v^3 = \delta \rho_c(z) \quad (\text{cluster form at constant over density})$$

$$GM/R \propto kT \quad (\text{virial theorem})$$

$$M_{\text{gas}} \propto M \quad (f_{\text{gas}} = \text{cst})$$

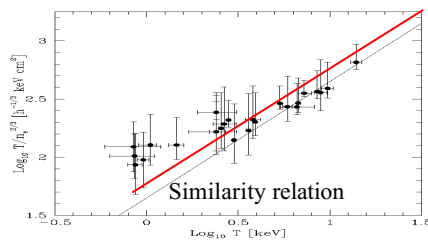
$$M_{\text{gas}} \propto T^{3/2} ; R_v \propto T^{1/2} ; L_x \propto T^2$$

Observed departure from self-similar scaling



- Steepening of the L_x - T relation

[Tozzi & Norman, 2001, *ApJ*, 546, 63
Data from Arnaud & Evrard, 1999;
Allen & Fabian, 1888, Ponman et al, 1996]



- Entropy excess

- Characteristic 'floor' value of $\sim 100 \text{ keV cm}^2$

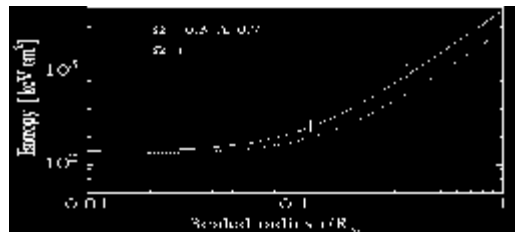
[Ponman et al, 1999, *Nature*, 397,135
See also Lyod-Davies et al, 2000,
MNRAS, 315, 689]

The evolution of the ICM is **not purely governed by gravitational effects**

Recent XMM observations suggest that entropy floor already established at high z

Physical origin not understood:

- **Pre-heating ?** by:
 - SN-driven early galactic winds thought to be responsible for the ICM enrichment
 - AGN
- **Cooling ?** (NB poorly understood cf XMM/RGS)
- variation of **galaxy formation efficiency** with cluster mass?
- **fundamental flaws in DM collapse model?**



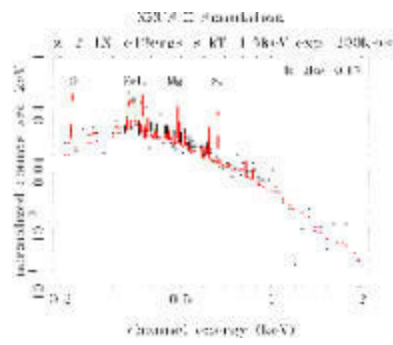
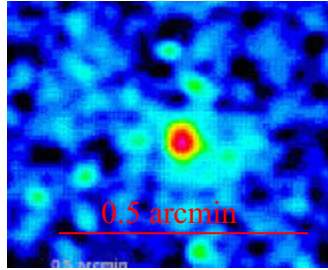
$Z=0.6$ cluster

[Arnaud et al, 2002]

What do we need to understand cluster (and structure) formation?

- Know the Universe in which they form and evolve
 - $P(k)$, Ω , Λ
 - **Planck**
 - Understand better the complex NE physics of merger events
 - > measure gas v (nearby clusters)
 - > **Bolometers (Astro-E II; Cons-X; XEUS)**
 - **Directly observe the history of present day clusters**
 - merging activity and evolution of subclustering up to z at least 2
 - thermodynamical (cooling, heating) evolution
 - including the physical properties of groups at high z , the 'seeds' of present day clusters
- **high throughput, E resolution (XEUS)**

XEUS simulation of a poor group at $z=2$





High redshift Sunyaev-Zel'dovich clusters and XEUS

R. Kneissl

Astrophysics Group, Cavendish Laboratory, University of Cambridge, Madingley Road, Cambridge CB3 0HE, UK

Abstract. Over the next 10 years a substantial number of ground-based and space-borne SZ cluster surveys will become available. They are expected to find $\approx 10^4$ massive clusters overall and, given the SZ selection function, a substantial fraction of these will be at redshift one and beyond, the numbers depending only on cosmology. X-ray observations with XEUS of this large sample of early clusters will reveal the details of cluster formation, and when combined with highly resolved, multi-frequency SZ images can determine the cluster's angular distances or bulk velocities, for example.

1. Introduction

Galaxy clusters, as the largest bound objects in the universe for which a mass and a radius can be determined, are interesting sites to study high temperature gas physics, to learn about structure formation in general and to probe properties of the universe as a whole. Tracing their evolution back to the high redshifts where they first formed is of great relevance to all these areas. However finding these rare objects at high redshift has been a problem in the past in all traditional wavebands. Now a new window is opening in the microwave and sub-mm bands where clusters can be studied using inverse Compton scattering of CMB photons, the Sunyaev-Zel'dovich effect (SZ, Sunyaev & Zel'dovich 1972). Indeed detection of the SZ effect in rich X-ray-selected clusters has become routine (see Birkinshaw 1999 for a review).

An instrument such as XEUS providing a deep X-ray view of the universe is unable to find these clusters at high redshift but is ideally matched to study those selected in the SZ effect, thanks to the high collecting area and energy resolution. In practice it compensates for the $(1+z)^{-4}$ cosmological dimming X-ray radiation suffers compared to the SZ flux, and allows studies of high-z clusters comparable and better to what is presently possible for nearby clusters.

Sunyaev-Zel'dovich and X-ray observations of galaxy clusters both probe the intra-cluster gas, but quite differently in many ways:

SZ	X-RAY
inverse Compton scattering	Bremsstrahlung + line emission
$\int n_e(r, \theta) T_e(r, \theta) dr$ integrated pressure, total thermal energy	$\int n_e n_p \Lambda(T_e) dr + \text{lines}$ density and composition sensitive
$M_{\text{gas}} \times \langle T_e \rangle_n$ redshift independent	density concentrations, gas clumping $(1+z)^{-4}$ dimming
	extragalactic confusion
Radio/GHz sources	AGN/XRB
	galactic confusion
Synch., HII, dust	$10^6 - 10^7 \text{K}$ gas, HI/metal absorp.

SZ and X-ray observations are complementary probes. Given their respective properties a promising strategy for the future appears to be SZ surveying and cluster selection followed by deep X-ray imaging and spectroscopy.

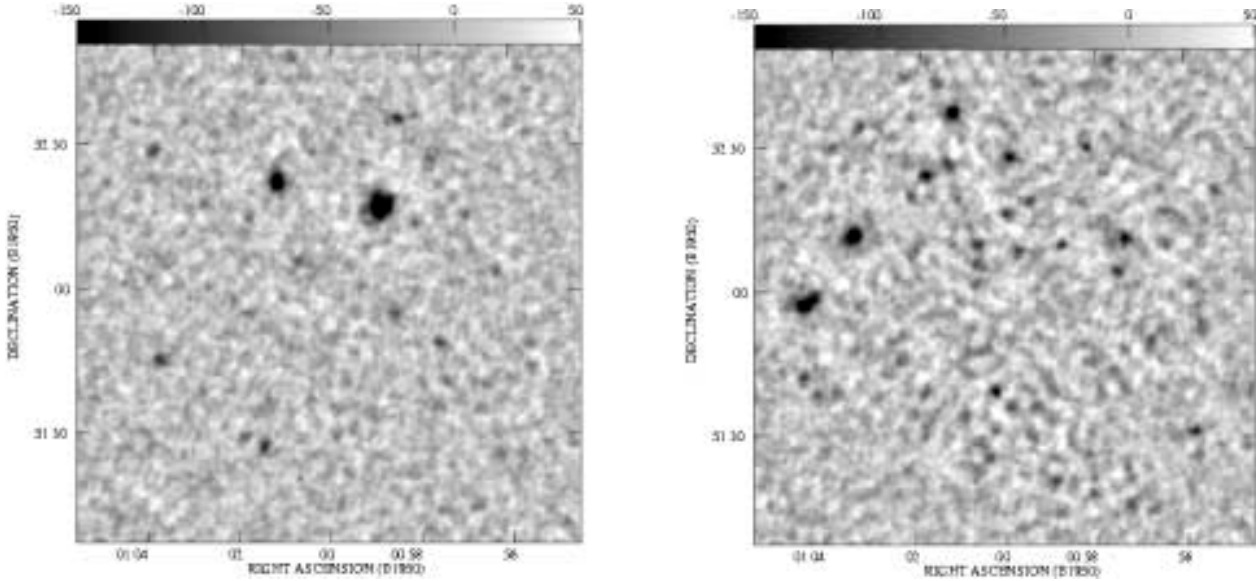


Fig. 1. Two simulated AMI observations of 20-arcmin radius fields showing the effects of the different cosmologies ($\Omega_0 = 1$ on the left and $\Omega_0 = 0.3$ on the right); units are $\mu\text{Jy beam}^{-1}$. The clusters show as dark (negative) features against the CMB. The simulation with low matter density has many more moderate mass clusters, because clusters form early and can be seen in SZ all the way to very high redshift.

2. SZ cluster surveys

Technological advances now allow the construction of very sensitive CMB telescopes. A large number of projects with the capability to search for clusters in blank fields via the SZ effect are proposed, planned or being build:

- arrays now / over next 2-3 years
 - interferometers
 - AMI(+Ryle): 12-18 GHz, 10 3.7-m + 8 13-m dishes
 - AMiBA: 85-95 GHz, 19 1-m dishes
 - SZA: 26-34 GHz, 6 3.5-m dishes (+OVRO/BIMA ?)
 - bolometers
 - ACBAR: 150-350 GHz, 4 arcmin
 - BOLOCAM(II): 150-270 GHz, 1 arcmin
- Planck (satellite; launch 2007)
 - 10 frequency channels, 30-800 GHz, 5-10 arcmin beams
- arrays over next 4-10 years
 - ACT
 - OCRA
 - SPT

In the following two examples, the ground-based interferometer AMI and and the satellite project Planck Surveyor are discussed in more detail.

2.1. The Arcminute Micro-Kelvin Imager (AMI)

The design requirements for an SZ survey instrument are: maximum sensitivity, hence low system temperature and high bandwidth and shortest baselines of $\approx 200\lambda$ (confusion from primary CMB anisotropies becomes a problem at shorter baselines). The approach adopted with AMI is to exploit the low system temperature available at low frequency, but to provide sufficient flux sensitivity at higher resolution to detect and then remove confusing radio point sources using the large antennas of the Ryle Telescope. Operating at 15 GHz from Cambridge it is possible to achieve total system temperatures below 25 K. The available bandwidth is the K_a waveguide band of 12–18 GHz; the minimum required baseline of $\approx 200\lambda$ fixes the antenna size at ≈ 4 m. The number of these antennas is fixed by the flux sensitivity available for source subtraction from the Ryle Telescope and the 15 GHz source counts (Taylor et al. 2001) to about

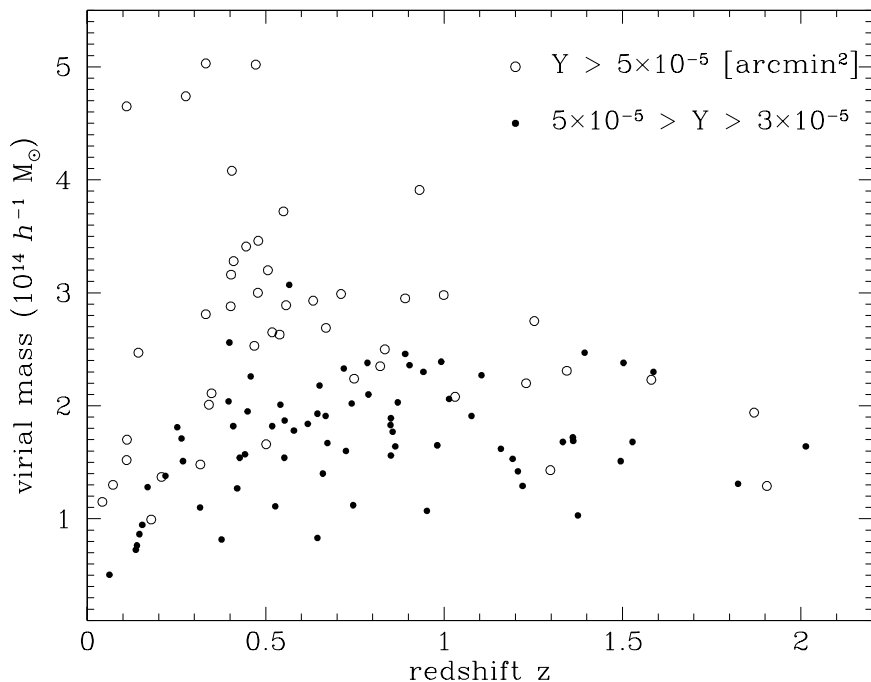


Fig. 2. Masses and redshifts of clusters detectable in the AMI survey for the $\Omega_0 = 0.3$ cosmology. Filled and empty points show two different flux cuts achievable in deep and shallow surveys. Clusters out to $z = 2$ can be seen. The lower flux cut corresponds to lower cluster masses, and more of these clusters exist at high redshift.

ten, i.e. a collecting area equal to about one RT antenna. More detail on the technical side of the AMI telescope are given in Jones (2002).

The flux sensitivities are $2 \text{ mJy s}^{-1/2}$ and $20 \text{ mJy s}^{-1/2}$ for the large and small arrays, in 6 and 20 arcmin fields of view respectively. The temperature sensitivity depends on the exact array configuration used; a representative number would be about $15 \mu\text{K}$ in a week, in a 1.5 arcminute beam and 20 arcmin field of view.

To determine how many galaxy clusters AMI can detect, it is useful to create realistic SZ sky maps simulated for different cosmologies. This approach is particularly helpful for interferometric measurements, because the limited coverage in Fourier space can lead to ringing in the map plane affecting the detection efficiency and to a reduction in the observed flux of a single cluster depending on its size and shape. To produce a map, the Press-Schechter expression is used in combination with individual cluster templates from ten ΛCDM hydrodynamical cluster simulations. Each cluster is observed at eight different redshifts out to $z \approx 1.1$, and templates are produced from three orthogonal directions to maximise the variety in the apparent cluster shapes.

We simulate the cluster detection process for a blank field AMI observation in two different ways: a detailed, but time consuming, simulation of the response of the interferometric array to the structure on the sky, and a simplified simulation, which only operates in the image plane and uses a compensated beam profile that is constructed to match the synthesised beam resulting from the more detailed simulations. We find that after one year of observation AMI will have completed a cluster survey down to roughly $1 \times 10^{14} M_\odot$ with 20 ($\Omega_0 = 1$) to 70 ($\Omega_0 = 0.3$) clusters for our pessimistic assumptions about σ_8 and f_g , or several hundred clusters for more realistic assumptions. Figure 2 shows the mass–redshift distribution we expect for the catalogued clusters in a $\Omega_0 = 0.3$ cosmology. The details of these results can be found in Kneissl et al. (2001). The SZ cluster catalogue and the differential cluster counts at different flux levels will be prime observational results from the AMI blank field survey and the data will become public.

Sunyaev-Zel'dovich cluster map

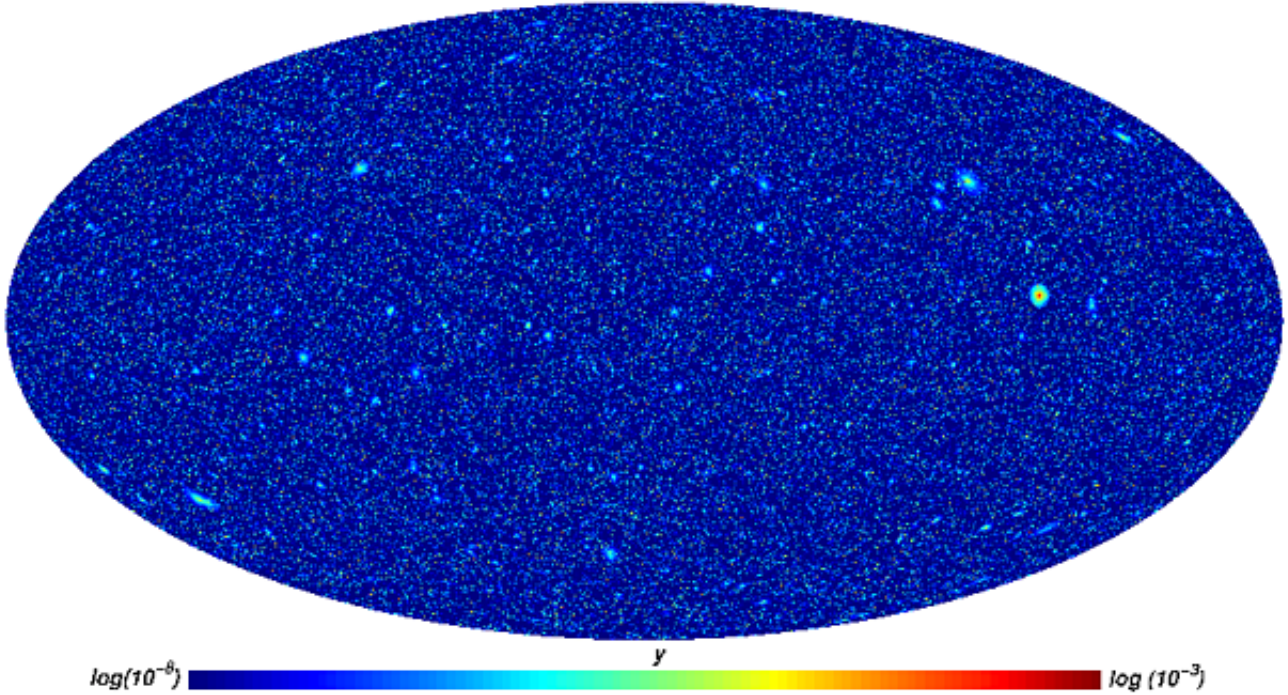


Fig. 3. Simulated SZ cluster for Planck component separation analysis. Hydro-simulation templates and the Press-Schechter expression have been combined in an $\Omega_0 = 0.3$, $\Omega_\Lambda = 0.7$ cosmology.

2.2. Planck Surveyor

The Planck Surveyor will map almost the entire sky with better than 10 arcmin resolution in 10 frequencies between 30 and 860 GHz:

Instrument		LFI (4 channels)				HFI (6 channels)					
Frequency	[GHz]	30	44	70	100	100	143	217	353	545	857
Beam FWHM	[arcmin]	33	23	14	10	10.7	8	5.5	5	5	5
Noise rms	[μK]	4.4	6.5	9.8	11.7	4.6	5.5	11.7	39.3	400.7	18182

This frequency coverage will allow a separation of the SZ signal via its distinct spectrum from other physical components in the cosmic microwave background. In Cambridge we perform a component separation on simulated all-sky data (see Figure 3) using a Maximum Entropy Method (Stolyarov et al. 2001). In broad terms there is agreement with other estimates (e.g. Bartelmann 2001, Kay et al. 2001) that the expected sensitivity to cluster fluxes is $Y = \int y d\Omega \approx 3\text{-}7 \times 10^{-4}$ arcmin² and cluster numbers are $1\text{-}5 \times 10^4$ with a considerable dependence on the cosmological and cluster gas models.

2.3. Cosmological Parameters

Several key cosmological parameters can be determined from various SZ cluster surveys. In Weller, Battye and Kneissl (2002) we assume different survey parameters as listed in Table 1. They can be categorised roughly as low sensitivity deep (I) / wide (II) and high sensitivity wide (III) and deep (IV). All of these different survey type instruments are either under construction or being proposed. AMI is an example of (I) whereas the instrument parameters of the Planck Surveyor have been used for (III). Future bolometer arrays (IV) with a large number of elements promise deep and fast surveying to cover a large area.

	(I)	(II)	(III)	(IV)	
S_{lim}	0.1	5	≈ 36	-	[mJy]
ν	15	30	≈ 100	-	[GHz]
$\Delta\Omega$	10	10^4	20600	4000	[deg 2]
M_{lim}	1.5	≈ 7.0	≈ 6.0	2.5	[$10^{14}h^{-1}M_{\odot}$]
N_{tot}	≈ 90	≈ 1970	≈ 5200	≈ 13600	

Table 1. The properties of the different classes of experiments and the number of clusters one would expect to observe in a fiducial cosmology ($H_0 = 65 \text{ km s}^{-1} \text{ Mpc}^{-1}$, $\sigma_8 = 0.925$, $\Omega_0 = 0.3$, $w_0 = -0.8$, $w_1 = -0.3$, where $p_Q = (w_0 + w_1z)\rho_Q$). The model parameters are being varied with respect to this cosmology.

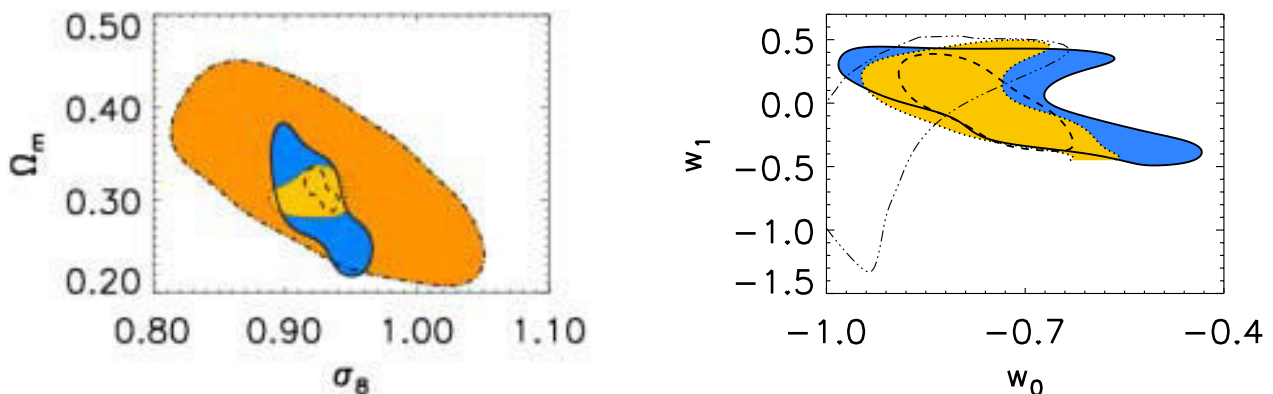


Fig. 4. The accuracy of parameter estimation is given as 68% confidence contours (marginalising over the other model parameters - no priors). The contours show constraints from the different types of survey. Left panel: The largest contour line corresponds to a type (I) survey, the solid contour line to type (II), the dotted contour line to type (III) and the dashed contour line to type (IV). Useful constraints on σ_8 and Ω_0 can be achieved. Right panel: Survey type (I) is omitted here. The additional contour line shows the expected constraints from supernovae with the SNAP satellite. Some constraints on the dark energy w_0 and its evolution w_1 seem possible.

It is particularly the larger cluster numbers even from shallower surveys which increase the precision of these measurements (see Figure 4). However assumptions about the scaling of SZ flux to mass at a given redshift have to be made, and the cluster by cluster scatter in this scaling has to be small. The validity of these assumptions will certainly be testable with the first generation of SZ survey telescopes and subsequent intensive optical and X-ray follow-up on these small, but deep samples.

3. Studying clusters at high redshift with XEUS

The SZ cluster surveys will provide a uniquely selected target list for XEUS to observe massive clusters at high redshifts. In quite a moderate observation time XEUS will be able to provide precision measurements of temperature and redshift for even the highest redshift SZ clusters (see Figure 6). It therefore appears feasible with XEUS to study an SZ selected cluster sample homogeneously with high quality X-ray data. These are indeed needed for some of the applications possible with the SZ effect.

The possibility to discover massive clusters at high redshift allows a number of further studies at various wavebands. Apart from X-ray and optical imaging and spectroscopy also deep SZ pointings below and above the peak in the Planck spectrum will become possible. Probing the whole SZ spectrum allows to separate the thermal and kinematic SZ effect, but also the temperature-dependent relativistic and the non-thermal components. With all these data at hand a wealth of information can be extracted from cluster studies over a very large range of redshifts. In the following two example, the ‘‘classical’’ H_0 determination carried to high- z and the measurement of the cluster’s peculiar velocity via the kinematic SZ effect, both of which require high quality X-ray data, are discussed in more detail.

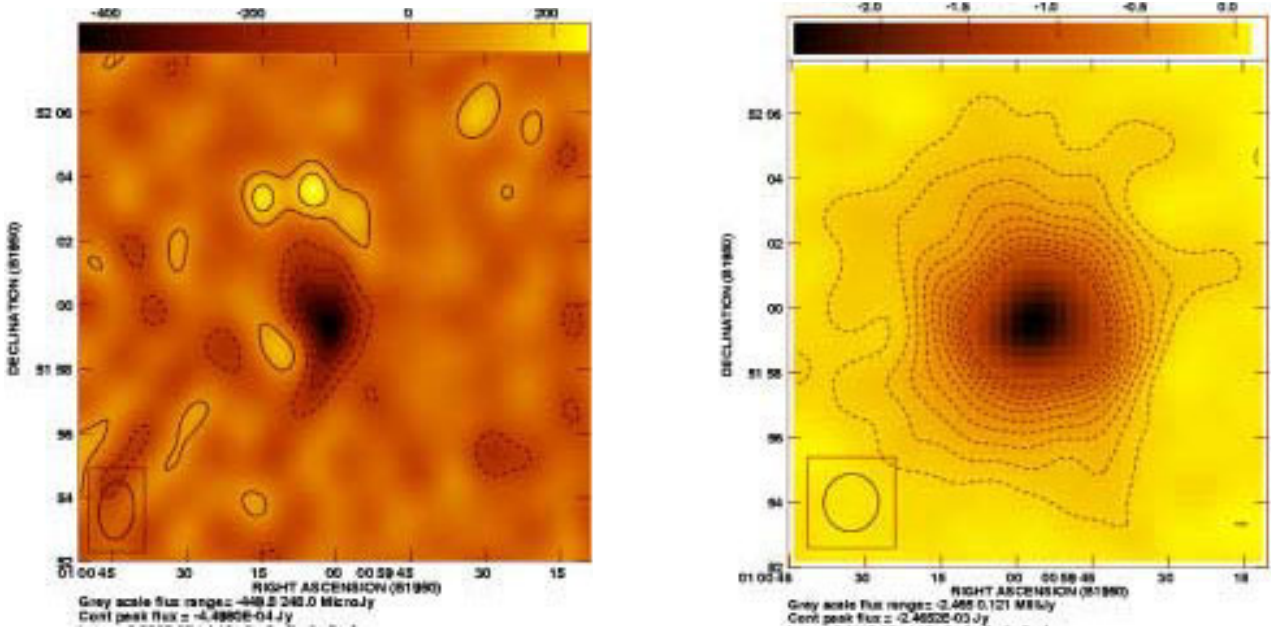


Fig. 5. Left: An image of 84 hours of RT data showing an SZ effect in Abell 1914 which is essentially unresolved. Right: A simulated observation of the cluster with AMI of the same integration time. The spatial dynamic range and signal-to-noise ratio are vastly increased, providing detailed structural information on the cluster gas; indeed no structure due to receiver noise is visible in the background. The input to this simulation is a rescaled ROSAT PSPC image.

3.1. Direct angular distances

Detailed SZ images of galaxy clusters at any redshift will be possible with the new SZ instruments (see Figure 5 for a simulation of an AMI observation). Matching X-ray data, in particular on the density structure, the gas temperature and the total X-ray flux are needed to determine the angular distance r_d to the clusters (e.g. Silk and White 1978; Cavaliere, Danese and De Zotti 1979). Given redshifts, it is possible to estimate $H(z)$ or to low order H_0 and q_0 (which depends on Ω_0 and Ω_Λ). In this absolute distance method no assumptions about cluster evolution have to be made. It works in principle for an individual cluster, as long as the parameters entering the relation for r_d can be measured reliably, and the cluster gas and temperature distributions can be modelled sufficiently accurately. We know there are uncertainties in this modelling process, for example through clumping, cooling, or temperature gradients. But we have found, from analytic modelling and the hydrodynamical simulation templates, that the effects on estimating H_0 and q_0 tend to cancel out even for a single cluster, and certainly for a larger sample (Grainger et al. in preparation). In a low density universe ($\Omega_0 = 0.3$) where many clusters, are expected at high redshifts, the AMI sample contains an about equal number of clusters below and above $z = 0.5$. For simplicity we divide the sample into one at $z = 0$ which determines H_0 and one at $z = 0.8$ which in comparison determines q_0 . To achieve an accuracy of about 5 % in the angular distance relation, which is at least comparable to the supernovae results (Riess et al. 1998; Perlmutter et al. 1999), we will need samples of 30 clusters each at low and high redshift, mainly to reduce the effect of unknown orientation. Given that the X-ray temperature enters the relation for r_d squared, an error of less than 10% is required for all clusters, in particular those at high redshift.

3.2. Cluster velocities

The random and pairwise velocities of galaxy clusters and their bulk flow in a large volume are important probes of the cosmological model since they show the effect of the total matter and can be calculated in linear theory. The SZ effect in particular allows to measure these over a large range in redshift probing the evolution of the velocity field. Furthermore it is a physical method which does not have to rely on distance indicators.

The radial cluster peculiar velocity can be measured directly via the kinematic SZ effect ($\Delta T/T = \tau v/c$; Sunyaev and Zel'dovich 1980) if the optical depth of the cluster is known. In principle even the transverse component of this velocity can be measured via its polarisation effect on the scattered radiation ($p \approx \tau (v/c)^2$). The optical depth can

be derived from either the X-ray surface brightness or can be inferred from the thermal SZ effect ($y \approx \tau kT_e/m_e c^2$) if the temperature of the cluster gas is measured, which would be done most accurately via X-ray spectroscopy. Given that a measurement uncertainty in the SZ of a few μK is anticipated, although there are uncertainties in this number, for typical clusters ($\tau \approx 0.01, v \approx 500$ km/s) again an accuracy of about 10% is required in the X-ray measurement.

4. Conclusion

XEUS is the ideal instrument to explore cluster physics back to the earliest times when clusters formed. The Sunyaev-Zel'dovich effect will be employed by a large number of specialised telescopes to find these early, but rare clusters, providing targets for XEUS observations. Applications of SZ observations requiring X-ray data, such as for example direct distance measurements, will become possible for a large sample of SZ selected clusters.

Acknowledgements. I like to thank my collaborators, Richard Battye, Vincent Eke, Jochen Weller, and my colleagues in the AMI team and in the Cambridge Planck Analysis Center.

References

- Bartelmann M., 2001, A&A, 370, 754
Birkinshaw M., 1999, Phys. Rept., 310, 97
Cavaliere A., Danese L. and De Zotti G., 1979, A&A, 75, 322
Jones M. E., 2002, in proc. 8th Taipei Astrophysics Workshop 'AMiBA 2001', ASP Conference Series, Vol. 999, eds. Chen L-W, Ma C-P, Ng K-W, Pen U-L (astro-ph/0109351)
Kay S.T., Liddle A. R., Thomas, P. A., 2001, MNRAS, 325, 835
Kneissl R., et al., 2001, MNRAS 328, 783
Perlmutter S., et al., 1999, ApJ, 517, 565
Riess A.G., et al., 1998, AJ, 116, 1009
Silk J., White S.D.M., 1978, ApJL, 226, L103
Stolyarov V., Hobson M. P., Ashdown A. J., Lasenby A. N., 2001, MNRAS submitted, (astro-ph/0105432)
Sunyaev R. A., Zel'dovich Ya., 1972, Comments Astrophys. Space Phys. 4, 173
Sunyaev R. A., Zel'dovich Ya., 1980, MNRAS, 190, 413
Taylor, A. C., et al., 2001, MNRAS 327, L1
Weller J., Battye R., Kneissl R., 2002, Phys. Rev. Lett., 88, 231301

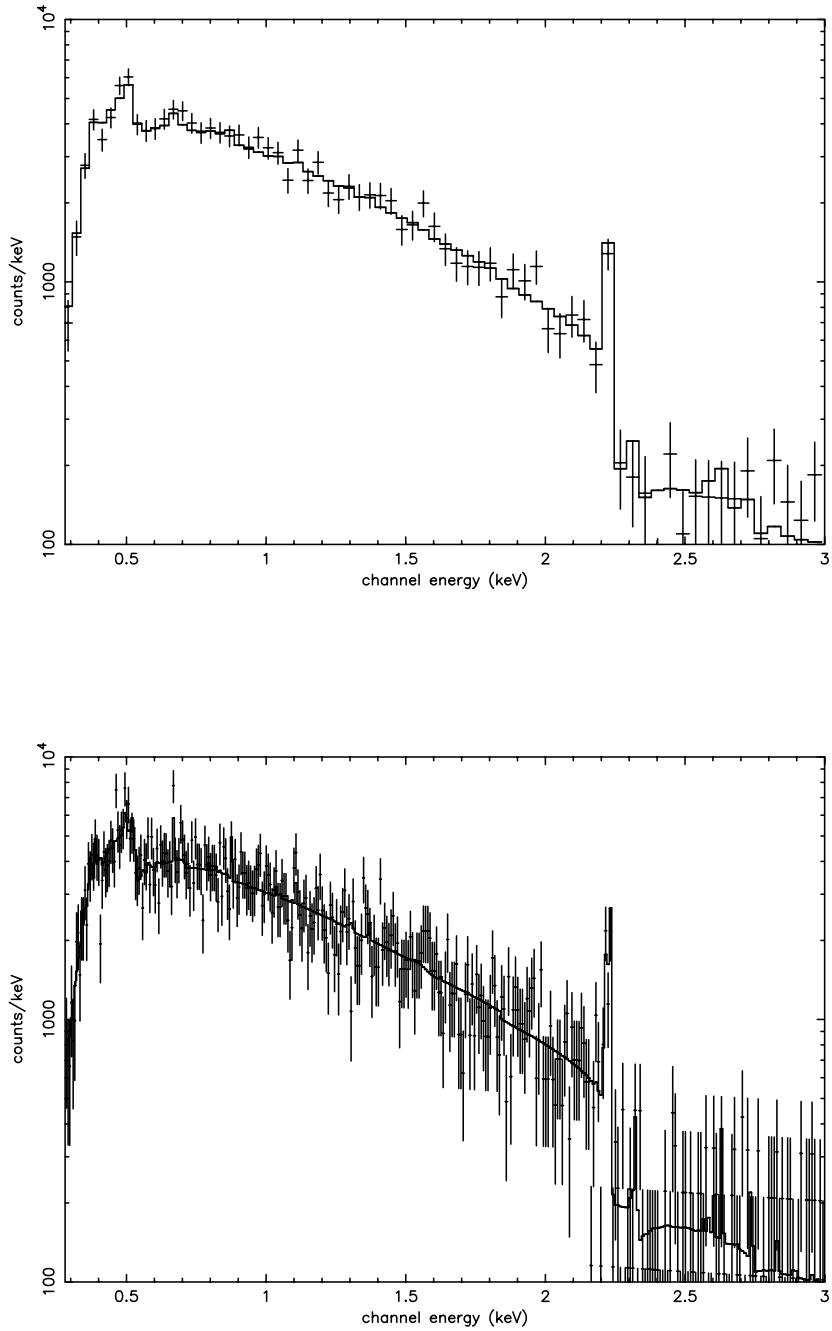


Fig. 6. Simulated XEUS-II spectrum with 20 ks exposure of a typical SZ survey cluster ($M = 2 \times 10^{14} h^{-1} M_{\odot}$, $L_x \approx 1 \times 10^{44} h^{-2} \text{ erg s}^{-1}$) at a redshift of $z = 2$ ($F_x = 3 \times 10^{-15} \text{ cgs}$). In the top panel the spectrum has been binned suitably (50 channels per bin) to detect the iron-K line. In the bottom panel the spectrum has been binned with 10 channels per bin suitable for fitting the MEKAL model spectrum. The resulting uncertainties in the temperature and redshift are $\delta T \approx 0.4 \text{ keV}$ and $\delta z \approx 0.002$. Note however that for $z = 2$ the iron-K line happens to lie just below the gold absorption edge of the telescope.

X-ray Absorption and Emission Spectroscopy of the Intergalactic Medium at Small Redshift

Frits Paerels¹, Andy Rasmussen¹, Steven M. Kahn¹, Jan Willem den Herder², and Cor de Vries²

¹ Columbia Astrophysics Laboratory and Department of Astronomy, 550 West 120th St., New York, NY10027, USA

² SRON National Institute for Space Research, Sorbonnelaan 2, 3584 CA Utrecht, the Netherlands

Abstract. Recent observations with *Chandra* and *XMM-Newton* have begun to probe the properties of the intergalactic medium (IGM) at small redshifts. We briefly present a recent new result on resonance absorption by highly ionized oxygen at $z \approx 0$ with the Reflection Grating Spectrometer on *XMM-Newton*, and then discuss the prospects for detecting line emission from the Warm-Hot phase of the IGM.

1. Introduction

The discrepancy between the baryon density predicted from Big Bang Nucleosynthesis and the results of a baryon census at small redshift (with only 50% of the predicted baryon density accounted for by galaxies and diffuse gas in groups and clusters; Fukugita, Hogan, and Peebles 1998) is thought to indicate that a large fraction of the baryons currently resides in the Intergalactic Medium (IGM), in a highly ionized phase that makes it difficult to detect. Two separate arguments support this belief: the baryon census at high redshift ($z \sim 3$) is essentially complete, with most of the baryons residing in the Ly α forest, and large scale coupled Dark Matter/Hydrodynamic simulations of structure formation (Cen & Ostriker 1999) naturally show that this high-redshift medium will be heated just by gravitational energy input alone to a very high degree of ionization at the current epoch, making it extremely difficult to observe in species with low ionization potential.

A search for this 'Warm-Hot Intergalactic Medium' (WHIM, Cen & Ostriker 1999) in high ionization species has recently begun. Observations with the *Far Ultraviolet Spectroscopic Explorer* have started to find significant amounts of O VI bearing gas out to redshifts of a few tenths (Tripp, Savage, & Jenkins 2000; Tripp & Savage 2000; Savage et al. 2002), and the first attempts to detect higher ionization species in absorption (primarily O VII and O VIII) with the diffraction grating spectrometers on *Chandra* and *XMM-Newton* have been conducted (Fang et al. 2001, 2002a). The latter have yielded null results, which are not surprising considering the limited sensitivity of the observations. Since we held the meeting, the results of the dedicated very deep *Chandra* LETG/ACIS observation of H1821+643 (which has strong intervening O VI absorption) have become available (Mathur, Weinberg, & Chen 2002). Marginal O VII and O VIII resonance absorption is found at or near the redshifts of some of the known O VI absorbers, but in view of the low significance of the result, it is probably safest to regard it as representing an upper limit to intergalactic O K absorption. The O VIII Ly α absorber at $z = 0.055$ recently reported by Fang et al. (2002b) in *Chandra* LETGS/ACIS data on PKS2155-304 is, unfortunately, probably spurious (see below). As far as detection of *emission* from the WHIM is concerned, the tip of the iceberg may have shown up in a number of deep *ROSAT* PSPC fields in the form of relatively dense filaments stretching between clusters (Scharf et al. 2000). Finally, a careful accounting of the intensity measured in the unresolved X-ray background (Kuntz, Snowden, & Mushotzky 2001) has yielded an average intensity of $7 \text{ keV cm}^{-2} \text{ s}^{-1} \text{ sr}^{-1} \text{ keV}^{-1}$ in the '3/4 keV' band that cannot be ascribed to unresolved point sources (Galactic or extragalactic). Some fraction of this is due to foreground Galactic diffuse emission, but a finite intensity may well remain after the Galactic and the most probable summed emission from clusters and Groups has been taken into account (Wu & Xue 2001).

The O VI absorption by itself, or even when combined with H I and C, N, and Si spectroscopy, does not (yet) allow a direct characterization of the nature of the absorbing medium: collisionally ionized or photoionized, single- or multiphase (Savage et al. 2002). Hence, we do not know whether the gas is associated with galaxy halos, the intragroup medium of small Groups, or the non-virialized IGM. The measurements do, however, yield a robust lower limit to the mass density associated with the O VI gas, based on the fact that the ionization fraction in O VI peaks

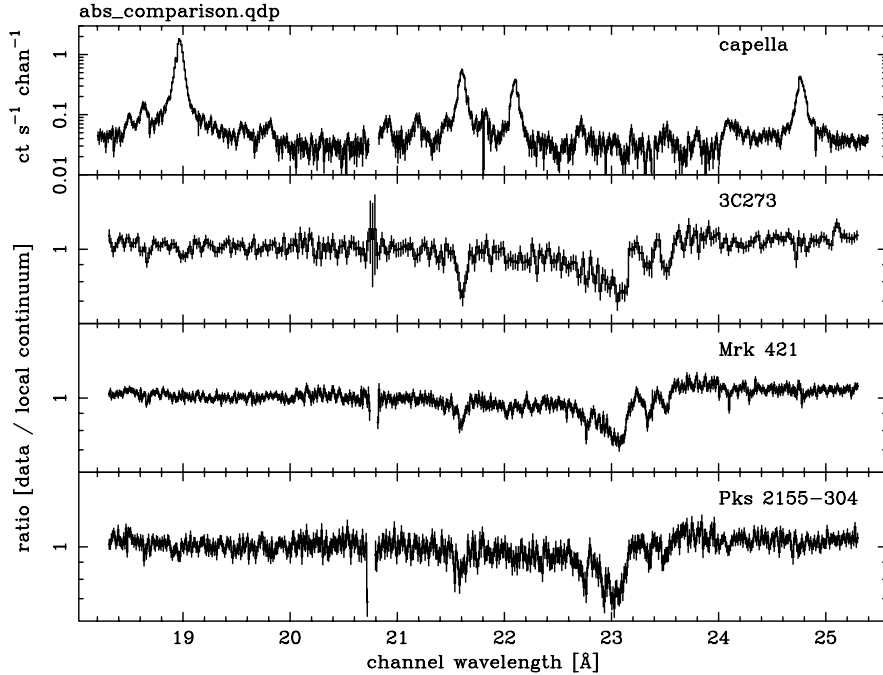


Fig. 1. XMM-Newton RGS spectra of Mkn 421, 3C273, and PKS2155–304 in the 18–26 Å band; the spectrum of Capella, using identical reduction methods, is shown at the top. O VII $\lambda 21.60$ Å resonance absorption is clearly visible in all three AGN spectra, while O VIII Ly α ($\lambda 18.97$ Å) is detected in PKS2155–304 and 3C273.

at $f_{\text{O VII}} = 0.2$, regardless of the ionization mechanism. Savage et al. (2002) find $\Omega_{\text{O VII}} > 0.0021h_{70}^{-1}$ at small redshift, for oxygen abundances 0.1 solar or smaller. The associated O VII/O VIII absorption reported by Mathur, Weinberg, and Chen (2002), when interpreted as an upper limit, similarly places an upper limit to the mass density in highly ionized gas of $\Omega_{\text{O VII}} + \text{O VIII} \lesssim 0.03h_{70}^{-1}$ for 0.1 solar abundance, along the line of sight towards H1821+643. This is to be compared with the baryon mass density derived from Big Bang Nucleosynthesis: $\Omega_b h_{70}^{-2} = 0.04$ (Burles and Tytler 1998).

But the first unequivocally positive detections of intergalactic X-ray line absorption have appeared at redshift *zero*. Fabrizio Nicastro and his colleagues first announced the positive detection of oxygen and neon absorption lines in the *Chandra* LETG/HRC spectrum of PKS2155–304 in January, 2002 (Nicastro et al. 2002), and oxygen absorption has been positively detected in three very deep observations of Mkn 421, 3C273, and PKS2155–304 with the RGS on XMM-Newton (Rasmussen et al., 2002). Fabrizio discussed his data at the meeting (Nicastro, this volume), and we will discuss the RGS spectroscopy below.

2. O VII Resonance Absorption at $z = 0$ with XMM-Newton RGS

XMM-Newton repeatedly observed the three (relatively) strong continuum sources Mkn 421, 3C273, and PKS2155–304 in its initial PV/Calibration phase. A total RGS exposure time of 280,000 (Mkn 421), 417,000 (3C273), and 255,000 (PKS2155–304) sec was accumulated. The data were processed with custom software written at Columbia, whose main features have meanwhile been incorporated into the standard SAS package. For the actual details of the analysis we refer to Rasmussen et al. (2002), since they don't really matter for the discussion below.

Figure 1 shows the RGS spectra of Capella, Mkn 421, 3C273, and PKS2155–304 in the 18–26 Å band, with the AGN spectra normalized to an empirical continuum model (without interstellar absorption). The Capella spectrum, processed with the identical software, is displayed to provide a 'calibration-independent' wavelength scale (not that the standard SAS wavelength calibration can not be trusted (den Herder et al. 2001), but directly comparing the AGN data to the strongest emission line source provides a striking, simple way to make the point that uncertainties in the absolute wavelength scale don't affect our discussion of the absorption features). Immediately visible by eye in the AGN spectra are three strong O VII resonance absorption lines at 21.60 Å. Weaker O VIII Ly α absorption at 18.97 Å is visible in 3C273 and PKS2155–304. The absorption edge at 23.1 Å is the O K edge, due mostly to oxygen absorption in the instrument (de Vries et al. 2002; this feature has since been incorporated in the standard spectrometer response

matrix), while the absorption line at 23.50 \AA is the $1s - 2p$ line in neutral atomic oxygen in the interstellar medium (Paerels et al. 2001). The absorption feature at 23.35 \AA is its analogue in oxygen-bearing molecules in the instrument. Other parts of the spectrum were searched, but no significant astrophysical absorption was found other than neutral Ne K and Fe L interstellar absorption; specifically, there is no evidence for Ne IX resonant absorption at 13.447 \AA , with upper limits to the equivalent width of $\lesssim 5 - 10 \text{ m\AA}$. Note that no absorption feature is visible at 20.02 \AA in PKS2155–304, where Fang et al. (2002) claim a redshifted O VIII Ly α feature in the *Chandra* LETGS spectrum. In the LETGS, the equivalent width of the redshifted O VIII line is similar to the equivalent width of the redshift zero O VII resonance line. The superior statistics in the RGS spectrum, in which the O VII line is easily detected, implies that the LETGS O VIII feature must be ascribed to a systematic or statistical fluctuation.

The measured properties of the O VII absorption lines are as follows. The redshifts are all consistent with zero ($|\Delta v| < 200 \text{ km s}^{-1}$). The lines are not resolved in Mkn 421 and 3C273 (velocity width $\lesssim 300 \text{ km s}^{-1}$ FWHM); there may be some resolved velocity structure in PKS2155–304, the exact nature of which depends on the detailed satellite aspect solution. Inferred column densities are $N_{\text{O VII}} \approx 0.5 - 1 \times 10^{16} \text{ cm}^{-2}$, $N_{\text{O VIII}} \approx 0.3 \times 10^{16} \text{ cm}^{-2}$ (and an upper limit of $N_{\text{O VIII}} < 0.1 \times 10^{16} \text{ cm}^{-2}$ in Mkn 421).

These results are consistent with the detections of O VII and O VIII $z = 0$ resonance absorption in the *Chandra* LETGS spectrum of PKS2155–304 (although the Ne IX $\lambda 13.45 \text{ \AA}$ absorption is not confirmed), but they now extend to three very different directions on the sky, and have much higher statistical significance, which, in the case of PKS2155–304, may already allow a hint of velocity substructure to be detected. Nicastro et al. interpret their result by requiring that the O VI, O VII, and O VIII absorption towards PKS2155–304 arises in a single-phased medium. The coexistence of these three oxygen ions then requires that the medium be photoionized, rather than be in collisional equilibrium. Since the intensity of the ionizing radiation field is known (it is the extragalactic soft X-ray background), this places a constraint on the density of the medium. This results in a very low density ($n \sim 6 \times 10^{-6} \text{ cm}^{-3}$), and, given the measured oxygen column densities, a linear extent of order $l \sim 3(Z/0.3Z_{\odot})^{-1} \text{ Mpc}$. From these constraints, Nicastro et al. conclude that we must be seeing absorption along the long direction of a filament in the WHIM.

We think it is more plausible that the O VI absorption instead arises in a separate component, either a separate phase of the medium, or in a physically distinct absorber much closer to the Galaxy. Column densities of order $N_{\text{O VI}} \sim 10^{14} \text{ cm}^{-2}$ have been measured in the Galaxy and the Galactic Halo (Jenkins 1978), not much below the measured column towards PKS2155–304. If we drop the O VI from the absorber, the O VII and O VIII bearing medium can still be in collisional equilibrium, be at higher density, and have much smaller linear extent. With only measured column densities, we can constrain only the product of density and size. But if we combine our result with the diffuse O VII and O VIII emission line intensities measured with the X-ray Quantum Calorimeter rocket flight experiment (McCammon et al. 2002), we can obtain rough separate constraints on density and size separately, since the line intensities scale as $n^2 l$. We treat the emission line intensities as upper limits to the intensity arising in the O VII and O VIII absorbing gas, since an unknown fraction of the line emission probably arises in our Galaxy or its halo. A finite fraction of the absorption we measure is of course also associated with this local gas; the Local Bubble probably contributes no more than $N_{\text{O VII}} \sim 10^{15} \text{ cm}^{-2}$, but one medium-aged SNR could conceivably contribute 10^{16} cm^{-2} . We have no independent constraints on this foreground absorption, and therefore proceed on the assumption that most of the absorption arises outside our Galaxy. Combining the absorption and emission constraints, we find that the absorbing medium has a density $n \lesssim 2 \times 10^{-4} \text{ cm}^{-3}$, and linear scale $l \gtrsim 0.15 \text{ Mpc}$ (assuming an oxygen abundance 1/3d of solar). It is therefore most likely the intragroup medium of our Local Group. From the O VII/VIII ionization balance (assumed to be collisional, the density is too high to be affected by photoionization by the XRB), we infer an electron temperature of $kT_e \approx 200 - 300 \text{ eV}$, consistent with the value for the virial temperature of the Local Group estimated from Local Group galaxy kinematics (Peebles 1995). The implied total gas mass is, unfortunately, not well constrained by these sparse data ($M_{\text{gas}} \gtrsim 5 \times 10^{10} M_{\odot}$). We also point out that the upper limit to the velocity broadening of the O VII lines we measure ($\Delta v \lesssim 300 \text{ km s}^{-1}$ FWHM) probably by itself puts limits on the linear size of the absorber—a truly intergalactic filament of linear extent $\sim 10 \text{ Mpc}$ viewed along the long direction would probably exhibit a significant velocity broadening due to the expansion of the Universe, of amplitude $\sim 700(l/10 \text{ Mpc})h_{70} \text{ km s}^{-1}$, depending on the degree to which the velocity field in the long direction has been affected by gravitational acceleration.

The implications are exciting (apart from finally having detected the long sought-for hot gas in our Local Group! cf. Kahn & Woltjer, 1959). If we can detect our Local Group in absorption, and the Local Group is relatively low mass ($M_{\text{virial}} \sim 5 \times 10^{13} M_{\odot}$, Peebles 1995) and is dominated by spirals, then we should be able to detect other, similarly low-mass groups in absorption, in spectra of similar quality.

We are also probably very close to detecting, or place significant constraints on, truly intergalactic absorption. The RGS datasets show no obvious oxygen absorption features at finite redshifts, which places rough upper limits on column densities of $N_{\text{O VII, VIII}}(z > 0) \lesssim 5 \times 10^{15} \text{ cm}^{-2}$. Recent calculations predict a density of $dN/dz \approx 5 - 10 \text{ O VIII}$

absorption systems per unit redshift with a column density above this limit (Perna & Loeb 1998; Hellsten, Gnedin, & Miralda-Escudé 1998; Fang & Canizares 2000; Fang, Bryan, & Canizares 2002; see also Xavier Barcons' contribution to these proceedings). The cumulative redshift interval sampled by these three spectra is approximately $\Delta z = 0.31$, so that we should expect to detect of order one absorption system in this data at this limit. With just a few more deep spectra extending out to redshifts of a few tenths, we should either find the first unambiguous detection, or start to place significant constraints on the cosmic density of diffuse O VII and O VIII bearing gas. This sounds easier said than done, of course: with the three sources discussed above, plus the very deep *Chandra* LETG/ACIS spectrum of H1821+643 we have picked the ripest fruit—it will be difficult to reach the required sensitivity on the next, weaker sources on the list of suitable targets.

3. Oxygen Emission Spectroscopy of the IGM

Considering the emission from the intergalactic medium, we enter the realm of (informed) speculation, because, apart from a few possible detections of emission from especially overdense filaments, no experimental data exist. It will be very difficult to detect the WHIM in emission, but such measurements are important if we want to reach a full characterization of its properties. Absorption spectroscopy-only studies will require many sightlines to reach an adequate sampling, and will be plagued by uncertainties in ionization balance and especially abundances. Without the aid of hydrodynamic simulations, we cannot translate the column densities into true space densities, linear sizes, and masses: a replay of the evolution of the study of the Ly α forest.

For the purpose of discussing the emission from the intergalactic medium, the critical fact is its extremely low average density. The average baryon density is $\langle n_b \rangle = 2.2 \times 10^{-7} \text{ cm}^{-3}$ for $\Omega_b h_{70}^2 = 0.04$, and the average overdensity of the WHIM at zero redshift, as found from simulations, is $\delta_{\text{WHIM}} = 10 - 30$ (Cen & Ostriker 1999). The other important characteristic is the very large range in density of the medium. The density distribution found in simulations is approximately Gaussian in $\log n$, with a width of order $\Delta \log n \approx 1$, so that the clumping factor is about $C \equiv \langle n^2 \rangle / \langle n \rangle^2 \approx 100$. At any given density, the material spans a wide range in temperature, reflecting the past thermodynamical history of heating by gravitational collapse; the average temperature at the average density is of order $T_e \sim 2 - 4 \times 10^6 \text{ K}$. Nothing is known with certainty about the metal abundances of the WHIM, except that the average metallicity in the high redshift Ly α forest is very low ($Z/Z_\odot \approx 10^{-2}$; Cowie et al. 1995), and the average abundance in the intragroup medium of small groups at the current epoch is suprisingly high ($Z/Z_\odot \sim 0.1 - 0.3$). The simulations by Cen et al. (2001) include a parameterized metallicity source, and, not suprisingly, they find that the metallicity is very strongly density-dependent, reflecting the nonlinear dependence of star formation and nucleosynthesis processing rate on density. Very little is known about dispersal (Aguirre et al. 2001).

The emission from this medium is dominated by thermal bremsstrahlung continuum plus collisionally excited atomic line radiation (the power balance at $3 \times 10^6 \text{ K}$, for 0.1 solar metallicity, is such that about 50% of the power comes out in metal emission lines, with $\sim 5\%$ of the total in the oxygen K shell lines); recombination emission contributes very little (see below). Since the emissivities for these processes all scale as n^2 , the sensitivity is weighted heavily towards the detection of rare high overdensities. In terms of the total mass, these regions only represent the tip of the iceberg, and we would have to reach something like the median overdensity in order to account for at least half the mass in the WHIM. It will be very difficult to uniquely detect the WHIM using broad-band X-ray photometric observations: at low spectral resolution, the point source contribution, foreground Galactic and Local Group emission, and particle background cannot be distinguished. The contribution from point sources can be taken care of with sufficiently high spatial resolution, but the diffuse foreground and particle background remain. And even with deep imaging, integrating over the WHIM emission from a finite range in redshift will lower the contrast in the images (*e.g.* Croft et al. 2001). The contrast can be dramatically enhanced by employing spatially resolved spectroscopy of the line emission from the WHIM, which suppresses the spectrally featureless particle background and remaining point source contribution (which also has a smooth spectrum), and separates out the local foreground. This also produces a true 3D map, which allows a proper separation of the WHIM from gas in virialized objects (groups and clusters). We therefore estimate the metal line contribution to the emission. Due to its likely high relative abundance, we concentrate on oxygen emission.

Since the densities are very low, it is important to consider the likely ionization balance of the metals in the WHIM with some care. Taking oxygen as the standard case, the collisional ionization timescale is (see for instance Mewe 1999):

$$t_{\text{ion, collisional}} \sim 10^{11} (n_e / 10^{-7} \text{ cm}^{-3})^{-1} \text{ yr} \quad (1)$$

assuming $T_e = 4 \times 10^6 \text{ K}$, which is high; the collisional ionization timescale increases exponentially with decreasing temperature. Most gas does not reach collisional ionization equilibrium over a Hubble time. Instead, as is now commonly realized, the rate of photoionization in the intergalactic radiation field exceeds the collisional rates. Using the intensity

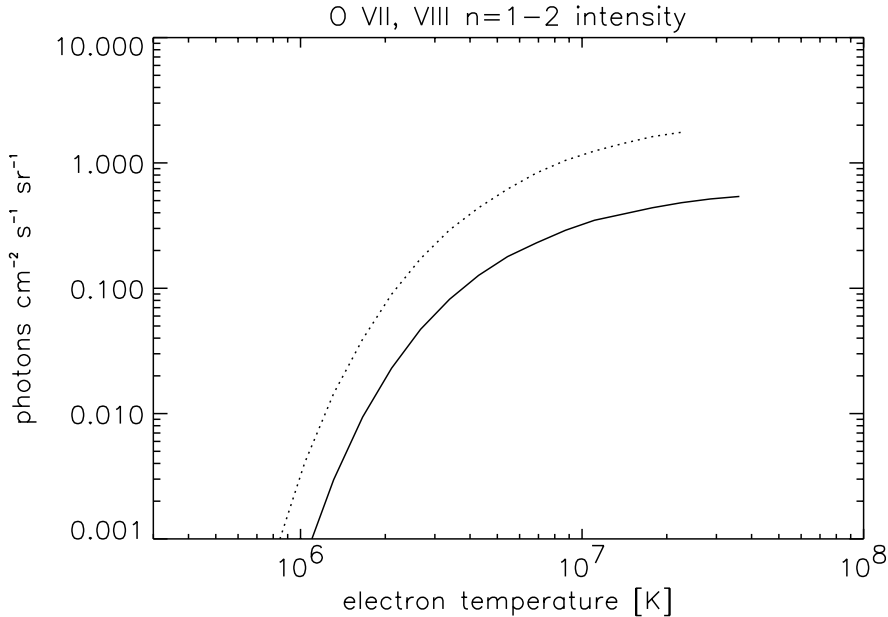


Fig. 2. Average photon count rates from the WHIM in the O VII triplet (dotted line) and O VIII Ly α (solid line) lines, as a function of electron temperature. See text for explanation.

of the soft X-ray background as measured in the *ROSAT* All-Sky Survey, and extrapolating the spectrum measured around 1–2 keV to lower energies to find the extragalactic component, the timescale for photoionization of the He-like to the H-like species of an atom of nuclear charge Z is

$$t_{\text{ion, photo}} \sim 10^9 (Z/8)^{2.8} \text{ yr}, \quad (2)$$

so that photoionization dominates below densities $n_e / \langle n_e \rangle \sim 100$. The timescale for recombination to the H- or He-like charge states is very long:

$$t_{\text{rec}} \sim 3 \times 10^{11} (Z/8)^{-2} (n_e / 10^{-7} \text{ cm}^{-3})^{-1} (T_e / 4 \times 10^6 \text{ K})^{0.75} \text{ yr}, \quad (3)$$

and the metals in the lower-density gas may not be in ionization equilibrium. This is a peculiar state: the metals in the WHIM are highly photoionized, possibly out of equilibrium, and mechanically heated to temperatures of order a million degrees (well above the photoionization equilibrium temperature).

The average line intensity scales very roughly as

$$\langle I \rangle \sim \frac{1}{4\pi} \langle n_e^2 \rangle l \cdot A \cdot f_i g(T_e) = \quad (4)$$

$$= \frac{1}{4\pi} C \langle n_e \rangle^2 l \cdot A \cdot f_i g(T_e) \text{ photons cm}^{-2} \text{ s}^{-1} \text{ sr}^{-1}, \quad (5)$$

with A the elemental abundance, f_i the fractions of atoms in the relevant ionization state, l the path length, C the clumping factor, and $g(T_e) \equiv \langle \sigma(v)v \rangle$ the thermal average of the collisional excitation cross section $\sigma(v)$ times the electron-ion velocity v . The average should really be carried out explicitly over redshift as well, since the WHIM rapidly evolves at small redshift. For the O VIII Ly α and O VII resonance lines, a very rough estimate for the rate is plotted as a function of electron temperature in Figure 2. We have assumed one-tenth solar abundance, $f_i = 0.5$ for both ions (the ionization fractions have to be calculated from the photoionization balance and depend mostly on density rather than on electron temperature; strictly speaking, f_i should have been taken inside the average for the density), and $l = 1/3 \cdot c/H_0$, with H_0 the Hubble constant.

To figure the count rate in any given instrument, these rates are multiplied by the 'grasp', the product of field of view and effective area. To establish a point of reference, we estimate the line count rates in the *XMM-Newton* PN camera. The effective area is about 1000 cm² at 500 eV, and a circular FOV of radius 20 arcmin corresponds to 10⁻⁴ sr, and so the total rate is about 10⁻² photons s⁻¹, not a small number. However, since the energy resolution is of order 1/5th at 500 eV, most of the counts out to redshifts of a few tenths end up in at most a few spectral resolution elements, in which the background will be very high. In careful analysis of deep images, the PN may see

the integrated emission from the WHIM, but we will not be able to tell where it is. Over time, a few high overdensity filaments will probably show up, though, simply by imaging in the soft band. *XEUS-II*, by coincidence, will have a similar grasp with the cryogenic spectrometer ($G \sim 7.5 \times 10^{-2} \text{ cm}^2 \text{ sr}$), but with much higher spectral resolution. At $\Delta E = 1 \text{ eV}$, the emission line contrast increases by almost two orders of magnitude compared to the PN, sufficient to produce large spectral contrast. But *XEUS*'s field of view will be very small, and unless a very large amount of time is devoted to observing a contiguous field, of order something like a square degree, with, say 10^4 sec exposure per field, the WHIM will primarily show as a few isolated background emission lines in every deep field, filling the field of view; this would still make for a valuable statistical description of the WHIM.

An efficient search could be conducted with a dedicated experiment. With a $1 \times 1 \text{ deg}$ field of view, and 100 cm^2 effective area, we have a grasp of order $10^{-2} \text{ cm}^2 \text{ sr}$. Since we are interested only in soft photons ($E < 1 \text{ keV}$), the graze angle on the optics can be large, and the focal length short, making for a relatively small detector. Matching the spectral resolution to the expected angular scale of condensations in the WHIM (of order an arcminute) produces $\Delta z \sim 3 \times 10^{-5}$ at $z = 0.1$, which implies a resolution narrower than the thermal Doppler width! Cryogenic spectrometers can perhaps be pushed to a resolution of order $\Delta E \sim 1 \text{ eV}$, corresponding to a resolution 1/500 at 500 eV, which undersamples the redshift dimension by a factor of order 60. More realistically, however, the peculiar velocity field in the WHIM due to gravitational motion is probably of order a few hundred km s^{-1} , so that redshift space distortions set the much less stringent resolution limit of $\Delta v/c \sim 10^{-3}$ if no loss of spatial information is our only criterion (at higher resolution one could measure the 'X-ray Kaiser effect'! [Kaiser 1987]). At $\Delta E \sim 1 \text{ eV}$, the spatial dimension would be undersampled by a mild factor ~ 2 . Diffractive options are probably ruled out altogether for any finite field of view: aberrations associated with an odd number of bounces severely limits either spectral resolution or field of view.

At the meeting, Eugene Churazov gave an inspired talk (with exquisite references to 19th century American literature), which provides an important insight: if we can spatially resolve most of the point sources that provide the diffuse intergalactic X-ray continuum radiation field, we will see the contribution of photoexcitation (or resonance scattering) to the line emission from the IGM. For the parameter values we have been discussing, the photoexcitation contribution is not small compared to the collisional excitation rate (Churazov et al. 2001). This raises the following exciting possibility: if we could observe the fully resolved O VII He-like triplet from a given region, we could simultaneously measure the emission measure (from the intercombination and forbidden transitions), which scales as $n^2 l$, while the relative intensity of the resonance line measures the optical depth across the region, which scales as nl . With a simultaneous measurement of the emission measure and the optical depth, the region can be fully characterized in terms of density and size, and spectroscopy of this kind is fully redundant with separate absorption and emission spectroscopy (*i.e.* we don't have to have a strong background continuum source to measure absorption through the region to break the degeneracy in n and l inherent in either separate absorption or emission spectroscopy). For this to work, one would have to be able to resolve the members of the triplet, which requires $\Delta E \approx 5/(1+z) \text{ eV}$, well within the range of cryogenic spectrometers.

References

- Aguirre, A., Hernquist, L., Schaye, J., Katz, N., Weinberg, D. H., & Gardner, J. 2001, *ApJ*, 561, 521
 Burles, S., & Tytler, D. 1998, *ApJ*, 507, 732
 Cen, R. & Ostriker, J. P. 1999, *ApJ*, 514, 1
 Cen, R., Tripp, T. M., Ostriker, J. P., & Jenkins, E. B. 2001, *ApJ*, 559, L5
 Churazov, E., Haehnelt, M., Kotov, O., & Sunyaev, R. 2001, *MNRAS*, 323, 93
 Cowie, L. L., Songaila, A., Kim, T., Hu, E. M. 1995, *AJ*, 109, 1522
 Croft, R. A. C., Di Matteo, T., Davé, R., Hernquist, L., Katz, N., Fardal, M. A., & Weinberg, D. H. 2001, *ApJ*, 557, 67
 den Herder, J. W. et al., 2001, *A&A*, 365, L7
 de Vries, C. et al. 2002, in preparation
 Fang, T., & Canizares, C. R. 2000, *ApJ*, 532, 539
 Fang, T., Marshall, H., Bryan, G., & Canizares, C. R. 2001, *ApJ*, 555, 356
 Fang, T., Davis, D., Lee, J. C., Marshall, H. L., Bryan, G. L., & Canizares, C. R. 2002a, 565, 86
 Fang, T., Marshall, H. L., Lee, J. C., Davis, D. S., & Canizares, C. R. 2002b, *ApJ*, 572, L127
 Fang, T., Bryan, G., L., & Canizares, C. R. 2002, *ApJ*, 564, 604
 Fukugita, M., Hogan, C. J., & Peebles, P. J. E. 1998, *ApJ*, 503, 518
 Hellsten, U., Gnedin, N. Y., & Miralda-Escudé, J. 1998, 509, 56
 Jenkins, E. B. 1978, *ApJ*, 219, 845
 Kaiser, N. 1987, *MNRAS*, 227, 1
 Kahn, F. D., & Woltjer, L. 1959, *ApJ*, 130, 705
 Kuntz, K. D., Snowden, S. L., & Mushotzky, R. F. 2001, *ApJ*, 548, L119

- Mathur, S., Weinberg, D. H., & Chen, X. 2002, astro-ph/0206121
- McCammon, D. et al., 2002, astro-ph/0205012
- Mewe, R. 1999, in *X-Ray Spectroscopy in Astrophysics*, J. van Paradijs & J. A. M. Bleeker (eds.), 109 (Springer)
- Nicastro, F., et al. 2002, ApJ, 573, 157
- Paerels, F., et al. 2001, ApJ, 546, 338
- Peebles, P. J. E. 1995, ApJ, 449, 52
- Perna, R., & Loeb, A. 1998, ApJ, 503, L135
- Rasmussen, A., Paerels, F., Kahn, S. M., den Herder, J. W., & de Vries, C. 2002, in preparation.
- Savage, B. D., Sembach, K. R., Tripp, T. M., & Richter, P. 2002, ApJ, 564, 631
- Scharf, C. et al. 2000, ApJ, 528, L73
- Tripp, T. M., & Savage, B. D. 2000, ApJ, 542, 42
- Tripp, T. M., Savage, B. D., & Jenkins, E. B. 2000, ApJ., 534, L1
- Wu, X.-P., & Xue, Y.-J. 2001, ApJ, 560, 544



The Local Group WHIM Filament

F. Nicastro¹

Harvard-Smithsonian Center for Astrophysics, Cambridge, MA 02138, USA

Abstract. In this contribution we present the strongest evidence so far, supporting the existence of Warm-Hot Intergalactic Medium (WHIM) filaments in the local Universe. In particular we show that our own Local Group is embedded in one of these filaments. Such filament is detected along the majority of the lines of sight against *Chandra* and FUSE spectra of background AGNs through weak $z \sim 0$ resonant absorption from highly ionized metals (OVI, OVII, OVIII and NeIX). Based on combined X-ray and UV data from the line of sight to PKS 2155-304, we estimate a temperature of $\log T \simeq 5.8$, a baryonic density of a $n_b = 4 - 6 \times 10^{-6} \text{ cm}^{-3}$, an equivalent hydrogen column density of $N_H = 4.5 \times 10^{19} [O/H]_{0.3\odot}^{-1} \text{ cm}^{-2}$, and so a size of 2-4 $[O/H]_{0.3\odot}^{-1}$ Mpc. Assuming a transverse size of 1 Mpc, this implies a total baryonic mass of $\sim 0.6 - 2 \times 10^{12}$ solar masses, comparable with the mass of the two main virialized components of the Local Group, M 31 and the Milky Way, and sufficient to stabilize the local group.

1. Introduction

The number of detected baryons in the “virialized Universe” at $z \lesssim 2$ (i.e. stars, neutral hydrogen associated with galaxies, and X-ray emitting gas in clusters) is far smaller than predicted by standard big bang nucleosynthesis (e.g. Burles and Tytler, 1998). It is also known since 1959 (i.e. Kahn & Woltjer, 1959) that, locally, more than $1.5 \times 10^{12} M_\odot$ are needed to dynamically stabilize our own Local Group.

A possible and intriguing solution to this problem, known as the “missing baryons” problem, is offered by recent hydrodynamical simulations. These predict that the majority of the total baryonic matter in the local ($z \lesssim 2$) Universe be concentrated in non-yet virialized filamentary structures of highly ionized gas (the so called Warm-Hot Intergalactic Medium, WHIM, e.g. Cen & Ostriker, 1999; Hellsten et al., 1998; Davé et al., 2001). Similar predictions have been recently made for our local Supercluster Environment (Kravtsov et al., 2002; Klypin et al., 2001).

The detection and study of this important component is needed for the proper understanding of large and small scale structures in the Universe. However, while X-ray emission from the virialized density peaks of the ICM and ISM has been detected and intensively studied in X-rays, the predicted highly ionized gas in the WHIM has been poorly studied so far, due to instrumental limitations. The low density of the WHIM leads to low emissivity, so that studies of the WHIM in emission are a formidable challenge. However, absorption depends only on the total column density of the medium, not on density, and background light sources in the form of quasars (Aldcroft et al., 1994) and gamma-ray bursts (Fiore et al. 2000) are readily available.

The WHIM is too hot for strong absorption to be found other than in the far-ultraviolet (FUV, OVI $\lambda 1031.93$) or soft X-ray bands (CVI, OVII, OVIII, NeIX, in the $\lambda = 10 - 40 \text{ \AA}$ range). The lack of appropriate, sensitive instruments prevented any candidates for such absorption being found until last year. The current candidates though are at almost zero redshift, and so it is hard to distinguish between material local to our own Milky Way galaxy, and material in the local filament of intergalactic gas that our galaxy is embedded in.

The first clear detection of associated OVI (FUV) and OVII-OVIII and NeIX (X-rays) absorption at $z \sim 0$ along the line of sight to the blazar PKS 2155-304, has been recently published (Nicastro et al., 2002a, N02a). In that paper we presented physical evidences supporting the identification of this absorbing medium, with a diffuse warm-hot gas in our Local Group (N02a). At the time this conference was held, this, and 2 more cases for which X-ray ionized absorption at $z \sim 0$ had been found (see F. Paresi’s contribution in this conference proceedings), were the only spectroscopic evidence supporting the identification of this absorbing medium with gas in the Local Group. Since then, however, we started a detailed study of the spatial and dynamical distribution of the ubiquitous High Velocity

(HV) and Low Velocity (LV) OVI absorbers discovered by FUSE (e.g. Savage et al., 2000, Sembach et al., 2002), in an effort to better constrain the location of this medium. Our conclusion is that while the LV-OVI are disk or halo clouds, at rest in the Local Standard of Rest (LSR), the vast majority of HV-OVI are instead at rest in the Local Group Standard of Rest. This evidence nicely support and complement the X-ray findings and so strongly implicate that the HV FUV lines and the X-ray lines at $z \sim 0$ are due to absorption by a primordial WHIM filament pervading our Local Group (Nicastro et al., submitted to Nature, N02b).

In this contribution, for the first time, we combine all evidence together, in an attempt to provide a clear and coherent picture of the current status of our knowledge of the local WHIM.

2. The Dynamics of the OVI Absorbers

FUSE observations of 11 Active Galactic Nuclei (AGN) showed two types of $z \sim 0$ OVI absorbers, similar to those observed in PKS 2155-304: (1) Low Velocity OVI clouds ($|v_{LSR}| < 100 \text{ km s}^{-1}$; Savage et al., 2000; Wakker et al., 2001, Savage et al., 2001; Howk et al., 2002; Hoopes et al., 2002); and (2) High Velocity OVI clouds ($|v_{LSR}| > 100 \text{ km s}^{-1}$, Sembach et al., 2000; Sembach et al., 2001, Heckman et al., 2002). To further investigate the nature of these absorbers we have examined a larger sample of AGNs having publicly available data in the FUSE archive, allowing us to clearly identify the HV-OVI component with diffuse gas in the Local Group.

2.1. The Sample

After a selection in signal-to-noise ratio, the final sample contains 54 different lines of sight with 45 detected OVI absorbers at $z \sim 0$ (83 % of the total sample), at our detection thresholds. Seven out of the remaining 9 objects have poor quality FUSE spectra, with detection threshold of $EW \geq 200 \text{ m}\text{\AA}$. Of these 45 lines of sight, 38 show LV-OVI absorption (70 % of the sample), and 32 (59 % of the sample) show HV-OVI components, with 22 objects showing both. Only 3 lines of sight show multiple LV or HV absorption.

2.2. OVI Velocity Distribution in the LSR

The OVI velocity distribution in the LSR (Fig. 1) shows a narrow peak between $\pm 100 \text{ km s}^{-1}$ (LV-OVI: dashed histogram) with a much broader, roughly symmetric distribution (Fig. 1, solid histogram) extending to $\pm 550 \text{ km s}^{-1}$ (HV-OVI). The bimodality of this distribution suggests that LV- and HV-OVI systems belong to two different populations of absorbers, as previously pointed out by Savage et al. (2000), and Sembach et al. (2000).

2.3. Spatial Distribution and Velocity Segregation of LV- and HV-OVI in the LSR

We note that “velocity segregation” of a homogeneous population of objects in a given reference frame suggests the presence of an average bulk motion of the objects in that reference frame. On the other hand, “velocity randomization” in a given reference frame (i.e. no segregation), suggests that the objects are on average at rest in that velocity frame.

A plot in Galactic coordinates of the LSR velocity distributions for the LV- (Fig. 2a) and HV-OVI (Fig. 2b) absorption systems shows that: (a) the HV-OVI absorbers are highly segregated in velocity space in the LSR, splitting the sky in two distinct halves (Fig. 2a), while (b) the LV-OVI are not velocity-segregated, and appear distributed randomly (FIG. 2b).

The hemisphere with $0^\circ \leq l \leq 180^\circ$ contains only HV-OVI lines with negative velocities, while the other hemisphere contains mostly HV-OVI absorbers with positive LSR velocity (Fig. 2a). There are three exceptions, (at $l \sim 254^\circ$, $b \sim -65.8^\circ$, $l \sim 202^\circ$, $b \sim -21.1^\circ$, and $l \sim 225^\circ$, $b \sim -83.2^\circ$). Of these, the first two lines of sight, however, contain the only two negative HV-OVI systems in our sample with LSR velocities very close to the threshold velocity of $|v_{LSR}| = 100 \text{ km s}^{-1}$, and so may well belong to the LV-OVI population. The remaining lies at very high latitude (where the concept of longitude becomes meaningless).

The systematic LSR velocity distribution of HV-OVI is strikingly similar to that shown by the Compact High Velocity Clouds of hydrogen (CHVCs, Braun & Burton, 1999), and is consistent with matter that is either: (1) counter-rotating, with respect with the Galaxy disk rotation, on orbits external to the sun’s orbit, (2) at rest in the Galactic halo or (3) at rest in the intergalactic space surrounding the Galaxy. The range of radial LSR velocities of the HV-OVI ($100 < |v_{LSR}|^{HV} < 550 \text{ km s}^{-1}$) greatly exceeds the range of observed radial velocities in the Galactic disk or halo, suggesting that the Galaxy related options [(1) and (2)] are unlikely. Moreover some of the HV-OVI velocities exceed a plausible measure of the escape velocity from the Milky way (Oort, 1926), as observed in CHVCs (Braun & Burton, 1999; de Heij, et al., 2002; Blitz, 2002).

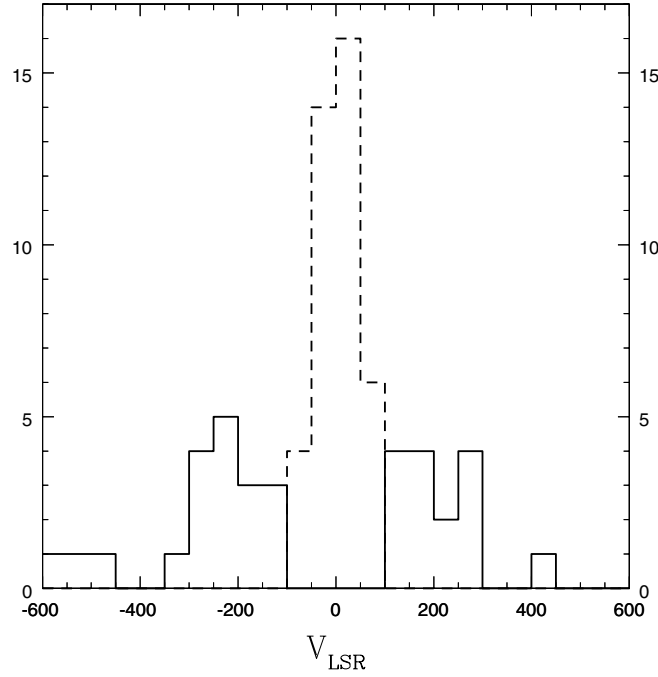


Fig. 1. Histogram of the HV-OVI (solid line) and LV-OVI (dashed line) velocity distributions in the LSR.

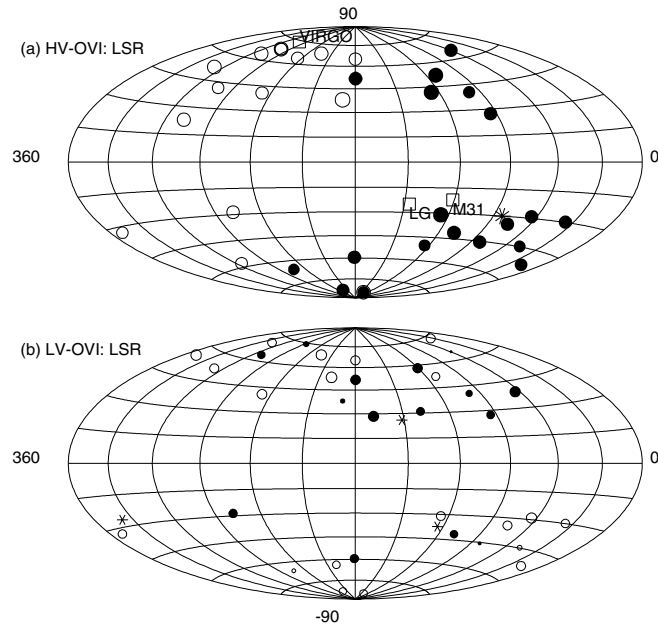


Fig. 2. Aitoff plots of the LSR velocity distributions for (a) the HV-OVI and (b) the LV-OVI absorption systems. In both panels filled circles correspond to negative velocities, while open circles correspond to positive velocities. In the upper panel the open squares indicate the position of (i) the barycenter of the Local Group (LG), (ii) M 31, and (iii) the Virgo cluster, as labeled. The star, instead, marks the position of the barycenter of the distribution. In the lower panel stars indicate absorbers effectively at rest in the LSR (i.e. $|v_{LSR}|^{HV} < 20 \text{ km s}^{-1}$, the FUSE resolution at 1032 \AA).

Finally, clouds in the Galaxy's halo, and at distances lower than $\sim 100 \text{ kpc}$ from the Galaxy's center, would be dynamically bound to the Galaxy's potential well, and so would probably be rotating on random orbits around the galaxy's center, as Globular Clusters do. This is clearly shown in Figure 3, where we show the aitoff plot of the spatial and velocity sign distributions of Globular Clusters with distance larger than 10 Kpc from the Galaxy's center in the LSR: no obvious velocity segregation is visible. The peculiar velocities of Globular Clusters along their orbits tend to

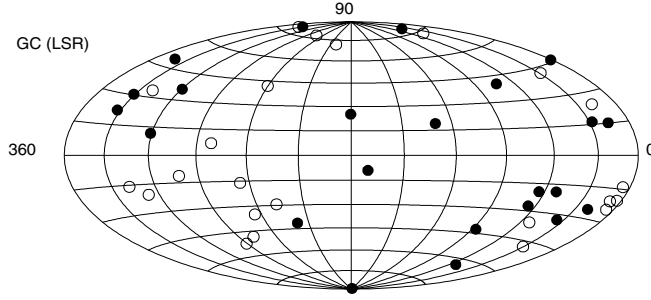


Fig. 3. Aitoff plots of the LSR velocity distributions of Globular Clusters with Galactocentric distance larger than 10 kpc. Symbols are the same as in Figure 2.

Table 1. Average (v, l, b) vectors, and associated uncertainties, for the LV- and HV-OVI absorbers, in the LSR, GSR and LGSR.

OVI Systems	Reference Frame	$\langle v \rangle$ km s ⁻¹	$\langle l \rangle$ deg.	$\langle b \rangle$ deg.
HV	LSR	125 ± 15	276 ± 10	30 ± 21
HV	GSR	60 ± 10	280 ± 18	38 ± 41
HV	LGSR	25 ± 10	293 ± 35	32 ± 78
LV	LSR	5 ± 3	333 ± 39	11 ± 62
LV	GSR	25 ± 17	90 ± 8	-11 ± 27
LV	LGSR	71 ± 12	93 ± 7	-17 ± 14

randomize the apparent symmetry induced in the LSR by the circular motion of the Sun in the Galaxy for matter effectively at rest in the halo. We then conclude that an intergalactic origin of the HV-OVI absorbers is more consistent with the data.

2.4. Spatial Distribution and Velocity Segregation of LV- and HV-OVI in the GSR and LGSR

The spatial distribution of the LV- and HV-OVI velocity signs in the LSR (Figure 2) strongly suggest that (a) the LSR is not the rest frame system for the HV-OVI clouds, while (b) the LSR is the rest frame for the LV-OVI absorbers.

To further test this hypothesis, we searched for velocity reference frames in which (a) the velocity of the HV-OVI absorbers appears randomized, (b) the velocity of the LV-OVI absorbers appears segregated, and (c) the amplitude of the average velocity vectors of LV- and HV-OVI is minimized. To compute the average velocity vector (v, l, b) in a given velocity reference frame, we projected (v, l, b) onto three Cartesian axis (X, Y, Z) , averaged the Cartesian components, and transformed back $(\langle X \rangle, \langle Y \rangle, \langle Z \rangle)$ into $(\langle v \rangle, \langle l \rangle, \langle b \rangle)$. Standard deviations for $(\langle v \rangle, \langle l \rangle, \langle b \rangle)$ were computed in the Cartesian space (i.e. $(\sigma_{\langle X \rangle}, \sigma_{\langle Y \rangle}, \sigma_{\langle Z \rangle})$) and then propagated in quadrature to obtain uncertainties on $(\langle v \rangle, \langle l \rangle, \langle b \rangle)$. Table 1 shows the average velocity vectors in the LSR, the Galactic Standard of Rest (GSR), and the Local Group Standard of Rest (LGSR). Translations to these systems have been performed first transforming LSR velocities into Heliocentric velocity (using the velocity conversion factor stored in the header of the FUSE data files) and then using the Heliocentric-to-GSR and Heliocentric-to-LGSR apex vectors given in the the NASA/IPAC Extragalactic Database (NED) velocity correction calculator¹.

If the HV-OVI absorbers were clouds of gas in the Galaxy's halo, one would expect the amplitude of the average velocity vector to be a minimum and close to zero in the GSR frame, and increase again for translation into the LGSR, where it should have amplitude and direction consistent with the motion of our Galaxy in the direction of the barycenter of the Local Group ($l = 147^\circ$, $b = -25^\circ$; Einasto et al., 1982). This is not observed. On the contrary, the amplitude of the HV-OVI average velocity vector decreases monotonically from the LSR to the LGSR, at which point it is only $\langle |v_{LGSR}|^{HV} \rangle = 25$ km s⁻¹ (Table 1), much smaller than the corresponding velocities in the LSR and GSR, and close to the FUSE resolution (~ 20 km s⁻¹ at 1032 Å). At the same time, the direction of the average vector becomes very poorly constrained (Table 1). Both the low value of the residual motion and the large dispersion in l and b of the average vector (Table 1) suggest that the LGSR is the rest frame of the HV-OVI absorbers. Moreover, the symmetry present in the LSR velocity distribution of the HV-OVI systems (Fig. 2a) disappears in the LGSR (Fig.

¹ http://nedwww.ipac.caltech.edu/help/velc_help.html#notes

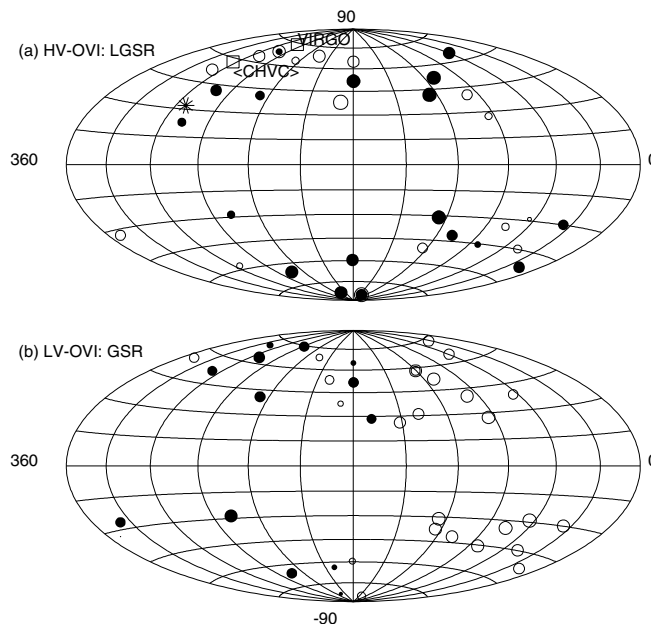


Fig. 4. Aitoff plots of (a) the LGSR velocity distribution of the HV-OVI absorbers and (b) the GSR velocity distribution of the LV-OVI absorption systems. Symbols are the same as in Figure 2.

4a) and instead appears random, again suggesting that the LGSR is a privileged reference frame for the HV-OVI absorbers. **This locates the population of HV absorbers in the intergalactic space of the Local Group.**

By contrast the velocity sign distribution of the LV-OVI absorbers appears strongly segregated in the GSR (Fig. 4b). The symmetry is opposite to that shown by HV-OVI in the LSR (Fig. 2a), with most of the positive velocity segregated in the $0^\circ < l < 180^\circ$ half of the sky. This distribution in the GSR is that expected for OVI clouds of gas orbiting around the center of the Galaxy, following the Galaxy’s disk rotation. Accordingly the amplitude of the average velocity vector of the LV-OVI absorbers has a minimum in the LSR (where it is consistent with zero) and increases monotonically for translations into the GSR and LGSR.

Based on the above evidence we conclude that (a) the LGSR is a privileged reference frame for the HV-OVI absorbers, and so the HV-OVI gas is located in the Local Group, while (b) LV-OVI absorbers are clearly at rest in the LSR, possibly clouds of ionized gas following the galaxy’s disk rotation.

3. Physical State of the Local Group WHIM Filament along the Line of Sight to PKS 2155-304

3.1. OVI-OVIII and NeIX Absorption in the Chandra and FUSE Spectra of PKS 2155-304

The very high quality ($\lesssim 700$ counts per resolution element, at 20 \AA), high resolution ($R \sim 400$ at 20 \AA) Chandra-LETG (“Low Energy Transmission grating”: Brinkman et al., 2000) spectrum of PKS 2155-304 shows absorption by highly ionized species of O and Ne, at redshift consistent with zero (N02a). Figure 5 shows 2 portions of the Chandra-LETG spectrum of PKS 2155-304 binned at a resolution of $0.0125 \text{ \AA}/\text{bin}$ (~ 4 times finer than the effective Chandra-LETG resolution), in which OVII $K\alpha$, OVII $K\beta$, OVIII $K\alpha$ and NeIX $K\alpha$ resonant absorption at $z \simeq 0$ are clearly visible, and labeled. The best fitting continuum-plus-absorption-lines model to this spectrum is also plotted (red solid line), as well as the typical 1-sigma errorbar over the selected wavelength ranges. The resonant absorption lines detected in the Chandra-LETG spectrum of PKS 2155-304 are all very weak, with typical equivalent widths (EW) of the order of 10 m\AA , corresponding to OVII-VIII and NeIX column densities of the order of $5 \times 10^{15} \text{ cm}^{-2}$.

The FUSE (Moos et al., 2000) spectrum of PKS 2155-304 (resolution $R \sim 15000$ at 1032 \AA , about 30 times the Chandra-LETG resolution) shows complex OVI at $z \sim 0$ (Figure 6), clearly structured in at least 2 components: a high velocity OVI component, with LSR centroid at $-135 \pm 14 \text{ km s}^{-1}$, and a stronger low velocity OVI component with LSR centroid at $36 \pm 6 \text{ km s}^{-1}$. The two OVI lines have EW of 137 m\AA (HV-OVI) and 180 m\AA (LV-OVI), and typical $1-\sigma$ errors of $\sim 10 \%$ (see N02a, for details).

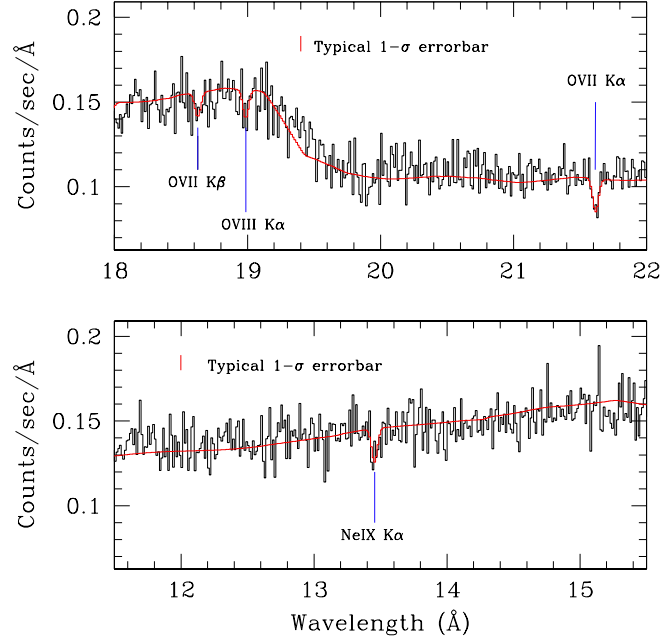


Fig. 5. Two portions of the Chandra-LETG spectrum of PKS 2155-304

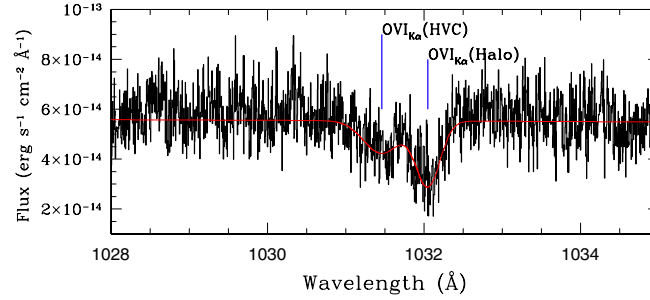


Fig. 6. 1028-1034 Å portion of the FUSE spectrum of PKS 2155-304.

3.2. Curve of Growth Analysis

The two lines of the OVI doublets ($\lambda_{rest} = 1031.9261 \text{ \AA}$ and $\lambda_{rest} = 1037.6162 \text{ \AA}$) in the FUSE spectra of PKS 2155-304 have ratios consistent with their oscillator strength ratios, and so with no saturation. The ratio between the OVII K α and K β lines is also consistent with no OVII saturation, but the large errors in the OVII K β line EW prevent us to unambiguously rule out saturation. A curve of growth analysis of all the detected lines, however, allow us to rule out saturation at $\geq 90 \%$ confidence level. Figure 7 shows the curve of growths for OVI($\lambda 1031.93$), OVII K α , OVIII K α and NeIX K α , built using our resonant absorption code (Nicastro, Fiore & Matt, 1999), for a doppler parameter of $b = 125 \text{ km s}^{-1}$ (the measured value for the total resolved OVI complex in FUSE). Horizontal lines correspond to the maximum possible observed EWs (best fit + 2σ).

From this analysis we conclude that lines are not saturated, and this allow us to apply EWs ratio diagnostics, to estimate the ionization balance in the UV and X-ray absorbers.

3.3. High Density (Galactic) versus Low Density (Extragalactic) Solutions

We distinguish between Galactic and extragalactic solutions, based on the linear size of the cloud along the line of sight, as derived by the ratio between the absorber equivalent hydrogen column and volume densities. The equivalent hydrogen column density depends (other than on metallicity compared to solar) on the gas ionization balance, which, in turn, depends critically on the mechanisms that contribute to the gas ionization. Here we consider collisional ionization as the main process, but allow for the additional contribution of photoionization by the diffuse extragalactic X-ray background. This becomes important only when the ratio between the photon density at the surface of the

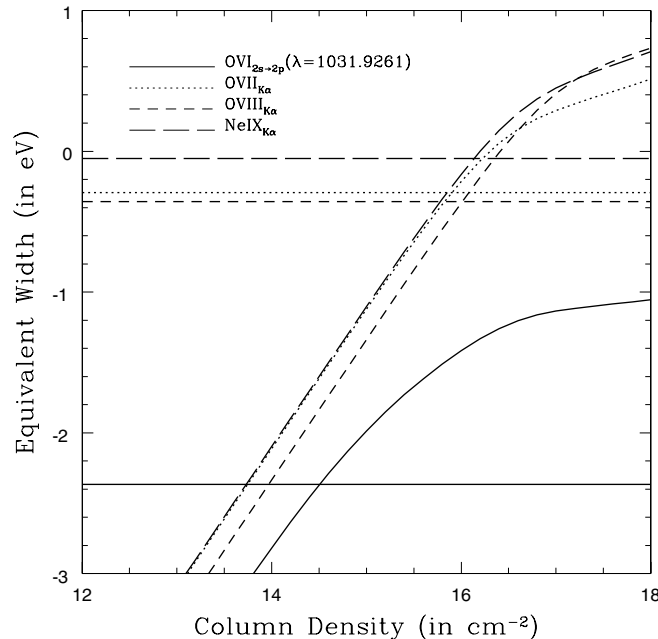


Fig. 7. Curves of Growth for the detected UV and X-ray.

cloud, and the cloud equivalent hydrogen volume density are comparable (i.e. baryonic densities $n_b \lesssim 10^{-4} \text{ cm}^{-3}$ and so ionization parameters $U \gtrsim 0.005$). Solutions that require a significant photoionization contribution, therefore, allow us to simultaneously estimate both the equivalent hydrogen column and volume density in the gas, and so the linear size of the cloud.

3.3.1. No Common UV-X-ray Galactic Solution

The Chandra-LETG resolution ($2\text{-}\sigma$ FWHM $\sim 800 \text{ km s}^{-1}$ at 21.6 \AA) does not allow us to resolve the OVI complex in the OVII, OVIII and NeIX lines, and so to securely associate one of the two OVI components to the X-ray absorber (see Fig. 3 in N02a). We then first searched for a common UV-X-rays solution that accounts for all the measured line EWs. Figure 8 shows ion relative abundance ratios curves built using CLOUDY for pure collisionally ionized gas (i.e. $n_e \gtrsim 10^{-4} \text{ cm}^{-3}$ and so negligible photoionization contribution), for temperatures between $T_e = 10^5 \text{ K}$ and 10^8 K . Superimposed on the equilibrium ionization balance curves are the allowed $2\text{-}\sigma$ intervals for each measured EW line ratio (a unit $[\text{Ne}/\text{O}]_{\odot}$ ratio is assumed to convert from NeIX/OVII EW ratio into NeIX/OVII relative abundance ratio). Clearly no such a solution can be found.

3.3.2. Three-Cloud Galactic Solution

Figure 8 shows that the allowed ranges for the OVII/OVI and OVIII/OVI ratios are too low for a single Galactic solution (involving all the OVI complex and the X-ray lines) to be found at a given temperature. However, UV data indicate that at least two different OVI absorbers, with different dynamics, are absorbing the radiation from PKS2155-304 at $z \sim 0$. We then searched for multi-cloud Galactic solutions looking for the largest possible fraction of OVI EWs, $f(\text{OVI})$, from one of the two lines in FUSE, that can be associated with the X-ray absorbing gas. Since we try to minimize the amount of OVI absorption produced by the X-ray cloud, it is natural to associate the weakest of the two OVI lines in FUSE (i.e. the HV line) with the X-ray absorber.

Figure 9 shows the 90 % confidence size of the allowed region, in the $f(\text{OVI})$ versus T_e plane: at most 25 % of the HV-OVI EW can be produced by the Galactic X-ray absorber in collisional ionization equilibrium at temperatures of $T_e \sim 10^{6.3-6.5} \text{ K}$.

We conclude that at least 3 different Galactic absorbers (i.e. $n_e \geq 10^{-4} \text{ cm}^{-3}$) in collisional ionization equilibrium, and with different apparent dynamics in the LSR, are needed to explain the FUSE and Chandra data of PKS 2155-304: (a) a relatively cold and low velocity cloud producing all the LV-OVI absorption, (b) a hotter and higher velocity cloud

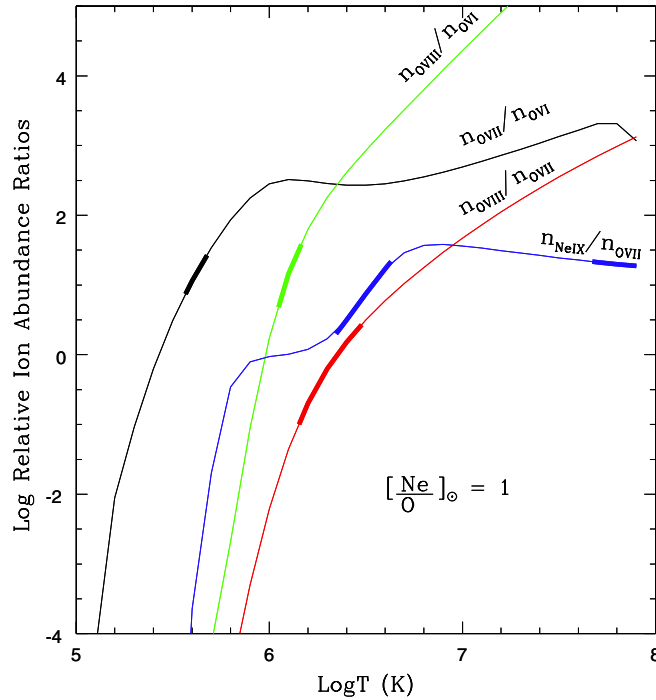


Fig. 8. Expected ion abundance ratio curves for gas in pure collisional ionization equilibrium, and allowed $2\text{-}\sigma$ intervals (thick segments) for each measured EW line ratio (a unit $[\text{Ne}/\text{O}]_{\odot}$ ratio is assumed to convert from NeIX/OVII EW ratio into NeIX/OVII relative abundance ratio).

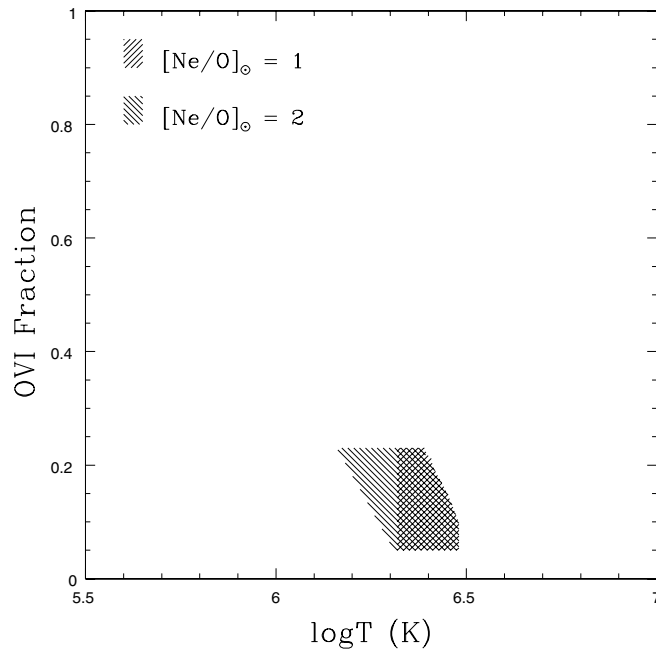


Fig. 9. Maximum fraction of HV-OVI that can be associated with a Galactic X-ray absorber, as a function of the electron temperature in the gas.

producing all the X-ray absorption and at most 25 % of the HV-OVI in FUSE, and (c) a third cloud with temperature similar to that of the LV-OVI cloud, but different dynamics, to produce the remaining ≥ 75 % HV-OVI absorption.

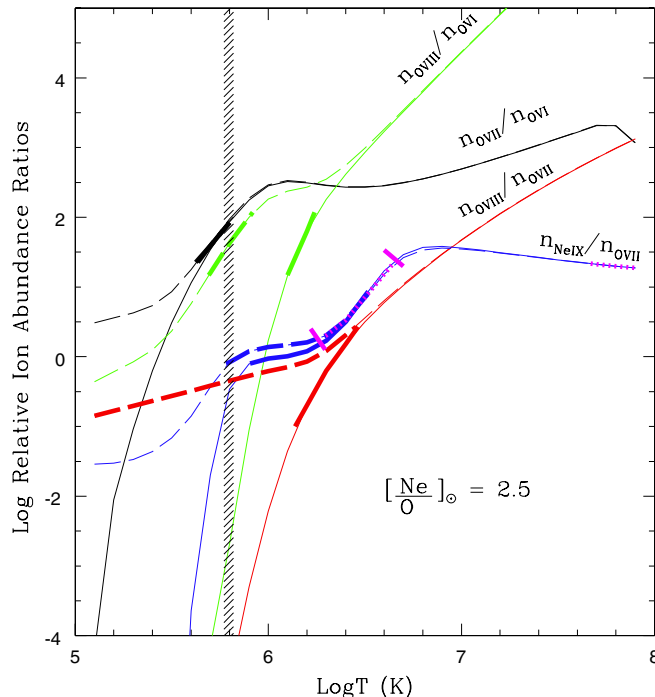


Fig. 10. Expected ion abundance ratio curves for high-density gas in pure collisional ionization equilibrium (solid curve), and low density gas ($n_e \simeq 4 - 6 \times 10^{-6} \text{ cm}^{-3}$; dashed curves). Thick segments on these curves are allowed $2\text{-}\sigma$ intervals for the measured EW line ratios.

3.3.3. Extragalactic Solution

An alternative solution, accounting for both the HV-OVI and the X-ray lines, is found allowing the gas volume density to be lower than $n_e \lesssim 10^{-5} \text{ cm}^{-3}$, and so the photoionization contribution by the diffuse extragalactic X-ray background to become relevant.

Figure 10 shows a plot similar to that shown in Figure 8, except now ion abundance ratio curves for low density gas ($n_e = 4 - 6 \times 10^{-6} \text{ cm}^{-3}$) are also plotted, as dashed curves. The corresponding high-density models (purely collisionally ionized gas) are drawn as solid curve for comparison. As in Figure 8, thick intervals on these curves are the $2\text{-}\sigma$ measured ion abundance ratios. We note that a $[\text{Ne}/\text{O}]_{\odot} = 2.5$ ratio has to be assumed to reconcile the measured strength of the NeIX absorption, relatively to OVII, with models. The vertical dashed black interval represent a possible solution, corresponding to a temperature of $T_e \simeq 10^{5.8} \text{ K}$.

This solution gives an equivalent hydrogen column density of $N_H = 4.5 \times 10^{19} [\text{O}/\text{H}]_{0.3\odot}^{-1}$, and so a linear size along the line of sight (assuming homogeneity) of $D = 2 - 4 [\text{O}/\text{H}]_{0.3\odot}^{-1} \text{ Mpc}$. This definitely locates the absorber in the intergalactic space surrounding our Galaxy (in the Local Group).

4. Discussion and Conclusions

The evidence presented in this contribution offers a self-consistent picture of the local high-ionization absorption observed along the majority of the lines of sight with FUSE, in OVI, and in few X-ray cases (all the lines of sight for which Chandra or XMM collected sufficient signal to noise spectra, so far). We propose that our own Galaxy and the entire Local Group are indeed embedded in a tenuous warm-hot medium, possibly shock-heated at temperature of about 10^6 K , and experiencing a non-negligible photoionization contribution by the diffuse X-ray background, due to its extremely low density. The density of this gas, as measured along the line of sight to PKS 2155-304, would be only about 20-40 times the average density in the Universe. Its total baryonic mass (assuming a transverse size of $1 \times [\text{O}/\text{H}]_{0.3\odot}^{-1} \text{ Mpc}$) would be of $0.6 - 2 \times 10^{12} M_{\odot}$, in principle enough to stabilize the Local Group, without any contribution from non-baryonic matter.

The physical and geometrical quantities derived for this medium fit nicely the predictions by simulations for the formation of structures in the Universe (i.e. Hellsten et al., 1998; Kravtsov et al., 2002). They predict that a major reservoir of baryons in the Local Universe ($z \lesssim 2$) lie in a filamentary web of matter shock-heated during the collapse

of density perturbations, up to temperature of $10^5 - 10^7$ K. Typical density peaks in the local IGM should reach overdensity values of $\delta \sim 10 - 50$ compared to the average density in the Universe, and should extend for few to few tens of Mpc.

Of course, our interpretation of the local UV-X-ray absorbing medium is not unique. Recently Heckman et al. (2002) proposed a model based on the ejection of matter from the Galaxy's disk, and its subsequent infall onto the Galactic plane, to explain the UV (CIV) and FUV (OVI) high velocity absorption. This model reproduces the observed differences in ionization degree, with stratified multi-temperature clouds of collisionally ionized gas in the Galaxy's halo. However the model overpredicts by factors from 3 to 10 the X-ray column densities observed along the line of sight to PKS 2155-304 (Heckman et al., 2002). Moreover, the absorbers would be dynamically bound to the Galaxy, and so would hardly reproduce the velocity segregation that HV-OVI clouds show in the LSR (§2).

Our model fits better both the observed dynamical behaviour of the HV-OVI absorbers, as well as the X-ray data. However, in this largely simplified version, it fails to explain all the HV-CIV absorption detected along the line of sight to PKS2155-304. A possible solution is that the WHIM filament of the Local Group is not homogenous. The gas could get denser when approaching the virialized structure of our Galaxy (and/or the other virialized components of the Local Group) and cool down to the temperature needed to produce the observed amount of CIV.

If our proposed interpretation is correct, any high resolution X-ray spectrum of an extragalactic source with absorption line detection threshold of few mÅ should show OVII-OVIII and NeIX absorption from the local WHIM. This detection threshold corresponds to excellent quality Chandra-LETG or XMM-RGS spectra with at least 1000-2000 counts per resolution element in the continuum. This is only reachable, for the brightest AGNs, with exposures of at least one million seconds. Alternatively, AGNs in outbursts (or Gamma-Ray-Burst X-ray afterglows, Fiore et al., 2000), can be used, with much more reasonable integrations (i.e. PKS 2155-304 was at a flux level of 21 mCrab in the 2-10 keV band - 4.2×10^{-10} cgs - during the 60 ks Chandra-LETG observation presented here). However, the current Chandra-LETG and XMM-RGS response time, allow only few of these observations to be performed in a year. Furthermore Target of Opportunity Observations (TOOs) require, of course, reliable triggers on reasonably short timescales, which are hard to obtain with the sensitivity of current X-ray all sky monitors (e.g. the XTE-ASM).

Current X-ray spectrometers (i.e. Chandra-HETG and -LETG, and XMM-RGS) have allowed us to detect for the first time this important baryonic component of the Universe, and will allow us, in the near future, to increase the number of WHIM detections. However, clearly, a systematic study of the WHIM (locally as well as at higher redshift) will have to wait for the next generation of X-ray satellites, with (a) large effective area; (b) high spectral resolution (at least 5-10 times larger than the current Chandra-LETG resolution), and (c) short-response times for TOOs. Particularly, **high resolution**, X-ray data are crucial to securely identifying the X-ray components associated to the UV and FUV components, and so to measure the ionization balance in the WHIM, which in turn allows us to measure its mass.

Acknowledgements. This work has been partly supported by NASA-Chandra grants GO2-3122A and the NASA-Chandra X-ray Center contract.

References

- Aldcroft T., Elvis M., McDowell J., & Fiore F., 1994, ApJ, 437, 584
 Blitz L., 2002, ASP Conference Proceedings Vol. 254, 215 Eds. Mulchaey J.S. & Stocke J., San Francisco: Astronomical Society of the Pacific
 Braun R. & Burton W.B., 1999, ApJ, 341, 437
 Brinkman A.C., et al., 2000, ApJ, 530, L111B
 Brules S., & Tytler D., 1998, SSRv, v.84, issue 1/2, p.65
 Cen R., & Ostriker J.P., 1999, ApJ, 514, 1
 Davé R., Cen R., et al., 2001, ApJ, 522, 473
 de Heij V., Braun R., Burton W.B., 2002, A&A, in press, astro-ph/0206333
 Einasto J., & Lynden-Bell, D., 1982, MNRAS, 199, 67
 Fiore F., Nicastro F., Savaglio S., Stella L., & Vietri M., 2000, ApJ, 544, L7
 Heckman T.M., Norman C.A., Strickland D.K., & Sembach K.R., 2002, ApJ in press, astro-ph/020556.
 Hellsten U., Gnedin N.Y., & Miralda-Escudé J., 1998, ApJ, 509, 65
 Hoopes C.G., Sembach K.R., Howk J.C., Savage B.D., Fullerton A.W., 2002, ApJ, 569, 233-244
 Howk J.C., Savage B.D., Sembach K.R., & Hoopes C.G., 2002, ApJ, 572, 264
 Kahn F.D., & Woltjer L., 1959, ApJ, 130, 705
 Klypin A., Hoffman Y., Kravtsov A., Gottloeber S., 2001, submitted to ApJ, astro-ph/0107104
 Kravtsov A.V., Klypin A., & Hoffman Y., 2002, ApJ, 571, 563

- Moos H.W., et al., 2000, ApJ, 538, L1
Nicastro F., et al., 2002, ApJ, 573, 157 (N02a)
Nicastro F., et al., 2002, submitted to Nature, astro-ph/0208012 (N02b)
Oort J.H., 1926, The Observatory, 49, 302
Savage B.D., et al., 2000, ApJ, 538, L27
Savage B.D., et al., 2001, AAS, 199, 6504
Sembach K.R. et al., 2000, ApJ, 538, L31
Sembach, K.R., AAS, 2001, 199, 11301
Wakker B.P., et al., 2001, AAS, 199, 6508



Detection of resonance absorption lines from the Intergalactic Medium by XEUS

X. Barcons¹

Instituto de Física de Cantabria (CSIC-UC), 39005 Santander, Spain

Abstract. Detecting hot and warm baryons in intergalactic space via resonance absorption lines is one of the main science goals of XEUS. I review the expectations and requirements regarding this topic, in the light of the new developments on both theoretical and observational side.

1. Introduction

The existence of a warm/hot component in the intergalactic medium (WHIM) is not under debate at present. On the one hand, all cosmological theories predict that the baryon density outside galaxies and clusters is a sizeable fraction of the total matter density in the Universe and that at low redshift most of these baryons will be at temperatures between $10^5 - 10^7$ K. Besides that, the first detections of resonant absorption lines from a hot gas filament probably associated with the local group with the spectrographs on board *Chandra* (Nicastro et al 2002) and XMM-Newton (Paerels et al 2002) has shown that this is not pure speculation, but based on reality. The situation is substantially different to that in 1999 when the first version of the XEUS science case was written (Arnaud et al 2000). The question now is no longer whether the WHIM exists, but to characterize it and to explore the important consequences that studying it will have to further our knowledge of the structure of the Universe.

XEUS will have two basic properties that are needed to detect resonance absorption lines: large collecting area (in order to obtain high S/N spectra of background sources at significant redshift) and moderate to high spectral resolution (in order to avoid dilution of the resonance absorption lines in the noise). A further feature of XEUS, which is its good angular resolution, will also enable to study with unprecedented detail, resonance absorption lines from many elements in more condensed systems (groups and clusters of galaxies), without the emission lines from the gas filling the resonance absorption lines.

With that in mind, the goals of XEUS in studying resonance absorption lines from tenuous warm and hot intergalactic gas, can be listed as:

- Measuring the baryon density as a function of redshift, trying to solve the problem of the missing baryons, i.e. those predicted by big-bang nucleosynthesis but not seen at low z in either galaxies or Lyman α absorption systems.
- Determining the thermal history of the baryons in the Universe.
- Measuring the chemical evolution of the Universe, by detecting lines from different elements in various ionisation states.
- Finding the relative contribution of various heating mechanisms, like gravitational heating, photoionisation by galaxies and active nuclei, etc.

I first discuss recent progress (both theoretical and observational) in this field, updating the XEUS science case (Arnaud et al 2000). Then I briefly discuss the expected sensitivity of XEUS with the NF11 detector (assumed to be an Superconducting Tunneling Junction -based device) and present some specific simulations. I finally review the prospects and limitations of the baseline XEUS concept, with special emphasis on those areas where technical progress would be much needed to achieve the specific science goals related to the study of the WHIM.

2. A strong science case for XEUS

The possibility that many baryons in the hot and warm phase ($T \sim 10^5 - 10^7$ K) could be present in filamentary structures filling intergalactic space was worked out with some detail by Perna & Loeb (1998), Hellsten et al (1998)

and Cen & Ostriker (1999). These papers performed hydrodynamical simulations of large volumes of the Universe, and studied random lines of sight through the resulting matter distributions. Given that a large fraction of the baryons at $z < 1$ happen to be in a warm/hot phase, resonance absorption lines would be detectable if bright background X-ray sources could be found. The “X-ray forest”, produced by many elements in the WHIM including O, Fe and Ne, was taking shape as a cosmological tool with a potential interest similar to that of the Lyman α forest that is routinely detected in optical/UV spectra towards distant QSOs.

The idea of using resonance absorption lines to study tenuous gas was not new. Krolik & Raymond (1988) and Sarazin (1989) suggested its use to study intracluster gas, and to eventually measure the distance to clusters by combining absorption and emission measurements. The absorbing column is $N \propto n_{gas}R$, where n_{gas} is the gas density and R the size of the absorber, while both the free-free and line emissivity scale as $\propto n_{gas}^2R^3$. Tenuous systems are easier to trace via absorption against a background source than via emission. For large condensations (groups and clusters), Sarazin (1989) also warns about the competing effect of the line emissivity filling the resonance absorption lines. Indeed this scales as the solid angle of the beam, and therefore for these large systems good angular resolution is needed for absorption line studies. XEUS will be unique in this respect, as it will be able to study both diffuse WHIM and intragroup and intracluster gas in absorption given its angular resolution.

2.1. How many trees in the X-ray forest?

Although much progress has been achieved in this field recently, it is enlightening to look back to the optical/UV absorption systems. It is nowadays widely accepted that strong Lyman α absorption systems, metal systems and damped Lyman α absorption systems (all of them having HI column densities in excess to $3 \times 10^{-14} \text{ cm}^{-2}$) arise in extended galaxy halos. If one were to predict the incidence of these systems based on, say, the deepest optical images, it would be difficult to guess that more than one galaxy-associated absorption line would be found in any line of sight, out to very large redshifts. But instead, hundreds of these systems are found in any random line of sight. The reason is that galaxies appear to possess extended (and to some extent metal enriched) galaxy envelopes which provide a much larger cross section than what is seen in emission. Similarly, if we were to predict X-ray absorption line number counts, accounting for groups and clusters, with the cross section defined by the X-ray emitting gas, we would end up with one absorber per many lines of sight. However, reality could be very different.

Substantial progress in this field has been achieved via hydrodynamical simulations of regions along extended lines of sight in the Universe. Most of the baryonic gas is in fact outside the virialized structures in the form of filaments (e.g., Davé et al 2001). Depending on the cosmological model, from 20 to 40% of the baryons in the universe can be in this warm to hot phase below $z < 1$. A similar fraction of the baryons go to collapsed structures, and then there is very little room for cold intergalactic gas at low z , as supported by the paucity of Lyman α absorbers at $z < 1$.

Fang & Canizares (2000) computed specifically column density distributions per unit redshift based on a semi-analytical formulation, which is valid for large systems. Again, depending on the cosmological models, they found $\sim 1 - 10$ OVIII absorbers per unit redshift with $N_{OVIII} > 10^{-16}$. Other ions (SiXIV, FeXXV) are expected to be much less frequent.

In a more recent paper, Fang, Bryan & Canizares (2002) carried out detailed simulations which confirmed and refined their previous estimates on line densities. As we will see later, a column density of $N_{OVIII} \sim 10^{-16}$ should be detectable with XEUS routinely against fairly faint background AGN, and therefore the “X-ray forest” should become a reality.

2.2. The Doppler velocity widths

In the simplest terms, an absorption line is defined by 3 parameters: its central wavelength, its column density (N) and its Doppler velocity parameter $b = \sqrt{\sigma}$, where σ is the velocity dispersion, assumed gaussian. Under these conditions, the line has a Voigt profile.

Depending on the spectral resolution, the line will or will not be resolvable. For unresolved lines, N and b cannot be separated, and only the line equivalent width can be measured. Fig 2.2 shows the “curve-of-growth” for the OVIII Lyman α transition, computed for various values of b , ranging from 100 to 500 km s^{-1} . The leftmost part of this curve is the “linear” part of the curve of growth, where the equivalent width $W \propto N$ with no Doppler velocity dependence. According to Fang & Canizares (2000) most of the lines found in the WHIM will be in this regime. The very few absorption lines associated to clusters could have larger columns and get into the saturated part of the curve of growth, where the equivalent width W is mostly a measure of b (for example due to gas turbulence) and is insensitive to the column density. The “damping” part of the curve of growth (on the right again), where damping wings dominate, is unlikely to be relevant to this discussion for elements other than Hydrogen.

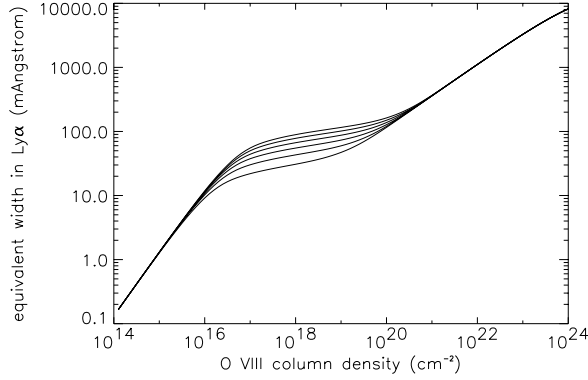


Fig. 1. Curve of growth for the OVIII Lyman- α transition for various values of the turbulent velocity.

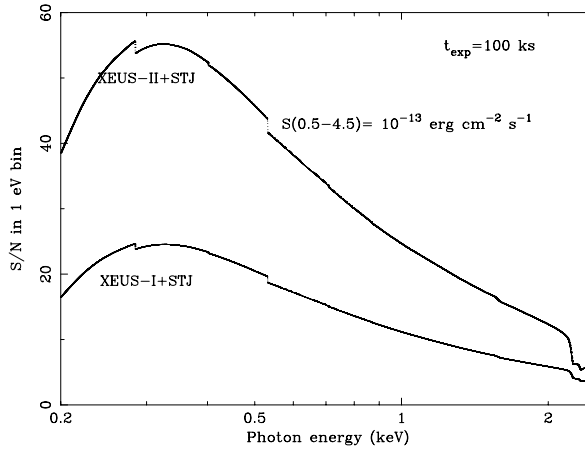


Fig. 2. Expected signal to noise ratio for a spectrum in 1 eV bins for a background source with a $\Gamma = 2$ power-law spectrum, absorbed by $N_H = 2 \times 10^{20} \text{ cm}^{-2}$ and a 0.5-4.5 flux of $10^{-13} \text{ erg cm}^{-2} \text{ s}^{-1}$.

Fang et al (2002) have computed the b -parameter distribution for a set of X-ray absorption lines: OVII, OVIII, SiXIII, SiXIV, FeXXV and FeXXVI. These distributions are fitted to log-normal functions, with peaks that range from under 50 km s^{-1} for the OVII and OVIII ions to over 100 km s^{-1} for the Fe ions. Again, only the absorbers coming from the groups and clusters are expected to have turbulent velocities of several hundreds of km s^{-1} .

It is interesting to note that for the absorption lines in the linear part of the curve of growth, high resolution spectroscopy of unblended absorption lines can deliver both N and b with very little correlation, via Voigt profile fitting. However, due to the small value of b for most systems, a spectral resolution of > 1000 would be needed to resolve the lines and > 3000 to permit a meaningful profile fitting.

3. Expected sensitivity

3.1. What background source do we need?

The key requirement to detect absorption lines is to have a bright enough background source. The required signal to noise to detect an absorption line with specified parameters, is not only a function of its equivalent width, but of both column density and Doppler width. Indeed, very broad lines with limited equivalent width tend to be confused with the continuum noise.

For unresolved lines (and most of the WHIM associated lines will be unresolved by XEUS+STJ), a rule of thumb is that with a $S/N = 10$ spectrum which samples the spectral resolution in $\sim 2 - 3$ channels, absorption lines with equivalent width as small as a fraction of the channel width can be detected. Spectra with S/N much smaller than 10 are basically useless for absorption line studies, as they can be confused with noise spikes.

The question is whether there are enough background sources in the Universe that will permit this type of study with XEUS. We have taken, as an example, sources with a 0.5-4.5 keV flux of $10^{-13} \text{ erg cm}^{-2} \text{ s}^{-1}$. There are 1-2 sources brighter than this in every XMM-Newton image, with a source density of $\sim 10 \text{ deg}^{-2}$, so these are not rare sources. The mean redshift of AGNs brighter than this flux level is ~ 0.5 , so most of these sources will be far enough to cross a significant patch of intergalactic space.

Fig 3.1 shows the expected S/N ratio for the spectrum of one such source, with a binning of 1 eV. A single power-law spectrum with $\Gamma = 2$ absorbed with $N_H = 2 \times 10^{20} \text{ cm}^{-2}$ has been assumed. We see that in the region where most of the interesting transitions are expected to occur, XEUS-II will obtain routinely high enough S/N spectra to search for WHIM absorption lines in the 0.2-1 keV band in a 100 ks integration. For XEUS-I brighter sources will be generally needed, in which case the redshift range probed will be more limited. In conclusion, the full XEUS-II configuration will be needed to properly explore the cosmic evolution of the WHIM, while XEUS-I will be helpful in probing the nearby intergalactic space.

3.2. Equivalent width detection limits

We have carried out simple `xspec` simulations to see how weak an absorption line can be detected with either XEUS-I and XEUS-II. For unresolved lines we have used the `notch` model, which simulates a completely saturated line with given equivalent width. We have used a line at the wavelength of an OVII absorption line at $z = 0$, but the sensitivity is reasonably flat within a relatively extended wavelength range (see fig 3.1). The flux and spectrum of the source is the same as in fig 3.1. Once the spectrum is simulated, a power law is fitted to a limited spectral range and we plot the data to model ratio in fig 3.2 (i.e., we normalize the spectrum to the continuum fit, as usual in absorption line studies).

The contribution of any background has been ignored, and that is likely to be a fair assumption with such a bright continuum. It must be stressed that it is important, in particular at the very low energy end, to keep this background low if significant redshifts have to be reached.

As it can be seen from fig 3.2, XEUS-I will be able to detect absorption lines as weak as $W \sim 0.3 \text{ eV}$ ($\sim 10 \text{ m}\text{\AA}$), while XEUS-II should be able to detect lines as weak as $W \sim 0.1 \text{ eV}$ ($\sim 3 \text{ m}\text{\AA}$). If we take the example of the OVIII Lyman α transition (fig. 2.2) we see that these limits translate into column density limits of 10^{16} cm^{-2} for XEUS-I and 10^{15} cm^{-2} for XEUS-II. According to Fang et al (2002), tens of absorption lines per unit redshift will be found by XEUS-II, in which case a true forest of X-ray absorption lines will be visible.

3.3. Velocity width limits

In more condensed structures, like groups and clusters, XEUS-II should be able to detect a number of absorption lines which will enable a detailed study of ionisation state and chemical abundances of the absorbing gas. To illustrate this we have computed the structure of a coronal plasma supposed to mimic the gas of a galaxy group or cluster at $z = 0.7$ with 0.5 solar metallicity, 100 kpc core radius and beta profile with $\beta = 0.65$. The equivalent width of a number of resonance absorption lines has been computed as a function of central particle density and temperature. Fig. 3.3 shows contours for an equivalent width limit of 0.2 eV.

Clearly, at low temperature, OVII, OVIII and NeX can be detected for the most tenuous systems. At higher temperatures, a wealth of resonance absorption lines appear which should be detectable in the realm of groups and clusters.

One potential problem for the detection of many species in groups and clusters is that turbulent velocity could make the absorption line disappear into the continuum noise. Again, a few `xspec` simulations have been performed for a $W = 1 \text{ eV}$ absorption line with gaussian profile and increasing Doppler parameter. Fig. 3.3 shows the simulated lines with a velocity dispersion of $\sigma = 800 \text{ km s}^{-1}$ (corresponding to a $b \sim 1100 \text{ km s}^{-1}$). The line is clearly detected in the XEUS-II spectrum, but its significance is very limited in the XEUS-I spectra. Taking into account that most of the resonance absorption lines will have equivalent widths significantly smaller than 1 eV (0.2 eV is probably more realistic, according to fig. 3.3), XEUS-II will be needed in most cases.

4. Outlook

If anything, the detection of resonance absorption lines from warm and hot gas has become a stronger science driver for XEUS following theoretical and observational developments in the recent years. Current models and simulations predict that XEUS (and XEUS-II in particular) will routinely detect the X-ray forest and that detailed physical studies of intervening could be performed.

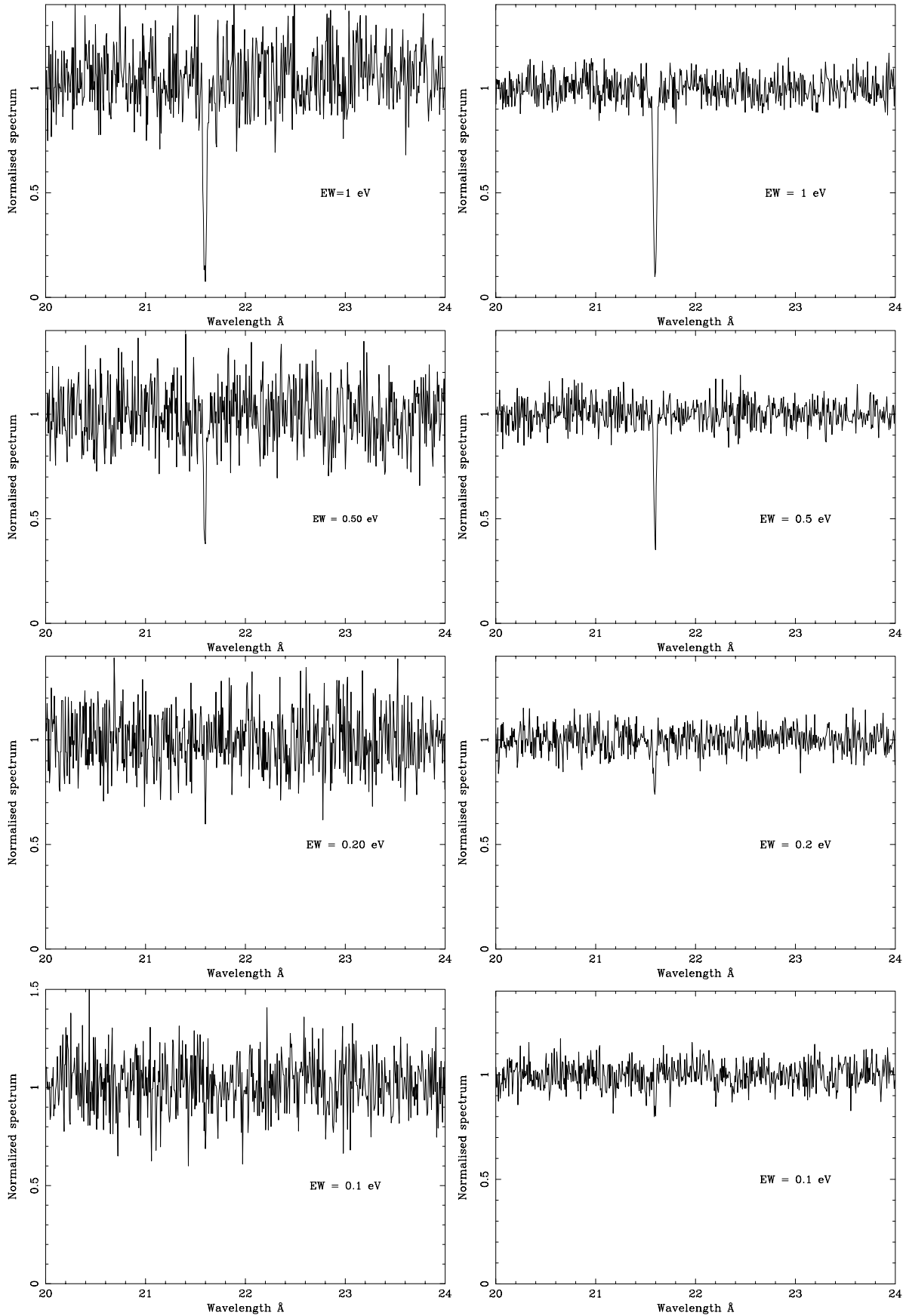


Fig. 3. Portions of simulated spectra with XEUS and the STJ detector for 100 ks exposure. On the left for the initial XEUS-I configuration and on the right for the fully grown XEUS-II. From top to bottom, a resonance absorption line has been simulated at 21.6\AA , with equivalent widths 1, 0.5, 0.2 and 0.1 eV.

Acknowledgements. I'm grateful to Francisco Carrera, Maite Ceballos, Fabrizio Nicastro, Frits Paerels and my colleagues at the XEUS Astrophysics Working Group and the XEUS Steering Committee for enlightening discussions. Partial financial support for this work was provided by the Spanish Ministry of Science and Technology, under project AYA2000-1690.

References

- Arnaud M., Barcons X., Barret D. et al, 2000. The XEUS Science case, ESA SP-1238.
- Cen R., Ostriker J.P., 1999, ApJ, 514, 1
- Davé R., Cen R., Ostriker J.P., Bryan G.L., Hernquist L., Katz N., Weinberg D.H., Norman M.L., O'Shea B., 2001, ApJ, 522, 473
- Fang T., Canizares C.R., 2000, ApJ, 539, 532
- Fang T., Bryan G.L. Canizares C.R., 2002. ApJ, 564, 604
- Hellsten U., Gnedin N.Y., Miralda-Escudé J., 1998, ApJ, 509, 56
- Krolik J.H., Raymond J., 1988, ApJ, 335, L39
- Nicastro F., Zezas A., Drake J., Elvis M., Fiore F., Fruscione A., Marengo M., Mathur S., Bianchi S., 2002, ApJ, submitted (astro-ph/0201058)
- Paerels F. Rasmussen A., Kahn S., 2002, these proceedings.
- Perna R., Loeb A., 1998, ApJ, 503, L135
- Sarazin C.L., 1989, ApJ, 345, 12



Resonant scattering of X-rays by the warm intergalactic medium

E. Churazov^{1,2}

¹ MPI für Astrophysik, Karl-Schwarzschild-Strasse 1, 85740 Garching, Germany

² Space Research Institute (IKI), Profsovnaya 84/32, Moscow 117810, Russia

Abstract. We discuss the possibility to investigate the warm IGM by its emission due to resonant scattering of X-ray background photons by He and H-like ions of heavy elements. For the low density filamentary and sheet-like structures in the warm ($\sim 10^4$ to $\sim 10^6$ K) IGM the resonant line scattering of X-ray background (XRB) photons can exceed the “local” thermal emission by a factor of a few or more. Due to the conservative nature of scattering this resonantly scattered radiation can only be identified if a significant fraction of the XRB is resolved and removed. While the combined spectrum of the resolved sources will contain X-ray absorption features, the residual background will contain corresponding emission features with the same intensity. At the relevant densities and temperatures the lines of He and H-like oxygen at 0.57 and 0.65 keV are most promising. These lines (which have a typical width of ~ 1 –2 eV) may contain up to 50% of the total 0.5–1 keV emission of the filament.

In order to detect a filament in resonant lines it is essential to have an instrument with a large field of view and low internal background (in addition to a usual requirement of high sensitivity and energy resolution).

1. Introduction

Numerical simulations predict that a considerable fraction of all baryons is contained in a warm IGM which traces the filamentary and sheet-like distribution of the dark matter (e.g. Ostriker & Cen, 1996, Cen & Ostriker 1999). This phase of the IGM should have densities of a few up to a few tens times the mean baryonic density. The temperatures should range between a “photoionization temperature” at low densities ($\sim 10^3$ – 10^4 K) and the virial temperature of sheets and filaments ($\sim 10^6$ K). This “warm” phase of the IGM is of special interest as it will contain a record of the energy and metals expelled from galaxies. The typical surface brightness of filaments due to local thermal emission of the diffuse gas is, however, a factor 100 or more smaller than that of the X-ray background. It was suggested that the warm IGM produces measurable absorption in the resonant transitions of heavy elements such as oxygen or iron if there is a bright quasar behind the gas (Shapiro and Bahcall 1980, Aldcroft et al., 1994, Hellsten, Gnedin, Miralda-Escude 1998, Perna and Loeb, 1998, Markevitch, 1999). This seems a promising method to study the warm IGM, especially as long as high energy resolution is only possible for bright sources (i.e. using gratings). It will, however, only give information along the line-of-sight to point sources. We explore here the possibility to investigate the warm IGM by its emission due to resonant scattering of X-ray background photons by He and H-like ions of heavy elements (Churazov, Haehnelt, Kotov & Sunyaev 2001). While for the high density and temperatures in galaxy clusters the local thermal emission clearly dominates over resonant scattering the opposite is true for the more moderate densities and temperatures expected in the sheet-like and filamentary structures of the warm phase of the IGM.

A Hubble constant of $H_0 = 50 \text{ km s}^{-1} \text{ Mpc}^{-1}$ and an Einstein-de-Sitter Universe was assumed throughout the paper. For the baryon density we take $\rho_{\text{bar}} = 3.6 \cdot 10^{-31} \text{ g cm}^{-3}$ ($\Omega_{\text{bar}} h^2 = 0.02$, Burles et al., 1999). The abundances of heavy elements were assumed to be a constant fraction of solar abundances as given by Feldman (1992). For the local XRB spectrum we use the simple approximation $I(E) = I_0 E^{-1.3} e^{-\frac{E}{40 \text{ keV}}}$ for energies $E \geq 1 \text{ keV}$ and a power law with a photon index of 2 below 1 keV, where $I_0 = 8 \text{ photons cm}^{-2} \text{ sec}^{-1} \text{ keV}^{-1} \text{ sr}^{-1}$ (e.g. Barcons & Fabian 1992, Miyaji et al. 1998).

2. Photoionization balance and emissivity of the warm gas

2.1. Typical densities and temperatures

The characteristic sheets and filaments seen in numerical simulations are the result of the non-linear collapse of density perturbation imprinted onto the matter distribution in the early Universe. Sheets form from perturbations which collapse along one axis (Zeldovich 1970) while filaments have collapsed along two axis. This results in typical overdensities of a few in sheets and a few tens in filaments. The typical Thomson optical depth scales linearly with the length scale of the density perturbation and will be about $(0.1, 0.5)h^{-1} \times 10^{-4} (R/8h^{-1} \text{ Mpc})$ for sheets and filaments, respectively. Note that $R = 8h^{-1} \text{ Mpc}$ is approximately the scale on which the present-day density field has gone non-linear. The space density of structures larger than this decreases exponentially. Typical temperatures in the warm IGM are somewhat uncertain but will be strongly correlated with density. In the absence of energy input from star formation and AGN the temperatures at low densities are set by the balance of photoheating and adiabatic cooling and lie in the range 3000 -10000 K (e.g. Hui & Gnedin 1997). At higher densities the gas will be shock-heated. In virialized regions the temperatures will be set by the virial temperature of sheets and filaments and should be about 10^6 K . The energy input from star formation and AGN will raise this temperatures especially at low densities. Ponman, Cannon & Navarro (1999) e.g. suggest a minimum “entropy” of $100h^{-1/3} \text{ keV cm}^2$ to explain the X-ray luminosity temperature relation of galaxy clusters at the faint end.

In the discussion below we consider two examples: emission from regions with an overdensity of (5,30), corresponding to a electron density of $(10^{-6} \text{ cm}^{-3}, 6 \cdot 10^{-6} \text{ cm}^{-3})$, a temperature of $(2 \times 10^5 \text{ K}, 10^6 \text{ K})$, and a metallicity of (10%,30%) solar which may resemble a typical sheet and filament, respectively. For a size of 8 Mpc a sheet and filament will have a Thomson optical depth of $(0.2, 1) \times 10^{-4}$ respectively. The emission spectra are calculated below for zero redshift.

2.2. Thermal emission of the gas in collisional equilibrium

For gas with given density and temperature in pure collisional equilibrium (coronal approximation) the following processes contribute to the X-ray emission: continuum emission (free-free and bound-free), recombination lines and emission lines excited by electron collisions. In the following we call these emission mechanisms collectively “thermal” emission. For our adopted parameters the X-ray emissivity of the gas in filaments and sheets is extremely low (due to both the low temperature and the low density of the gas). Detecting these structures requires very high sensitivity. The thermal emission from a typical filament in the 0.5–1 keV energy band (in units of $\text{keV sec}^{-1} \text{ cm}^{-2} \text{ keV}^{-1} \text{ sr}^{-1}$ to facilitate comparison with the XRB surface brightness) is shown in Fig. 1 by the dotted curve. For comparison the intensity of the XRB is shown by the solid line. For our canonical sheet the emissivity is several orders of magnitude lower and well below the limits of the plot.

The intrinsic width of the lines should be dominated by the Hubble flow, peculiar and turbulent velocities rather than thermal broadening. In the considered energy range of 0.5–1 keV the velocity dispersion of 500-1000 km s^{-1} implies a width of $\sim 1\text{--}2 \text{ eV}$. The spectra shown in all figures are convolved with a Gaussian with a FWHM of 2 eV. We note here that this kind of resolution may be achieved by projected X-ray missions like Constellation-X or XEUS.

2.3. Influence of the XRB on the thermal emission

The IGM is exposed to XRB photons. These photons change the ionization balance of the IGM, producing ions at higher ionization stage than expected for pure collisional ionization at a given temperature. The importance of photoionization depends on the temperature and density of the gas. The characteristic time for photoionization of oxygen ions by XRB photons, $t = (4\pi \int I(E)\sigma_{\text{ph}}(E)dE)^{-1}$ is $\sim 3.5 \times 10^9 \text{ yr}$ for O VII and $\sim 10^{10} \text{ yr}$ for O VIII. Here $I(E)$ is the background intensity ($\text{photons cm}^{-2} \text{ sec}^{-1} \text{ keV}^{-1} \text{ sr}^{-1}$) and $\sigma_{\text{ph}}(E)$ is the photoionization cross section. This is somewhat shorter than the Hubble time and ionization equilibrium is approximately established. At the densities and temperatures typical for the warm IGM the oxygen is mainly in the form of He and H-like ions, as shown in Fig.3. The contours show the areas on the temperature/overdensity plot where the fraction of He and H-like ions of oxygen is larger than 30%. O VII and O VIII more or less trace the density temperature relation of the warm IGM. A fraction larger than 30% is expected for practically the whole range of densities and temperatures prevalent in the warm IGM (see also Hellsten et al. 1998).

The change of the ionization balance due to photoionization affects the bound-free radiation, recombination lines and strength of the lines excited by electron collisions. The free-free emission does not change compared to the gas at the same temperature in collisional equilibrium. The corresponding thermal emission spectra (i.e. the sum of the free-free, bound-free continuums, recombination and collisionally excited lines) are shown by the grey lines in Fig.1,2

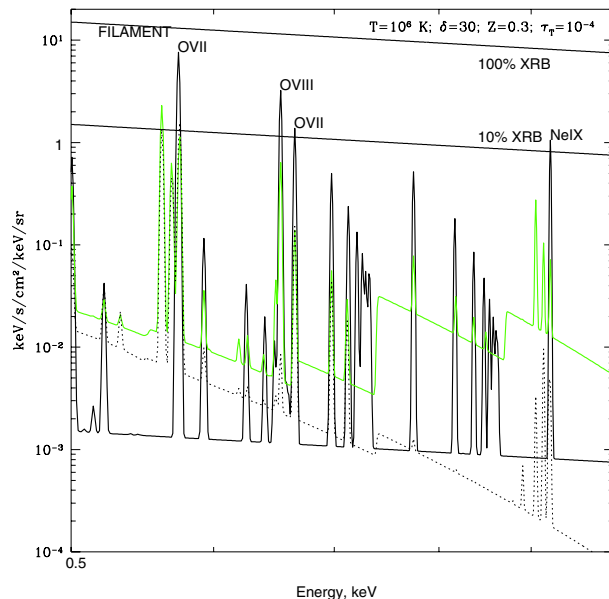


Fig. 1. The X-ray spectrum of warm gas with an overdensity of $\delta = 30$, a temperature of $10^6 K$, a Thomson optical depth of 10^{-4} and a metallicity of 30% solar. These conditions should be typical for a filamentary structure in the warm IGM. The dotted curve shows the emission spectrum due to collisional excitation and ionization. For the light solid curve photoionization by the XRB was taken into account. The dark solid curve shows Thomson plus resonantly scattered radiation. The upper solid line is the intensity of the XRB from the same region. The lower solid line shows 10% of the XRB intensity (the level to which discrete source may be removed). The spectra were convolved with a Gaussian with a FWHM of 2 eV.

for our canonical filament and sheet, respectively. The change of the ionization state due to photoionization strongly enhances the X-ray emissivity of the gas. Photoabsorbed XRB photons are effectively converted into recombination radiation (in the form of bound-free radiation and recombination lines). The effect is especially strong when the temperature of the gas is low, e.g. around $10^5 K$. In this case the gas does hardly emit any X-rays if photoionization is neglected.

2.4. Resonant scattering vs local thermal emission

Resonant scattering of XRB photons is even more important than the enhancement of the thermal emission of the gas due to photoionization. The emissivity of resonantly scattered radiation ($\text{cm}^{-3} \text{sec}^{-1}$) can be written as,

$$\epsilon_{\text{rsc}}(E_l) = 4\pi I(E_l) n_i \sigma_0, \quad (1)$$

where E_l is the line energy and n_i is number density of a given ion. Hereby $\sigma_0 = \frac{\pi e^2}{m_e c} f_{ul} F$, where f_{ul} is the oscillator strength, e is the electron charge, m_e is the electron mass, c is the speed of light, and $F = 4.14 \times 10^{-18}$ is the conversion factor from Hz to keV. The number density of a given ion is

$$n_i = n_H Z_\odot Z f_x, \quad (2)$$

where n_H is the hydrogen density in the warm IGM, Z_\odot is the solar abundance of a given element relative to hydrogen, Z is the abundance of the element relative to solar abundance and f_x is the fraction of atoms in a given ionization state.

The resonantly scattered flux in a given line is proportional to the number density of the ion. It is convenient to express its intensity in terms of the intensity of the Thomson scattered continuum, which is proportional to the density of the electrons. The emissivity of the Thomson scattered continuum is given by,

$$\epsilon_{\text{tsc}}(E_l) = 4\pi I(E_l) n_e \sigma_T, \quad (3)$$

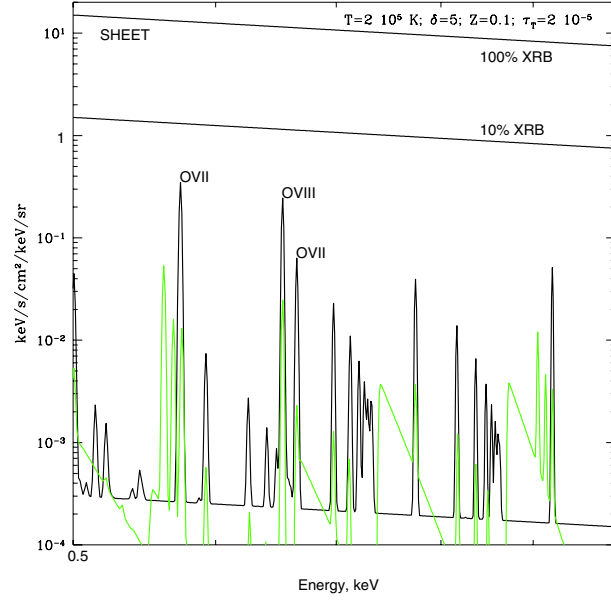


Fig. 2. The same as in Fig.1 but for warm gas with an overdensity of $\delta = 5$, a temperature of $2 \cdot 10^5$ K, a Thomson optical depth of 0.2×10^{-4} and a metallicity of 10% solar. These conditions should be typical for a sheet-like structure in the warm IGM. The thermal emission from such a gas in pure collisional equilibrium is orders of magnitude below the limits of the plot.

Table 1. Equivalent width of the resonant lines of H and He-like ions relative to the Thomson scattered continuum assuming unity for the fraction of the ionization state and solar abundances. The abundances are taken from Feldman (1992).

Ion	Abundance (Z_{\odot})	Energy (keV)	E_{EW} (keV)
CV	3.98E-04	0.31	46.6
CVI		0.37	27.5
NVI	1.00E-04	0.43	11.7
NVII		0.50	6.9
OVII	8.51E-04	0.57	99.6
OVIII		0.65	58.9
NeIX	1.29E-04	0.92	15.1
NeX		1.02	8.9
MgXI	3.80E-05	1.34	4.4
MgXII		1.47	2.6
SiXIII	3.55E-05	1.85	4.1
SiXIV		2.00	2.4
SXV	1.62E-05	2.45	1.9
SXVI		2.62	1.1
FeXXV	3.24E-05	6.67	3.8
FeXXVI		6.97	2.2

where n_e is the electron density and σ_T is the Thomson cross section. The total scattered spectrum (i.e. the sum of resonantly and Thomson scattered radiation) is shown in Fig.1,2 by the thick solid curves¹.

The ratio of resonantly and Thomson scattered emissivity (i.e. the equivalent width) is,

$$E_{EW} \sim \frac{\pi e^2}{m_e c} f_{ul} \frac{Z_{\odot} Z f_x}{\sigma_T} \quad (4)$$

¹ Here we use the list of the strong resonant lines compiled by Verner (<http://www.pa.uky.edu/verner/atom.html>).

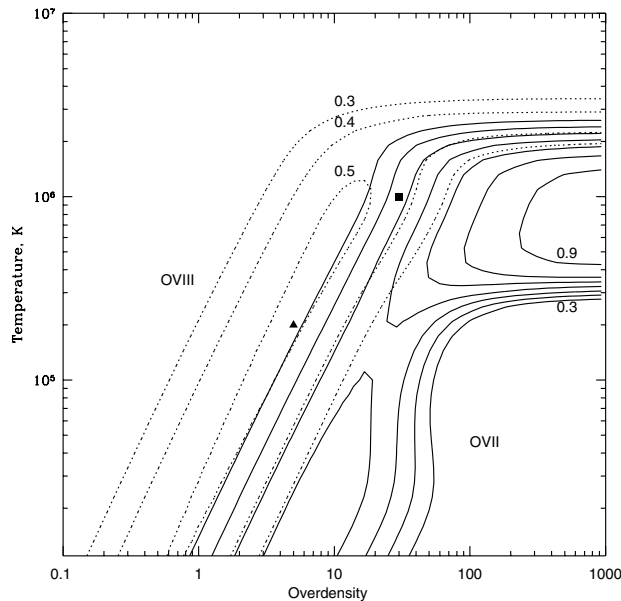


Fig. 3. Contours show the fraction of OVIII (dotted lines) and OVII (solid lines) ions as a function of temperature and (over)density. Contours start with 0.3 with 0.1 increment. Some of the contours are labeled. Ionization equilibrium was calculated taking into account photoionization by XRB photons. Black square and triangle mark the typical parameters of a filament and sheet respectively.

This expression is of course only valid for an optically thin medium. The equivalent widths for He and H-like ions are given in Table 1 assuming unity for the fraction of the ionization state and solar abundances. Along an isoelectronic sequence (e.g. for He-like ions of heavy elements) the oscillator strength for a given transition is approximately constant. Not surprisingly the resonant transitions of H and He-like oxygen (OVII and OVIII) are particularly strong due to the high oxygen abundance.

We now compare the emissivity of the gas due to scattering and that due to thermal emission (taking into account photoionization by XRB). The ratio depends strongly on the temperature and density of the gas as shown in Fig. 4. Both scattered and thermal emission were integrated over the energy range 0.5–1 keV. At low densities and low temperatures the ratio is about 3–4. For these parameters photoionization strongly dominates over collisional ionization. As a result the ratio of the scattered and thermal emission (the latter being dominated by recombination radiation) is proportional to the factor $\frac{\sum n_i I(E_i) \sigma_0}{\sum n_i \int I(E) \sigma_{ph}(E) dE}$, where the summation in the denominator is over all ions and in the numerator over all ions and lines. For strong individual lines this ratio is about 3–4. For our canonical filament the 0.5–1 keV emissivity of the gas due to resonant scattering exceeds the thermal emission of the photoionized gas by a factor of about 2. In Fig. 5 we compare the emissivity (including scattered radiation) of the gas photoionized by the XRB to the pure thermal emission of the gas if it were in collisional ionization equilibrium. The ratio of the emissivities (integrated over the 0.5–1 keV energy band) is shown as a contour plot. For our canonical filament this ratio is about 5–10 while for the sheet it is more than 10^5 . We conclude that estimates for the detectability of the warm IGM which neglect either scattering of the soft X-ray background and/or photoionization of the IGM by the soft X-ray background are overly pessimistic.

Finally, we compare the emissivity due to resonant scattering in the OVII line which is likely to be the strongest line at the relevant temperature and densities, to the total integrated emissivity in the energy range 0.5–1 keV (Figure 6). For a typical filament about 30 percent of the total flux is emitted in the resonant line of OVII.

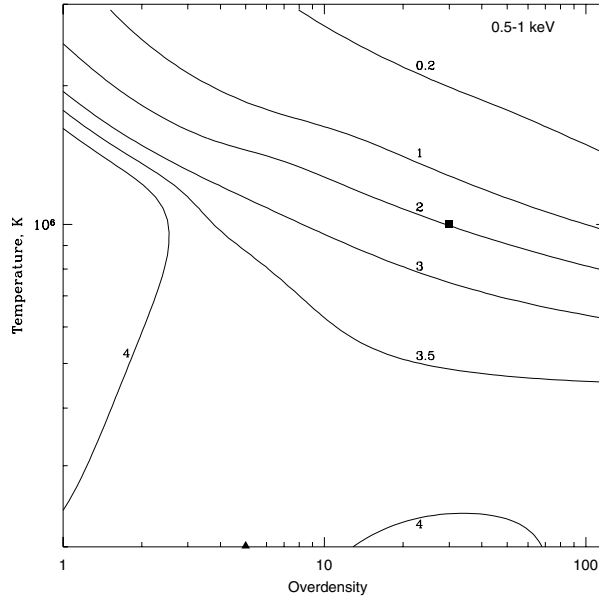


Fig. 4. Contour plot of the ratio of scattered emission to thermal emission in the energy range 0.5–1 keV for typical temperatures and (over)densities. The solid square and triangle mark the parameters of the canonical filament and sheet, defined in Section 2.1, respectively.

3. Detectability of filamentary structures in the warm IGM

3.1. Detecting resonance scattering from diffuse gas in emission

Note that neither the number nor the energy of photons change during resonant scattering. Resonant scattering would not change the XRB flux if the XRB were completely homogeneous and isotropic². However, the XRB is emitted by discrete sources and resonance scattering converts photons emitted by compact sources into a diffuse background.

The resonantly scattered emission will be detectable in images in which discrete sources making up a significant fraction of the total background have been removed. This is demonstrated in Fig. 7 which shows the spectrum of our canonical filament (taking into account the XRB) and the case where 90 percent of the background has been removed. ROSAT has e.g. resolved 70–80% of the XRB in the energy range 0.5–2 keV (Hasinger et al., 1998). At the lower end of this range the situation is somewhat unclear mainly due to the emission of our own Galaxy.

The spectral resolution of X-ray instruments is dramatically increasing. XMM and Chandra are the first instruments with high spectral resolution (using gratings) but only for bright compact sources. With projected missions like Constellation-X and XEUS imaging with a spectral resolution of about 2 eV will become possible. The large ratio of resonantly scattered emission to the Thomson scattered continuum and the local thermal emission makes the search for the spectral feature of resonantly scattered radiation very worthwhile. Detecting the warm IGM by photons scattered in the OVII or OVIII resonant transitions has another big advantage. Filaments and sheets contain a large number of faint galaxy clusters and galaxy groups. The emission from the dense hot gas in these clusters and groups generally dominates the thermal emission from filaments. However, in this dense and hot gas oxygen is generally completely stripped from electrons and no resonant scattering will occur in these regions. The resonantly scattered radiation will thus be a good tracer of the diffuse gas in filaments. The only contamination should be due to resonant oxygen scattering by the warm gas which may be contained in the galaxies within the filaments.

The highest signal to noise ratio can be achieved if OVII or OVIII absorption lines are observed in the spectrum of a very bright compact source located behind the filament as first suggested by Shapiro and Bahcall (1980). The longest exposures (deep surveys) however are usually collected for fields without strong X-ray sources. For such fields the detection of OVII or OVIII resonant lines in emission in the residual background is favorable compared to the detection of these lines in absorption using the combined spectrum of all resolved background sources in the field. The number

² To a smaller extent this is also true for the photoabsorbed photons of the XRB which are reemitted as recombination photons.

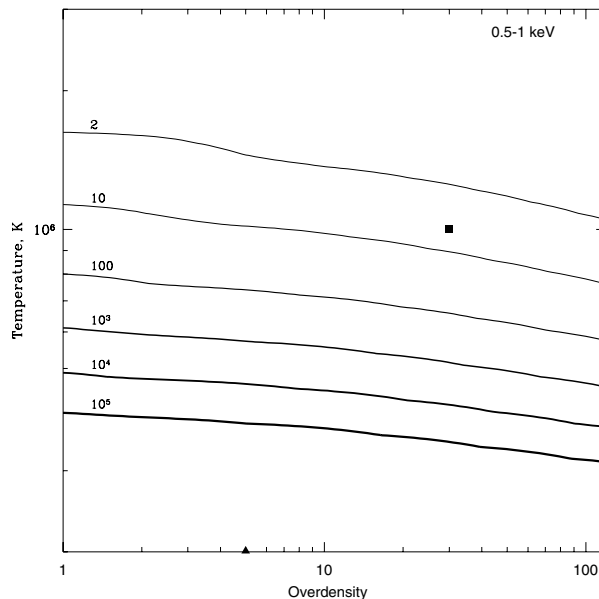


Fig. 5. Contour plot of the ratio of the total emissivity (including scattered radiation) of gas photoionized by the XRB and the thermal emission from gas at the same density and temperature in pure collisional equilibrium. The emissivities are integrated over the 0.5–1 keV band. The solid square and triangle mark the parameters of the canonical filament and sheet, defined in Section 2.1, respectively.

Table 2. Parameters of different X-ray missions. The number quoted in the table are very approximate and should only be used for rough estimates. For XEUS the parameters are quoted for the Narrow and Wide field imagers, respectively. The total number of (resonantly scattered) photons in the OVII line which will be collected from a filament filling the field of view (FOV) of the telescope is proportional to the product of the effective area and the size of the FOV (AF). The signal-to-noise ratio (assuming pure statistical errors mainly due to background photons from unresolved sources and Galactic emission in a band pass set by the energy resolution of the telescope) is proportional to the factor $\sqrt{\frac{AF}{\Delta E}}$ which is given in the last row of the table.

	XMM	XEUS	Constellation-X
Area@0.5 keV (A), cm^2	1000	300000	15000
FOV (F), arcmin ²	25×25	$(1 \times 1; 5 \times 5)$	3×3
ΔE , eV	60	(2;50)	2
AF	$6 \cdot 10^5$	$(3 \cdot 10^5; 8 \cdot 10^6)$	$1.4 \cdot 10^5$
$\sqrt{\frac{AF}{\Delta E}}$	100	(400;400)	260

of line photons in the residual background is approximately equal to the number of line photons absorbed from the spectra of all resolved sources. The intensity of the residual background is, however, lower if most of the background is resolved. This results in a higher signal-to-noise ratio for the residual background. It means that in order for such a method to be useful the particle and other “non cosmological” detector backgrounds have to be low compared to the combined intensity of the resolved sources in the field.

3.2. Detecting filaments with upcoming satellite missions

In an Einstein de Sitter Universe our canonical filament of comoving size ($16h^{-1}$ Mpc \times $3h^{-1}$ Mpc has angular extent ($183' \times 34'$, $50' \times 9'$, $31' \times 6'$) at $z = (0.1, 0.5, 1)$, respectively. Estimates of the effective area, FOV and energy resolution are summarized in Table 2. In the case of a filament, completely filling the FOV the expected number of counts in the

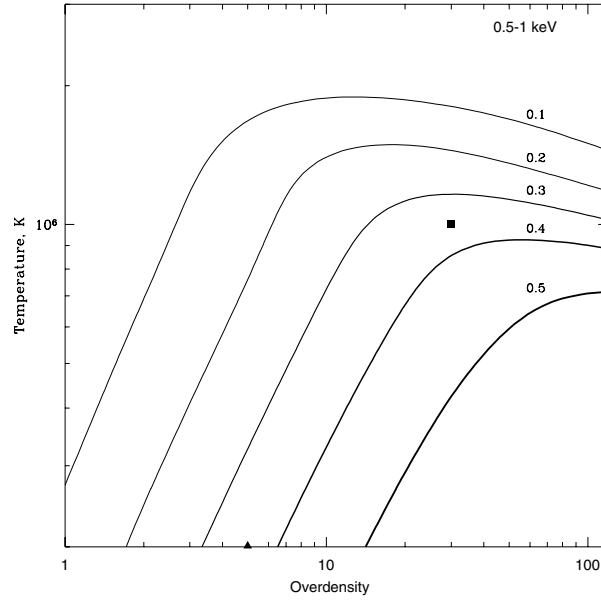


Fig. 6. Contour plot of the fraction of the total emissivity in the 0.5–1 keV band which is due to resonantly scattered radiation in the OVII line at 0.57 keV. The solid square and triangle mark the parameters of the canonical filament and sheet, defined in Section 2.1, respectively.

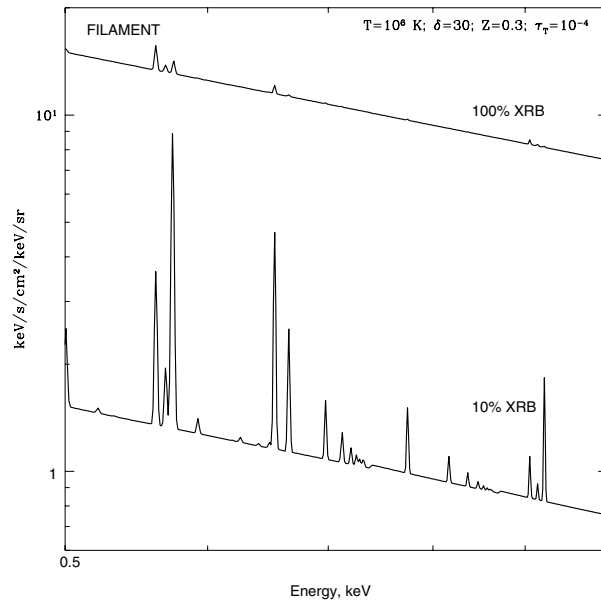


Fig. 7. The upper curve shows the total spectrum of a region of the sky containing a filament with Thomson optical depth of 10^{-4} . This spectrum is a sum of the thermal emission of the filament, scattered XRB and emission of the background sources, part of which is either absorbed or scattered by the filament. Note that resonance scattering does not change the XRB flux and only emission lines due to the thermal emission of the filament are visible in this spectrum. The lower curve shows the spectrum of the same region if 90% percent of the background is resolved into compact sources and removed. Note that the most prominent OVII line at 0.57 keV becomes visible only in this spectrum. In the hypothetical case when all XRB is resolved and removed the residual spectrum should be equal to the sum of the thermal emission of the filament and scattered XRB emission. These two components are shown in Fig. 1.

oxygen line is proportional to the product of the effective area (A) and the FOV (F) of the telescope. This value is largest for the Wide field imager of XEUS. For a nearby ($z \lesssim 0.1$) filament with Thomson optical depth of 10^{-4} WFI of XEUS will detect about few 1000 counts in the OVII line in a 10^5 s exposure. The signal-to-noise ratio (assuming pure statistical errors mainly due to background photons from unresolved sources and Galactic emission in a band pass set by the energy resolution of the telescope) is proportional to the factor $\sqrt{\frac{AF}{\Delta E}}$ which is given in the last row of the table. This value is comparable for all missions. The above estimates assume that internal background is small compared to cosmic X-ray background (which may not be true). The anticipated FOV of Constellation X and of the Narrow field imager of XEUS is rather small (see Table 2). The total number of photons detected in the OVII and OVIII lines for a filament filling the whole FOV will therefore be even lower than for a XMM class mission. It is clear that for an efficient study of the diffuse emission of filaments a larger FOV would be very important. If it were possible to increase the FOV to e.g. $5' \times 5'$ (below 1 keV) for high energy resolution detectors like those of Constellation X and XEUS then these missions should be able to detect resonantly scattered emission of filaments along any line of sight during a 50ks exposure.

4. Conclusions

For the temperatures and densities prevalent in the the filamentary and sheet-like structures of the warm intergalactic medium illumination by XRB photons significantly increases the X-ray emissivity of the medium. The strongest contribution to the X-ray emissivity is due to resonant scattering of XRB photons. This resonantly scattered emission can be detected in images from which a significant fraction of the XRB due to compact sources has been removed.

Resonant lines of He and H-like oxygen are most promising for detecting filamentary structures in the warm IGM. The fraction of oxygen in the ionization states OVII or OVIII is larger than 30 percent practically for the whole range of densities and temperatures expected in the warm IGM.

Successful detection of low density filaments demands a combination of a low internal background and large field of view of an instrument along with the large effective area and high energy resolution.

References

- Aldcroft T., Elvis M., McDowell J., Fiore F. 1994, ApJ, 437, 584
 Barcons X., Fabian A.C. 1992 , ARA&A, 30, 429
 Burles S., Nolett K.M., Truran J.N., Turner M.S. 1999, Phys.Rev.Lett,82
 Cen R., Ostriker J.P. 1999, ApJ, 514, 1
 Churazov E., Haehnelt M., Kotov O., Sunyaev R. 2001, MNRAS, 323, 93
 Feldman U. 1992 , Physica Scripta , 46 , 202
 Hasinger G., Burg R., Giacconi R., Schmidt M., Truemper J., Zamorani G. 1998, A&A, 329, 482
 Hellsten, U., Gnedin, N. Y. and Miralda-Escudé, J. 1998, ApJ, 509, 56
 Hui L., Gnedin N.Y., 1997, MNRAS, 292, 27
 Markevitch, M. 1999, ApJ, 522, L13
 Miyaji T., Ishisaki Y., Ogasaka Y., Ueda Y., Freyberg M.J., Hasinger G., Tanaka Y. 1998, A&A, 334, 13L.
 Ostriker J.P., Cen R. 1996, ApJ, 464, 270
 Perna R., Loeb A. 1998, ApJ, 503, 135
 Ponman T.J., Cannon D.B., Navarro J.F., 1999, Nature 397, 135
 Shapiro P.R., Bahcall J.N. 1980, ApJ, 241, 1
 Zeldovich Ya.B. 1970 A&A, 5, 84



The XEUS Mission

A.N. Parmar

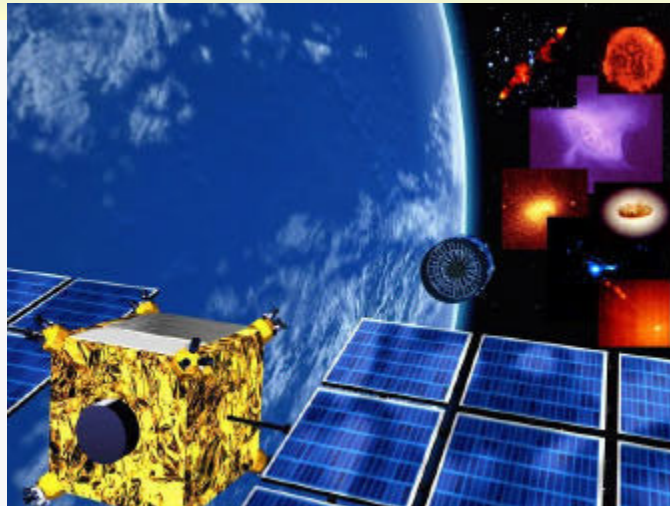
Astrophysics Mission Division, Research and Scientific Support Department of ESA, ESTEC, 2200 AG Noordwijk, The Netherlands

Abstract. XEUS is a potential follow-on to XMM-Newton, ESA's Cornerstone X-Ray Spectroscopy Mission currently in operation, and is under study as part of the Horizon 2000+ plan to utilize the International Space Station (ISS) for astronomical applications. XEUS will be a long-term X-ray observatory with an initial aperture of 6 m², an energy range of 0.05–30 keV and a spatial resolution of 2'' to 5'' at 1 keV. The focal plane detectors will consist of both narrow and wide-field imagers with fields of view of 1 and 5–10', respectively. The narrow field imagers are expected to have an energy resolution of <2 eV at 1 keV and the wide field imager 50 eV at 1 keV. Following refurbishment at the ISS the mirror area of 30 m² at 1 keV will allow sources as faint as 4 10⁻¹⁸ erg cm⁻² s⁻¹ to be detected.

The enormous low-energy collecting area and good spatial resolution of XEUS will allow the detection of massive black holes in the earliest AGN and estimates of their mass, spin and redshift through studies of relativistically broadened Fe-K lines and variability to be made. XEUS will allow the study of the formation of the first gravitationally bound, dark matter dominated, systems ie. small groups of galaxies and the tracing of their evolution into today's massive clusters. High resolution spectroscopy will allow the study of the evolution of metal synthesis down to the present epoch, using in particular, observations of the hot intra-cluster gas while the hot filamentary structure will be studied using absorption line spectroscopy to allow the mass, temperature and density of the intergalactic medium to be characterized.

Acknowledgements. We gratefully acknowledge the permission by the Springer Verlag to use their A&A L^AT_EX document class macro.

The X-ray Evolving Universe Spectroscopy Mission



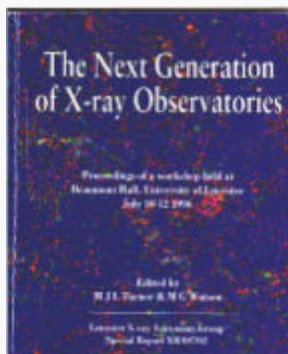
XEUS – Introduction

- XEUS status
- Deep Universe science objectives and requirements
- Mission design
- Expanding the science objectives

XEUS – Current Status

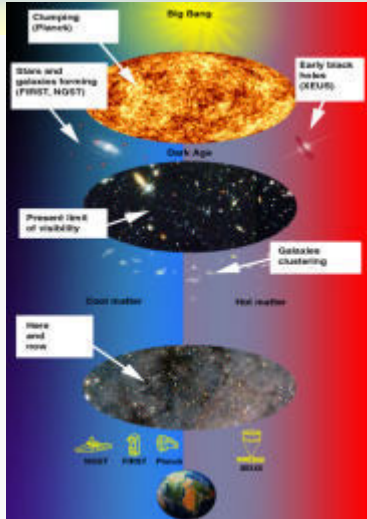
- XEUS is one of the established priorities of the ESA Space Science Programme and is classed as a “mission under study”.
- A concept study conducted by industry showed no potential “show stoppers”.
- 18 month System Study to begin in April. Jointly supported by DSCI and DMSM and in collaboration with our ISAS colleagues. (Analysis of critical subsystems (AOCS, thermal, baffling, etc), study of ISS interfaces, costs and mirror logistics).
- Technological emphasis is on demonstrating the mirror capabilities in the next 2 to 3 years.
- Goal is to be ready with a technically feasible, affordable, mission together with our international partners for launch soon after 2012.

XEUS – Origins in 1996



- Horizon 2000+ called for a study of the utilization of the ISS for a major high-energy astrophysics mission.
- How should we follow XMM-Newton?
- What will be the science topics for high-energy astronomy at the end of the first decade of the 21st century

XEUS Science Topics



Observations of the hot Universe at high redshifts will provide crucial complimentary information to NGST, ALMA, Herschel etc on:

- The formation and evolution of the first massive blackholes
- The large scale structure of the Universe and hot filamentary components at high redshift
- Study of the first small groups of galaxies and their evolution to today's massive clusters
- Study of the formation of the first metals, in the hot inter-galactic medium

XEUS - Requirements

- Study of first galaxy groups and evolution into today's clusters
- Absorption line spectroscopy of hot filamentary material
- Spectra of first accreting black holes



Sensitivity: $4 \times 10^{-18} \text{ erg cm}^{-2} \text{ s}^{-1}$
Angular resolution: $< 5''$
Spectral resolution: $2 \text{ eV @ } 1 \text{ keV}$
Bandpass: $0.05 - 30 \text{ keV}$



Mirror effective area: $30 \text{ m}^2 @ 1 \text{ keV}$, $3 \text{ m}^2 @ 8 \text{ keV}$
Lightweight high resolution optics ($5''$, goal $2''$) with 50m focal length
Imaging wide field semiconductor and cryogenic high γ E instruments

X-ray Astronomy Satellites



XMM-Newton:

- Mirror area 0.4 m²
- Spatial resolution 15'' HEW
- Limiting sensitivity: 10⁻¹⁵ erg cm⁻² s⁻¹



Chandra:

- Mirror area 0.08 m²
- Spatial resolution 0.5'' HEW
- Limiting sensitivity: 10⁻¹⁶ erg cm⁻² s⁻¹

XEUS – The Challenge

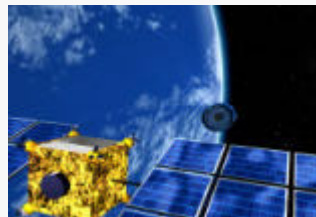
XMM-Newton



0.4 m² 15'' HEW



XEUS



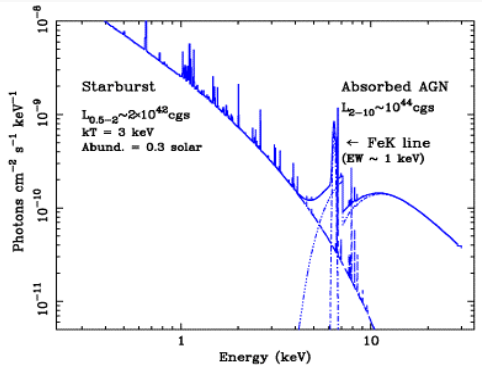
30 m² 2-5'' HEW

Via the ISS and in
partnership with
ISAS



XEUS is under study as part of the
Horizons 2000+ programme and is one of
the established priorities of the ESA
Science Programme

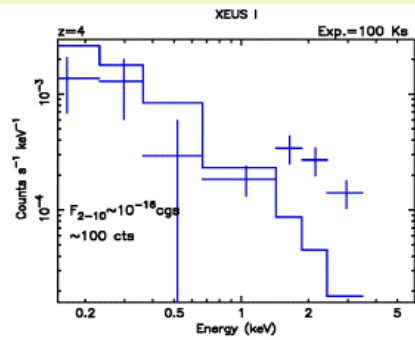
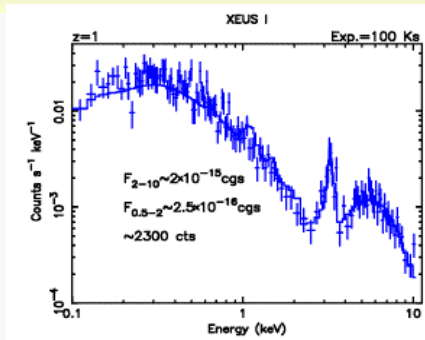
XEUS – AGN versus Starbursts



Credit: A. Comastri & M. Cappi

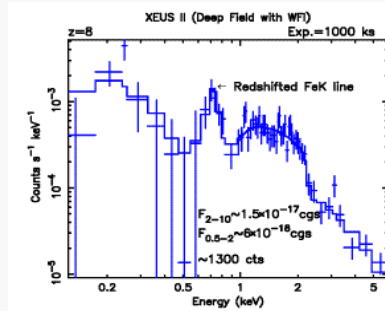
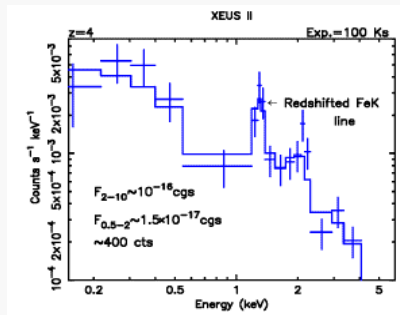
- Figure shows a composite spectrum of a $kT=3$ keV $0.3x$ solar metallicity thermal gas and an absorbed AGN with a strong ($EW=1$ keV) Fe line, primarily due to reflection.
- Source luminosity assumed the same as the nearby galaxy NGC 6240.
- XEUS can study dust enshrouded AGN at high redshifts and separate the contributions from starbursts and AGN.

XEUS – AGN versus Starbursts



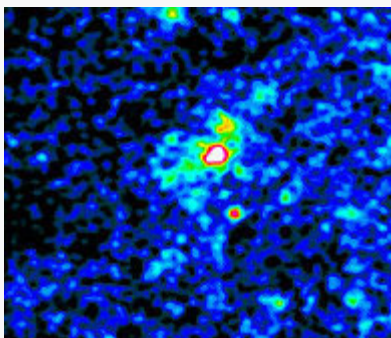
- Simulated XEUS spectra of the composite starburst-AGN for $z=1$ and $z=4$ for the initial XEUS configuration. An exposure of 100 ks is assumed.

XEUS – AGN versus Starbursts



- Simulated XEUS spectra of the composite starburst-AGN for the final XEUS configuration. These show that with a deep field exposure, the spectra of sources at $z=8$ could be obtained and their Fe-K lines detected.

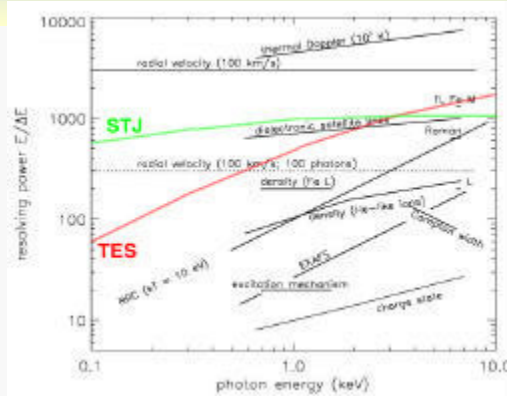
XEUS – Studying structure formation



Credit: H. Böhringer

- In standard cosmology, galaxy groups with masses of $\sim 10^{13} M_{\odot}$ are the first emerging massive objects at redshifts of 2-3.
- These groups have sufficiently deep gravitational potential wells that the intra-group gas is heated to X-ray temperatures and remains essentially trapped.
- XEUS will be a powerful tool for observing the formation of large-scale structure in the Universe.
- Such groups are expected to be found serendipitously in regular XEUS observations.
- Simulated XEUS image of a $10^{43} \text{ erg s}^{-1}$ Hickson-type group at $z=2$ with $5''$ HEW angular resolution.

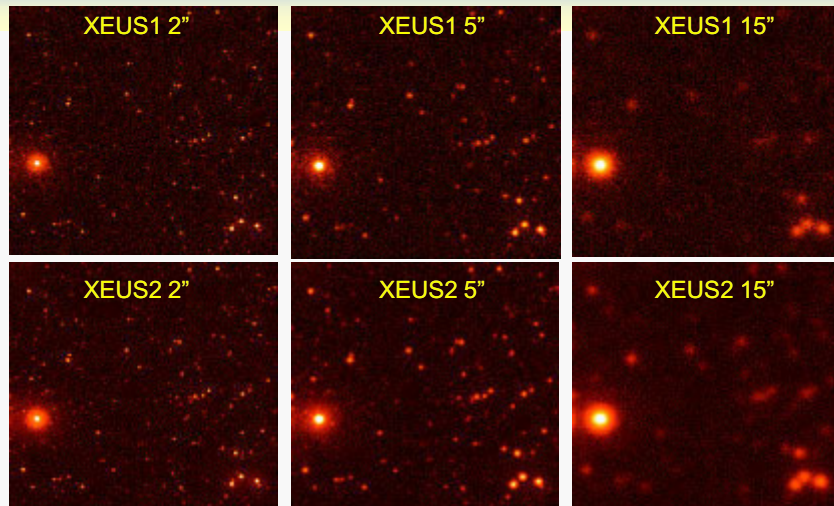
XEUS – Spectral Resolving Power



Credit: F. Paerels

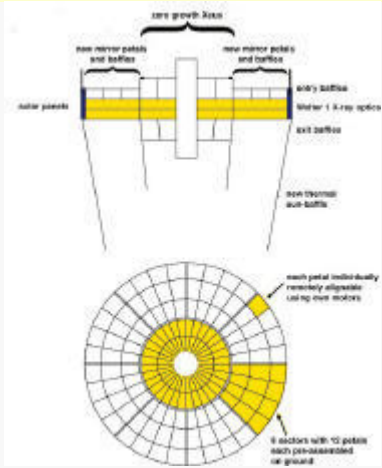
- Plot of resolving power against photon energy. The red line shows the resolving power of the strawman TES instrument; green the strawman STJ instrument.

XEUS – Observing the deep Universe

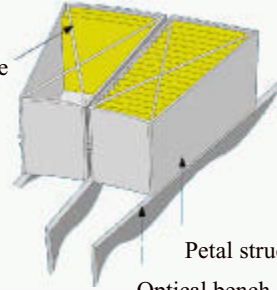


100 ks
0.5-2 keV

XEUS – Mirror Technology



Mirror plate



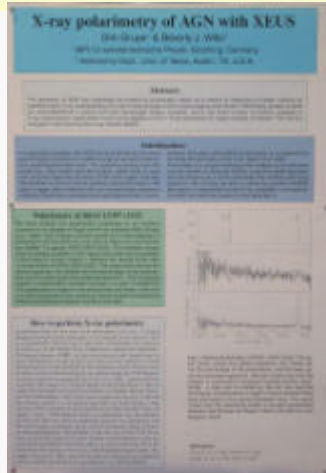
Petal structure
Optical bench (=MSC)



XEUS – The Movie

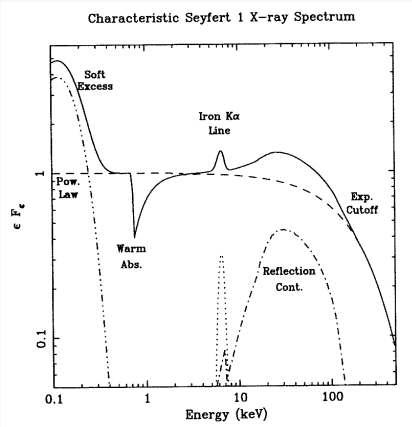


XEUS – Expanding the Science Case



- X-ray Polarimetry?
- Grupe & Wills
- Presentation by Costa as well.

XEUS – High-energy Extension?

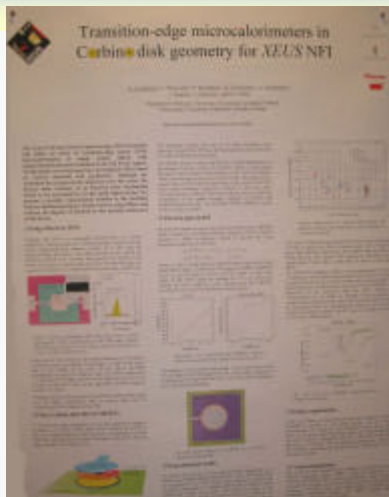


- Important classes of objects such as Seyfert galaxies can show strong reflection components which peak at ~30 keV and provide important astrophysical constraints.
- Talk by Y. Ogasaka.

XEUS – A Fast Timing Capability?

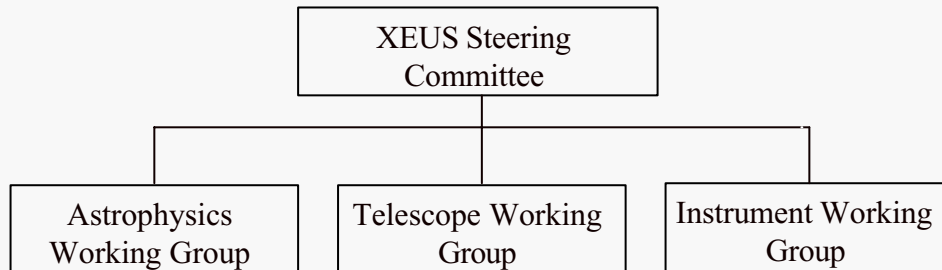
- XEUS could provide an order of magnitude sensitivity improvement in timing studies over RXTE – if a suitable capability in the focal plane was present.
- This will provide sufficient sensitivity to search for the signatures of the innermost stable orbit around neutron stars (as seen from 4U 1820-30 by RXTE) allowing the Equation of State of ultra-dense material to be directly constrained and the effects of strong gravity on the metric to be directly tested.
- Talk by D. Barret

XEUS – Focal Plane Detectors



- An alternative micro-calorimeter configuration for XEUS?
- Luukanen et al.

XEUS – Organisation



XEUS Astrophysics Working Group

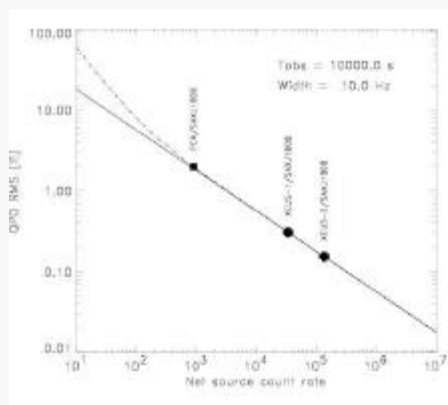
Gunther Hasinger, [AIP Potsdam, D](#)
 Monique Arnaud, [CEA Saclay, F](#)
 Xavier Barcons, [CSIC-UC Santander, ES](#)
 Didier Barret, [CESR-CNRS/UPS, F](#)
 Alain Blanchard, [Strasbourg, F](#)
 Hans Böhringer, [MPE Garching, D](#)
 Massimo Cappi, [TESRE Bologna, I](#)
 Andrea Comastri, [Bologna Obs, I](#)
 Thierry Courvoisier, [Geneva, CH](#)
 Andy Fabian, [IoA Cambridge, UK](#)
 I. Georgantopoulos, [IA&A, Athens, G](#)
 Richard Griffiths, [Carnegie Mellon U, USA](#)

Nobuyuki Kawai, [RIKEN, J](#)
 Katsuji Koyama, [Kyoto University, J](#)
 Kazuo Makishima, [U of Tokyo, J](#)
 Pino Malaguti, [TESRE Bologna, I](#)
 Keith Mason, [MSSL/UCL, UK](#)
 Mariano Mendez, [SRON, NL](#)
 Takaya Ohashi, [Tokyo Metro. Univ, J](#)
 Frits Paerels, [Columbia U, USA](#)
 Arvind Parmar, [ESA/ESTEC, NL](#)
 Luigi Piro, [IAS Roma, I](#)
 Jürgen Schmitt, [U of Hamburg, D](#)
 Michiel van der Klis, [Amsterdam, NL](#)
 Martin Ward, [U of Leicester, UK](#)

XEUS – Baseline Parameters

Parameter	Specification (goal)
Energy Range	0.05 – 30 keV
Telescope focal length	50 m
Mirror area @ 1 keV	6m ² (XEUS I) 30 m ² (XEUS II)
Mirror area @ 8 keV	3m ² (XEUS I) 3m ² (XEUS II)
Fields of view	5' (WFI) 1' (NFI)
Energy resolution @ 1 keV	50 eV (WFI) 2 (1) eV (NFI)
Energy resolution @ 8 keV	100 eV (WFI) 5 (2) eV (NFI)

XEUS – A Fast Timing Capability?



- Simulations by Barret et al. show the sensitivity of XEUS to QPO from the *only* known accreting milli-second X-ray pulsar SAX J1808-3658. RXTE did not find QPO.
- Detection of both coherent P and kHz QPO from the same source would immediately allow conformation or rejection of many QPO models.
- XEUS would likely detect both types of signal from a number of LMXRB.
- These systems may be powerful sources of gravitational radiation. Accurate P measurements could help LISA etc in searches for gravitational radiation.



Metrology for the XEUS mirror plates

R. Willingale

Department of Physics and Astronomy, University of Leicester, University Road, Leicester, LE1 7RH, UK
email: rw@star.le.ac.uk

Abstract. XEUS is a single focus Wolter type I telescope with aperture diameter 10 m and focal length 50 m providing a collecting area $> 20 \text{ m}^2$ at 1 keV with angular resolution 2-5 arc seconds. The aperture is divided into sectors and the Wolter surfaces are manufactured as sector plates rather than continuous surfaces of revolution. The major technological challenges in constructing the mirror system are (i) manufacture of very high quality mirror plates (ii) handling and fixing of the plates during integration into a sector module and (iii) metrology of the reflecting surfaces before and during integration to ensure the desired angular resolution is met. This paper discusses techniques that can satisfy challenge (iii). A metrology scheme which can be used for monitoring the figure of the mirror plates during production, handling and integration is proposed. The scheme has the potential for sub arc second accuracy which is more than adequate to satisfy the requirements for XEUS.

1. Major technological challenges in the construction of the XEUS mirror system

The basic concept for the construction of the XEUS mirror system is shown in Fig. 1. The mirrors consist of two reflection surfaces, a paraboloid and a hyperboloid, joined together as a continuous thin plate. The change in gradient at the join is small, just three times the grazing incidence angle. The right-hand panel shows dummy

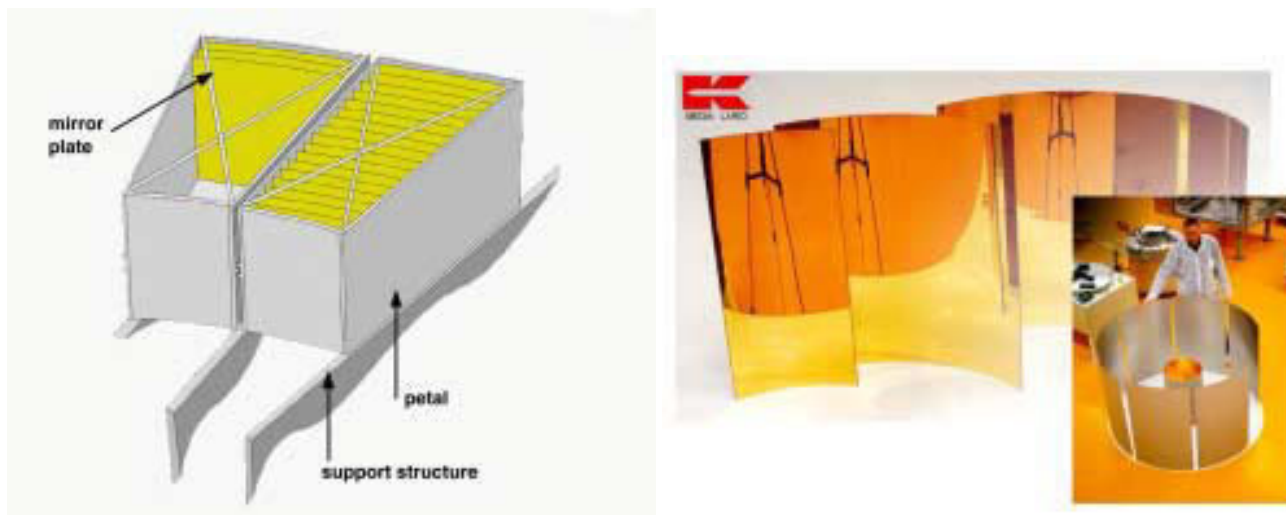


Fig. 1. Schematic of a XEUS mirror petal and examples of full size dummy mirror plates manufactured from nickel with a gold coating

XEUS mirror plates manufactured from nickel with a coating of gold made in the same way as the XMM-Newton mirror shells. Full details of the proposed mirror design and a discussion of the available mirror technologies is provided in the report of the XEUS Telescope Working Group, ESA (2001). Typical plate dimensions are an axial

length of 2×500 mm (both the paraboloid and hyperboloid sections are 500 mm in length) and a width of 500 mm. The plate thickness is ~ 1 mm and the grazing reflection angles range from 0.3 to 0.67 degrees depending on the radial position of the plate in the full mirror aperture. The axial mirror profiles are almost conical however a slight curvature is required to produce the exact paraboloid and hyperboloid form so that the X-rays are focused to arc second accuracy. Fig. 2 shows the deviation of the surface generators from simple straight lines. The maxi-

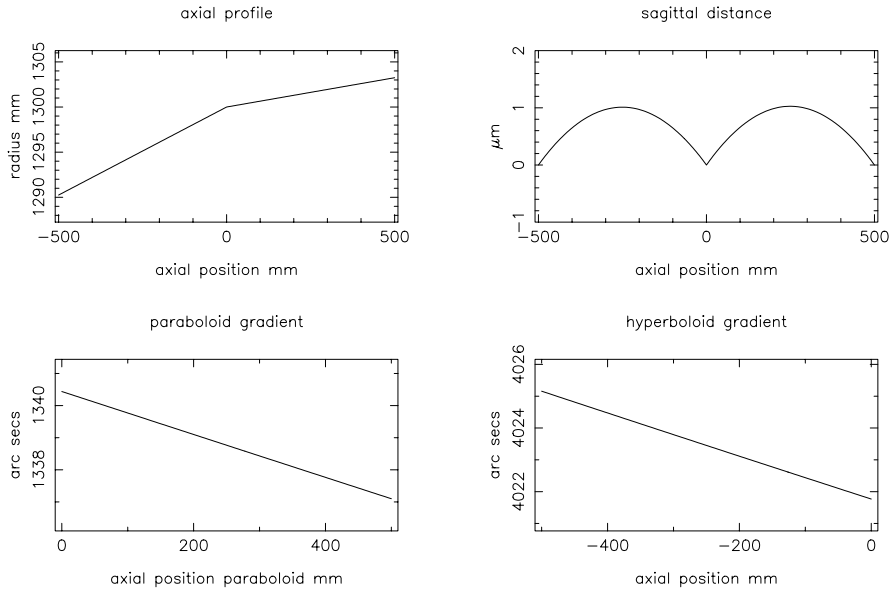


Fig. 2. A typical axial plate profile, top-left. The top-right panel shows the difference between a straight line generator and the true Wolter I surface profiles. The lower panels show the change in gradient along the paraboloid and hyperboloid surfaces.

imum sagittal distance is ~ 1 μm and the grazing angles only change by ~ 3 arc seconds over the axial length of 500 mm.

The challenges are:

- Manufacture of mirror plates. They are very thin, large area, low mass mirrors with arc second figure accuracy and a super-smooth reflecting surface of high-Z material.
- Handling and fixing of the mirror plates to produce an integrated petal structure. This requires μm precision across the full length and breadth of the plates.
- Plate metrology before and during integration. The angular resolution goal is ~ 2 arc seconds and the rms surface roughness must be ~ 3 \AA . Very high precision metrology is needed to verify plate manufacture and monitor the handling and fixing processes at all times.

2. Plate alignment and plate distortions

Fig. 3 shows the basic geometry of the plate alignment. The focusing is insensitive to rotation about the Z or Y axes. Tilt (rotation about X) and translation in Z and Y shifts the focal spot. Translation in X defocuses the image. Fig. 4 shows the lowest order distortions which can be introduced into the plate figure. It is important that any alignment and integration scheme does not introduce figure errors that can seriously degrade the X-ray focusing. Focusing quality is largely determined by axial gradient errors introduced by the low order plate distortions illustrated. Table 1 lists the typical alignment and distortion amplitudes measured at the corners of a plate that will contribute a ~ 1 arc second blur at the focus. The elements on the left-hand side of the table are rather insensitive and are easily controlled by conventional mechanical metrology. The elements on the right-hand side require μm accuracy and must probably be monitored optically to ensure that the angular resolution goal is met.

3. Metrology requirements and difficulties

As indicated above the alignment and integration of the XEUS Wolter I mirror plates into a petal module calls for very high precision if the focusing of the completed petal is to meet the goal of a few arc seconds. The plates must

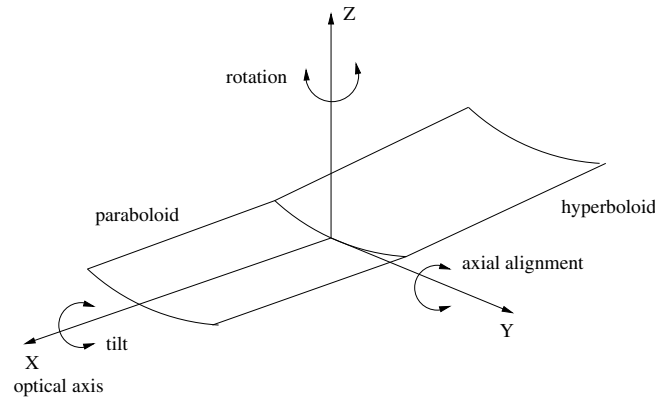


Fig. 3. The alignment geometry of a single mirror plate

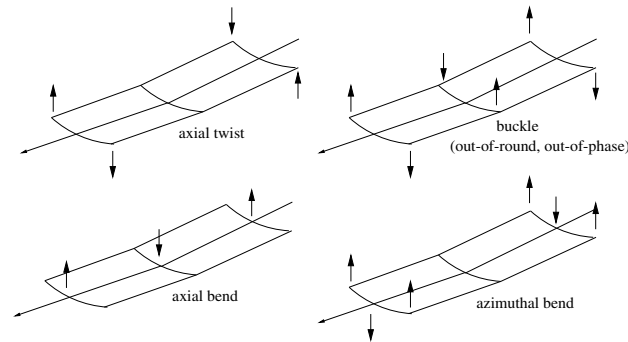


Fig. 4. The lowest order plate distortions

X shift	2.4 mm	Rotation (about X)	46 μm
Rotation (about Z)	2.1 mm	Azimuthal bend	41 μm
Rotation (about Y)	2.1 mm	Axial bend	2.4 μm
Axial twist	2.1 mm	Buckle	1.2 μm
Y shift	0.24 mm		
Z shift	0.24 mm		

Table 1. Distortion amplitudes measured at the corners of a plate which produce ~ 1 arc second blur at the focus

be fixed such that their figure is very close to the ideal Wolter I surfaces and each plate must be very accurately positioned with respect to its neighbours.

The XMM mirror shells were aligned and integrated using a Vertical Optical Bench (VOB) utilising the so-called Hartmann test. In this test the front aperture of the shell is illuminated with visible light such that plane wavefronts are perpendicular to the optical axis, effectively a point source at infinity in the centre of the field of view. The Wolter I shell then produces an optical image at the 2-reflection focus in much the same way as with X-rays. However, because the shell aperture annulus is very narrow (1-3 mm) the optical image is severely diffraction limited. In such an arrangement the intra-focal and extra-focal images seen forward of or behind the optimum focus are annula rings. Individual sectors of the shell surface can be isolated using a mask in front of the aperture and there is a direct correspondence between the azimuthal position around the intra-focal and extra-focal images and the azimuthal position of the mask. If the mask is scanned around the aperture the alignment of the individual sectors of the mirror can be checked and adjusted.

The shape of the hyperbola focus (due to single reflections from the second surface only) which can also be seen in this arrangement is very sensitive to the tilt of a shell with respect to the axis (the wavevector associated with the incident wavefronts). It is very easy to adjust the tilt to provide alignment with respect to the incoming beam.

Unfortunately the sensitivity of the Hartmann test and the hyperbola focus derives from the fact that the shell is a complete surface of revolution. In the case of XEUS the mirror plates cover only a narrow sector of the aperture, 11-22 degrees. The arrangement used for XMM shells gives some sensitivity to Y shift and tilt (about X) but the 2-reflection image and the intra-focal and extra-focal images are insensitive to Z-shift and axial alignment errors

largely because of diffraction at visible wavelengths.

The metrology requirements:

- Must be sensitive to all distortions and shifts that degrade the angular resolution by ≥ 1 arc second.
- Must be quick because we have 1000s of plates to screen and integrate.
- Must be reliable because we can't disintegrate the plates once they have been integrated.
- Must use mechanical and/or optical techniques to ensure an acceptable X-ray performance. X-ray testing can only be used as a spot check.

The metrology difficulties:

- The XEUS plates are aspheric. In fact they are very close to cylindrical or straight cone sections. We can't utilise standard normal incidence methods based on spherical wavefronts.
- The 2-reflection X-ray focusing paths cover a very narrow annular aperture which is severely diffraction limited at visible wavelengths.
- The plates are not complete surfaces of revolution so we can't exploit rotational symmetry.

4. The proposed metrology scheme

We can gain sensitivity to the angular and shift alignments shown in Fig. 3 and to the low order plate distortions shown in Fig. 4 if we illuminate the surface with wavefronts near parallel to the surface, i.e. with the reference beam wavevector at near normal incidence. If we set the wavefronts parallel to the optical axis of the Wolter I geometry the beam will provide an absolute reference that can be used to monitor the alignment between the plates as they are integrated as well as being sensitive to distortions of the individual plates.

The paraboloid and hyperboloid sections are well approximated by cylindrical mirrors since the axial profile radius of curvature is very large and the azimuthal radius of curvature doesn't change very much from the top to the bottom (X-high to X-low) of each of the surfaces as shown in Fig. 2. Therefore we should use cylindrical wavefronts incident on the mirror plates as shown in the schematic view of the proposed scheme, Fig. 5. This arrangement is essentially a Twyman-Green interferometer. The use of cylindrical wavefronts to measure grazing incidence optics has been described before, see for example Geary and Maeda (1987) who propose a Fizeau interferometer arrangement, but for XEUS the area of surface to be monitored is very large and we also want an absolute reference between successive plates. A cylindrical lens produces a line focus on the optical axis of the Wolter I geometry. Cylindrical wavefronts are accurately tilted by a beam tilt device to exactly match the grazing angle (axial gradient) of the reflecting surface. The return wavefronts can be focused using a telescope objective to produce an image or they can be used to produce an interferogram with the reference beam. Initial crude alignment can be effected by adjusting the plate until the focused spot of the reference beam and the focused spot returned from the mirror plate are coincident. Fine tuning of the surface profile can then be monitored using the interferogram. Integration of a petal will start with the outer plate (largest radius). Once this is fixed the next plate can be introduced. The deviation angle of the beam tilt device must be reduced very slightly to match the grazing angle of the new plate. So the process proceeds from plate to plate. During this sequence the only adjustment required in the metrology set up is the deviation angle of the beam tilt device and switching between using a telescope to focus the beams and producing an interferogram. The incident beam, cylindrical lens and the interferometric optics remain fixed as an absolute reference. This combination produces the line focus on the optical axis and this must remain fixed in space. Providing the beam tilt device is sufficiently accurate all the plates will be correctly aligned as a confocal set.

The sensitivity of the proposed scheme depends on a number of factors:

- An input beam width of ~ 100 mm will give a diffraction limit of ~ 1 arc second if the wavelength is 630 nm.
- The beam tilt must cover a grazing angle range of 0.3-0.67 degrees for the paraboloid and 0.9-2.0 degrees for the hyperboloid.
- The beam tilt must have an absolute accuracy and sensitivity of ≤ 1 arc second.
- We need at least 1 device for the paraboloid surface and 1 device for the hyperboloid surface. More would be preferable so that we can monitor most of the plate surface simultaneously.
- To illuminate the full plate width the cylindrical lens must be $\sim f/2.6$.

Further development of this metrology concept is required:

- A suitable beam tilt device must be designed, tested and calibrated.

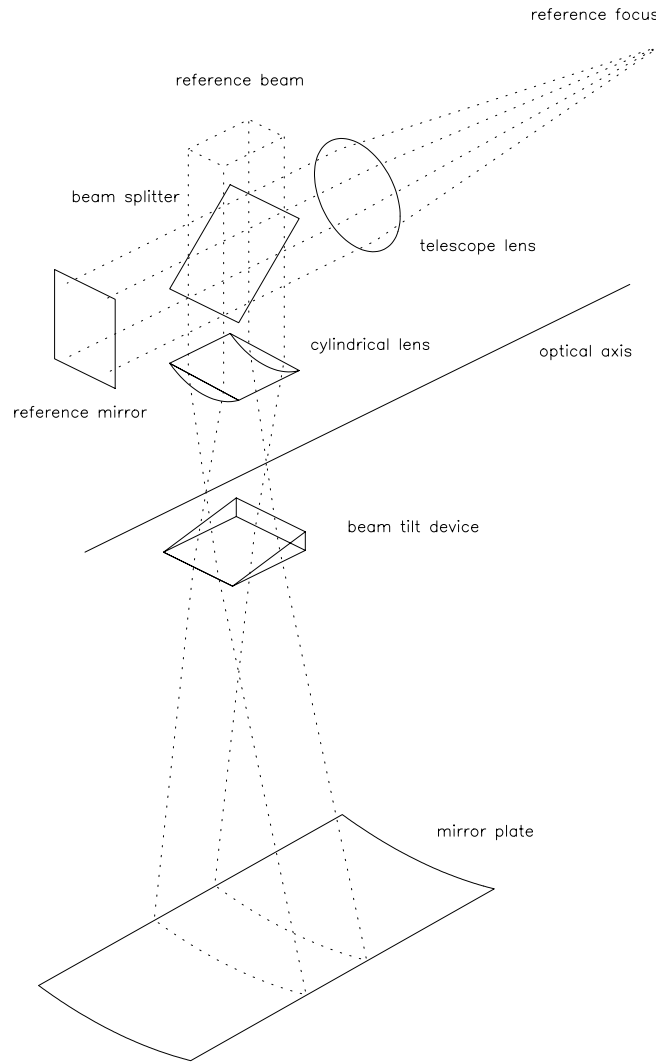


Fig. 5. An optical metrology scheme which illuminates the plate surfaces with cylindrical wavefronts

- Ray tracing must be used to assess the sensitivity of the scheme in the alignment and adjustment of plates which exhibit a combination of misalignments and/or distortions.
- Ray tracing should be used to assess the diffraction limited performance we can expect. The cylindrical lens and beam tilt device will be subject to aberrations. Small correction plates may be needed to achieve a diffraction limited performance over the full aperture of the metrology scheme.
- An algorithm must be developed to utilise data from the device in a fast and effective alignment and integration procedure.

Fig. 6 illustrates the principle of a possible beam tilt device. The device comprises a small angle liquid prism formed between two optical flats. The angle between the optical flats can be adjusted to change the beam tilt produced. The beam deviation is $\delta = (n - 1)\alpha$ where α is the prism angle and n is the refractive index of the liquid. If $n = 1.33$ (water!) then α must be set to an accuracy of ~ 3 arc second to give a final accuracy/sensitivity of ~ 1 arc second. A larger gearing will result if the refractive index of the liquid is closer to unity.

If the radius of the plate at the join plane is R and the focal length is F then the grazing angle is given by $4\theta_g = \tan^{-1}(R/F) \approx R/F$. If the plate thickness is T and the axial length of the paraboloid (or hyperboloid) section is L then the change in radius to move to the next plate is $\Delta R = L \sin \theta_g + T \approx L\theta_g + T$. Therefore the change in grazing angle moving from one plate to the next is $\Delta\theta_g \approx (L\theta_g + T)/4F$. If $F = 50000$ mm, $L = 500$ mm, $T = 1$ mm and $0.3^\circ \leq \theta_g \leq 0.67^\circ$ then the change in grazing angle required is $3.7'' \leq \Delta\theta_g \leq 7.1''$. The gradient of the hyperboloid

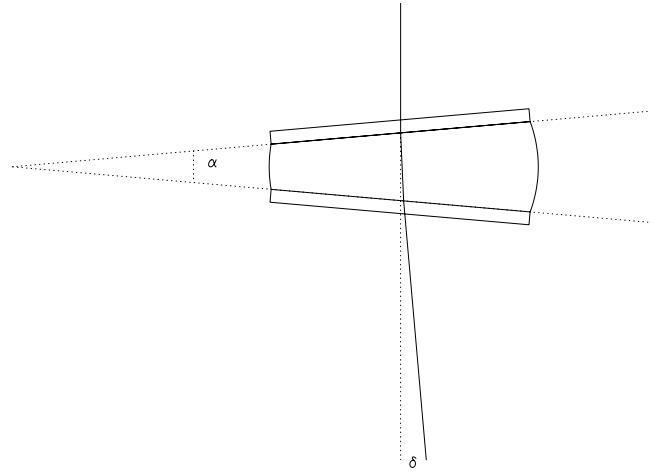


Fig. 6. A thumb nail sketch of a simple beam tilt device

section is 3 times that of the paraboloid section. Therefore the beam tilt device for hyperboloid section must be set and adjusted by 3 times these values moving from plate to plate.

5. Conclusions

I believe we will only achieve arc second imaging if the figure quality of the plates is fully monitored with the highest accuracy throughout the manufacture, handling and integration processes required to produce a completed mirror petal. If we measure the plates with the scheme proposed above we will be able to tell when figure errors are introduced and identify the particular process which is at fault.

The proposed metrology scheme requires full normal incidence access to the reflecting surfaces at all times. Therefore integration must start with the outer radius plates and move inwards towards the smaller radius plates within a petal module. This probably implies that the plates must be supported along the axial edges throughout the handling and integration process.

A relatively simple Twyman-Green interferometer working in visible light with the addition of a beam tilt device as described can be used to measure plate quality and monitor alignment and distortions as the plates are integrated into a petal. An accuracy/sensitivity of ~ 1 arc second or better is possible and therefore the integration of XEUS petals would and should not be limited by the available metrology.

Acknowledgements. I would like to thank Tommi Karhunen for help in ray tracing possible designs for the plate metrology.

References

- ESA SP-1253, 2001, Aschenbach B., Bavdaz M., Beijersbergen M., Kunieda H., Willingale R. and Yamashita K., "The XEUS Telescope", ISBN 92-9092-612-0
 Geary J. and Maeda R., 1987, SPIE Proc. Vol. 830, 268-272

Alternative mirror technologies

O. Citterio¹, M. Ghigo¹, F. Mazzoleni¹, G. Pareschi¹, B. Aschenbach² and H. Bräuninger²

¹ Osservatorio Astronomico di Brera – INAF, Via E. Bianchi 46, 23807 Merate (Lc), Italy

² Max-Planck-Institut für extraterrestrische Physik, Postfach 1603, 85741 Garching, Germany

Abstract. One of the major components of the XEUUS scientific payload is given by the X-ray optics that, in spite of its enormous size, has even to be characterized by optimal imaging capabilities (the HEW goal is of just 2 arcsec). The enormous mirror dimensions give rise to a number of problems that make very challenging to meet a so ambitious request. It is impossible to realize so large mirror shells with a close symmetrical Wolter I structure (which would guarantee a high mechanical stiffness), but instead they will be formed by a series of segments (size of the order of 1 m x 0.5 m), known as petals, to be assembled together. Moreover, the Mass/Geometric-Area ratio foreseen for the mission is very small (just of 0.08 Kg/cm²), much lower than for the XMM-Newton (0.24 Kg/cm²). Finally, the optics will operate in prohibitive thermal conditions (the mirror temperature will oscillate between -30 and -40° C), that tend to exclude the epoxy-replication approach because of the mismatch between the CTE of the substrate and that of the resin, that would cause a deformation of the mirror profile. These considerations make very attractive the use of light weight materials with high thermal-mechanical parameters like glass or ceramics to realize the XEUUS petals. In particular, in this paper we will describe the basic ideas concerning an on-going development activity devoted to the realization of the XEUUS petal by large segments of thin borofloat glass. The technique to be explored is based on a thermal precision slumping of flat glass panels to produce the optics. To get the right final mirror profile, the segments will be directly grinded and superpolished. After the evaporation of the reflecting coating, the segments will be integrated in the mounting structure in appropriate way, in order not to deform the mirror profile. Some elements for the evaluation of the real feasibility of the process will be also given.

Acknowledgements. We gratefully acknowledge the collaboration with Dr. W. Egle from C. Zeiss (Germany) and Dr. T. Döhring from Schott (Germany) for their valuable support concerning the development activities on course.

References

Citterio O., Ghigo M., Mazzoleni F., et al, 2001, SPIE Proc. 4496, 23

Citterio O., Ghigo M., Mazzoleni F., et al, 2002, in SPIE Conf. AS18, in press.

Alternative Mirror Technologies

O. Citterio, M. Ghigo, F. Mazzoleni, G. Pareschi

*Osservatorio Astronomico di Brera - INAF
Via e. Bianchi 46
23807 Merate -- Italy*

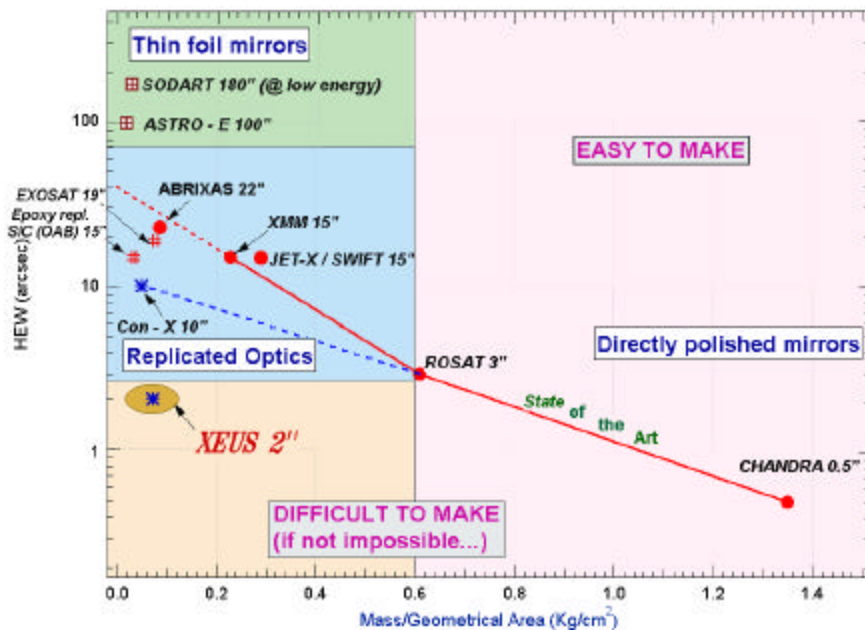
B. Aschenbach, H. Bräuninger

*Max-Planck Institut fur extraterrestriche Physik
Postfach 1312, Giessenbachstrasse
85741 Garching - Germany*



***XEUS Workshop**
MPE Garching March 11-13, 2002*

HEW vs. the Mass/Collecting-Area Ratio for past and future X-ray telescopes



The high demanding requirements in terms of:

- **angular resolution**
- **low mass**
- **large temperature operative range***

for the next generation X-ray telescopes like **XEUS** require development of new technological approaches for the manufacture of the X-ray optical systems

*NOTE: the present XEUS configuration foresees a thermal operative range for the optics between -30° – 40° C

Assuming a petal configuration with segmented mirrors which is imposed by the large diameter foreseen for the **XEUS** optics, in this presentation we will analyze the use of:

- *new materials*
- *new manufacturing processes*

that we think could meet the stringent requirements of XEUS

Envisaged approaches for the **XEUS** segmented mirrors manufacturing

Materials and manufacturing techniques under investigation:

□ Borofloat glass

- Slumping of the shell
- ↓
- Fast Polishing
- ↓
- Active integration

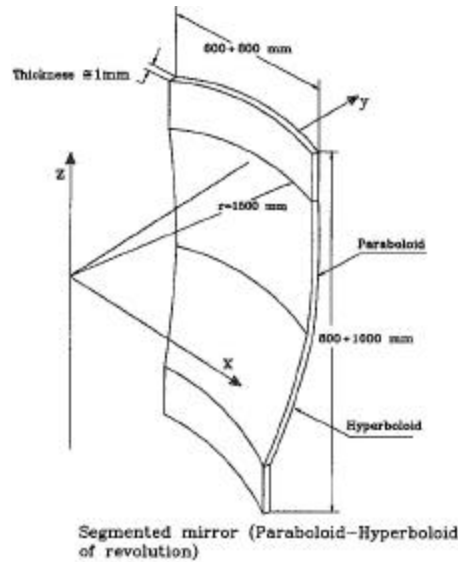


□ Ceramic SiC

- Tape casting of the shell
- ↓
- Silicon infiltration
- ↓
- Fast polishing
- ↓
- Active integration



Possible layout of a XEUS mirror segment



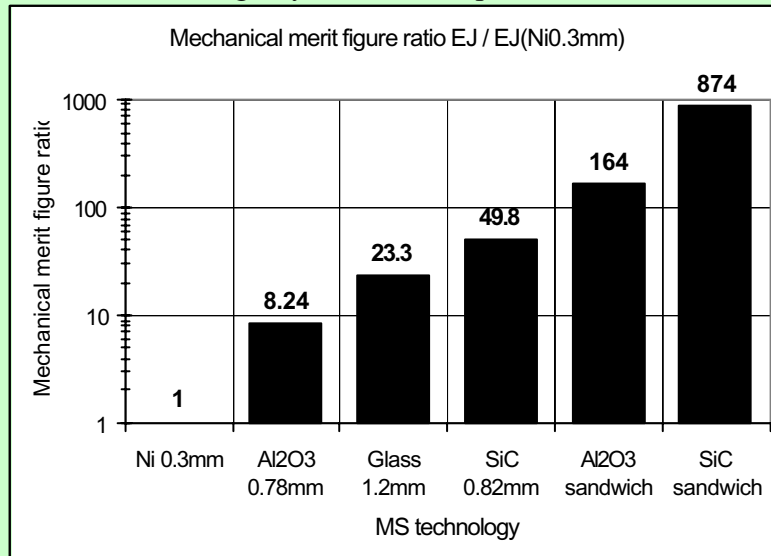
Thermal-mechanical parameters of some materials used in past missions or candidate for future projects like XEUS.

Material	ρ Density [Kg x m ³ x 10 ³]	α CTE [K ⁻¹ x 10 ⁶]	C Specific Heat [J x kg ⁻¹ x K ⁻¹]	k Therm. Conduct. [W x m ⁻¹ x K ⁻¹]	E Elastic Modulus [GPa]	$k \times \alpha^{-1}$ Therm. Dist. Par. [W x m ² x 10 ²]	$E \times \rho^{-1}$ Specific Stiffness [MN x Kg ⁻¹ x 10 ⁶]
<i>Electrof. Ni</i>	8.8	14	444	90	180	0.6	20.5
<i>Plasma spray Al₂O₃</i>	3.37	5.5	880	25	87	0.45	25.8
<i>Al</i>	2.7	25	899	237	76	0.95	28.1
<i>UIE (7971)</i>	2.2	0.03	708	1.3	67	4.3	30.4
<i>Zerodur</i>	2.55	0.15	820	6.0	90	4.0	33.3
<i>CFRP</i>	1.55	1.6	710	17	70	1.06	45.1
<i>CVD SiC</i>	3.21	2.4	700	25	466	10.4	145
<i>Be</i>	1.85	11.4	1880	216	305	1.9	164

If we fix the unitary mass equal to 2.64 Kg/m², corresponding to the mass budget foreseen for a single panel (segment) of the most external mirror shell of the XEUS mirror mission (see below for details), we can spend such a mass using:

1. 0.3 mm of electroformed Ni;
2. 1.2 mm solid glass;
3. 0.78 mm solid Al₂O₃;
4. 0.82 mm CVD SiC;
5. an Al₂O₃ sandwich having a foamed core 2 mm thick and two skins 0.3 mm each;
6. a SiC sandwich having a foamed core 2 mm thick and two skins 0.3 mm each;

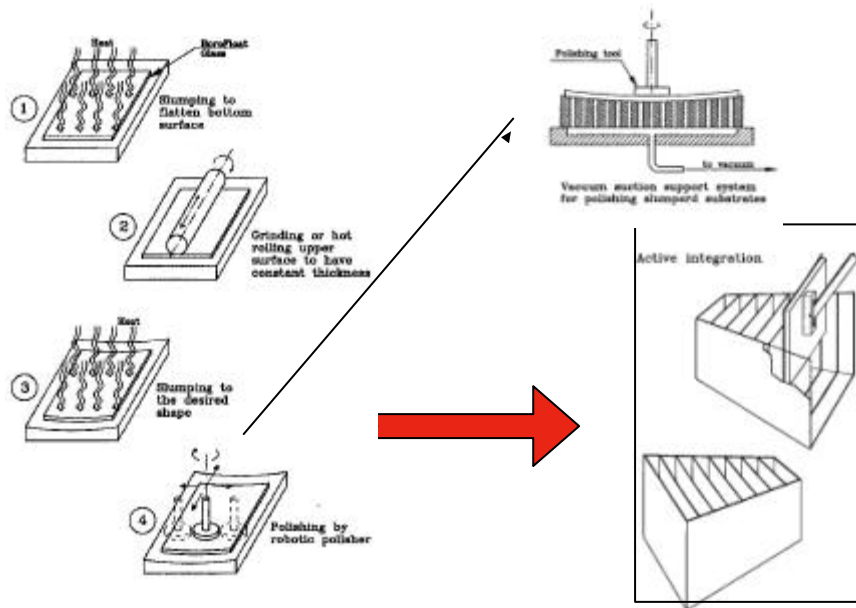
Flexural Rigidity for a XEUS panel 1 m x 0.5 m



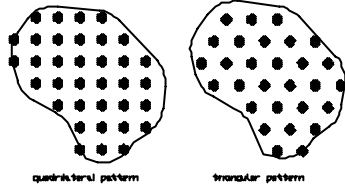
NOTE: E = Elastic Modulus
J = Moment of Inertia



XEUS petals based on slumped glass segments: production sequence and assembling



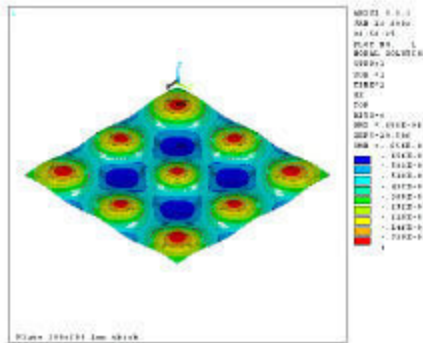
Mirror supporting in measuring and integration conditions



Simulations by a finite elements code applied to the case of a borofloat glass segment 1 mm thick showed that the quadrilateral pattern gives the better performances.

During the testing phase the mirror segments have to be opportunely supported by a matrix of astatic actuators, in order to avoid as better as possible the deformations due to the gravitation.

Two possible patterns have been considered for the distribution of the actuators: the quadrilateral and triangular patterns.



Slumped glass approach: rough estimation for the manufacturing time

Phase A: Slumping of the shell segments

1. Investments:

- *Measuring machine*
- *Slumping mould*
- *New building*

2. Time schedule

- *1 year for preparation*
- *3 year for production (XEUS 1)*

Phase B: Fast Polishing of the shells:

1. Investments

- *3 machines for 3D tests*
- *10 robotic polishing machines*
- *4 Promap or Wyko profilometers*
- *building + clean room*

2. Time schedule

- *1 year for preparation*
- *4 year for production (XEUS 1)*

Activity in progress

MPE and OAB/INAF have initiated a preliminary study to verify the feasibility of the *borofloat* glass approach:

- The slumping process is investigated with the support of the Schott Company (Germany);
- the fast polishing with robotic machine will be investigated with the support of the Zeiss company (Germany);

In addition:

- OAB/INAF is investigating a possible manufacturing program based on SiC ceramics.



First results on the slumping process expected in a time frame of 5 months

Conclusions

- The production of the **XEUS** optics present a real challenge;
- We presented some technological approaches that could be a viable solution for the manufacture of the **XEUS** optics;
- Experimental verification is required to prove the feasibility of these concepts;
- For the slumped *borofloat* glass approach a preliminary feasibility study is currently in progress (first results are expected in a time frame of = 5 months).

NOTE:

Part of the concepts above presented have already been published in: O. Citterio, M. Ghigo, F. Mazzoleni, G. Pareschi, G. Parodi, H.W. Bräuninger, W. Burkert, G. Hartner, "Development of Soft and Hard X-ray optics for astronomy: progress report II and considerations on the production methods of large diameter segmented optics for future missions", 2001, *SPIE Proc.*, **4496**, 23. We also plan to present the first results of the MPE/OAB activity for the development of borofloat segments in: O. Citterio, M. Ghigo, F. Mazzoleni, G. Pareschi, B. Ascenbach, H. Bräuninger, G. Hasinger, P. Friedrich, "Large-size glass segments for the production of the XEUS X-ray mirrors: basic ideas and concepts", during the SPIE Conf. "Astronomical Telescopes and Instrumentation", Waikoloa - Hawaii 22-28 Aug 2002 (Conf. AS18).



Cryogenic Detectors (Narrow Field Instruments)

Henk Hoervers¹ and Peter Verhoeve²

¹ SRON National Institute for Space Research, Sorbonnelaan 2, 3584 CA Utrecht, The Netherlands

² Research and Scientific Support Department, ESTEC/ESA, P.O. Box 229, 2200 AG Noordwijk, The Netherlands

Abstract. Two cryogenic imaging spectrometer arrays are currently considered as focal plane instruments for XEUUS. The narrow field imager 1 (NFI 1) will cover the energy range from 0.05 to 3 keV with an energy resolution of 2 eV, or better, at 500 eV. A second narrow field imager (NFI 2) covers the energy range from 1 to 15 keV with an energy resolution of 2 eV (at 1 keV) and 5 eV (at 7 keV), creating some overlap with part of the NFI 1 energy window. Both narrow field imagers have a 0.5 arcmin field of view. Their imaging capabilities are matched to the XEUUS optics of 2 to 5 arcsec leading to 1 arcsec pixels. The detector arrays will be cooled by a closed cycle system comprising a mechanical cooler with a base temperature of 2.5 K and either a low temperature ³He sorption pump providing the very low temperature stage and/or an Adiabatic Demagnetization Refrigerator (ADR). The ADR cooler is explicitly needed to cool the NFI 2 array.

The narrow field imager 1 Currently a 48 × 48 element array of superconducting tunnel junctions (STJ) is envisaged. Its operating temperature is in the range between 30 and 350 mK. Small, single Ta STJs (20–50 μm on a side) have shown 3.5 eV (FWHM) resolution at $E = 525$ eV and small arrays have been successfully demonstrated (6 × 6 pixels), or are currently tested (10 × 12 pixels). Alternatively, a prototype Distributed Read-Out Imaging Device (DROID), consisting of a linear superconducting Ta absorber of 20 × 100 μm², including a 20 × 20 μm² STJ for readout at either end, has shown a measured energy resolution of 2.4 eV (FWHM) at $E = 500$ eV. Simulations involving the diffusion properties as well as loss and tunnel rates have shown that the performance can be further improved by slight modifications in the geometry, and that the size of the DROIDS can be increased to 0.5–1.0 mm without loss in energy resolution. With a DROID-based array of 48 × 10 elements covering the NFI 1 field of view of 0.5 arcmin, the number of signal wires would already be reduced by a factor 2.4 compared to a 48 × 48 array of single pixels. While the present prototype DROIDS are still covered with a 480 nm thick SiO_x insulation layer, this layer could easily be reduced in thickness or omitted. The detection efficiency of such a device with a 500 nm thick Ta absorber would be > 80% in the energy range of 100–3000 eV, without any disturbing contributions from other layers as in single STJs. Further developments involve devices of lower T_c -superconductors for better energy resolution and faster diffusion (e.g. Mo). *The narrow field imager 2* The NFI 2 will consist of an array of 32 × 32 detector pixels. Each detector is a microcalorimeter which consists of a superconducting to normal phase transition edge thermometer (transition edge sensor, TES) with an operating temperature of 100 mK, and an absorber which allows a detection efficiency of > 90% and a filling factor of the focal plane in excess of 90%. Single pixel microcalorimeters with a Ti/Au TES have already shown an energy resolution of 3.9 eV at 5.89 keV in combination with a thermal response time of 100 μs. These results imply that they the high-energy requirement for XEUUS can be met, in terms of energy resolution and response time. It has been demonstrated that bismuth can be applied as absorber material without impeding on the detector performance. Bi increases the stopping power in excess of 90% and allows for a high filling factor since the absorber is can be modeled in the shape of a mushroom, allowing that the wiring to the detector and the thermal support structure are placed under the hat of the mushroom. In order to realize the NFI 2 detector array, there are two major development areas. Firstly, there is the development of micromachined Si and SiN structures that will provide proper cooling for each of the pixels and the production of small membranes to support the detector pixels. Micromechanical prototypes of this cooling and support structure have been made and are currently characterized. Secondly, the read-out of the array has to be developed. The current baseline for research is frequency division multiplexing (FDM) which will allow that a large detector can be read-out with a minimum of low-temperature electronics (Superconducting Quantum Interference Devices) and with a minimum of wires to the detector, thus reducing the thermal load on the detector cooling. Significant progress has been achieved since a microcalorimeter has been successfully biased at a frequency of 46 kHz, showing a performance which is very similar to that under conventional dc-bias conditions, proving the FDM concept.

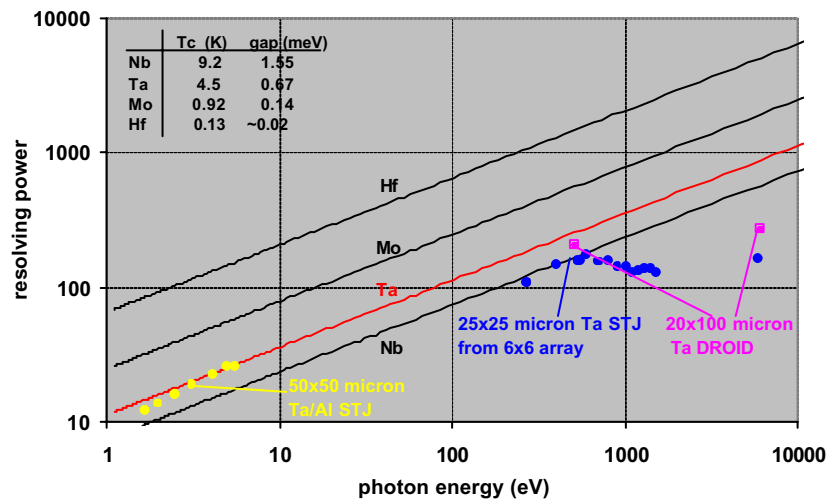
Cryogenic Detectors (Narrow Field Instruments)

Part 1: The narrow field imager 1

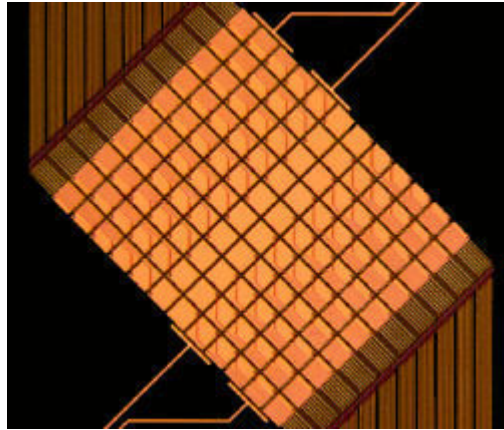
Peter Verhoeve
 Research and Scientific Support Department
 ESTEC/ESA
 P.O. Box 229
 2200 AG Noordwijk
 The Netherlands



Resolving power

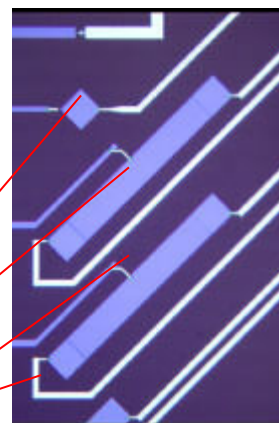
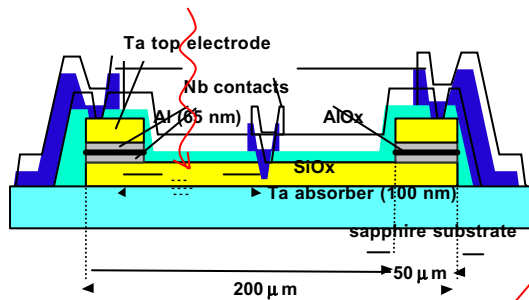


S-Cam 3 array: 10x12 pixels ($33 \times 33 \mu\text{m}^2$)



- Individual pixel read-out
- 4 groups of 32 pixels (FEE modules of 32#)

Distributed Read-Out Imaging Devices

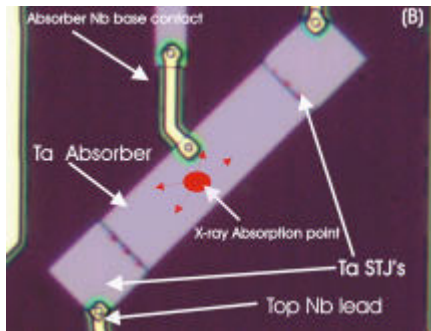


50x50 μm^2 single STJ

50x400 μm^2 absorber with 50x50 μm^2 STJs

niobium wiring to prevent QP outdiffusion

Soft X-ray detection with 1D DROIDS



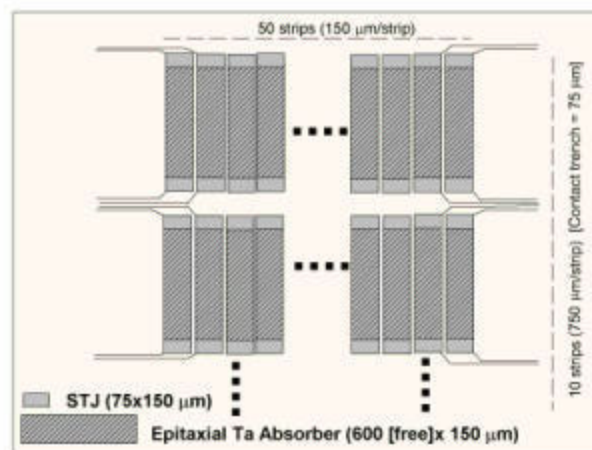
Title:
Graphics produced by IDL
Creator:
IDL Version 5.2 (Win32 x86)
Preview:
This EPS picture was not saved
with a preview included in it.
Comment:
This EPS picture will print to a
PostScript printer, but not to
other types of printers.

100x20 μm^2 absorber with 20x20 μm^2 STJs

$\Delta E=2.4$ eV (FWHM) at $E=500$ eV, $\Delta E=21$ eV at $E=5.9$ keV

R. den Hartog et al., LTD-9

Possible array format for XEUS



ISIRO Cryogenic Detectors (Narrow Field Instruments)

NI

Part 2: The narrow field imager 2

Henk Hoervers

SRON National Institute for Space Research

Sorbonnelaan 2

3584 CA Utrecht

The Netherlands

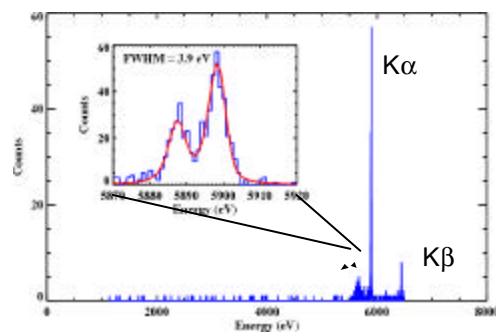
ISIRO Voltage biased X-ray microcalorimeter - performance

NI

- Single pixel microcalorimeter; 1.5 keV: $\Delta E = 2$ eV (NIST) and 2.8 eV (GSFC)
- Single pixel microcalorimeter; 5.89 keV: $\Delta E = 3.9$ eV (SRON):
resolving power $E/\Delta E = 1,500$



Single pixel microcalorimeter
(photo: SRON)



Pulse height spectrum of an ^{56}Fe source, $\Delta E = 3.9$ eV (under dc-voltage bias, SRON)

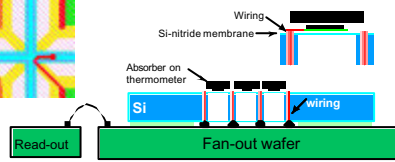
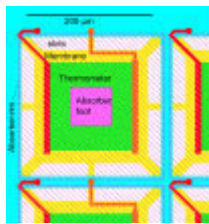
ISIRO

Imaging arrays of TES based sensors

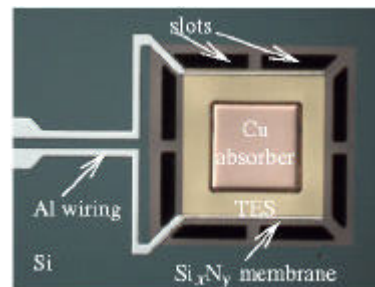
Ni

Present devices: a single pixel on a closed membrane

- A closed membrane leads to unacceptable thermal cross-talk for an array
- Solution: slotted membranes, tune G with aspect ratio of support beams



Cross section array support



TiAu TES on a slotted membrane (photo SRON-MESA)

ISIRO

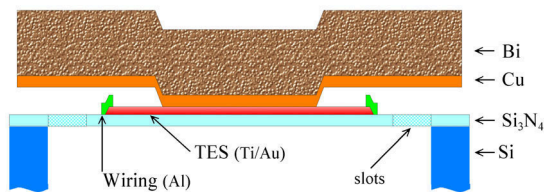
Imaging arrays of TES based sensors

Ni

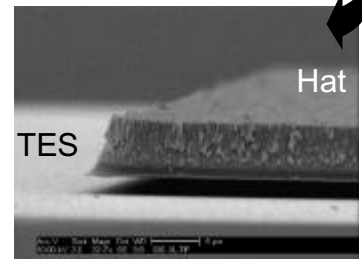
Present devices do not reach the required stopping power/pixel area

- Solution: mushroom shaped bismuth absorbers

$\Delta E = 5.2$ eV at 5.89 keV
92% stopping power
2 μm Cu and 5 μm Bi



Cross section mushroom-shaped absorber

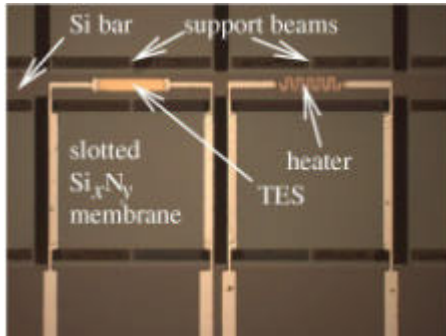


Detector with Cu/Bi absorber (photo SRON-MESA)

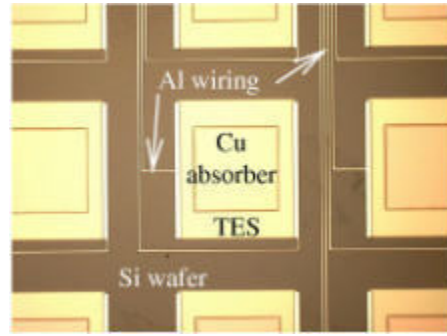
ISIRO

Imaging arrays of TES based sensors

Slotted membranes suspended by array support structure



Micromechanical 5 x 5 prototype, Si (111) bars, slotted membranes photo: SRON/MESA



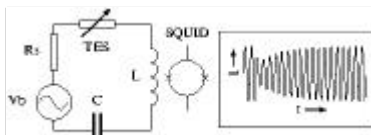
Detector 5 x 5 prototype on solid Si wafer photo: SRON/MESA

ISIRO

Read-out of an imaging array

Read-out of an array of $m \times m$ pixels

Option	# SQUIDs	remark/electronics
Direct read out (dc-bias)	$m \times m$	1) back-up option 2) m^2 FLL systems 3) ~ 4,000 wires to base
Frequency Division Multiplexing	m	1) SRON-VTT, LLNL, Berkeley, ISAS 2) m FLL + m frequencies + lock-in 3) ~ 150 wires to base
Time Division Multiplexing	$m(m+1)$	1) NIST 2) m FLL + m channel MUX 3) ~1500 wires to base



FDM requires AC-biasing of a microcalorimeter
Proof of principle: AC-bias at 46 kHz, shown by SRON-VTT
Measured $\Delta E = 6.9$ eV (5.5 eV with DC bias) at 5.89 keV

Resonant bias circuit used for ac-bias experiment; the carrier frequency is amplitude-modulated by an X-ray photon



The Wide Field Imager for XEUS

L. Strüder¹, P. Lechner²

MPI Halbleiterlabor, Otto-Hahn-Ring 6, 81739 München

¹ Max-Planck-Institut für extraterrestrische Physik, Giessenbachstr., 85741 Garching

² PNSensor GmbH, Römerstr. 28, 80803 München

1. Introduction

The Wide Field Imager (WFI) on XEUS is one of three scientific instruments in the focal plane of the X-ray telescope with a field of view of about 5 arcmin. The large collecting area (up to 30 m²) and high angular resolution (2 - 5 arcsec) of the X-ray optics requires new detector technologies. The physical quantities of interest are imaging (position resolution) spectroscopy (energy resolution) with a high detection probability (quantum efficiency) in a single photon counting mode at a high photon rate (time resolution without pile-up). The first choice for the WFI is mainly driven by its count rate capabilities and the flexibility of operation. As the collecting area of XEUS in phase A is already a factor of 20 larger than XMM-Newton and a factor of 100 in the fully-grown phase B configuration, it becomes clear, that a new device concept is needed rather than improvements of existing schemes. Active Pixel Sensors (APS) will be in the focus of our considerations, being able to match the relevant physical parameters of the WFI. The concept of the DEpleted P-channel Field Effect Transistor (DEPFET) allows to measure position, arrival time and energy with a sufficiently high detection efficiency in the range from 0.1 to 30 keV.

As a fallback solution fully depleted backside illuminated frame store pn-CCDs and frame store MOS-CCDs are considered. In a modified way both systems have proven their feasibility and reliability throughout the first 2 years of operation on XMM-Newton. They will be briefly described in section 7 and 8. Two possible extensions to the WFI focal plane, a fast timing channel and an expanded field of view detector, which would increase the power of the instrument by transient and serendipity observations, are treated in section 9.

The wide field imager is considered (in many cases) to be a pathfinder for the two Narrow Field Imagers (NFI) with restricted field of views in the order of 0.5 arcmin. Once a selected target is found and characterised in terms of position and energy by the WFI, detailed spectroscopic studies can be made with one of the two NFIs with an E/ΔE up to a factor of 50 better than the Fano limited WFI.

2. The Device and System Concept

In all CCD-type concepts charges are transferred slowly over large distances, therefore they are intrinsically sensitive to radiation damage due to the presence of traps in the bulk silicon. In addition, because of the relatively slow charge transfer, X-rays may hit the CCD during the

readout time. This gives rise to events whose position is erroneously assigned – the so-called out-of-time events.

In the DEPFET active pixel sensor every pixel is a complete single detector sub-unit, i.e. detector and amplifying electronics in one. The readout concept of the DEPFET allows for flexible windowing on the detector during the readout. Up to 1.000 full frames per second can be processed and therefore most of the constraints inherent to CCDs are overcome.

The XMM-EPIC pn-CCD system is limited with pile-up at count rates in the order of 10 counts per HEW* and sec. (Note that the pile-up limit is given by the product of pixel area and readout time per pixel. This is correct as long as the signal charge cloud is significantly smaller than the pixel size). But with the anticipated collecting area up to 30 m² several hundreds of counts per HEW and second are expected for comparable observations. That means that a factor of 20 or more in the XEUS phase A and a factor of about 100 when XEUS is fully grown in frame speed is needed as compared to the pn-CCD camera on EPIC-XMM, to exploit the capabilities of the XEUS mirror system and therefore its astrophysical significance.

The challenge of the wide field imager system is that 10⁶ pixels can be read out 1.000 times per second, delivering several Gigabyte of data. This is the unavoidable drawback of detection systems with high position resolution and simultaneous fast readout. This absolutely requires an efficient data reduction immediately after the analog-to-digital conversion.

2.1 Perspectives of the DEPFET System

The DEPFET detector system belongs to the family of 'active pixel sensors'. That means, that every pixel has its own amplifier and can be addressed almost individually by external means. This results in a high degree of operational freedom and performance advantages.

The major advantages of DEPFET type devices are:

- Operation with high spectroscopic resolution at temperatures as high as –50 °C, keeping the total readout noise below 5 electrons (rms).
- The charge does not need to be transferred parallel to the wafer surface over long distances. That makes the devices very radiation hard, because trapping, the major reason for degrading the charge transfer efficiency in CCDs, is avoided.
- The ratio between photon integration time and readout time can be made as large as 1.000:1 for a full frame mode, that means that the so called out-of-time events are suppressed to a large extent.
- As the integration time per event will be in the order of 1msec and the readout time per line about 1 µsec, more than 1000 counts per second per HEW (2 arcsec, i.e. 7 x 7 pixel) can be detected with a pile-up probability below 6 %.
- No additional frame store area is needed; the device is as large as the sensitive area.
- Any kind of windowing and sparse readout can be applied easily, different operation modes can be realised simultaneously.

* Half Energy Width of the telescope point spread function

- The DEPFET transistor amplifier structure offers the possibility for a Repetitive Non-Destructive Readout (RNDR). Under those conditions the readout noise can be reduced to below 1 electron (rms) by a repetitive reading of the physically same signal charge. This readout mode can be applied in selected areas, while the rest of the device is operated in the standard readout mode.

From the conceptional point of view this is the most advanced semiconductor X-ray pixel detector as it offers a lot of additional features like e.g. the analog storage of 2D X-ray images.

The standard DEPFET devices are p-channel devices on n-type material. The use of p-type base material is very interesting for the inverse DENFET* device. The reason for that is, that the use of n-channel JFETs and MOSFETs becomes possible by using holes as the signal charges. This offers an increased transconductance g_m of the transistors by a factor of three improving the equivalent noise charge at least by a factor of 1.5.

2.2 Device Concept and Functional Principle

The proposed DEPFET concepts are based on a detector-amplifier structure, which consists of a field effect transistor working on a depleted high resistivity substrate. The cross section of such a device is shown in figure 1.

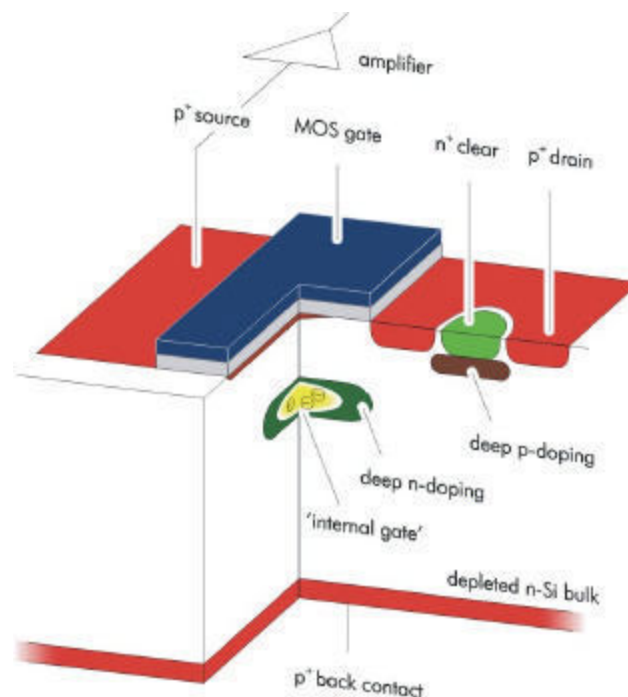


Figure 1: Cross section of a DEPFET structure based on an enhancement mode MOSFET.

* Depleted N-Channel Field Effect Transistor

The device, which was proposed by Kemmer and Lutz in 1986, makes use of the sideward depletion principle. Assuming that n-type semiconductor material is used, one can deplete a detector chip in such a way, that there remains a potential minimum for electrons under the channel of a field effect transistor being capable of storing the signal charges for a long time – if needed, up to several seconds depending on the operating temperature. It is straightforward to use such a device as detector, where signal charges (electrons) are collected in the potential minimum, from where they can steer the transistor current, acting as a so-called 'internal gate'. The signal charges change the transistor current by inducing charges inside the p-type channel of the DEPFET. The result is a simultaneous integration of the first amplifier stage on the detector chip with a detection fill factor of 1. Figure 2 shows the zoom of an APS layout plot, based on DEPFET structures with hexagonal outline.

The potential distribution and the electron density in the device, calculated by the 2-D TOSCA code, are shown in figure Figure 3. The potential maximum of the internal gate (minimum for electrons) is clearly visible and is separated from the external gate by the p-channel. The potential difference in the pixel area to its direct surroundings is about 1V, sufficient to collect and store more than 100.000 electrons in one pixel.

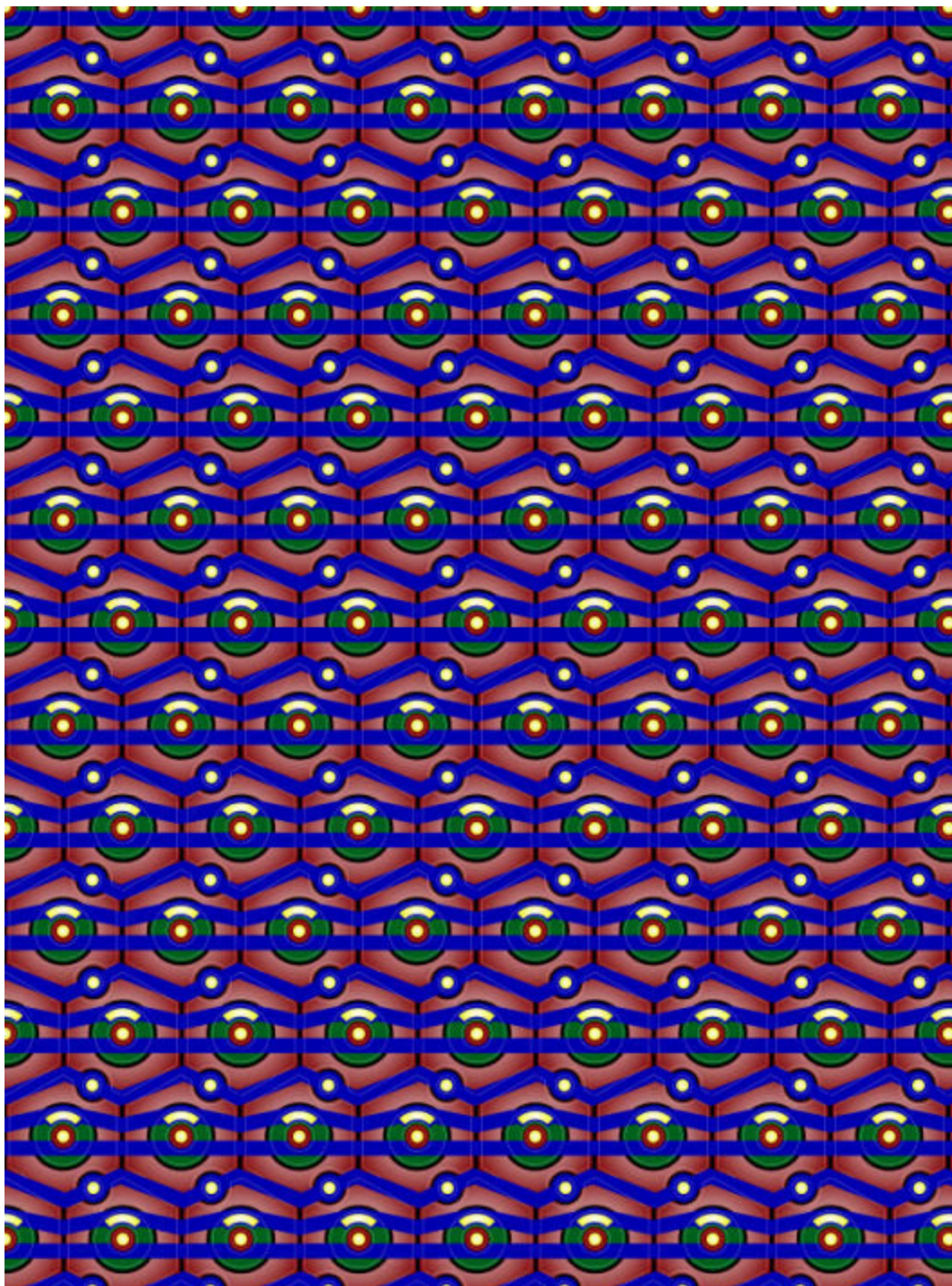


Figure 2: Layout plot of an Active Pixel Sensor with hexagonal pixel outline. Each hexagon is a DEPFET with cylindrical symmetry: the source in the centre of each pixel (red) is enclosed by the ring shaped gate (green) and drain (red). The blue lines are metal connections. The yellow regions are contact holes for inter-layer connections.

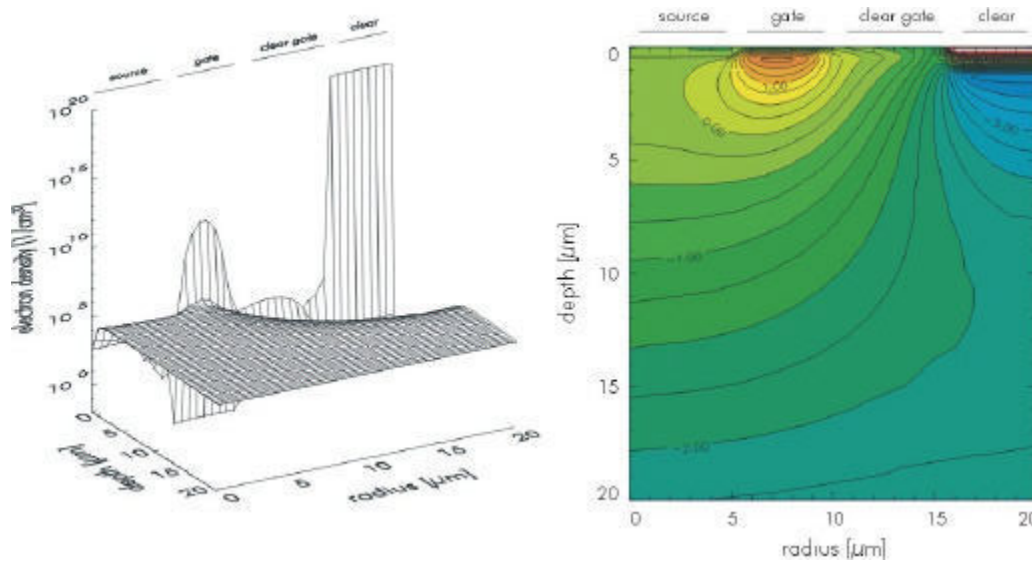


Figure 3: Two-dimensional simulation showing the electron density (left side) and the potential maximum (minimum for electrons; right side), also called internal gate, in which electrons generated in the bulk are collected. The simulation was done with the program TOSCA for a DEPFET with cylindrical symmetry where the source is in the centre of the structure.

Since the electrons are collected in a potential minimum – signals as well as leakage current – the device has to be reset from time to time by emptying the corresponding internal gate. One straightforward way of doing it, is applying a positive voltage to an adjacent n⁺ contact, which acts as a drain for electrons.

In a first approach devices were built, where periodically (hundreds of μs) all charges are removed from the potential minimum beneath the transistor. This is done by applying a positive voltage at the n⁺ substrate contact for a short time (hundreds of nsec). The result of a two-dimensional simulation shows the continuous rise of the bulk potential between the region under the transistor and the substrate contact for this particular case (figure 4). After the clear procedure signal electrons can be collected and stored in the potential minimum under the transistor channel. As the signal charges have to be removed explicitly and as the internal gate is continuously filled up with thermally generated electrons, the clear procedure can be applied upon request or in a repetitive manner. The clear mechanism acts locally where the clear pulses have been applied. The information about the amount of signal charges stored can be recorded by measuring the rise of the transistor current. This measurement does not disturb the stored charges, therefore the readout process can be repeated several times and opens the option of a multiple non-destructive readout. If a row of DEPFETs is activated by the selective application of the external gate voltages, the charge content can be measured, a clear pulse can be applied and the charge measurement repeated without having signal electrons in the potential minimum. The difference between both measurements is the net signal of electrons in the internal gate.

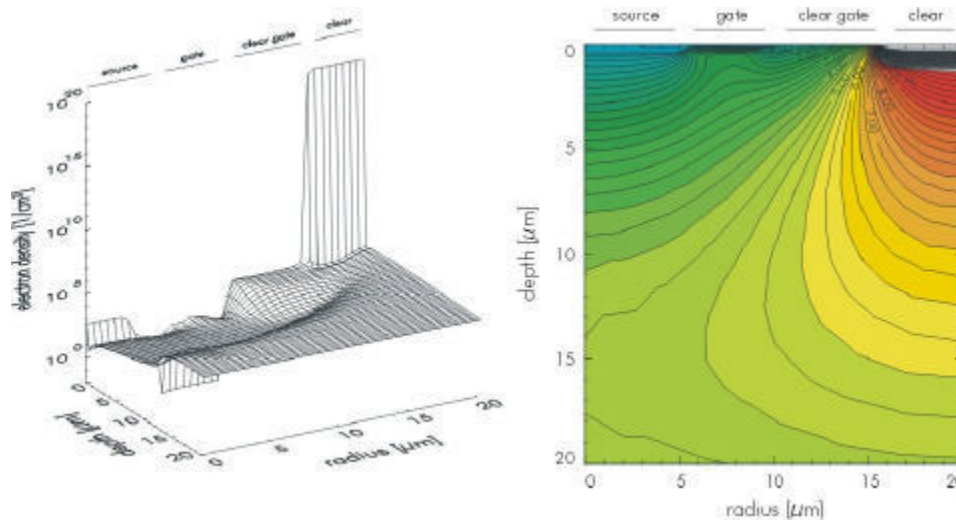


Figure 4: Result of a two dimensional simulation of the clear procedure; one can see the electron density (left side) and the potential (right side) inside the detector chip while there is a positive voltage pulse (+ 15 V) applied to the substrate contact; the simulation was done with the program TOSCA for a DEPFET with cylindrical symmetry where the source is in the centre of the structure.

3. System Performance

The key parameters of the DEPFET system are listed in the table below. Their values have been derived from prototype measurements or, if transferable, from measurements with the XMM-Newton pn-CCDs. The main properties are summarised in the chapters 'Energy Resolution and Noise', 'Position Resolution', 'Count Rate Capabilities' and 'Quantum Efficiency'.

3.1 Energy Resolution and Noise

Beside the statistical fluctuations of the ionisation process (Fano fluctuations) the electronic noise is the dominant limitation of the energy resolution. Therefore physical models of the devices with the aim to understand its basic noise sources are of great importance.

Considering the noise behaviour of the DEPFET, the so-called 'total detector capacitance' present in conventional detector-amplifier combinations can be neglected. Only the capacitance of the internal gate is relevant, all kinds of stray capacitances and the capacitance of the external gate are avoided. This leads to very low equivalent noise charges for the series noise contribution. The parallel noise of the structure has its origin in the volume generation of charges inside the fully depleted substrate and surface generated currents.

To examine the noise characteristics, measurements of the energy resolution were done with the help of an ^{55}Fe source. Figures 5 and 6 show spectra of a ^{55}Fe source – recorded with a DEPFET at room temperature and at $-60\text{ }^\circ\text{C}$ – with the Mn-K_α and the Mn-K_β -line at 5.895 eV and 6.492 keV.

Table 1: Expected performance figures of the DEPFET focal plane detector system

Parameter	Value
Integration + Readout	
read time per row (128 channels)	2.5 μ sec
total read time	1.25 msec
integration: read time	500:1
window mode	160 μ sec for 128 x 128 pixel
Response to Radiation without Blocking	
QE* @ 100 eV	100 %
QE @ 110 eV	85 %
QE @ 282 eV (C K_{α})	90 %
QE @ 1.740 eV (Si K_{α})	100 %
QE @ 8050 eV (Cu K_{α})	100 %
QE @ 10.000 eV	96 %
QE @ 20.000 eV	45 %
depletion depth	500 μ m
rejection efficiency of MIPs	100 %
Spectroscopy	
Fano noise at 5.9 keV	118 eV FWHM
system noise	3 – 5 el (rms)
system noise with RNDR	~ 1 el (rms) for n=16
^{55}Fe resolution	125 eV
C K_{α} resolution	50 eV
Radiation Hardness	
no change up to	10^{10} p per cm^2
Focal Plane Geometries	
device size	7.5 x 7.5 cm^2
device format	1.024 x 1.024 pixel
pixel size	75 x 75 μm^2
position resolution	= 30 μm
fill factor of focal plane	1
operating temperature	~ 200 K

* Quantum Efficiency

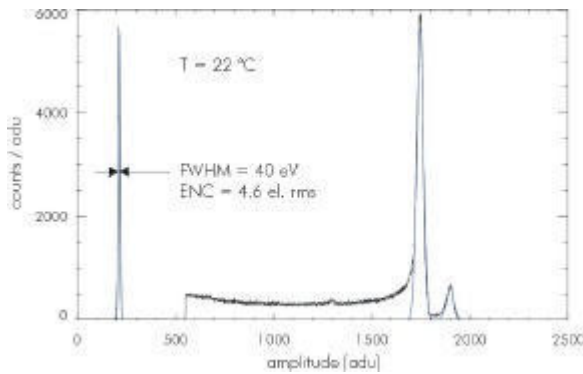


Figure 5:

⁵⁵Fe spectrum recorded with a DEPFET structure at 22 °C.

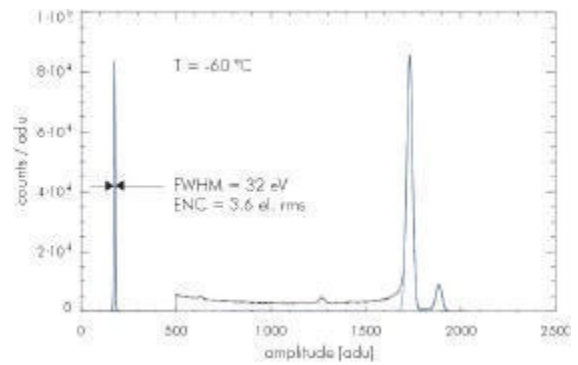


Figure 6:

⁵⁵Fe spectrum recorded with a DEPFET structure at -60 °C.

The noise peaks in the spectra of figures 5 and 6 have been measured separately while the detector was not exposed to radiation. The energy calibration is done by comparing the position of the Mn-K_α line with the position of the noise peak.

The electronic readout noise at room temperature (22 °C) is 4.6 el. (rms). Reducing the parallel noise contribution of the leakage current by cooling the device to -60 °C results in an improved noise figure of 3.6 el. (rms). Both spectra have been obtained at shaping times of a few μsec.

The obtainable energy resolution with a DEPFET detector is shown in figure 7. In the standard full frame mode the FWHM, including readout noise and Fano fluctuations is shown. Down to 1 keV incident photon energy, the energy resolution is mainly determined by the Fano noise. The improvement in energy resolution from 50 eV to 500 eV with the RNDR is clearly to be seen in the dashed graph, indicating the 1 el. rms read noise.

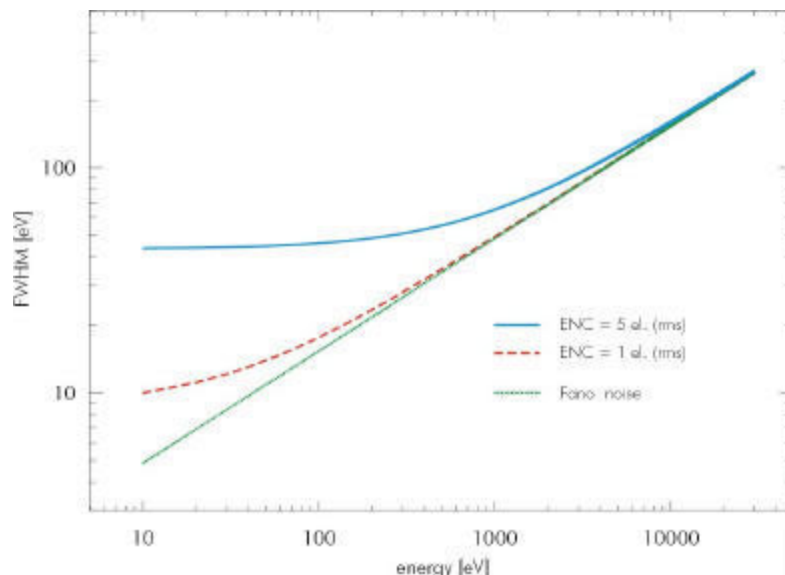


Figure 7: Calculated energy resolution as a function of the photon energy. The Fano noise is taken into account as well as 5 el. rms and 1 el. rms equivalent noise charge respectively.

3.2 Position Resolution

Due to the diffusion of the signal charges during their drift from the conversion point inside the silicon bulk into the potential minimum of the pixel, the spatial measurement precision can be improved substantially, with relatively large pixel sizes. The improvement is significant, if the signal charge cloud diameter is in the order of the pixel size. Taking into account the thicker silicon wafer (500 μm thickness for 6inch wafer) and the longer transit times, i.e. collection times for the generated electrons, the charge cloud, containing 96 % ($\pm 2\sigma$) of all signal charges will have a diameter of about 40 μm . For a pixel size of 75 μm about 70 % of all events will be split events and 30 % are contained within one pixel. Under those conditions, the position resolution will always be better than 20 μm , but for most of the cases better than 5 μm (see also figure 8). A position resolution of 0.2 μm for X-ray photons absorbed at the pixel boundaries was verified experimentally. Those values may be changed by (a) the temperature, (b) by the pixel layout and (c) by the operating voltages. The relatively weak photon energy dependence of the position precision is neglected for this estimation.

A theoretical and experimental study on the position resolution using the charge spreading technique and their impact on energy resolution must be considered. But it seems reasonable that a pixel size of 75 μm to 100 μm is adequate for the anticipated angular resolution and focal length. This pixel size can even handle the expected FWHM of the point spread function below 1 arcsec.

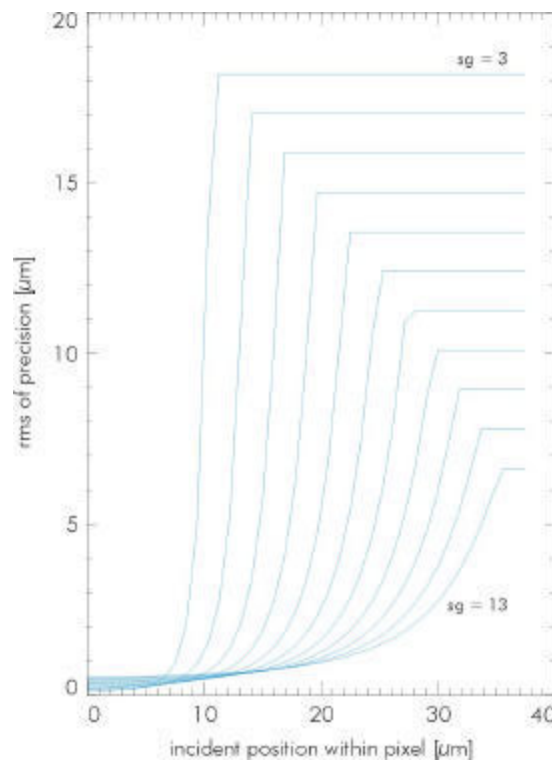


Figure 8: Improvement of the position precision as a function of the Gaussian spreading of the electron charge cloud. The typical sigma of the Gaussian ('sg') of the Gaussian electron distribution is 7 μm . The assumed pixel size is 75 μm . 1.000 el. have been

generated and processed with a noise level of 5 el. (rms).

Figure 8 demonstrates the effect of charge spreading and position reconstruction of the incident photon. The improvement of the position resolution because of the extension of the electron charge cloud is equally true for the pn-CCD detector. The x-axis indicates the position of the photon hit: At $x=0$ the photon hits the pixel exactly at the boundary to the neighbouring pixel. Here the position resolution is at its optimum. As the physical situation is symmetrical with respect to the centre of the pixel, the x-axis ends at half the pixel size. On the ordinate we plotted the position resolution (rms). This number must be multiplied by a factor of three, if the position precision of more than 90 % of the photons should be better than the rms value on the ordinate. The parameter 'sg' (sigma of the Gaussian) scales the lateral signal spread before arriving in the pixel well. The upper curve indicates a $sg = 3 \mu\text{m}$ and increases to $sg = 13 \mu\text{m}$ at the bottom. For a $500 \mu\text{m}$ thick detector the typical sg is between $7 \mu\text{m}$ and $9 \mu\text{m}$.

3.3 Count Rate Capabilities

As the count rate capabilities of the WFI are of major importance to the overall performance of XEUS mission, the flux losses and pile-up behaviour are treated in more detail. The calculations shown below are taking into account a point spread function similar to XMM with an angular resolution of 1 arcsec (FWHM).

With preliminary parameters describing the envisaged telescope performance, it is possible to simulate the effect of pileup for the CCD as focal plane instrument. Pileup is the effect of changing either a pattern type and/or the energy information of a photon event due to the occasional hitting of an adjacent (flux loss) or the same (classical pileup) pixel by more than one photon in a readout cycle.

For the case of the DEPFET detector together with the XEUS-telescope (see figure 9), one finds that for a rate of one photon per readout cycle (1.000 photons per frame), only 6% of the incident flux is lost, and the contamination of the spectrum is about 0.1 % (1.000 photons per second correspond roughly to a source of 5 mCrab for the phase A telescope configuration). A telescope with 1 arcsec angular resolution, together with a focal length of 50 m is assumed, corresponding to 10 pixels HEW on the detector.

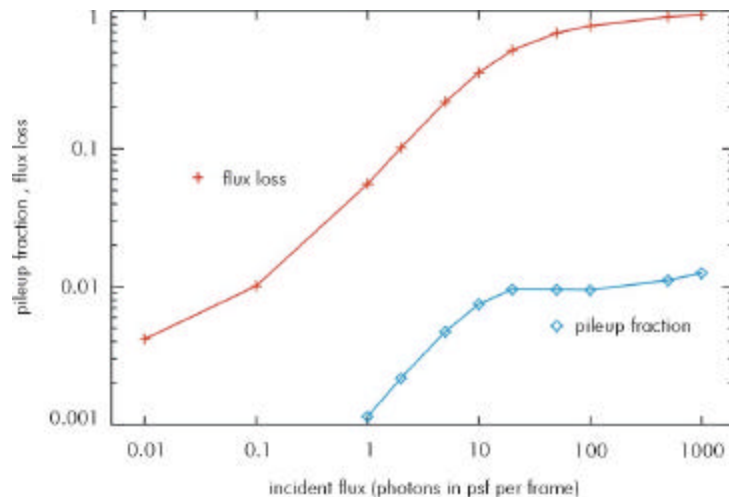


Figure 9: Flux loss and pile-up fraction as a function of the incoming photons. Note, that around 1.000 frames will be read out per second.

Note that the flux loss is a scalar correction factor that can be rather easily handled, while the more complicated case of spectral contamination due to conventional pileup is more than one order of magnitude smaller.

3.4 Quantum Efficiency

As the XEUS mission intends to achieve high sensitivity from the very low energies (around 50 eV) up to 30 keV the detector entrance window as well as the sensitive thickness must be optimised. The practical thickness of such a detector is limited to 500 μm because the Compton background of the spacecraft increases with detector thickness. On the low energy side the studies on $\langle 100 \rangle$ oriented silicon will continue, in order to improve the spectroscopic response down to 50 eV. The limiting quantity for the low energy response is clearly the optical blocking filter. As a baseline we propose a 100 \AA thick monolithically integrated Al filter on the radiation entrance side.

For Xrays in the range of 0.1 keV up to 30 keV the response is shown in figure 10. It is remarkable, that the change of absorption depth in silicon over 5 orders of magnitude is reduced to a quantum efficiency variation of less than 30 % in the detectors over the whole bandwidth.

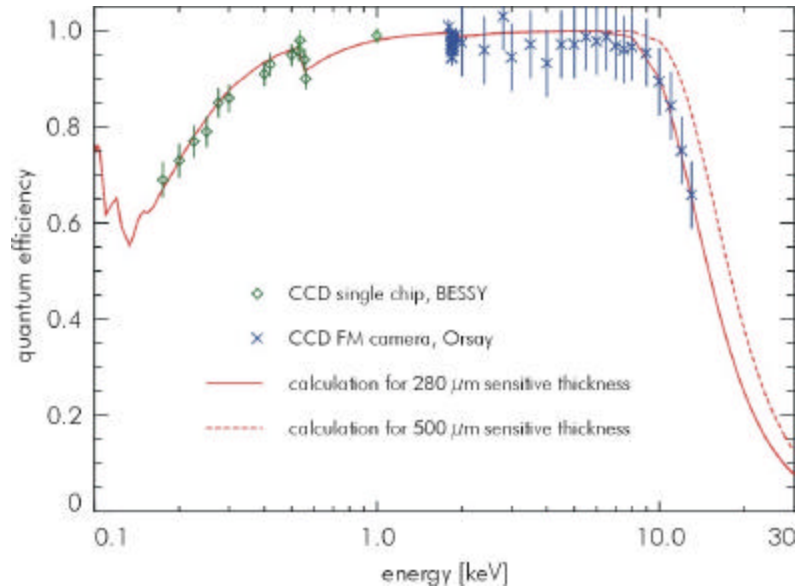


Figure 10: Quantum efficiency (QE) measured with pn-CCDs in a single photon counting mode at the synchrotron facilities BESSY in Berlin and LURE in Orsay. The lines show the QE calculated from the photon absorption coefficients for 280 μm (solid) and 500 μm (dashed) thick detectors. The calculated QE for a 500 μm thick detector is still 35 % QE at 20 keV.

The experience with XMM-Newton has revealed the advantages of avoiding very thin optical blocking filters: free standing 7 x 7 cm² large pinhole-free filters with a thickness below 0.2 μm are difficult to fabricate, to calibrate and to operate throughout the integration, test and launch of the camera. Technical precautions for preventing the destruction of the filter due to acoustic noise load during transport and launch are necessary. As X-ray observations without any light filter would not lead to the desired spectral resolution because of the optical loading, it would be advantageous to integrate a thin aluminum layer directly on the radiation entrance window of the detector, such that the detector itself serves as the mechanical support for the filter.

First tests of very thin Al layer deposition on silicon detectors have already been made and show very promising results with respect to homogeneity and layer thickness. It seems that a 500 \AA thick Al deposition can reliably be made.

A 100 nm thick aluminum layer would already reduce the flux of optical light between 200 nm and 700 nm by a factor of $5 \cdot 10^6$, in the case of a 150 nm thick Al layer the optical light flux is attenuated by a factor of 10^{10} (see figure 11). The price to pay is the worsening of the low energy cut-off for X-rays: 100 nm of Al yields just 5% of quantum efficiency (QE) at 100 eV (see figure 12). The C-K _{α} line at 282 eV can already be detected with a QE of about 50 %.

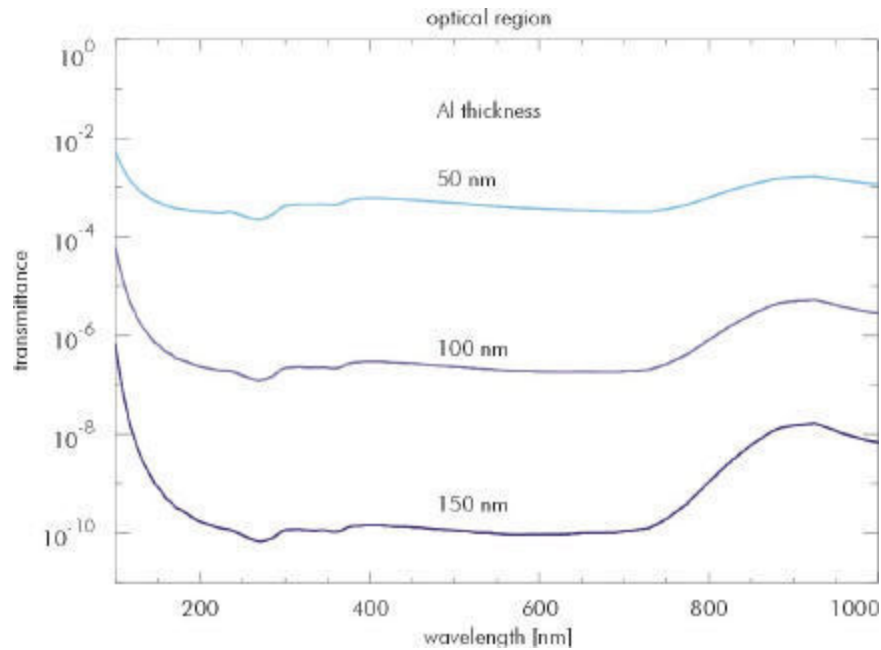


Figure 11: Attenuation of optical photons from the UV to the near IR as a function of wavelength. The transmission of aluminum layers of 50 nm, 100 nm and 150 nm was calculated. It is assumed, that the aluminum layers are integrated directly on the detector's entrance window.

Future research in this field will include the test of the light-tightness of the filters as well as their uniformity and long-term stability. Depending on the astrophysical X-ray input spectrum through the telescope and on the ionising particle background in orbit the fluorescence light, generated in the on-chip filter must be studied.

Both proposed camera systems, DEPFET active pixel sensors and frame store pn-CCDs, will be equipped with the integrated aluminum filters. As the thickness of the aluminum layer strongly affects the quantum efficiency up to 2keV (see figure 12) a thin on-chip filter could be envisaged, while a thicker, mechanically more stable filter may still be required to block the visible light from very bright sources in the field of view.

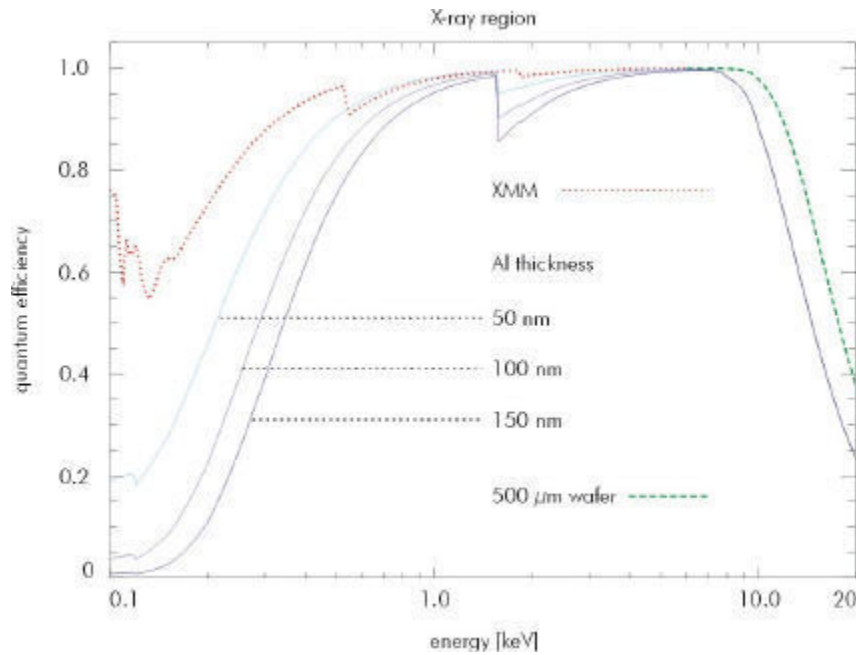


Figure 12: Reduction of quantum efficiency as a function of X-ray energy and aluminum thickness. The upper graph shows the XMM pn-CCD performance with no aluminum on the CCD. The assumed detector thickness is 300 μm and 500 μm .

4. Pixel Matrix System

According to the present experience a monolithic focal plane up to 8 arcmin seems to be possible. But all estimations for the current XEUS design are based on a 5 arcmin field of view (FOV).

4.1 Focal Plane Layout and Mechanics

Figure 13 shows the photograph of a small DEPFET-based APS prototype with 64 x 64 pixels and a pixel size of 50 x 50 μm^2 . In normal operation the transistors of one row after the other are turned on, read and cleared by CMOS control chips ('SWITCHER'). While the DEPFETs of the one active row are read in parallel by a multi-channel CMOS preamplifier/multiplexer ('CARLOS'), the rest of the pixels is turned off and in integration mode thus keeping dead time short and power consumption low.

As shown in figure 14, the principle layout of the focal plane is the same with the size and number of pixels scaled to the requirements of the XEUS instrument. The central part is the pixel matrix chip. It is logically divided into 16 sections according to the control and readout scheme (see below). However, its internal design remains completely uniform. Around the sensitive area the readout (upper and lower sides) and control (left and right sides) chips are placed. The pixel size is 75 μm x 75 μm . The matrix consists of 1.024 x 1.024 pixels resulting in a sensitive area of 76.8 mm x 76.8 mm. The exposed area assuming a FOV of 5 arcmin and a

resulting diameter of 72.7 mm is totally covered by the detector's geometry. The number of spatial resolution elements is at least 4.000 x 4.000 (see chapter 3.2).

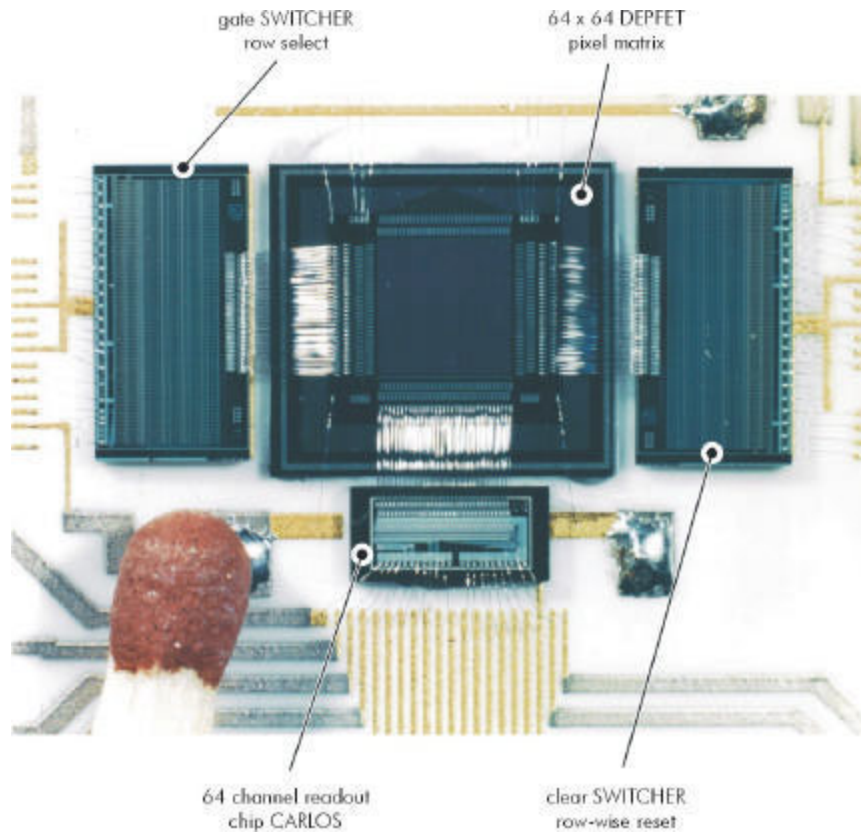


Figure 13: APS prototype with 64 x 64 pixels and $50 \times 50 \mu\text{m}^2$ pixel size.

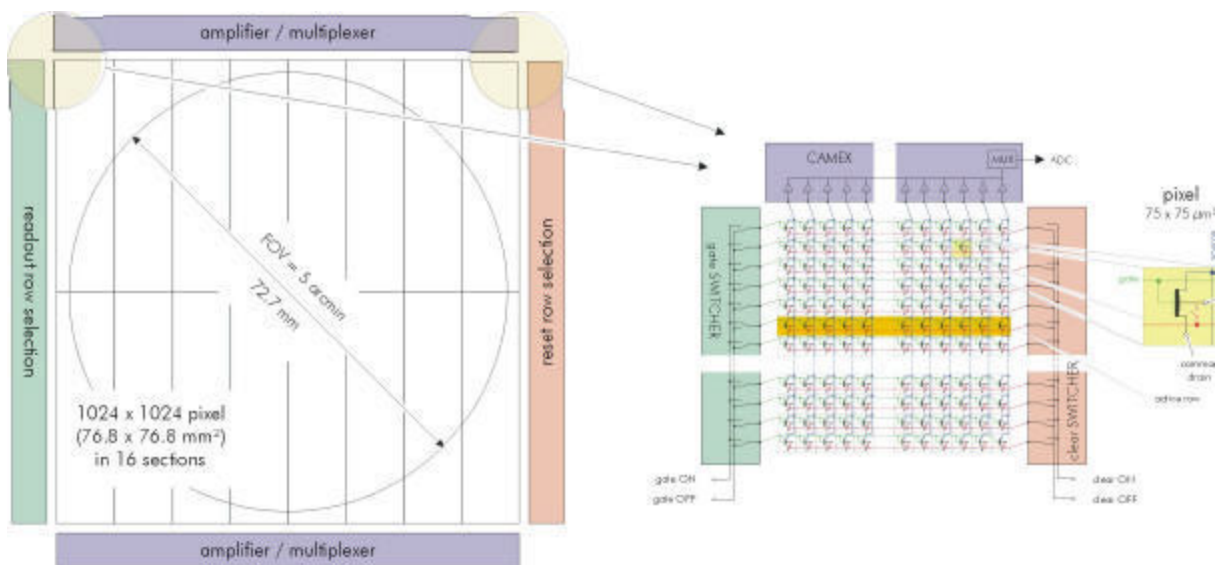


Figure 14: Layout of the focal plane pixel matrix system, consisting of the detector chip and surrounding readout and control electronics. The figure shows the sensitive area and its logical division.

A cross section of this arrangement is sketched in figure 15. Connections to the ASIC chips and to further signal processing components are realized by wire bonding. An additional detector layer for hard X-rays, which have a high probability to pass the Active Pixel Sensor or CCD without interaction, may be placed underneath.

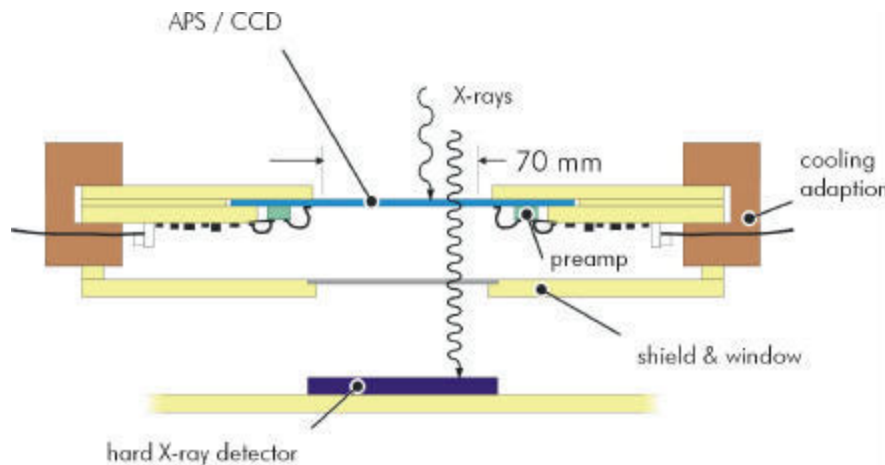


Figure 15: Cross section through the mechanical arrangement of the focal plane.

4.2 Electronic Control and Analog Readout

The pixel matrix system is divided into two identical monolithically integrated subunits (upper and lower), each having their independent control and analog readout electronics. The following description refers to one such unit. All actions mentioned may happen in both subunits simultaneously. The pixel matrix needs a control scheme to selectively activate a row of pixels for readout or reset. These units are placed along the left and right sides of the matrix in figure 14. From the left side one (horizontal) row of pixels is selected for readout. This is achieved by applying an appropriate gate voltage to all pixels of this row, which switches on the transistor currents. From the other side a clear pulse can be sent to a selected row. The control chips are identical, however a dedicated voltage supply and timing scheme has to account for either clearing or selection-for-readout.

Each column (512 pixels) of a subunit is fed into one channel of a multiplexing preamplifier chip. This ASIC has 128 inputs and one output. A subunit is such subdivided in 8 readout units of 128 x 512 pixels each.

The analog readout is done in four steps:

- current to voltage conversion and amplification
- multi-correlated sampling/filtering with offset subtraction,
- storage of the amplified analog signals in sample & hold stages,
- output of these signals.

The first three steps are done for $n \times 128$ pixels (channels) in parallel, n being the number of amplifiers read out (1 - 8). In step four the signals are sequentially sent to ADCs (1 ADC/readout unit).

4.3 Readout Modes

The readout has a high flexibility originating from:

- its non-destructive character,
- a random access to single rows and columns (channels),
- independent and parallel readout of subunits,
- and readout units.

Depending on the scientific goal of an observation at different readout modes can be selected, e.g.:

- *full frame readout*: search for regions of interest (ROIs, can have an arbitrary shape),
- *masked full frame readout*: after ROIs have been defined, all other pixels are either suppressed or readout at much lower frequency,
- *timing mode*: a selected image region is read out at highest possible frequency,
- *mixed mode*: different readout modes can be applied to dedicated image regions.

4.4 Data Processing

As described above, the 2×8 readout units are followed by one multiplexing amplifier and one ADC each. One readout unit operating at maximum speed generates 32 MegaPixel/sec (assuming a frame rate of 500 Hz). Data processing mainly aims to reduce this to a manageable rate in several steps:

- According to the selected readout mode only part(s) of the pixel matrix is read out and AD-converted at maximum speed.
- After A/D-conversion the data are masked, i.e. only pixels in ROIs are further processed, bad pixels and pixels outside the exposed area are rejected.
- Necessary correction is applied, like offset subtraction and gain factors.
- An event filter is applied, i.e. only pixels above an individual threshold are accepted.

Also this chain of data processing will be done in parallel for each of the 16 readout units.

4.5 Calibration

In a first calibration step each pixel is read out an appropriate number of times (typically 100), with the detector matrix shielded from any incoming radiation. By statistical evaluation the average offset and fluctuation (noise) of each pixel are calculated. Pixels with excess noise are stored in a 'bad pixel map'. For 'good pixels' the offsets and event thresholds are recorded.

In the second calibration phase the matrix will be flat field exposed to an on-board X-ray source. Another set of calibration frames are taken and evaluated to determine and store each pixel's gain factor. 'Blind' pixels are identified and added to the bad pixel map.

4.6 Power Consumption

An active pixel (i.e. a pixel selected for readout) delivers a current of typically 200 μA into 5 V. At maximum, 2 x 1.024 pixels can be simultaneously active resulting in a power consumption of about 2W for the pixel matrix. Amplifier/multiplexer chips consume about 16 x 1 W, clear-and readout-selectors about 2 x 1 W. The total power dissipation in the focal plane adds up to about 20 W.

5. The Repetitive Non-Destructive Readout (RNDR)

Provided that the count rate does not exceed the pile-up limit and/or the area of interest is restricted to a smaller window, e.g. 2 x 2 cm^2 the same signal charge can be read out several times. The field of interest for RNDR in the focal plane can be chosen relatively free, leaving the rest of the detector in its conventional readout mode.

Because the electrons are confined in the electric field below the sensing gate of the DEPFET amplifier (floating gate amplifier) and are not mixed with other charges the measurement of the amount of signal charges can be repeated as often as required.

The noise as shown in equation (1) can be reduced by

$$ENC(n) = ENC \times n^{1/2} \quad (1)$$

where n is the number of readings of the signal charges and ENC is the noise of a single reading.

We expect a single read noise of the DEPFET structure of 4 el. (rms) at -50°C with a shaping time of 1 μsec for the reading of two pixels we could achieve a single electron noise floor, corresponding to an energy resolution of less than 10 eV (FWHM). This would allow to expand the usable X-ray bandwidth down to 50 eV. As the areas which make use of the non-destructive readout can be selected during operation, we can imagine to run the detector slowly in areas where sources have been detected and fast (without RNDR) where it is not required.

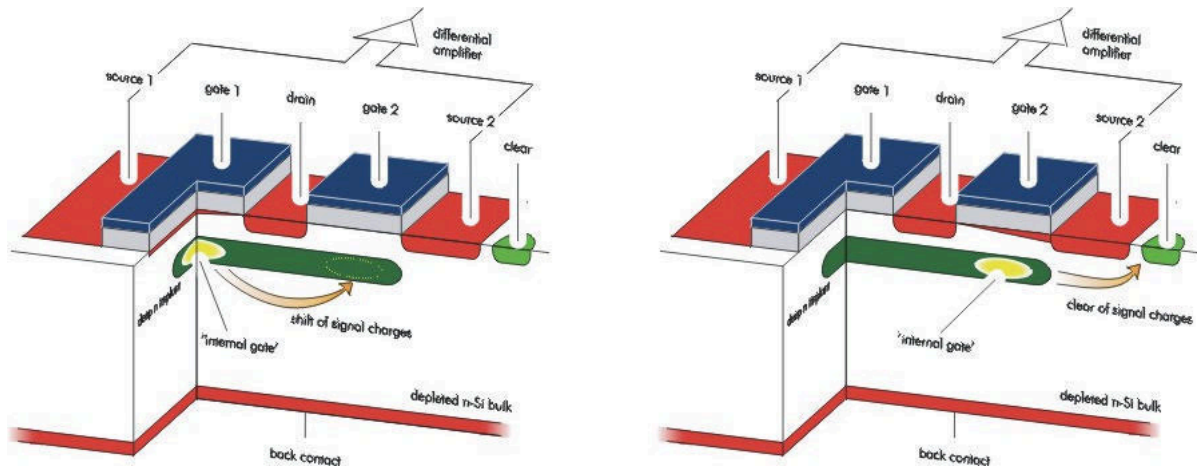


Figure 16: Two adjacent DEPFET devices are able to transfer the signal charges from one floating gate amplifier to the neighbouring one, reading the same signal charges several times. The read noise is reduced by $n^{1/2}$, where n is the number of readings.

6. Resources

The power and mass requirements for the WFI are summarised below. If compared to the XMM pn-CCD camera the weight is only slightly increased, but due to the 50 times higher pixel throughput, the power consumption goes up significantly:

power:	200 W,
mass:	150 kg.

A detailed engineering study is needed to derive the resources with a precision of better than 10 %.

7. Frame Store pn-CCDs for XEUS

As in conventional CCDs also pn-CCDs can be designed in a frame store format. The area to be processed in a quasi defect free manner increases by the size of the store area. A $7 \times 7 \text{ cm}^2$ large image area can be realized monolithically on a 6 inch wafer (see figure 17). If pn-CCDs should be used also for the $14 \times 14 \text{ cm}^2$ focal plane a possible extension of the focal plane camera is shown in figure 18. By that technique the whole field of view could be covered with a minimum of insensitive gaps in between the buttoned devices. The central part, the inner diameter of 7 cm, would be homogeneously sensitive.

The major change in concept besides the smaller pixel size is the dramatic increase in frame rate because of the modified readout philosophy: By doubling the processed area and dividing it in an image and store section we will get the required readout speed for the large collecting area of the XEUS mirrors. As will be shown later, we expect to get a frame rate of the whole camera of 200 per sec. That will lead us to a count rate capability of more than 200 counts per sec and HEW.

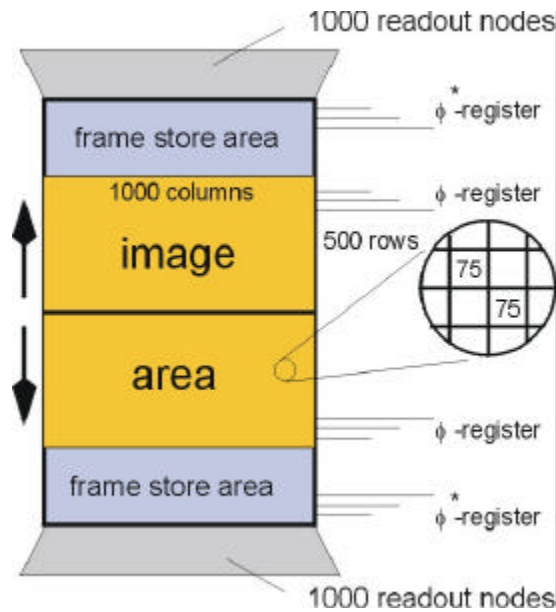


Figure 17: Example for a pn-CCD operated in a frame store mode. The imaging area has a pixel size of $75 \times 75 \mu\text{m}^2$.

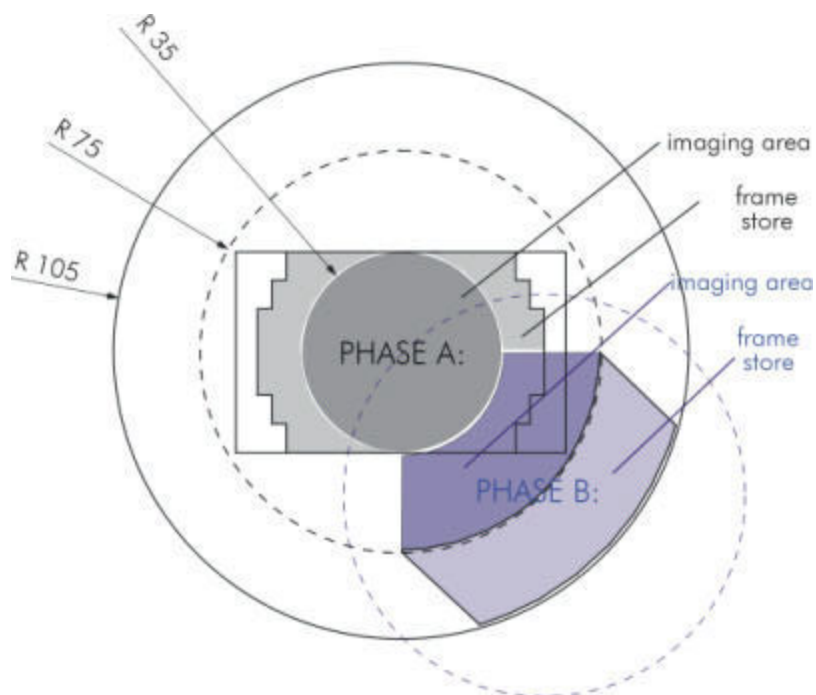


Figure 18: Composition of the whole focal plane with frame store pn-CCDs. The outer CCDs are slightly cylindrically shaped. The phase A configuration has a diameter of 70 mm, covering a FOV of 5 arcmin, while phase B configuration covers the 10 arcmin FOV.

As the pixel size shrinks, the number of read nodes and transfers increases. At the same time, the system will be requiring more readout time and being more sensitive to radiation damage due to the higher number of transfers. If charge sharing of signal charges among more than one pixel is needed for the improvement of position resolution, the effective read noise per event will be higher by a factor n (n is the number of pixels involved). To maintain the high readout speed of the pn-CCD EPIC-XMM system, the signal processing must be speeded up by a factor of two. The solution of the above 'constraints' seems to be realistic, but must be proven experimentally.

To date, the signals of one row (64 pixels) are processed in parallel in 22 μsec . The extension to 128 channels on the CAMEX amplifiers, to match the new pixel pitch, was already realized for applications in high energy physics, but it would involve a redesign of the CAMEX64B for the low noise operation. In addition the signal process time must be shortened by a factor of two. The increased readout speed will certainly have an impact on the power consumption, which is actually below 1 W for the 36 cm^2 array.

If 128 channels were read out with 12.8 MHz, 10 μsec would be required for the parallel readout of one pixel line. For the parallel transfer from the image to the storage area 100 nsec are needed for one transfer. A device of 1.000 x 1.000 pixels would be divided (as in the XMM-EPIC case) in two identical halves of the image area, i.e. 500 x 1.000 pixel each. For the parallel 500 shifts 50 μsec would be needed for the transfer from the image to the insensitive storage area. The readout time for the storage area while integrating X-rays in the image part, would then be $500 \times 10 \mu\text{sec} = 5 \text{ msec}$. That means, within 5 msec the whole focal plane would be read out. The out-of-time probability for the X-ray events will then be 1:100. In this operation mode 200 image frames can be taken in 1 sec with a full frame time resolution of 5 msec.

8. A Frame Store MOS-CCD System

MOS-CCDs have been developed in collaboration with industry with great success. Large format devices were integrated in the XMM-Newton focal plane. Significant improvements were made with respect to detection efficiency at the low and high-energy end from 200 eV up to 10 keV. The energy resolution was Fano limited and readout algorithms allowed for pattern recognition of useful events. The pixel sizes can also be tailored according to the requirements given by the X-ray telescope.

They could be further improved to depletion thicknesses up to 300 μm keeping all other relevant parameters unaffected. As in the case of the pn-CCDs, they have the potential to match the XEUS requirement, with all restrictions inherent to CCDs in general. By increasing the number of read nodes and by improving the readout speed of the front-end electronics up to several hundred full frames per second seem to be feasible.

The 5 arcmin FOV could also be covered by one monolithic MOS-CCD with dimensions of 7.5 x 7.5 cm^2 plus the store areas (c.f. figure 19). The limiting fact is the parallel transfer time, which could be speeded up by using a double metal process to overcome the high resistance poly-silicon gates. Most probably this would require a backside-illuminated device.

With a read speed of 1 MegaPixel per second at a read noise of 5 el. (rms) about 200 read nodes would be required to match the XEUS requirement of at least 200 frames per second. This must be coupled to a high-speed event recognition system, which keeps track at the anticipated pixel rates.

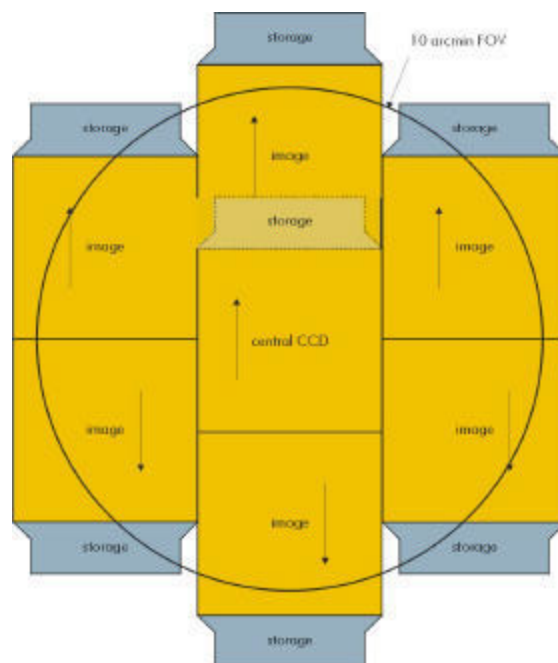


Figure 19: Example of the 10 arc minutes FOV for a MOS-CCD. The central CCD is vertically displaced with respect to the others. A FOV of 5 arcmin would be realized by one monolithic CCD.

9. Extensions to the XEUS Wide Field Imager

9.1 Fast X-ray Timing Capability

Science rationale

The X-rays generated in the inner accretion flows around black holes and neutron stars carry information about regions of the strongly curved space-time in the vicinity of these objects. This is a regime in which there are extreme predictions of general relativity still to be tested. High resolution X-ray spectroscopy and fast timing studies can both be used to diagnose the orbital motion of the accreting matter in the immediate vicinity of the collapsed star, where the effects of strong gravity become important.

The spectroscopic approach is already well covered in the current XEUS detector baseline, but the fast timing one should also be considered. Exciting new opportunities have arisen in the last few years through the discovery with the ROSSI X-ray Timing Explorer of (sub-)msec quasi-periodic timing phenomena and brightness oscillations during X-ray bursts in weakly magnetized accreting neutron stars. These discoveries have unambiguously demonstrated that fast X-ray timing provide the potential to accurately measure the motion of matter in strong gravity fields and to constrain masses and radii of neutron stars.

Fast X-ray timing requires extremely good photon statistics. In view of its huge collecting area, XEUS could therefore make a major contribution to this field. With a better than one order of magnitude improvement in sensitivity for timing studies, XEUS will enable for the first time the testing of predictions of general relativity in strong gravity fields, such as frame dragging effects and fully relativistic periastron precession. In addition, XEUS will allow, in exquisite detail, the waveform of coherent brightness burst oscillations to be studied. The waveform is directly affected by gravitational light deflection and relativistic Doppler shifts, and yields direct constraints on the mass and radius of the neutron star, and hence the equation of state of dense matter. Similarly, the modelling of the waveform of the high frequency quasi-periodic oscillations (which will for the first time be observed on their coherence time scales) can place important constraints on the mass and spin of the black hole.

A fast timing capability on XEUS would also extend its field of applications, by allowing the study of the X-ray variability of a wide class of objects, such as low-mass X-ray binaries in external galaxies (owing to the zero background, kHz quasi-periodic oscillations could be detected up to 20 keV for the brightest objects), accreting and isolated pulsars, accreting white dwarfs, and X-ray transients, especially the so-called micro-quasars. Accretion and jet formation are crucial in understanding aspects of astrophysics from normal stars to super-massive black holes. The fast timing capability can be combined with good energy resolution and broad band coverage allowing time resolved spectroscopic observations. For instance, the space-time geometry close to black holes could be probed using variability in the Fe-K α line.

Science requirements

The science requirements derive from the ability of the fast timing capability to observe the brightest X-ray sources in the sky, mostly X-ray binaries, either transient or persistent:

- Simulations using the current effective area of the mirrors show that the Crab would produce about 250 kcps* and about 800 kcps in XEUS phase A and B respectively. Sco X-1, bright transients and X-ray bursts can be ten times brighter. This leads to a requirement to be able to handle up to 3 Mcps (phase A) and 10 Mcps (phase B).
- The arrival time of each photon should be recorded with a timing resolution of 10 μ sec.
- The energy resolution of the detector should be around 200 eV, i.e. an improvement by a factor of 10 over current instrumentation for timing studies.
- The detector energy range should cover the high-energy response of the mirrors (as timing signals tend to become stronger at higher energies).

Detector implementation

The Wide Field Imager will be able to provide timing information, but only up to 500 kcps, even in a fast window mode of the APS. This means that an alternative solution should be considered. Although a pixel detector, placed out of focus, could be a possible solution, the most promising one appears to be a small size Silicon Drift Detector (SDD) in the focal plane.

The SDD is a completely depleted volume of silicon in which an arrangement of increasingly negative biased rings drives electrons generated by the impact of ionising radiation towards a small readout node in the centre of the device (fig 20). The main advantage of the SDD over conventional silicon PIN diodes is the small physical size and consequently the small capacitance of the anode, which translates to the capability to handle high count rates with simultaneous high energy resolution. To take the full advantage of the small capacitance the first transistor of the amplifying electronics is integrated on the detector chip. That way the stray capacitance of the interconnection between detector and amplifier is minimised and the system is practically insensitive to mechanical vibration and electronic pickup.

* cps: counts per second

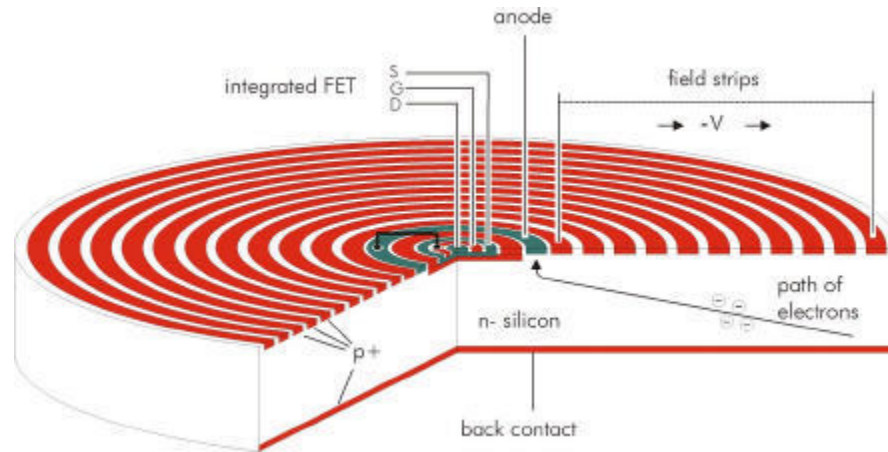


Figure 20: Schematic cross section of a cylindrical Silicon Drift Detector. Electrons are guided by an electric field towards the small sized collecting anode in the centre of the device. The first transistor of the amplifying electronics is integrated on the detector chip.

Silicon Drift Detectors have been proved to be capable of handling count rates exceeding 1 Mcps with pile-up less than 20%. Energy resolution of better than 200 eV at 6 keV is readily achieved with moderate cooling to -20 °C. The device could be implemented in the XEUS focal plane independently of the WFI or integrated monolithically on the APS wafer, sharing the mechanical structure and cooling mechanism with the central imaging detector.

SDDs are currently produced with thicknesses of 300 μm . Although there are on-going efforts to thicken these devices, the best match of the high energy response of the mirror could be achieved by associating the SDD with a higher density fast semiconductor detector located underneath (e.g. CdTe, CdZTe, GaAs).

Technical implications

The requirements in terms of power, real estate, and cooling are not constraining. High-speed data processing electronics will be needed to handle the data. 15 Mbits/sec of telemetry is desirable but if some limitations (e.g. reduced energy information) are accepted for the brightest sources, this could be reduced by an order of magnitude.

9.2 Extended Field of View

Science Case

Given the increased plate scale of the XEUS optic, there is a case to be made for an extension to the field coverage of the WFI whose prime goal is aimed at serendipitous science and extended object work. This could be accomplished by a mosaic 'ring' of detectors around the inner APS array.

The formation of super massive black holes is very probably an integral feature of the initial galaxy formation process, and these should originate at high red-shift at $z > 5$, even 10. They are likely to have a luminosity in the 10^{43} - 10^{44} erg sec⁻¹ range and the study of these, the first quasars can only be done in the X-ray band. The study will aim to examine the evolution of these objects with red-shift. Clearly it is important to detect as many as possible in the deep looks that will be necessary to exploit the limiting sensitivity of XEUS at around 10^{-18} erg cm⁻² sec⁻¹.

At the same time XEUS will also address the formation of the first galaxy groups, later to form clusters of galaxies. These groups follow the dark matter distribution resulting from inhomogeneities after the big bang, and can be recognised by spectral lines from the hot gas accumulating in the potential well created by the dark matter. The evolution of these groups with red-shift is a key scientific aim.

The WFI instrument is the prime for studies of the very high red-shift universe, combining high efficiency with moderate energy resolution and a wide field of view. Because of the long focal distance of XEUS, 50 m, the physical size of the focal plane is significantly larger than e.g. the CCD arrays of XMM-Newton. Because of the high throughput the central region where pointing targets will be located requires the use of a fast counting detector, the APS,

that allows high counting rates and a broad energy range coverage. The size of the APS is such as to cover a 7 arcmin square of the FOV. This is much larger than the FOV of the cryogenic imaging spectrometer, which is less than 1 arcmin, but is still much smaller than the XMM-Newton cameras, which cover a 30 arcmin diameter FOV. As the XEUS mirror will have a good off-axis performance an extension of the FOV should be considered.

Given the expected performance of the XEUS mirror the extension of the field of view to a diameter of 15 arcmin would more than double the number of exploitable scientific objects per deep field observation.

Detector Technology

A possible way to implement the FOV extension is a ring of large area CCDs either pn- or MOS-type around the central imager, providing an independent sub-system to the WFI to fit within defined thermal, mechanical and electrical interfaces. The tentative scheme of the Extended Wide Field Imager (E-WFI) is outlined in fig. 21.

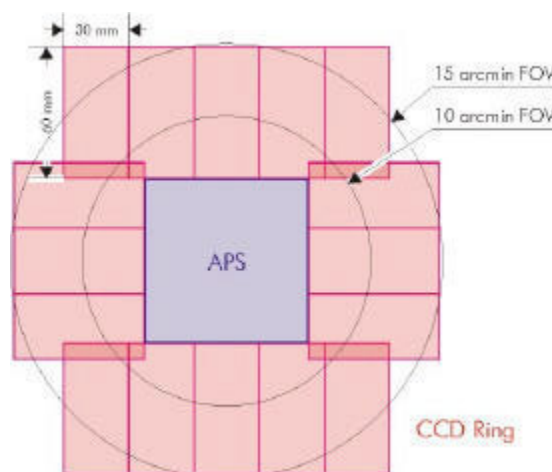


Figure 21: Focal plane geometry of the Extended Wide Field Imager (E-WFI).

E-WFI Focal Plane

i. Layout

Optimum layout of the focal plane will require an extensive study of the XEUS optimum focal surface, the system architecture to be used, and the size and associated yield of CCDs. The mosaic array options for the E-WFI are varied, with a trade-off to be made between a few ultra-large CCDs and many 'smaller' detectors each having a higher production yield. In the example shown in fig. 21, the baseline is a 3x6 cm² detector format which is a standard format for contemporary astronomical detectors. In this example, the E-WFI detection ring is formed using a mosaic of 16 detectors. Overlapping sensitive areas of the detectors will minimise the dead space between adjacent modules.

ii. Readout Modes

The detectors of the E-WFI ring will not be performing a target-science role, and consequently it is not foreseen to implement a variety of complex operating modes. The CCDs will be operated in one basic frame transfer mode routinely covering the whole of the outer field. A windowing mode similar to that used on XMM-Newton could also be included for bright sources but would complicate the array's readout cycle.

10. Conclusion

For the application as X-ray imaging spectrometers Active Pixel Sensors are the most advanced detectors as they combine a high degree of operational flexibility with performance figures close to the theoretical limits. The DEPFET concept satisfies the scientific requirements of the XEUS Wide Field Imager:

- low electronic noise, Fano-limited energy resolution,
- position resolution in the order of 20 μm ,
- count rate capability of more than 1000 counts per sec in one resolution element of the X-ray telescope, high-speed readout by parallel multi-channel processing,
- random accessibility of the pixels, flexible readout in full-frame, window or mixed mode,
- analog storage of energy and position information, possibility of repetitive non-destructive readout,
- high quantum efficiency from 0.1 – 30 keV by an optimised entrance window and a fully depleted bulk,
- improved radiation hardness,
- low power consumption.

The powerful XEUS mirror telescope suggests to enhance the observational potential of the instrument by the extension of the Wide Field Imager focal plane:

- A fast timing channel will offer an insight to the exciting physics of the inner regions of accretion flows around black holes and neutron stars.
- A larger field of view detector surrounding the central imager will considerably increase the number of scientific exploitable objects by serendipity observations.



XEUS observations of hard X-ray sources

H. Inoue

Institute of Space and Astronautical Science, Sagami-hara, Kanagawa 229-8510, Japan

Abstract. Thanks to invitation by the European colleagues, we, the Japanese X-ray astronomy group, started participating in various studies for the XEUS mission a few years ago. We are now intending to make significant contributions to this mission mainly by fabricating the detector spacecraft (Mitsuda et al., this workshop) and by introducing an imaging capability in the hard X-ray band to the XEUS X-ray telescope (Ogasaka et al., this workshop). Here, I will present some interesting scientific objectives of the XEUS hard X-ray observations. By using the multi-layer technique, it will be possible to extend the mirror-energy range up to $\sim 40\text{--}50$ keV and the source detection limit in $10\text{--}40$ keV will roughly be 10^{-15} erg cm $^{-2}$ s $^{-1}$ in a 10^2 sec observation. With this sensitivity, the cosmic X-ray background (CXB) in $10\text{--}40$ keV, which has the largest power in CXB, could be able to be fully resolved into discrete sources. We would expect to detect a number of highly obscured, nearby ($z < 1$) AGNs in this energy band which cannot be observed in the soft energy band below 10 keV. On the other hand, it will be possible to detect highly obscured, distant ($z > 1$) AGNs with its very high sensitivity in the soft X-ray band because of the large redshift. By combining the hard observations of the nearby sources and the soft observations of the distant sources, we will be able to perform a complete survey of the highly obscured AGNs. At the same time, it will become possible to observe non-thermal emission from SNRs, galaxies and clusters of galaxies in detail. In particular, due to a large evolution of the cosmic micro-wave background (CMB) with z , we could expect to detect inverse Compton emission of the CMB by accelerated electrons in a number of SNRs associated with a star-burst activity of a proto-galaxy.

References

- Bowyer, S., Berghofer, T.W., Korpela, E.J., 1999, ApJ 526, 592.
Deiss, B.M., Reich, W., Lesch, H., Wielebinski, R., 1997, A&A 321, 55.
Dogiel, V.A., 2000, A&A 357, 66.
Done, C., Madejski, G.M., Smith, D.A., 1996, ApJ 463, L63.
Elbaz, D., Arnaud, M., Vangioni-Flam, E., 1995, A&A 303, 345.
Fusco-Femiano, R., Dal Fiume D., Feretti, L., et al., 1999, ApJ 513, L21.
Hasinger, G., Altieri, B., Arnaud, M., et al., 2001, A&A 365, L45.
Koyama, K., Petre, R., Gotthelf, E.V., et al., 1995, Nature 378, 255.
Naito, T., Yoshida, T., Mori, M., Tanimori, T., 1999, Astron.Nachr. 320, 205.
Sarazin, C.L., Kempner, J.C., 2000, ApJ 533, 73.
Sreekumar, P., Bertsch, D.L., Dingus, B.L., et al., 1998, ApJ 494, 523
Tanimori, T., Sakurazawa, K., Dazeley, S.A., et al., 1998, ApJ 492, L33.

XEUS Observations of Hard X-Ray Sources

H. Inoue (ISAS, Japan)

Probable Contributions of Japan to the XEUS Mission

- DSC (Detector Spacecraft)
 - A Poster by Mitsuda
- Extension of the mirror-energy-range up to ~ 50 keV by using the multi-layer technique
 - A Talk by Ogasaka
- Detectors
- Science

High Sensitivity in 10 - 40 keV

A rough estimation of the source detection limit

$$S_{L, 10-40} \sim 10^{-15} \text{ erg/cm}^2/\text{s}$$

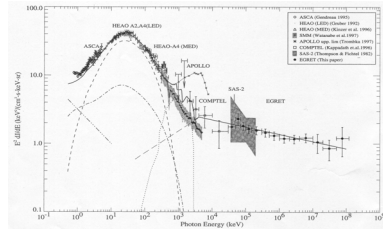
in a 10^2 ksec observation.

(When $dF/dE \propto E^{-1.7}$, $S_{1-10} \sim S_{10-40}$)

Possible observational objectives

- Resolving the Cosmic X-ray Background in 10 - 40 keV into discrete sources.
- Search for hidden AGNs
- Non-thermal emission from clusters of galaxies
- Detection of initial star burst activities in our universe.

Resolving the Cosmic X-ray Background into discrete sources



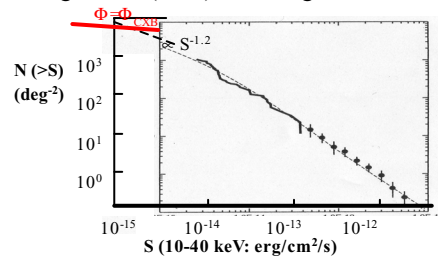
(Sreekumar et al. 1998)

The largest power of the CXB is emitted in 10-40 keV.

When $N \propto S^{-1.2}$,
integrated flux above S_0 ,
 $\Phi = 6N(>S_0)S_0$.

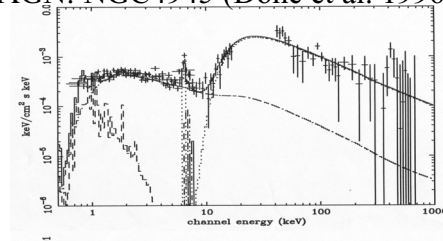
The CXB in 10 - 40 keV
could be fully resolved
into discrete sources.

Extrapolation from log N-log S in 5-10 keV by
Hasinger et al. (2001), assuming $dF/dE \propto E^{-1.7}$.

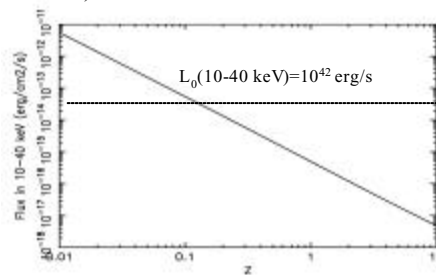


Search for hidden AGNs

Highly obscured AGN: NGC4945 (Done et al. 1996)



When $dF/dE \propto E^{-1.7}$, $F(10-40 \text{ keV}) = L_0(10-40 \text{ keV})(1+Z)^{0.3}/4\pi D_L^2$
(D_L : luminosity distance)



Non-thermal Emission from Clusters of Galaxies

Some observational evidences for presence of Non-thermal emission from clusters of galaxies

For example: **Coma Cluster**

- Radio Deiss et al. 1997
- EUV Bowyer et al. 1999
- X-ray Fusco-Femiano et al. 1999

Emission mechanism of X-rays

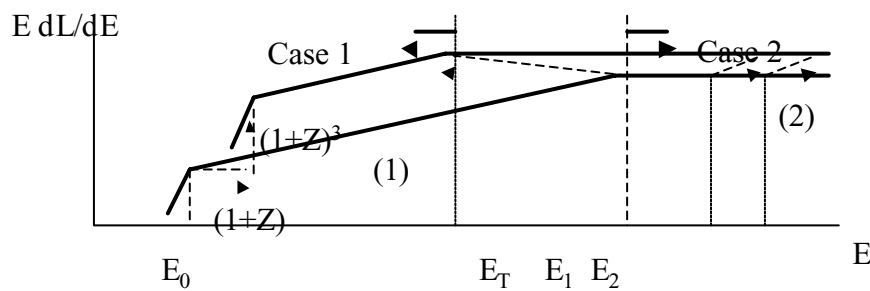
Inverse Compton scattering of cosmic microwave background

(Fusco-Fermiano et al. 1999)

Non-thermal Bremsstrahlung

(Sarazin & Kempner 2000; Dogiel 2000)

Spectral Evolution of the IC Emission with Z



Electron Dist. $\propto \gamma^p$

$E_0 \propto T_{\text{CMB}}$

$dL/dE_{(1)} \propto T_{\text{CMB}}^{(p+5)/2} E^{-(p-1)/2}$

$dL/dE_{(2)} \propto T_{\text{CMB}}^{(p+5)/2} E_T^{1/2} E^{-p/2}$

$T_{\text{CMB}} \propto (1+Z)$

$\gamma_T \propto (t_U U_{\text{CMB}})^{-1} \propto (1+Z)^{3/2} (1+Z)^{-4} \propto (1+Z)^{-5/2}$

$E_T \propto \gamma_T^2 T_{\text{CMB}} \propto (1+Z)^4$

$E_1, E_2 \propto (1+Z)$

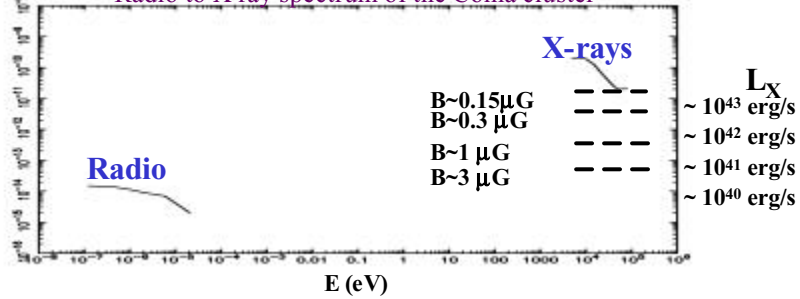
$L(E_1, E_2; Z) = L(E_1, E_2; 0) (1+Z)^4$: Case 1

$L(E_1, E_2; Z) = L(E_1, E_2; 0) (1+Z)^{3/2}$: Case 2

(when $p=2$)

Expected Flux from A Cluster of Galaxies for Inverse Compton Emission of CMB

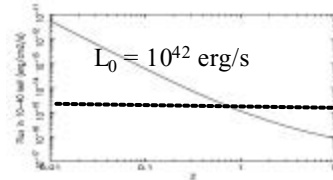
$E^2 dF/dE$ Radio to X-ray spectrum of the Coma cluster



$$F(10-40 \text{ keV}) = L_0(10-40 \text{ keV})(1+Z)^{3/2} / 4\pi D_L^2$$

In a case of clusters of galaxies,
 $E_T \sim 50 (t_U/10^{10} \text{ years})^{-1} (T_{\text{CMB}}/2.7 \text{ K})^{-4} \text{ eV}$

Hence, **Case 2 for X-ray emission**



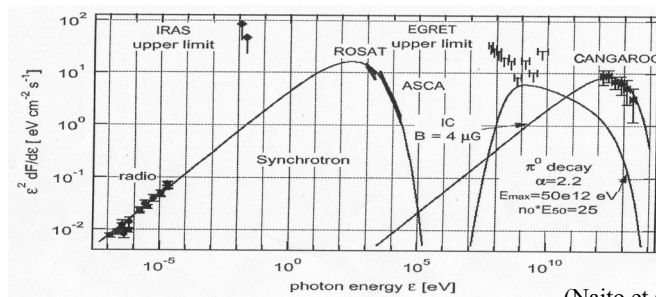
A Possibility to detect Initial Star-Burst Activities in our Universe

ASCA Observation of SN1006 (Koyama et al. 1996)

- Detection of a prominent non-thermal component
- Synchrotron-emission from rim of the remnant Electrons accelerated up to 10^{14} eV

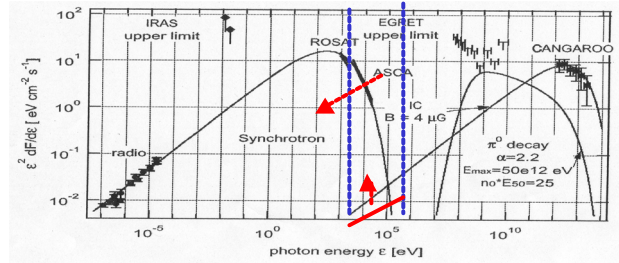
CANGAROO Observation of SN1006 (Tanimori et al. 1998)

- Detection of TeV gamma-rays
- Inverse Compton scattering of CMB by high energy electrons with $\gamma \sim 10^8$



(Naito et al. 1999)

Evolution of IC X-rays from a SNR with Z



In this case, $E_1, E_2 \ll E_T$ Case 1

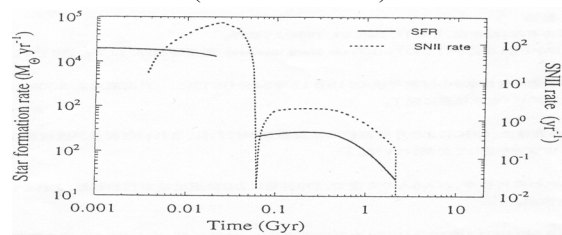
$$F_{\text{SNR}} = L_0 (1+Z)^4 / 4\pi D_L^2$$

Estimated IC liminosity in 0.5 - 10 keV

$$L_{\text{SNR},0}(0.5-10 \text{ keV}) \sim 10^{31} \text{ erg/s}$$

Integrated IC emission from star formations in a proto-elliptical galaxy

A prediction for SNR rate in a proto-elliptical galaxy
(Elbaz et al. 1995)



$\sim 10^{10}$ SNRs in $10^{7.5}$ years

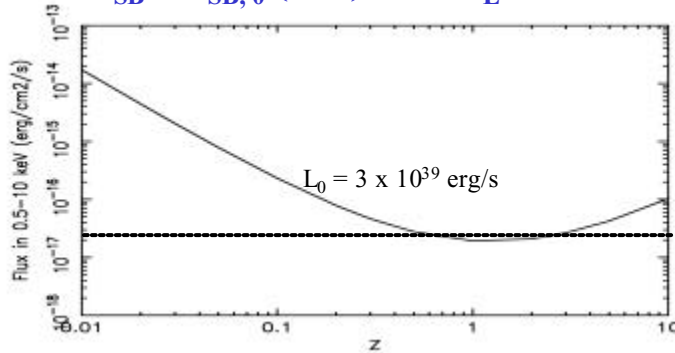
Integrated IC luminosity from such a star bursting
Proto-elliptical galaxy

$$L_{\text{SB}} \sim N_{\text{SNR}} (\tau_e / \tau_{\text{SB}}) L_{\text{SNR}} \\ \sim 10^{39.5} (N_{\text{SNR}}/10^{10})(\tau_e/10^6 \text{ years}) \\ (\tau_{\text{SB}}/10^{7.5} \text{ years})^{-1} (L_{\text{SNR}}/10^{31} \text{ erg/s}) \text{ erg/s}$$

(τ_e : life time of electrons responsible for IC X-ray
Emission, roughly given by $2.5 \times 10^7 n_e^{-1}$ years)

Integrated IC X-ray emission from
a star bursting proto-elliptical galaxy

$$F_{SB} = L_{SB,0} (1+Z)^4 / 4\pi D_L^2$$



It could be possible to detect star-burst activities from
proto-elliptical galaxies.

Summary

Possible scientific objectives of XEUS hard X-ray observations

- Observations of Micro-quasars on a time scale of a milli-second
- Deepest survey in 10 - 40 keV
- Study of non-thermal emission from clusters of galaxies
- A possibility to discover star-bursting proto-elliptical galaxies.



The Neutron Star Equation of State From Fast Timing of X-ray Bursts

Cole Miller, University of Maryland

Importance of the high-density EOS.

Burst oscillations.

Current constraints from bursts.

Benefits of XEUS timing.

Frontiers in High-Density Matter

The state of matter beyond nuclear saturation bears on many aspects of astrophysics and nuclear physics.

Primordial BH and dark matter.

Black holes at QCD phase transition?

Core-collapse supernovae.

Maximum mass of NS?

Prevalence of black holes in universe.

Gamma-ray bursts.

Origin of short bursts is unknown.

Phase transition from accretion?

Gravitational radiation waveforms.

NS-NS source for VIRGO, LIGO.

Previous Astrophysical Constraints

Neutron stars have core densities $\rho > \rho_s$, so observations of them may bear on the EOS.

Many methods have been tried.

Mass estimates from binary pulsars.

$$M_{\max} = 1.44 M_{\odot}.$$

Eliminates very soft EOS.

Limits from observed spin rates.

$$\nu_{\max} = 642 \text{ Hz}.$$

Eliminates very hard EOS.

Radius estimates from thermal models.

Mass estimates from QPOs.

All suffer from unknown systematics and/or are weakly constraining.

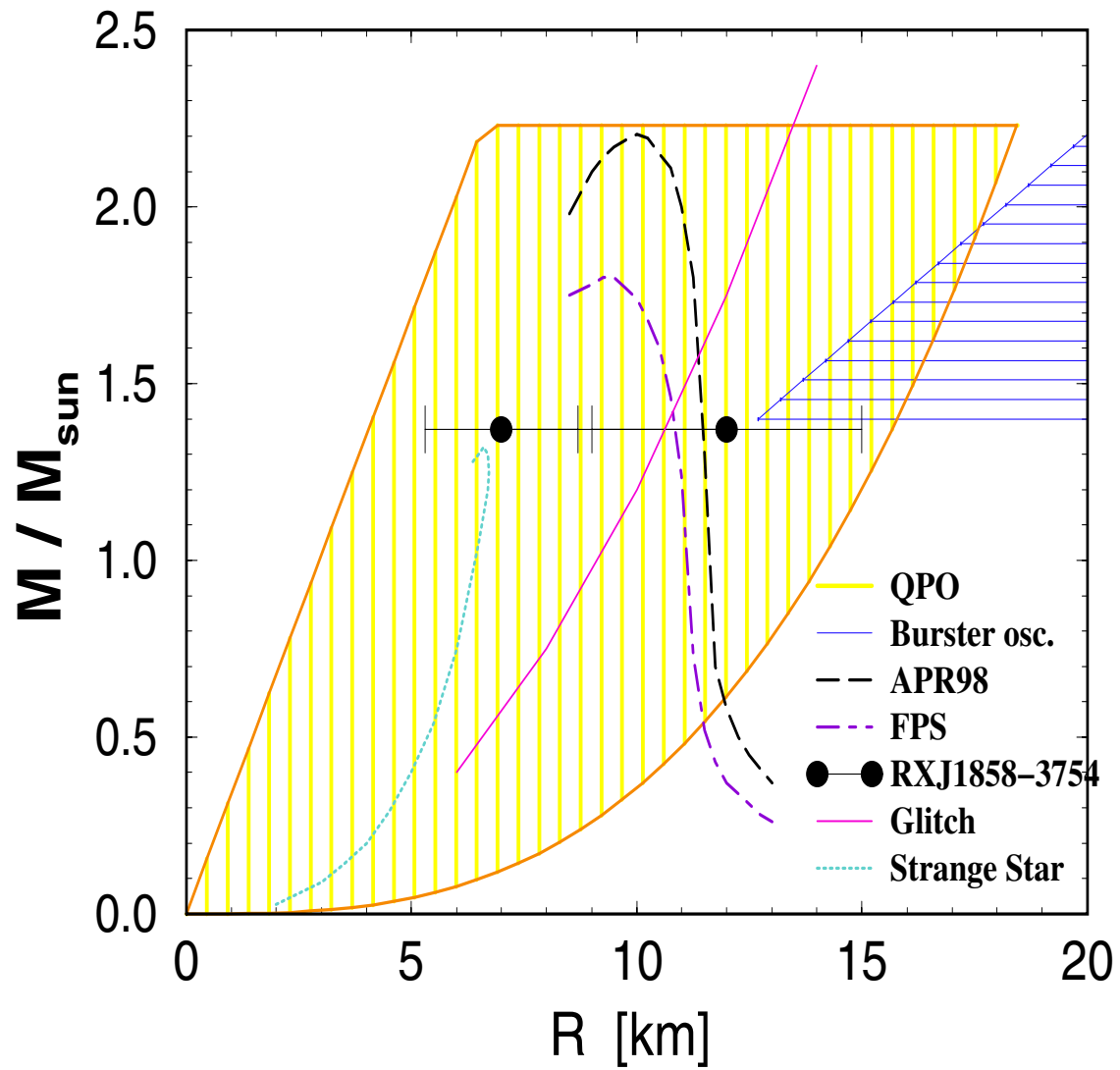


Fig. 1.— Astrophysical mass and radius constraints from neutron star modeling. From H. Heiselberg 2002, astro-ph/0201465.

Burst Brightness Oscillations

NS LMXBs have X-ray bursts.

Thermonuclear flash on surface.

In 1996, coherent oscillations discovered with RXTE.

$\nu_{\text{burst}} \sim 300 \text{ Hz}$ or $\sim 600 \text{ Hz}$.

Hot spot rotating at ν_{spin} or $2\nu_{\text{spin}}$.

Muno et al. (2002): Some $P_{\text{tot}} > 2000$.

High ν , M/R mean that light curve encodes unique information.

Little observation time is needed.

Many sources burst frequently.

Two with ~ 20 burst oscillations.

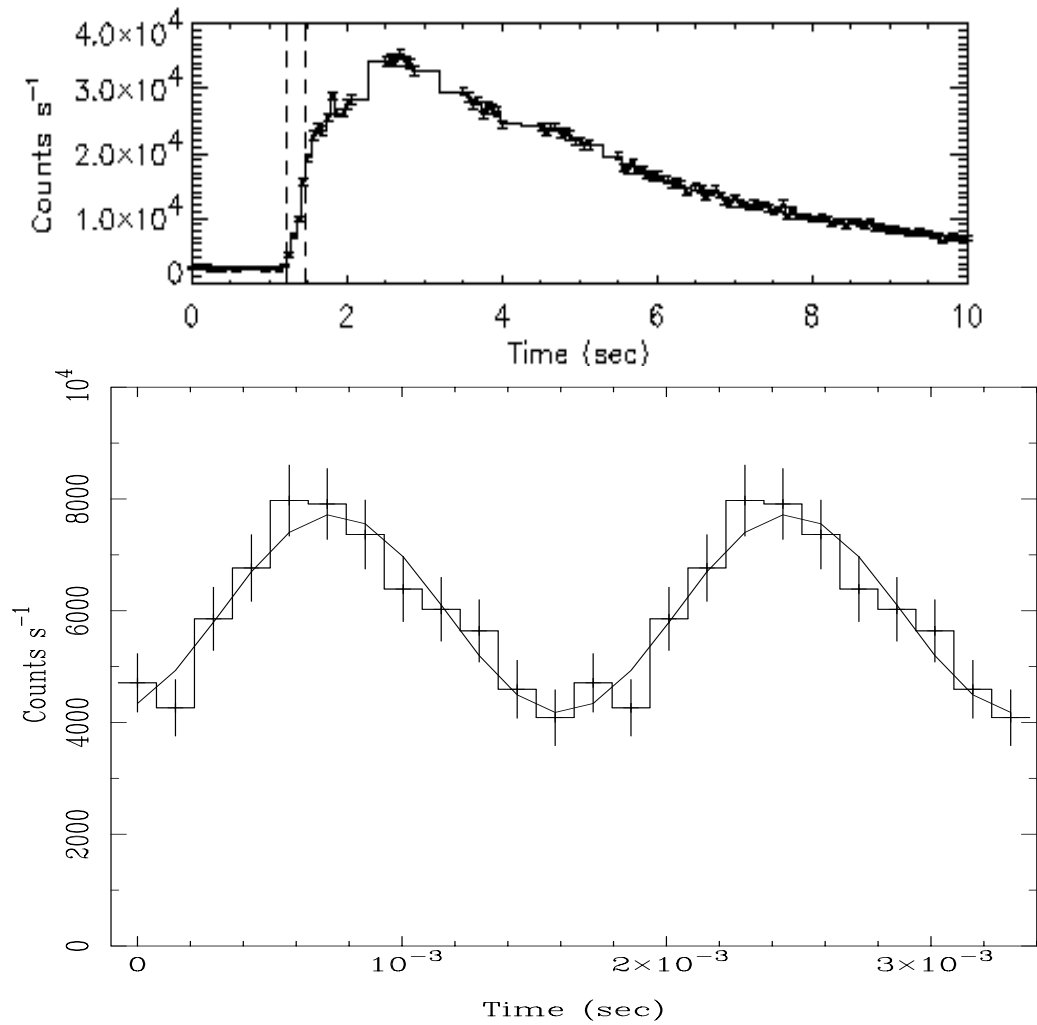


Fig. 2.— Light curves of thermonuclear bursts from the source 4U 1636-536, from T. Strohmayer et al. 1998, ApJ, 498, L135. Upper panel: overall light curve in Rossi X-ray Timing Explorer counts per second versus time. Lower panel: folded light curve, clearly showing frequency of 581 Hz.

Current Constraints

Some constraints possible with RXTE data.

Nath & Strohmayer (2002): amplitude.

Ford (1999, 2000): phase lags.

Muno et al. (2002): pulse profile.

Low area hampers constraints.

Simple modeling of simulated light curves:

$$P=2000 \Rightarrow \Delta M/M > 0.5.$$

Also, $j = a/M$ is undetermined.

Analysis of data is pending (Muno et al.).

Benefits of XEUS Timing

With a much larger instrument, constraints are overwhelmingly better.

Assuming Leahy power of 4×10^4 :

$$\Delta M/M < 0.1.$$

$$\Delta R/R < 0.1.$$

Detection of frame-dragging.

Together, unprecedented constraints on the state of high-density matter.

May constrain thermonuclear propagation.

In some bursts, $2\nu_{\text{spin}}$ may dominate.

See speed of propagation.

$v > \text{few} \times 10^8 \text{ cm s}^{-1}$ means detonation.

Only possible with high area.

Bears on novae, Type Ia supernovae.

Highly Resolved X-ray Spectra with Chandra: Dynamics of Neutral and Ionized Matter

Norbert S. Schulz

Massachusetts Institute of Technology, Center for Space Research, Cambridge, MA 02139, USA

Abstract. The High Energy Transmission Grating Spectrometer (HETGS) onboard the Chandra X-ray Observatory has so far produced a large number of high resolution X-ray spectra with unprecedented spectroscopic details. Spectra from outflows in galactic and extragalactic X-ray sources indicate plasmas with a wide range of properties. Optically thick fluorescent matter and warm photoionized regions play as much a role as very hot regions where collisional ionization and scattering dominate the emission. Through the measurements of blue- and redshifts the complex dynamics of these plasmas is revealed. Quite intriguing in this respect is the case of X-ray absorption of neutral matter. In many cases spectral features are found to be of high complexity though the detection of edges from intermediate Z elements as well as absorption lines from monatomic species to molecular compounds. With the application of line diagnostic tools and more accurate atomic data bases we are now able to model the properties of these plasmas as well as measure line shifts and shapes to constrain their spatial distribution and dynamics. In various examples, i.e. plasmas from accretion disks, winds, stationary clouds as well as the ISM, the power of highly resolved X-ray spectra is demonstrated and the scientific capability of XEUS in this context is explored.

1. Introduction

With the launch of the Chandra X-ray Observatory in 1999 we entered a new era of high resolution X-ray spectroscopy that enriched our views throughout the entire field of high energy astrophysics. Specifically the two grating spectrometers, the HETGS and the Low Energy Transmission Grating Spectrometer (LETGS), with a spectral resolving power of over an order of magnitude larger than most previous space-born X-ray spectrometers have already quite impressively demonstrated the importance and need for high resolution instruments in the field. While focussing mostly on bright galactic X-ray sources, I will explore some aspects of X-ray spectroscopy and plasma diagnostics using the HETGS which are now state of the art in the field.

X-ray binaries are the brightest X-ray sources in the sky and their bright X-ray emission is a consequence of the accretion process of material from a close companion onto a compact object, likely a neutron star or a black hole (BH). The result is a strong X-ray continuum that can be detected and measured with fairly low resolution detectors like proportional or gas scintillation counters. The latter offer spectral resolving powers of about $\Delta E/E$ of 1 to 10 depending on energy. These continua have been modeled to be of either thermal nature like blackbody radiation from the surface of a neutron star, disk blackbody radiation from a hot inner disk surface, thermal bremsstrahlung with high energy cut-offs, power laws from synchrotron radiation and/or reprocessed radiation through inverse Compton scattering, just to name a few. These spectra are generally modified by continuum (photoelectric) absorption in the ISM and optically thick matter intrinsic to the sources. Discrete emission like Fe K lines was merely detected as local perturbations in the continuum modeling process. Lewin et al. (1995) offers a more complete review with references. With the advent of charge coupled devices (CCDs) the resolving power increased to the order of 10 to 60. Some good progress was made to detect discrete line emission and absorption predominantly from faint extragalactic sources like warm absorbers and relativistic iron lines in active galactic nuclei. Spectra from very bright X-ray binaries offered quite little in this respect. Here only a few are to name like 4U 1626-67 (Angelini et al. 1995), Cyg X-3 (Kitamoto et al. 1994), and various high mass X-ray binaries like Vela X-1, Cen X-3 and GX 301-2 (Nagase et al. 1994). The problem with X-ray binaries was thought to be photon pile up in the CCD frame, which at such brightness levels wiped out potential line emission.

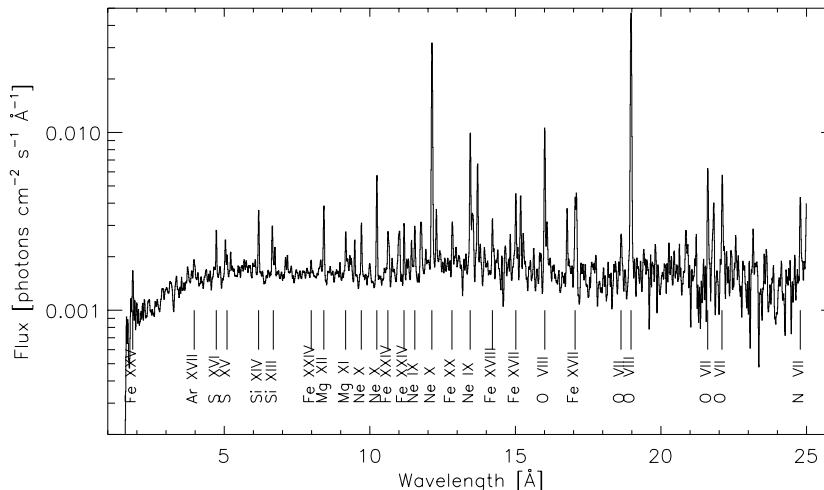


Fig. 1. HETGS spectrum of II Pegasi (from Huenemoerder, Canizares & Schulz 2001).

Why do we expect discrete emission in X-ray binaries in the first place? The answer is that there are many different plasma environments in these systems that re-process the radiation of the central source. In the following I chose a few examples of such environments and focus on the fact that we need various levels of spectral resolving powers to not only detect discrete features but also resolve them. The range of parameters in these plasmas is quite large as we observe temperatures between 10^4 and 10^8 K, densities from as low as $\sim 10^8$ cm^{-3} in winds to as high as $\sim 10^{18}$ cm^{-3} in accretion disks, optical depths between 0.01 and 100, ionization parameters of up to 2×10^4 and a vast range of ionization stages. For in-depth reviews I recommend Liedahl (1997) and Paerels (1997). Many times conditions are complicated by the fact that most of these plasmas are neither in ionization equilibrium nor at rest and we thus have to deal with all kinds of plasma dynamics.

The observation of X-rays in stars was discovered with *Einstein*, but the fact that many stars exhibit significant X-ray emission was finally established with the advent of *ROSAT* in 1990. Observation and analysis of stellar spectra is difficult and highly complex. Although most of the stars show X-ray emission at some level, but it is primarily the emission from very young late type and early type stars or stars that are very close to the sun that dominate the observations. The reason is that the two former show X-ray luminosities that are many orders of magnitude higher than most late type main sequence stars. On the other hand, the X-ray spectra of stars are more or less pure line spectra that need high spectral resolving power.

2. Line Emission

Chandra so far has produced a wealth of X-ray spectra showing discrete line emission, most of these spectra are attributed to either coronal emission or wind emission (or both) from stars. Coronal emission in general reflects emissivity conditions in the corona of our sun, which is a hot gas of temperatures above 10^6 K at relatively low densities ($\sim 10^{10}$ cm^{-3}). Figure 1 shows the example of such a spectrum observed in II Pegasi with the HETGS (Huenemoerder, Canizares & Schulz 2001). II Pegasi is what we call a coronally active binary and its plasma has a range of temperatures, densities, velocities, and nonequilibrium states. In order to diagnose this plasma we usually oversimplify conditions and assume a coronal approximation where we assume collisional excitation and ionization from the ground state and radiative and dielectronic recombination only. Photoexcitation of metastable states and photoionization are assumed to be negligible, except for density sensitivity. The spectrum shows - besides some thermal bremsstrahlung continuum - a manifold of lines from most abundant ions between $Z=7$ (nitrogen) and $Z=26$ (iron). In order to determine emission measure distributions and abundances (in flare and non-flare states) we need to resolve as many lines in the spectrum as possible. At a region between 10 \AA and 10 \AA we specifically observe a large line density, which is primarily due to the fact that here we find dominant lines from Fe L shell ions. The mean resolving power of the Medium Energy Grating (MEG) here is 1200 with an absolute wavelength scale of 50 to 100 km^{-1} allowing for unambiguous line identifications and line flux determinations. At lower wavelength below 10 \AA the resolving power of the gratings decrease, but so does the line density in the spectrum. For example lines from H- and He-like sulfur ions can be observed at a resolving power of 500.

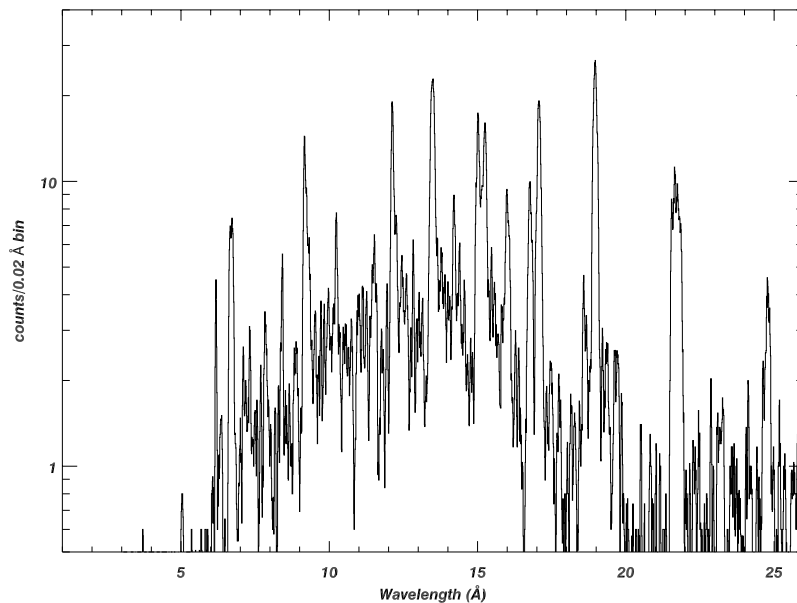
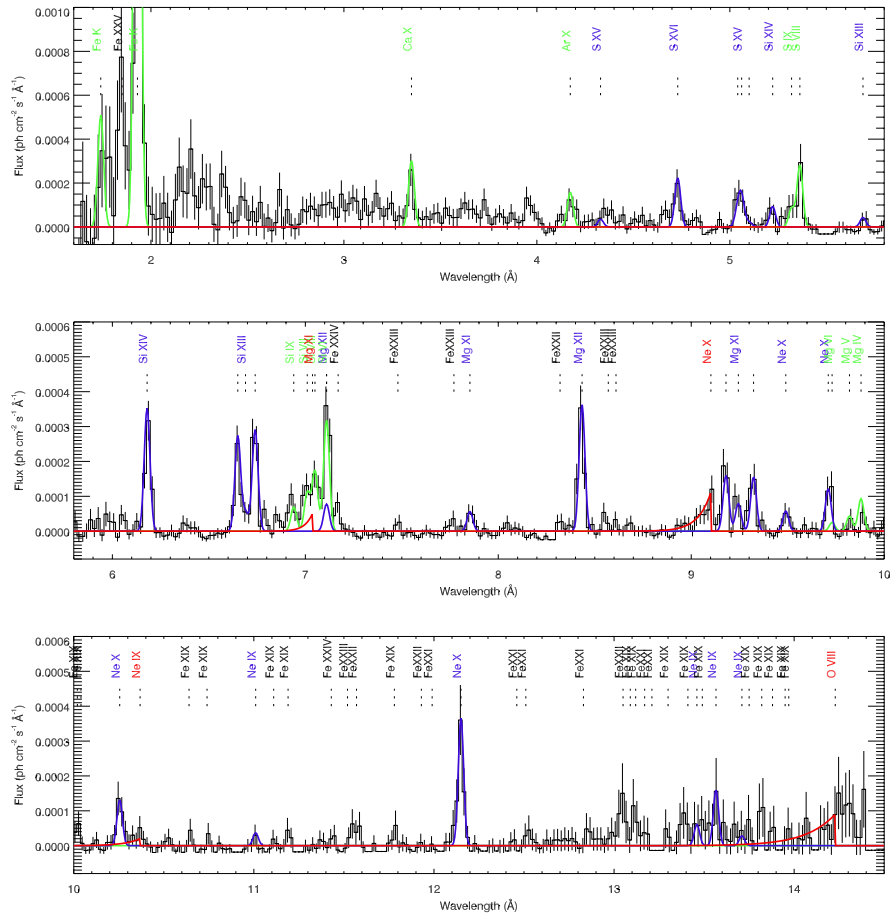


Fig. 2. Preliminary HETGS count spectrum from ι Ori.

Of course, this is valid only if the lines are not significantly broadened and shifted due to motions in the plasma. Figure 2 shows the example of ι Orionis, a highly eccentric early type binary (O9 III + B1 III), where we expect lines from a high velocity stellar wind ($v \sim 2500 \text{ km s}^{-1}$) and a collisionally ionized plasma of a temperature of $6 \cdot 10^6 \text{ K}$. Here the lines appear severely Doppler broadened, which allows us to fully resolve the lines with a much lower power but at the expense of line confusion. The O VII triplet, for example well resolved in II Peg, appears as one broad line in ι Ori although the resolving power of the instrument is the same. The reason is that in II Peg the lines are generated in coronal loops near the stellar surface, while in ι Ori the lines are generated in the wind a few stellar radii away from the surface of the star where the terminal velocity is reached.

When we observe line emission from accreting X-ray binaries we primarily find that plasmas are predominantly photo-ionized, at most hybrid plasmas (Bautista and Kallman 2000, Porquet and Dubois 2000). Exceptions from this are rare, like high temperature outflow in the jet of SS 433 (Marshall, Canizares, & Schulz 2002) or possible contributions from shock instabilities in the stellar wind of high mass X-ray binary (HMXBs) companions as was speculated in Cyg X-1 (Schulz et al. 2002), just to name a few.

Reprocessed X-rays in a stellar winds result in discrete emission lines. Figure 3 shows an example of an HETGS spectrum of the ionized stellar wind in Vela X-1 during eclipse (see Schulz et al. 2002). The spectrum shown is a residual spectrum, i.e. the scattered continuum from the central source has been subtracted and it thus appears entirely resolved into emission lines. The lines originate from at least two dynamically different regions. First, we observe lines from the photo-ionized wind (blue). The lines itself are actually not resolved, i.e. we do not observe any measurable Doppler-broadening above the resolution limit, which at Ne X corresponds to about 250 km s^{-1} . There are also no line shifts. A detailed analysis of the spectrum reveals signatures of photo-excitation in the plasma (Schulz et al. 2002). This is most prominently visible in the He-like triplets as the resonance lines appear much too strong as expected from a photo-ionized or hybrid plasma (Porquet & Dubois 2000). Wojdowsky et al. (2002) in an analysis of a similar spectrum of Cen X-3 interprets this effect as resonant scattering of the source continuum in the resonance line. We also observe radiative recombination continua (RRCs, red) from the photo-ionized gas from Mg XII, Ne X, and O VIII ions, although the one from Mg XII is blended in with another line complex. RRCs appear narrow at low temperatures and broad at high temperatures and it thus critically depends on the resolution of the instrument how accurately we can measure the temperature of the photoionized gas. In the HETGS spectrum they appear fully resolved at a temperature of $1.2 \cdot 10^5 \text{ K}$. The most remarkable lines in the spectrum in Figure 3, however, are the fluorescence lines, specifically the ones at S, Si, and Mg. Here the observation of some L-shell ions is most likely an indicator of cold material of high column density. The challenge we face here from the point of spectroscopy is that low excitation fluorescence lines (House 1969) cannot be resolved with the HETGS resolution and the determination of the ion type becomes strongly model dependent.



1

Fig. 3. The residual line spectrum of Vela X-1 during eclipse observed with the HETGS.

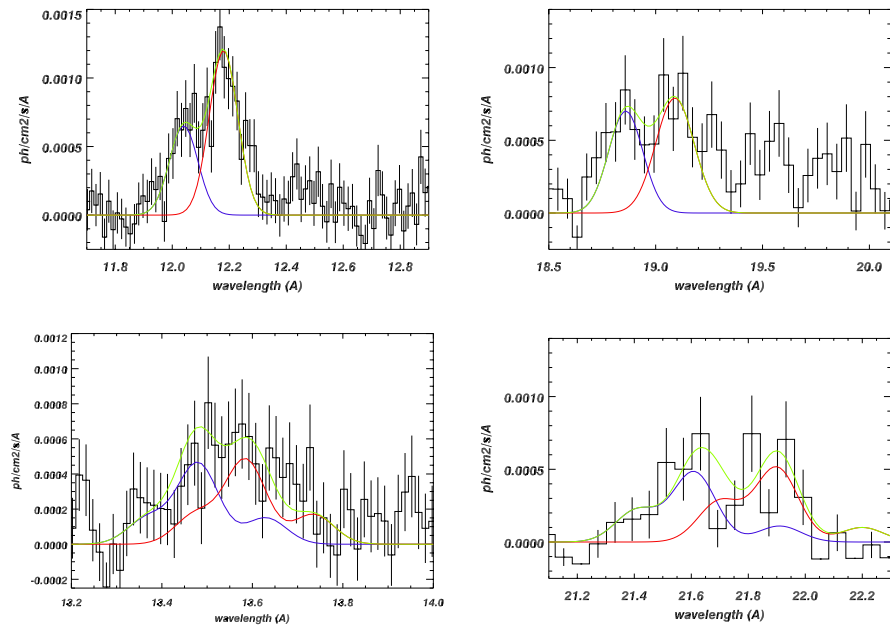


Fig. 4. Doppler line pairs from the accretion disk in 4U 1626-67 (from Schulz et al. 2002a)

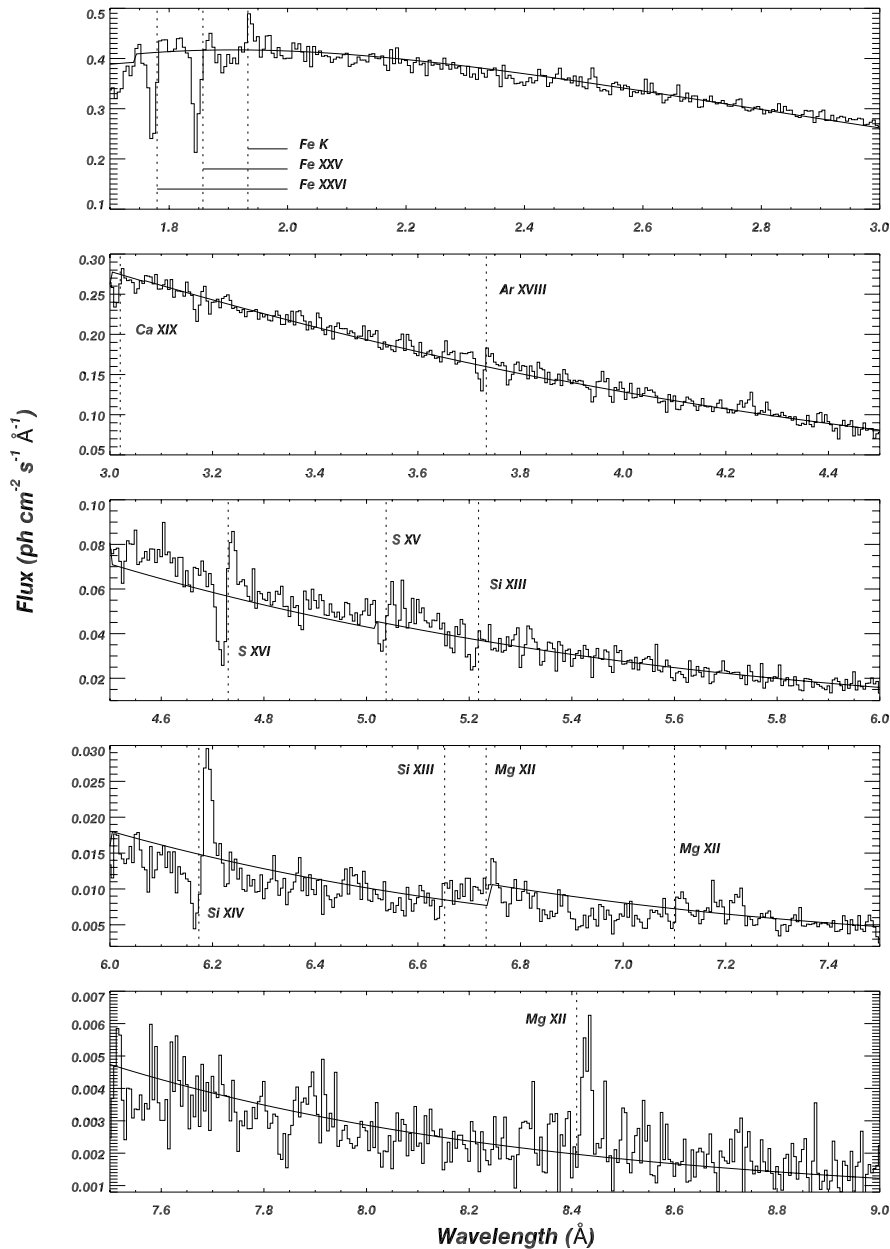


Fig. 5. HETGS spectrum from a deep intensity dip of Cir X-1 during periastron (from Schulz & Brandt 2002)

Emission lines are also observed with the HEGTS from accreting disks in low-mass X-ray binaries (Brandt & Schulz 2001, Cottam et al. 2001, Schulz et al. 2002a). In 4U 1626-67 it was well known from previous *ASCA* and *BeppoSAX* observations that the spectrum shows strong Ne and O lines (Angelini et al. 1995, Owens, Oosterbroek, & Parmar 1997). The HETGS spectrum basically confirms these observations as only the lines from H-like and He-like ions of Ne and O were detected. Surprisingly the lines appeared fully resolved and extremely broad, which turns out to be an effect of blue- and red-shifted line components as shown in Figure 4. At velocities between 1550 to 2610 km s⁻¹ for the blueshifted and 770 to 1900 km s⁻¹ for the redshifted line components, spectral resolution does not seem to be that crucial and in fact only a factor of resolution higher than CCD resolution would have sufficed to detect the Doppler split. However, it becomes critical again when we want to model the He-like triplets, which now take on a very complex shape in which the resonance, intercombination, and forbidden line components of the blueshifted line triplet now mix with the redshifted triplet (see bottom of Figure 4).

3. Resonant Absorption

Besides line emission we on many occasions observe resonant line absorption. Most illustrative in this respect is the case of Cir X-1, in which we found P Cygni line profiles for the first time in X-rays (Brandt & Schulz 2000). Figure 5 shows the spectrum of Cir X-1 during a major dip, i.e. when major parts of the spectrum appear heavily absorbed (from Schulz & Brandt 2002). Besides strong emission lines from all H- and He-like ions of abundant elements we observe strong and blueshifted absorption accompanying these lines. Brandt & Schulz (2000) interpret these absorption lines as a consequence of a fast outflow/wind originating at the line production site resulting in P Cygni lines. These lines are narrow with blueshifts ranging from 400 to 2000 km s⁻¹. With medium resolution detectors like ASCA these lines were not seen and only barely detected with the XMM-RGS (Shirey 2001, priv. comm). These absorption lines appear variable on timescales of one to a few hours (Schulz & Brandt 2001). A detailed analysis revealed that this variability is most likely the consequence of fluctuations in the ionization fraction of the outflow (Schulz and Brandt 2002). A result like this could not have been possible without the superb spectral resolution of the instrument.

Other examples includes HETGS spectra of Cyg X-1. Here the situation appears similarly complex. We observed this black hole binary at various orbital phases and find a series of weak and narrow absorption lines (Schulz et al. 2002b, Marshall et al. 2001, Miller et al. 2002). Parts of HETGS spectra from two phases are illustrated in Figure 6. The top two panels show spectra from an orbital phase where we view the focussed stellar wind of the star with a significant velocity component that points away from the observer. As a consequence we observe red-shifted absorption lines (Marshall et al. 2001) by about 450 km s⁻¹. The bottom panel in Figure 6 shows an orbital phase, where there is no such velocity component and here we see absorption lines without measureable red-shifts (Miller et al. 2002). I have to point out again that the detection of these dynamic lines require the maximum resolution of the HETGS device (in 1st order).

4. Photoelectric Absorption

The understanding of photo-electric absorption of X-rays is of immediate importance for the analysis of X-ray spectra. With the high resolution X-ray spectrometers onboard *Chandra* and *XMM-Newton* we can now directly measure the depth and structure of major photo-electric edges. The treatment of photo-electric absorption has a longstanding history in determining energy dependent photoionization crosssections of the interstellar medium ISM from the far UV to X-rays (Strom & Strom 1961, Brown & Gould 1970, Morrison and McCommon 1983). Most recently Wilms, Allen & Mc Cray (2000) presented the latest improvements on the abundance distribution of the ISM. We have started a survey of observations with the HETGS of bright X-ray binaries in the galactic plane in order to determine the optical depths of low energy absorption edges from Ne, Fe, O, and possibly N. In two pilot studies by Paerels et al. (2000) and Schulz et al. (2002) several remarkable features have been found ranging from strong absorption of the 1s-2p atomic absorption line from oxygen as well as indications of narrow absorption from various oxides.

Figure 7 shows three examples of measured Fe L edges observed in X-ray binaries with different interstellar column densities. Of course, in general we cannot easily distinguish between source intrinsic and ISM contributions and here we have an opportunity to advance our understanding of cold matter structure. The spectra around 710 eV show that the edge shows considerable structure, mainly a three-fold absorption pattern corresponding to a very weak Fe L1 (844 eV, not included in Figure 7) and strong Fe L2 (719 eV) and Fe L3 (706 eV). The values here are given for metallic Fe. The Fe L edge structure from metallic iron was measured recently by Kortricht & Kim (2000) and we used their cross sections to fit the data (straight lines in Figure 7). Clearly, as this edge shows significant structure over a large range of column densities (here 1 to 9 10²¹ cm⁻²) it probably caused residuals in spectral fits with low resolution detectors which ultimately were interpreted as low energy Fe lines. However, even if we include the basic structure of this edge, the three examples in Figure 7 show that there is more detailed structure accompanying these edges. Here we see great challenges for the future.

5. Scattering

This topic is very much related to the previous one as we now enter an era of solid state astrophysics in the X-ray domain. The understanding of absorption and scattering of X-rays is not only of immediate importance for the analysis of X-ray spectra, but also fundamentally contributes to our understanding of the composition and structure of the ISM and the circumstellar medium. X-ray absorption fine structure (XAFS) are produced by the interference effect of a back-scattered electron wave from nearby atoms on the final state of the out-going electron wave. XAFS thus depend on the type, structure, and state of the intervening matter. It now allows us to study the properties of interstellar grains and molecules in the spectra that have passed through interstellar matter (Woo 1995).

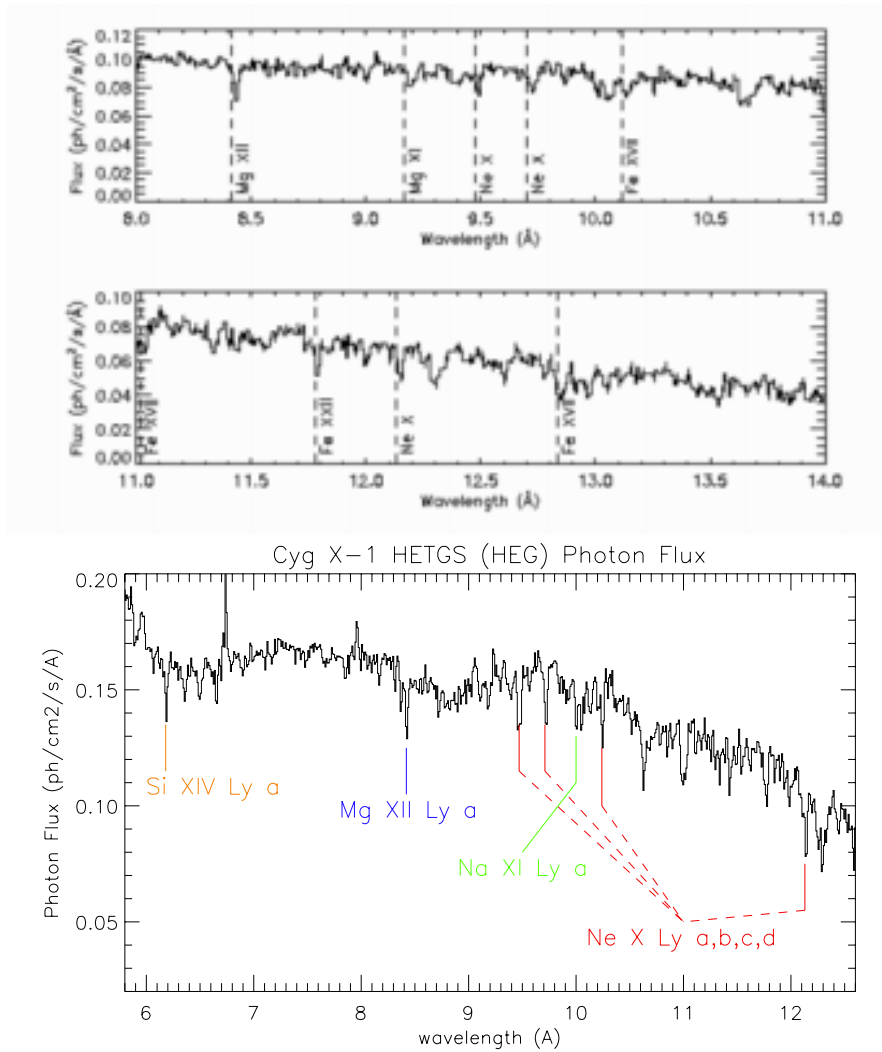


Fig. 6. Top: redshifted absorption lines in the spectrum of Cyg X-1 at orbital phase 0.82 (Marshall et al. 2001). Bottom: Unshifted lines at phase 0.74 (Miller et al. 2002).

Figure 8 shows two examples where we likely observe solid matter signatures from circumstellar matter (left) and ISM matter (right). In HETGS spectra of GRS 1915+105, Lee et al. (2002) found XAFs signatures near the Si edge, but also indications near S and Mg. This is quite important in the context of observations of clouds and dust in the IR and UV as well as from meteorites and interplanetary dust, where it is generally believed that interstellar grains are composed of various combinations of ice (H_2O), graphite (C), silicates (e.g. FeSiO_3 , MgSiO_3), magnetites (e.g. Fe_3O_4), to name a few. From the instrumental point of view, two factors are important here: spectral resolution *and* effective area as most of these features are extremely weak. GX 5-1 is exceptionally bright even though it lies in the galactic bulge at a projected distance of 10 kpc and is thus strongly affected by absorption. The right part of Figure 8 shows a strong edge signal in the count spectrum at Si K. Once the instrumental contribution, which is largely affected by contributions from SiO_2 , is removed we still observe large residuals of SiO_2 . The signal is significantly stronger than what would be expected from calibration uncertainties and it is quite likely that we observe interstellar SiO_2 .

6. Implications for XEUS

These last sections clearly demonstrated that highly resolved spectroscopy opened a new window to our galaxy in X-rays. A common thread in these new discoveries is that they were clearly not possible without the unprecedented spectral resolving power of the HETGS. XEUS, with specification of 2 eV (narrow field of view) in the range of 0.05

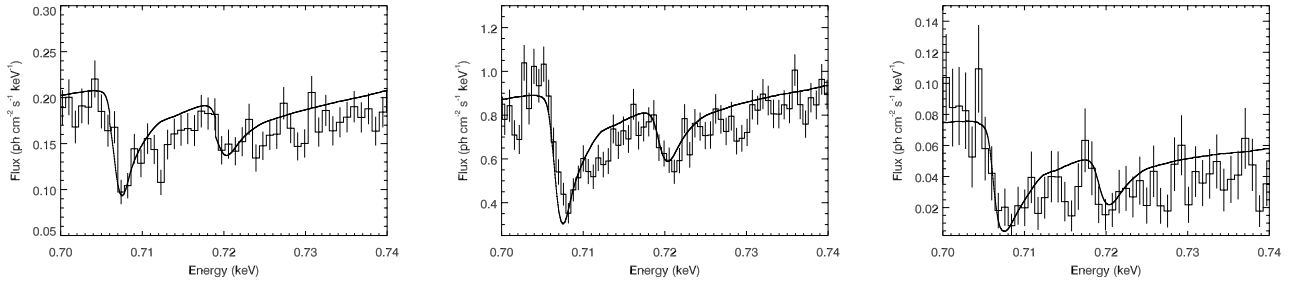


Fig. 7. Three examples of Fe L 2 and 3 edge observations at various column densities: 4U1636-53 at $3 \cdot 10^{21} \text{ cm}^{-2}$ (left), Cyg X-1 at $6 \cdot 10^{21} \text{ cm}^{-2}$ (middle), and GX 349+2 at $9 \cdot 10^{21} \text{ cm}^{-2}$ (right)

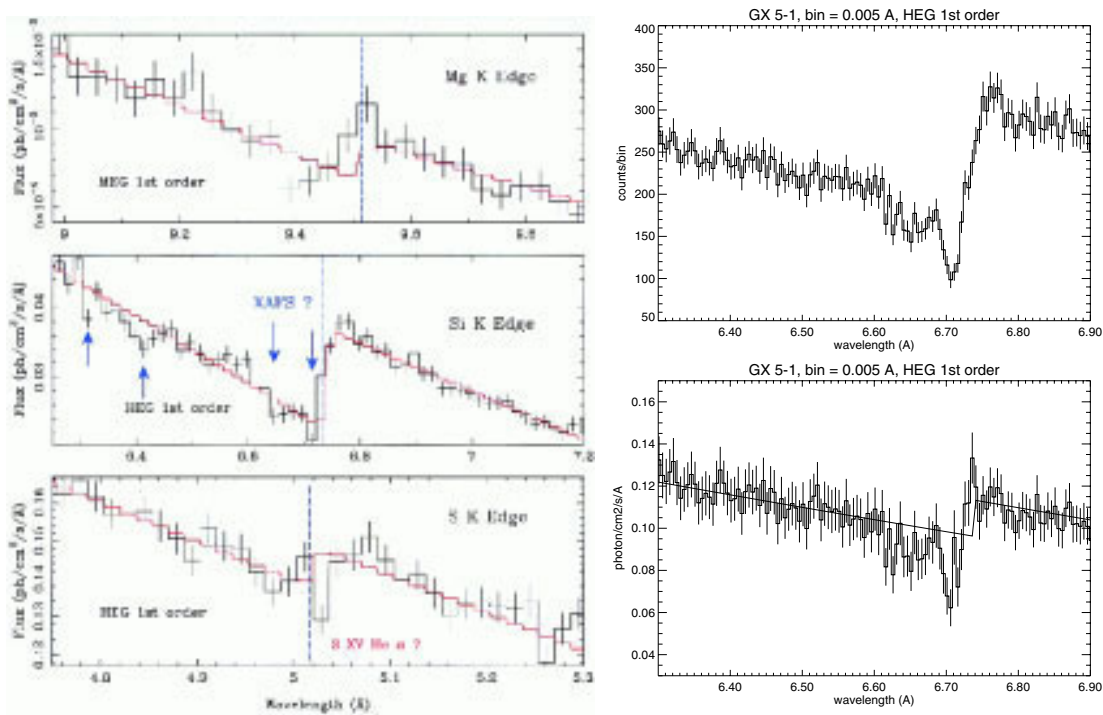


Fig. 8. Left: XAFS near edges in GRS 1915+105 (from Lee et al. 20012). Right: Strong residual structures in the Si K edge of GX 5-1.

to 30 KeV (250 to 0.4 \AA), offers not only a continuation of these capabilities, but will extend our currently accessible bandpass. Here are a few science topics, which I can identify in this respect:

- line shape studies - Doppler tomography in accretion disk lines
- line variability studies - reverberation mapping
- weak edge structures - cold matter in X-ray sources and the ISM
- XAFS in the ISM - grains and molecules
- ionized absorption in the IGM
- extended source - abundance, temperature, velocities in SNRs

As the observation of fainter sources with the HETGS and XMM-Newton -RGS is quite exposure time consuming and the study of line variability is exposure limited, its so much larger effective area will clearly push our current limits. At higher energies the extended bandpass will allow to include the observation of the full Fe XXIV Lyman α series, H- and He-like Ni ions, as well as highly resolved synchrotron absorption lines. The increased resolving power at high energies is specifically interesting as we will be able to better resolve narrow Fe K fluorescence lines, which are already found in quite a variety of sources. As for the continuation of our current efforts, however, it also has

to be concluded that a resolving power of 1 eV at 1 keV, which is currently only listed as a goal for the mission, is clearly more desired than the current specification of 2 eV. The latter would severely limit our diagnostical potential for spectroscopic features similar to the ones shown in this presentation.

Acknowledgements. Work at MIT was supported by NASA through the HETG contract NAS 8-38249 and through the Smithsonian Astrophysical Observatory (SAO) contract SVI-61010 for the Chandra X-ray Center. In addition I want to thank Raquel Morales for critically reading through the manuscript as well as the CXC and HETG team at MIT for their continuing support.

References

- Angelini L., White N. E., Nagase F., et al. 1995, *ApJ* , 449, L41
Bautista M.A., & Kallman, 2000, *ApJ* , 544, 581
Brandt W.N., & Schulz N.S., 2000, *ApJ* , 544, L123
Cottam J., Kahn S.M., Brinkman A.C., et al., 2001, *A&A*, 365, L277
House L.L., 1969, *ApJ Suppl.*, 18, 21
Huenemoerder D.P., Canizares C.R., & Schulz N.S., 2001, *ApJ* , 599, 1135
Kitamoto S., Kawashima K., Negoro H., et al. 1994, *PASJ*, 46, L105
Kortright J.B., and Kim S.-K., 2000, *Phys. Rev. B*, 62, p. 12216
Lee J.C., Reynolds C.S., Remillard R.R., et al., 2002, *ApJ* , 567, 1102
Lewin W.H.G., van Paradijs J., van den Heuvel E.P.J., 1995, "X-ray Binaries", Cambridge: Cambridge Univ. Press
Liedahl D.A., 1997, in "X-ray Spectroscopy in Astrophysics", eds. J. van Paradijs and J.A.M. Bleeker, Springer Berlin-Heidelberg-New York, p. 189
Marshall H.L., Schulz N.S., Fangt T., et al., 2001, in "X-ray Emission from Accretion onto Black Holes", eds.: T. Yaqoob and J.H. Krolik, Baltimore, published electronically, E45
Marshall H.L., Canizares C.R., & Schulz N.S., 2002, *ApJ* , 564, 941
Miller J.M., Schulz N.S., Marshall H.L., et al., 2002, *ApJ* , submitted
Morrison R., & McCommon D., 1983, *ApJ* , 278, 1082
Paerels F., 1997, in "X-ray Spectroscopy in Astrophysics", eds. J. van Paradijs and
Paerels F., Brinkman A.C., van der Meer R.L.J, et al., 2001, *ApJ* , 546, 338
Porquet D., & Dubau J., 2000, *A&AS*, 143, 495 J.A.M. Bleeker, Springer Berlin-Heidelberg-New York, p. 347
Nagase F., Zylstra G., Sonobe T., , 1994, *ApJ* , 436, L1
Owens A., Oosterbroek T., & Parmar A. N. 1997, *A&A*, 324, L9
Schulz N.S., & Brandt W.N. 2001, in "X-ray Astronomy 2000", Eds. R. Giacconi, L. Stella, and S. Serio, ASP conference series, p. 263
Schulz N.S., & Brandt W.N. 2002, *ApJ* , 572, 971
Schulz N.S., Canizares C.R., Lee C.R., & Sako M., 2002, 564, L21
Schulz N.S., Chakrabarty D., Marshall H.L., 2002a, *ApJ* , 563, 941
Schulz N.S., Cui W., Canizares C.R., et al., 2002b, *ApJ* , 565, 1141
Strom S.E., & Strom K.M., 1961, *PASP*, 73, 43
Wilms J., Allen A., & McCray R., 2000, *ApJ* , 542, 914
Wojdowski P.S., Liedahl D.A., Sako M., et al., 2002, astro-ph/0206065
Woo J.W., 1995, *ApJL*, 447, L129



AGN iron lines: the complex picture from *XMM-Newton* and *Chandra*

Paul O’Brien, James Reeves, Ken Pounds, Kim Page and Martin Turner

Department of Physics & Astronomy, University of Leicester, University Road, Leicester, LE1 7RH, U.K.

Abstract. Observations of AGN by the *XMM-Newton* and *Chandra* satellites have revealed a wide variety of spectral features in the iron K-band. Some objects, particularly the Seyfert 1 galaxies MCG $-6 - 30 - 15$ and Mrk 766, show a neutral, broad iron K line. Several AGN, for example Mrk 205 and Mrk 509, show an ionised, broad iron K line. In contrast, broad iron lines, whether neutral or ionised, are difficult to delineate in high luminosity quasars. The observed distribution in broad iron-line features could be due to an increase in the average accretion disc ionisation with X-ray luminosity.

A narrow, neutral iron line is a common feature in low to moderate luminosity type 1 AGN. The width and strength of the narrow iron line suggests it originates in the outer BLR and/or the putative molecular torus invoked in AGN unification schemes. The narrow line is far less obvious in high luminosity AGN possibly due to a reduction in the BLR covering factor or in the solid angle subtended by the molecular torus, as predicted by some torus models.

The new observations make it clear that the iron K band contains a wealth of detail. Despite their already substantial contributions to our knowledge of AGN, neither *XMM-Newton* nor *Chandra* have sufficient capability to fully exploit the diagnostic potential of this waveband. Rather, the new data show even more clearly that a mission with a large effective area, high energy resolution and broad bandpass, is required if we are to disentangle the various emission and absorption features, determine the origin of the broad and narrow emission features, determine the physical parameters with which these features correlate, and extend the current detailed studies to high-redshift, where the first black holes were formed. More effective area is required to provide high-quality data for large AGN samples in a reasonable time. High energy resolution is required to separate the narrow and broad features. Broad bandpass is required to determine the continuum shape and hence reliably measure the absorption and emission features. *XEUS* would provide all of these capabilities.

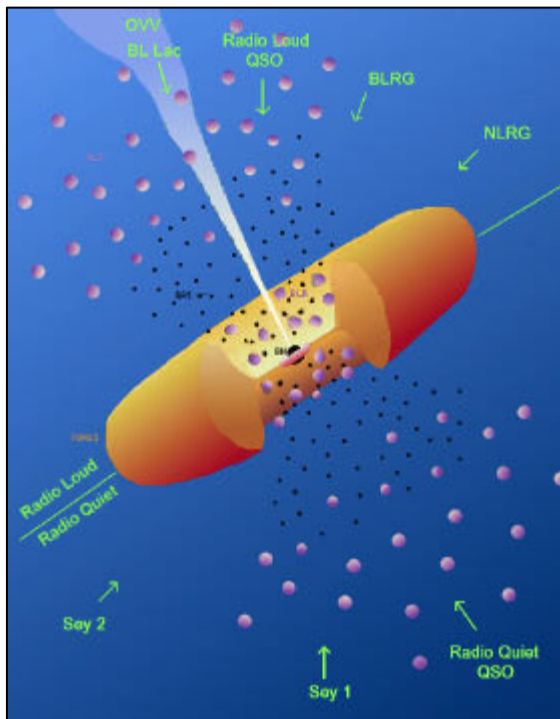
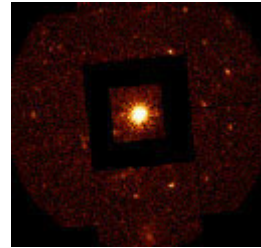
Acknowledgements. We gratefully acknowledge the permission by the Springer Verlag to use their A&A L^AT_EX document class macro.

**AGN iron lines:
the complex picture from
XMM-Newton and *Chandra***

- Paul O'Brien
- James Reeves
- Ken Pounds
- Kim Page
- Martin Turner
- plus collaborators

X-ray and Observational
Astronomy Group
University of Leicester, UK

X-ray and Observational Astronomy Group

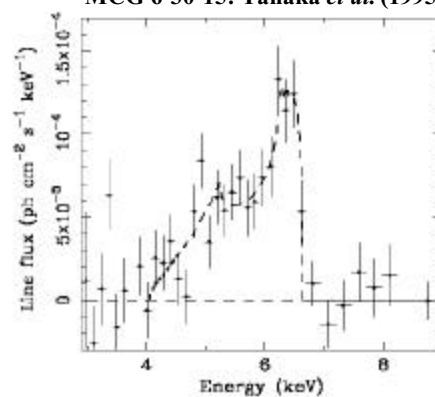


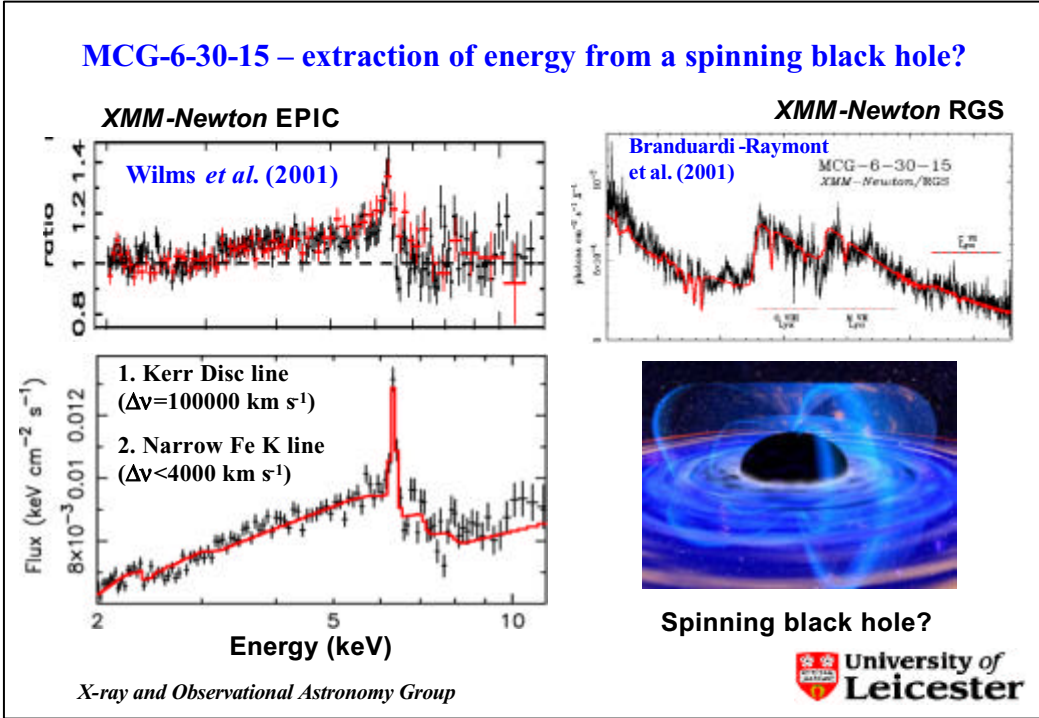
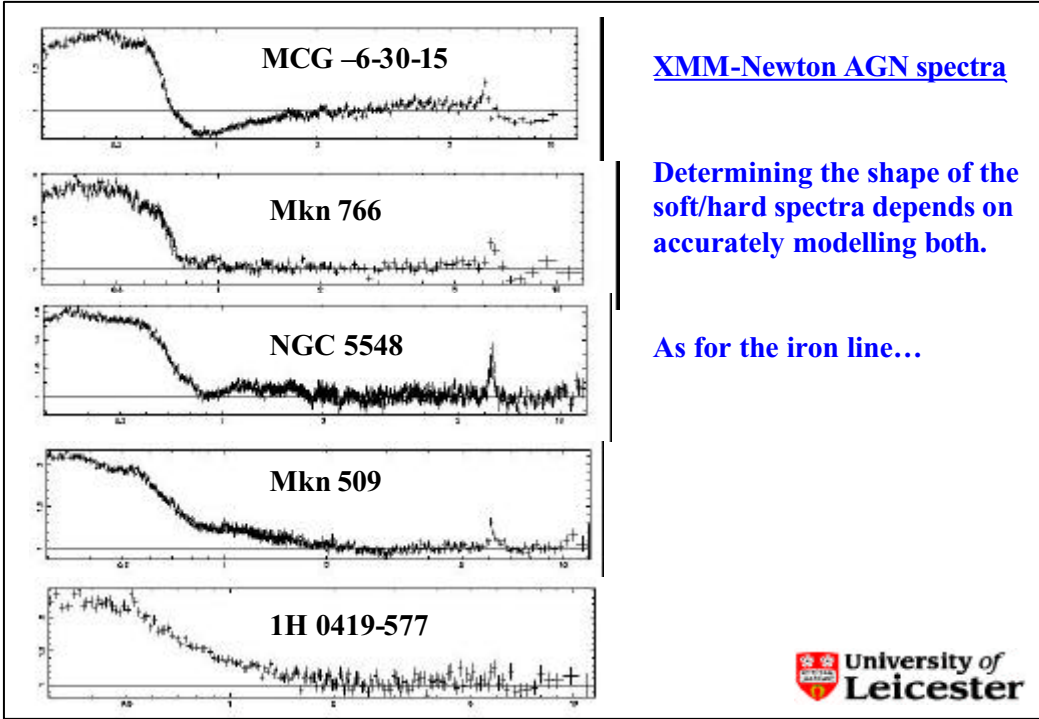
**Hard X-rays illuminate 'cold' inner
accretion disc and BLR/torus**

Broad (disc) Fe K α

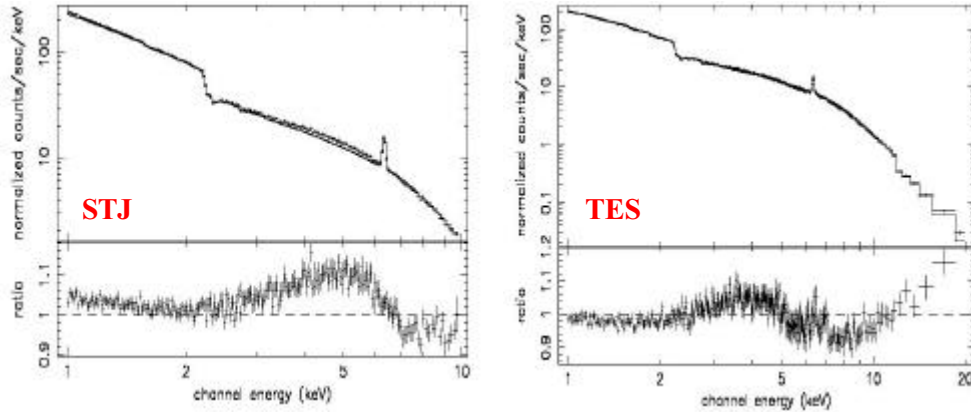
Narrow (BLR/torus) Fe K α

MCG-6-30-15: Tanaka *et al.* (1995)





Simulation of MCG-6-30-15 observed with XEUS I for 5 ksec



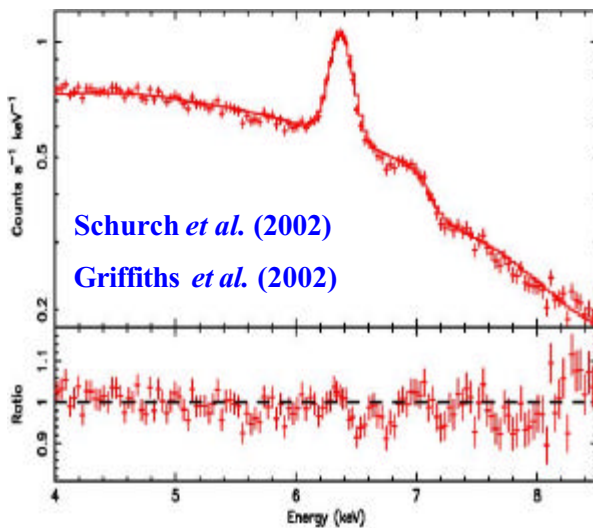
Model from Wilms et al. (2001) excluding absorption

X-ray and Observational Astronomy Group



No Broad Iron K Line in NGC 4151?

XMM-Newton observation



Schurch et al. (2002)

Griffiths et al. (2002)

NGC 4151 in low flux state
 $F_{2-10} = 4.25 \times 10^{-11} \text{ ergs cm}^{-2} \text{ s}^{-1}$

Iron $K\alpha$ emission is narrow
 during the XMM-Newton
 observation:

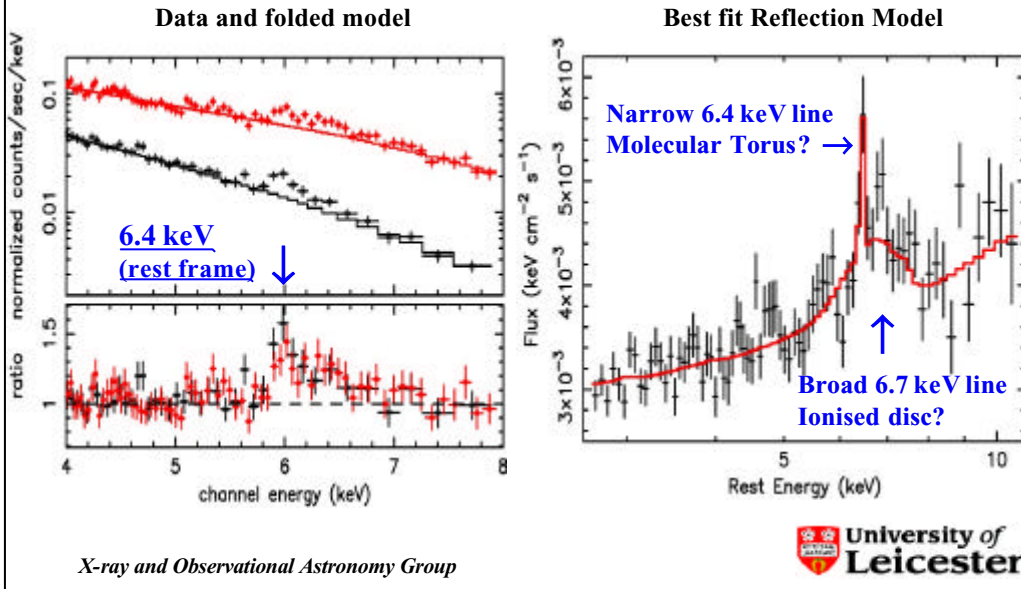
$E = 6.40 \text{ keV}$, $EW \sim 180 \text{ eV}$
 $\sigma \sim 30 \text{ eV}$ (FWHM $\sim 3000 \text{ km/s}$),

No Broad iron K line is required

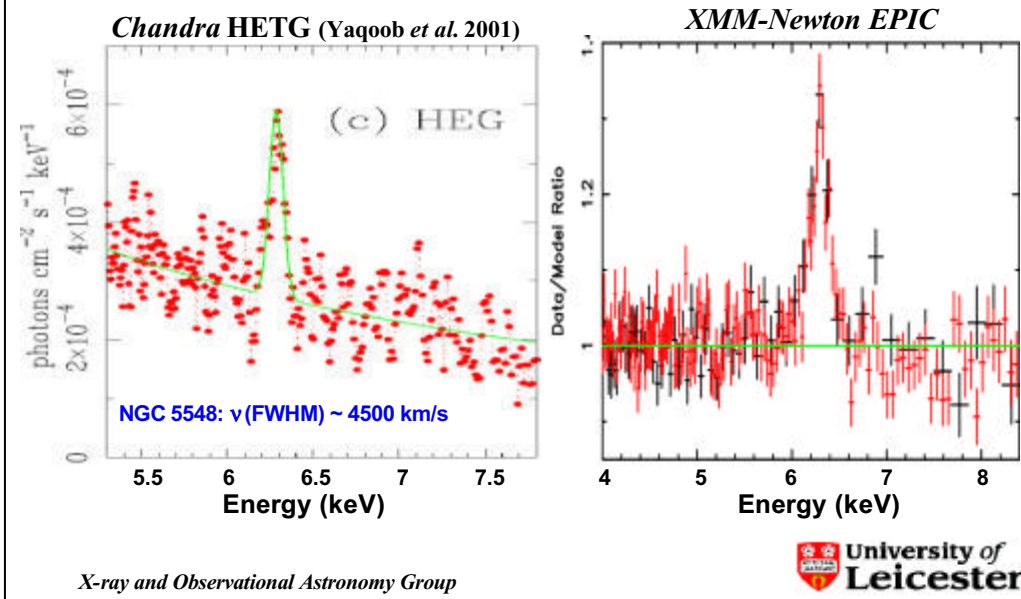
X-ray and Observational Astronomy Group



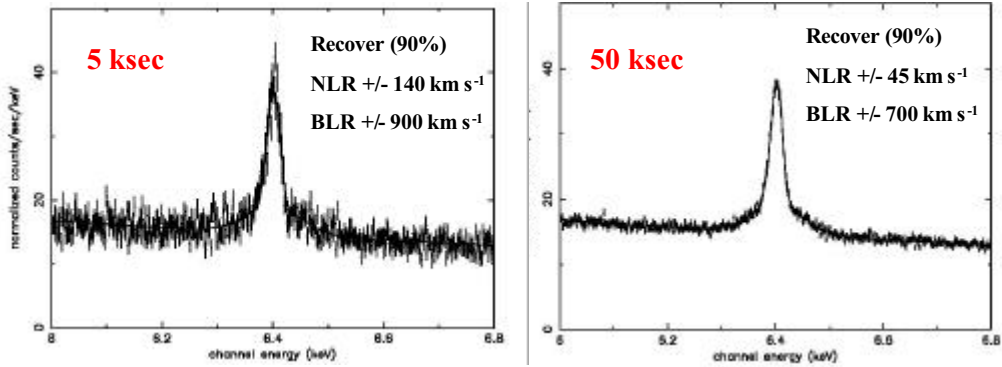
Markarian 205: EPIC MOS+PN (Reeves et al. (2001))



The Narrow Iron K α line in the Seyfert 1 Galaxy NGC 5548



XEUS I simulation of NGC5548 narrow Fe K α line with STJ detector



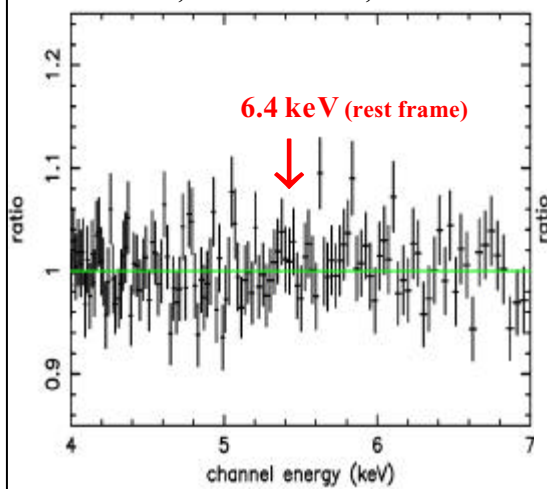
Model: “NLR/Torus” Fe K α (doublet) FWHM = 1000 km s⁻¹ +
“BLR” line FWHM = 5000 km s⁻¹. Total EW ~ 70 eV.

X-ray and Observational Astronomy Group

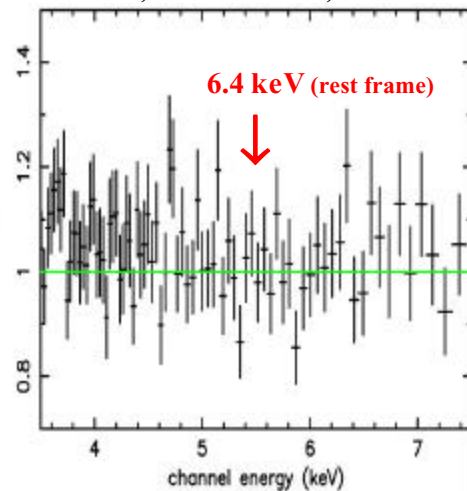


Luminous Quasars – No narrow iron K lines

3C 273; Iron K α Line, EW<10eV



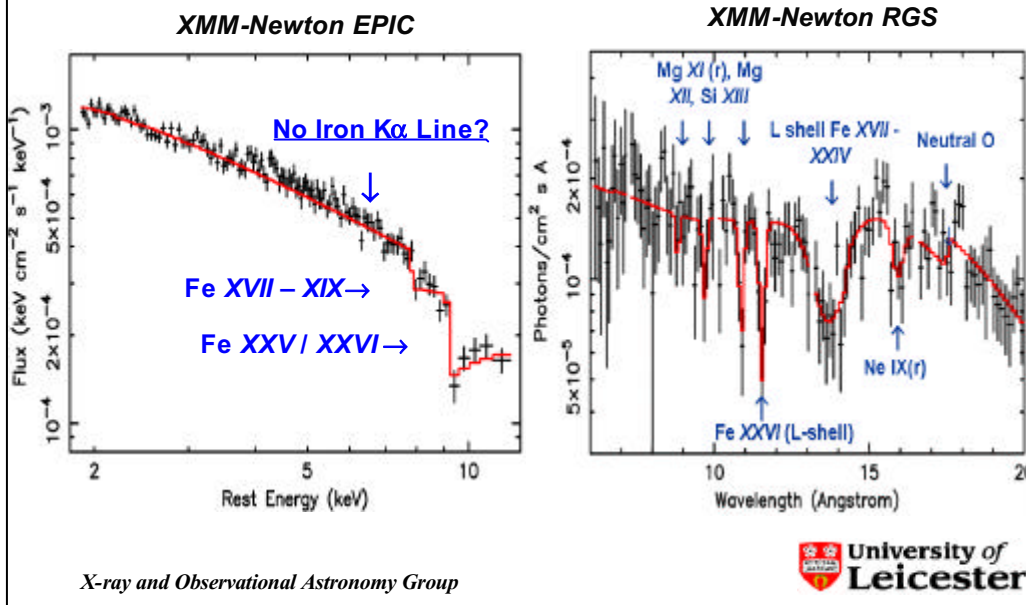
PDS 456; Iron K α Line, EW<12eV



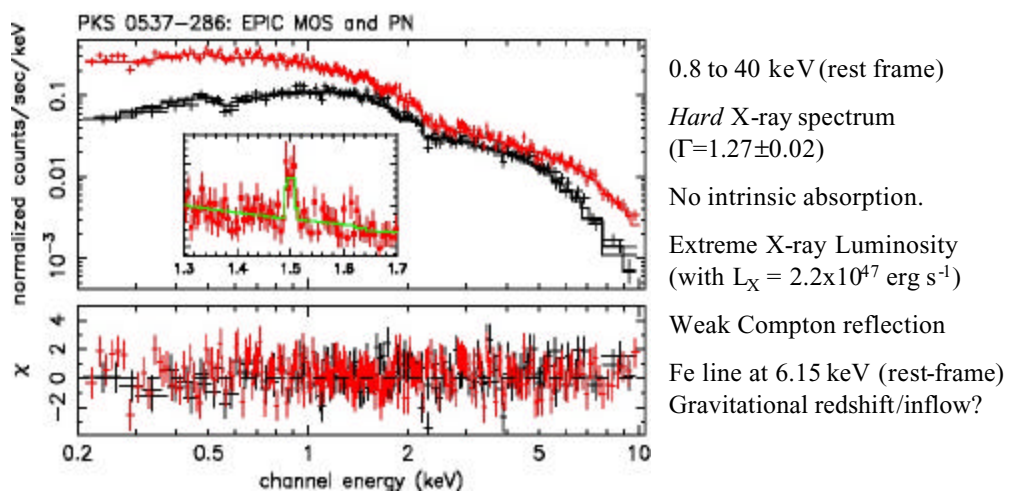
X-ray and Observational Astronomy Group



X-ray Absorption in the High Luminosity Quasar PDS 456

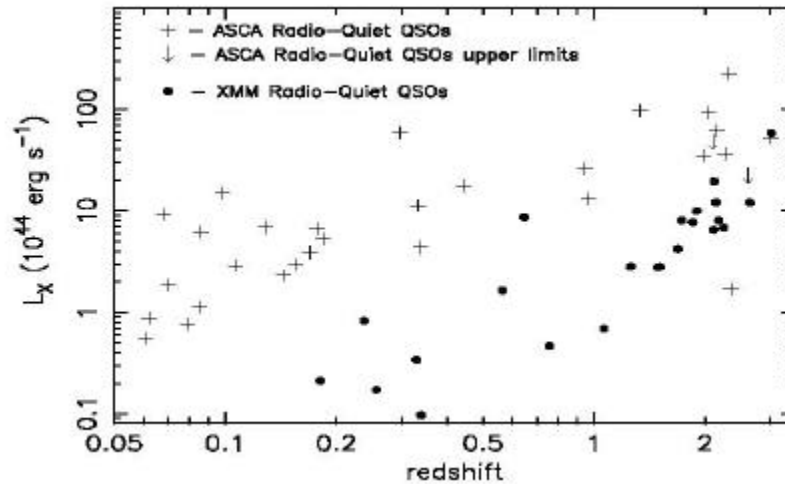


Observation of the $z=3.104$ quasar, PKS 0537-286 (Reeves et al. (2001))



XMM-Newton – push AGN studies at high z to lower L, but hard work!

(Page et al. (2002))



X-ray and Observational Astronomy Group



Conclusions - Iron K band features in AGN

- **Broad, redshifted, neutral iron K lines most prominent in the Seyfert 1 galaxies, Mrk 766 and MCG-6-30-15** - linked to RGS spectrum?
- **Ionised iron K lines found in luminous Seyfert 1s, Mrk 205 and Mrk 509**
Lines centred near 6.7 keV.
- **Strong narrow iron lines in many low/moderate luminosity type-1 AGN: Mrk 359, IC 4329A, Fairall 9 (Gondoin et al. 2001), NGC 5548, NGC4151, NGC 3783 (Chandra, Kaspi et al. 2001), Mrk 205, Mrk 509 ...**
Widths/EWs similar ($\sigma < 5000 \text{ km s}^{-1}$; $EW \sim 75 \text{ eV}$); **Origin: Torus and/or outer BLR?**
- **Broad or narrow iron K lines weak in most luminous quasars, 3C 273, PDS 456...**
Disc ionised? Torus/BLR covering factor reduced?
- **Disc and/or torus properties appear to correlate with luminosity/accretion-rate**
- **Need XEUS to probe low L at high z, to monitor AGN and measure BH mass**

X-ray and Observational Astronomy Group



High resolution spectroscopy of nearby AGN

J.S. Kaastra¹

SRON National Institute for Space Research, Sorbonnelaan 2, 3584 CA Utrecht, The Netherlands

Abstract. In this paper the potential of high resolution spectroscopy of nearby AGN with XEUUS is discussed. The focus is upon the energy resolution that is needed in order to disentangle the different spectral components. It is shown that there is an urgent need for high spectral resolution, and that a spectral resolution of 1 eV, if possible, leads to a significant increase in diagnostic power as compared to 2 eV resolution.

1. Introduction

Since the launch of Chandra and XMM-Newton, with their high resolution spectrometers, our insight into the astrophysics of Active Galactic Nuclei (AGN) has changed dramatically. It is now possible to study in detail the geometry, dynamics and physical state of the warm absorber, as well as the underlying continuum spectrum, including the exciting possibility of relativistic emission lines. While with XMM-Newton and Chandra high resolution, high signal-to-noise ratio spectra of the brightest (and in general the nearest) AGN can be taken, the large resolving power and effective area of XEUUS will allow us to study AGN spectra out to large redshifts or low intrinsic luminosities. It will also allow time-resolved spectroscopy of the most rapidly varying AGN. A detailed understanding of the astrophysics and spectral signatures of the nearest AGN is an absolute requirement in order to understand the properties of the most distant AGN that will be observed by XEUUS, which will have much noisier spectra. In this contribution spectral simulations are presented that show the potential and limitations of AGN spectroscopy with XEUUS.

2. Spectral simulations

I have performed a set of spectral simulations of a bright Seyfert 1 galaxy as will be observed with XEUUS. For the effective area of the instrument I took the area as foreseen in the final configuration of XEUUS (taken from the XEUUS web page).

For the spectral resolution a parameterization of what currently is thought to be feasible was taken: a constant full width at half maximum (FWHM) of 2 eV below 1 keV, 10 eV above 14 keV and in between a linear interpolation. A spectral response matrix was generated with a Gaussian energy resolution consistent with the FWHM and effective area mentioned above. All spectral simulations were done using the SPEX package version 2.0 (Kaastra et al. 2002b).

For the Seyfert 1 spectrum I took a prototype of a bright and nearby AGN: NGC 5548. This Seyfert 1 galaxy was the first to be observed at high spectral resolution (Kaastra et al. 2000). It has a moderate redshift of 0.017, and a low Galactic column density. The spectral model I used is described below, and is based upon the modeling of the Chandra LETGS data (Kaastra et al. 2002a) for most energies, supplemented by the Fe-K line emission as modeled by Yaqoob et al. (2001) based upon the Chandra HETGS data.

The ingredients of our spectral model are:

- a power law continuum
- a modified blackbody spectrum, describing the accretion disk continuum at low energies
- a warm absorber, consisting of three ionization and five velocity components, with a range of -160 to -1060 km/s outflow velocity
- narrow forbidden emission lines from O VII and Ne IX
- a narrow Fe-K line component at 6.4 keV

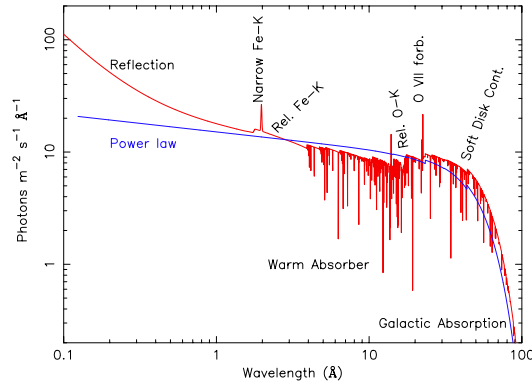


Fig. 1. Model spectrum at high spectral resolution for NGC 5548, with the different spectral components as indicated. The blue line indicates the underlying power law component. Note that nowhere in the spectrum the total model spectrum looks similar to the underlying power law!

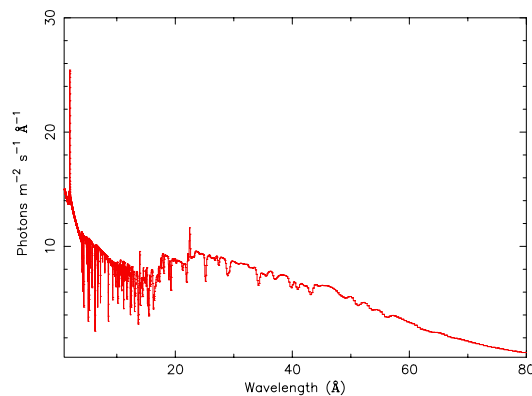


Fig. 2. Model spectrum for NGC 5548, folded with the energy resolution of XEUS.

- a relativistic Fe-K line
- weak relativistic O VIII and N VII Ly α lines
- a reflection component at high energies

The model photon spectrum corresponding to the above model, as would be seen with very high energy resolution, is shown in Fig. 1. The model spectrum, but now folded with the XEUS spectral resolution, is shown in Fig. 2. Note that nowhere in the model spectrum there exists an energy range where the spectrum agrees fully with the underlying power law component. At high energies there is the excess of the reflection component, around 6 keV the broad iron line component causes excess flux, then at lower energies the warm absorber reduces the observed flux, followed by excess emission at the lowest energies, due to emission from the accretion disk, including the modified blackbody as well as any possible relativistic Ly α lines from oxygen and nitrogen.

Thus, in order to derive the underlying AGN continuum or any of the other spectral components, the spectrum must be fitted over the entire wavelength range, taking into account all contributions. It is also seen that due to the fact that XEUS will use non-dispersive X-ray detectors, the spectral resolution at low energies is relatively poor and not all the spectral lines can be resolved (compare Fig. 1 with Fig. 2). I come back later to this point.

3. Finding relativistic lines

The presence of relativistic emission lines from O VIII and N VII Ly α has been discussed first by Branduardi-Raymont et al. (2001) based upon XMM-Newton RGS observations of the narrow line Seyfert 1 galaxies MCG -6-30-15 and Mrk 766. In these two galaxies the relativistic lines are very strong, although another group disputes this result (Lee et al. 2001). The flux level in both sources is quite strong, so statistics is not really the problem, but the debate depends heavily upon disentangling the different spectral components. A stronger warm absorber would produce deeper oxygen absorption edges, and hence would leave less room for a relativistic oxygen emission line. But in order to get a reliable

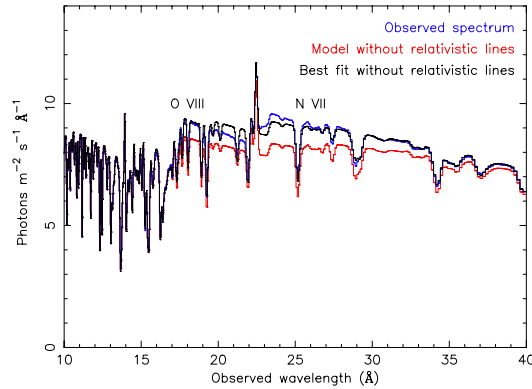


Fig. 3. Model spectrum of NGC 5548 with the XEUS resolution near the region of the relativistic oxygen and nitrogen lines. The blue curve is the simulated spectrum for 40 ks integration time (error bars are very small and invisible); the red curve is the same model spectrum but with the relativistic lines left out; the black curve is the best fit model for a model that does not take into account the relativistic lines.

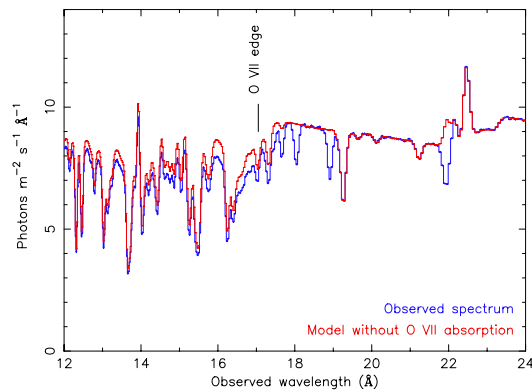


Fig. 4. Blue line: model spectrum of NGC 5548 with the energy resolution of XEUS. Red curve: same model, but with the O VII column density put to zero.

estimate of the depth of the oxygen absorption edges, which are strongly contaminated by several other absorption lines and edges, a detailed modeling of the absorption lines is needed, and for that purpose high spectral resolution is a necessary condition.

In NGC 5548 the relativistic lines are much weaker, as is shown in Fig. 3. It is seen from this figure that the maximum amplitude of these lines is at most $\sim 15\%$, around 24 \AA . It is also seen that when the relativistic lines are not taken into account, the resulting spectral fit agrees quite well with the observed spectrum. The differences in the continuum are less than a few percent, in a region where very likely also instrumental neutral oxygen edges will be present. This therefore poses severe constraints on the calibration of the effective area, which must be better than a percent over broad energy ranges.

A way out is of course by looking to the spectral lines in order to constrain the depth of the absorption edges. But for that purpose the highest possible spectral resolution is needed.

4. Complexity of the warm absorber

The complexity of the warm absorber is illustrated in Fig. 4. From the difference of the model with and without the O VII it is seen that in the observed photon spectrum the K-edge of O VII cannot be distinguished, due to strong blending by several weak inner shell iron lines (see below). The apparent "edge" is rather smooth, and moreover from the jump in the continuum between 16 \AA and 18 \AA it is not possible to measure directly the depth of the oxygen edge: the effective depth of the "edge" is significantly deeper than just the contribution from O VII alone. Again, high resolution is needed in order to estimate accurately the depth of the O VII edge, based upon the equivalent width ratios of the absorption lines from the same ion. Due to blending, which is in particular important at low spectral resolution,

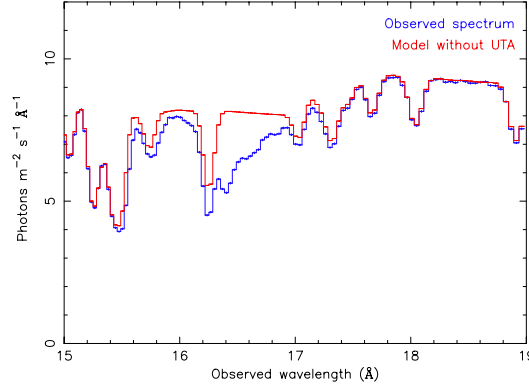


Fig. 5. Blue curve: model spectrum of NGC 5548 with the energy resolution of XEUS; red curve: same model, but with the column densities of the Fe-M ions put to zero.

but which cannot always be avoided even at high energy resolution due to the finite velocity width of the absorption complexes, it is important to observe several lines of the same ion.

One of the reasons for the complexity of the spectrum near the O VII edge is demonstrated in Fig. 5. In this range of the spectrum there are many weak inner-shell absorption lines due to lowly ionized iron (in our model Fe IX–Fe XVI). These lines were first recognized by Sako et al. (2001) in their analysis of the quasar IRAS 13349+2438. It is seen that these lines constitute a broad, unresolved blend. They are very important from a diagnostic point of view, since they measure directly the strength of the less ionized material in the warm absorber, for ionization parameters that yield otherwise only spectral lines mostly in the inaccessible (E)UV range.

5. Why high spectral resolution is needed

High spectral resolution is important in order to determine the spectral line parameters of the warm absorber and thereby the continuum spectrum. This is illustrated in Fig. 6. This figure simulates the transmission of a slab composed of pure O VIII. For other ions the effects illustrated in this figure are qualitatively similar. The model spectrum has been convolved with the currently adopted XEUS spectral resolution of 2 eV.

For the reference model (O VIII column 10^{22} m^{-2} , velocity dispersion $\sigma_v = 250 \text{ km/s}$, outflow velocity $v = 0 \text{ km/s}$ and covering factor $f_{\text{cov}} = 1$), the Ly α , Ly β and Ly γ lines are strongly saturated, and hence doubling the column density does not change these line profiles significantly. Note that for this velocity dispersion, the intrinsic width of the Ly α line is about 1.2 eV and hence unresolved with the 2 eV instrumental resolution. In many Seyfert galaxies the intrinsic line width can be even smaller than the value used here. The difference in column density can only be seen for the higher order lines (Ly δ and higher) but these lines start becoming blended with each other (in the model, I took all lines up to $n = 10$ into account). And of course the difference in column density can be seen near the continuum edge, but as I have shown before the continuum edge is often very hard to measure due to severe contamination by various spectral lines and line blends, and due to the unknown underlying continuum spectrum.

Measuring the intrinsic velocity broadening σ_v appears at a first glance more promising. By doubling σ_v to 500 km/s, the Ly α and Ly β lines become significantly deeper, while the higher lines of the series become less deep, because they are smeared out. The Ly α and Ly β lines become deeper because their (equivalent) width doubles and now becomes comparable to the instrumental resolution. However it should be noted that the intensity at the deepest point of the *observed* Ly α line is still not zero, despite the fact that the line core in the original *model* spectrum is completely black. This is due to the limited spectral resolution of the instrument.

This, in fact, causes that the apparent sensitivity for changes in σ_v is partially an illusion, as is illustrated with the light blue curve, where the same enhanced σ_v of 500 km/s was adopted but now with a covering factor of only 75 %. Now the observed line profiles are very similar to the original reference model with σ_v of 250 km/s and full covering factor! The difference would be most clearly visible in the continuum edge, where the transmission differs by 25 %, but as was pointed out before these continuum edges are difficult to measure accurately.

Finally, Fig. 6 also shows the sensitivity to measure outflow velocities. Outflow velocities of 500 km/s can be measured by using line centroiding. For the Ly α line, this velocity corresponds to a 1 eV shift, so can be easily detected. Note however that in many AGN the absorption lines are composed of several velocity components, which are separated by velocity differences on the hundred km/s velocity scale. Each velocity component may have its own

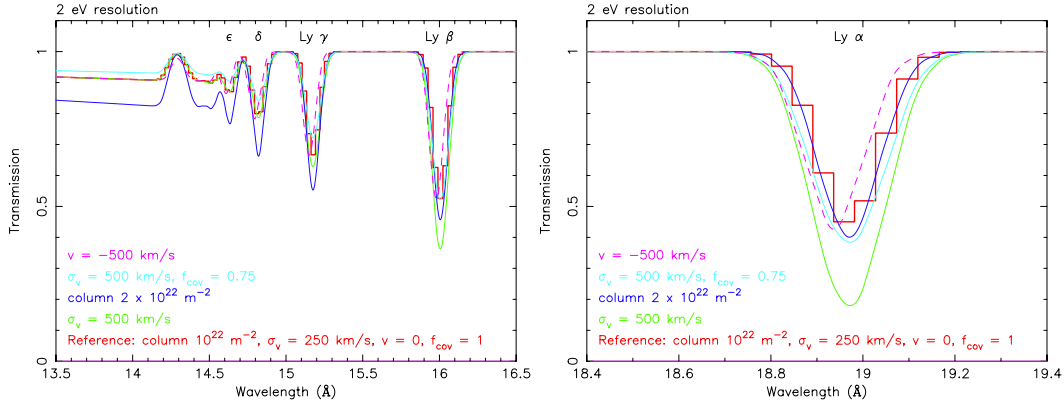


Fig. 6. Different models for the transmission of a slab composed of pure O VIII. The model spectra are folded through an instrument with an energy resolution of 2 eV (as is used for the present XEUS simulations). Right panel: the Ly α line; Left panel: the higher Lyman lines and the O VIII edge. The reference model (red curve) has an O VIII column of 10^{22} m^{-2} , a velocity dispersion of 250 km/s, an outflow velocity of 0 km/s and a covering factor of unity. The other curves have the same parameters except the ones indicated in the caption.

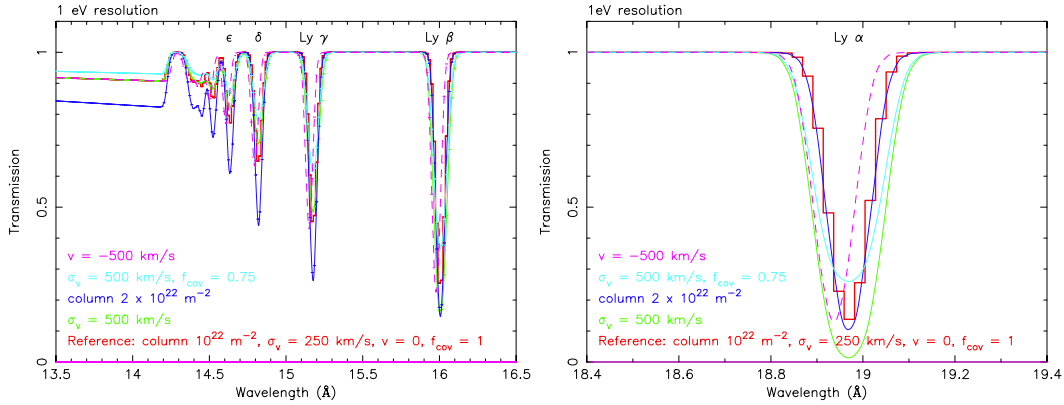


Fig. 7. Same as Fig. 6, but instead a 1 eV instrumental resolution.

ionization structure, hence what is observed as a single broad absorption line is actually composed of a complex set of line components, hence any gain in spectral resolution is extremely useful.

Needless to say that for cosmologically redshifted AGN the situation becomes even more problematic, due to the fact that the lines shift to lower energies with poorer instrumental resolution.

Therefore I have also made a set of calculations for the line profiles with a spectral resolution of 1 eV instead of 2 eV (Fig. 7). Such a factor of two improvement of the spectral resolution does not seem impossible from a technical point of view, in particular if the spectral resolution is optimized for these lower energies (below 2 keV). Improving the spectral resolution by a factor of two also enhances the sensitivity for weak lines with a factor of two, without even increasing the effective area! Comparing both figures, it is seen that the observed lines now appear much deeper, and hence the accurate measurement of covering factors can be done more easily. The differences between the various cases shown in the figure are much more pronounced.

Apart from a significant improvement in the determination of the intrinsic line widths and centroids, a major advantage of a higher spectral resolution is also that contamination due to blending by lines from other ions can be severely reduced. Note that our above simulation was done for a slab consisting of pure O VIII, but in reality the spectrum is composed of a mixture of absorption lines from many ions with different velocity and ionization structure.

This is illustrated in Fig. 8, where I compare the original model spectrum with the model spectrum folded through 1 and 2 eV instrumental resolution. It is clear that for both instrumental resolutions the velocity fine structure of the absorption lines cannot be resolved. This is currently a great advantage of the UV band, where instruments like FUSE or the STIS instrument of HST are able to provide very high spectral energy resolution (down to the 10 km/s scale). In fact, STIS observations served as the basis for our velocity model applied in this figure. Nevertheless, it is evident from this figure that a 1 eV spectral resolution is a significant improvement over a 2 eV spectral resolution.

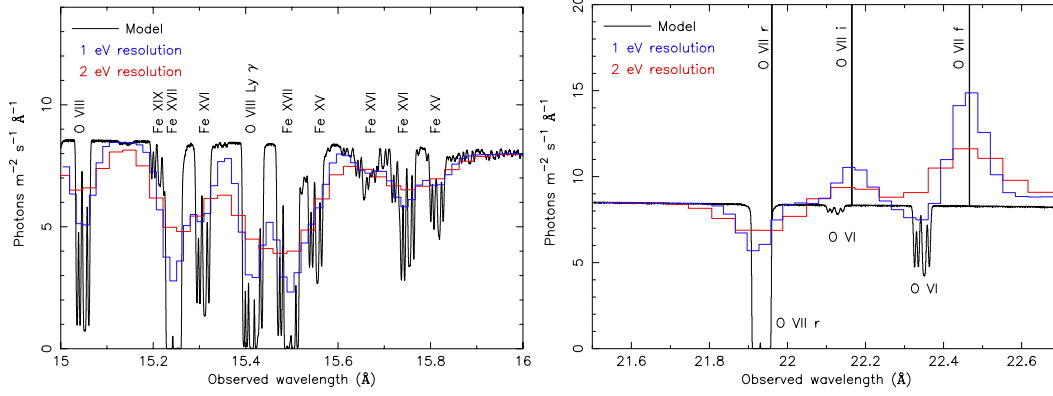


Fig. 8. Model spectrum at high resolution (black line), convolved with an instrumental resolution of 1 eV (blue line) and 2 eV (red line). Left panel: region near 15 Å containing O VIII, Fe XVII and other important diagnostic lines; right panel: region near the O VII triplet.

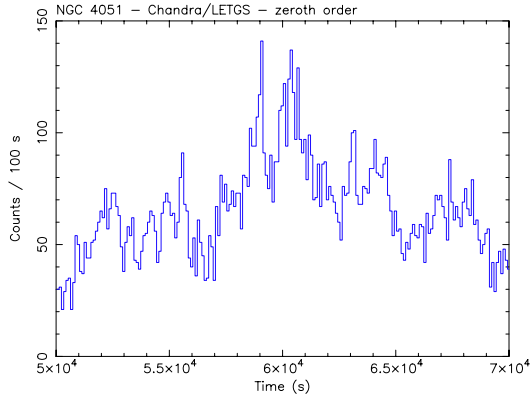


Fig. 9. Chandra LETGS light curve in first order of NGC 4051. Time bins: 100 s.

For example, the O VIII Ly γ line at 15.18 Å (observed here at 15.4 Å due to the cosmological redshift) and the Fe XVII line at 15.27 Å (observed at 15.5 Å) are not separated with 2 eV resolution but can be distinguished clearly at 1 eV resolution. With 2 eV resolution, it would be difficult to see if it is a blend of two narrower components, or for example a single broad, red/blueshifted line. The same holds for separating the Fe XV and Fe XVI lines around 15.8 Å.

Also near the O VII triplet a gain in spectral resolution is very important. With 2 eV resolution the intercombination line of O VII cannot be measured, and also the important O VI inner shell absorption line, observed at 22.35 Å is only visible with 1 eV resolution, since it is so close to the strong forbidden emission line. This O VI line, as well as similar inner shell absorption lines from O I – O V at slightly longer wavelengths, are very important, as they cover a broad range of ionization parameter with ions from the same chemical element, thus avoiding modeling difficulties due to unknown elemental abundances. Although the inner shell Fe-lines (the UTA mentioned before) around 15–17 Å also cover this range of ionization parameter, the analysis of these lines is much more complicated due to the strong blending, while the oxygen lines are in a relatively clean part of the spectrum (the 21–24 Å range).

6. Time variability

The large effective area of XEUS makes it ideal to study rapid time variability. For the high luminosity AGN variability typically occurs on time scales of days or longer, so for those sources variability studies are limited by the finite exposure time available for each target. However, for low luminosity AGN the intrinsic variability time scales can be much faster. An example is given in Fig. 9. This AGN shows rapid variability, down to the time scale of 100 s.

With the current generation of grating spectrometers it is not possible to obtain high quality spectra with such a short integration time on the minute time scale. However with the effective area of XEUS this is not a problem. This is illustrated in Fig. 10. XEUS is able to obtain high S/N spectra for bright Seyfert 1 galaxies in just 100 s integration time. This allows a study of the intrinsic variations of the accretion disk spectrum on this time scale. For

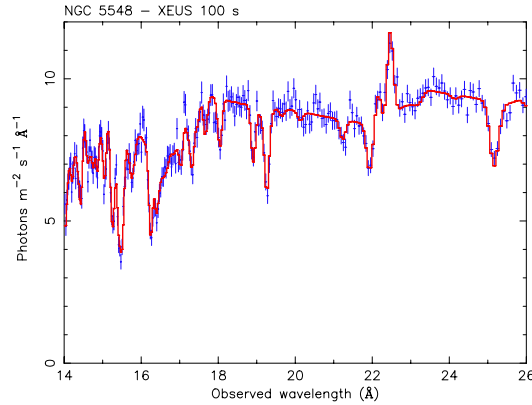


Fig. 10. Simulated spectrum for NGC 5548 with a 100 s integration time.

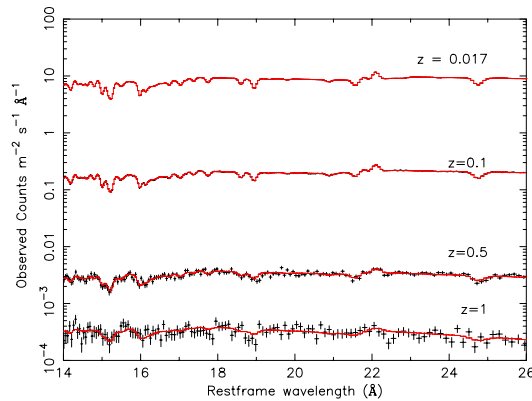


Fig. 11. Simulated spectra for NGC 5548 with 40 ks exposure time, for redshifts of 0.017, 0.1, 0.5 and 1 (from top to bottom). The y-axis represents the fluxed spectrum in the *observers* frame, however for easy of comparison the x-axis has been shifted to the rest frame wavelength. For the lowest redshift, the error bars on the spectrum are barely visible.

example, if an AGN has strong relativistic oxygen and nitrogen lines, and it varies rapidly on this time scale, all kinds of reverberation methods can be applied and the geometry of the innermost part of the accretion disk can be well constrained.

The large effective area of XEUS is of course not only excellent for high time resolution observations of bright and nearby AGN, it also will allow to obtain good spectra of distant AGN. This is illustrated in Fig. 11. In that figure NGC 5548 is put at redshifts of 0.017 (its true redshift), 0.1, 0.5 and 1. Good quality spectra within a reasonable net exposure time (half a day) is possible up to $z = 0.5$. At $z = 1$, the spectrum becomes too noisy at the highest spectral resolution, and also due to the cosmological redshift the spectral resolution degrades, making it harder to disentangle the narrow spectral components. For example, for $z = 1$, the O VII triplet cannot be resolved, both due to the low source flux and the factor of 2 poorer spectral resolution, as compared to the case of $z = 0.017$. Of course, for higher luminosity AGN good spectra can be obtained out to larger redshifts.

Acknowledgements. SRON is supported financially by NWO, the Netherlands Organization for Scientific Research.

References

- Branduardi-Raymont, G., Sako, M., Kahn, S.M., et al., 2001, A&A 365, L140
 Kaastra, J.S., Mewe, R., Liedahl, D.A., Komossa, S., & Brinkman, A.C., 2000, A&A 354, L83
 Kaastra, J.S., Steenbrugge, K.C., Raassen, A.J.J., et al., 2002a, A&A 386, 427
 Kaastra, J.S., Mewe, R., & Raassen, A.J.J. 2002b, in *New Visions of the X-ray Universe in the XMM-Newton and Chandra Era*, ed. F.A. Jansen, ESA, in press
 Lee, J.C., Ogle, P.M., Canizares, C.R., et al., 2001, ApJ 554, L13
 Sako, M., Kahn, S.M., Behar, E., et al. 2001, A&A 365, L168
 Yaqoob, T., George, I.M., Nandra, K., et al., 2001, ApJ 546, 759



Reverberation revisited

A.C. Fabian¹

Institute of Astronomy, Madingley Road, Cambridge CB3, U.K.

Abstract. Continuum – iron line X-ray reverberation will enable the black hole mass of AGN to be determined directly from X-ray data and the inner accretion flow to be mapped. Such work will only be possible with the next generation of telescopes such as Constellation-X and Xeus, which have the collecting area to give good count rates in the iron band. The puzzling time behaviour of the iron line in the Seyfert galaxy MCG–6-30-15 is used to demonstrate that the response of the iron line to continuum variations may not be straightforward. It is possible however that this behaviour is due to the strong gravity of the black hole.

1. Introduction

Deducing the absolute size and structure of the inner regions of Active Galactic Nuclei (AGN) by observing the response of emission lines to continuum variations, i.e. reverberation (Blandford & McKee 1982), has proven to be a powerful technique in the optical and UV bands (Peterson & Wandel 2000). Generally this probes regions at 100s to 1000s of gravitational radii ($1000r_g = 1000GM/c^2$). Extending the method to the X-ray band (Fabian et al 1989; Stella 1989; Reynolds et al 1999; Young & Reynolds 2000) should enable the innermost regions to be mapped down to within a few gravitational radii. In principle it enables the mass and spin of the black hole to be measured.

The relevant emission line is the broad iron line (Fabian et al 1989; Laor 1990) produced by fluorescence on the surface of the accretion disc by the X-ray continuum radiation from flares above the disc. Gravitational redshift and doppler shifts skew and broaden the line so that different parts of it originate from different radii (in gravitational units). If the line has the rest energy of lowly ionized iron at 6.4 keV and part of the broadened line at 4 keV is seen to vary, then that part originates at about $6r_g$. The continuum is the powerlaw produced by Comptonization in the flare regions and is commonly observed to be highly variable. If the location of the flare is known, then the time delay between a continuum outburst and the response of the line enables distances in gravitational units to be converted to real time units and thus the absolute scale of the system and the mass of the black hole to be found. The time development of the line profile, which can be complex owing to gravitational time delays (Reynolds et al 1999), can itself be used to constrain possible locations for the flare.

No X-ray reverberation has so far been reported for an accreting black hole. The best targets would be AGN, since Galactic Black Hole Candidates (GBHC) have a much smaller flux per light crossing time. Even for AGN, the flux per light crossing time is too small for reverberation to have been detected with current instruments, unless there are exceptional flares. The effect only becomes routinely detectable with Constellation-X (Young & Reynolds 2000) and can be well studied with Xeus.

For reverberation to be useful, the line has to respond in a well understood way to changes in the continuum. Although the short term response has not yet been tested, the long term response in some objects is puzzling. For example, in the Seyfert galaxy MCG–6-30-15 the line appears to be constant while the continuum varies by factors of two or more on timescales of $10^3 - 10^4$ s.

2. AGN vs GBHC

Broad iron lines have recently been confirmed in several GBHC (Miller et al 2001; 2002; Martocchia et al 2002) so they could appear to be good reverberation targets. However the key quantity for reverberation is the flux per light crossing time. If we adopt $1r_g$ for the typical length then the light crossing time of that length is about a factor of 10^5 or more

longer for an AGN (mass greater than $10^6 M_{\odot}$) than for a GBHC (mass $\sim 10 M_{\odot}$). This more than compensates for the faintness of the typical flux of a ‘bright’ AGN, which may be only one per cent of that of a GBHC.

As examples and for XMM-Newton, the GBHC XTE J1650 may give only about 1 ct total per light crossing time of a few R_g whereas the AGN MCG–6-30-15 gives about 1000. The problem for reverberation in AGN is then that only a handful of those 1000 ct are in the iron line (The iron line in a bright Seyfert like MCG–6-30-15 gives about $2 \text{ ph m}^{-2} \text{ s}^{-1}$). Single event reverberation with XMM-Newton would only be possible for highly exceptional events in very massive AGN.

If reverberation leads to a similar pattern of behaviour in the line every variation time (i.e. every few crossing times), then a statistical analysis might be able to show that some reverberation signal exists.

3. MCG–6-30-15: a case study

The Seyfert 1 galaxy MCG–6-30-15 shows a very clear example of a broad iron line, first clearly seen in a long ASCA observation (Tanaka et al 1995; Fabian et al 1995). Variations in that line have been seen (Iwasawa et al 1996, 1999; Vaughan & Edelson 2001).

However, the line variations seen during a long joint ASCA/RXTE observation of MCG–6-30-15 during 1997 show no correlation with the continuum flux (Vaughan & Edelson 2000; see also Lee et al 2000 and Reynolds 1999). This result extends to an even longer observation made in 1999 (Matsumoto et al 2002; Shih et al 2002), where there is little evidence for the line varying at all. Several explanations have been proposed. One is that the disk is so highly ionized by intense flares as to give no line (Lee et al 2000; Reynolds 1999). A second is that the corona is not static but undergoes mildly-relativistic motions during flaring. Then if the emitting gas is moving towards us we see an increase in continuum, but the disk is less irradiated than usual (Reynolds & Fabian 1997; Beloborodov 1999; Matsumoto et al 2002; Lu & Yu 2001). The problem with this explanation is that it would be expected that the continuum would become harder when approaching us (since the Comptonizing emission region would see fewer soft disk photons) whereas the opposite effect is observed. Obscuration of the emission region by a marginally optically thick corona is another possibility (the ‘thundercloud’ model of Merloni & Fabian 2001).

A final simple empirical model is discussed by Shih et al (2002). Here the spectrum consists of an approximately constant, reflection dominated component, together with a steeper, rapidly varying, continuum. This explains the observed behaviour including that of the continuum, and is supported by the apparent saturation of the spectral index at high fluxes (Shih et al 2002). The two components are tentatively identified with the main disk (the line bearing component) and the magnetized plunge region from just within the innermost stable orbit of the disk (see e.g. Krolik 1999; Gammie 1999; Hawley & Krolik 2002; Armitage et al 2001). The model also fits the long XMM-Newton data (Figs. 1-3, Fabian et al 2002; Fabian & Vaughan in preparation), where again no line variations have been found despite a fivefold variation in continuum.

Why the powerlaw continuum produces no corresponding iron line which varies with it probably requires that the continuum be anisotropic. (The breadth of the iron line precludes the possibility that the lack of response is due to the reflector being very distant from the source of continuum.) The behaviour could be due to the extreme gravity at the inner edge of the disc, where most of the continuum originates. There doppler boosting of the continuum and light bending by the strong gravity of the black hole could be very important, so making returning radiation (Cunningham 1975) create a strong reflection component (Martocchia, Matt & Karas 2002).

It appears that for MCG–6-30-15 at least, the response of the broad iron line is unexpected and could be complex. If this is due to strong gravity then more powerful instruments such as Xeus will be able to probe this region directly.

4. Summary

Routine X-ray reverberation studies are not expected to be possible before the large effective areas of the next generation telescopes such as Con-X and Xeus are available. Preliminary work on the temporal behaviour of the broad iron line in at least one bright Seyfert galaxy, MCG–6-30-15, has revealed a puzzling lack of line variability. This could be due to the dominance of returning radiation in the close proximity to the black hole implied by the breadth of the iron line. If this is correct then Xeus offers the prospect of exploring through reverberation the strong gravity environment around the ergosphere of a rapidly spinning black hole.

Acknowledgements. I thank the Royal Society for support.

References

Armitage P.J., Reynolds C.S., Chiang J., 2001, *Astrophys. J.*, **548**, 868

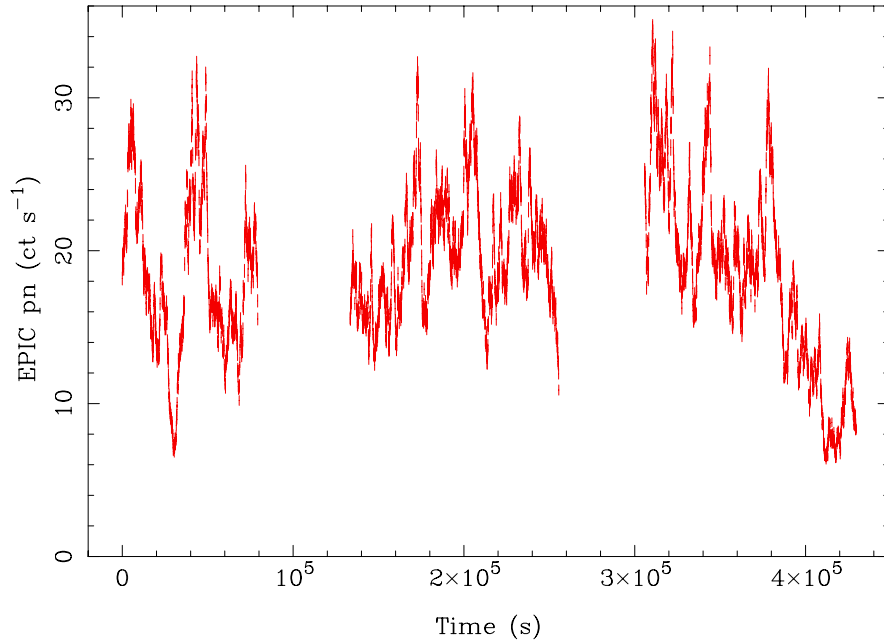


Fig. 1. The XMM-Newton lightcurve of the 325 ks long look at MCG-6-30-15 (Fabian et al 2002).

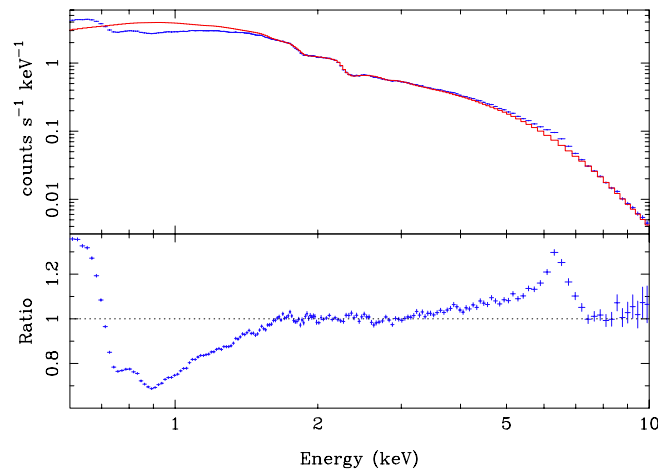


Fig. 2. EPIC/MOS spectrum of MCG-6-30-15 (Fabian et al 2002).

- Beloborodov A.M., 1999, *Astrophys. J.*, 510, 123
 Blandford R.D., McKee C.F., 1982, *Astrophys. J.*, 255, 419
 Cunningham C.T., 1975, *Astrophys. J.*, 202, 788
 Fabian A.C., Rees M.J., Stella L., White N.E., 1989, *Mon. Not. R. astr. Soc.*, 238, 729
 Fabian A.C., Nandra K., Reynolds C.S., Brandt W.N., Otani C., Tanaka Y., Inoue H., 1995, *Mon. Not. R. astr. Soc.*, 277, L11
 Fabian A.C. et al 2002, *Mon. Not. R. astr. Soc.*, 335, L1
 Gammie C.F., 1999, *Astrophys. J.*, 522, L57
 Hawley J.F., Krolik J.H., 2002, *Astrophys. J.*, 566, 164
 Iwasawa K., Fabian A.C., Young A.J., Inoue H., Matsumoto C., 1999, *Mon. Not. R. astr. Soc.*, 306, L19
 Iwasawa K., et al., 1996, *Mon. Not. R. astr. Soc.*, 282, 1038
 Krolik J.H., 1999, *Astrophys. J.*, 515, L73
 Laor A., 1991, *Astrophys. J.*, 376, 90
 Lee J.C., Fabian A.C., Reynolds C.S., Brandt W.N., Iwasawa K., 2000, *Mon. Not. R. astr. Soc.*, 318, 857
 Lu Y., Yu Q., 2001, *Astrophys. J.*, 561, 660
 Martocchia A., Matt G., Karas V., 2002, *Astr. Astrophys.*, in press (astro-ph/0201192)
 Matsumoto C., Inoue H., Iwasawa K., Fabian A.C., 2001, PASJ, submitted
 Merloni A., Fabian A.C., 2001, *Mon. Not. R. astr. Soc.*, bf 328, 956

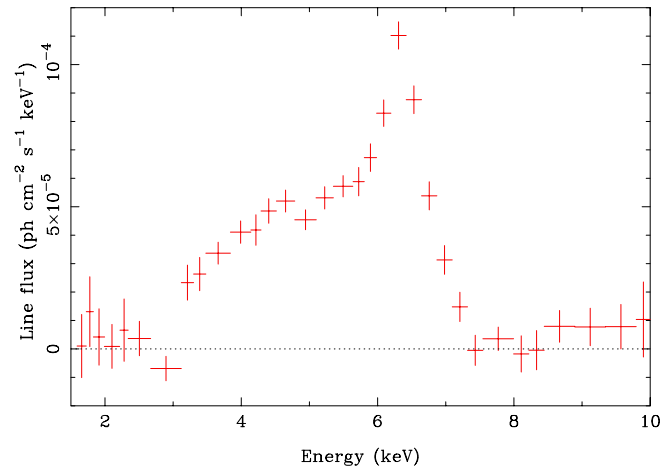


Fig. 3. The broad iron line in MCG-6-30-15 (Fabian et al (2002)).

Miller J.M., et al 2002, *Astrophys. J.* , 570, L69

Miller J.M., et al 2002, *Astrophys. J.* in press (astro-ph/020375)

Peterson B, Wandel A., 2000, *Astrophys. J.* , 540, L13

Reynolds C.S., Fabian A.C., 1997, *Mon. Not. R. astr. Soc.* , 290, L1

Reynolds C.S., Young A.J., Begelman M.C., Fabian A.C., 1999, *Astrophys. J.* , **514**, 164

Reynolds C.S., 2000, *Astrophys. J.* , **533**, 811

Shih D., Iwasawa K., Fabian A.C., 2002, *Mon. Not. R. astr. Soc.* , 333,687

Stella L., 1990, *Nature*, **344**, 747

Tanaka Y., et al., 1995, *Nature*, **375**, 659

Vaughan S., Edelson R., 2001, *Astrophys. J.* , **548**, 694

A fast X-ray timing capability on XEUS

D. Barret¹, G. K. Skinner¹, E. Kendziorra², R. Staubert², P. Lechner³, L. Strüder³, M. van der Klis⁴, L. Stella⁵, and C. Miller⁶

¹ Centre d’Etude Spatiale des Rayonnements, CESR-CNRS/UPS, France (Didier.Barret@cesr.fr)

² University of Tübingen, Germany

³ MPI Halbleiterlabor, Germany

⁴ University of Amsterdam, The Netherlands

⁵ University of Roma, Italy

⁶ University of Maryland, United States

Abstract. Fast X-ray timing can be used to probe strong gravity fields around collapsed objects and constrain the equation of state of dense matter in neutron stars. These studies require extremely good photon statistics. In view of the huge collecting area of its mirrors, XEUS could make a unique contribution to this field. For this reason, we propose to include a fast X-ray timing capability in the focal plane of the XEUS mirrors. We briefly outline the scientific motivation for such a capability. We compute some sensitivity estimates, which indicate that XEUS could provide better than an order of magnitude sensitivity improvement over the Rossi X-ray Timing Explorer. Finally, we present a possible detector implementation, which could be an array of small size silicon drift detectors operated out of focus.

1. Introduction

The X-rays generated in the inner accretion flows around black holes (BHs) and neutron stars (NSs) carry information about regions of the strongly curved space-time in the vicinity of these objects. This is a regime in which there are important predictions of general relativity still to be tested. High resolution X-ray spectroscopy and fast timing studies can both be used to diagnose the orbital motion of the accreting matter in the immediate vicinity of the collapsed star, where the effects of strong gravity become important. With the discovery of millisecond aperiodic X-ray time variability (QPO) from accreting BHs and NSs, and brightness burst oscillations in NSs, the Rossi X-ray Timing Explorer (RXTE, Bradt et al. 1993) has clearly demonstrated that fast X-ray timing has the potential to measure accurately the motion of matter in strong gravity fields and to constrain masses and radii of NSs, and hence the equation of state of dense matter.

Although the prime objectives of XEUS are to perform spectroscopy of faint X-ray sources to trace the origin and evolution of hot matter back to the early ages of the Universe (see Hasinger et al. 2000; Bleeker et al. 2000), the large collecting area required to meet these objectives could also be used for X-ray timing studies. In this paper, we briefly outline how XEUS could broaden its science by having a fast X-ray timing capability in the focal plane (section 2). The potential of X-ray timing studies is described in more details in two companion papers by Michiel van der Klis and Cole Miller. In section 3, we give some sensitivity estimates for XEUS. Finally, in section 4, we present a possible implementation for the fast X-ray timing capability.

2. Summary of scientific objectives

2.1. Probing strong gravity fields

RXTE has detected high-frequency QPOs from both BH and NS binary systems (see van der Klis 2000 for an extensive review). In neutron stars, several types of QPOs are commonly observed, including the two “kilohertz” QPOs at $\nu_1 = 200 - 800$ Hz and $\nu_2 = 500 - 1300$ Hz. The upper end of this frequency range represents the highest-frequency oscillations ever seen in astronomy. Indeed, the frequencies are so high that any plausible mechanism requires that their origin be deep in the gravitational well of the neutron star. For example, the orbital frequency 20 km from a $1.4 M_\odot$ neutron star is 770 Hz, so the majority of the upper kilohertz QPOs must be generated in regions of strong

spacetime curvature. As a consequence, detailed study of these QPOs has great promise for discoveries about strong gravity and the dense matter of the neutron stars themselves.

The precise interpretation of the QPOs depends on the model proposed. Ideas include beat-frequency models (Miller, Lamb, & Psaltis 1998), where an orbital frequency is modulated by emission at the stellar spin frequency; pictures in which the observed frequencies are related to geodesic frequencies modified by additional, possibly fluid, interactions (Stella & Vietri 1998; Psaltis & Norman 2002); and disk oscillations (Titarchuk & Osherovich 1999). Independent of the detailed origin of the QPOs, there is wide agreement that the upper kilohertz frequency ν_2 is close to the frequency of a nearly circular orbit at some special radius near the star. From this alone one expects a number of crucial phenomena to be detected with a high-area timing detector on XEUS. For example, an upper limit to ν_2 is set by the orbital frequency at the innermost stable circular orbit (ISCO). With a highly sensitive detector, one expects to see a clear upper limit to the frequency corresponding to the ISCO in several sources. Suggestive evidence for this has been found for the source 4U 1820–30 (Zhang et al. 1998), but it is not yet conclusive. Detection of such a ceiling on the frequency will establish the existence of unstable circular orbits, a fundamental prediction of general relativity that is essential to the description of accreting black holes of all masses as well as to neutron stars. It will also allow precise estimation of the mass of the neutron star, and is likely to provide evidence for frame-dragging. The detection of even higher frequencies than have yet been seen would allow the elimination of several candidate equations of state of dense matter (Miller et al. 1998). In addition, the detailed predictions of specific models will be tested severely by the new data (e.g., Miller et al. 1998; Stella & Vietri 1999).

Models for black hole QPOs will also be illuminated greatly by high-area timing observations. The detection of a pair of high-frequency QPOs in three black hole candidates (Strohmayer 2001a,b; Miller et al. 2001), combined with their dynamical mass estimates, has already provided clinching evidence for spinning black holes in these sources. However, there is much ambiguity about the physical origin of these oscillations. A timing instrument with the area of XEUS would make profound contributions to such study, not least because the oscillations would be detectable on their coherence time, or even during a single oscillation. This will allow detailed characterization of the brightness variations. Specifically, because the cycle waveform depends on the Doppler shifts associated with the local velocity of the radiating matter in the emitting blob or spot, as well as on the curved-spacetime light propagation effects, fitting of the waveform yields the mass and spin of the compact object. In fact, along with detailed models of the QPOs themselves, the problem is overdetermined so the underlying theories can be tested in critical ways.

2.2. Equation of state of dense matter

Nearly coherent oscillations at ~ 300 Hz or ~ 600 Hz have been observed during type I X-ray bursts from about 10 NS so far (see Strohmayer 1998 for a review). These oscillations are probably caused by rotational modulation of a hot spot on the stellar surface. The emission from the hot spot is affected by gravitational light deflection and Doppler shifts (e.g. Miller & Lamb 1998). With XEUS, the oscillation will be detected within one cycle. The composition and properties of the NS cores have been the subject of considerable speculation, and remain a major issue in modern physics: at the highest densities, matter could be composed of pion or kaon condensates, hyperons, quark matter, or strange matter. By fitting the waveform, it will be possible to investigate the spacetime around the NS, and simultaneously constrain its mass and radius, and hence determine the equation of state of its high density core (see e.g. Nath et al. 2002).

2.3. Additional science

A fast X-ray timing capability would allow XEUS to investigate the physics of a wide range of astrophysical sources, such as accreting millisecond pulsars, microquasars, X-ray pulsars, dippers, CVs, novae, soft gamma-ray repeaters, anomalous X-ray pulsars. For instance, there are only three accreting millisecond pulsars known so far; the first one discovered being the famous SAXJ1808-3658 (Wijnands & van der Klis 1998; Chakrabarti & Morgan 1998). Its properties suggest that all NS systems should show pulsations at some level. In most models, pulse amplitudes cannot be suppressed below $\sim 0.1\%$ (RMS) without conflicting with spectroscopic or QPO evidence. This is a factor of 10 above the sensitivity XEUS could achieve (millisecond pulsations at the 0.01% RMS level would be detected in 1000 seconds in Sco X-1). Detection of such pulsations in objects also showing kHz QPOs and burst oscillations would immediately confirm or reject several models for these phenomena involving the NS spin (e.g. Miller et al. 1998). In addition, it has been suggested that such objects could be among the brightest gravitational radiation sources in the sky, emitting a periodic gravitational wave signal at the star's spin frequency (Bildsten 1998). Undirected searches in frequency space for such radiation lose sensitivity because of statistical considerations. Independently measuring the spin period very accurately would therefore be of great importance for periodicity searches with gravitational wave antennae (e.g. Brady et al. 1997).

Another important area of astrophysics where the fast X-ray timing capability could contribute concerns micro-quasars. In these systems, the link between the very fast disk transitions observed in X-rays and the acceleration process could be studied on very short time scales, allowing the non steady state disk properties and their link to the formation of relativistic jets to be explored (Belloni et al. 1997; Fender et al. 1999). This would be of direct relevance to understanding the properties of AGNs, where presumably similar jet formation mechanisms operate on a much larger scales. In addition, through time-resolved spectroscopic observations, the spacetime close to the black holes could be probed using the variability of the iron $K\alpha$ line.

3. XEUS sensitivity for timing studies

For the sensitivity computations, we have assumed the energy response of the XEUS mirrors as given in the most recent report of the telescope working group (Aschenbach et al. 2001). We have further assumed the proposed high energy extension in which the inner mirror shells of the telescope are coated with supermirrors (the effective area is thus $\sim 20000 \text{ cm}^2$ at $\sim 9 \text{ keV}$ and $\sim 1700 \text{ cm}^2$ at 30 keV). Finally we have assumed that the timing detector is made of 300 microns of Silicon lying above 2 mm of CdZnTe (see below). Table 1 gives the count rates expected from some sources.

Table 1. Examples of total count rates above 0.5 keV and above 10 keV ($C_{E>10\text{keV}}$) in kcts/s. The spectrum of Sco X-1 which is variable is such that it would produce 60 kcts/s in the RXTE/PCA (2.5–30 keV). The X-ray burst input spectrum is a blackbody of 1.5 keV with a normalization yielding an Eddington luminosity at 8.5 kpc. SAXJ1808-3659 is the millisecond pulsar taken at the peak of its 1996 outburst.

Source name	XEUS-1	XEUS-2	$C_{E>10\text{keV}}$
Crab	250	800	5
Sco X-1	1200	3800	10
GC X-ray burst	120	220	2
SAXJ1808-3659	30	130	0.3

Let us now compute the sensitivity for QPO and coherent signal detections. First the signal to noise ratio n_σ at which a QPO is detected in a photon counting experiment is approximately:

$$n_\sigma = \frac{1}{2} \frac{S^2}{B+S} r_S^2 \left(\frac{T}{\Delta\nu} \right)^{1/2}$$

where S and B are source and background count rate, respectively, r_S is the (RMS) amplitude of the variability expressed as a fraction of S , T the integration time and $\Delta\nu$ the bandwidth of the variability. The bandwidth $\Delta\nu$ is related to the coherence time τ of a QPO as $\Delta\nu = 1/\tau$. On the other hand, for a coherent signal ($T < 1/\Delta\nu$), the more familiar exponential detection regime applies, with false-alarm probability $\sim \exp[-S^2 r_S^2 T / 2(B+S)]$.

From the above formulae, assuming $B \sim 0$ appropriate for XEUS, one can estimate the RMS amplitude corresponding to a 5σ QPO detection as a function of the source count rate (Figure 1 left). Similarly one can compute the RMS for the detection of a coherent signal at a given false alarm probability (Figure 1 right). These two plots demonstrate that with its huge collecting area XEUS provides an order of magnitude sensitivity improvements in timing studies over RXTE. The sensitivity reached is such that QPOs could be detected within their coherence times and the oscillations detected within one cycle. The scaling of the above formula implies also that a QPO detected at 5σ with the PCA would be detected at 100σ with XEUS-1. Similarly, XEUS-1 will detect signals at the same level of significance as the PCA but for an observing time 100 times shorter.

4. Detector implementation

4.1. Science requirements

The detector needs to be able to handle up to 3 Mcts/s (XEUS-1) and 10 Mcts/s (XEUS-2) (equivalent to a 10 Crab source, see Table 1) with a timing resolution of $\sim 10\mu\text{s}$ and a deadtime less than $\sim 1\%$. In addition, the detector energy range should match closely the high energy response of the mirrors.

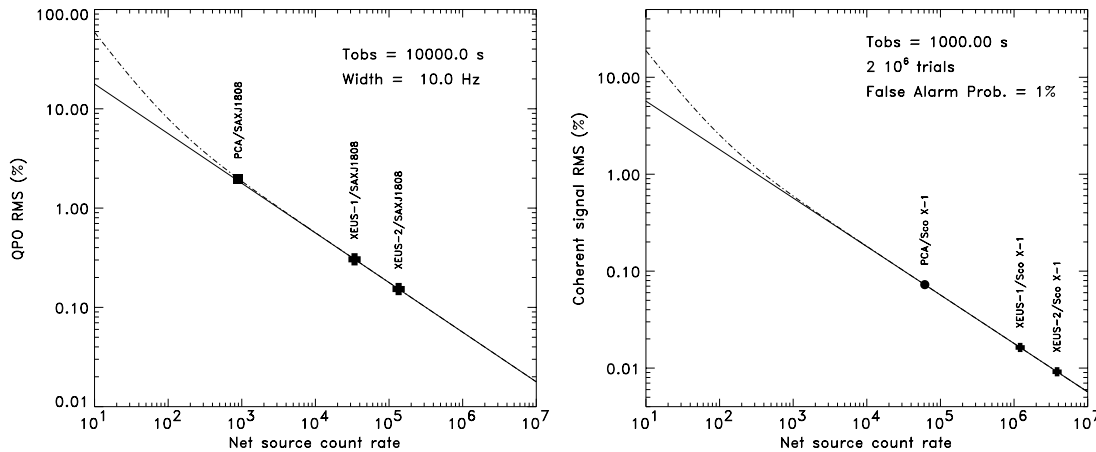


Fig. 1. left: Comparison between the XEUS (solid line) and RXTE/PCA (dot-dashed line) sensitivity for QPO detection (5σ in 10 ksec, signal width 10 Hz). An illustrative example is provided by the millisecond pulsar for which RXTE failed to detect QPOs. As can be seen, a factor of ~ 10 improvement in sensitivity over the RXTE/PCA is obtained with XEUS. Right: Comparison between the XEUS (solid line) and RXTE/PCA (dot-dashed line) sensitivities for coherent signal detection (1 ksec). The detection level corresponds to a false alarm probability of 1% for 2×10^6 trials. So far, no pulsations have been detected from Sco X-1. The XEUS-1 sensitivity is 10 times better than the current RXTE/PCA sensitivity, and failure to detect pulsations at this level would demand major revision of our current ideas about low-mass X-ray binaries.

4.2. Silicon Drift Detector

In the current XEUS detector baseline, the Wide Field Imager (WFI) has the highest count rate capabilities. However, even in the most optimistic case, it will only be able to provide timing information up to 500 kcts/s (by using a fast window mode). This means that an alternative solution should be considered.

Among the fast X-ray detectors currently available, Silicon Drift Detectors (SDDs) are the most promising (Strüder 2000; Lechner et al. 2001). The SDD is a completely depleted volume of silicon in which an arrangement of increasingly negative biased rings drive the electrons generated by the impact of ionising radiation towards a small readout node in the center of the device. The time needed for the electrons to drift is much less than $1 \mu\text{s}$. The main advantage of SDDs over conventional PIN diodes is the small physical size and consequently the small capacitance of the anode, which translates to a capability to handle high count rates simultaneously with good energy resolution. To take full advantage of the small capacitance, the first transistor of the amplifying electronics is integrated on the detector chip (see Fig. 2). The stray capacitance of the interconnection between the detector and amplifier is thus minimized, and furthermore the system becomes practically insensitive to mechanical vibrations and electronic pickup.

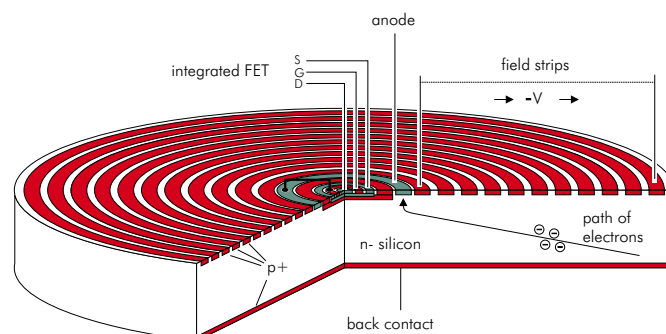


Fig. 2. Schematic cross section of a cylindrical Silicon Drift Detector (SDD). Electrons are guided by an electric field towards the small collecting anode located at the center of the device. The first transistor of the amplifying electronics is integrated on the detector chip (drawing kindly provided by P. Lechner).

Energy resolution of better than ~ 200 eV (at 6 keV, equivalent to a low energy threshold ~ 0.5 keV) is readily achieved with modest cooling (-20°C) for count rates below 10^5 cts/s (e.g. Lechner et al. 2001, see Fig. 3).

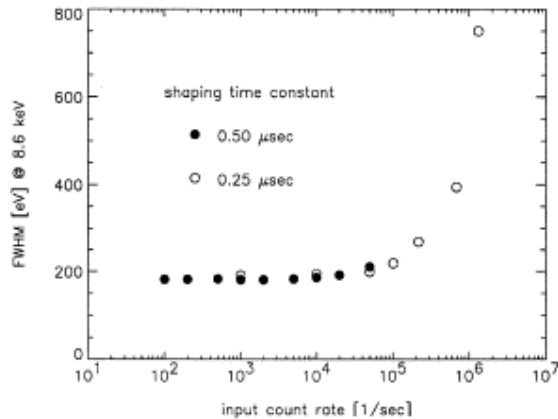


Fig. 3. Dependence of energy resolution of a SDD with integrated FET on the rate of incoming photons (Lechner et al. 2001).

With such a low energy threshold, the fast timing capability would explore completely new windows of X-ray timing by getting below ~ 2.5 keV (current threshold of RXTE-like proportional counters). Such device would also allow the investigations of the frequency domain up to $\sim 10^4$ Hz, where signals have been predicted from accreting neutron stars (Sunyaev & Revnivtsev 2000).

4.3. Deadtime and implications

For timing studies, deadtime is always a critical issue. Deadtime will include contributions from the signal rise time, the charge sensitive amplifier, the shaping amplifier. The first two of these can be very short, and the limiting contribution is that of the amplifier, where a trade-off between speed and energy resolution is necessary. Shaping time constants as short as 50 nanoseconds (ns) have been found to be usable (Strüder 2000). This translates to a minimum feasible deadtime of ~ 100 ns. Using currently available devices and pipelining techniques, the analog-digital conversion stage is not a limiting factor at these speeds.

A 100 ns deadtime per event corresponds to a 1% deadtime for a source producing 10^5 cps/s. To handle 10^6 cps/s, one must therefore distribute the focal beam over ~ 10 pixels. The best and easiest solution could be a detector made of an ensemble of about ~ 10 separate SDDs on a single wafer. Such SDD arrays already exist, as shown in Figure 4. *This detector should therefore be operated out of focus.* For XEUS-1, the out of focus distance is of the order of 10 cm. This could be accomplished either by a mechanical construction, or by changing the distance between the detector and mirror spacecraft. Although this will require a careful study, both solutions appear to be feasible within the current XEUS mission design. The requirements in terms of real estate on the detector spacecraft are not constraining, in particular because no complicated cooling systems will be necessary. Finally, the SDD array could be easily implemented on the side of the wide field imager chip.

4.4. Radiation hardness

The detector will be exposed to high radiation doses and one must therefore consider its radiation hardness. The main limitation in the maximum acceptable dose arises from the JFET connected to the collecting anode on the back of the device (Leutenegger et al. 2001). High energy photons absorbed in the transistor region increase the amount of oxide charge and interface traps, thus reducing the charge carrier lifetimes, and thus contributing to increase the leakage current. Laboratory measurements indicate however that a 300 micron thick SDD survives a radiation dose of $\sim 10^{13}$ incoming high energy photons ($E > 12$ keV) (Leutenegger et al. 2001). This is equivalent to a continuous exposition of 3 years at 10^5 photons/s. Similarly, the detector will be exposed to particles at a moderate rate (1-2 particles/cm²/s). Again, the XMM-Newton EPIC PN cameras which have similar detector technology have not shown any degradations in performance in space (Strüder et al. 2001). So, the device selected can be clearly considered as radiation hard.

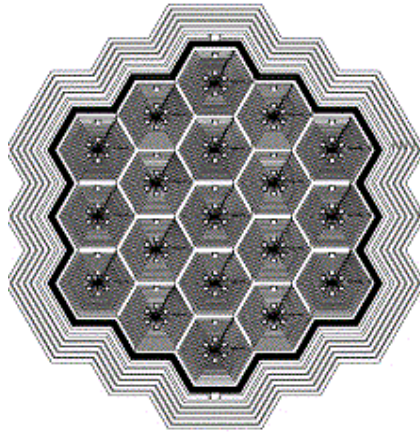


Fig. 4. SDD array made of 19 hexagon cells of 5 mm^2 (Lechner et al. 2001). The overall size of the detector is just about 1 cm^2 .

4.5. High energy extension

As mentioned above, a high energy extension (above 40 keV) is proposed for the mirrors (Aschenbach et al. 2001). SDDs are currently produced with thicknesses of 300 microns, which is adequate to cover the energy range below 10 keV. Although there are on-going efforts to make thicker devices, the best match of the high energy response of the mirrors will require the SDD array to be associated with a higher density detector located underneath. Among the potential high energy semi-conductor detectors, CdZnTe as the one presented in Budtz-Jørgensen et al. (2001) stands today as a very promising solution. Such a detector would both ensure the overlap in energy range with the SDD array, and provide a flat energy response up to $\sim 80 \text{ keV}$ and 10 microsecond timing resolution (Budtz-Jørgensen et al. 2001).

4.6. Telemetry and data handling

The goal is to send to the ground the time and energy information of every photon. For most sources, data compression will make this possible (within a 2 Mbits/s data rate) without compromising either time or energy resolution. For the very brightest sources, this can still be done with a restricted number of energy channels.

5. Conclusions

Probing strong gravity fields, constraining the equation of state of dense matter, and more generally studying the brightest X-ray sources of the sky with fast X-ray timing could be achieved with XEUS with the addition of a fast X-ray timing capability in the focal plane. This would greatly extend the capabilities of XEUS at low cost, with little impact on the primary objectives of the mission, which remain the spectroscopy of the most distant X-ray sources of the Universe. Current detector technology meet the science requirements for the timing of the brightest X-ray sources. The most attractive detector implementation would consist of an array of small size silicon drift detectors operated out of focus.

Acknowledgements. We are grateful to the following colleagues who are supporting the proposal for a fast X-ray timing capability in XEUS: J.L. Atteia, T. Belloni, H. Bradt, L. Burderi, S. Campana, A. Castro-Tirado, D. Chakrabarty, P. Charles, S. Collin, S. Corbel, C. Done, G. Dubus, M. Gierlinski, J. Grindlay, A. Fabian, R. Fender, E. Gourgoulhon, J.M. Hameury, C. Hellier, W. Kluzniak, E. Kuulkers, S. Larsson, J.P. Lasota, T. Maccarone, D. de Martino, K. Menou, C. Miller, F. Mirabel, M. Nowak, J.F. Olive, S. Paltani, R. Remillard, J. Rodriguez, R. Rothschild, T. di Salvo, R. Sunyaev, M. Tagger, M. Tavani, L. Titarchuk, G. Vedrenne, N. White, R. Wijnands, J. Wilms, A. Zdziarski, W. Zhang.

The authors are also grateful to A. Parmar, G. Hasinger and M. Turner for helpful information about the XEUS mission in general.

References

- Aschenbach, B., et al., 2001, ESA Pub. Division, ESA SP-1253
- Belloni, T., Mendez, M., King, et al. 1997, ApJL, 479, L145
- Bildsten, L. 1998, ApJL, 501, L89

- Bleeker, J. A. M., et al., 2000, ESA Pub. Division, ESA SP-1242
- Bradt, H. V., Rothschild, R. E., & Swank, J. H. 1993, A&AS, 97, 355
- Brady, P. R., et al. 1998, Phys. Rev. D, 57
- Budtz-Jørgensen, C., Kuvvetli, I., Westergaard, N. J., et al., 2001, Astrophysics and Space Science, 276, 281
- Chakrabarti, D. & Morgan, E. H., 1998, Nature, 394, 346
- Fender R. P., Garrington S. T., McKay D. J., et al. 1999, MNRAS, 304, 865
- Hasinger, G., et al., 2000, ESA Pub. Division, ESA SP-1238
- Lechner, P., Fiorini, C., Hartmann, R. et al. 2001, Nucl. Inst. Meth., 458, 281
- Leutenegger, P., Kemmer, J., Lechner, P., et al., 2000, SPIE, 4012, 579
- Miller, J. M. et al. 2001, ApJ, 563, 928
- Miller, M.C., Lamb, F. K., & Psaltis, D. 1998, ApJ, 508, 791
- Miller, M.C. & Lamb, F.K., 1998, ApJ, 499, L39
- Nath, N. R., Strohmayer, T. E., & Swank, J. H. 2002, ApJ, 564, 353
- Psaltis, D. & Norman, G., 2002, ApJ, submitted
- Stella, L. & Vietri, M., 1998, ApJ, 492, L59
- Stella, L. & Vietri, M., 1999, Physical Review Letters, 82, 17
- Strohmayer, T., 1998, The Active X-ray Sky, 69, 129
- Strohmayer, T. 2001a, ApJ, 552, L49
- Strohmayer, T. 2001b, ApJ, 554, L169
- Strüder, L., 2001, Nucl. Instr. and Meth., 454, 73
- Strüder, L. et al. 2001, A&A, 365, L18
- Sunyaev, R. & Revnivtsev, M., 2000, A&A, 358, 617
- Titarchuk L. & Osherovich V., 1999, ApJ, 518, L95-98
- Van der Klis, M., 2000, ARA&A, 38, 717
- Wijnands, R. & Van der Klis, M., 1998, Nature, 394, 344
- Zhang W., Smale A. P., Strohmayer T. E., Swank J. H., 1998, ApJL, 500, L171



The importance of soft X-ray spectroscopy in the 0.1–0.5 keV range with XEUS

Th. Boller, D. Breitschwerdt, L. Strüder, P. Predehl

Max-Planck-Institut für extraterrestrische Physik, Postfach 1312, 85741 Garching

Abstract. We work out the astrophysical importance of X-ray spectroscopy in the 0.1-0.5 keV energy range with XEUS for (i) exploring the soft X-ray absorption up to the most distant quasars and (ii) studying diffuse soft X-ray emission from the local interstellar medium up to distant external galactic halos. The large collecting area and the high spectral resolution of XEUS allows to precisely measure the low-energy cutoffs which immediately probe absorption along the line of sight up to the most distant quasars. Observations of high redshift quasars are of wide cosmological importance since these objects are thought to be associated with the earliest collapsed structures. Large column densities may be reasonably expected in young objects. A strong correlation of the amount of soft X-ray absorption with distance is presently found for quasars up to a redshift of $z=4.72$ (the most distant matter yet probed with soft X-ray spectroscopy in the 0.1-0.2 keV range: GB 1428+4217 (Boller, Fabian, Brandt, Feyberg 2000)). To study soft X-ray absorption at redshifts above $z=5$, observations in the extreme soft X-ray range down to about 0.1 keV are required. Moreover, XEUS allows to perform precise plasma diagnostics (line ratios, metal abundances, equilibrium studies). The most important lines of oxygen and iron with rest frame energies between 0.5 and 0.9 keV will be shifted into the lowest energy band. We work out the scientific importance of precise measurements in the soft 0.1-0.5 keV energy range with XEUS for studying the formation and history of gas associated with our own galaxy up to the most distant quasars. First technical feasibility studies will also be presented.

Acknowledgements. We gratefully acknowledge the permission by the Springer Verlag to use their A&A L^AT_EX document class macro.

The importance of soft X-ray spectroscopy in the 0.1- 0.5 keV with XEUS

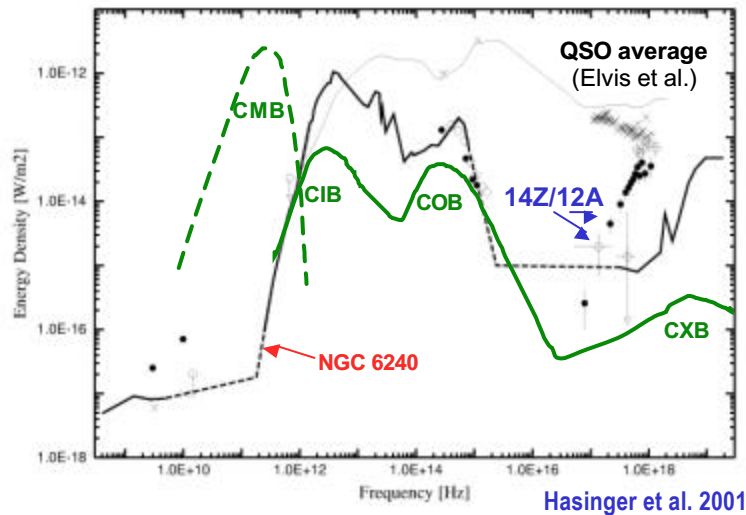
Th. Boller, D. Breitschwerdt, L. Strüder, P. Predehl

Max-Planck Institut für extraterrestrische Physik Garching

Absorbing gas is connected with youth and formation of the host galaxy

- Rees 1988:** Formation of galaxies involves infall of gas from radii ~ 100 kpc
Two-phase infalling gas (neutral and ionised)
- Fabian 1999:** Spectrum of X-ray background requires that most accretion power is absorbed
- Hasinger 1999**
Comastri 1995 Important requirement is presence of large column densities
- Matt 1994** High absorbing fractions are required (~ 90 % with $N_{\text{H}} > 10^{22} \text{ cm}^{-2}$)
- Madau 1994**
Setti 1989 Covering factor must approach 4π sr and it must be fairly neutral and cold to absorb X-rays
- Hasinger 2001** Compton thick sources resemble SED of nearby obscured sources 

Type II AGN and the XRB

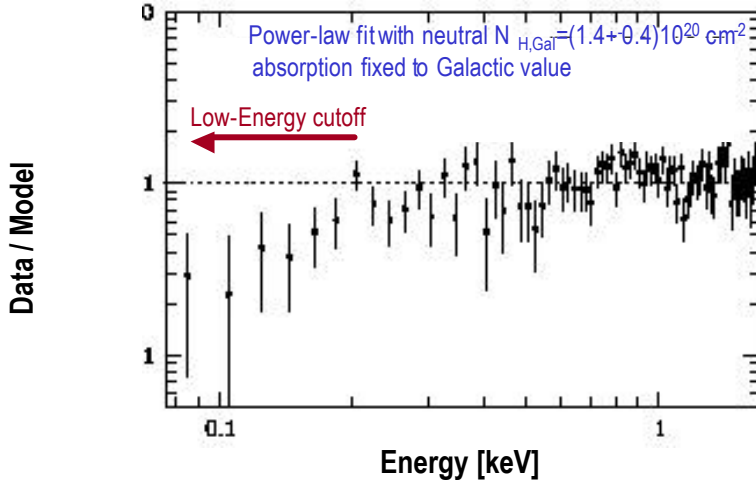


Absorbing gas is connected with youth and formation of the host galaxy

- Rees 1988: Formation of galaxies involves infall of gas from radii ~ 100 kpc
Two-phase infalling gas (neutral and ionised)
- Fabian 1999: Spectrum of X-ray background requires that most accretion power is absorbed
Hasinger 1999: Important requirement is presence of large column densities
Comastri 1995: High absorbing fractions are required ($\sim 90\%$ with $N_H > 10^{22}$ cm⁻²)
Matt 1994: Covering factor must approach 4π sr and it must be fairly neutral and cold to absorb X-rays
Madau 1994: Covering factor must approach 4π sr and it must be fairly neutral and cold to absorb X-rays
Setti 1989: Covering factor must approach 4π sr and it must be fairly neutral and cold to absorb X-rays
- Hasinger 2001: Compton thick sources resemble SED of nearby obscured sources 
- Fiore 1998: Detection of low-energy cutoffs in radio-loud quasars
Elvis 1994: Number of cutoffs increases with redshift
- Boller 2000: Detection of a low-energy cutoff in a $z=4.72$ quasar 

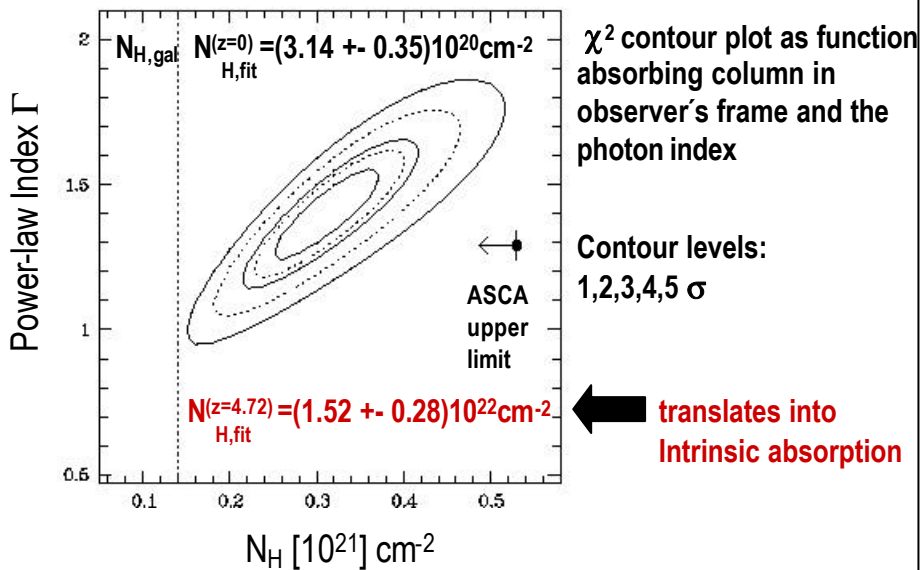
The most distant low-energy cutoff GB 1428+4217 (z=4.72)

(Boller, Fabian, Brandt, Freyberg 2000)

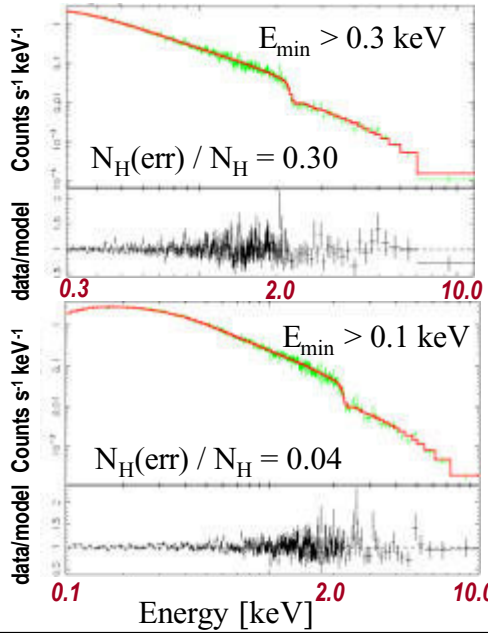


Low-Energy cutoff already shifted into the 0.1-0.2 keV band
This type of science can not be done with XMM-Newton

The excess absorption in GB 1428+4217



XEUS Simulation for AGN in LH



AGN in rest frame at $z = 1$

$$L = 10^{44} \text{ erg s}^{-1}$$

$$N_{\text{H}} = 1.0 \cdot 10^{20} \text{ cm}^{-2}$$

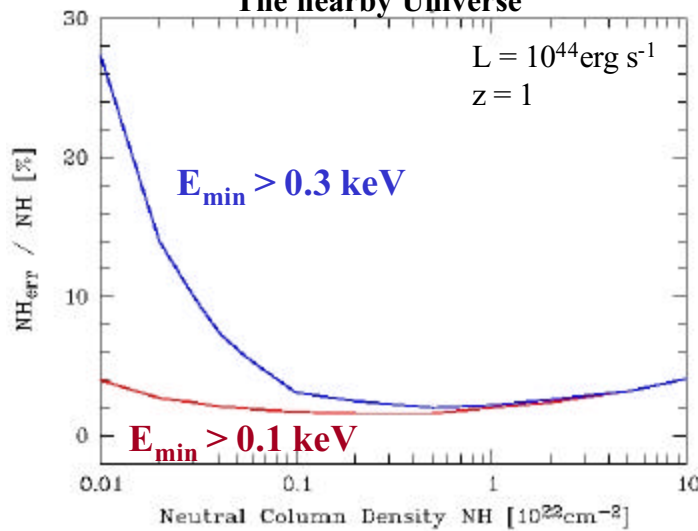
Exposure = 40 ksec

Cutoff precision = 30 %

Cutoff precision = 4 %

XEUS Simulation - Varying N_{H} from (0.01-10) 10^{22} cm^{-2}

'The nearby Universe'



Low column densities require measurements in the soft $>0.1 \text{ keV}$ band

Optical Light from the dawn of the Universe

Number of optical photons: $R=25.13$ $F = 1.55 \cdot 10^{-15} \text{ erg cm}^2 \text{ s}^{-1}$ **Fan 2000**
 SDSS 1044-0125
 $z=5.80$

$$F = 2 \cdot 10^{-19} * 4000 \text{ erg cm}^2 \text{ s}^{-1} \sim 10^{-15} \text{ erg cm}^2 \text{ s}^{-1}$$

Goodrich 2001

$$\text{Number of photons} = \frac{\int f d\lambda}{\int E d\lambda} = 1 \text{ Photon cm}^{-2} \text{ s}^{-1}$$



Number of Photons from high z Quasar: $10^{-1} \text{ Photons s}^{-1} \text{ PSF}^{-1}$

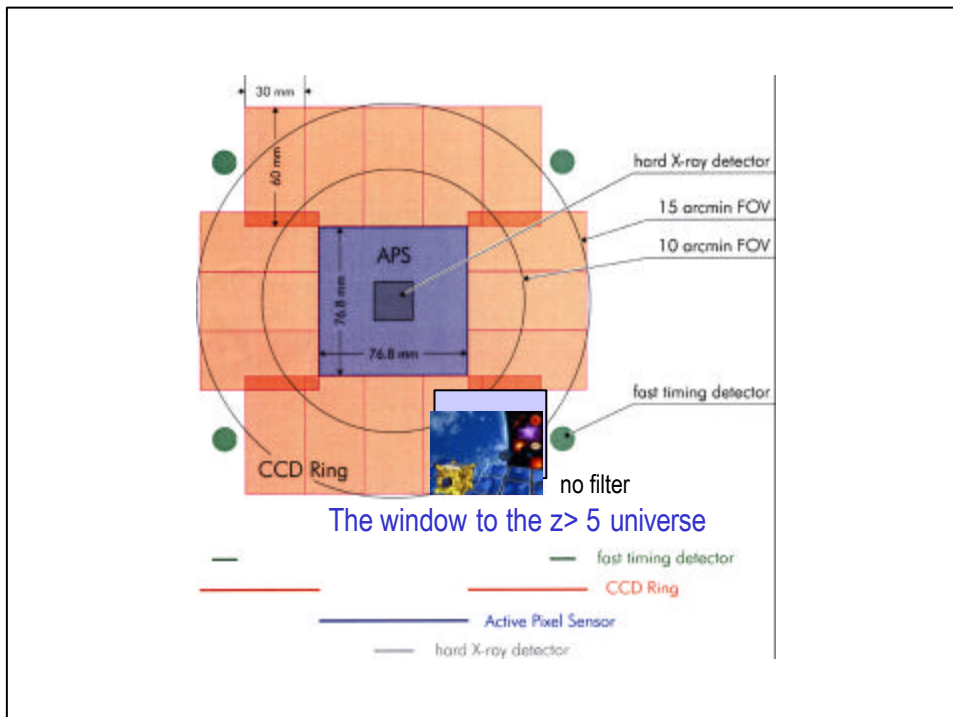
Number of optical photons
 in detector to achieve
 a 1 % error at 1.0 keV

Read-out time: 1 ms per pixel
 10 Photons \rightarrow 7 e⁻ Hole pairs \rightarrow ~ 20 eV
 $\rightarrow \Delta E / \text{pixel} \sim 10 \text{ eV} \rightarrow 1 \% @ 1 \text{ keV}$

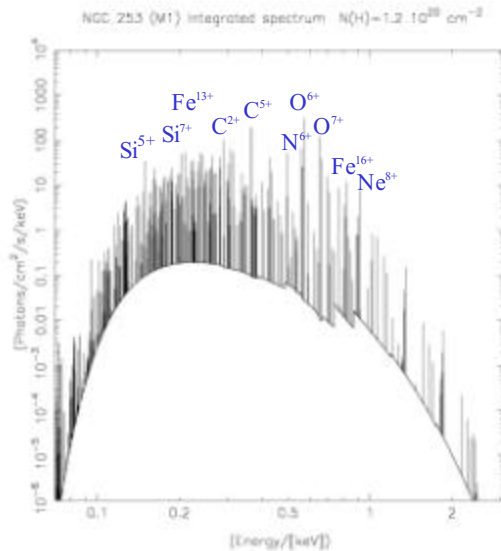


allowed number of photons in detector $\sim 10^4 \text{ Photons s}^{-1} \text{ PSF}^{-1}$

No filter required to observe objects in the XEUS high redshift (ignoring scattered light)



Importance of soft X-ray spectroscopy for plasma diagnostics



- Integrated spectrum of galactic wind (NGC 253)
- “multi-temp.” structure
- NEI spectrum has many diagnostic lines (OVII, OVIII, FeXVII) in soft energy range

Summary and suggestion for the XEUS Steering Group

Ignoring the soft X-ray band $> 0.1 \text{ keV}$ → formation and growth of high- z quasars can not be studied
→ we lose an important science case

XEUS II allows precise measurements of the gas in the first galaxies forming above 0.1 keV

Aluminum filter cuts out $\sim 90\%$ of your photons @ 0.1 keV
Decreases statistics for all type of timing and spectral analysis

The XEUS $z = 5 - 10$ universe may not require any additional filter on the detector

Proposal: discuss whether part of the detector can be made without a filter

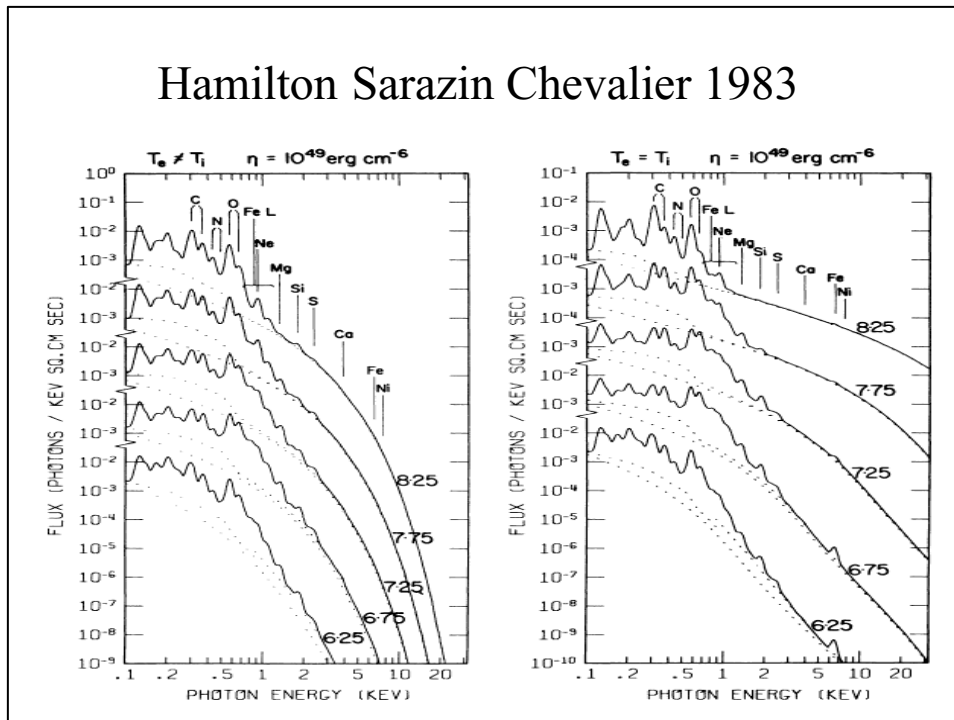
Scientific and technical aspects of a low energy imaging spectrometer for XEUS

R. Lieu

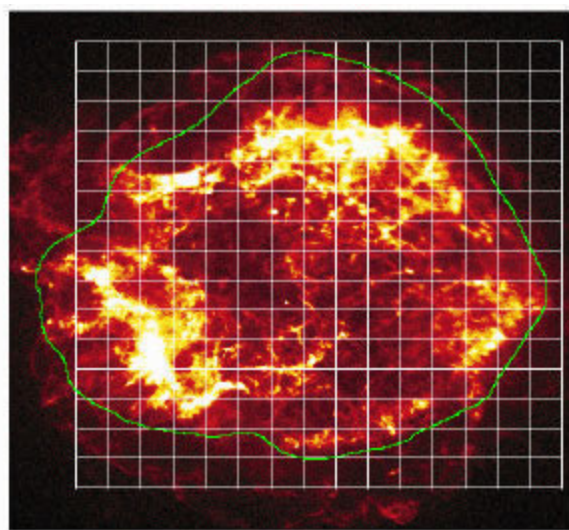
Abstract. My presentation aims at emphasizing that a mission of XEUS class should demonstrate superior capability in imaging spectroscopy (of both point and extended sources) in soft X-rays and EUV passbands. As illustrated by the plot of Fig. 1, the key radiative transitions of elemental species occur in a temperature range where the corresponding emission/absorption line lies in the above passband. We show some of the many real astrophysical examples. Fig. 2 contains a Chandra LETG spectrum of the bright coronal star Capella, where the abundance of lines towards the lower energy X-ray range is clear (EUVE data indicate that this object exhibits numerous emission lines from soft X-rays all the way to the FUV). Next, for understanding the physics of a supernova remnant (Fig. 3) one needs high resolution imaging spectroscopy down to at least the soft X-rays (see Fig. 4 for the soft X- lines from a shocked plasma). For our interstellar medium, it has been known for some time already that the entire set of many line emissions detected at energies ≤ 1 keV (Fig. 5 top panel) do not match well even the best of existing models (bottom panel, Fig. 5), and further investigation necessitates the same demand on instrument performance as that outlined for supernovae (in Fig. 6 we highlight the reproducibility (hence credibility) of the soft X-ray data by showing two totally independent observations). Lastly there is an area of importance to cosmology that XEUS can make significant advances on - the discovery of soft excess emission from clusters of galaxies (Lieu et al 1996, ApJL & Science) is now confirmed by the XMM/Newton mission (Nevalainen et al 2002, ApJ in press), which also identified redshifted O VII emission in the soft excess spectrum (Kaastra et al 2002, A & A in press) thus proving also the correctness of our original proposition that the soft component is signature of many missing baryons in a warm intergalactic medium. The next four figures highlight some results of the forementioned two papers: Figs. 7 and 8 illustrate the reliability of the XMM EPIC calibration by showing the residuals of power-law fits to standard candle spectra, while Figs. 8 and 9 illustrate the soft excess witnessed by EPIC when an approx. $kT = 8$ keV hot plasma emission is fitted to the spectra of two regions of the Coma cluster (1-2 and 4-6 arcmin annuli, where in each case the blue color represents ROSAT data and model and the other three colors represent EMOS1,2 and EPN). Fig. 10 shows the predicted performance of XEUS by applying various best-fit XMM models of the soft excess in the cluster A1795, where it can be seen that thermal and non-thermal models are readily distinguishable. The final figure is excerpted from recent works that demonstrated how low energy passband filters of high sensitivity, with capability of excluding unwanted long wavelength background radiation (like Lyman alpha, and the HeI and HeII geocoronal lines at 304 and 584 Å) to a high degree.

Acknowledgements. We gratefully acknowledge the permission by the Springer Verlag to use their A&A L^AT_EX document class macro.

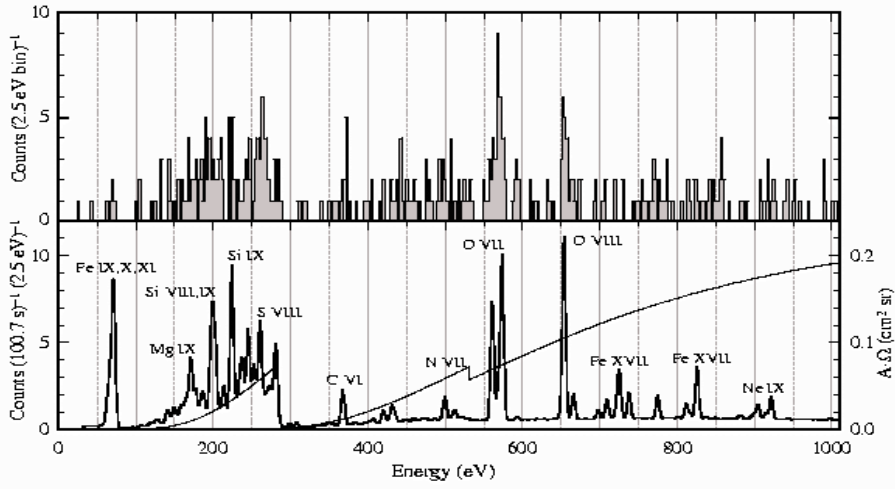
Hamilton Sarazin Chevalier 1983



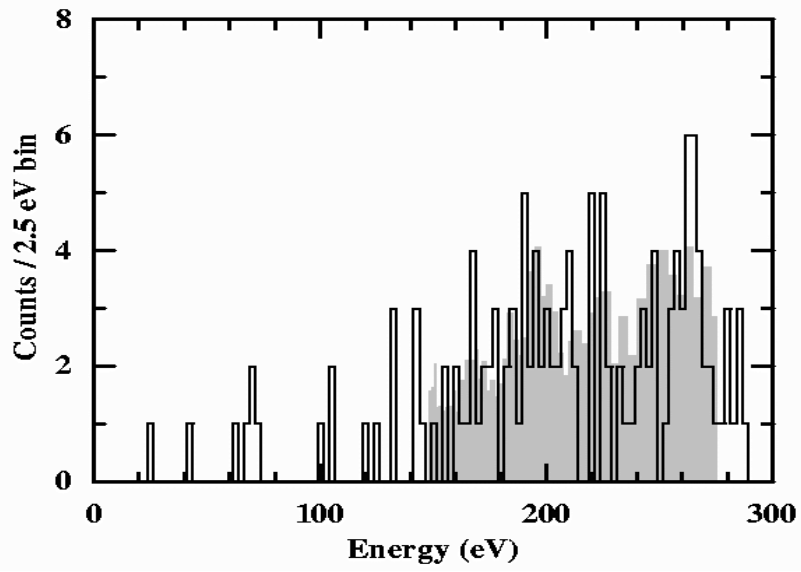
Willingale et al 2002



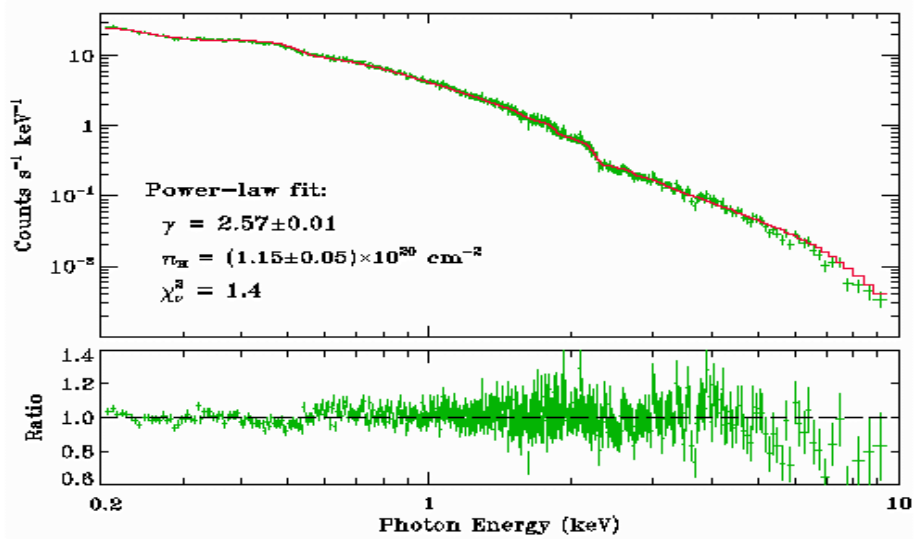
McCammon et al 2002



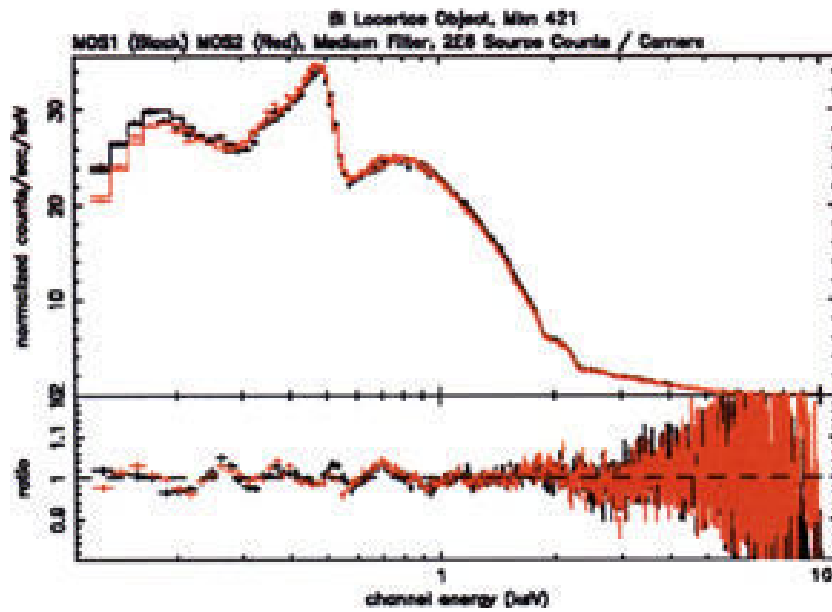
McCammon et al 2002



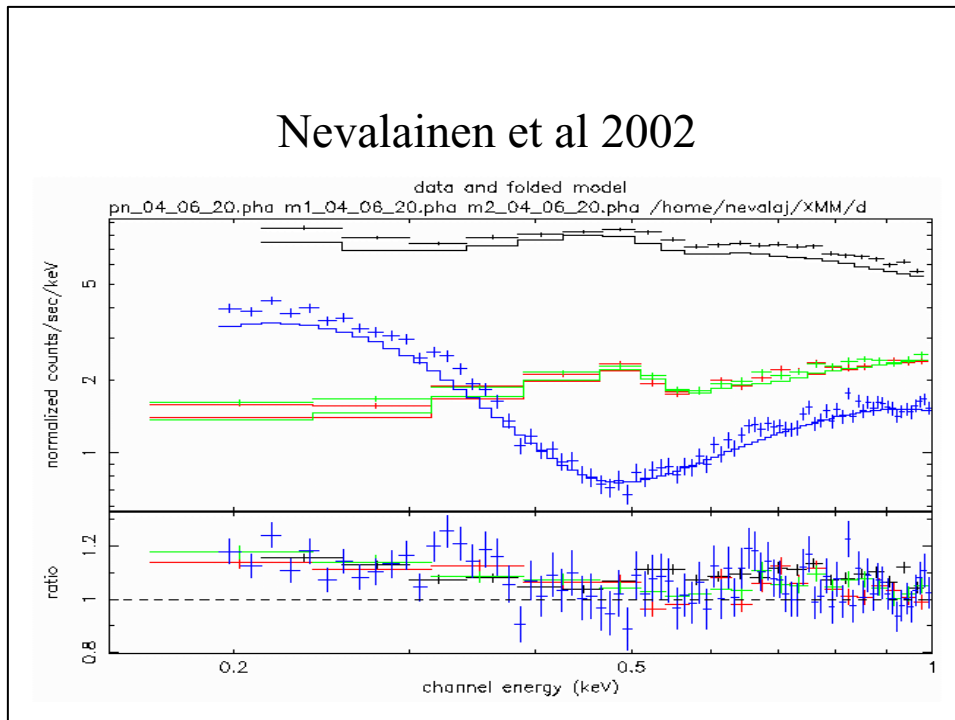
Briel et al 2001



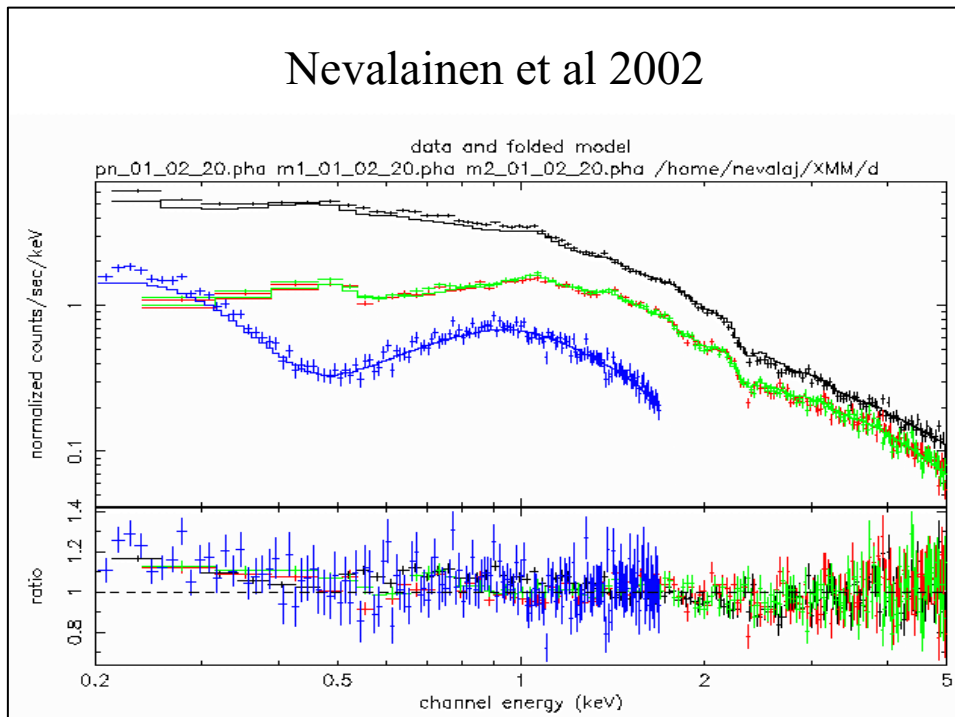
Ferrando et al 2001



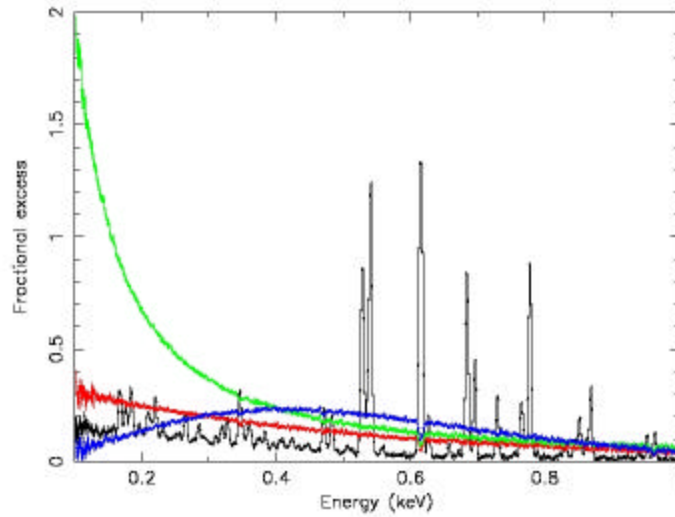
Nevalainen et al 2002



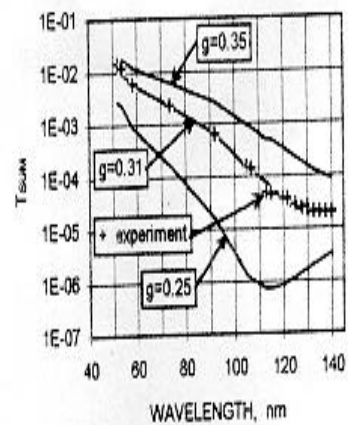
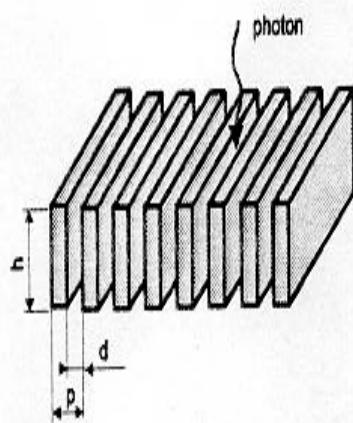
Nevalainen et al 2002



Simulated XEUS spectrum of A1795's extended soft emission



Gruntman et al 1997





X-ray Astronomical Polarimetry in the X_{EU}S Era

E. Costa¹, P.Soffitta¹, G.Di Persio¹, M.Feroci¹, L.Pacciani¹, A.Rubini¹ and R.Bellazzini², A.Brez², L.Baldini², L.Latronico², N.Omodei², G.Spandre²

¹ IASF-CNR, Rome, Italy

² INFN, Sezione di Pisa, Italy

Abstract. X-ray Polarimetry is almost as old as X-ray Astronomy. Since the first discovery of X-ray sources theoretical analysis suggested that a high degree of linear polarization could be expected due either to the, extremely non thermal, emission mechanism or to the transfer of radiation in highly asymmetric systems. The actual implementation of this subtopic was, conversely, relatively deceiving. This is mainly due to the limitation of the conventional techniques based on the Bragg diffraction at 45°, or on Thomson scattering around 90°. Actually no X-ray Polarimeter has been launched since 25 years. Nevertheless the expectations from such measurement on several astrophysical targets including High and Low Mass X-Ray Binaries, isolated neutron Stars, Galactic and Extragalactic Black Holes is extremely attractive. We developed a new technique to measure the linear polarization of X-ray sources. It is based on the visualization of photoelectron tracks in a, finely subdivided, gas filled detector (micropattern). The initial direction of the photoelectron is derived and from the angular distribution of the tracks the amount and angle of polarization is computed. This technique can find an optimal exploitation in the focus of X_{EU}S-1. Even in a very conservative configuration (basically the already existing prototype) the photoelectric polarimeter could perform polarimetry at % level on many AGNs. Further significant improvements can be expected from a technological development on the detector and with the use of X_{EU}S-2 telescope.

1. Introduction

Historically we can group the measurements performed on Astronomical X-ray Sources into four groups:

- Timing Photometry (Geiger, Proportional Counters, MCP) with Rockets, UHURU, Einstein, EXOSAT, ASCA, SAX, XMM, Chandra.
- Imaging:
 - Pseudo-imaging (modulation collimators, coded masks), SAS-3, XTE-ASM, SAX-WFC, HETE-2
 - Real Imaging (grazing incidence optics + Position Sensitive Detectors: IPC, MCA, CCD) with Rockets, Einstein, EXOSAT, ROSAT, ASCA, SAX, Chandra, Newton.
- Spectroscopy:
 - Non dispersive (Proportional Counters, Si/Ge and CCD) Rockets, Einstein, EXOSAT, HEAO-3, ASCA, SAX, Chandra, Newton.
 - Dispersive: (Bragg, Gratings) Einstein, Chandra, Newton
- Polarimetry (Bragg, Thomson/Compton) with rockets Ariel-5, OSO-8

While in the domain of Photometry, Imaging and Spectroscopy the observing techniques have been tremendously improved, Polarimetry has only been based on the same, conventional techniques, producing important but very limited results. In fact, after OSO-8, no astronomical Polarimeter has been flown any more.

2. Why X-ray Astrophysical Polarimetry?

Polarization from celestial sources may derive from:

- Emission processes themselves: cyclotron, synchrotron, non-thermal bremsstrahlung (Westfold, 1959; Gnedin & Sunyaev, 1974; Rees, 1975)

- Scattering on aspherical accreting plasmas: disks, blobs, columns (Rees, 1975; Sunyaev & Titarchuk, 1985; *Mészáros* et al. 1988).
- Resonant scattering of lines in hot plasmas (Sazonov 2002).
- Vacuum polarization and birefringence through extreme magnetic fields (Gnedin et al., 1978; Ventura, 1979; *Mészáros* & Ventura, 1979)

3. Polarization expected in X-ray Pulsators

The role that polarimetry can play in these sources is straightforward. We know that the emission mechanisms and we know, because we directly measure, the rotation period of the neutron star (from the light curve) and, in some cases, the intensity of the magnetic field (from cyclotron lines), and the masses (or at least the mass ratio) from optical spectroscopy and possibly from doppler effect on the X-ray period. But other important parameters such as the inclination of the magnetic to the mechanical axis or the inclination of the rotation axis on orbit plane are free parameters to be derived from fitting data of spectral variability. So far we do not know whether or when the emission is in the form of a fan or of a pencil. As computed in detail by *Mészáros* et al. (1988) the polarization of the cyclotron emission and the different scattering cross section produces a high degree of linear polarization strongly variable with energy and phase. With a pencil beam the degree of polarization will be anticorrelated with the luminosity, while for a fan beam it will be correlated. We will actually *see* the magnetic axis swinging around the rotation axis projected on the sky. All the geometry of the system will be completely frozen.

4. Polarization expected in isolated Neutron Stars

Radiation can be polarized when crossing an extreme magnetic field for the birefringence. Soft thermal X-ray radiation is produced by a NS atmosphere at T_{eff} of 0.3 to 3×10^6 K. The opacity of a magnetized plasma depends on polarization. While the effects of magnetic field on the spectrum are negligible the effects on polarization are outstanding. The degree of polarization (10%-30 %) depends on photon energy, T_{eff} , magnetic field and mass-to-radius ratio. Pavlov & Zavlin, 2000. In radio pulsars with thermal X-ray emission, phase resolved polarimetry, will provide mapping the magnetic field. Even more dramatic effects are expected in Soft Gamma Repeaters, in the frame of the magnetar model.

5. Polarization from Scattering in Accretion Disks and General Relativity effects

Intrinsically unpolarized radiation can be polarized by scattering as well, provided that scattering angles to the observer are selected by the system geometry. Chandrasekhar (1960) computed the maximum polarization (17%) that can derive from an infinitely extended, infinitely thin scattering cloud. In accretion disks around compact objects photons are Compton scattered by high energy electrons have an energy substantially different from parent population. Therefore in the X ray range the radiation can be highly polarized either in the direction perpendicular to the major axis of the disk or in that parallel (Lightman & Shapiro, 1976, Sunyaev & Titarchuk, 1985).

The polarization properties are altered by gravitational effects. The polarization plane rotates continuously with energy because of light bending predicted by General Relativistic effects combined with the radial temperature distribution in the disk. This is a signature of the presence of a black-hole (Stark & Connors, Connors & Stark, 1977, Connors, Piran & Stark, 1980).

6. Polarization of AGNs

In Seyfert Galaxies and QSOs the effects of scattering, kinematics and GR are all combined. Moreover the disk/torus geometry produces significant selection effects in the scattering angles. Also, in condition of high accretion rate, the X-ray illuminated disk can be altered in its ionization and temperature structure producing polarized radiation at energies of 2-6 keV (Matt, Fabian & Ross, 1995).

Blazar emission will be synchrotron at lower energies and is expected to be highly polarized (as in IR). At higher energies inverse compton will prevail and the degree of polarization should decrease and the angle rotate. From the energy resolved polarimetry the geometry and energy distribution of the electrons within the jet can be studied (Poutanen, 1994).

7. Miscellaneous Targets

- Non thermal X-ray emission from pulsars (for Crab P < 8%)

- Pulsations in LMXB (QPOs and millisecond pulsar)
- Edge-on X-ray binaries (polarized lines?)
- Jets in Galactic Mini-quasars (synchrotron?)
- Non thermal components in thermal Supernova Remnants (local or extended)
- Non thermal component in Galaxy Clusters
- Gamma-Ray Burst Afterglows
- Solar Flares

8. Conventional Techniques

Compared with great expectations of the theoretical analysis, the experimental results are quite meagre. In the beginning of X-ray astronomy polarimeters were flown aboard rockets, and satellites ARIEL-5 and OSO-7. In practice the only positive result was the detection of polarization by Crab Nebula by the team of Columbia University, with a rocket and with OSO-8: 19.2 % at 2.6 keV (Weisskopf et al., 1978).

This is mainly due to the limitations of the conventional techniques of Bragg diffraction and Compton scattering. A Bragg crystal, operated at 45° , and rotated around the optical axis, is an excellent analyzer of Polarization. It preserve imaging but the efficiency is very poor. Compton around 90° is a good compromise of efficiency and modulation, but, unless the energy lost in the scattering is measured (what is typically possible at higher energies only), completely destroys positional information and results in set-up huge, with high background and very serious systematic effects, that are partially removed by rotating the whole set-up. The best implementation of these two techniques is the Stellar X-Ray Polarimeter (Kaaret et al. 1990), made for the SPECTRUM-X-Gamma Mission, so far not flown.

9. Photoelectric Polarimetry

The distribution of electrons in photoelectric effect is good analyzer of polarization, almost at the same level of Bragg diffraction, but involves a large slice of the X-Ray spectrum. When the photon is absorbed by the inner shells of an atom, a photoelectron is ejected with a kinetic energy which is the difference of the photon energy and the binding energy of the electron. The photoelectron is preferentially ejected (actually with a \cos^2 distribution) on a plane perpendicular to the incoming photon. Within this plane the ejection directions are peaked around the electric field of the photon (again with a \cos^2 distribution).

The photoelectron interacts with the matter around the initial atom by several processes, two of which are almost exclusively determining its kinematics: it is slowed by ionizing collisions with atomic electrons and scattered by coulomb diffusion on the charge of the nuclei. The photoelectron, just like any electron of any other origin, leaves in the absorber a track, namely a string of electron/ion pairs, topologically connected, marking the path from the creation to the stopping point. All this Physics was studied in detail by Auger in 1926 by means of a cloud chamber filled with various mixtures of gas. The tracks of the photoelectrons, created along the X-ray beam path, are visualized by the cloud chambers as chains of bright dots. Incidentally by studying the images Auger discovered the presence of an additional electron of fixed energy produced by the self-ionization of the excited ion, since then named the Auger Electron. The cloud chamber, thanks to the low density of the conversion/detection material, is an ideal tool to microscopically resolve the photoelectron track. But a cloud chamber is definitely a ground based device.

Many workers tried in the past to design sensitive x-ray polarimeters based on the photoelectric effect but with scarce or no success. Some are based on a combination of a solid photo-cathode and an electronic detector and they require very high grazing incidence and pointing stability, while they do not provide energy information on the X-ray flux. Other attempt, with a single integrated analyser and detector, were frustrated. Actually they detected polarisation only as an 'edge' effect, either by counting coincidence in neighbors proportional counters wires (Riegler G.R. et al. Bull. Am. Phys. Soc., 15, 1970, 635.) or in neighbors CCD pixels (Tsunemi et al., NIM, 1992). Only with the advent of finely segmented gas detectors it now possible to detect polarization, with the highest sensitivity, in the canonical energy band for X-ray Astronomy. This approach has been attempted by means of gas luminescent detectors read with a CCD through an imaging optics (Austin 1993, La Monaca 1998, Sakurai 2001), but the capability to efficiently apply this method to low energy X-rays is still to be verified. In the following we present a newly developed detector, already available for a space experiment.

10. A new device: the MICROPATTERN DETECTOR

Position sensitive gas detectors, such as the Multi-Wire Proportional Chamber, typically come out with a single information on a X-ray event such as the center of gravity or the cross-over time. This information includes all data

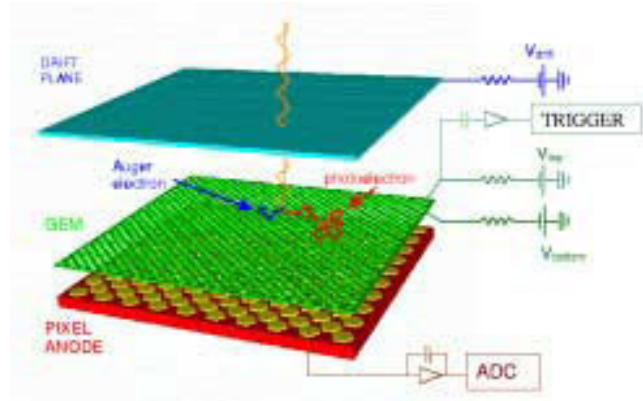


Fig. 1. Design of the Micropattern detector with GEM and readout plane with exagonal pads

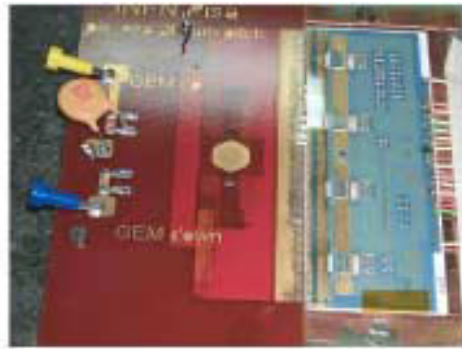


Fig. 2. Detector plane with exagonal pads currently working as laboratory prototype

on the photoelectron track. In this sense the extension of the track is usually considered as a *noise*, something to be kept as small as possible in the design. For the Multi-Wire Proportional Counter the extension of the track is considered the ultimate limit to the space resolution. Our approach is orthogonal. We image the track to reconstruct the interaction point and the prime direction of the photoelectron: something very similar to the cloud chamber but including electronic read-out, measurement of the deposited energy, self trigger capability, moderate encumbrance .

This modern Cloud Chamber is the Micropattern Gas Chamber (Costa, Bellazzini et al., Nature 2001). It consists (fig. 1, fig.2) of a gas cell with a drift region, a multiplication stage (actually a Gas Electron Multiplier) and a multi pixel true bi-dimensional read-out anode. We have constructed a multi-pixel hexagonal read-out built on an many-layer PCB (fig.3). The high granularity allows the tracks of individual photoelectrons emitted by each incident X-ray to be followed. The device combines almost the best performances of gas detectors: pixel sizes from 50 to 200 μm are feasible, the signal is very fast (tens of ns), and the energy resolution reasonable, close to the optimum for such devices (10% at 6 keV). Each pixel is connected to a pre-amplifier and ADC channel which allow to detect the energy lost in that pixel. The images of the tracks contain therefore also the information of the dynamics of the photoelectron energy loss and of the energy of the primary photon. By taking the signal from the GEM we trigger the acquisition of the anode signal and perform an optimal pulse height analysis. We collect a track for each detected photon (see fig 4).

The actual track is made as a skein and from its analysis is always possible to identify the 'head' which carries most of the information on the polarization from the tail which does not. We collected tracks from a very finely collimated 5.4 keV unpolarized sources. The loci of the centroids of each track are located on a circular region around the interaction points indicating the tracks, even at this low energy, are not randomized (fig.5). From each track we reconstructed the emission angle. The histogram of the emission angles is indicative of the presence of polarization in the incoming X-ray photons. In case of non polarised X-ray photons, such as fluorescence lines, all the emission angles have the same probability and the histogram is, therefore, a flat curve. We measured a flat curve from the fluorescence line produced by an Fe^{55} source at 5.9 keV or Chromium lines at 5.4 keV indicating that no major spurious effects

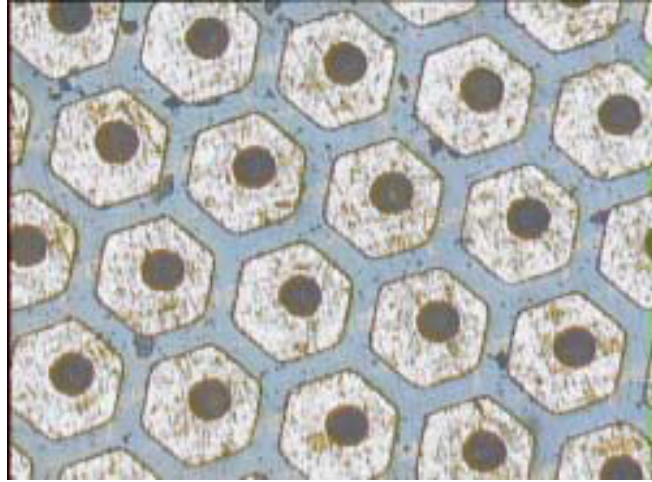


Fig. 3. Close-up view of the hexagonal pads as readout plane of the laboratory prototype

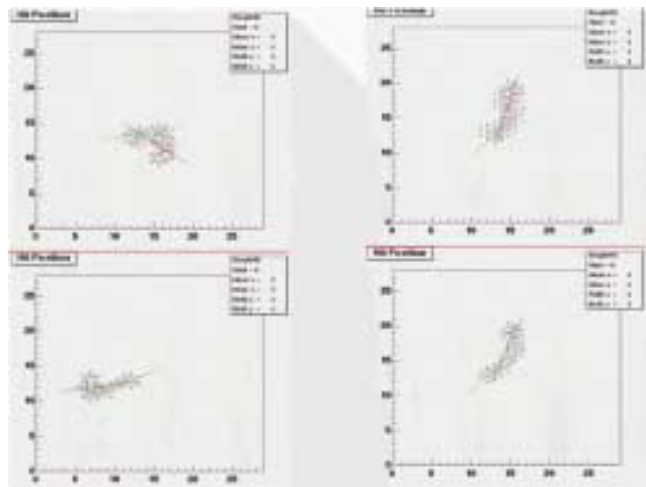


Fig. 4. Photoelectron tracks produced in gas in the laboratory prototype by 5.4 keV photons

were present (fig. 6.1). We, instead measured a significant deviation from a flat curve when we shined the detector with a polarized X-ray source of 5.4 keV (fig.6.2).

This data are well modelled, also quantitatively, with what we expect if we take into account the theoretical distribution of the photoelectron and the smearing effect due to the scattering and to the lateral diffusion of electrons in the drift from the absorption point to the GEM.

Therefore we built a detector with combined Polarimetric, Imaging, Spectral and Timing capabilities and master the simulation tools to design different configurations dedicated to a particular experiment set-up.

11. A MICROPATTERN detector in the focus of XEUS-1.

In order to evaluate the capabilities of such a device in the focus of XEUS we follow a very conservative approach. We assume to build a detector with the main features of an existing prototype, extended to include the whole XEUS PSF. We compute the expected counting rates from sources and from background (from literature data) and the modulation factor from monte.carlo simulations confirmed from our prototype measurements. This can be mounted within a conventional set-up for gas counters such as the BeppoSAX MECS GSPC, with a ceramic body and a thin ($50\mu\text{m}$) Beryllium window. This is far from an optimal device but is something of which we can guarantee, since now the feasibility, and is capable to perform on a representative sample of celestial objects the large majority of measurements foreseen in the literature, including AGNs.

In Tab.1 we show the Minimum Detectable Polarization for a sample of bright AGNs with a one day observation with such a device in the focus of XEUS-1. Energy resolved Polarimetry in 3-4 bands is possible as well at 1-2 % level

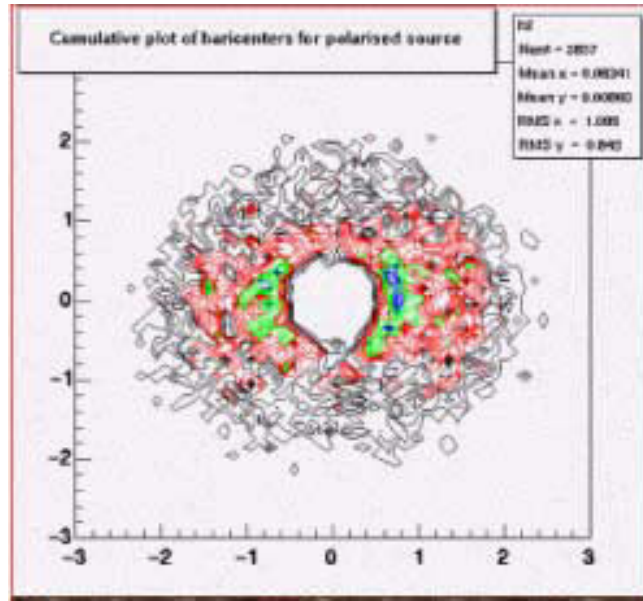


Fig. 5. Locations of the Baricentres for 5.4 keV polarized photons as derived by the tracks detected by the Micropattern

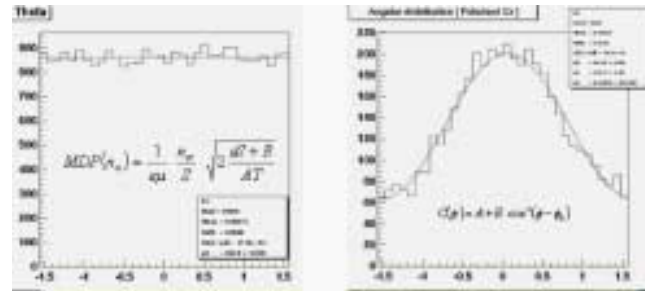


Fig. 6. Modulation curve measured with an unpolarized source Fe^{55} (left panel) and a polarized 5.4 keV source (right panel)

Table 1. MDP for AGNs in 10^5 s in the 2-10 keV energy band with XEUS-1

AGNs	MDP%
CENA	0.6
NGC4151	0.7
NGC5548	0.8
MCG 6-30-15	1.2
Circinus Galaxy	2.8
IC4329A	0.7
Fairall 9	1.6
MKN501 (Outburst)	0.5
MKN421	0.7
3C273	0.9

on all of them. Of course a much more detailed study is possible on Galactic Sources. We stress the point that in our imaging we can use the reconstructed absorption point (an not the centroid an in a MWPC). This means that we have a (experimentally verified) position resolution of around $100\mu\text{m}$, suitable to exploit all the quality of XEUS optics. Therefore XEUS could perform angular resolved polarimetry: e.g. independent polarimetry of an AGN and of its jet; polarimetry of individual knots of a SNR, polarimetry of regions of a cluster suspect to host non-thermal components. Also the system wold have full timing capability and could perform time-resolved polarimetry: e.g. phase and energy resolved polarimetry of binaries and of radiopulsars and SGR. A last point we want to stress is that, as verified at first

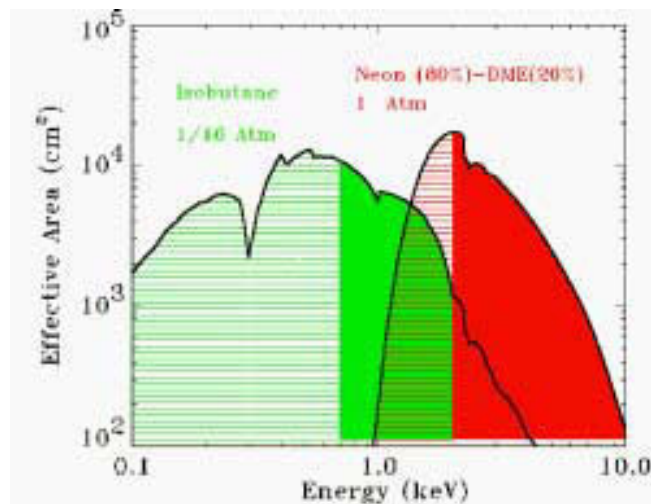


Fig. 7. Effective area of two micropattern detector for low-energy (0.1-2 keV) and high-energy (2-10 keV) application at the focus of zero-growth XEUS-1 mirrors. In full colors are represented the energy bands of X-ray polarimetric sensitivity.

order with laboratory testing, systematic effects on this polarimeter are well under control and no rotation is needed to remove them (as in a conventional scattering or bragg polarimeter).

12. Improvements with XEUS-1 and XEUS-2

The conservative configuration giving the results in the table is in no way optimal. The efficiency and modulation of the detector can be improved by increasing the absorption gap and modifying the gas filling mixture to reduce the scattering and/or the diffusion on the drift, the two major effects that smear the track. Also the algorithms so far used are relatively simple and can be improved by techniques of pattern recognition.

Another important improvement may be achieved by using instead of one detector, covering the whole energy range, two detectors optimized in two different bands. The complexity increases but the total time to achieve a broad band measurement will be significantly reduced. In fig.7 we show the effective area of our conservative configuration (on the right), effective from 2 to 10 keV, and (on the left) of a low energy detector, optimized in the band 0.6 - 3 keV. Such a low energy device could allow for 1% polarimetry of MK421 in 10^4 s.

A further important improvement can derive from the implementation of XEUS-2 optics. From statistics the MDP will scale with the square root of areas. Even though we cannot nowadays be sure of our capability to control systematic effects to perform reliable polarimetry below 1%, the observations will be significantly shorter and the sample will become much richer including AGNs at higher red-shift.

13. Conclusions

We conclude that with the new MICROPATTERN device, the Polarimetry of Astrophysical sources is now feasible, provided that a high throughput optics is used. This will open a new window in the sky and dramatically improve our understanding of Physics of X-ray emitting regions around NS and Black Holes. With XEUS-1 optics, and with moderate assumptions on technological developments, polarimetry to the % level of tens of AGNs will be feasible.

Therefore we think that the inclusion of a MICROPATTERN photoelectric polarimeter in the baseline payload for XEUS-1 should be seriously considered.

References

- K.C. Westfold, *Astrophys. J.* **130** (1959) 241.
- I.N. Gnedin & R. A. Sunyaev, *Astron. Astrophys.* **36**, (1974) 379.
- M.J. Rees, *Mon. Not. R. Astron. Soc.* **171** (1975) 457.
- R.A. Sunyaev & L.G. Titarchuk, *Astron. Astrophys.* **143** (1985) 374.
- P. Mészáros, R. Novick, A. Szentgyorgyi, G.A. Chanan & M.C. Weisskopf, *Astrophys. j.* **324** (1988) 1056.
- S.Y. Sazonov, A. Churazov & R.A. Sunyaev *Mon. Not. R. Astron. Soc.* **333** (2002) 191.
- Y.N. Gnedin, G.G. Pavlov & Y.A. Shibanov, *Sov. Astron. Lett.* **4** (1978) 117.

- J. Ventura, *Phys. Rev.*, **D 19** (1979) 1684.
- P. Mézàros, J. Ventura, *Phys. Rev.*, **D 19**, (1979), 3565.
- A.P. Lightman & S.L. Shapiro *Astrophys J.* (1976) **203**, 701.
- R.F. Stark & P.A. Connors, *Nature* **266** (1977) 429.
- P.A. Connors & R.F. Stark, *Nature* **269** (1977) 128.
- P.A. Connors, T. Piran & R.F Stark *Astrophys J.* **235** (1980), 224.
- G. Matt, A.C. Fabian & R.R. Ross *Mon. Not. R. Astron. Soc.* **264** (1993) 839.
- J. Poutanen *Astrophys J. Supp. Ser.* **92** (1984) 607.
- M.C. Weisskopf, E. Silver , H.L. Kestenbaum, K.S. Long, R. Novick , *Astrophys. J.* **220** (1978) L117.
- P. Kaaret, R. Novick, C. Martin, T. Hamilton, R.A. Sunyaev, I. Lapshov, E. Silver, M. Weisskopf, R., Elsner, G. Chanan, G. Manzo, E. Costa, G. Fraser, G.C. Perola, *Opt. Eng.* **29** (1990) 773.
- Riegler, G. R. et al., *Bull. Am. Phys. Soc.* **15** (1970) 635.
- Tsunemi, H. et al., *Nucl. Instr. and Meth* **A321** (1992) 629.
- Austin, R., A., Minamitani T., Ramsey B.D. , *SPIE* **2010** (1993) 118.
- La Monaca, A., Costa E., Soffitta P., Di Persio G., Manzan M., Martino B., Patria G., Cappuccio G., Zema N., *Nucl. Instr. and Meth* **A416** (1998) 267.
- Sakurai H., Saito S., Gunji, Noma N., Kanase and Suzuki Y., *IEEE Trans. Nucl. Sci.* **44** (1999) 481.
- E. Costa, P. Soffitta, R. Bellazzini, A. Brez, N. Lumb & G. Spandre, *Nature* **411** (2001) 662.

LMXRB in Elliptical Galaxies

L. Angelini^{1,2}, S. Snowden^{1,2}, M. Loewenstein¹, R. Mushotzky¹

¹ LHEA, NASA's GSFC, Greenbelt, MD 20771, USA

² USRA

Abstract. Chandra observations of the elliptical galaxies have shown that the large fraction of the 2-10 keV X-ray emission is resolved into high luminous point sources (Sarazin et al. 2000 & 2001; Blanton et al. 2001; Angelini et al. 2001). These findings were possible thanks to the angular 0.5" resolution on Chandra. The point source contribution to the total flux is about 80 % in the hard band (> 2 keV). These sources are most likely Low Mass X-ray Binaries (LMXRBs) similar to those observed in our own galaxy, as suggested by the composite spectra consistent with a bremsstrahlung of $kT \sim 6$ keV. These X-ray sources are very luminous with many super-Eddington (assuming a $1.4 M_{\odot}$ neutron star). The luminosity distribution sampled down to 5×10^{37} erg/s function is very similar in faint and bright ellipticals suggesting a scaling with the number of sources. Within a single Chandra observation no strong variability was detected for the brightest sources.

Elliptical galaxies host a large number of Globular Clusters (GC). There is an enormous variation in the number of GCs per galaxy with the highest found in galaxies at the center of clusters. The GC two color distribution seen in ellipticals has been interpreted as evidence that during the merger time, when the ellipticals are formed, of a more recent star formation activity (Asham & Zepf 1992). The lifetime of LMXRB is a few Gyrs and their abundance in elliptical would be an indicator of the last epoch of star formation, a fossil record of its last merger event. A correlation between Chandra and HST images have shown that about 66% and 44% of the X-ray sources in NGC1399 (Angelini et al. 2001) and NGC4472 (Angelini et al. 2002) respectively are located within GCs. This association confirms that the point sources are LMXRB and suggests that in giant elliptical galaxies luminous X-ray binaries preferentially form in GCs. This fraction is higher compared to faint ellipticals (Sarazin et al. 2000, Kraft et al 2001) but larger of that observed in our galaxy. Many of the GC sources have super-Eddington luminosities (for an accreting neutron star) and their average luminosity is higher than the non-GC sources. The X-ray spectral properties of both GC and non-GC sources, inferred from hardness ratio and combined spectra, are similar to those of LMXRBs in our Galaxy. There is no distinction in colors between the GC and non GC sources. In some cases it is possible to identify an ultra-soft spectrum, similar to that seen in the high state of black hole candidates.

A future mission, such as X_{EU}S, equipped with large effective area will allow to obtain high quality spectra of these individual sources and study in detail their timing characteristics, if the angular resolution is sufficient. We present here simulations based on the NGC1399 Chandra results using different angular resolution and conclude that at least 2" resolution is required.

Acknowledgements. We gratefully acknowledge the permission by the Springer Verlag to use their A&A L^AT_EX document class macro.

References

- Angelini L., Loewenstein M., Mushotzky R., 2001, ApJ, 557, 35.
Angelini L., Loewenstein M., Mushotzky R., 2002, ApJ, submitted
Ashman and Zepf, 1992, ApJ, 384, 50
Blanton E. L., Sarazin, C. L., Irwin J. A., 2001, ApJ, 552, 106
Kraft et al., 2001, ApJ, 560, 675.
Sarazin C.L., Irwin J. A., Bregman J. N., 2000, ApJ 544, L101.
Sarazin C.L., Irwin J. A., Bregman J. N., 2001, ApJ 556, 533.

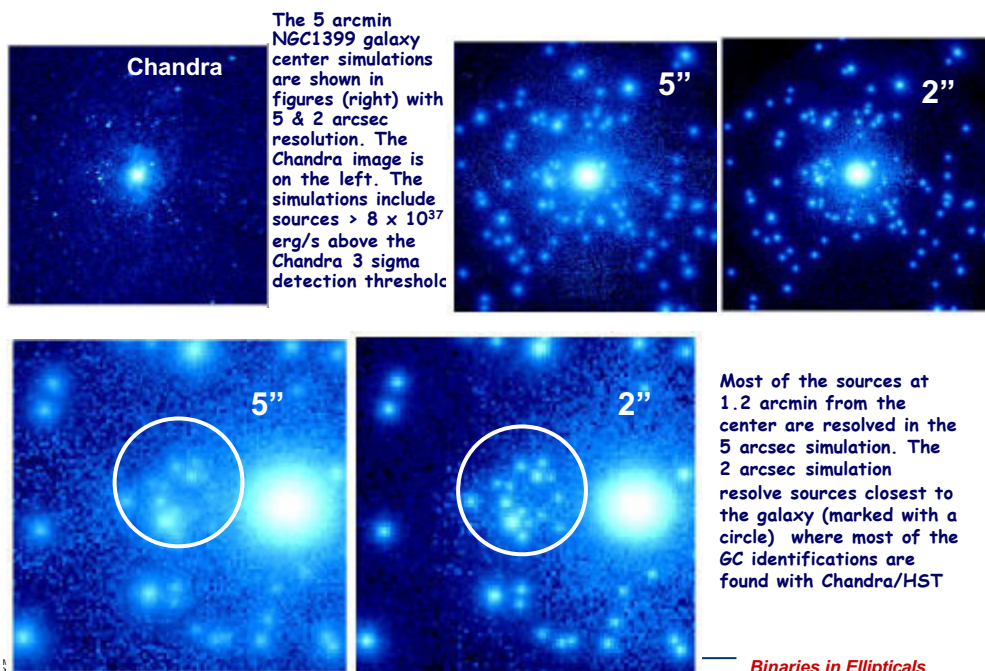
Implications for XEUS

- o While Chandra can collect positions and monitoring the long term variability of these sources, it will not obtain the necessary counts for detailed spectroscopy and timing studies of these sources
- o To achieve this is needed a mission that carries a much larger effective area with a good angular resolution: **I.e. XEUS**
- o We made XEUS simulations using the results obtained from the Chandra observation of NGC1399 with the following parameters :
 - The effective area to be 250 of the XMM (~about XEUS 2)
 - Because of the longer focal length we assumed 10 times the PN background on XMM (per arcmin²)
 - The simulations contained 160 sources (3 sigma from Chandra)
 - With a flux range of 1.6×10^{-15} - 7.4×10^{-14} ergs/cm²/s (0.5-10 keV luminosities of 8×10^{37} - 3.6×10^{39} erg/s for a distance of 20.5 Mpc)
 - With an input power law spectra of photon index 1.5
 - The extended central emission was modelled by a double gaussian as measured in the Chandra data with an 1 keV thermal input spectra
 - Exposure was set to 50 ksec to compare with Chandra
 - The PSF was set at 5 and 2 arcsec resolution

March 11-13 2002
Xeud Workshop

Binaries in Ellipticals

Simulation for XEUS



Binaries in Ellipticals

Other facts for XEUS

- o The simulation does not include low luminosity sources (down to 10^{36} erg/s) expected to be more numerous from the luminosity function. The effective area on XEUS will allow to explore and match the LMXRB luminosity range observed in our galaxy. The 2 arc sec resolution "goal" is desirable to avoid/limit confusion in these dense source galaxies.
- o A 50 ksec observation gives a 4,692 counts for the faint and 219,755 for the bright source
 - Spectra properties can be constrained with high accuracy and be searched for possible line emissions
 - Lightcurves can be searched for periodic or quasi periodic signal
- o The quality of data for this galaxy and others will be equivalent to observe LMXRB in our own galaxy with an ASM at the effective area of 10% the Ariel V ASM!
- o A 2 arc sec resolution will allow similar studies ~500 ellipticals galaxies at distance up to twice the distance of Virgo (~30 Mpc).



A new class of X-ray binaries to observe with XEUUS?

L. Boirin^{1,2} and A. N. Parmar¹

¹ Astrophysics Mission Division, Research and Scientific Support Department of ESA, ESTEC, Postbus 299, NL-2200 AG Noordwijk, The Netherlands

² Centre d'Etude Spatiale des Rayonnements, CNRS/UPS, 9 Av. du Colonel Roche, 31028 Toulouse Cedex 4, France

Abstract. We have observed the X-ray transient XTE J0421+56 in quiescence with XMM-Newton. The observed spectrum is highly unusual being dominated by an emission feature at ~ 6.5 keV. We fit the spectrum using a partially covered power-law and Gaussian line model, in which the emission is almost completely covered (covering fraction of $0.98_{-0.03}^{+0.02}$) by material with an abundance consistent with solar and is strongly absorbed with an N_{H} of $(48_{-16}^{+24}) \times 10^{22}$ atom cm^{-2} . The Gaussian has a centroid energy of (6.4 ± 0.1) keV and can be interpreted as a fluorescent emission line from iron. The strongly absorbed X-ray emission from XTE J0421+56 could result from the compact object being embedded within a dense circumstellar wind emitted from the supergiant B[e] companion star, in agreement with the picture drawn from optical spectroscopy of the source. XTE J0421+56 is the first high-mass X-ray binary with such a supergiant B[e] companion. Its very peculiar geometry and the emission mechanisms involved in the system are still to be explored. We show how they could be tightly constrained with a short (5 ks) observation of XTE J0421+56 with XEUUS I.

1. Introduction

XTE J0421+56 was discovered by the All-Sky Monitor onboard RXTE as a soft X-ray transient during an outburst on 1998 March 31 (Smith et al. 1998). This outburst was observed by CGRO (Paciesas & Fishman 1998), RXTE (Revnivtsev et al. 1999; Belloni et al. 1999), ASCA (Ueda et al. 1998) and BeppoSAX (Frontera et al. 1998; Orr et al. 1998). The outburst X-ray spectra from XTE J0421+56 are complex and can not be fit by any of the models usually applied to soft X-ray transients. A two temperature bremsstrahlung model was used to describe the spectra of the ASCA and two BeppoSAX outburst observations.

XTE J0421+56 is identified with CI Cam (Wagner & Starrfield 1998; Hjellming & Mioduszewski 1998; Robinson et al. 1998). It is a supergiant B[e] star (Clark et al. 1999; Robinson et al. 2002), or a sgB[e] star, following the notation of Lamers et al. (1998), i.e. a supergiant showing the B[e] phenomenon. The B[e] phenomenon concerns many objects of different masses and evolutionary phases (see e.g., Lamers et al. 1998). One of the common properties of stars exhibiting the B[e] phenomenon is to show forbidden emission lines in their optical spectra. Another common property is to show a strong IR excess attributed to hot circumstellar dust. Stars with the B[e] phenomenon clearly differ from the ordinary Be stars which are rapidly rotating stars near the main sequence losing mass in an equatorial wind. CI Cam/XTE J0421+56 is the first high-mass X-ray binary (HMXB) with a sgB[e] mass donor companion.

Optical high-dispersion spectroscopy of CI Cam led Robinson et al. (2002) to the conclusion that CI Cam emits a two component wind. One component is a hot, high-velocity wind. The other component is a cool, low-velocity and very dense wind. It is roughly spherical and continuously replenished. The circumstellar material around CI Cam is much denser, far more extended and much less confined to the equatorial plane than the circumstellar material around a Be star. The compact object travels through that complex environment, which makes XTE J0421+56 unique among the X-ray binaries.

Recently, Robinson et al. (2002, Sect. 2.3) estimated that the distance to the source was much larger than previously thought, making XTE J0421+56 among the most luminous transients. The 2–25 keV luminosity at the peak of the outburst was 3.0×10^{38} erg s^{-1} , assuming the revised distance of 5 kpc (Orlandini et al. 2000; Robinson et al. 2002).

The unusual nature of CI Cam makes the interstellar absorption towards the star difficult to estimate. From an analysis of diffuse interstellar bands in the optical spectrum of CI Cam, Clark et al. (2000) derive an interstellar $E(B-V)$ of 0.65 ± 0.20 and an A_v of 2.0 ± 0.6 , which should imply an interstellar X-ray absorption N_{H} of

$(0.36 \pm 0.11) \times 10^{22}$ atom cm^{-2} (Parmar et al. 2000, Sect. 3). Extinction at soft X-ray wavelengths yielded an absorption, N_{H} , of $(3.76 \pm 0.36) \times 10^{22}$ atom cm^{-2} near the peak of the outburst, and N_{H} decreased to $\sim 0.22 \times 10^{22}$ atom cm^{-2} as XTE J0421+56 approached quiescence (Belloni et al. 1999). This rapid change in the X-ray extinction, as well as the change in the IR flux after the outburst (Clark et al. 2000), indicate that much of the extinction to CI Cam is local, not interstellar (Robinson et al. 2002).

The absence of neutron star signatures (bursts, pulsations), as well as the large ratio of peak to quiescent luminosity is evidence for the compact object being a black hole (Robinson et al. 2002).

XTE J0421+56 was observed in quiescence by BeppoSAX (Orlandini et al. 2000; Parmar et al. 2000). In 1998 September, the source was soft (power-law photon index, α , of $4.0_{-0.9}^{+1.9}$) with low absorption (N_{H} of $(0.11_{-0.11}^{+0.49}) \times 10^{22}$ atom cm^{-2}). In 1999 September, the source had hardened (α of $1.86_{-0.32}^{+0.27}$) and brightened and became strongly absorbed with an N_{H} of $(40 \pm 8) \times 10^{22}$ atom cm^{-2} .

Here, we report on the XMM-Newton observation of XTE J0421+56 in quiescence performed on 2001 August 19. The detailed analysis and results are reported in Boirin et al. (2002). In this paper, we present and discuss the nature of the X-ray spectrum. Furthermore, using a simulation, we show how easily a 5 ks XEUS observation of the source would allow to precise the nature of the X-ray emission, and constrain tightly the physical parameters involved.

2. The XMM-Newton spectrum

2.1. Observations and data analysis

The region of sky containing XTE J0421+56 was observed in quiescence by XMM-Newton on 2001 August 19 between 07:05 and 16:16 UT. Here, we present the EPIC PN spectrum in the 0.1–12 keV energy range, where the source is detected. The exposure after excluding high background periods and selecting single pixel events is ~ 12 ks. Source counts were extracted from a circular region of $30''$ radius centered on XTE J0421+56. Background counts were obtained from a circular region of $90''$ radius offset from the source position. Subtracting the source and background count rates gives a net count rate of 0.024 counts s^{-1} (0.1–12 keV). This corresponds ~ 280 net counts detected. In order to ensure applicability of the χ^2 statistic with so few counts, we rebinned the spectrum such that at least 25 net counts per bin were present. The resulting spectrum has 11 significant bins which allows only simple models to be tested. All spectral uncertainties are given at 90% confidence.

2.2. Fitting the spectrum

The PN spectrum of XTE J0421+56 is shown in Fig. 1 (left). Its shape is highly unusual. It is clearly dominated by an emission feature at ~ 6.5 keV. Both a broad and a narrow component seem to be needed to account for this high-energy feature. Considering the broad high-energy feature as a highly absorbed continuum component, we fit the spectrum with a partially covered power-law model, the *pcfabs(powerlaw)* model within XSPEC in which some absorbing material covers a fraction (from 0 to 1) of a power-law emission. The abundances of the absorbing neutral material were fixed at solar values. This model gives a χ^2_{ν} of 2.45 for 7 d.o.f.. With a narrow Gaussian added to the model (*pcfabs(powerlaw+gaussian)*), the χ^2_{ν} is 0.76 for 4 d.o.f.. An F-test indicates that the probability, P_{rej} , of rejecting the hypothesis that the fit is better including the Gaussian is 5.5%. This means that the Gaussian is significant at 94.5% confidence. The best-fit parameters obtained for this partially covered power-law and Gaussian model are an N_{H} of $(48_{-16}^{+24}) \times 10^{22}$ atom cm^{-2} , a covering fraction of $0.98_{-0.03}^{+0.02}$, α of $1.1_{-0.6}^{+0.7}$, a Gaussian centroid energy of (6.4 ± 0.1) keV, width $\sigma < 0.47$ keV and equivalent width of 900_{-460}^{+660} eV. The model described above is our best-fit model and is shown in Fig. 1 (left). It is equivalent to the sum of an absorbed (and covered) plus an unabsorbed (and uncovered) component. The contributions of both these components are shown separately in Fig. 1 (left). The unabsorbed component (dashed line) dominates the emission $\lesssim 5$ keV and will be referred to as the low-energy component. On the contrary, the absorbed component (dotted line) clearly dominates the emission $\gtrsim 5$ keV and will be referred to as the high-energy component. Using the partially covered power-law and Gaussian model, we derive a 1–10 keV unabsorbed luminosity of 3.3×10^{33} erg s^{-1} , at a distance of 5 kpc. The low-energy component contributes 9.2% to the total absorbed flux in the 1–10 keV range.

In order for the uncovered component to be at least absorbed by the line of sight interstellar medium, we included an additional photo-electric absorption component (the *phabs* component within XSPEC) to the previous model. The resulting model (*phabs(pcfabs(powerlaw+gaussian))*) fits the spectrum well, with a χ^2_{ν} of 1.02 for 3 d.o.f., although an F-test indicates that the addition of the absorption component does not improve the fit (P_{rej} of 88%). The best-fit parameters are similar to the ones obtained previously with the partially covered power-law and Gaussian model. The N_{H} of the additional absorption component (*phabs*) is $< 0.2 \times 10^{22}$ atom cm^{-2} .

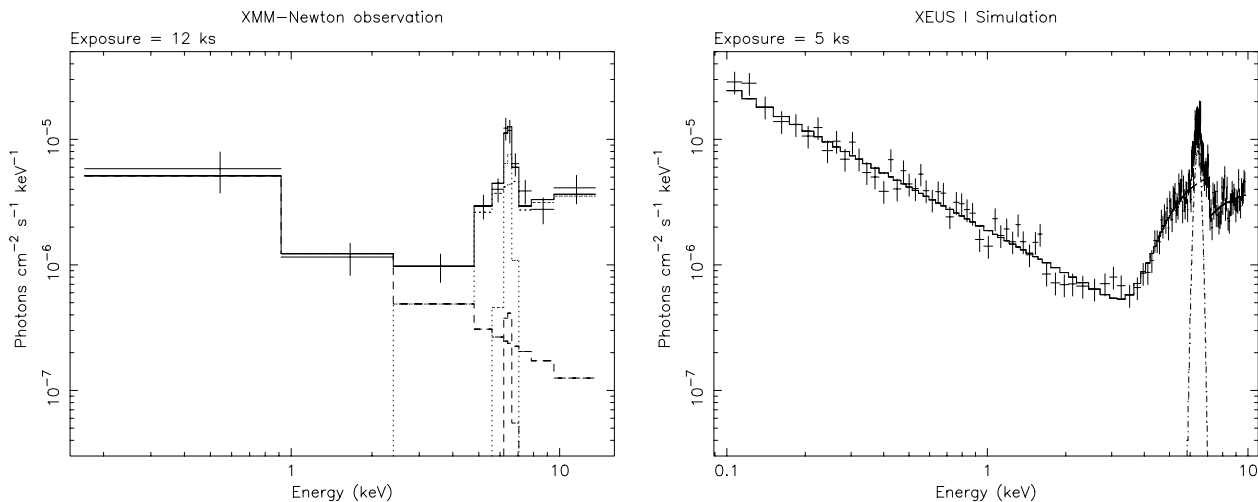


Fig. 1. Left: The XMM-Newton PN spectrum of XTE J0421+56 in quiescence. The solid line is the best-fit using the partially covered power-law and Gaussian model. The dotted line shows the contribution of the unabsorbed and uncovered component (the low-energy component) to the total model. The dashed line shows the contribution of the absorbed and covered component (the high-energy component). **Right:** The simulated XEUS I spectrum of XTE J0421+56 assuming the best-fit parameters obtained from the XMM-Newton observation. The solid line is the best-fit using the partially covered power-law and Gaussian model.

3. The XEUS I simulated spectrum

We have simulated the spectrum of XTE J0421+56 that would be obtained within a 5 ks XEUS I (initial configuration) observation. We chose 5 ks because it will probably be the shortest exposure allowed with XEUS. We assume the partially covered power-law and Gaussian model and the best-fit parameters derived from the XMM-Newton observation (sect. 2.2). We use the response matrix of the Low-energy STJ detector (`xeus_init_stj_mesh+al.rsp`) provided at <ftp://astro.estec.esa.nl/pub/XEUS/RESPONSE/> (January 2000), assuming no pile-up. Fig 1 (right) shows the XEUS I simulated spectrum and model (solid line). Using XEUS I, the best-fit parameters would be tightly constrained to an N_{H} of $(51 \pm 3) \times 10^{22}$ atom cm^{-2} , a covering fraction of $0.979_{-0.003}^{+0.002}$ and α of 1.15 ± 0.05 . The emission line parameters would be a Gaussian centroid energy of (6.41 ± 0.02) keV, a width σ of (0.17 ± 0.02) keV and an equivalent width of 775_{-86}^{+92} eV.

Furthermore, to test the detectability with XEUS of other lines potentially emitted by the source, we have simulated a XEUS spectrum assuming the previous model including an additional Gaussian. As an example, we included a Gaussian corresponding to emission from the ion O VIII, with a line energy of 0.654 keV, a width σ of 0.01 keV and a normalization corresponding to an equivalent width of 34 eV. We fit the obtained spectrum using both the model with and without the additional Gaussian included. Using an Ftest, we then concluded that the fit was better with the Gaussian included and that the line was significant at a confidence level of 99.99%. Similarly, XEUS could detect at a confidence level of 98.7% a comparable line with an equivalent width of only 22 eV.

4. Discussion

The quiescent X-ray spectrum of XTE J0421+56 during the 2002 XMM-Newton observation can be fit by a partially covered power-law and Gaussian model, in which the emission is almost completely covered by material and strongly absorbed by an N_{H} of $(48_{-16}^{+24}) \times 10^{22}$ atom cm^{-2} . The fitting approach adopted here is supported by the fact that a similarly strongly absorbed emission, with an N_{H} of $(40 \pm 8) \times 10^{22}$ atom cm^{-2} , was already reported from the source during the 1999 BeppoSAX observation (Parmar et al. 2000).

When absorption is added to the partially covered power-law and Gaussian model used to fit the XMM-Newton spectrum, the N_{H} of this component is $<0.2 \times 10^{22}$ atom cm^{-2} . This value is consistent with that obtained when XTE J0421+56 approached quiescence after the outburst (Belloni et al. 1999). These low values of N_{H} confirm that the *interstellar* column towards XTE J0421+56 is not high. On the other hand, X-ray results show that the column density intrinsic to the system can be very high, and as inferred from the large range of absorption obtained (from roughly 0.2 to 50×10^{22} atom cm^{-2}), very variable. Thus, this confirms the picture that most of the absorption towards XTE J0421+56 is local and not interstellar.

The partially covered power-law model suggests the presence of two components. The covered (high-energy) component possibly results from the compact object being embedded within the dense circumstellar wind emitted from the sgB[e] companion star, in agreement with the picture drawn from optical spectroscopy of the source (Robinson et al. 2002). The large range of observed N_{H} (from roughly 0.2 to 60×10^{22} atom cm^{-2}) at X-ray wavelengths could reflect the complexity of the B[e] star environment in which the compact object is traveling.

The uncovered (low-energy) component could be due to X-ray emission from the sgB[e] star itself. The X-ray emission from OB stars is intrinsically soft (up to ~ 4 keV, Long & White 1980). Orlandini et al. (2000) estimate that the X-ray luminosity of the companion star in XTE J0421+56 could be $\sim 5 \times 10^{32}$ erg s^{-1} , while Robinson et al. (2002, Sect. 2.4) estimate that the sgB[e] star could emit up to 10^{34} erg s^{-1} in the 0.2–4.0 keV band. The 0.2–4.0 keV luminosity observed from XTE J0421+56 during the XMM-Newton observation is 1.5×10^{33} erg s^{-1} at 5 kpc. Thus, we cannot exclude that the low-energy emission, or part of it, originates from the companion star.

Another possibility is that the low-energy component is due to the scattering of higher-energy X-ray photons in an ionized corona or wind, such as observed in some low-mass X-ray binaries. The flux of the low-energy component in XTE J0421+56 is about 9% of the total 1–10 keV flux. In dipping, eclipsing or accretion disk corona sources, the ratio observed between the flux attributed to scattered emission and the total flux is usually $\sim 5\%$ (see e.g., Parmar et al. 1986). Thus, at least a part of the low-energy emission could be due to scattering in XTE J0421+56. Emission from the companion star and scattering from an ionized corona or wind could both play a role in the low-energy emission observed from XTE J0421+56.

XTE J0421+56 is the first identified member of a new class of HMXB with sgB[e] companion. The emission processes involved in the system and its geometry have still to be explored. The XMM-Newton observation, although very important because it shows that the transient is still substantially emitting in quiescence, does only allow us to test simple emission models. Our simulation of a 5 ks XEUS I spectrum from XTE J0421+56 shows how easily XEUS would allow first to distinguish between different possible models for the X-ray emission, and second, to tightly constrain the physical parameters involved.

Acknowledgements. This work is based on observations obtained with XMM-Newton, an ESA science mission with instruments and contributions directly funded by ESA member states and the USA (NASA). L. Boirin acknowledges an ESA Fellowship.

References

- Belloni, T., Dieters, S., van den Ancker, M. E., et al. 1999, *ApJ*, 527, 345
 Boirin, L., Parmar, A. N., Oosterbroek, T., et al. 2002, *A&A*, submitted
 Clark, J. S., Miroshnichenko, A. S., Larionov, V. M., et al. 2000, *A&A*, 356, 50
 Clark, J. S., Steele, I. A., Fender, R. P., & Coe, M. J. 1999, *A&A*, 348, 888
 Frontera, F., Orlandini, M., Amati, L., et al. 1998, *A&A*, 339, L69
 Hjellming, R. M. & Mioduszewski, A. J. 1998, *IAU Circ.*, 6862
 Lamers, H. J. G. L. M., Zickgraf, F., de Winter, D., Houziaux, L., & Zorec, J. 1998, *A&A*, 340, 117
 Long, K. S. & White, R. L. 1980, *ApJ*, 239, L65
 Orlandini, M., Parmar, A. N., Frontera, F., et al. 2000, *A&A*, 356, 163
 Orr, A., Parmar, A. N., Orlandini, M., et al. 1998, *A&A*, 340, L19
 Paciesas, W. & Fishman, G. 1998, *IAU Circ.*, 6856
 Parmar, A. N., Belloni, T., Orlandini, M., et al. 2000, *A&A*, 360, L31
 Parmar, A. N., White, N. E., Giommi, P., & Gottwald, M. 1986, *ApJ*, 308, 199
 Revnivtsev, M. G., Emel'yanov, A. N., & Borozdin, K. N. 1999, *Astronomy Letters*, 25, 294
 Robinson, E. L., Ivans, I. I., & Welsh, W. F. 2002, *ApJ*, 565, 1169
 Robinson, E. L., Welsh, W. F., Adams, M. T., & Cornell, M. E. 1998, *IAU Circ.*, 6862
 Smith, D., Remillard, R., Swank, J., Takeshima, T., & Smith, E. 1998, *IAU Circ.*, 6855
 Ueda, Y., Ishida, M., Inoue, H., et al. 1998, *ApJ*, 508, L167
 Wagner, R. M. & Starrfield, S. G. 1998, *IAU Circ.*, 6857

Investigating galactic halos with XEUS

D. Breitschwerdt, M.J. Freyberg, and W. Pietsch,

Max-Planck-Institut für extraterrestrische Physik, Giessenbachstraße, 85740 Garching, Germany

Abstract. Many normal spiral and starburst galaxies possess extended diffuse X-ray halos. The X-ray morphology is often correlated with radio continuum and H_α emission, suggesting star formation as the driving agent. However, *direct* observational evidence for outflows is scanty, due to the low surface brightness of galactic halos. It is also an open question if galactic fountains or winds are the prime sources of outflows. Plasma diagnostics in soft X-rays offers a unique possibility to discriminate between static and dynamic halos, since it allows to probe the temperature and density structure. We show preliminary results from XMM-Newton observations and modeling of NGC 253 that stress the necessity for improved sensitivity, high spectral and spatial resolution and, above all, a large collecting area as offered by XEUS.

1. Introduction

The detection of galactic halos around early-type galaxies dates back to observations with the EINSTEIN IPC in the late '80s (s. Fabbiano 1989 and references therein). The diffuse nature of an extended halo in M86, a member of the Virgo cluster, was clearly seen by its deformed X-ray isophotes (due to its interaction with the intracluster medium) compared to the optical images. Clear evidence for a huge halo was also found in M82, an irregular, which underwent a massive starburst, and an indication for an outflow from the nuclear region (“plume”) could be deduced from the X-ray images of the starburst galaxy NGC 253. An earlier search for X-ray halos around normal spirals with EINSTEIN produced essentially negative results (Bregman & Glassgold 1982). Only with the launch of ROSAT (Trümper 1983) with its high sensitivity and low-background PSPC instruments it became possible to study diffuse soft emission in the 0.1 – 2.4 keV range. Bregman & Pildis (1984) reported the detection of a diffuse X-ray halo around the normal spiral NGC 891. Subsequently, more diffuse X-ray halos were detected, e.g., around NGC 4631 (Wang et al. 1995; Vogler & Pietsch, 1996), amongst others.

Despite these observational efforts, the nature of diffuse X-ray halos remained unclear. Available theoretical models argued for a hot corona (Spitzer 1956), or outflows in the form of galactic fountains (Bregman 1980), galactic winds (Breitschwerdt et al. 1987; Breitschwerdt & Schmutzler 1994) or a special form of clustered fountain/wind, called “chimney”, model (Norman & Ikeuchi 1989). The onset of an outflow, however, was not directly seen, except for an extreme case like M82, where the presence of a high central supernova rate in conjunction with a low gravitational potential and a huge X-ray *and* radio halo, made the conclusion for a galactic wind inescapable. In fact, starburst galaxies seem to be the objects for which the physics of galactic halos can be best studied. Although the question of break-out in normal spirals – and in particular the rôle of magnetic fields as an obstacle – has not been conclusively solved so far, the morphology and also the spectral properties, as we shall see, are not too different with respect to starburst galaxies. We shall therefore confine ourselves to the X-ray characteristics of these latter objects in this paper.

2. Spectral studies of X-ray halos

The development of CCD cameras for X-ray observations made it possible to go beyond the study of hardness ratios for observed sources, and with the launch of CHANDRA and XMM-NEWTON a new door in X-ray spectroscopy has been opened. While CHANDRA is superior in spatial resolution and thus in the detection of point sources, XMM-NEWTON is clearly more suited for the study of diffuse low-surface brightness objects, including a sensitivity below the CHANDRA limit of 0.5 keV, down to 0.2 – 0.3 keV. In the case of X-ray halos, the latter is a clear advantage that cannot be

underestimated. This has been demonstrated in the case of NGC 253, which according to CHANDRA data point to a “hollow cone” emission (Strickland et al. 2000), whereas XMM-Newton EPIC pn data reveal a distributed diffuse emission emanating from the plume (Pietsch et al. 2001). The XMM-Newton view of this galaxy (Fig. 1) shows most impressively the large extension of the soft X-ray halo in the $0.2 - 0.5$ keV range for the EPIC pn thin filter observation. In Fig. 1 (left), the base of an outflow, connected to the nuclear region and stretching along the minor axis for almost 2 arcmin, can be seen. Comparison between the nuclear and the plume region (Figs. 2 left and right, respectively) show a similar spectrum between $1 - 2$ keV, with some soft excess emission between $0.2 - 0.5$ keV that can be attributed to the diffuse component; this is corroborated by a similar behaviour for the NE(N) and NE(S) spectra. Between those too, however, the NE(N) shows an additional harder component between 0.5 and 1 keV (extending up to ~ 2 keV), indicating a hotter plasma with contributions from ions like OVII and FeXVII, which have already been identified as diagnostic lines from ROSAT PSPC observations in conjunction with non-equilibrium outflow models (Breitschwerdt & Freyberg, 2002). The outflowing gas, driven by the starburst, undergoes substantial adiabatic cooling on time scales considerably shorter than the recombination time scale. Hence collisional ionization equilibrium (CIE) cannot be maintained and non-equilibrium ionization (NEI) effects can dominate in the form of delayed recombination. In Fig. 5, which is a snapshot of the plasma flow at a certain distance, a stark discrepancy between CIE and NEI is visible. Integrating over the whole halo region of NGC 253 (NE), the NEI model, based on a self-consistent calculation of a galactic outflow model (for details, see Breitschwerdt & Schmutzler, 1999) shows again the importance of the diagnostic lines (s. Fig. 4) of OVII and FeXVII. Finally, the bright nucleus and associated plume regions have been observed at high dispersion with the RGS instrument (s. Fig. 3) aboard XMM-Newton, which unambiguously establishes the thermal nature of the diffuse emission and provide clear evidence for Fe-L line emission. For a more detailed discussion of Figs. 1, 2 we refer to Pietsch (2002).

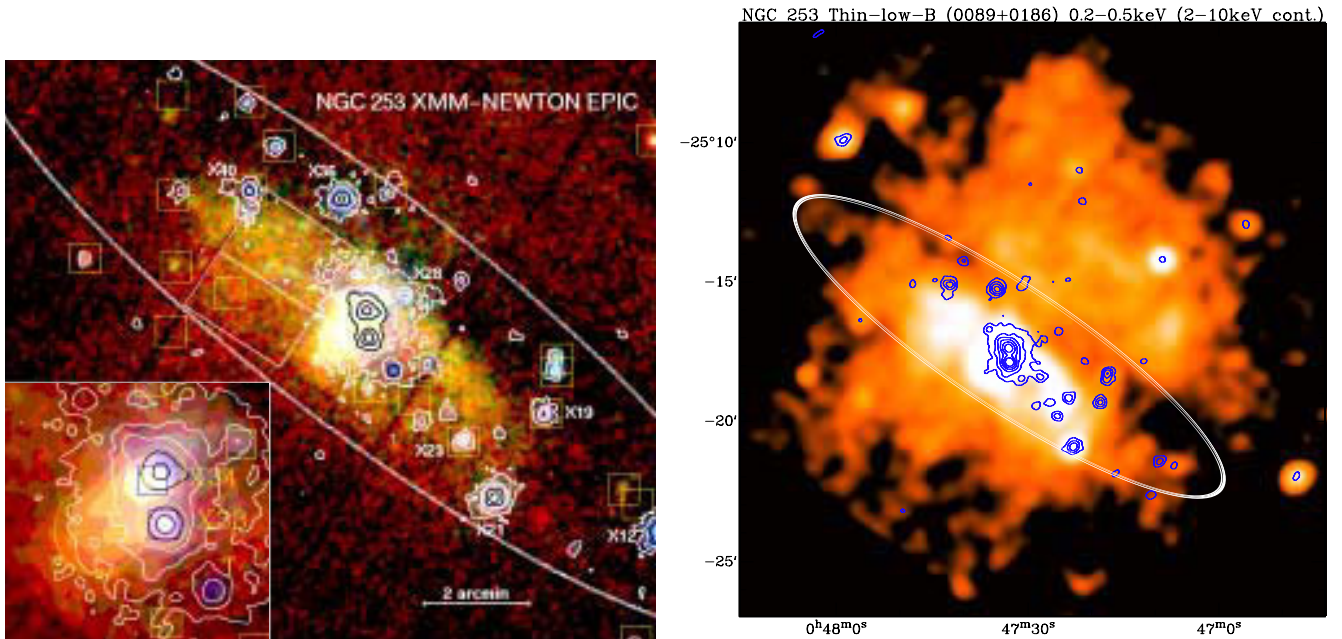


Fig. 1. XMM-Newton EPIC low-background images, slightly smoothed, the white ellipse indicates the optical D_{25} diameter of the galaxy. *Left:* NGC 253, EPIC pn and MOS, red: $0.2 - 0.5$ keV, green: $0.5 - 0.9$ keV, blue: $0.9 - 2.0$ keV, where the $2 - 10$ keV emission is shown superimposed as white contours, ROSAT sources are indicated by squares. The lower left corner shows a blow-up of the centre region. *Right:* NGC 253 with EPIC pn thin filter in the $0.2 - 0.5$ keV band with the $2 - 10$ keV emission superimposed as blue contours.

3. Future perspectives in galactic halo research with XEUS

So far spectral analysis of halos is available only for the nearest galaxies, and, in order to separate disk from halo emission, an edge-on view is preferable, thus reducing the number of useful objects to a mere handful. With its smaller FOV, but larger collecting area and arcsec spatial resolution, XEUS offers the perspective to observe a statistically

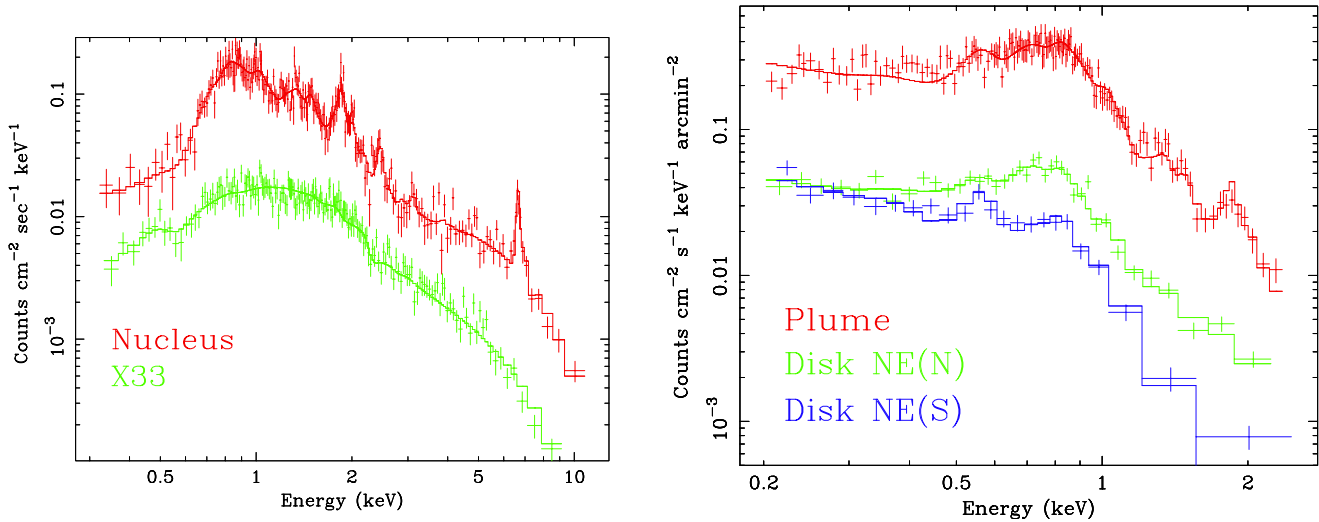


Fig. 2. EPIC pn background subtracted spectra with spectral models indicated: (*Left*) spectra of the extended nucleus of NGC 253 and the XRB NGC 253-X33. (*Right*) spectra of the NGC 253 SE X-ray plume and two areas of the disk NE of the nucleus (see left panel of Figure 1).

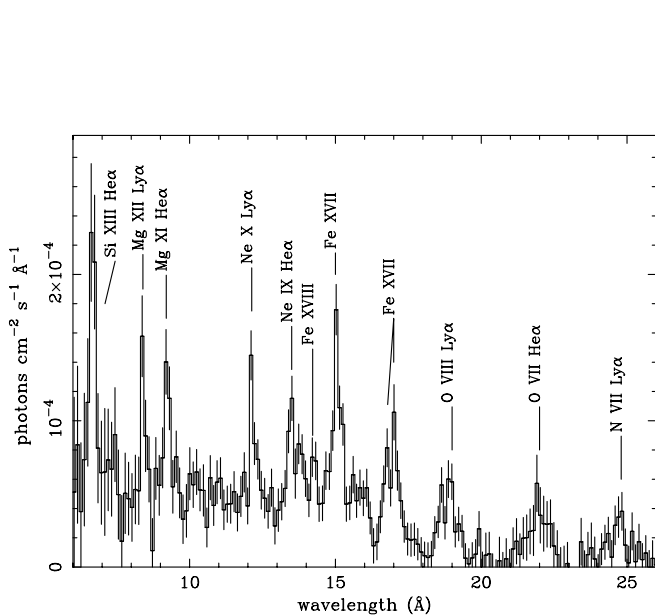


Fig. 3. XMM-Newton RGS spectrum of the bright nuclear area of NGC 253 covering nucleus and plume; bright emission lines are identified.

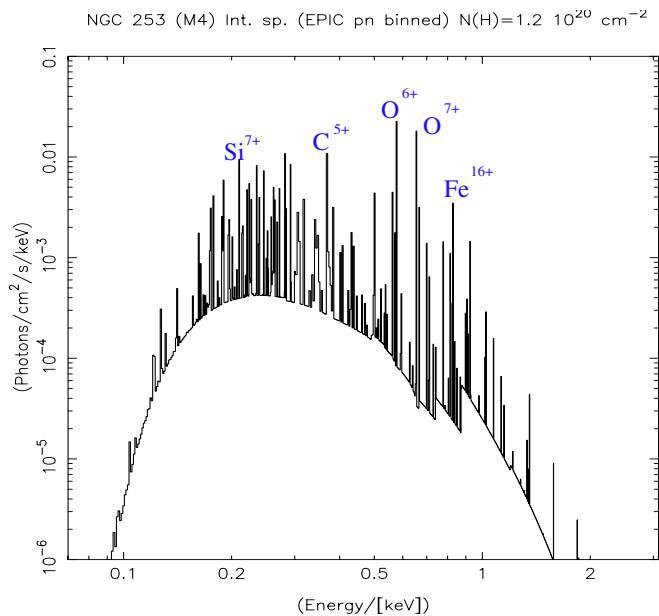


Fig. 4. Non-equilibrium outflow model spectrum (not folded through telescope and instrument), integrated over the whole NE halo region of NGC 253.

significant sample of galactic halos at larger distances, such as e.g. the starburst galaxy NGC 3079 (s. Fig. 6). At ~ 17 Mpc, a 2 arcsec resolution would correspond to ~ 170 pc, sufficient to study the outflow region, as recent CHANDRA observations have shown (Cecil et al. 2002), although, again, they suffered from the sensitivity limit below 0.5 keV and a reasonably large collecting area. XEUS would ideally combine arcsec resolution (to separate diffuse emission from point sources), i.e. a narrow PSF with narrow wings, with a high collecting power to ensure good photon statistics for spectral analysis. The XMM-Newton EPIC pn image of NGC 3079 obtained from the Guaranteed Time Program (Fig. 6) already shows a glimpse of an extended halo, but does not allow a detailed spectral analysis.

Thus the desiderata for instruments aboard XEUS to investigate galactic halos would be:

1. High sensitivity and throughput at low energies, down to 0.1 keV
2. Low internal (camera) background as well as low external (particle) background

3. No filter absorption edges near the diagnostic lines expected in the spectra (carbon, oxygen)
4. High spectral resolution (~ 2 eV) to accurately determine ratios of diagnostic lines, including different ionization stages of the same element (this would give abundance-independent information on CIE or NEI emission processes)
5. Large field-of-view to cover also background environment of galaxies.

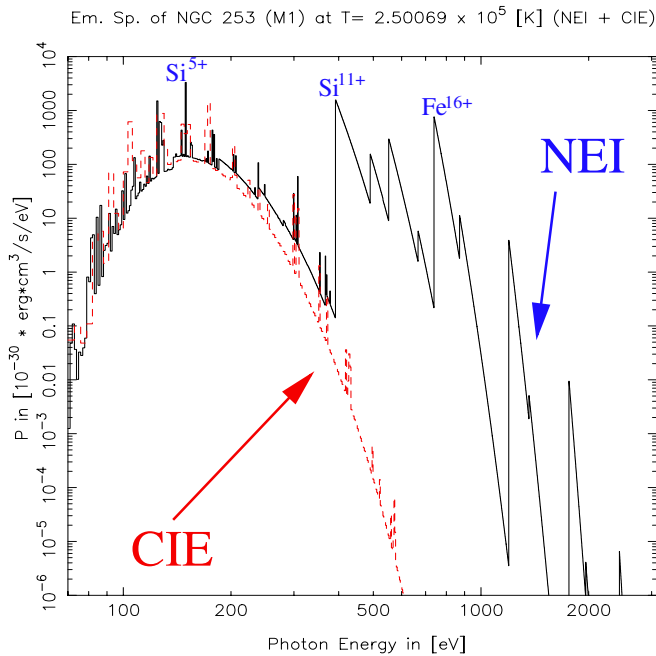


Fig. 5. *Intrinsic spectrum* of the outflow region in NGC 253 at a distance where the flow has cooled down to $T = 2.5 \times 10^5$ K. The effect of *delayed recombination* can be clearly seen since in the case of CIE there is hardly any emission above 0.6 keV, whereas in the NEI case, there is still recombination contributing up to 1.0 keV.

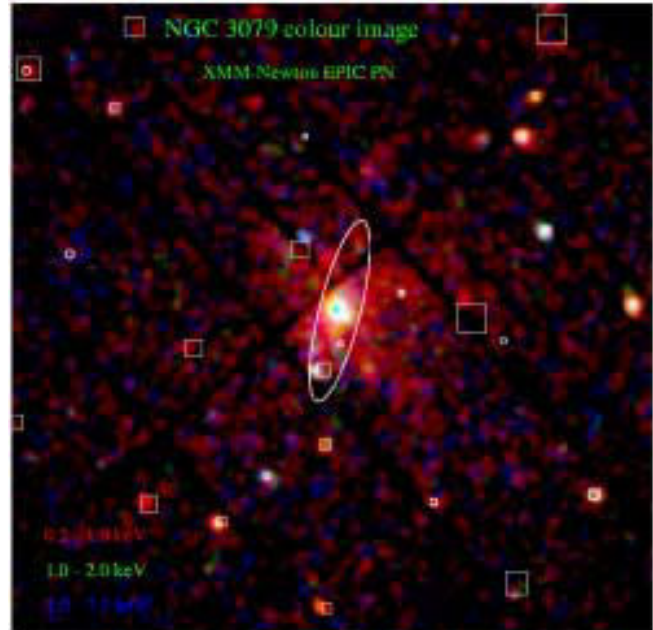


Fig. 6. NGC 3079 field, XMM-Newton EPIC pn only, red: 0.2 – 1.0 keV, green: 1.0 – 2.0 keV, blue: 2.0 – 7.2 keV, ROSAT PSPC sources indicated by squares, HRI sources by circles. The position of SN 2001ci is indicated by the blue cross north of the centre of NGC 3079.

References

- Bregman J.N., 1980, ApJ 236, 577
 Bregman J.N., Glassgold A.E., 1982, ApJ 263, 564
 Bregman J.N., Pildis R.A., ApJ 420, 570
 Breitschwerdt D., Freyberg M.J., 2002, A&A (in preparation)
 Breitschwerdt D., McKenzie J.F., Völk H.J., 1987, In: “Interstellar Magnetic Fields”, Springer, p. 131, eds. R. Beck, R. Gräve, Heidelberg
 Breitschwerdt D., Schmutzler T., 1994, Nature 371, 774
 Breitschwerdt D., Schmutzler T., 1999, A&A 347, 650
 Cecil G., Bland-Hawthorn J., Veilleux S., astro-ph/0205508
 Fabbiano G., 1989, ARA&A 27, 87
 Norman C.A., Ikeuchi S., 1989, ApJ 345, 372
 Pietsch W., Roberts T.P., Sako M., et al. 2001, A&A 365, L174
 Pietsch W., 2002, In: Proc. of the Symposium “New Visions of the X-ray Universe in the XMM-Newton and Chandra Era”, ESTEC, ESA SP-488, eds. F. Jansen et al. (in press)
 Spitzer L. jr., 1956, ApJ 124, 20
 Strickland D.K., Heckman T.M., Weaver K.M., Dahlem M., 2000, AJ 120, 2965
 Trümper J., 1983, Adv. Space Res., 2(4), 241
 Vogler A., Pietsch W., 1996, A&A 305, 74
 Wang Q.D., Walterbos R.A.M., Steakley M.F., Norman C.A., Braun R., 1995, ApJ 439, 176

Investigating the “missing baryon problem” with XEUS: Mapping and spectral analysis of the Galactic soft X-ray emission

M.J. Freyberg and D. Breitschwerdt

Max-Planck-Institut für extraterrestrische Physik, Giessenbachstraße 1, 85748 Garching, Germany

Abstract. The *X-ray Evolving Universe Spectroscopy* (XEUS) mission is primarily designed to study contents and structure of the primordial universe and thus to look back to redshifts of $z \sim 10$. To investigate this distant matter in the X-ray regime emission from the nearby universe has to be taken into account as a line-of-sight samples all emission and thus times from now until the early epochs. It is therefore necessary to have a handle on the thermal galactic emission components. Furthermore, higher energetic lines are redshifted into the “galactic” energy range and are thus blended. A successful XEUS mission therefore needs high spectral resolution at the low-energy band-pass.

Cosmological simulations predict that about 30 – 40% of the baryonic matter in the Universe should be heated to temperatures of $10^5 - 10^7$ K during structure formation to account for the discrepancy of baryons from observations between redshifts $z = 3$ and $z = 0$. Due to limiting sensitivity and spectral resolution of X-ray telescopes and detectors, no positive detections have been reported hitherto, and only crude upper limits for the contribution of a warm-hot intergalactic medium (WHIM) exist. The problem has been exacerbated due to recent deep pointed XMM-Newton and Chandra observations, in which more than 80% of the diffuse soft X-ray background has been resolved into point sources (mainly AGN) between 0.5 – 2 keV.

We show that the key to the determination of the WHIM contribution lies in the detailed mapping and spectral analysis of the galactic foreground and background emission. Our preliminary results from XMM-Newton EPIC shadowing experiments show that improved spectral resolution at the softest energies offers the unique possibility to disentangle diffuse emission components. Thus XEUS will be ideal for probing the diffuse galactic and intergalactic medium at increasing redshifts.

1. Introduction

The so-called “missing baryon” is as simple as it is puzzling and disturbing. Not only that we live in a universe which is dominated gravitationally by a dark matter component, but we are faced with the problem that luminous baryonic matter in the local universe is deficient by a large amount. Inventories of locally observed material (stars and gas in galaxies, and intergalactic gas in groups and clusters of galaxies) can only account for roughly 20 % of the baryons that have been observed at redshifts $z \geq 2$ in the form of diffuse photoionized intergalactic medium (IGM) as absorption lines in spectra of distant quasars. Even more surprising, these observations are in good agreement with the baryon content inferred from big bang nucleosynthesis models (Burles & Tytler 1998) so we are forced to admit that during structure formation, baryons seem to “disappear”. Cosmological hydrodynamical simulations (Cen & Ostriker 1999, Davé et al. 2001, Croft et al. 2001) offer an attractive explanation that during gravitational collapse cold gas is successively heated to temperatures of $10^5 - 10^7$ K forming a so-called widespread warm hot intergalactic medium (WHIM), which should account for 30 – 40 % of the baryons at $z \approx 0$, but which has so far escaped detection. The reason is twofold. Firstly, at the high energy end of the WHIM gas (i.e. above 1 keV), most of the X-ray background has been resolved into point sources (e.g. Hasinger et al. 2001), leaving little room for a substantial WHIM contribution. Secondly, in the lower energy range (0.1 – 1 keV) the X-ray flux is dominated by diffuse Galactic foreground emission.

The ROSAT PSPC All-Sky Survey has established the existence of *local* thermal emission but also a significant contribution from *beyond* the bulk of the absorbing neutral gas of our Galaxy (Snowden et al. 1995, 1997, 1998). The latter may be comprised of galactic halo emission but may also contain contributions from the WHIM. For its determination it is crucial to be able to perform a detailed mapping and spectral analysis of the galactic foreground

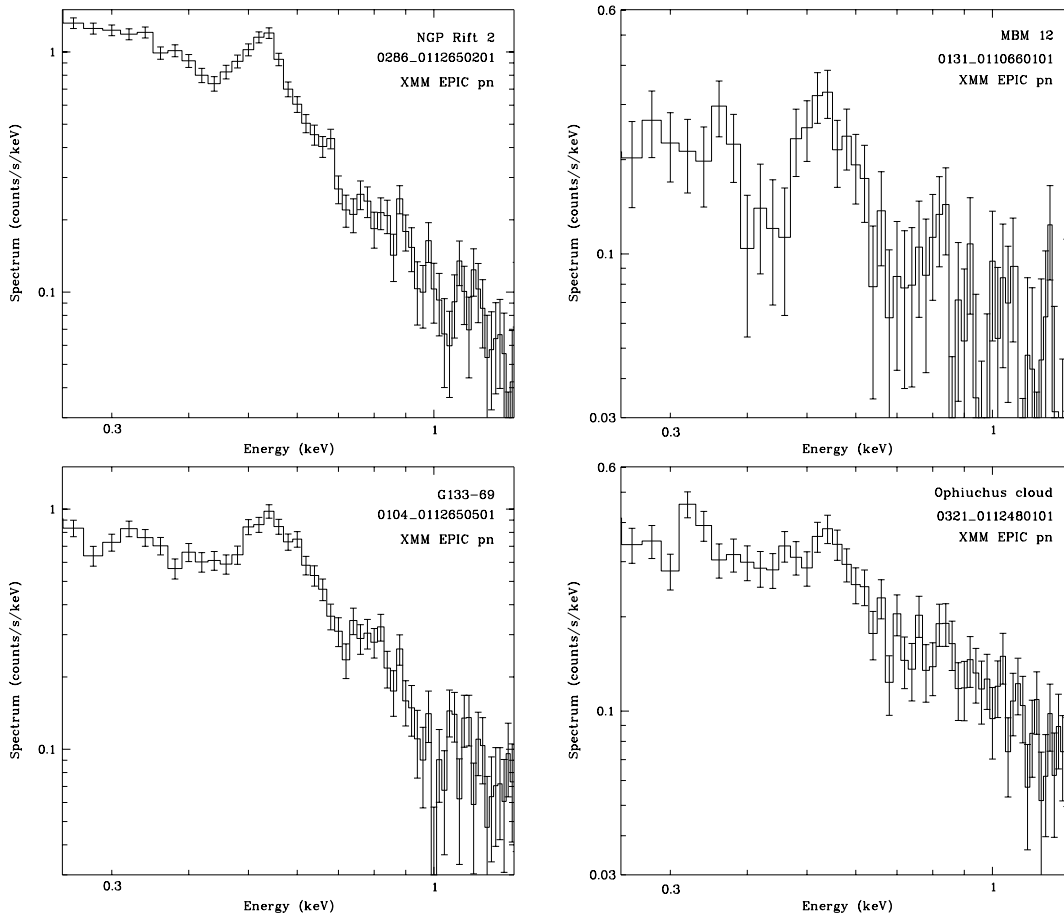


Fig. 1. XMM-Newton EPIC pn spectra taken at various sight lines through the local interstellar medium and the galactic halo. The internal instrumental background has already been subtracted. *Upper left:* North Galactic Pole Rift, *Lower left:* high galactic latitude absorption feature in the southern hemisphere, G133-69, *Upper right:* nearby molecular cloud MBM 12, *Lower right:* Ophiuchus molecular cloud. The spectra clearly show that galactic spectral features like O VII and O VIII lines strongly depend on the chosen direction. Any analysis of spatial variations beyond the Galactic halo requires therefore detailed knowledge of the foreground structures.

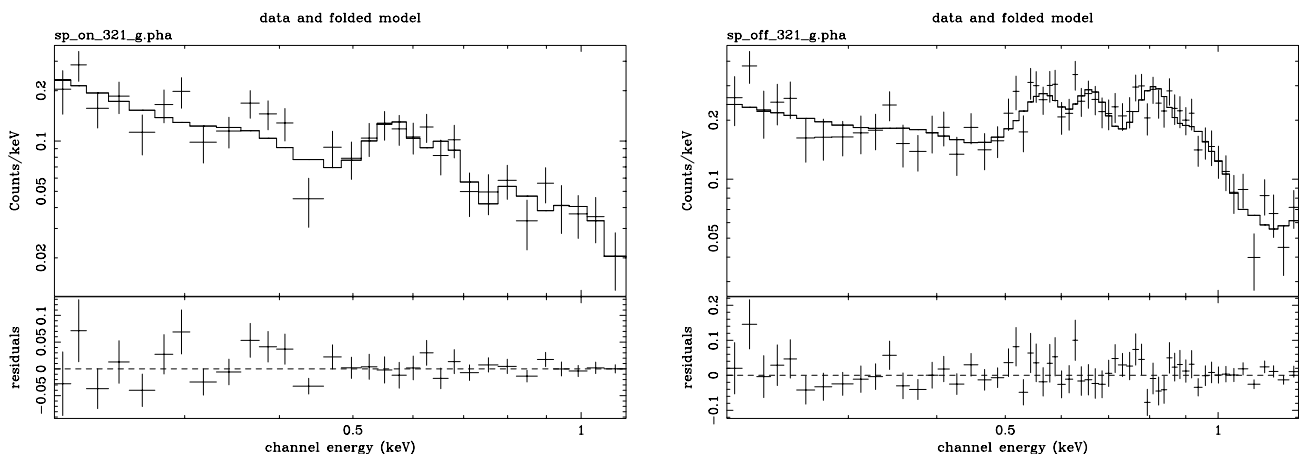


Fig. 2. XMM-Newton EPIC pn spectra of an *on-cloud* direction (*left*) and an *off-cloud* line-of-sight (*right*). The spectra are significantly different, e.g. the off-cloud direction samples much more of the Loop-I superbubble emission and appear to be hotter (e.g. strong iron lines) than the on-cloud gas. Moreover, a spectral analysis has indicated a complex temperature structure also in the case of the on-cloud emission which may be interpreted in terms of either non-equilibrium plasma models or by significant local excess emission in the 0.5 – 0.7 keV range.

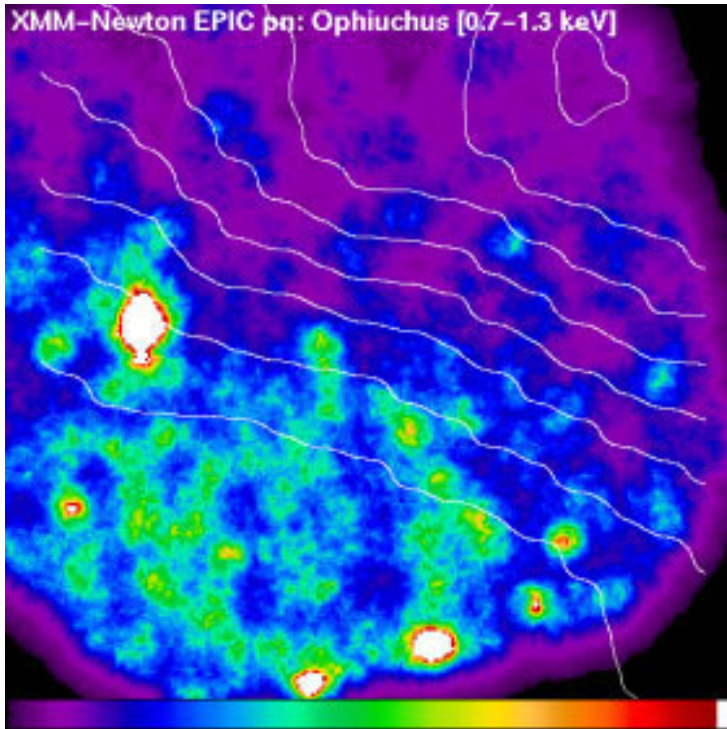


Fig. 3. XMM-Newton EPIC pn intensity image of the Ophiuchus molecular cloud region (located just outside Local Bubble in the Loop-I superbubble) in the energy band 0.7 – 1.3 keV. The white lines show the IRAS 100 μm contour lines, increasing from the lower left to the upper right, and show a clear anti-correlation of X-ray intensity (where blue indicates low, and red and white high intensity, respectively) and absorbing material (X-ray shadow).

and background emission. Moreover, this will not only tell us about cosmological implications but also reveal the origin and structure of the Local Bubble and the Galactic halo.

X-ray shadows cast by opaque molecular clouds at various distances have been used to constrain the three-dimensional emission distribution of soft X-rays on larger scales. However, the limited spectral resolution of the ROSAT PSPC instrument prevented the unique discrimination of foreground and background spectral parameters. Therefore higher spectral and spatial resolving capabilities are required to disentangle the emission components.

2. First XMM-Newton EPIC pn results

Studies of extended low-surface brightness objects need low internal camera background and low external particle and non-cosmic -X-ray background. While the ROSAT PSPC had an anti-coincidence rejection and a low-earth-orbit that reduced particle events the EPIC pn camera aboard XMM-Newton suffers from the eccentric orbit that exposes the instruments to the solar wind causing flare-like background enhancements and also internal X-rays in the camera. Using a proper spatial (Freyberg et al. 2002b) and spectral background subtraction (Freyberg et al. 2002a) along with careful time selection first promising results have been obtained (Freyberg & Breitschwerdt 2002).

Figure 1 gives (time-filtered and background-subtracted) spectra of observations pointing toward very different directions and thus sampling different contributions of the local interstellar medium and the galactic halo. On the left the North Galactic Pole Rift (top) and the ROSAT All-Sky Survey absorption feature G133-69 (bottom) show typical high-galactic latitude spectra, dominated by strong soft emission at 300 eV and O VII lines at ~ 560 eV. MBM 12 (top right) and the Ophiuchus Molecular Cloud are examples of close-by dense clouds that absorb most of the 0.5 keV emission from behind and can be used to determine the local contribution to X-ray spectra. The relative contribution of the O VII lines is similar as for the high-latitude fields, and there is still indication for O VIII line emission (~ 660 eV). Spectral modeling shows that a complex temperature structure is required to give satisfying fit results. Both MBM 12 and Ophiuchus need two equilibrium temperatures components for the foreground emission at about 0.09 and 0.14 keV, respectively.

Figure 2 illustrates the spectral difference between the Ophiuchus on-cloud (left) and off-cloud (right) directions in more detail. The spectra are clearly different: while most of the distant emission is blocked off in the on-cloud case this is also seen in the off-cloud spectrum. This is most evident at the strong Fe-L complex (~ 0.8 keV).

The spatial emission distribution is shown in Fig. 3 where the 0.7 – 1.3 keV EPIC pn image is overlaid with IRAS 100 μm contours and illustrates the anti-correlation with the absorbing material. This is the first example of an X-ray shadow detected with EPIC aboard XMM-Newton.

A detailed analysis of the spectral and spatial properties of this shadow will be presented elsewhere. The purpose of this paper is to demonstrate the local emission variations that have to be taken into account in any analysis of distant emission variations.

3. Scientific subjects and resulting instrumental requirements:

The XEUS observatory with its wide-field and narrow-field imagers is ideal to study the following highly important topics:

- Warm-Hot intergalactic medium (WHIM) line emission due to oxygen at 0.5 – 0.7 keV for $z = 0$, and at ~ 0.15 keV for $z \sim 3$
- Galactic local and halo emission in the $\sim 0.1 - 1.0$ keV energy band
- Galactic emission that exhibits strong *spatial* and *spectral* variations even within the EPIC field-of-view
- The three-dimensional structure of the diffuse emission from the nearest to the most distant contributions

To investigate these scientific highlights the following instrumental specifications should be available:

- A large collecting area in the 0.1 – 2 keV band to obtain enough statistics for spectral and spatial analysis for low surface brightness emission
- Low internal (camera) background as well as low external (particle) background to obtain an accurate zero-level for intensity variations
- No filter absorption edges near the most important lines expected in the spectra (0.3 keV, 0.57 keV, 0.66 keV), as well as high filter transmission at the lowest energies (for redshifts $z > 0$)
- High spatial resolution in order to detect and exclude point-like objects and to sample true variations
- Moderate time resolution is sufficient.

4. Conclusions

The discrepancy between the amount and distribution in the local and the distant universe is one of the most disturbing problems in modern astrophysics and needs to be resolved in the near future. The most direct way is to detect diffuse intergalactic line emission at low redshifts. With the expected performance of XEUS, characteristic OVII, OVIII and FeXVII lines of a WHIM filament at redshift of e.g. $z \sim 0.1$ should be clearly distinguishable from local foreground emission. Depending on the spatial distribution of the WHIM, the emission measure could be embarrassingly low. However, an upper limit of the WHIM to the baryon contribution could be obtained from a detailed study of the local foreground (Local Bubble and Galactic halo) emission, leaving the WHIM as the residual component. Thus the best targets for this study are clouds at different distances, including nearby objects inside the Local Bubble or very nearby, such as the Ophiuchus cloud. In particular, most valuable spectral information could be obtained by pointing at the regions of highest densities and those of the highest density *gradients*. The excellent spectral resolution of the XEUS instruments would also give us important additional information about the ionization state of the foreground plasma and whether it is out of collisional ionization equilibrium, as our XMM results already indicate.

References

- Burles S., Tytler D., 1998, ApJ 499, 699
 Cen R., Ostriker J.P., 1999, ApJ 514, 1
 Croft R.A.C., Di Matteo T., Davé R., et al., 2001, ApJ 557, 67
 Davé R., Cen R., Ostriker J.P., et al., 2001, ApJ 552, 473
 Freyberg M.J., Breitschwerdt D., 2002, In: Proc. of the Symposium “New Visions of the X-ray Universe in the XMM-Newton and Chandra Era”, ESTEC, ESA SP-488, eds. F. Jansen et al. (in press)
 Freyberg M.J., Briel U.G., Dennerl K., Haberl F., Hartner G., Kendziorra E., Kirsch M., 2002a, In: Proc. of the Symposium “New Visions of the X-ray Universe in the XMM-Newton and Chandra Era”, ESTEC, ESA SP-488, eds. F. Jansen et al. (in press)
 Freyberg M.J., Pfeffermann E., Briel U.G., 2002b, In: Proc. of the Symposium “New Visions of the X-ray Universe in the XMM-Newton and Chandra Era”, ESTEC, ESA SP-488, eds. F. Jansen et al. (in press)
 Hasinger G., Altieri B., Arnaud M., et al., 2001, A&A 365, L45
 Snowden S.L., Freyberg M.J., Plucinsky P.P., et al., 1995, ApJ 454, 643
 Snowden S.L., Egger R., Freyberg M.J., et al., 1997, ApJ 485, 125
 Snowden S.L., Egger R., Finkbeiner D.P., Freyberg M.J., Plucinsky P.P., 1998, ApJ 493, 715

X-ray polarimetry of AGN with X_{EU}S

D. Grupe¹ and B.J. Wills²

¹ Max-Planck-Institut für extraterrestrische Physik, Giessenbachstraße, 85740 Garching, Germany

² Astronomy Dept., Univ. of Texas, Austin, TX 78712, U.S.A.

Abstract. The geometry of AGN can potentially be probed by polarimetry, either as a means of observing a hidden nucleus by scattered light, or by understanding the role of dust and gas in the central engine environment. Polarimetry studies of AGN are well-established in optical and radio wavelength ranges. However, due to the small number of photons available in X-ray observations, polarimetry could not be applied so far in X-ray astronomy for large numbers of objects. This can be changed in the future by the X-ray mission X_{EU}S.

1. Introduction

It is generally accepted that AGN are all powered by the same type of engine: accretion of matter through an accretion disk onto a supermassive black hole. The questions arising from this model are, what matter fuels the engine, where does it come from and what does the structure of the inner region look like? The problem is that we cannot spatially resolve this region. We have to apply other methods that can answer these questions indirectly. Polarimetry and especially spectropolarimetry in combination with other observational techniques is a powerful tool to study the geometry of the inner region of an AGN.

Polarimetry is a unique technique that enables us to look even into the centers of obscured AGN by using the matter that scatters the photons as a mirror to study their intrinsic soft X-ray spectrum. We will be able to clarify the question of whether absorption is responsible for the X-ray variability in at least some AGN and what the location of the absorber is.

2. Polarimetry of IRAS 12397+3333

We have studied the polarimetric properties of all northern sources of our sample of bright soft X-ray selected AGN (Grupe et al. 1998). Two of these sources turned out to have degrees of polarization of more than 4% in B. One of these sources is the Seyfert 1.5 galaxy IRAS12397+3333. This example shows what is already possible in the optical and what will be possible in the future in X-rays. Figure 1 displays the results of the optical polarimetry of IRAS12397+3333. The upper panel shows the optical spectrum, the middle one the percentage of the polarization and the lower panel the spectrum of polarized flux density. The increasing degree of polarization towards the blue is a sign of scattering. The polarization is higher in the broad lines and lower in the narrow lines compared to the continuum which locates the absorbing material somewhere between the Broad and Narrow Line Regions (BLR and NLR).

3. How to perform X-ray Polarimetry

In principle there are two ways to do polarimetry in X-rays: 1) using a Bragg polarimeter in the light path, or 2) using the X-ray detector itself as a polarimeter. The first case is the more conventional case and will be used e.g. in the Stellar X-ray Polarimeter onboard the Spectrum-X-Gamma mission (SXP, see hea-www.harvard.edu/kaaret/sxp for more information). In the second case there are two options: a) using the dependence of the direction of the elongation of the electron cloud by the E-vector of the incoming X-ray photon inside the CCD detector or using a detector as suggested by Costa et al. (2001, and his contribution in these proceedings). The advantage of a rotating Bragg crystal polarimeter is that its use has been approved and this technique is available already. However, the disadvantage is that it puts more weight on the spacecraft and the rotating crystal is a mechanical part that can break during a long

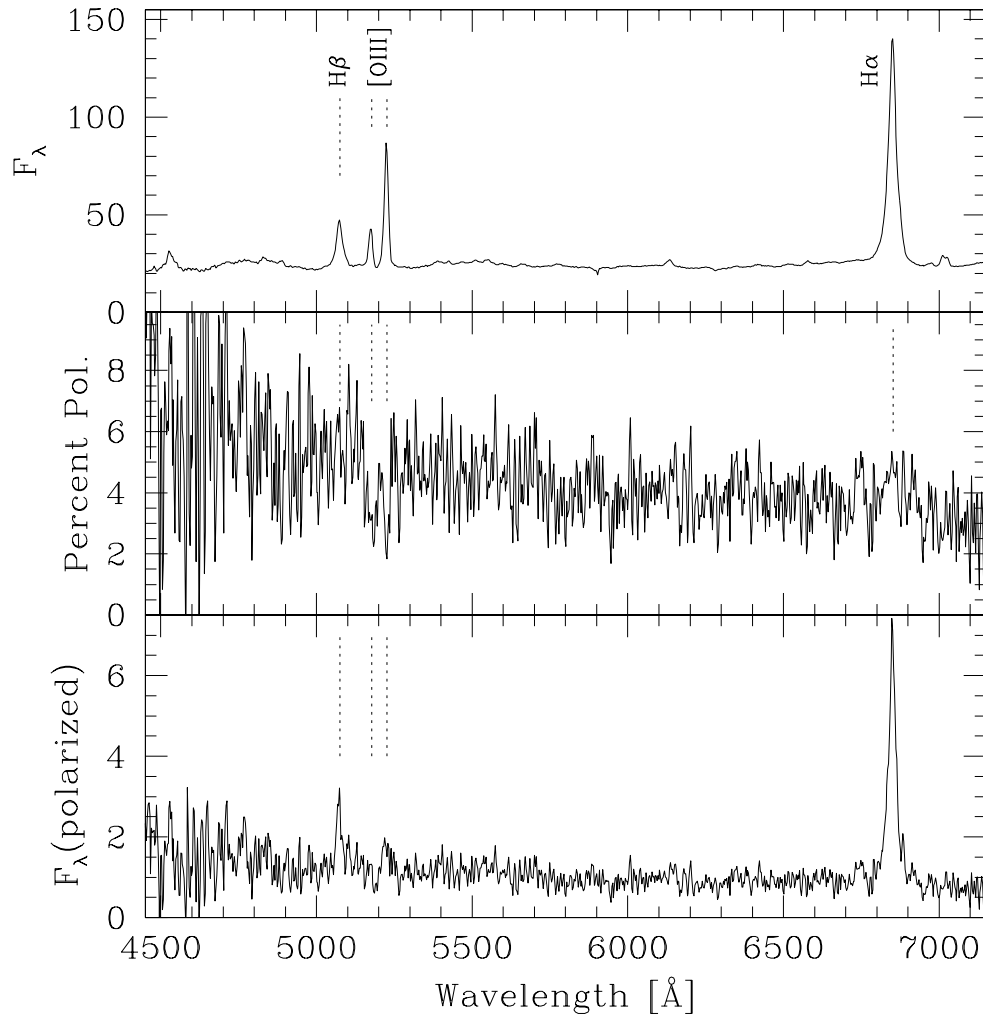


Fig. 1. Optical spectropolarimetry of IRAS 12397+3333. The upper panel shows the optical spectrum, the middle panel the percentage of the polarization, and the lower panel the polarized spectrum. We can clearly see that the degree of polarization increases towards shorter wavelength - a clear sign of scattering. We can also see that the degree of polarization is higher in the broad permitted lines and lower in the narrow forbidden lines. This result means that the absorbing matter is located somewhere between the Broad-Line Region (BLR) and Narrow-Line Regions (NLR).

mission. With a detector as the polarimeter the latter problem does not appear. Using a CCD detector itself as a polarimeter has the advantage that one does not need an additional detector and the good energy resolution can be used for moderate energy resolution spectropolarimetry. The problem is that the sizes of the CCD pixels have to be on the order of 1-2 μm . Studies of CCD detectors that can be used for polarimetry have been done e.g. at the solid state lab at the University of Leicester (www.src.le.ac.uk/solidstate/xraypoly.htm). Recently, Costa et al. (2001, and also his contribution in these proceedings) have proposed a micro pattern gas detector as a polarimeter e.g. onboard XEUS.

References

- Costa, E., Soffitta, P., Bellazzini, R., et al., 2001, *Nature* 411, 662
 Grupe, D., Wills, B.J., Wills, D., Beuermann, K., 1998, *A&A* 333, 827

The Compton-thick AGN in the GPS radio source OQ+208

M. Guainazzi¹, C. Stanghellini², and P. Grandi³

¹ XMM-Newton Science Operation Center, RSSD, ESA, VILSPA, Apartado 50727, E-28080 Madrid, Spain

² Istituto di Radioastronomia del CNR- CP 141 , I-96017 Noto, Italy

³ IAS/CNR - Via Fosso del Cavaliere 100, I-00133 Roma, Italy

Abstract. We report in this *paper* the ASCA discovery of the first (to our knowledge) radio-loud Active Galactic Nucleus (AGN) covered by a Compton-thick X-ray absorber, in the GigaHertz Peaked Spectrum radio source OQ+208. It represents one of the few available direct measurements of dense matter in the nuclear environment of this class of sources, which may provide the confining medium to the radio-emitting region if GPS sources are indeed "frustrated" classical radio doubles. The perspective of future studies with XEU_S are discussed.

1. Introduction

GigaHertz Peaked Spectrum radio sources are a class of powerful ($L_{radio} \sim 10^{45}$ erg s⁻¹) radio sources, defined by a simple convex spectrum peaking near 1 GHz. They represent $\simeq 10\%$ of the 5 GHz selected sources, *i.e.* a significant fraction of the powerful radio sources in the universe. They are characterized by compact radio cores, most likely not extending beyond the narrow-line regions (NLRs; ≤ 1 kpc). Some of them exhibit very faint extended radio emission on scales larger than the host galaxy (Baum et al. 1990; Stanghellini et al. 1990; Fanti et al. 2001), but rarely on Mpc scales (Schoenmakers et al. 1999). Their radio morphologies and host galaxies are generally consistent with classical 3CR doubles. Emission-lines optical spectra suggest interaction between the radio source and emission-line gas, as well as dust obscuration. Mid-IR measurements suggest the existence of a powerful hidden active nucleus (Heckman et al. 1994: see, however, de Vries et al. 1998 and Fanti et al. 2000 for a different point of view).

Two scenarios are currently proposed to explain the nature of GPS sources:

1. the *young scenario*: GPS could be young versions of large scale radio galaxies at an earlier stage of their formation (Carvalho 1985; Mutel & Philips 1988; Fanti et al. 1995; Readhead et al. 1996; O'Dea & Baum 1997). In this scenario, objects which are ~ 100 pc in size are about 10^4 years old, which is consistent with proper motion measurements on about 10 of them (Fanti 2000)
2. the *frustrated scenario*: GPS may represent "aborted" classical doubles, which will never reach their full maturity because they are embedded in a dense and turbulent medium, able to confine and trap the radio-emitting region on the scale-length of the NLRs (van Brueghel et al. 1984; O'Dea et al. 1991)

X-ray observations can provide an important contribution to elucidate the nature of this class of objects. In facts:

- measurements of hot gas, through its optically thin emission peaking in the soft X-rays, may provide indication for the presence of hot confining medium (O'Dea et al. 1996) . Constraints on the presence of such a gas phase from other wavelengths are not conclusive (Kameno et al. 2000; Marr et al. 2001)
- measurements of heavy X-ray absorption (in the most extreme case Compton-thick, $N_H > \sigma_T^{-1} \simeq 10^{24}$ cm⁻²) may indicate the presence of cold confining matter, to be compared with hydrodynamical models (De Young 1993; Carvalho 1994, 1998) to identify possible mechanisms responsible for the confinement of the jet
- the detection of large-scale X-ray jets may challenge one or more of our current assumptions on the nature of GPS sources (Siemiginowska et al. 2002)

The properties of the cold and hot phases, that one can derive from the X-ray spectral fitting may therefore provide a test for the "frustration" scenario.

Unfortunately, GPS sources are X-ray weak: only 3 out of 9 GPS sources observed in the soft X-rays have been detected. Hints that this low rate may be due to absorption were put forward by Elvis et al. (1994) and Zhang &

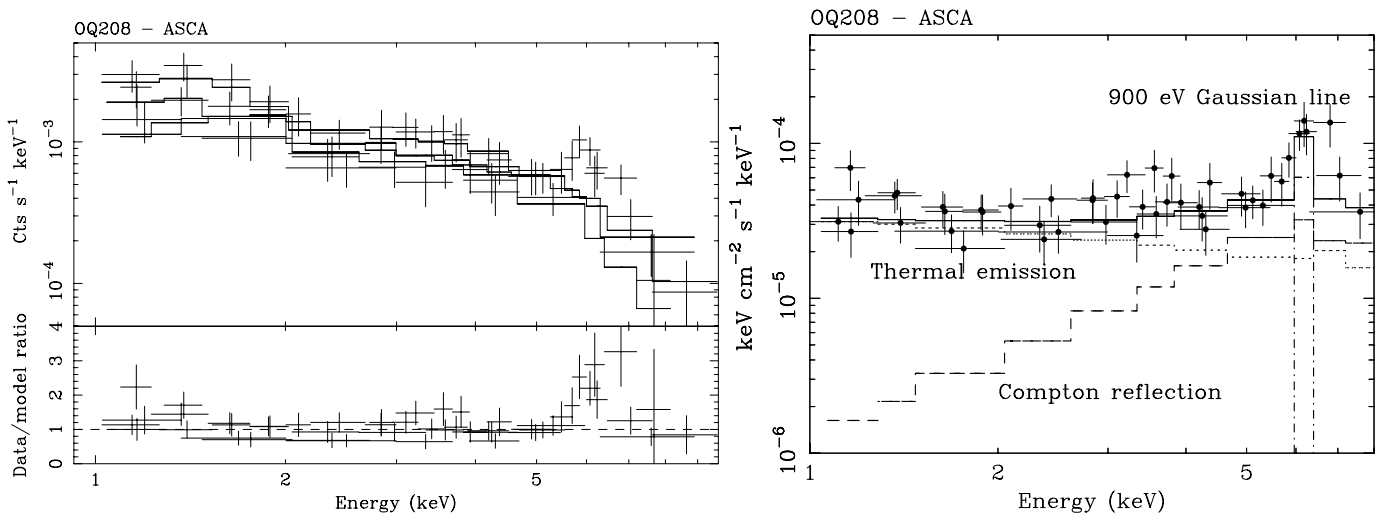


Fig. 1. *Left panel:* 1404+286 ASCA spectra (*upper panel*) and residuals in units of data/ratio models (*lower panel*) when a simple power-law model is applied. Photoelectric absorption column density due to our Galaxy ($N_H = 1.4 \times 10^{20} \text{ cm}^{-2}$) is assumed. *Right panel:* Unfolded best-fit model superimposed to the ASCA spectra of the same objects in the Compton-reflection plus thermal plasma scenario. The individual components are labeled

Marscher (1994). O’Dea et al. (1996) report the detection of a luminous ($L_X \sim 2 \times 10^{43} \text{ erg s}^{-1}$) and highly absorbed ($N_H \simeq 4 \times 10^{22} \text{ cm}^{-2}$) hard X-ray source in 1314+125 ($z = 0.122$). Siemiginowska et al. (2002) recently discovered with *Chandra* a prominent X-ray jet on scales $\sim 300h_{50}^{-1}$ in PKS 1127-145 ($z = 1.187$).

2. OQ+208: discovery of the first radio-loud Compton-thick AGN

We present in this paper results of the January 1999 ASCA observation of the GPS radio galaxy OQ+208 (1404+286; $z = 0.077$). The inverted X-ray spectrum (see Fig. 1; energy index $\alpha = -0.17 \pm 0.16$) and the remarkably strong (Equivalent Width, EW, $900 \pm 400 \text{ eV}$) K_α fluorescent neutral iron line ($E_{\text{centroid}} = 6.49 \pm 0.09 \text{ keV}$) are best explained if the X-ray emission is dominated by the Compton-reflection of an otherwise invisible continuum. The column density covering the AGN is likely to be as large as 10^{24} cm^{-2} . If this explanation is correct, 1404+286 would be *the first radio-loud Compton-thick AGN ever observed*. The alternative possibility of a Compton-thin absorber (still with $N_H \simeq 1.2 \times 10^{23} \text{ cm}^{-2}$) is equally viable from the statistical point of view, although in this scenario there is no clear explanation for the extreme intensity of the iron line (Leighly & Creighton 1993). In both cases, a soft excess below 3 keV is present, which can be explained as thermal emission from an optically thin hot gas, whose temperature is, however, loosely constrained ($T > 3.8 \times 10^7 \text{ K}$; cf. the right panel of Fig. 1). Again, the quality of the ASCA data is not good enough to rule out alternative explanations for the soft X-ray emission, as electron scattering of the primary nuclear emission. The observed fluxes are 0.7 and $5.5 \times 10^{-13} \text{ erg cm}^{-2} \text{ s}^{-1}$ in the 0.5–2 keV and 2–10 keV bands, respectively. They correspond to rest-frame unabsorbed luminosities of 1.7×10^{42} and $1.4 \times 10^{43} \text{ erg s}^{-1}$ in the same energy bands. However, if the bulk of the hard X-ray emission is indeed due to Compton-reflection, the true intrinsic 2–10 keV luminosity of 1404+286 is likely to be at least one order of magnitude higher (Guainazzi et al. 1999; Awaki et al. 2000).

Although the measurement of the iron line is robust, and points unambiguously to a reflection-dominated spectrum, the overall spectral deconvolution is still ambiguous. Time has been allocated for the XMM-Newton 2^o observational cycle (January–September 2003) to reobserve this target. The unprecedented collecting power of XMM-Newton in the hard X-rays (Jansen et al. 2001) will allow us to unambiguously characterize all the spectral components in this intriguing source.

3. The XEUS perspective

Only with XEUS one can get spectroscopic information on GPS sources at cosmological redshifts, where most of them are located (cf. Fig. 2). Simulations have been done, placing at redshift of $z = 1$ (Fig. 3; *upper* and *central* panels) and $z = 3$ (*lower* panels) the two GPS sources for which hard X-ray measurements are available (see above). An exposure time of 50 ks has been assumed throughout, and the CIS Superconducting Tunneling Junctions detectors response

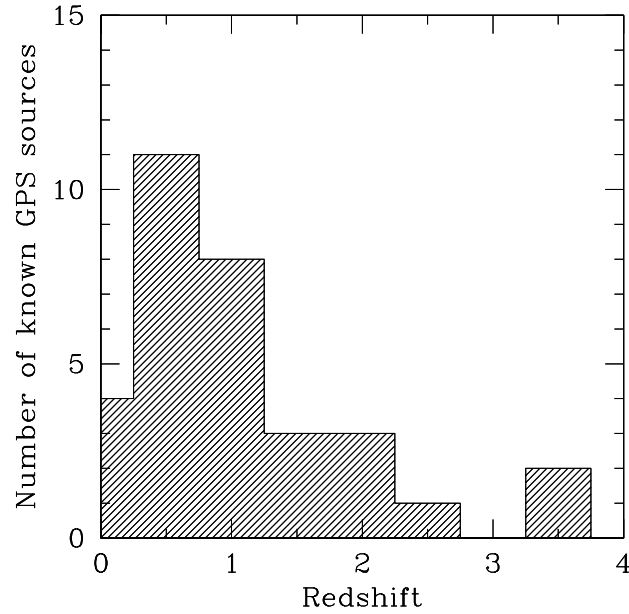


Fig. 2. Redshift distribution of the known GPS sources after O'Dea 1998.

matrices employed. In each spectral plot, the lower curve corresponds to the initial configuration, the upper curve corresponds to the final configuration one. The iso- χ^2 contours plots refer to the latter case.

References

- Awaki H., et al., 2000, ApJ, 542, 175
 Carvalho J.C., 1985, MNRAS, 215, 463
 Elvis M., et al., 1994, ApJ, 422, 60
 Fanti C., et al., 1985, A&A, 143, 292
 Fanti C., 2000, Proceedings of the 5th European VLBI Network Symposium, ISBN 91-631-0548-9
 Guainazzi M., et al., 1999, MNRAS, 310, 10
 Hatziminaoglou E., et al., 2001, ApJ, 547, 90
 Heckman T., et al., 1994, ApJ, 428, 65
 Jansen F., et al., 2001, A&A 365, L1
 Kamenno S., et al., 2000, PASJ, 52, 209
 Leahy D.A., Creighton J., 1993, MNRAS, 263, 314
 Marr P., et al., 2001, ApJ, 550, 160
 O'Dea C.P., et al., 1991, ApJ, 380, 66
 O'Dea C.P., et al., 1996, AJ, 111, 92
 O'Dea C.P. & Baum S.A., 1997, AJ, 113, 148
 O'Dea C.P., 1998, PASP, 110, 493
 O'Dea C.P., et al., 2000, AJ, 119, 478
 Readhead A.C.S., et al., 1996, 460, 612
 Schoenmakers A.P., et al., 1999, A&A, 341, 44
 Siemiginowska A., et al., 2002, ApJ, 570, 543
 Stanghellini C., et al., 1990, A&A, 233, 379
 van Brueghel W., Heckman T., Miley G., 1984, ApJ, 276, 79

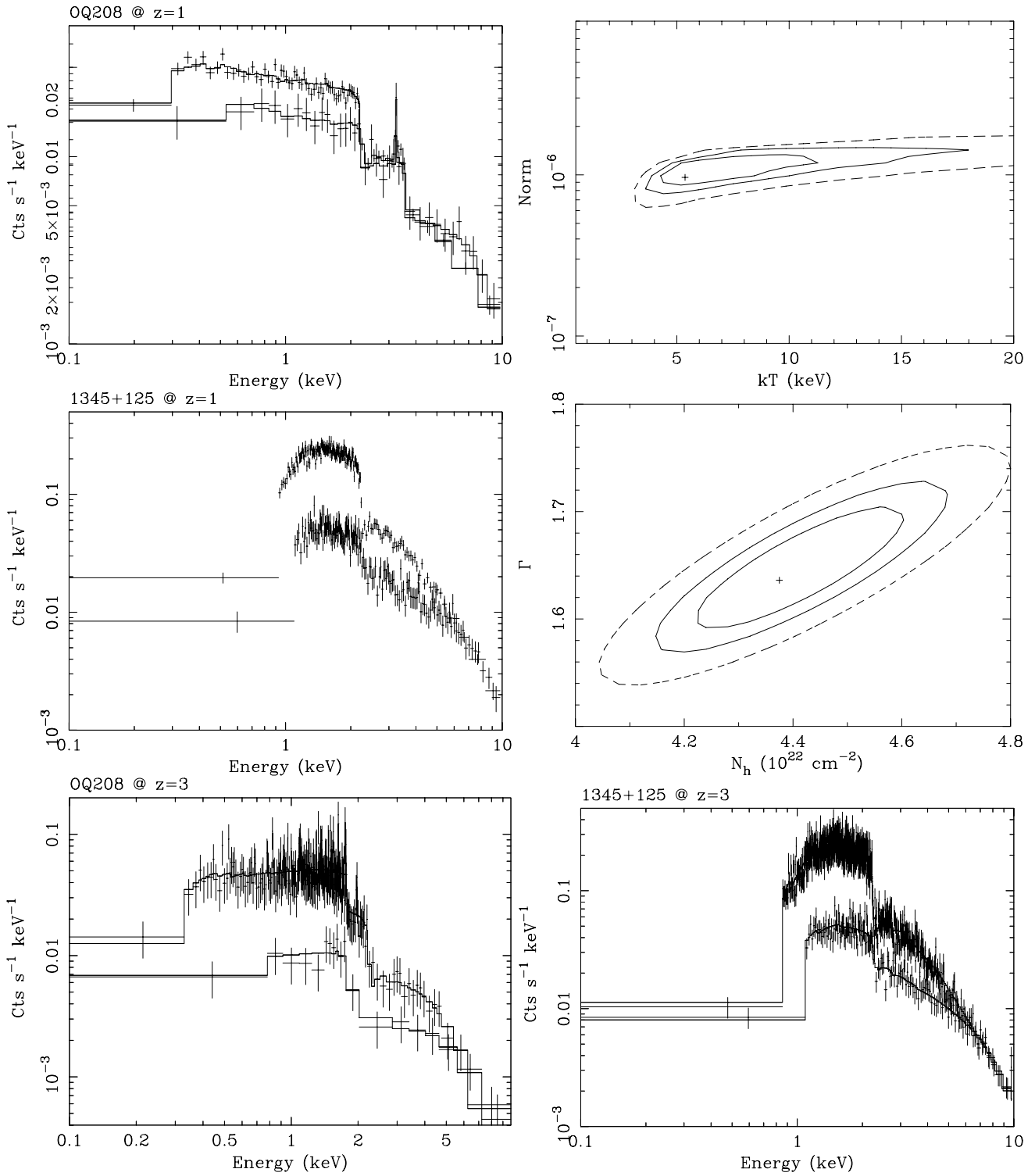


Fig. 3. XEUS simulation of GPS sources at cosmological redshifts. Details in text.

Light-weight X-ray optics for XEUS: alternative technologies

R. Hudec¹, L. Pína², A. Inneman³, V. Brožek⁴, P. Chráska⁵, K. Neufuss⁵, M. Zentková⁶, and A. Zentko⁶

¹ Astronomical Institute, Academy of Sciences of the Czech Republic, CZ-251 65 Ondřejov, Czech Republic

² Czech Technical University, Faculty of Nuclear Science, Prague, Czech Republic

³ Center for Advanced X-ray Technologies, Reflex s.r.o., Prague, Czech Republic

⁴ Institute of Chemical Technology, Prague, Czech Republic

⁵ Institute of Plasma Physics, Academy of Sciences of the Czech Republic, Prague, Czech Republic

⁶ Institute of Experimental Physics, Academy of Sciences of the Slovak Republic, Košice, Slovak Republic

Abstract. The XEUS mission requires very light-weight but large and precise X-ray mirror shells. Clearly, the developments of innovative techniques and approaches are necessary. We discuss the possible alternative techniques with focus on the technologies and experience available in the Czech Republic. They include light ceramics replication by plasma spraying as well as by CVD and PVD technologies, SiC, thin glass technology, improved electroforming, composites, as well as glossy metals.

1. Introduction

The future X-ray astrophysics missions such as the ESA's XEUS (Aschenbach et al. 2001) will require innovative technologies and approaches resulting in lighter mirror shells in order to achieve high sensitivity and high angular resolutions at a still reasonable weight of the mirror assembly.

Initiated by the expected participation in the ESA XEUS mission, we have started a wide collaboration among the Czech and Slovak scientific institutes in order to exploit the possibilities of the suitable alternative technology to recently widely used electroforming replication.

2. Glass

Glass has 4 times less volume density if compared with nickel in common use. Highly flat and highly smooth thin glass foils may serve in various future experiments. The recently developed advanced Lobster Eye X-ray optics modules (Hudec et al. 2002) are based on such gold-coated foils, only 100 microns thick, spaced at 300 microns. The recently developed mirror test assembly module (Fig. 1) is based on 50 30 x 30 cm gold-coated glass foils 0.75 mm thick, spaced at 12 mm, with possible thickness decrease up to 0.1 mm in future. The test array with curved foils has been also designed and developed and the study of innovative methods of shaping of glass foils to achieve the required geometry with high accuracy and stability is under way.

3. Composites

We have developed double-sided X-ray reflecting foils and flats of various thickness within the US - Czech Science and Technology Program. They are based either on a combination of composite and electroforming technologies, or on gold-coated composites, and exhibit a low weight and a very smooth surface. Analogous flats and foils may find applications in future X-ray optics experiments.

4. Ceramics

The recently available technologies such as the thermal spray deposition allow the ceramics materials to be considered as carriers or shell material of the X-ray mirrors. Their volume density may be up to four times less than electroformed nickel.

Plasma spraying belongs to the fast growing family of thermal spraying. It has been proved, that the water stabilised plasma (WSP) spraying is a complementary and useful method of thermal spray. Plasma units based on this principle,



Fig. 1. The optical tests (with the focal image) of the prototype of a segmented mirror assembly based on gold-coated 30 cm x 30 cm glass foils



Fig. 2. The test shells produced by plasma spraying (light ceramics replication)



Fig. 3. The plasma spraying facility at the Institute of Plasma Physics in Prague

produced by the IPP Prague, were successfully applied in several countries in Europe, in the USA and Japan. The high energy density and the high temperature result in a very high throughput, in some cases one order of magnitude higher than that for the gas stabilised systems. Therefore the best use of WSP is for large area coatings, for production of self-supporting or free-standing ceramic parts and for powder processing.

The recently available device allows to deposit tubes up to 1.65 m length and 0.5 m diameter. Also flats, plates, and shaped surfaces are possible. The spraying output is up to 40 kg Al₂O₃/hour and up to 100 kg metal/hour.

Plasma spraying can be used for the production of free-standing parts (FSP) such as required for future X-ray optics, with a large variety of shapes. Plates, tubes/shells, pipes, bowls, crucibles or specially shaped bodies can be sprayed from many different feedstocks, such as alumina, alumina based materials, mullite, zircon (and their combinations with alumina), garnet, basalt, etc. Cermet parts produced from ceramic and metallic powders, functionally graded

Table 1. The comparison of mechanical parameters of selected amorphous and crystalline metals and alloys

Material	Elast. lim. [kg/mm ²]	Tens. strength [kg/mm ²]	Young's mod. [kg/mm ²]	Cryst.Temp. [K]
Fe80P13C7 Amorphous	235	310	12 400	420
Fe72Cr8P13C7 Amorphous	342	385		
Fe72Ni8P13C7 Amorphous	210	270		410
Fe60Ni20P13C7 Amorphous	190	250		390
Fe40Ni40P14B6 Amorphous		175	14 700	
Fe32Ni36Cr14P12B6 Amorphous		195	14 700	
Ni49Fe29Al2P14B6 Amorphous		200	9 100	
Ni _{1-x} P _x Amorphous				~ 560
(Fe _{0.5} Ni _{0.5}) _{1-x} P _x Amorphous				~ 590
(Co _{0.5} Ni _{0.5}) _{1-x} P _x Amorphous				~ 620
Ni Crystalline		50	18 000	
Cu Crystalline	3	20	10 000	
Fe Crystalline	5	35	19 000	
Carbon steel	33	75	20 000	
Molybdenium Steel	60	150	22 000	

structures and sandwich” bodies consisting of ceramic/ metal/ ceramic layers have been deposited. From the materials already sprayed with the WSP, the fused basalt, garnet almandin, mullite, cordierite, steatite, wollastonite, Si, and AlSi (10) seem to be promising (due to low volume densities of 2 ... 3) for the production of X-ray optics carriers/shells.

Tests with replication of light ceramics layers (to produce free standing shells) have been carried out, with deposit thickness between 0.2 and 1.0 mm. Various materials including SiC, Al₂O₃, ZrSiO₄, TiB₂, MoSi₂, B₄C, Ti-TiN-TiO₂, Al₂O₃-13TiO₂, and mullite have been investigated and tested.

The mechanical strength was tested in compression on standard samples (0.785 cm² in area, 1.0 mm in thickness), while the pressure needed for destruction was registered. The mechanical resistance measured amounts to 60 ... ≥ 800 kPa depending on the sample material.

The roughness measurements has indicated that all the surfaces of replicated layers adjacent to the masters have the same roughness as the corresponding substrate.

The residual internal stresses in replicated layers have been also investigated. The excellent planar test replicated flats were produced by the deposition on Mo substrates and following separation at 970° C, all the residual stresses are then minimized and the resulting flat replica is undeformed.

5. Amorphous-glossy metals

The metallic amorphous alloys have very interesting physical properties. The principal mechanical parameters of some metallic amorphous alloys are summarised in the Table I. It can be seen from this table the huge differences between the crystalline pure elements and amorphous materials. Mechanical properties of amorphous alloys are comparable with those of high strength steel. As an example, the mechanical properties of amorphous Ni/Fe alloy are nearly four times better than those of crystalline Ni.

The amorphous metallic materials may be formed by different techniques such as

1. Rapid quenching of the melt. In this case a molten alloy is ejected onto the surface of a rotating roller and cooled immediately into a long ribbon. The obtained amorphous ribbons are up to 50 mm wide and about 50 microns thick. This technique is ideal for preparation of magnetic amorphous alloys, however for optical purposes is unsuitable (rough surface).

2. Mechanical alloying. In this case the powders of the required components are mixed together to give the starting composition. The mechanical alloying process is performed in a low energy ball mill rotated at a speed of about 120 rev/min. Stainless steel vials and balls are used. The obtained powder is amorphous, however for practical use must be pressed into pellets.

3. Electrodeposition. The preparation of amorphous metallic layers can be accomplished by an electrodeposition process. The following Ni containing amorphous layers were prepared: Ni_{1-x}P_x, (Fe_{0.5}Ni_{0.5})_{1-x}P_x, (Co_{0.5}Ni_{0.5})_{1-x}P_x, where x is from interval 0.13 up to 0.25. The layer thickness varies from 0.1 to 100 microns. In

special cases the samples were prepared by electrodeposition onto carefully polished copper tube, which was dissolved after preparation. The tube-shaped samples were 40 to 80 mm in length, about 6 mm in diameter, and about 0.3 mm in thickness. The structure and physical properties of the deposit depend sensitively on the rate of deposition, the temperature and the composition of the electrolyte. However, the addition of small amounts of certain inorganic or organic substances to electrolyte can profoundly affect the structure and the other properties of the electrodeposit. The great advantage of this method is the possibility of preparation of samples with a mirror-like surface determined primarily by the smoothness of the substrate. Besides this, the advantage of this method is also the possibility of preparation of the samples of special form (X-ray optics shells) and preparation of modulated multilayers.

6. Conclusion

There are several promising alternative methods to produce large precise and lightweight X-ray mirror shells for future X-ray astronomy satellite missions. The first prototypes and tests have indicated that the glass foils, double-sided composite flats, light ceramics as well as amorphous metal alloys are among the suitable techniques to be further exploited.

Acknowledgements. We appreciate the support provided by the Grant Agency of the Czech Republic, grant 102/99/1546 and by the Ministry of Industry and Trade of the Czech Republic, project FB-C3/29 "Centre of Advanced X-ray Technologies".

References

- Hudec R. 2002, this volume.
Aschenbach B. et al., 2001, ESA-SP 1253.





Large X-ray Optics: Lobster alternative

R. Hudec¹, L. Pína², and A. Inneman³

¹ Astronomical Institute, Academy of Sciences of the Czech Republic, CZ-251 65 Ondřejov, Czech Republic

² Czech Technical University, Faculty of Nuclear Science, Prague, Czech Republic

³ Center for Advanced X-ray Technologies, Reflex s.r.o., Prague, Czech Republic

Abstract. The Wolter 1 geometry suggested for the X_{EU}S X-ray telescope is the widely used one. The Wolter X-ray optics provides fine angular resolution, but on the other side, the field of view is rather limited, mostly by less than 1 degree. We discuss alternative arrangements which could provide much larger field of view. They focus on various modifications of the Lobster Eye X-ray optics. We discuss this alternative approach and show some examples and results obtained by Lobster Eye test prototypes. The astrophysical preferences of such solution are also addressed.

1. Introduction

The wide field X-ray optics discussed in this paper represents an analogy to the reflecting superposition eyes of shrimps and lobsters. The shrimps and lobsters have quite different eye structures if compared with other crustaceans and insects. While the insects exhibit optical elements from high refractive index structures behaving as two-lens telescopes, by contrast, the structures in shrimps eyes are square boxes made of more or less homogeneous jelly. Since this is hardly a good basis for any kind of known optical system, the shrimps were believed for a relatively long time that they could not see (Vogt, 2000). Vogt (1975, 1980) has first recognized that the jelly blobs of crayfish eyes were silvered, and that they were not lenses at all, but mirror boxes. Shortly afterwards the same mechanism was found in a decapod shrimp, and it now appears that this reflecting system is the rule throughout the long-body crustaceans - the shrimps, prawns, lobsters, crayfish and the anomuran squat lobsters.

It is evident that these eyes work as grazing incidence devices and that they provide very large fields of view, up to 180 degrees. These findings were described by Land (1978) and it was this paper published in Scientific American who lead to the notice of Angel (1978) who has recognized the great importance of this system for wide field X-ray imaging. The recent efforts to develop the real system for astrophysical applications are described and explained in this paper.

2. The wide field alternative

The Lobster-Eye wide field X-ray optics has been suggested in 70ies by Schmidt (Schmidt, 1975, orthogonal stacks of reflectors) and by Angel (Angel, 1979, array of square cells) but has not been constructed until recently. Up to 180 deg FOV may be achieved. This novel X-ray optics offers an excellent opportunity to achieve very wide fields of view (FOV, 1 000 square degrees and more) while the widely used classical Wolter grazing incidence mirrors are limited to roughly 1 deg FOV. Wide field X-ray telescopes with imaging optics are expected to represent an important tool in future space astronomy projects, especially those for deep monitoring and surveys in X-rays over a wide energy range.

Various Lobster-eye X-ray telescope prototypes have been finished. As an example, the medium-sized prototype of the Schmidt geometry represents one module and consists of two perpendicular arrays of double-sided X-ray reflecting flats (36 and 42 double-sided flats 100 x 80 mm each). The flats are 0.3 mm thick and gold-coated. The microroughness is below 1 nm. The focal distance is 400 mm from the midplane. The FOV of one module is about 6.5 degrees. More such modules may create an array with substantially larger FOV. The optical and X-ray tests have confirmed performance close to those calculated and expected (e.g. by ray tracing).

The Mini-Schmidt modules represent another an another example. These prototypes are based on 0.1 mm thick glass plates 23 x 23 mm, gold coated, spaced at 0.3 mm. 60 such plates are used for one module, the double focusing device is created by two such modules. The aperture/length ratio is 80, the reflecting surface microroughness amounts

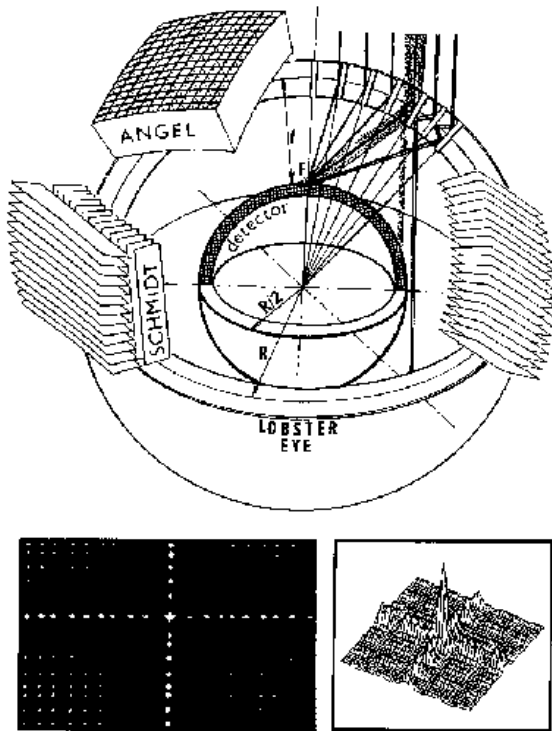


Fig. 1. The schematic arrangements of the Lobster-Eye X-ray optics of the Angel and Schmidt type. Below the focal image of the distant point-like source in optical light (left) and the calculated focal plane intensity distribution

to 0.2 - 0.5 nm. The FOV of the module is 2.5 deg. Recently, both large Lobster Schmidt modules (30 x 30 cm) as well as Micro Lobster Schmidt modules (3 x 3 mm) have been designed and developed.

For the alternative Angel geometry, numerous square cells of very small size (about 1x1 mm or less at lengths of order of tens of mm, i.e. with the size/length ratio of 30 and more) are to be produced. This demand can be also solved by modified innovative replication technology. The test modules with LE Angel cells have been successfully produced. First linear test module has 47 cells 2.5 x 2.5 mm, 120 mm long (i.e. size/length ratio of almost 50), surface microroughness 0.8 nm, $f = 1.3$ m. Second test module is represented by a L-shaped array of 2 x 18 = 36 cells of analogous dimension. The third test module with 6 x 6 = 36 cells is finished recently. The surface microroughness of the replicated reflecting surfaces is better than 1 nm. An innovative technique for production of 120 x 120 mm sized modules with large number of 3 x 3 mm cells, 120 mm long, is under development.

The various prototypes of lobster eye X-ray lenses of both the Schmidt as well as Angel geometries demonstrate the feasibility that the wide field telescopes may be constructed in the future based on this type of reflective X-ray optics.

The LE X-ray telescopes are extremely important since the discovery of X-ray afterglows of Gamma Ray Burst (GRBs) sources in 1997. Almost every GRB is accompanied by a X-ray afterglow. The expected rate of GRBs is 1 per day, however the theoretical prediction assumes larger beaming angle in X-rays if compared with gamma rays, hence the actual rate of X-ray afterglows is expected to be larger than the rate of GRBs. The calculated sensitivity of LE telescopes is sufficient enough to detect the recently discovered X-ray GRB afterglows. For pointed observations, limits better than $10^{-14} \text{ erg sec}^{-1} \text{ cm}^{-2}$ (0.5 - 3 keV) can be obtained ($10^{-12} \text{ erg sec}^{-1} \text{ cm}^{-2}$ for daily observations). The localization accuracy of the LE telescopes is of order of 1 arcmin, substantially exceeding the recent localization accuracy of most gamma ray instruments (2 deg and more). This is sufficient to localize the fading X-ray GRB counterpart to 1 arcmin or better, as well as obtain the light curve. It is hence obvious that the LE telescopes can provide a substantial contribution to the science and statistics of GRBs.

The additional science of LE X-ray telescopes includes various areas of X-ray astronomy and astrophysics such as supernova explosions, high energy binary sources, AGNs, blazars, X-ray novae, X-ray flares on stars, X-ray transients,

cataclysmic variables etc. The use of LE telescopes will allow these objects to be detected and studied by sky patrol monitoring.

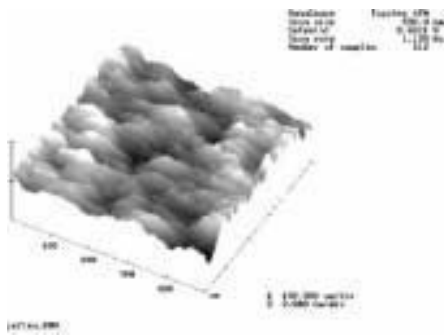


Fig. 2. The results of AFM measurements of the glass foils used in the LE telescopes: the measured microroughness rms amounts to 0.3 nm.

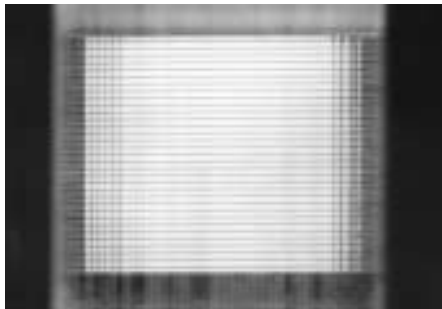


Fig. 3. The front view of the Mini-Schmidt Lobster module, 23 x 23 mm, with 100 micron thick gold-coated foils spaced by 300 microns

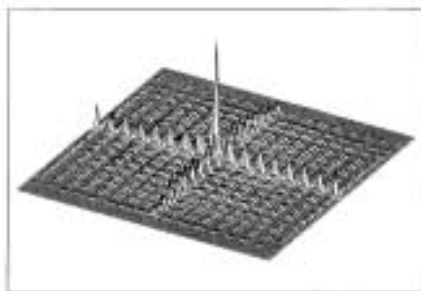


Fig. 4. The focal plane intensity distribution for the Schmidt LE prototype, 80 x 100 mm plates, detector area 40 x 40 mm, distant point like source, assumed microroughness 1 nm (computer ray-tracing).

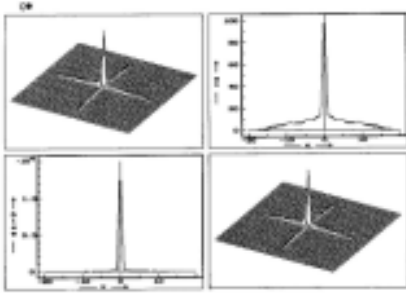


Fig. 5. Intensity distribution in the focal plane (15 x 15 mm detector) for the 23 x 23 mm Schmidt LE objective, mathematical ray tracing for the wavelength of 1 nm and microroughness of 1 nm.

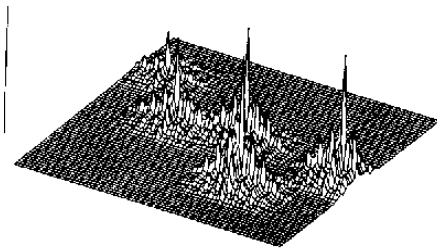


Fig. 6. The Cassiopeia constellation as seen by the Lobster Eye telescope (computer ray-tracing).

3. Discussion

The use of very wide field X-ray imaging systems could be without doubts very valuable for many areas of X-ray and gamma-ray astrophysics.

Results of analyses and simulations of lobster-eye X-ray telescopes have indicated that they will be able to monitor the X-ray sky at an unprecedented level of sensitivity, an order of magnitude better than any previous X-ray all-sky monitor. Limits as faint as $10^{-12} \text{ erg cm}^{-2} \text{ s}^{-1}$ for daily observation in soft X-ray range are expected to be achieved, allowing monitoring of all classes of X-ray sources, not only X-ray binaries, but also fainter classes such as AGNs, coronal sources, cataclysmic variables, as well as fast X-ray transients including gamma-ray bursts and the nearby type II supernovae. For pointed observations, limits better than $10^{-14} \text{ erg sec}^{-1} \text{ cm}^{-2}$ (0.5 to 3 keV) could be obtained, sufficient enough to detect X-ray afterglows of GRBs.

The various prototypes of both Schmidt as well as Angel arrangements have been produced and tested successfully for the first time, demonstrating the possibility to construct these lenses by innovative but feasible technologies. This makes the proposals for space projects with very wide field lobster eye optics possible.

The future steps toward the real lobster eye telescope for both Schmidt and Angel arrangements should be focussed to application of additional layers, to extent the energy range to higher energies, to further improve the surface quality (microroughness, slope errors), and to further improve the reflectivity and the angular resolution. The construction of larger or multiple modules to achieve a larger FOV of order of at least 1 000 square deg or more will be necessary as well as the further reduction of the cell apertures (Angel) and/or spacing and plate thickness (Schmidt) and to enhance the length/aperture ratios to achieve a better angular resolution.

Acknowledgements. We appreciate the support provided by the Grant Agency of the Czech Republic, grant 102/99/1546 and by the Ministry of Industry and Trade of the Czech Republic, project FB-C3/29 "Centre of Advanced X-ray Technologies".

References

Angel J. R. P. 1979, *Astroph. J.* 364, 233.

- Land M. F. 1978, *Sci. Am.* 239, 126
Land M. F. 2000, *Pure Appl. Opt.* 2, R44
Schmidt W. H. K. 1975, *Nucl. Instr. and Methods* 127, 285
Vogt K. 1975, *Z. Naturf.* 30, 691
Vogt K. 1980, *J. Comput. Physiol.* 135, 1



Theory of Compact Stars

M. Hanauske¹, D. Zschesche¹, U. Eichmann¹, L.M. Satarov^{1,2}, I.N. Mishustin^{1,2,3}, J. Schaffner-Bielich⁴,
H. Stöcker¹, and W. Greiner¹

¹ Institut für Theoretische Physik, J. W. Goethe-Universität, D-60054 Frankfurt, Germany

² The Kurchatov Institute, 123182 Moscow, Russia

³ The Niels Bohr Institute, DK-2100 Copenhagen O, Denmark

⁴ Department of Physics, Columbia University, 538 West 120th Street, New York, NY 10027, USA

Abstract. This article gives a short introduction into the theory of highly compact stellar objects. In addition to traditional neutron stars, we will introduce different types of compact objects, namely strange quark stars, hybrid stars and hypercompact hyperon stars. We show that the relation between mass and radius of compact stars depend sensitively on the equation of state (EoS). Properties of compact stars, detected with the planned XEUS detector will allow to determine the main features of the EoS realized in nature.

1. Introduction

Compact stars are composed out of the densest matter known in the universe. The observable properties of these stars strongly depend on the EoS of hadronic and quark matter, which yet is still poorly known. Some global properties of the EoS at high temperatures and moderate nuclear densities can be extracted from Heavy-Ion and High-Energy experiments. Present and planned terrestrial accelerator experiments will determine the EoS further. In this paper, the new perspective of determining the EoS uses astrophysical data of compact stars will be outlined. In the first section, the theoretical description of the interior of neutron stars within the chiral hadron $SU(3)$ model is presented. In the second section, the properties of strange quark stars within the Nambu–Jona-Lasinio model are discussed. In the third section, the theory of hybrid models with phase transitions are presented. The last section focuses on the possibility of determining the EoS with the planned XEUS detector.

2. Neutron Stars

If one restricts the consideration to weakly magnetized, equilibrated neutron stars, only two forces determine the behavior of the system, namely the strongest (QCD) and the weakest force (gravity).

Unfortunately QCD is not solvable in the nonperturbative regime and, up to now, numerical solutions of QCD on a finite space-time lattice are unable to describe neutron star matter or even finite nuclei or infinite nuclear matter [1]. As a consequence various effective models of hadronic interaction have been proposed [2, 3, 4, 5]. Especially the Walecka model and its nonlinear extensions have been quite successful and widely used for the description of hadronic matter and finite nuclei. These models are relativistic quantum field theories of baryons and mesons, but they do not consider essential features of QCD, like approximate $SU(3)_R \times SU(3)_L$ chiral symmetry or broken scale invariance. This has lead us to construct a QCD-motivated hadronic chiral $SU(3)_R \times SU(3)_L$ model (HCM) as an effective theory of strong interactions, which contains the main features of QCD. The model has been found to describe reasonably well the hadronic masses of the various $SU(3)$ multiplets and the properties of finite nuclei, hypernuclei and excited nuclear matter [4].

In this section, we present the composition and structure of neutron star matter with hyperons in this chirally invariant model. Energy density and pressure in the core follow from the Gibbs-Duhem relation, $\varepsilon = \Omega/V + \sum_{k=i,l} \mu_k \rho_k$ and $P = -\Omega/V$. At a given baryon density ρ_B , the field equations are obtained by extremizing Ω/V and are solved self-consistently in conjunction with the charge neutrality and β -equilibrium conditions (for details see [6]). We use the results of [7, 8] to describe the neutron star crust.

The metric $g_{\mu\nu}$ outside a nonrotating spherical symmetric neutron star is the well known Schwarzschild metric [9]. The inside solution of $g_{\mu\nu}$, can be determined by solving the Tolman-Oppenheimer-Volkoff equations (TOV) [11] with the corresponding EoS as input, assuming that the energy-momentum tensor $T_{\mu\nu}$ is that of an ideal fluid [10],

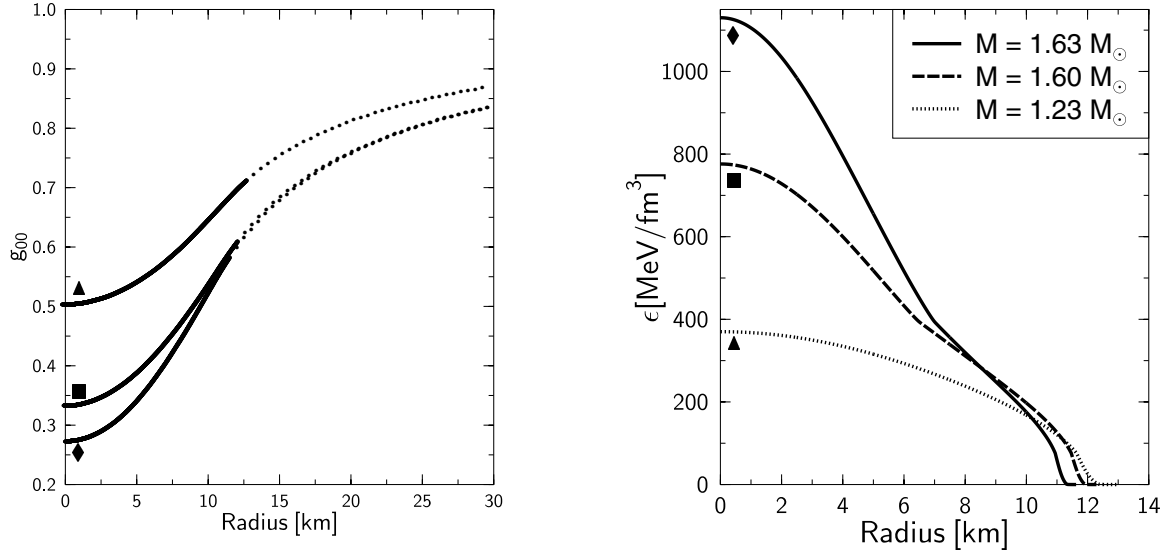


Fig. 1. a: Inside and outside solution of the metric component g_{00} for neutron stars having three different central energy densities (\blacklozenge , \blacksquare and \blacktriangle see Fig. 1b) calculated within the chiral model with hyperons. The solid curves represent the inside part calculated within the TOV equations, whereas the dotted curves are the outside solutions coming from the Schwarzschild metric. b: Energy density profiles $\epsilon(r)$ for three different central energy densities. The curve marked with the symbol \blacklozenge represents the star with the highest mass $M_{\max} = 1.63M_{\odot}$. The symbol \blacktriangle marks a star with a quite low central energy density, which does not contain any hyperons in the center of the star.

Figure 1a shows the metric component g_{00} as a function of the radius for three different central energy densities ($\epsilon_c^{\blacktriangle} = 370$ MeV/fm³, $\epsilon_c^{\blacksquare} = 780$ MeV/fm³, $\epsilon_c^{\blacklozenge} = 1130$ MeV/fm³) using the EoS as derived from the chiral model including hyperons [6].

The behavior of the energy density profiles is displayed in Fig. 1b, while the radii and masses of these stars can be seen in Fig. 2a.

The stars marked with the symbols \blacksquare and \blacklozenge have practically the same outside solutions of the metric $g_{\mu\nu}(r > R)$, because of their nearly identical masses ($M_{\blacksquare} = 1.60M_{\odot}$ and $M_{\blacklozenge} = 1.63M_{\odot}$). However, their inside metrics are quite different due to different energy density profiles.

Stars of higher masses or higher central densities than the most massive star \blacklozenge : ($M_{\max} = 1.63M_{\odot}$, $R_{M_{\max}} = 11.7$ km, $\rho_c^{M_{\max}} = 6.5\rho_0$) are not stable against radial oscillations and therefore will collapse to black holes [10, 12, 13]. In Fig. 1b the change in the slope of the energy density profiles at $\epsilon \cong 400$ MeV/fm³ is caused by the appearance of the hyperons Λ , Σ^- which softens the EoS considerably. From the present calculation using the HCM, we find that only the hyperons Λ , Σ^- , Ξ^- can be formed in neutron stars. The highest possible strangeness fraction is $f_S \approx 1/3$ for the most massive star (for details see Ref. [6]).

3. Strange Quark Stars

In contrast to neutron stars, (strange) quark stars are not composed out of hadronic matter. The interior of these stars consist of the fundamental fermionic particles of QCD, namely the quarks. The Nambu–Jona-Lasinio (NJL) model [14, 15], which is dealing with constituent quarks and respects chiral symmetry, is one of the most popular effective quark model. This model has been used to investigate the EoS of β -equilibrated matter appropriate for quark stars [16, 17, 19].

Below we use the SU(3)-flavour version of the NJL model proposed in [18]. We assume that the quark matter is in chemical equilibrium with respect to the strong and weak interactions. If neutrinos accompanying weak processes

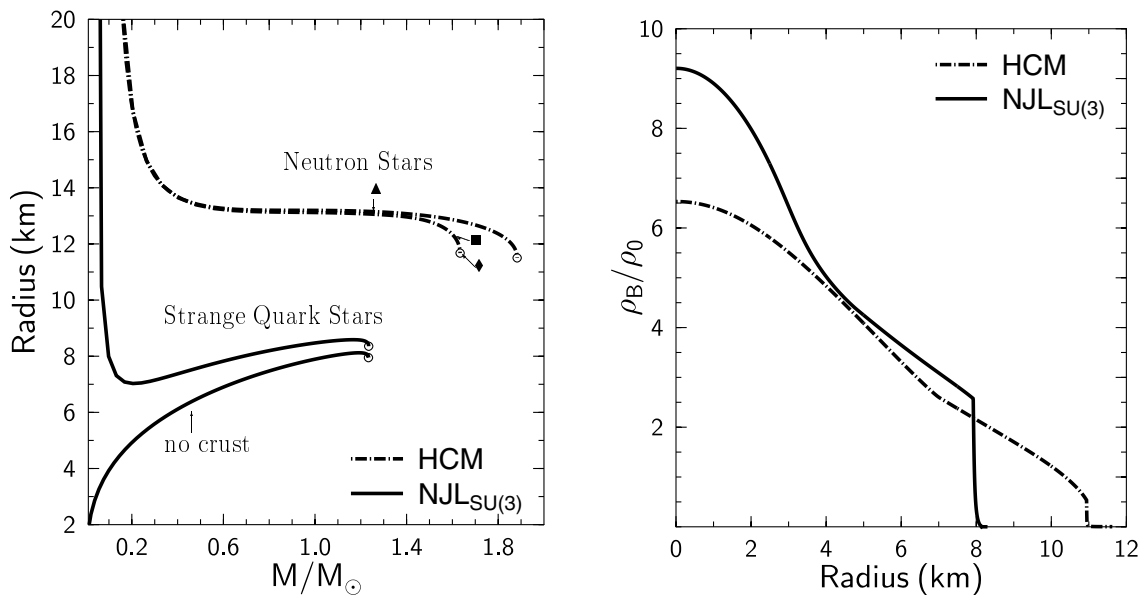


Fig. 2. a: The radius as a function of mass for neutron and strange quark stars. The neutron star curves with the lower value of M_{\max} represent calculation done within the HCM including hyperons; the arrows with \blacklozenge , \blacksquare and \blacktriangle represent the neutron stars marked in Fig. 1. The curve with the higher value of M_{\max} to the right of these curves shows the result when effects from hyperons are ignored. b: Baryon density profiles for the maximum-mass neutron and quark stars predicted by the HCM (with hyperons) and the NJL model.

escape freely ($\mu_\nu = 0$), one obtains the following conditions $\mu_d = \mu_s = \mu_u + \mu_e$ which relates the chemical potentials μ_i for u, d, and s-quarks and electrons (for details see Ref. [19]).

The calculated mass–radius relations are presented in Fig. 2a. The maximum mass of the strange quark star has a quite low value $M_{\max} = 1.23 M_\odot$ with a high central baryon density $\rho_c^{\max} = 9.2 \rho_0$ and a small radius $R_{(M_{\max})} \simeq 8.4$ km, which is typical for quark matter stars [12, 13]. Note, that the curves for self-bound quark matter start from the origin if they are naked, i.e. if there is no nuclear crust present.

Fig. 2b depicts the baryon density profiles $\rho_B(r)$ predicted by the NJL model as well as by the HCM (with hyperons). In both cases the results are shown for the respective maximum-mass star. The density of the quark star rapidly decreases at the star’s surface at a radius of $r \simeq 8$ km. The baryon density jumps from $\rho_B \simeq 2.6 \rho_0$ to a much lower value, the neutron-drip density with $\rho_B \simeq 10-3 \rho_0$, or to zero if the crust is neglected. The energy density profile of a maximum-mass star predicted by the HCM starts at a much lower central baryon density than that for a strange quark star, $\rho_c \simeq 6.5 \rho_0$, and extends smoothly towards the surface resulting in a somewhat larger radius.

4. Strange Compact Objects with Phase Transitions

In section 2 and 3, we have investigated pure hadronic and quark stars. The more realistic situation, where the outer layer of the compact star is hadron like and only the inner core of the star consists of deconfined quark matter, calls for the consistent inclusion of a quark-hadron phase transition [20]. Such hybrid models of the EoS can be formulated with the use of a Gibbs construction between the hadronic and quark model. From the outside to the inside, the resulting hybrid star structure is roughly as follows: The outer surface consists of a thin atmosphere and a typical neutron star crust; then one finds the hadronic matter regime with neutrons, protons, electrons and more to the inside also hyperons. Some kilometers below the surface where the density reaches 2–4 times normal nuclear matter the mixed phase region starts. At the beginning of the mixed phase, the first small bubbles of deconfined quark matter appears, whereas at its inner end only a few bubbles of hadronic matter remain. In between this widely extended (some

kilometers) mixed phase region geometrical structures of the matter (rods (like Spaghetti) and plates (like Lasagne)) appear, because of the balance of coulomb and surface energy [12, 13]. The inner nucleus of this hybrid star, where quark matter is more stable than hadronic matter, is composed out of purely deconfined charge neutral quark matter in β -equilibrium. However, the properties of such a hybrid star strongly depend on the used models for the hadronic and quark phase; even the existence of having a mixed phase between the hadron and quark phase is not certain [21].

Besides the quark-hadron phase transition, it is also possible that another type of phase transition takes place in compact stars, which is due to a highly attractive hyperon-hyperon interaction (for details see [22]). It was found that a hadronic EoS with hyperons allows for a first order phase transition to hyperonic matter. The signals for such a hadronic phase transition would be similar to the ones proposed for the deconfinement transition to quark matter. Such hyperon stars can have rather small radii of $R \sim 8$ km. Another possibility is the transition to Δ -matter, corresponding to the appearance of a density isomer in normal nuclear matter [23, 24].

5. Determining the EoS with X-Ray Detectors

In the foregoing sections, we have introduced different types of compact stellar objects in addition to neutron stars. The detection of compact stars with small radii combined with small masses ($M \approx M_{\odot}$ or below) will signal the existence of a novel form of matter, be it strange quark matter or hyperon matter. Recently, the radius of the isolated 'neutron (?)' star RX J185635-3754 has been extracted by various groups using X-ray data [25]. The radius for a black-body emitter turns out to be only $R_{\infty} := R/\sqrt{1 - 2GM/Rc^2} = 6$ km. Nevertheless, effects of an atmosphere can increase that value up to $R_{\infty} = 15 \pm 3$ km [25].

The knowledge of the radius and mass of various compact stars would help to determine the properties of the EoS favored by nature. The hope is that the amount of known compact stars will increase and that the accuracy of the extracted observational properties of these stars will be better. The X-ray Evolving Universe Spectroscopy Mission (XEUS) would be a major step into that direction.

Acknowledgements. We thank the Hessische Landesgraduiertenförderung, the DPG and the Gesellschaft für Schwerionenforschung for their support. JSB is supported by the U.S. Department of Energy under Contract No. DE-FG-02-93ER-40764. We also gratefully acknowledge the financial support of MPE giving us the opportunity to attend this workshop.

References

- J.D. Walecka, *Theoretical Nuclear and Subnuclear Physics* (Oxford University Press, New York, 1995).
 B.D. Serot and J.D. Walecka, *Adv. Nucl. Phys.* **16** (1986) 1.
 R.J. Furnstahl, C.E. Price, and G.E. Walker, *Phys. Rev. C* **36** (1987) 2590.
 P. Papazoglou, D. Zschesche, S. Schramm, J. Schaffner-Bielich, H. Stöcker, and W. Greiner, *Phys. Rev. C* **59** (1999) 411.
 S. Pal, M. Hanauske, I. Zakout, H. Stöcker, and W. Greiner, *Phys. Rev. C* **60**, 015802 (1999).
 M. Hanauske, D. Zschesche, S. Pal, S. Schramm, H. Stöcker, and W. Greiner, *Astrophys. J.* **537**, 958 (2000).
 G. Baym, C. Pethick, and P. Sutherland, *Astrophys. J.* **170**, 299 (1971).
 J. Negele and D. Vautherin, *Nucl. Phys.* **A207**, 298 (1973).
 K. Schwarzschild, *Sitzber. Deut. Akad. Wiss. Berlin, Kl. Math.-Phys. Tech.*, 189-196 (1916).
 C.W. Misner, K.S. Thorne and J.A. Wheeler, *Gravitation* W.H. Freeman and Company (San Francisco), 1973.
 J. R. Oppenheimer and G. M. Volkoff, *Phys. Rev.* **55**, 374 (1939).
 N.K. Glendenning, *Compact Stars* (Springer, New York, 1997).
 F. Weber, *Pulsars as Astrophysical Laboratories for Nuclear and Particle Physics* (IoP, Bristol, 1999).
 Y. Nambu and G. Jona-Lasinio, *Phys. Rev.* **122**, 345 (1961); **124**, 246 (1961).
 V.G. Vaks and A.I. Larkin, *Sov. J. JETP* **13**, 192 (1961).
 K. Schertler, S. Leupold, and J. Schaffner-Bielich, *Phys. Rev. C* **60**, 025801 (1999).
 A.W. Steiner, M. Prakash, and J.M. Lattimer, *Phys. Lett.* **B486**, 239 (2000).
 P. Rehberg, S.P. Klevansky, and J. Hüfner, *Phys. Rev. C* **53**, 410 (1996).
 M. Hanauske, L. M. Satarov, I. N. Mishustin, H. Stöcker, and W. Greiner, *Phys. Rev. D* **64**, 043005 (2001)
 N.K. Glendenning, *Phys. Rev. D* **46** (1992) 1274.
 M. Hanauske, A. Bhattacharyya, L. M. Satarov, I. N. Mishustin, H. Stöcker, and W. Greiner, (to appear soon on astro-ph)
 J. Schaffner-Bielich, M. Hanauske, H. Stöcker, W. Greiner astro-ph/0005490 (submitted to PRL)
 D. Zschesche, P. Papazoglou, S. Schramm, J. Schaffner-Bielich, H. Stöcker, W. Greiner *Phys. Rev. C* **63**, 025211 (2001)
 D. Zschesche, M. Hanauske, S. Schramm, H. Stöcker, and W. Greiner (in progress)
 F. M. Walter, *Astrophys. J.* **549**, 433 (2001); V. Burwitz, V. E. Zavlin, R. Neuhäuser, P. Predehl, J. Trümper, A. C. Brinkman, *Astron. Astrophys.* **379**, L35-L38 (2001); J. A. Pons, F. M. Walter, J. M. Lattimer, M. Prakash, R. Neuhäuser and P. An, *Astrophys. J.* **564**, 981 (2002); D. L. Kaplan, M. H. van Kerkwijk, J. Anderson, astro-ph/011117 (2001); J. J. Drake et al., astro-ph/0204159 (2002); F. M. Walter and J. M. Lattimer, astro-ph/0204199 (2002).

The population of X-ray binaries and background AGN in the field of the Large Magellanic Cloud

P. Kahabka¹

Sternwarte, Universität Bonn, Auf dem Hügel 71, 53121 Bonn, Germany

Abstract. A sample of ~ 30 (candidate) X-ray binaries and ~ 140 (candidate) background AGN in the LMC field was derived from the *ROSAT* PSPC survey and has been discussed in Kahabka (2002). A $\log N - \log S$ analysis of background sources in the LMC field with more than 50 observed counts has been performed by Kahabka et al. (2002). Here a summary of the X-ray binary and background AGN sample is given taking a few new identifications into account. The catalog of 50 X-ray sources with unabsorbed fluxes (0.5 – 2.0 keV) in excess of $1.4 \cdot 10^{-14}$ erg cm⁻² s⁻¹ and used for the $\log N - \log S$ analysis in the LMC field is given. Consideration of obscuration by dark absorbing clouds of 15% of the LMC field used for the $\log N - \log S$ analysis gives consistency between the observed $\log N - \log S$ and the theoretical $\log N - \log S$ of background sources (Gilli et al. 2001). The estimated mass associated with these clouds is $\sim 5 \cdot 10^7 M_{\odot}$, consistent with the total mass of molecular clouds in the LMC inferred from CO surveys.

1. Introduction

Recent X-ray surveys of several near-by galaxies with *ROSAT*, *Chandra*, and *XMM-Newton* have revealed a large number of point-like X-ray sources. Most of these sources are associated with these galaxies and are either high-mass X-ray binaries (HMXB) or low-mass X-ray binaries (LMXB). The evolutionary ages of HMXB and LMXB are different ($\lesssim 10^7$ yr and $(5 - 15) \cdot 10^9$ yr respectively, cf. van den Heuvel 1994) and thus HMXB and LMXB are preferentially found in galaxies of different age and Hubble type (HMXB in late-type spiral galaxies and LMXB in early-type elliptical galaxies). Recent deep surveys of near-by spiral and elliptical galaxies with *Chandra* have confirmed this picture (cf. Pence et al. 2001 for M101, Swartz et al. 2002 for M81, Irwin et al. 2002 for NGC 1291, Sarazin et al. 2000; 2001 for NGC 4697, and Finoguenov & Jones 2002 for M 84). As HMXB descend from massive progenitor stars they are still found close to the site of their formation (the spiral arms in spiral galaxies). The number of observed background AGN can be derived from the $\log N - \log S$ of background sources (cf. Hasinger et al. 1998; Gilli et al. 2001).

The LMC is a late-type irregular galaxy which is presently at a distance of ~ 50 kpc to the Milky Way and thus suited for a detailed study of the X-ray source populations.

2. X-ray binaries

Recent X-ray surveys of the Small and the Large Magellanic Cloud with *ROSAT*, *ASCA*, *RXTE* and *XMM-Newton* have revealed a large number of Be-type X-ray binaries associated with these galaxies (cf. Yokogawa et al. 2000; 2002 and Haberl & Sasaki 2000 for the SMC and Haberl & Pietsch 1999b, hereafter HP99, for the LMC). The presence of this young stellar population has been explained by a recent epoch of enhanced star formation (cf. Yokogawa et al. 2002). The sample of (candidate) X-ray binaries in the LMC has e.g. been discussed by Haberl & Pietsch (1999b), Negueruela & Coe (2002), and Kahabka (2002, hereafter Paper II).

Optical identifications exist for 15 X-ray binaries (cf. Negueruela & Coe 2002, cf. Tab.1) and there are further 18 candidate X-ray binaries which have not yet been optically identified. In Paper II X-ray color-color diagrams have been used to classify spectrally hard sources as X-ray binaries or background AGN (see also Kahabka et al. 2001). But a few of these classifications are insecure as X-ray binaries can have as steep powerlaw spectra as AGN. One source, RX J0530.1-6551 (HP 183), already classified in Paper II as an X-ray binary, has also been classified by Haberl (2002) as an X-ray binary from the hard powerlaw spectral index derived from *XMM-Newton* observations.

It is of interest to compare the number of X-ray binaries in the LMC with those found in the Small Magellanic Cloud as there may have been a recent close encounter of both galaxies which may have triggered star formation in

Table 1. Optically identified X-ray binaries in the LMC field. Column (1) gives the *ROSAT* source name, column (2) the *Einstein* source name, column (3) the *ROSAT PSPC* catalog index of HP99, column (4) the *ROSAT HRI* catalog index of SHP00, column (6) the V magnitude, column (7) the spectral type, column (8) the orbital period, column (9) the pulse period, column (10) the identification, and column (11) references.

(1) Source	(2) Ein	(3) HP	(4) SHP	(5) LMC	(6) V	(7) Sp	(8) P_{orb}	(9) P_{puls}	(10) Identification	(11) Ref.
J0538.9-6405		41	306	X-3	16.5–17.3	B2.5V	1.7 d		BH candidate (HMXB)	a
J0531.5-6518		106			16.0	B2V			HMXB	
J0532.5-6551		184			13.1	B0II			Sk-65 66 (HMXB)	a,b,c
J0529.8-6556		204			14.8	B0.5V		69.5 s	GSC 8891.0213 (HMXB, Be/X trans)	a,c,d
J0532.8-6622		316	239	X-4	14.0	O8III	1.4 d	13.5 s	HMXB	
J0502.9-6626	CAL E	331			14.3	B0V		4.06 s	[W636b]564 (HMXB, Be/X trans)	a,e,f
J0535.6-6651		436			14.8	B0.5III	16.6 d (?)	69 ms	AO538-66 (HMXB, Be/X trans)	a
J0535.0-6700		462			14.9	B0V	241 d (?)		RGC 28 (HMXB)	a,c
J0520.5-6932		946			14.4	O9V	24.5 d		HMXB	a,e,d
J0539.6-6944		1001	311	X-1	14.5	O8III	4.2 d (?)		BH candidate (HMXB)	e
J0544.1-7100		1225	364		15.3	B0-B1		96 s	1SAX J0544.1-710 (HMXB)	d
J0520.4-7157		1325		X-2	18–19		8.16 h (?)		LMXB	g,h
J0501.6-7034	CAL 9				14.5	B0V			HV 2289	a,c
EXO 0531.1-6609						B0.7V	24.5 d	13.7 s	HMXB, Be/X transient	a
H 0544-665					15.5	B0V			HMXB, Be/X transient	a

Ref.: (a) Negueruela & Coe 2002; (b) Haberl, Pietsch, & Dennerl 1995; (c) Liu et al. 2000; (d) Haberl et al. 1997; (e) Haberl & Pietsch 1999b; (f) Schmidtke et al. 1995; (g) Smale & Kuulkers 2002; (h) Liu et al. 2001.

both galaxies. In Paper II it has been found that the number of HMXB (with luminosities in excess of 10^{36} erg s $^{-1}$) found in both galaxies is comparable. The total mass of both galaxies differs by a factor of 10, but the gas mass is comparable. The star formation rate (and the number of HMXB) scales with the gas mass of a galaxy.

3. Background AGN

The majority of the spectrally hard X-ray sources detected during deep *ROSAT PSPC* observations of the field of the LMC are (candidate) background AGN. These background AGN can be used to construct the $\log N - \log S$ function in the LMC field and to compare with the $\log N - \log S$ of the soft extragalactic X-ray background derived in other fields of the sky. From this comparison constraints can be derived for the amount of intervening absorbing gas (associated with the Galaxy and the LMC). In Paper II a sample of ~ 140 (candidate) background AGN has been derived in the LMC field from classification in an X-ray color-color diagram. 50 of these AGN have more than 50 observed counts and have been used for a $\log N - \log S$ analysis (cf. Tab. 2). It has been found that the observed $\log N - \log S$ corrected for incompleteness due to the *ROSAT PSPC* exposure and absorption due to intervening galactic and LMC gas closely matches the theoretical $\log N - \log S$ of Gilli et al. (2001) derived to reproduce the soft extragalactic X-ray background (cf. Hasinger et al. 1998). But there remained some deficiency of the observed $\log N - \log S$ with respect to the theoretical $\log N - \log S$ for which three likely effects have been proposed: (a) incompleteness of the selected AGN sample, (b) deviation of the theoretical $\log N - \log S$ in the LMC field from a mean $\log N - \log S$ derived in other fields of the sky and (c) gas additional to the H I (galactic and LMC) measured with the *Parke*s telescope. Kahabka et al. (2002, hereafter Paper III) have discussed the likely contribution of these effects to explain the observed deficiency.

4. Addition

An option which is closely related to (a) will be discussed here: Some of the classified X-ray binaries are indeed background AGN. At least one source which has been classified as an X-ray binary coincides with an background AGN. The source RX J0507.6-6847 (with catalog index 727 of HP99, cf. Chu, et al 2000) has been found from *Chandra* observations to coincide with the background quasar OGLE 050736.52-684751.7 (Dobrzycki et al. 2002). The source has more than 50 observed counts and has to be included in the $\log N - \log S$ analysis. Consideration of RX J0507.6-6847 in the $\log N - \log S$ analysis does not qualitatively change the result. An additional quasar, OGLE 050833.29-685427.5, identified in the *Chandra* observations with a *ROSAT* source, RX J0508.5-6854, is contained in our sample of background sources used for the $\log N - \log S$ analysis (cf. Tab. 2).

In order to search for additional background sources (with more than 50 observed counts) which have been classified as X-ray binaries and which may be background AGN and contribute to the $\log N - \log S$ we considered all classifications for X-ray binaries which have no optical identification. There are two additional sources, RX J0532.4-6536 (HP 137),

Table 2. Sample of (candidate) background X-ray sources (AGN) in the LMC field with more than 50 observed counts which have been used for the $\log N - \log S$ analysis (cf. Paper III). The source coordinates, Column (2) and (3), and the 90% confidence error radius, Column (4), are from HP99. The flux (0.5 – 2.0 keV) in units of 10^{-14} erg cm $^{-2}$ s $^{-1}$ (for $N_{\text{H}} = N_{\text{HI}}$) is given in Column (5). The hardness ratios, Column (6) and (7), and the source classification, Column (9), are from Paper II.

(1)	(2)	(3)	(4)	(5)	(6)	(7)	(8)	(9)	(10)
Source	R.A.	Decl.	P_{err}	f_{X}	HR1	HR2	HP	Class	Remarks
Name.	(J2000) (h m s)	(J2000) ($^{\circ}$ ' ")	(")						
RX J0546.6-6415	5 46 40.0	-64 15 02	23.4	180.5±6.6	0.65±0.03	0.22±0.03	54	QSO	[1],[a]
RX J0528.8-6539	5 28 50.2	-65 39 38	15.2	10.0±0.8	0.74±0.11	0.25±0.06	147	AGN	[2],[a]
RX J0529.0-6603	5 29 00.6	-66 03 04	5.1	4.7±0.6	0.86±0.21	0.29±0.12	233	AGN	[2],[a]
RX J0503.1-6634	5 03 02.7	-66 33 43	9.0	85.3±2.1	0.86±0.03	0.22±0.02	380	AGN	[3],[a]
RX J0454.1-6643	4 54 11.3	-66 43 27	11.3	30.0±1.3	0.99±0.06	0.39±0.04	411	AGN	[4],[a]
RX J0522.7-6928	5 22 46.9	-69 28 34	12.0	5.2±0.8	1.15±0.23	0.35±0.19	931	AGN	[2],[a]
RX J0524.0-7011	5 24 01.6	-70 11 05	1.5	80.2±1.8	0.94±0.02	0.26±0.02	1094	AGN	[5],[a]
RX J0534.1-7018	5 34 08.2	-70 18 58	5.0	22.6±1.7	0.88±0.09	0.54±0.07	1124	AGN?	[2],[a],[b],[c]
RX J0534.1-7037	5 34 07.6	-70 37 37	10.5	6.5±1.3	0.68±0.25	0.32±0.15	1169	AGN	[a]
RX J0532.9-7040	5 32 56.2	-70 40 35	15.6	7.0±1.4	0.61±0.27	0.23±0.14	1178	AGN	[a]
RX J0536.0-7041	5 36 00.7	-70 41 28	3.7	11.8±1.2	0.89±0.12	0.26±0.09	1181	AGN	[2],[6],[a]
RX J0548.4-7112	5 48 28.7	-71 12 41	3.2	13.8±1.1	1.01±0.12	0.26±0.09	1247	AGN	[2],[a]
RX J0532.4-6401	5 32 27.4	-64 01 33	19.7	25.4±2.2	0.37±0.09	0.12±0.04	36	AGN	
RX J0541.2-6411	5 41 13.2	-64 11 59	7.7	11.7±1.1	0.45±0.10	0.23±0.05	50	AGN	
RX J0541.3-6415	5 41 20.2	-64 15 42	29.7	11.8±1.0	0.82±0.12	0.26±0.07	56	AGN	
RX J0528.1-6541	5 28 09.2	-65 41 03	17.6	4.1±0.6	0.94±0.23	0.04±0.15	150	AGN?	
RX J0529.2-6543	5 29 17.4	-65 43 46	11.8	1.6±0.3	0.69±0.32	0.36±0.15	156	AGN?	
RX J0531.5-6544	5 31 35.6	-65 44 22	9.7	1.9±0.4	0.51±0.31	0.28±0.14	158	AGN	
RX J0531.0-6544	5 31 01.1	-65 44 43	9.3	4.1±0.5	0.67±0.20	0.30±0.09	161	AGN?	
RX J0531.5-6549	5 31 32.8	-65 49 23	8.0	1.5±0.4	0.68±0.41	0.36±0.19	177	AGN?	
RX J0529.6-6553	5 29 40.3	-65 53 19	6.1	1.6±0.3	0.99±0.45	0.40±0.23	189	AGN	
RX J0528.9-6554	5 28 55.5	-65 54 27	8.8	1.8±0.4	1.25±0.60	0.25±0.28	193	AGN?	
RX J0529.5-6556	5 29 35.8	-65 56 04	7.5	1.4±0.4	1.04±0.57	0.01±0.26	200	AGN?	
RX J0532.7-6556	5 32 49.7	-65 56 27	18.1	2.6±0.5	1.09±0.42	-0.00±0.19	203	AGN?	
RX J0530.5-6556	5 30 35.0	-65 56 54	14.1	1.9±0.4	1.06±0.46	0.29±0.23	205	AGN?	[7]
RX J0531.8-6602	5 31 53.8	-66 02 21	7.8	2.1±0.4	1.28±0.45	0.52±0.25	229	AGN?	
RX J0530.1-6606	5 30 09.8	-66 06 56	12.4	3.3±0.7	0.83±0.36	0.17±0.18	251	AGN?	
RX J0531.0-6612	5 31 00.8	-66 12 36	9.3	4.7±0.6	1.07±0.26	0.24±0.14	267	AGN	
RX J0530.3-6615	5 30 21.7	-66 15 38	13.6	4.6±0.6	0.48±0.14	0.28±0.07	281	AGN?	
RX J0600.1-6625	6 00 10.5	-66 25 12	5.1	5.5±0.8	0.25±0.14	-0.04±0.06	327	AGN?	[8]
RX J0558.6-6626	5 58 38.5	-66 26 04	9.4	5.5±0.9	0.33±0.19	0.12±0.07	332	AGN	[8]
RX J0602.6-6629	6 02 40.3	-66 29 19	16.4	4.3±0.8	0.58±0.33	0.32±0.13	347	AGN?	[8]
RX J0559.5-6630	5 59 31.5	-66 30 03	8.8	5.1±0.7	0.51±0.20	0.35±0.09	352	AGN?	[8],[9]
RX J0559.9-6632	5 59 59.8	-66 32 41	5.1	3.3±0.6	0.25±0.17	-0.02±0.07	371	AGN?	[8]
RX J0600.8-6635	6 00 52.0	-66 35 35	8.2	3.3±0.6	0.44±0.25	0.32±0.10	388	AGN	[8]
RX J0603.2-6636	6 03 15.4	-66 36 54	23.1	3.8±0.8	0.72±0.44	0.32±0.30	391	AGN?	[8]
RX J0601.9-6642	6 01 57.6	-66 42 04	32.4	3.8±0.9	0.99±0.67	0.34±0.26	408	AGN?	[8]
RX J0455.0-6644	4 55 04.6	-66 44 16	8.5	7.8±1.0	0.48±0.16	0.20±0.08	417	AGN?	
RX J0510.9-6719	5 10 59.9	-67 19 59	45.9	24.2±3.5	0.63±0.20	0.22±0.11	519	AGN?	
RX J0512.3-6732	5 12 23.1	-67 32 15	12.5	8.3±1.4	0.99±0.35	0.26±0.18	545	AGN?	[2]
RX J0507.6-6847	5 07 37.9	-68 47 49	7.1	12.8±2.1	0.99±0.19	0.14±0.17	724	AGN	[2],[10]
RX J0508.5-6854	5 08 34.0	-68 54 23	7.3	11.7±1.7	0.87±0.14	0.46±0.12	756	AGN?	[11]
RX J0512.7-6938	5 12 42.6	-69 38 54	11.4	10.7±2.2	0.78±0.23	0.08±0.17	976	AGN?	
RX J0516.4-6948	5 16 24.3	-69 48 22	9.5	13.7±1.7	0.85±0.15	0.23±0.11	1019	AGN	
RX J0548.4-7055	5 48 29.9	-70 55 54	16.9	5.1±0.9	0.57±0.23	0.05±0.11	1214	AGN	
RX J0544.9-7056	5 44 59.0	-70 56 53	17.9	10.9±1.7	1.02±0.33	0.34±0.19	1216	AGN	
RX J0547.8-7117	5 47 53.0	-71 17 22	17.0	12.3±1.0	1.05±0.13	0.28±0.09	1252	AGN	
RX J0546.9-7122	5 46 57.7	-71 22 59	13.2	2.5±0.8	0.46±0.33	0.67±0.23	1261	AGN?	
RX J0553.1-7144	5 53 08.3	-71 43 05	78.1	16.0±2.7	1.11±0.37	0.22±0.20	1303	AGN?	
RX J0517.6-7151	5 17 36.0	-71 51 46	21.3	4.4±1.1	0.72±0.39	0.25±0.18	1318	AGN	
RX J0521.7-7205	5 21 47.0	-72 05 22	9.5	5.2±1.1	1.09±0.39	0.14±0.22	1340	AGN	

Remarks: [1] Quasar PMN J0546-6415, $z=0.323000$ (NED); [2] [hard]; [3] AGN Sy1, $z=0.064$ (SCF94), CAL); [4] AGN, $z=0.2279$ (CGC97); [5] AGN Sy, $z=0.151$ (SCF94); [6] no ID in CSM97; [7] extended (cf. Haberl et al. 2002); [8] South ecliptic pole; [9] GSC2.2 S0112000140562, $B=15.7$, at 6.5'' distance; [10] quasar OGLE 050736.52-68475.1.7, $z=0.53$ (DGM02); [11] quasar OGLE 050833.29-685427.5, $z=0.61$ (DGM02); [a] Paper I; [b] or X-ray binary; [c] not included in the $\log N - \log S$ analysis.

and RX J0527.1-7005 (HP 1078). RX J0532.4-6536 has been favored by Haberl & Pietsch (1999b) to be an X-ray binary but a background AGN could not be excluded. Even if in addition RX J0532.4-6536 and RX J0527.1-7005 would be background AGN, the result of the $\log N - \log S$ analysis would give for the best-fit gas additional to the HI in the high column ($> 10^{21}$ cm $^{-2}$) regime measured with Parkes but the total amount of absorbing gas becomes less constrained.

An option which has also been considered in Paper III to explain the deficit in AGN is a partial coverage of the LMC field by dense dark clouds. Assuming a fractal size distribution for these clouds an area covered by these clouds

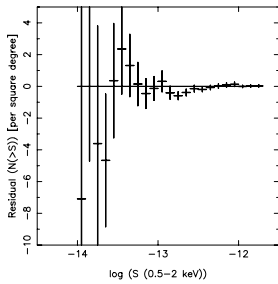


Fig. 1. Residua in the number of AGN with flux in excess of S , $N(> S)$ (data points with error bars) minus “fast evolution” model of the cosmic X-ray background of Gilli et al. (2001), for the classified AGN sample in the LMC field (15.2 square degrees) derived from the observed count rates in the spectrally hard (0.5 – 2.0 keV) band for off-axis angles < 19.5 . The chosen sample of AGN is complete for ≥ 50 counts. Reduction of the area of the observed LMC field by 15% due to dark absorbing clouds.

of 2.5 to 3.1 square degrees has been derived. If these clouds are restricted to a radius of 2 degrees then they would cover 20% to 25% of this area. About 60% of the pointings for the $\log N - \log S$ analysis are within a radius of 2 degrees from the 30 Dor complex and could be obscured by clouds. A $\log N - \log S$ analysis has been performed by reducing the area of the observed field by 15%. The result of this analysis is (cf. Fig. 1) that the observed $\log N - \log S$ is within the errors consistent with the theoretical $\log N - \log S$ of Gilli et al. (2001). One can estimate the mass associated with these absorbing clouds. Assuming column densities of $5 \cdot 10^{21} \text{ cm}^{-2}$, one obtains a total mass in these clouds of $5 \cdot 10^7 M_{\odot}$. With *NANTEN* a mass for molecular hydrogen of $(3 - 7) \cdot 10^7 M_{\odot}$ has been inferred (e.g. Rubio 1999; Fukui et al. 1999; Mizuno et al. 2001, see also the high-resolution hydrodynamic simulations of the multiphase interstellar medium of the LMC by Wada et al., 2000). The mass for molecular clouds as inferred with *NANTEN* would be consistent with the mass estimated above for the required dark absorbing clouds.

Acknowledgements. The *ROSAT* project is supported by the Max-Planck-Gesellschaft and the Bundesministerium für Forschung und Technologie (BMFT). PK is supported by the Graduiertenkolleg on the “Magellanic Clouds and other Dwarf galaxies” (DFG GRK 118). It has been made use of the GSC2.2 catalog operated at CDS.

References

- Chu, Y.-H., Kim, S., Points, S.D., et al., 2000, *AJ* 119, 2242
 Dobrzycki, A., Groot, P.A., Macri, L.M., et al., 2002, *ApJ* 569, L15 [DGM02]
 Finoguenov, A., & Jones, C., 2002, *ApJ* (subm.)
 Fukui, Y., Mizuno, N., Yamaguchi, R., et al., 1999, *PASJ* 51, 745
 Gilli, R., Salvati, M., Hasinger, G., 2001, *A&A* 366, 407
 Haberl, F., 2002, in Proc. of the Symp. on New Visions of the X-ray Universe in the XMM-Newton and Chandra Era
 Haberl, F., Pietsch, W., & Dennerl, K., 1995, *A&A* 303, L49
 Haberl, Dennerl, K., Pietsch, W., & Reinsch, K., 1997, *A&A* 318, 490
 Haberl F., & Pietsch W., 1999a, *A&A* 139, 277 [HP99]
 Haberl F., & Pietsch W., 1999b, *A&A* 344, 521
 Hasinger, G., Burg, R., Giacconi, R., et al., 1998, *A&A* 329, 482
 Irwin, J.A., Sarazin, G.L., & Bregman, J.N., 2002, *ApJ* 570, 152
 Kahabka P., 2002, *A&A* (in press, Paper II)
 Kahabka P., de Boer K.S., & Brüns, C., 2001, *A&A* 371, 816
 Kahabka P., de Boer K.S., & Brüns, C., 2002, *A&A* (in press, Paper III)
 Liu, Q.Z., van Paradijs, J., & van den Heuvel, E.P.J., 2000, *A&AS* 147, 25
 Liu, Q.Z., van Paradijs, J., & van den Heuvel, E.P.J., 2001, *A&A* 368, 1021
 Mizuno, N., Yamaguchi, R., Mizuno, A., et al. 2001, *PASJ* 53, 971
 Negueruela, I., & Coe, M.J., 2002, *A&A* 385, 517
 Pence, W.D., Snowden, S.L., Mukai, K., et al. 2001, *ApJ* 561, 189
 Rubio, M. 1999, in New views of the Magellanic Clouds, IAU Symp. No. 190, eds. Y.-H. Chu et al., p.67
 Sarazin, C.L., Irwin, J.A., & Bregman, J.N., 2000, *ApJ* 544, L101
 Sarazin, C.L., Irwin, J.A., & Bregman, J.N., 2001, *ApJ* 556, 533
 Sasaki M., Haberl F., & Pietsch W., 2000, *A&AS* 147, 75 [SHP00]
 Schmidtke, P.C., Cowley, A.P., McGrath, T.K., et al., 1995, *PASP* 107, 450
 Smale, A., & Kuulkers, E., 2002, *ApJ* 528, 702
 Swartz, D.A., Ghosh, K.K., Suleimnanov, V., & Tennant, A.F., 2002, *ApJ* (subm.)
 van den Heuvel, E.P.J., 1994, in *Interacting Binaries*, ed. H. Nussbaumer & A. Orr, Springer, Saas-Fee 22, p.263
 Wada, K., Spaans, M., & Kim, S., 2000, *ApJ* 540, 797
 Yokogawa, J., Imanishi, K., Tsujimoto, M., et al. 2000, *ApJ* 128, 491
 Yokogawa, J., 2002, PhD thesis, Kyoto University

The X-ray evolving universe: (ionized) absorption and dust, from nearby Seyfert galaxies to high-redshift quasars

Stefanie Komossa, Günther Hasinger

Max-Planck-Institut für extraterrestrische Physik, Giessenbachstraße, 85748 Garching, Germany

Abstract. Cold and warm absorbers have been detected in all types of active galaxies (AGN) from low to high redshift. This gas, located in the black hole region of AGN, is thought to play an important role in AGN unification scenarios, in explaining the X-ray background, in black hole growth and AGN evolution.

High-resolution spectroscopy with *Chandra* and *XMM-Newton* has recently revealed the signatures of warm absorbers in the form of many narrow absorption lines from highly ionized material. The richness in spectral features will provide a wealth of information on the physical processes in the central region of the few X-ray brightest, most nearby Seyfert galaxies. The long-term goal is to obtain this information for a much larger number of objects, particularly at higher redshift. This will be possible with the future X-ray observatory *XEUS*.

We provide a review of the observations of dusty and dust-free warm and cold absorbers at low and high redshift, including most recent results and exciting questions still open. Emphasis is on the science issues that we will be able to address with *XEUS* for the first time, particularly at high redshift, including: (i) determination of metal abundances of X-ray (cold) absorbers by detection of metal absorption edges, (ii) analysis of the composition of dust mixed with cold and ionized gas (K-edges of metals in cold dust and cold gas will be resolvable from each other for the first time), (iii) measurement of the velocity field of the gas, (iv) utilization of these results to investigate the *evolution* of gas and dust in AGN from high to low redshift: the evolution of abundances, dust content, ionization state, amount and velocity of gas, and its role in feeding the black hole.

We emphasize the importance of iron absorption measurements with *XEUS* at high redshift for two key issues of cosmology: the early star formation history of the universe, and the measurement of cosmological parameters. As an example, we discuss recent *XMM-Newton* observations of the high-redshift BAL quasar APM 08279+5255.

1. Introduction

Neutral (‘cold’) or ionized (‘warm’) gaseous material is ubiquitous in the AGN/SMBH environment, and therefore of utmost importance in understanding the AGN phenomenon, the evolution of active galaxies, their link with starburst galaxies and ULIRGs, and the X-ray background. X-ray absorption and emission features provide valuable diagnostics of the physical conditions in the X-ray gas and, in particular, allow to measure elemental abundances at high redshift, with profound consequences for our understanding of the star formation history in the early universe.

Here, we provide a short overview of previous X-ray observations of absorption in AGN, and discuss how exciting questions still open can be addressed with the *XEUS* observatory. We apologize in advance for incompleteness in citations due to space limitations.

2. (Warm) absorbers in nearby Seyfert galaxies

2.1. Dust-free and dusty ionized absorbers

With *ROSAT*, the signatures of warm absorbers, absorption edges of highly ionized oxygen ions at $E_{\text{OVII}} = 0.74$ keV and $E_{\text{OVIII}} = 0.87$ keV, were first detected in the X-ray spectrum of MCG-6-30-15 (Nandra & Pounds 1992), following earlier *Einstein* evidence for highly ionized absorbing material in AGN (Halpern 1984). Detailed studies of many other AGN followed, and the signatures of warm absorbers have now been seen in about 50% of the well-studied Seyfert galaxies (e.g., George et al. 1998; see Komossa 1999 for a review). First constraints placed the bulk of the

ionized material outside the BLR (e.g., Mathur et al. 1994, Komossa & Fink 1997b). Depending on its covering factor and location, the warm absorber may be one of the most massive components of the active nucleus.

Some (but not all) ionized absorbers were suggested to contain dust, based on otherwise contradictory optical–X-ray observations (e.g., Brandt et al. 1996, Komossa & Fink 1997b, Komossa & Bade 1998). The first possible direct detection of Fe-L dust features in the X-ray spectrum of MCG–6-30-15 was recently reported by Lee et al. (2001). See Komossa (1999) for a pre-*Chandra*/*XMM* review on warm absorbers.

Chandra and *XMM-Newton* detected a wealth of absorption features originating from ionized gas in nearby Seyfert galaxies (e.g., Kaastra et al. 2000, 2002; Kaspi et al. 2000, 2001; Sako et al. 2001; Collinge et al. 2001; Branduardi-Raymont et al. 2001; Lee et al. 2001; Komossa et al. 2001; Netzer et al. 2002; Yaqoob et al. 2002). These observations confirmed the presence of ionized absorbers, but also showed that spectra are more complex than previously modeled: The ionized absorbers are often multi-component, with a range of ionization parameters and outflow velocities (e.g., Kaastra et al. 2002, Kaspi et al. 2001), and absorption-dips previously mainly attributed to oxygen edges are in some cases similarly well or better explained by Fe-M absorption-line complexes (e.g., Sako et al. 2001, Behar et al. 2002). In the case of MCG-6-30-15 a discussion has started on how much of the “saw-tooth” spectral structure at soft X-ray energies originates from a warm absorber (which is independently detected by narrow absorption lines; Branduardi-Raymont et al. 2001, Lee et al. 2001), or whether it is dominated by relativistically broadened accretion-disk lines (Branduardi-Raymont et al. 2001, Fabian 2001).

The presence of ionized absorbers may also be responsible for a number of X-ray phenomena in X-ray-weaker objects, where previous X-ray spectroscopy did no longer allow to resolve individual spectral features from the absorber, but the collective effect of the absorbing gas on the X-ray spectrum is still visible. We give two examples: for instance, (i) with *ROSAT* it was generally not possible to distinguish between black bodies and ionized absorbers to account for the very *steep* observed soft X-ray spectra of Narrow-line Seyfert-1 galaxies (Komossa & Fink 1997a). (ii) The idea that *variations* of the ionized absorber in response to intrinsic luminosity variations can mimic continuum-shape variations in case of insufficient spectral resolution is an old one, and was discussed in the early days of warm-absorber studies (e.g., Kunieda et al. 1992). More recently, it was applied to some cases of unusual variability among AGN: the narrow-line Seyfert 1 galaxy RXJ0134-4258 (Komossa & Meerschweinchen 2000) and the Seyfert galaxy NGC 3516 (Netzer et al. 2002).

2.2. Cold absorption

Cold absorption plays a fundamental role in Seyfert galaxies of type 2. In this field, the *BeppoSAX* mission recently led to great progress: large X-ray absorption columns were measured in many Seyfert 2 and intermediate-type Seyfert galaxies, including a number of Compton-thick candidate sources (e.g., Maiolino et al. 1998, Guainazzi et al. 1999, Bassani et al. 1999). According to Bassani et al., the mean absorption column in Seyfert 2 galaxies is about $N_{\text{H}} \simeq 10^{23.5}$ cm^{-2} , while about 20-30% of the sources of their sample exceed $N_{\text{H}} > 10^{24}$ cm^{-2} . The X-ray absorption columns appear to be variable on the timescale of months to years (e.g., Risaliti et al. 2002). Interestingly, some Seyfert galaxies seem to change their X-ray spectra from reflection-dominated to transmission-dominated within several years (Guainazzi et al. 2002, and ref. therein). For the relevance of cold absorption in the context of models for the X-ray background, see Hasinger (these proceedings).

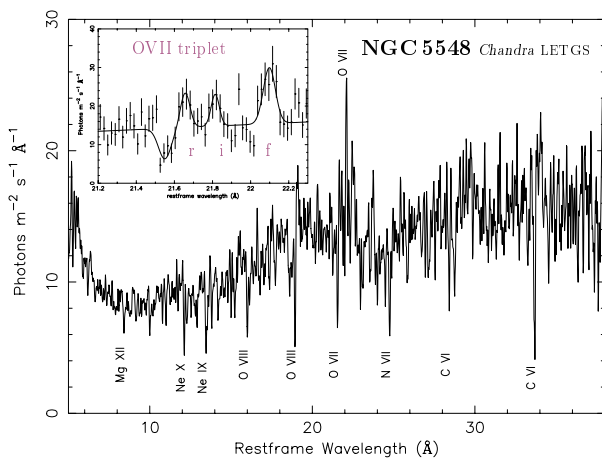


Fig. 1. High-resolution X-ray spectrum of NGC 5548 (Kaastra et al. 2000) obtained with the LETGS aboard *Chandra*. The inset shows a zoom of the O VII triplet to which a resonance line, two intercombination lines (unresolved), and a dipole-forbidden line contribute.

2.3. Open questions which we will be able to address with XEUS

Chandra and *XMM-Newton* provided high-quality spectra for the nearest Seyfert galaxies. The long-term goal is to obtain this information for a much larger number of objects, particularly at higher redshift. High spectral resolution and sensitivity will allow to detect even weak lines, measure line-profiles, resolve multiple components, perform line-reverberation mapping in X-rays, and obtain the velocity fields of the absorber(s).

Questions of particular interest are: how many components are warm absorbers composed of?, what are their densities, locations, covering factors, and metal abundances?, is the ionized material in or out of photoionization equilibrium?, is the velocity field similar to that measured in the UV? Finally, are UV- and X-ray absorber identical (e.g., Mathur et al. 1997, Brandt et al. 2002)?, what is the origin and evolution of ionized absorbers?

Concerning *dusty* warm absorbers, dust-created metal K-shell absorption edges will be spectrally resolvable from gas-created K-shell edges for the first time. Measuring dust absorption in X-rays will be a powerful new tool to determine the dust composition in other galaxies (e.g., Komossa & Bade 1998, Komossa 1999).

Finally, all kinds of peculiar or extreme properties of AGN, partly suggested to be linked to ionized absorption (e.g., Komossa & Meerscheinchen 2000), can be studied with *XEUS* observations of high resolution and sensitivity.

3. Broad absorption line (BAL) quasars

3.1. Previous observations

BAL quasars are characterized by broad UV absorption lines. It has been suggested that these lines arise in a flow of gas which rises vertically from a narrow range of radii from the accretion disk. The flow then bends and forms a conical wind moving radially outwards (Elvis 2000). Variants of radiatively-driven disk-winds were explored (e.g., Murray et al. 1995, Proga et al. 2000, Proga 2001, Everett et al. 2002). In some of these models, an X-ray absorber shields the wind downstream from soft X-rays, allowing resonant-line driving to remain effective and accelerate the outflowing BAL wind up to $\sim 0.1c$.

Pre-*Chandra*/*XMM* detections of BAL quasars in X-rays were rare. Generally, BAL quasars are X-ray weak, which is usually interpreted in terms of strong excess absorption (e.g., Green et al. 1995, Gallagher et al. 1999, Brinkmann et al. 1999, Brandt et al. 2000, Wang et al. 2000). Although *Chandra* provided valuable new constraints on the amount of absorption towards selected BALs (e.g., Sabra & Hamann 2001, Oshima et al. 2001, Gallagher et al. 2002) almost all data still suffer from low S/N (typically 50 to few hundred X-ray photons detected). There are indications that the BAL material is ionized instead of neutral. This is definitely the case for the quasar APM 08279+5255 which has the best-measured X-ray spectrum of any BAL quasar we are aware of. A recent *XMM-Newton* observation led to the detection of a strong absorption feature of ionized iron, interpreted as K-edge, arising from a warm absorber of high

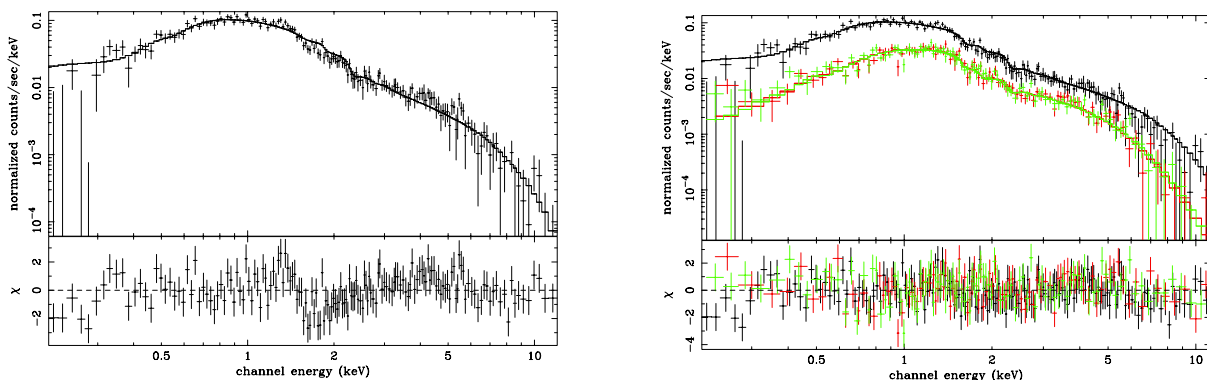


Fig. 2. *XMM-Newton* spectrum of the BAL quasar APM 08279+5255 at redshift $z=3.91$ (Hasinger et al. 2002). *Left:* *XMM* EPIC-pn spectrum, fit with a single powerlaw. An absorption feature is visible at an energy corresponding to ionized, redshifted iron. *Right:* Combined EPIC and MOS spectra, fit with a powerlaw plus an absorption edge of highly ionized iron.

column density (Hasinger et al. 2002; for *Chandra* results on this quasar, just posted at astro-ph, see Chartas et al. 2002)¹. No doubt, APM 08279+5255 is a top target for *XEUS* (see also Section 6).

3.2. Open questions which will be addressed with XEUS

One basic question related to the X-ray BAL flow is: are we directly seeing the outflowing gas in X-rays, or is the X-ray absorber at rest, shielding the UV absorbing gas to ensure the line-driving remains effective even for high ionization parameters? Are UV and X-ray absorber identical? Is radiation pressure from UV lines indeed the main driving mechanism of the outflow? What are the X-ray column densities and the corresponding mass outflow rates? What is the geometry of the BAL flow?

Of fundamental importance will be the simultaneous measurement of *column density* and *outflow velocity* of the gas. (With present X-ray missions, and as long as the X-ray spectrum is dominated by iron *absorption edges* it is very difficult to distinguish between dominant ionization stage and outflow velocity of the gas.) Such measurements will allow to solve one major uncertainty in BAL models, mentioned above: is the (high-column-density) X-ray absorber outflowing with high speed, or at rest? In fact, the high X-ray column density measured in some BALs, most reliably for APM 08279+5255, *in combination with high outflow velocities* would pose a problem for radiation-driven outflows (see, e.g., discussion by Hamann 1998) and may give indications that other mechanisms are at work to drive the BAL flows. The new X-ray measurements with *XEUS* will have profound implications for our understanding of massive and energetic outflows in AGN, their launch and acceleration mechanism.

Abundance measurements will tell the history and origin of the BAL gas, and its role in metal-enriching the environment. According to a recent model by Elvis et al. (2002), BAL environments are expected to be dusty. In the X-rays regime, absorption features from dust will provide a clean way to measure the dust composition.

4. Absorption in high-redshift quasars

4.1. Previous observations

Evidence for excess X-ray absorption was found in high-redshift, mostly radio-loud, quasars (e.g., Elvis et al. 1994, Schartel et al. 1997, Yuan 1998). The ionization state of the absorber remained largely unknown. However, there is now growing evidence that these absorbers are not cold but warm. As shown by Schartel et al. (1997) the spectrum and spectral changes of the high-redshift quasar PKS 2351-154 ($z=2.67$) are well explained by the presence of an ionized absorber of column density $\log N_w = 22.4$ which changes its ionization state in response to intrinsic luminosity changes of the quasar. PKS 2351-154 is one of the very few high- z quasars which show a *variable* UV absorption system as well. For several years, this quasar held the record of being the most distant X-ray warm-absorber candidate known, recently exceeded by GB 1428+42 and PMN J0525-33 (Fabian et al. 2001a,b). In contrast, Yuan et al. (2000) argued that the X-ray absorber of the high-redshift quasar RXJ1028.6-0844 is very likely cold. An interesting puzzle is, why the UV spectrum of this object does not show any signs of the X-ray cold absorber.

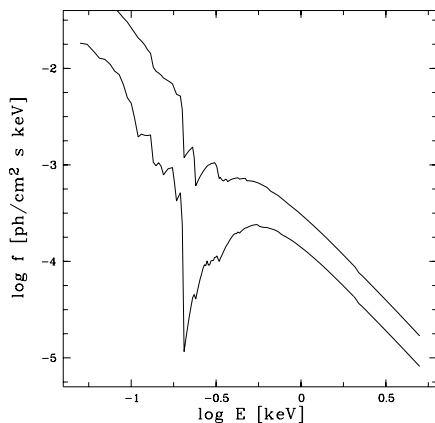


Fig. 3. Best-fit warm absorber which was used to model the X-ray spectrum of the $z = 2.69$ quasar PKS 2351-154 in high-state (upper curve) and low-state (lower curve; Schartel et al. 1997). For even higher redshifts, edges of the ionized absorber are shifted ever closer to the low-energy sensitivity cut-off of current X-ray instruments. In case of insufficient S/N, the edges and lines of the warm absorber may easily be confused with cold hydrogen absorption, and thus mimic the presence of a *cold* absorber of high column density (Komossa, e.g., 1999).

¹ Chartas et al. presented a *Chandra* spectrum of APM 08279+5255 and modeled the absorption structure by two iron absorption lines which then have huge outflow velocities of 0.2 and 0.4c. Both observations are consistent with each other, if variability is assumed.

4.2. Open questions which will be addressed with XEUS

What is the origin and nature of the high- z excess absorbers? Is this material warm or cold? Why has it been more abundant in the past? How does it evolve? Why is excess absorption mainly seen in high-redshift radio-*loud* quasars whereas a number of (non-BAL) high- z radio-*quiet* quasars appear to be absorption-free? Answers to these questions are crucial for understanding the formation and evolution of AGN.

Apart from measuring ionic column densities, a very interesting prospect is to determine element abundances in dust and gas at high redshift. This topic will be discussed in more detail in Section 6.

5. Absorption lines from the intergalactic medium

An exciting new aspect of having access to high-resolution spectroscopy in X-rays is the search for absorption lines from the intergalactic medium. First results were recently reported by Mathur et al. (2002). (Weak) OVII and OVIII absorption lines in the direction of the bright quasar H1821+643 were interpreted as arising from a moderate density, shock-heated intergalactic medium predicted by cosmological scenarios. (See Fang et al. 2002 for detection of OVIII Lyman-alpha absorption from intra-group gas along the sightline towards PKS 2155-304).

With XEUS, we will be able to measure more lines of sight, and greatly improve the statistics, to measure reliably high-ionization lines from filaments of low column density.

6. Prospects for studying absorbers at high redshift with XEUS: constraints on early star-formation history and cosmological parameters from iron abundance measurements

The spectral richness and complexity of AGN, observed with *Chandra* and *XMM*, will provide a wealth of information on the physical processes in the central region of the few X-ray brightest, most nearby Seyfert galaxies. The long-term goal is to obtain this information for a much larger number of objects, particularly at higher redshift.

We concentrate here on the aspect of deriving metal abundances at high redshift. Below, we summarize open questions and how they can be addressed with the greatly improved sensitivity and resolution (Arnaud et al. 1999) of XEUS.

6.1. Abundances at high redshift: constraints on early star-formation history of the universe, and on cosmological parameters

Two types of quasars show excess absorption at high redshift: radio-loud quasars on the one hand, BAL quasars on the other hand. ((Interestingly, though, very few BALs are radio-loud; but whether these facts tell us something about the similar/different origin of the excess absorbers in both types of objects, is unclear.))

Here, we will concentrate on the iron *edge* features which offer some valuable advantages over Fe emission lines in usage as abundance indicators (for interesting aspects of studying relativistically broadened iron *lines* at high redshift we refer to the XEUS science case; Arnaud et al. 1999).

The iron absorption features and K-edges provide a unique probe of matter at high redshift because, firstly, they are easy to measure even, or, *particularly*, at high redshift z , and secondly, Fe(/O) abundance measurements in the early universe are important for key issues of cosmology, as elaborated on below. The relevance of UV-FeII emission in deriving Fe/Mg abundances at high z was discussed by Hamann & Ferland (1999) and Yoshii et al. (1998). In particular, Yoshii et al. (1998) used the emission-line ratio FeII/MgII to estimate the iron-to-magnesium abundance in the distant quasar QSO B1422+231. Here, we would like to emphasize the role of the X-ray FeK α edges as one of the ‘cleanest’ diagnostics of iron – of column density and ionization state in a first step, and of Fe/O abundance in a second step:

- Firstly, the iron absorption is easy to measure: At high redshift, the iron-K edges are redshifted to a region, where the detector sensitivity is high. As a bonus, the continuum shape is very well constrained since redshift shifts the high-energy part of the quasar spectrum into the observable band.
- Absorption edges are, in principle, more reliable than emission lines because they do not depend on parameters like gas density and temperature, and provide a direct measurement of the ionic column densities. In addition, the iron edge is better suited than the iron K α emission line which appears to be less common at high redshift.

In the UV-band, no strong Fe-lines are present, apart from the FeII emission complexes which are still subject to high uncertainties, (i) in model predictions (e.g., the role of photo-excitation by Lyman α photons), and (ii) in measurement interpretation (some Fe may be depleted into dust, some Fe may be of higher ionization state than FeII, with reduced contribution to FeII emission in both cases); see Hamann & Ferland (1999) and references therein.

- The iron edges do not coincide with any other strong absorption-line transitions at the same energies (as opposed to some low-energy features, where K-shell and L- and M-shell features of different species partly overlap).
- Absorbers of *high column density* have been observed in high-redshift quasars in X-rays, particularly in radio-loud quasars and BAL quasars, so they are known to be present. A high column density is indeed required for the optical depths in the edges to become measurable. E.g., a column density in neon-like iron of $N_{\text{FeXVII}} = 10^{19} \text{ cm}^{-2}$ corresponds to an optical depth of $\tau = 0.27$ in the absorption edge (with cross section from Verner & Yakovlev 1995).
- The element iron plays a special role in chemical enrichment scenarios, because its production is delayed relative to other elements (e.g., Fig 1 of Hamann & Ferland 1993), since it is believed to be mostly produced in supernovae of type Ia (e.g., Nomoto et al. 1984, Sect. 2.1 of Greggio & Renzini, 1984, Sect.4.6 of Hamann & Ferland 1993, and references therein). Its role as “cosmic clock” was therefore realized early (e.g., Tinsley 1979). Hamann & Ferland (1993) also pointed out its role in determining cosmological parameters: A certain age of the universe is required to produce iron in sufficient amounts. The detection of high Fe abundances at high redshift would therefore point to a larger age of the universe at the same redshift, thus to a different set of cosmological parameters than an Einstein-deSitter universe with deceleration parameter $q_0 = 0.5$ (Fig. 4).

It is these last two science issues, which are of special interest. The usage of iron as a “cosmic clock” depends on our understanding of supernovae of type Ia, which are thought to play the dominant role in the enrichment of iron relative to alpha elements. Given the long lifetime of SNIa precursors, it takes about 0.3-1 Gyr until SN Ia start to form in significant numbers (e.g., Fig. 9 of Hamann & Ferland 1993; Fig. 4 of Matteucci 1994). The iron production is delayed correspondingly ($t > 1 \text{ Gyr}$). Therefore, even with a high rate of SNIa, detection of large amounts of iron in the very early universe would require another mechanism to be at work. It would most likely imply a larger age of the universe at a given redshift, to provide more time for the formation of iron (Hamann & Ferland 1993, Yoshii et al. 1998).

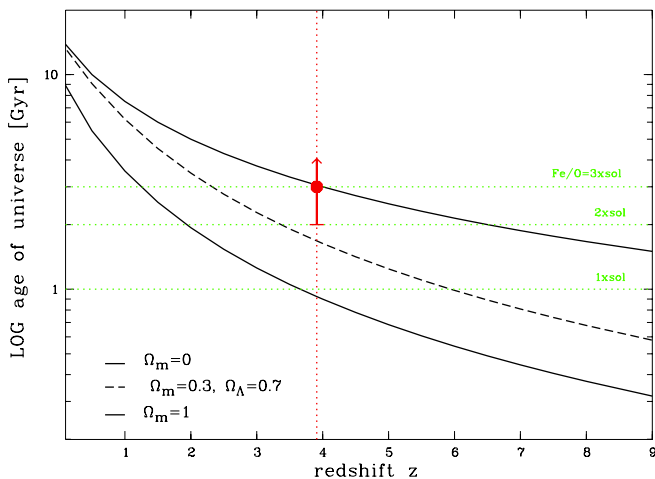


Fig. 4. Age of the universe in units of 10^9 years versus redshift for different cosmologies, using a Hubble constant $H_0 = 65 \text{ km/s/Mpc}$. Upper solid line: $\Omega_m=0$, lower solid line: $\Omega_m=1$ ($\Omega_\Lambda=0$ in both cases), dashed line: $\Omega_m=0.3$ and $\Omega_\Lambda=0.7$. The dotted horizontal lines correspond to the timescale to produce a Fe/O abundance ratio of solar, 2 and 3 \times solar (Hamann & Ferland 1993; their model ‘M4a’), as marked in the figure. The vertical dotted line corresponds to a redshift $z = 3.91$ measured for APM 08279+5255. The filled circle with the error bar gives the timescale necessary to produce the observed amount of iron in APM 08279+5255 (based on model M4a of Hamann & Ferland). XEUS will be crucial in determining Fe abundances at high redshift. It will allow to significantly narrow down the error bars for APM 08279+5255, and to study more high-redshift objects in a similar way.

To demonstrate these issues further, we use the recent X-ray results of Hasinger et al. (2002) on the BAL quasar APM 08279+5255 at redshift $z=3.91$, which shows an Fe/O ratio of about 3. Such high ratios are not produced by SNIa and imply that SNIa are involved. However, assuming an Einstein-deSitter world model with $\Omega_m=1.0$ and $\Omega_\Lambda=0$, at the redshift of the quasar the universe was too young ($t \approx 0.9 \text{ Gyr}$; Tab. 1) to produce the observed

cosmological model	age of universe	age of universe at $z=$			
	$t_{\text{look-back}, z \rightarrow \text{inf}}$	9.0	6.0	3.9	1.0
$\Omega_m=0, \Omega_\Lambda=0$	15 Gyr	1.5 Gyr	2.1 Gyr	3.0 Gyr	7.5 Gyr
$\Omega_m=0.3, \Omega_\Lambda=0.7$	14.5	0.6	1.0	1.7	6.1
$\Omega_m=1, \Omega_\Lambda=0$	10	0.3	0.5	0.9	3.5

Table 1. Age of the universe (in Giga years) at different redshifts for several cosmologies.

overabundance of iron. According to models of Hamann & Ferland (1993; their model M4a) a timescale of ~ 3 Gyr is required to produce an abundance ratio of $\text{Fe}/\text{O}=3$.²

The *XMM-Newton* X-ray observations of APM 08279+5255 therefore favor cosmological models which predict a slightly larger age of the universe *at the redshift of the quasar*, like recent models involving a low value of Ω_{matter} and a cosmological constant (e.g., Fig. 7 of Perlmutter et al. 1999). The idea is illustrated in Fig. 4, which plots the age of the universe in dependence of redshift z (e.g., Carrol et al. 1992) for several cosmological models.

The excellent spectral resolution and sensitivity of *XEUS* will not only allow us to scrutinize the presence of the iron feature in APM 08279+5255 and its interpretation, it will also provide similar information for many more objects. We will thus obtain valuable information about nucleosynthesis in the early universe, and we will be able to follow another path to measure cosmological parameters.

6.2. Soft X-ray sensitivity of future X-ray missions

An important design feature of future X-ray missions, particularly those aiming at high-redshift studies, is the *soft* X-ray sensitivity. In order to determine metal abundance ratios of Fe/O and Fe/Ne , it will be essential to detect oxygen and neon edges out to as high redshift as possible³. The high sensitivity of *XEUS* in its final configuration will be crucial to study iron absorption features at high redshifts, since the iron abundance is expected to decline significantly beyond a redshift $z \approx 4$, as discussed above.

7. Summary

Science issues that we will be able to address with *XEUS* for the first time, particularly at high redshift, include: measurement of metal abundances of X-ray (cold) absorbers by detection of metal absorption edges, determination of the composition of dust mixed with cold and ionized gas (K-edges of metals in cold dust and cold gas will be resolvable from each other for the first time), measurement of the velocity state of the gas, and usage of these results to investigate the *evolution* of gas and dust in AGN from high to low redshift: the evolution of abundances, dust content, ionization state, amount and velocity of gas, and its role in feeding the black hole.

A particularly exciting aspect is to use the iron absorption features, especially the K-edges, for abundance determinations, which will have fundamental implications for our understanding of the early star formation history of the universe, and which will provide another means to measure cosmological parameters. In order to determine Fe/O and Fe/Ne ratios out to large redshifts, *soft* X-ray energy sensitivity (to reliably measure O, Ne) of future X-ray missions is essential.

Acknowledgements. StK thanks Hartmut Schulz for very useful discussions on cosmological models.

References

- Arnaud M., et al., 1999, *The XEUS Science Case*, ESA
 Bassani L., et al., 1999, *ApJS* 121, 473
 Behar E., 2002, in: X-ray spectroscopy of AGN with *Chandra* and *XMM-Newton*, MPE report, in press

² The timescale to reach an abundance ratio of $\text{Fe}/\text{O}=\text{solar}$ is *at least* 1 Gyr in all models of Hamann & Ferland (HF93), and is basically given by the lifetime of SNIa precursors. Different models of HF93 then predict a different evolution of Fe/O , and we caution that in model predictions there is some scatter in the time at which Fe/O reaches $3\times\text{solar}$. Model ‘M4’ is the quasar model favored by HF93. In several other models they studied, Fe/O never reaches $3\times\text{solar}$, whereas in their extreme model ‘M6’ (cf. their Fig. 1) Fe/O reaches $3\times\text{solar}$ already after 2 Gyr.

³ For that purpose, the edges have to be disentangled from other potential absorption lines at similar energies, and any potential black body contribution at the softest X-ray energies has to be measured carefully, since it can influence the oxygen-iron ionization structure, thus affecting the measured ratio of Fe/O and Fe/Ne (Hasinger, Komossa et al., in prep.). The possibility of partial re-filling of absorption features due to scattering also has to be kept in mind carefully.

- Brandt W.N., Fabian A.C., Pounds K.A., 1996, MNRAS 278, 326
Brandt W.N., et al., 2000, ApJ 528, 637
Brandt W.N., et al., 2002, in: New Century of X-ray astronomy, ASP Conf. Ser. 251, 128
Branduardi-Raymont G., et al. 2001, A&A 365, L140
Brinkmann W., et al., 1999, A&A 345, 43
Carroll S.M., Press W.H., Turner E.L., 1992, ARA&A 30, 499
Chartas G., et al., ApJL in press [astro-ph/0207196]
Collinge, et al., 2001, ApJ 557, 2
Fang T., et al., 2002, ApJ, in press [astro-ph/0206264]
Elvis M., 2000, ApJ 545, 63
Elvis M., et al., 1994, ApJ 422, 60
Elvis M., Marengo M., Karovska M., 2002, ApJ 567, L107
Everett J., Königl A., Arav N., 2002, ApJ 569, 671
Fabian A., 2001, in : Proceedings of Texas Conf., astro-ph/0103438
Fabian A., et al., 2001a, MNRAS 324, 628
Fabian A., et al., 2001b, MNRAS 323, 506
Gallagher S., et al., 1999, ApJ 519, 549
Gallagher S., et al., 2002, ApJ 567, 37
George I., et al., 1998, iApJS 114, 73
Green P., et al., 1995, ApJ 450, 51
Greggio L., Renzini A., 1983, A&A 118, 217
Guainazzi M., et al., 1999, MNRAS 310, 10
Guainazzi M., 2002, in: X-ray spectroscopy of AGN with *Chandra* and *XMM-Newton*, MPE report, in press
Halpern J.P., 1984, ApJ 281, 90
Hamann F., 1998, ApJ 500, 798
Hamann F., Ferland G.J., 1993, ApJ 418, 11
Hamann F., Ferland G.J., 1999, A&AR 37, 487
Hasinger G., 2002, these proceedings
Hasinger G., Schartel N., Komossa S., 2002, ApJ 573, L80
Kaastra J., et al. 2000, A&A 354, L83
Kaastra J., et al. 2002, A&A in press, [astro-ph/0202481]
Kaspi S., et al. 2000 ApJ 535, L17
Kaspi S., et al. 2001, ApJ 554, 216
Komossa S., 1999, in: ASCA/ROSAT Workshop on AGN and the X-ray Background, T. Takahashi, H. Inoue (eds), ISAS Report, p. 149; [also available at astro-ph/0001263]
Komossa S., Bade N., 1998, A&A 331, L49
Komossa S., Fink H., 1997a, in: Accretion Disks - New Aspects, Lecture Notes in Physics 487, 250
Komossa S., Fink H., 1997b, A&A 327, 483
Komossa S., Meerschweinchen J., 2000, A&A 354, 411
Komossa S., et al., 2001, in: The central kiloparsec of starbursts and AGN, ASP Conf. Ser. 249, 411
Kunieda H., et al., 1992, ApJ 384, 482
Lee J., et al., 2001, ApJ 554, L13
Maiolino R., et al., 1998, A&A 338, 781
Mathur S., et al., 1994, ApJ 434, 493
Mathur S., 1997, in: Mass Ejection from AGNs, ASP conf. ser. 128, 161
Mathur S., Weinberg D., Chen X., 2002, ApJ in press [astro-ph/0206121]
Matteucci F., 1994, A&A 288, 57
Murray N., Chiang J., 1995, ApJ 454, L105
Nandra K., Pounds K.A., 1992, Nature 359, 215
Netzer H., et al. 2002, ApJ in press, [astro-ph/0112027]
Nomoto K., et al., 1984, ApJ 279, L23
Oshima T., et al., 2001, ApJL in press, [astro-ph/11410]
Perlmutter S., et al., 1999, ApJ 517, 565
Proga D., Stone J.M., Kallman T.R., 2000, ApJ 543, 686
Proga D., 2001, in: Mass Outflow in Active Galaxies, ASP Conf. Ser., in press [astro-ph/0109092v1]
Risaliti G., Elvis M., Nicastro F., 2002, ApJ 571, 234
Sabra B.M., Hamann F., 2001, ApJ 563, 555
Sako M., et al., 2001, A&A 365, L168
Schartel N., et al., 1997, A&A 320, 421
Tinsley J., 1979, ApJ 229, 1046
Verner D.A., Yakovlev D.G., 1995, A&AS 109, 125
Wang T.G., et al., 2000, ApJ 545, 77
Yaqoob T., et al. 2002, ASP conf. series, in press [astro-ph/0111428]
Yoshii Y., et al., 1998, ApJ 507, L113
Yuan W., 1998, PhD Thesis, TU München
Yuan W., et al., 2000, ApJ 545, 625

XMM-Newton Deep Survey in the Lockman Hole & The population of type-2 QSO

I. Lehmann¹, G. Hasinger¹, V. Mainieri², and the Lockman Hole team

¹ Max-Planck-Institut für extraterrestrische Physik, Giessenbachstrasse, Postfach 1312, 85741 Garching, Germany

² European Southern Observatory, Karl-Schwarzschild-Strasse 2, 85748 Garching, Germany

Abstract. Deep *Chandra*, *XMM-Newton* and *ROSAT* surveys (Giacconi et al. 2001, Brandt et al. 2001, Hasinger et al. 1998, 2001) have shown that the cosmic X-ray background (XRB) is largely due to the accretion onto supermassive black holes, integrated over the cosmic time. The soft X-ray background is dominated by X-ray and optically unobscured AGNs (Quasars, Sy1). The characteristic hard spectrum of the XRB can be explained if most of the AGN are heavily absorbed (type-2). The first deep *XMM-Newton* survey was performed in the Lockman Hole region. We present the X-ray properties of the population of faint newly detected *XMM-Newton* sources and their optical/near-infrared identification. The majority of these sources seems to be intrinsically absorbed type-2 AGN. We have found several heavily obscured type-2 Quasars (some of them already seen with *ROSAT*)

Acknowledgements. We gratefully acknowledge the permission by the Springer Verlag to use their A&A L^AT_EX document class macro.

References

- Giacconi R., Rosati P., Tozzi P., et al., 2001, ApJ 551, 624
Brandt W.N., Hornschemeier A.E., Alexander D.M., et al., 2001, AJ 122, 1
Hasinger G., Burg R., Giacconi R., et al., 1998, A&A 329, 482
Hasinger G., Alteri B., Arnaud M., et al., 2001, A&A 365, 45

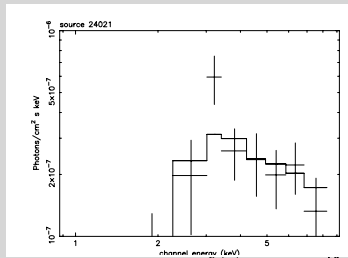
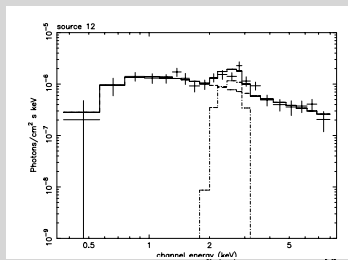
XMM-Newton Deep Survey in the Lockman Hole field & The population of type-2 QSO

Ingo Lehmann, Günther Hasinger, Vincenzo Mainieri (ESO) & the Lockman Hole team

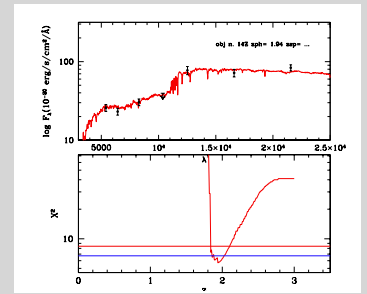
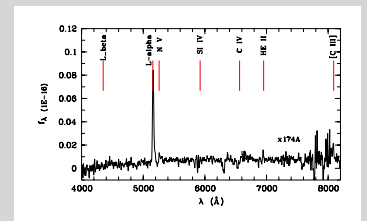
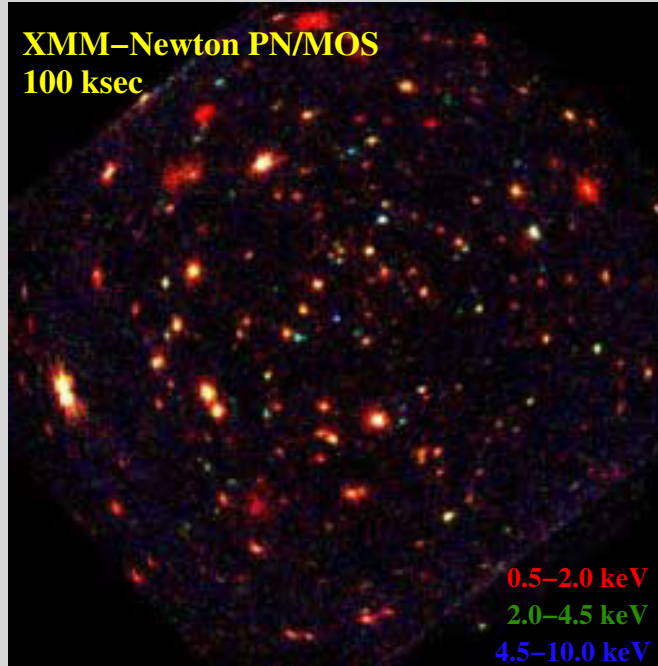
Abstract

Deep *Chandra*, *XMM-Newton* and *ROSAT* surveys (Giacconi et al. 2001, Brandt et al. 2001, Hasinger et al. 1998, 2001) have shown that the cosmic X-ray background (XRB) is largely due to the accretion onto supermassive black holes, integrated over the cosmic time. The soft X-ray background is dominated by X-ray and optically unobscured AGNs (Quasars, Sy1). The characteristic hard spectrum of the XRB can be explained if most of the

AGN are heavily absorbed (type-2). The first deep *XMM-Newton* survey was performed in the Lockman Hole region. We present the X-ray properties of the population of faint newly detected *XMM-Newton* sources and their optical/near-infrared identification. The majority of these sources seems to be intrinsically absorbed type-2 AGN. We have found several heavily obscured type-2 Quasars (some of them already seen with *ROSAT*).



The X-ray spectra of type-2 Quasars show intrinsic absorption of $\log N_H > 22$. The upper spectrum includes a Fe-K α line.

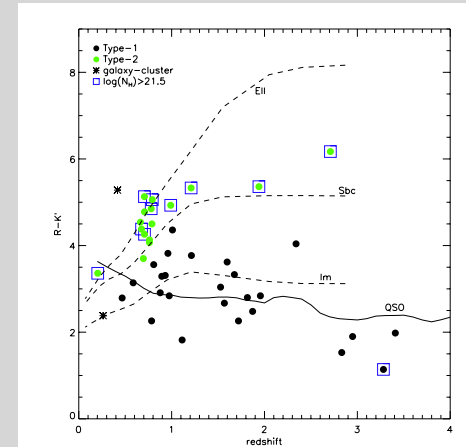
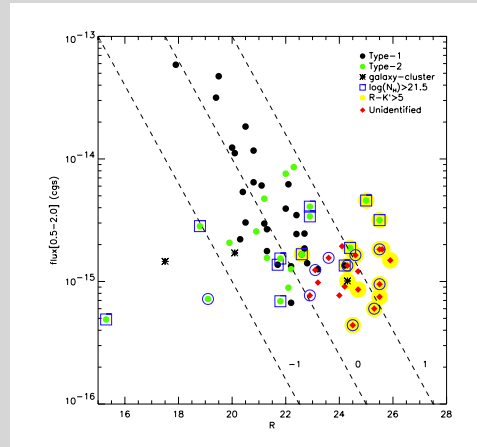
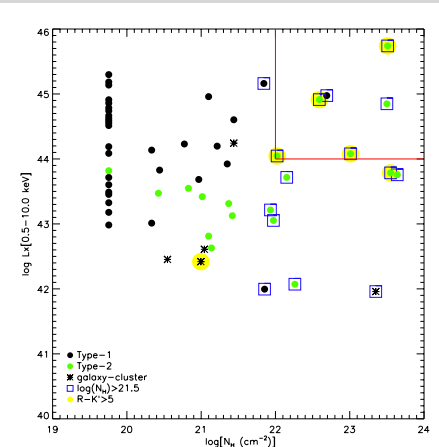


Keck spectrum of a type-2 Quasar at $z = 3.240$ (narrow L α , He II and [C III]). Phot.-z determination of a type-2 Quasar.

Hard X-ray sources: type-2 AGN/ type-2 Quasars

The new *XMM-Newton* sources, previously not detected in the Ultra Deep ROSAT Survey, are fainter and typically harder than the *ROSAT* sources. They are probably intrinsically absorbed sources, which is in good agreement with the predictions from the X-ray background models. About 25% of the new sources with sufficient number of photons (> 70) show very hard spectra, which can be described by a powerlaw (plus soft excess) and significant intrinsic absorption $\log N_H > 22$. The majority of these sources have

extremely red optical/near-infrared counterparts ($R - K' > 5$). Most of the so far identified new sources are type-2 AGN at $z < 1$. However, we have identified about five type-2 Quasars at $1 < z < 3$ using optical/near-infrared spectra and photometric redshift technique. The optical/near colours of type-2 AGN/Quasars are dominated by their host galaxies (ellipticals and spirals). Furthermore we find some examples of optically classified type-1 Quasars showing intrinsic X-ray absorption $\log N_H > 21.5$. See figures below.



Transition-edge microcalorimeters in Corbino disk geometry for XEUS NFI

A. Luukanen¹ and J. Huovelin², P. Keinänen¹, K. Kinnunen¹, A. Nuottajärvi¹, J. Pekola¹, J. Schultz², and O. Vilhu²

¹ University of Jyväskylä, Department of Physics, Surfontie 9, FIN-40351 Jyväskylä, Finland

² Observatory, University of Helsinki, Helsinki, Finland

Abstract. The X-ray Evolving Universe Spectroscopy (XEUS) mission will utilise an array of transition-edge sensor (TES) microcalorimeters to image cosmic objects with unprecedented spectral resolution in the soft X-ray regime. To this point, several groups have investigated TESs based on various materials and geometries. Although the resolution has progressively improved over the years, the devices show evidence of an internal noise mechanism which is not accounted for in the small signal model. We present a possible experimental solution to the problem with an idealised geometry which removes edge-effects and reduces the degrees of freedom in the dynamic behaviour of the device.

1. Edge effects in TESs

Typically, the TES is a rectangular bi-metal film on a Si_3N_4 membrane, which provides the required thermal isolation for the sensor. Superconducting contacts (usually Al or Nb) feed the current through the device. The edges parallel to the current are defined by lift-off or by wet-etch, and generally the quality of the metals at the edges is questionable due to the fact that the edges are exposed to chemicals or contamination from the resist, respectively.

In the case of Ti/Au bilayers, the wetting behaviour of Ti leads to a situation where the relative Ti thickness is larger at the edges than in the middle of the film. All the above described nonidealities can lead to a situation where the critical temperature T_c is different at the edges. Moreover, the edges have proven to be a source of flux flow noise, as the impurities introduce trapping centers for vortices. A method used by some groups is to add thick normal metal banks over the edges, maintaining them at normal state and not contributing to the dynamics of the TES [Hilton 2001].

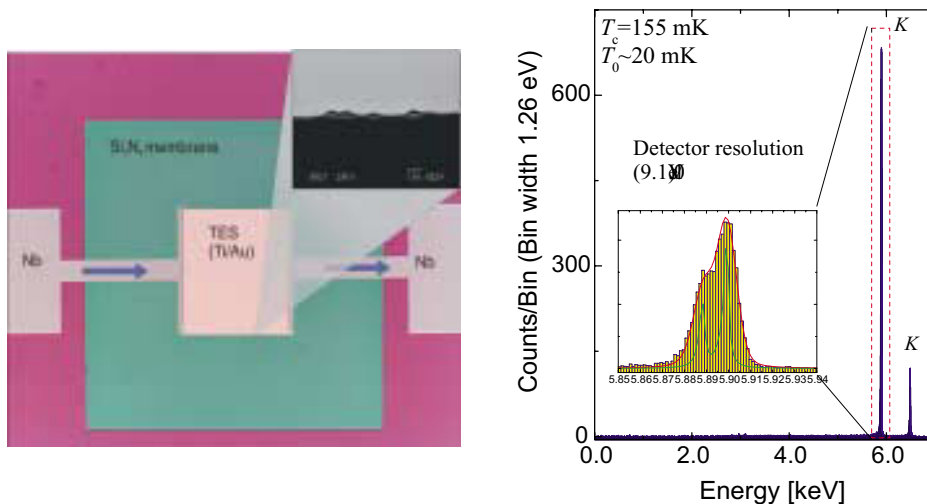


Fig. 1. (Left) A typical rectangular TES. The inset shows a SEM micrograph of the non-idealities at the TES edge. (Right) With this type of TES we were able to reach a resolution of 9.1 ± 0.1 eV for 5.89 keV X-rays

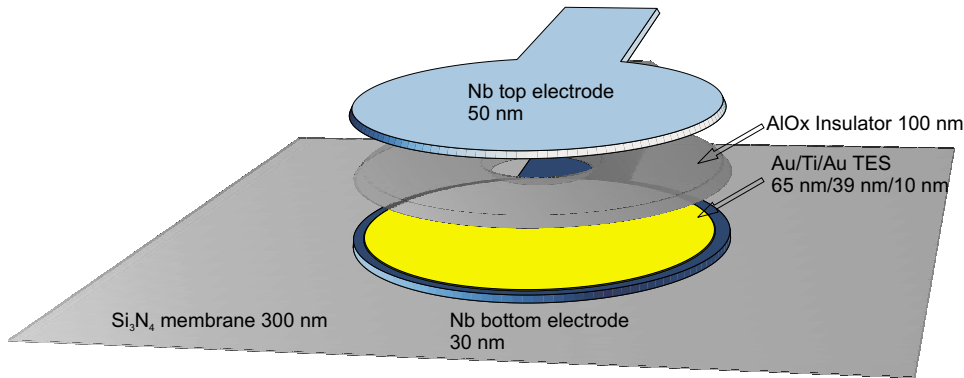


Fig. 2. A schematic of the geometry and the layers of the CORTES. The top electrode forms the central superconducting contact.

2. The Corbino disk TES (CORTES)

To rule out the edges altogether, we are investigating an edgeless geometry, a so-called Corbino disk. In this scheme, the current is fed via a superconducting outer electrode, circumfering a circular TES film, and collected at another at the apex of the TES. Thus, no edges parallel to the current exist.

The geometry requires the use of an extra insulating layer deposited between the TES and the top electrode which also acts as a superconducting ground plane. The current density in the CORTES has a radial dependence on the distance from the centre, $j(r) = I/(2\pi rt)$, where I is the current through the device, and t is the thickness of the Au/Ti/Au trilayer. Thus, more dissipation takes place in the centre of the disk, and we assume that a normal state hot-spot forms in the centre of the TES, with a phase boundary located at a distance r_b from the centre. This mechanism is different from that of square devices, where the propagation of the phase boundary depends on defects and imperfections in the film. The resistance of the CORTES is given by $R(r_b) = \rho \ln(r_b/r_0)/(2\pi t)$.

3. The hot-spot model

We have developed an elementary thermal model for the CORTES, which is based on calculating diffusion equations of the S- and N- domains in radial co-ordinates, taking in account the Joule dissipation within the N-state part:

$$-\kappa_N \nabla^2 T = j(r)^2 \rho \quad (1)$$

$$-\kappa_S \nabla^2 T = 0 \quad (2)$$

where κ_N and κ_S are the thermal conductivities in the normal state region and S region, respectively. We require boundary conditions $T(r_b) = T_c$, $T(r_2) = T_0$, and $\kappa_N \nabla T(r_b) = \kappa_S \nabla T(r_b)$, where r_2 is the outer radius of the TES. Using the solution for $T(r)$ we obtain the solution for $r_b(V_b)$, where V_b is the voltage across the CORTES, and thus the $I(V_b)$ curve for the device, shown in Fig. 3. The limitation of this steady state model is that it does not account for the effect of the SiN membrane; All of the heat is assumed to be transported via the TES film itself. Also the dynamic properties have not yet been calculated.

4. Experimental results

To pattern the devices, we use electron beam lithography on a double layer PMMA/MAA-MAA electron resist. The metal films are evaporated at an UHV electron gun evaporator, whereas the insulator is deposited at a separate electron gun evaporator while rotating the sample at an angle. This makes the edges of the insulator less abrupt, as step coverage as proven to be difficult. Of the materials tried, AlOx has proven to be most reliable in terms of lack of pinholes. The thickness of the insulator has varied from 250 nm to 50 nm. The order of deposition has also proven to be an issue. Previously, we used to deposit the films in inverse order, with a Nb ground plane deposited first, followed by the insulator, then the TES, and finally the top ring contact. We consistently measured critical temperatures of the order of 200 mK, as shown in Fig. 4. We attribute the saturation of the T_c to the contamination of the Ti-Au interface, which reduces the proximity effect of the Au. Earlier, in square devices, we were able to remove this screening effect by sandwiching the Ti between two Au layers. In the CORTES, the deposition of the Au/Ti/Au after the AlOx resulted

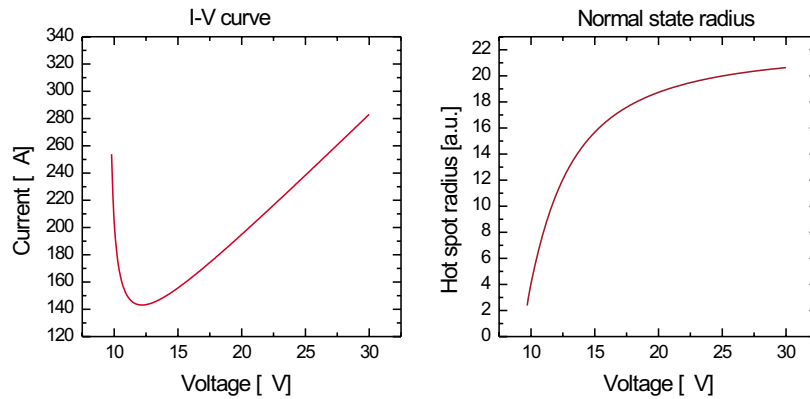


Fig. 3. Calculated I-V curve for the CORTES, and the radius of the normal state region as a function of V_b .

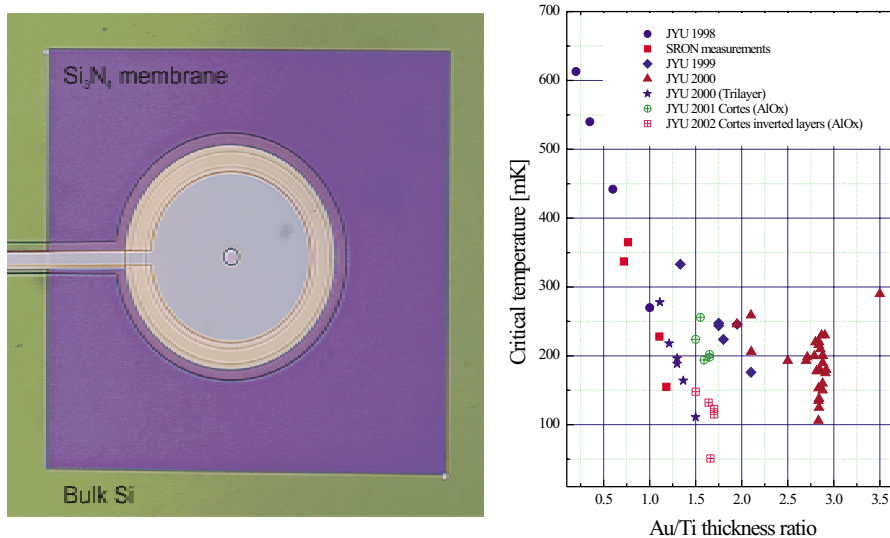


Fig. 4. (Left) An microscope image of a CORTES on a 300 nm thick Si_3N_4 membrane. (Right) Critical temperatures of various TES designs. An indicative of poor Au-Ti interface is the saturation of T_c to about 200 mK.

to uncontrollable T_c s, an effect we attribute to the desorption of contaminants (water) from the AlOx. We discovered that inverting the deposition order, i.e. depositing the insulator after the TES metals removed the problem. An $R - T$ curve of a CORTES with a $T_c=123$ mK is shown in Fig. 5.

5. Future experiments

In the near future we shall measure the noise properties of the CORTES to compare it with square devices. Also an X-ray measurement run is planned. One interesting idea to test is the direct use of the top superconducting contact as a superconducting absorber of X-rays. A benefit in this case is that most of the heat deposited by the X-rays will be conducted through the centre of the CORTES, removing any possible spatial dependence of the absorption location.

Acknowledgements. This work has been funded by the Academy of Finland and the Finnish technology agency TEKES within the framework of National ANTARES space research programmes High Energy Astrophysics and Space Astronomy (HESA)

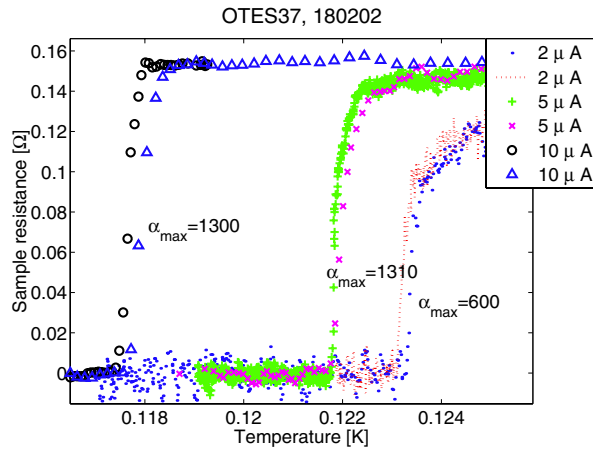


Fig. 5. The $R - T$ curve of a CORTES, measured with a constant current bias.

consortium and by the Academy of Finland under the Finnish Centre of Excellence Programme 2000-2005 (Project No. 44875, Nuclear and Condensed Matter Programme at JYFL).

References

Hilton G.C., Martinis John M., Irwin K.D., et al., 2001 IEEE Trans. Appl. Supercond. 11 (1), p. 739

Submillimetre evidence for the coeval growth of X-ray absorbed QSOs and galaxy bulges

M.J. Page¹, J.A. Stevens², and F.J. Carrera³

¹ Mullard Space Science Laboratory, University College London, Holmbury St. Mary, Dorking, Surrey, RH5 6NT, UK

² Instituto de Fisica de Cantabria (CSIC-UC), Avenida de los Castros, 39005 Santander, Spain

³ Royal Observatory, Edinburgh, EH9 3HJ, UK

Abstract. We present submillimetre observations of a sample of eight X-ray absorbed AGN with luminosities and redshifts which are likely to be characteristic of the sources which built up the majority of present day black hole mass. Half of the sources are detected at 850 μm with flux densities between 5 and 10 mJy, and are therefore ultraluminous or hyperluminous infrared galaxies. Interpreting the submillimetre flux as emission from dust heated by starbursts, these results suggest that the majority of the stars in spheroids were formed at the same time as their central black holes built up most of their mass by accretion. In the next decade, submillimetre observations using *Herschel* and ALMA should revolutionise the study of obscured star formation in the early galaxies; X-ray observations with *XEUS* will be vital if we are to understand the role played by massive accreting black holes in these objects.

1. Introduction

It now appears very likely that the creation and fuelling of AGN is related to galaxy formation. The luminosity function of AGN has evolved strongly with cosmic time, declining dramatically since the apparent peak of AGN activity at redshift ~ 2 (e.g. Boyle et al. 2000). Data from a variety of sources now show that star formation also peaked at redshift ~ 2 (Blain et al 1999 and references therein). This redshift corresponds to the epoch at which galaxies are expected to have assembled according to the hierarchical cold dark matter cosmology. The discovery and demography of massive dark objects, remnants of once luminous AGN in the bulges of many nearby galaxies (Magorrian et al. 1998), further demonstrates that the creation and fuelling of AGN is likely to be linked with the formation of galaxies, possibly occurring during the major growth phase of galaxy bulges. We have investigated this hypothesis by observing a sample of X-ray absorbed QSOs in the submillimetre. If the host galaxies of these objects were forming their stellar bulges in dusty starbursts we would expect them to be strong emitters of far infrared radiation.

2. The sample of X-ray absorbed QSOs

Our sample consists of eight X-ray selected, X-ray absorbed, broad line QSOs from our survey of hard spectrum *Rosat* sources (Page, Mittaz and Carrera 2000, 2001). The column densities and luminosities of the sources are shown in Fig. 1. They are characteristic of the sources that built up most of the mass that is now present in supermassive black holes:

- Their redshifts are in the range 1-3 where the integrated accretion luminosity density of AGN was at its peak.
- Their luminosities are close to the break in the luminosity function, which is where the majority of AGN accretion luminosity is produced.
- They are X-ray absorbed; of order 80% of AGN are expected to be absorbed X-ray sources, and many are now being discovered in deep X-ray surveys.
- All but one of them are radio quiet – in similar proportion to the overall AGN population at these luminosities.

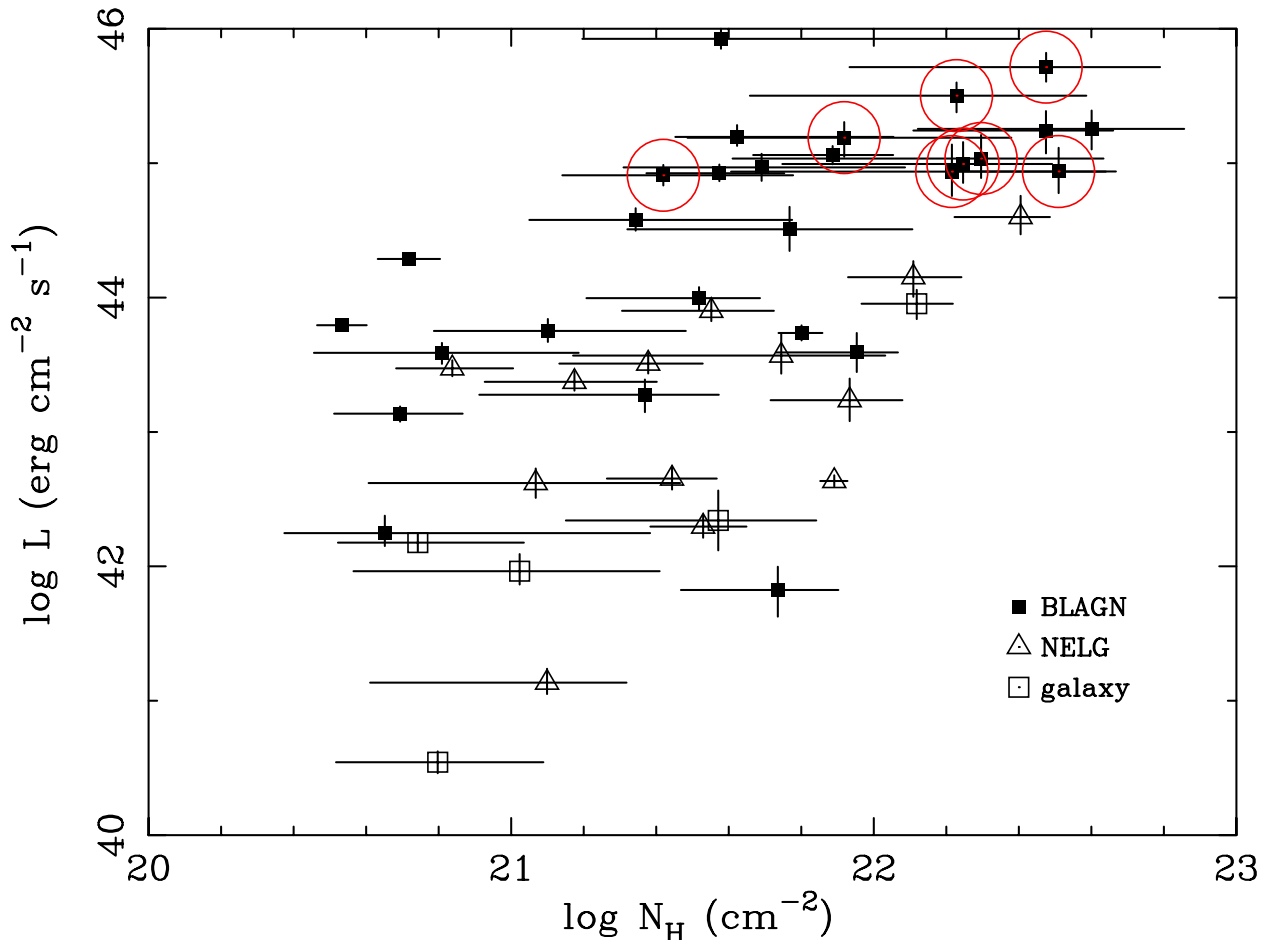


Fig. 1. X-ray column densities and intrinsic 0.5-2 keV luminosities for the identified AGN in our hard spectrum Rosat sample. The sources which have been observed in the submillimetre are circled.

3. Submillimetre observations

The sources were observed at $850\mu\text{m}$ using the Submillimetre Common User Bolometer Array (SCUBA; Holland et al. 1999) on the James Clerk Maxwell Telescope. Half of the objects were detected (all those with $z > 1.5$) with flux densities between 5 and 10 mJy as shown in Fig. 2. This means that these sources are extremely luminous in the far infrared – of order $10^{13} L_{\odot}$, similar to the sources that produce the majority of the submillimetre background radiation (Smail et al. 2002). Their far infrared luminosities are larger or similar to the entire bolometric output expected from the AGN components detected in X-rays, suggesting that the far infrared radiation is powered by regions of intense star formation (see Page, Stevens, Mittaz and Carrera 2001 for more details). The ratios of AGN to star formation luminosity in these objects are similar to what is expected from the present day ratio of black hole mass to stellar bulge mass.

Our results imply a significant overlap between the growth phases of massive black holes and galaxy bulges. However, the manner in which the two components influence each other and the overall galaxy formation process is now the subject of much speculation. For example, in the model developed by Archibald et al. (2001) the dimming of the AGN component is brought about by the consumption of its gas supply by star formation. In contrast, in the model proposed by Fabian (1999) the AGN eventually generates a powerful wind which expels the remaining reservoir of gas, terminating the growth of the stellar bulge. Understanding the interaction between the accretion and star formation processes, and their relative roles in galaxy formation will be an important objective for future observational programmes.

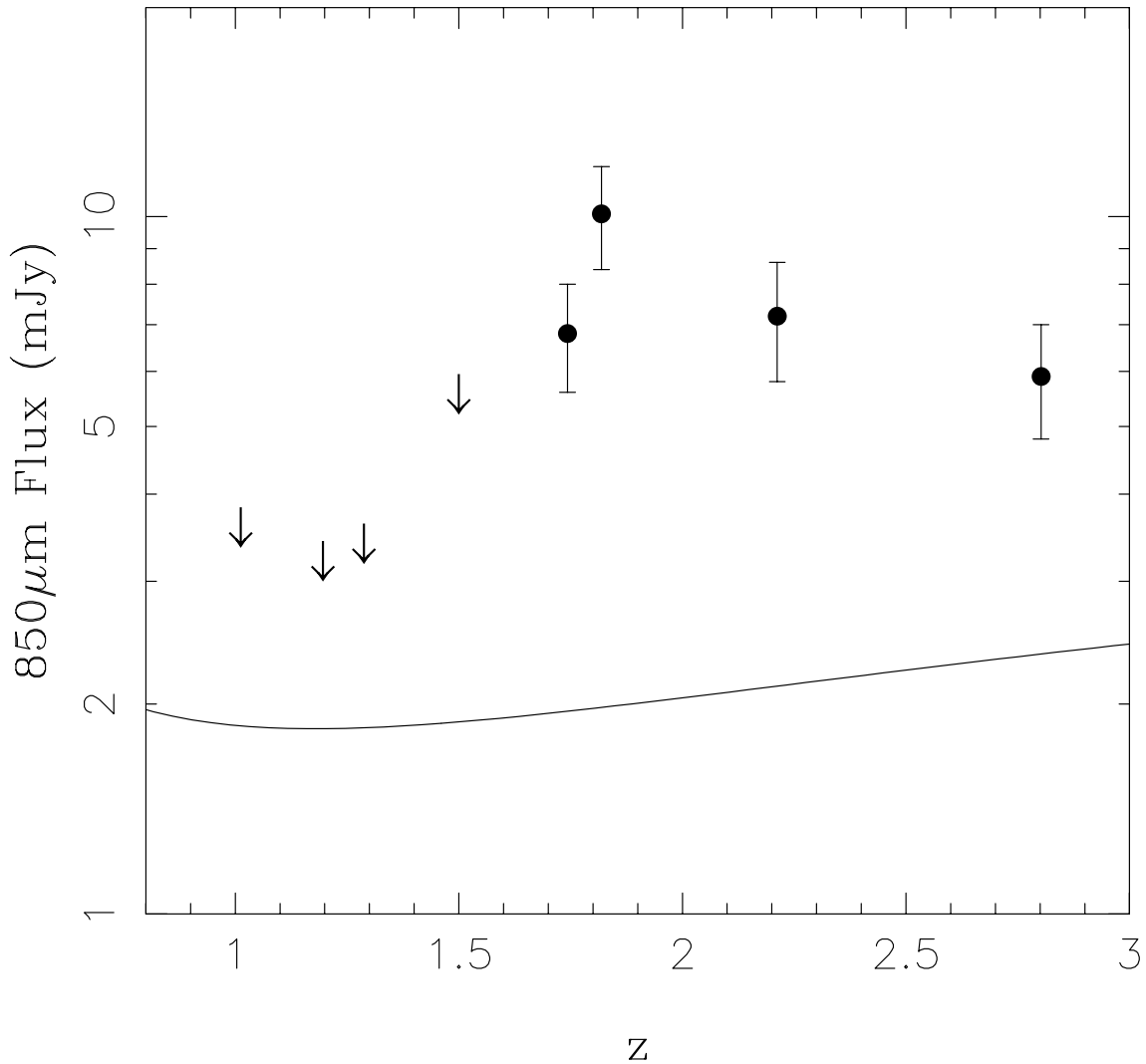


Fig. 2. $850\mu\text{m}$ flux densities of the X-ray absorbed QSOs as a function of their redshifts. For comparison we show the flux density which would be observed from Mrk 231 at similar redshifts.

4. Implications for XEUS

This study shows the importance of combining X-ray observations to detect emission from obscured AGN and submillimetre observations to detect dramatic episodes of star formation. If the bulk of the faint submillimetre sources contain AGN, a large fraction of AGN accretion may have been embedded in dusty starbursts at early epochs. Therefore, if we are to understand the relationship between the histories of star formation and accretion, we will require observations of both the hot and the cold Universe.

In the era of XEUS, the Atacama Large Millimetre Array (ALMA) will be operating with a hundred-fold improvement in submillimetre sensitivity compared to today's state of the art. Deep surveys in the infrared and submillimetre with the ESA *Herschel* satellite will have found many dusty galaxies, opening up the cold Universe at high redshift.

If the first massive black holes were embedded deep in highly obscured star forming galaxies, sensitive X-ray observations with XEUS will be required to constrain their masses and accretion rates. Observations of molecular lines with ALMA are likely to be vital to determine their redshifts, as such objects may be far too faint for optical or infrared spectroscopy. Observations of molecular lines can also provide gas masses for these early galaxies, indicating their evolutionary status and star forming potential. This means that the complementary capabilities of ALMA and XEUS together offer excellent prospects for determining the role of supermassive black holes in the formation of the first galaxies.

References

- Archibald E.N., Dunlop J.S., Jimenez R., Friaca A.C.S., McLure R.J., Hughes D.H., 2002, astro-ph/0108122
- Blain A.W., Jameson A., Smail I., Longair M.S., Kneib J.-P., Ivison R.J., 1999, MNRAS, 309, 715
- Boyle B.J., Shanks T., Croom S.M., Smith R.J., Miller L., Loaring N., Heymans C., 2000, MNRAS, 317, 1014
- Fabian A.C., 1999, MNRAS, 308, L39
- Holland W.S., et al., 1999, MNRAS, 303, 659
- Page M.J., Mittaz J.P.D., Carrera F.J., 2000, MNRAS, 318, 1073
- Page M.J., Mittaz J.P.D., Carrera F.J., 2001, MNRAS, 325, 575
- Page M.J., Stevens J.A., Mittaz J.P.D., Carrera F.J., 2001, Science, 294, 2516
- Smail, I., Ivison R.J., Blain A.W., Kneib J.-P., 2002, MNRAS, 331, 495

X-Ray Survey with High Spectral Resolution Microcalorimeters

L. Piro¹, L. Colasanti¹, E. Costa¹, P. Soffitta¹, G. Gandolfi¹, M. Feroci¹, L. Pacciani¹, M. De Pasquale¹, A. De Rosa¹, F. Gatti², D. Pergolesi², M. Razeti², A. Ferrara³, R. Maiolino³, F. Mannucci³, M. Orio⁴, A. Ferrari⁴, E. Trussoni⁴, F. Fiore⁵, L. Stella⁵, G. Stratta⁵, D. McCammon⁶, T. Sanders⁶, M. Galeazzi⁶, A. Szymkowiak⁷, S. Porter⁷, and R. Kelley⁷

¹ IASF-CNR, Roma, Italy

² INFN-Universita' di Genova, Genoa, Italy

³ Osservatorio Astronomico Arcetri, Florence, Italy

⁴ Osservatorio Astronomico Torino, Torino, Italy

⁵ Osservatorio Astronomico Monte Porzio, Rome, Italy

⁶ Wisconsin University, Madison, USA

⁷ GSFC-NASA, USA

Abstract. IMBOSS (Intergalactic-Interstellar Medium and Burst Observatory Spectroscopy Survey) is an experiment based on X-ray microcalorimeters aimed to perform a high resolution (4-10 eV) all-sky survey. The experiment is proposed to be allocated on the International Space Station (ISS). One of the primary scientific goal is the observation of the baryon "missing" matter at $z < 2$. This is expected to be in the form of a hot medium (WHIM: Warm-Hot Integalactic Medium) emitting in soft X-rays. We aim to detect and study the WHIM via X-ray emission lines. Another key goal is the detection of X-ray features in the prompt emission of GRBs, ultimately leading to a measurement of z for those class events (like X-ray rich, dark GRBs and short GRBs) still embedded in the mystery. Finally, a high resolution spectroscopy survey of the Galaxy will clarify the origin of the many components thought to make up the diffuse galactic X-ray emission.

1. Instrumental mission profile

IMBOSS is an experiment proposed to be allocated on a space platform (the External Pallett of the ISS) and designed to perform an all-sky survey. To match the different requirements from the scientific aims, the baseline design employs two detectors with different fields of view (FOV). The first one, with a collimator of $10^\circ \times 10^\circ$, will perform a survey of the diffuse X-ray emission produced by Interstellar and Intergalactic Media. The second, with a collimator with a FOV of $60^\circ \times 60^\circ$, will scan the sky to detect GRBs and to perform a high resolution spectroscopy of their X-ray prompt emission. Two arrays of 36 silicon microcalorimeters will be employed as detectors, with similar properties: a HgTe absorber, a total area of 1.44 cm^2 and an energy resolution of 4-10 eV in the 0.1-10 keV energy band. An Adiabatic Demagnetization Refrigerator (ADR) will cool the detectors to their working temperature (few tens of mK), while 5 parylene-aluminium filters will stop the IR radiation. The ADR will be kept in its working temperature range by a He⁴ dewar. We are studying the option of using pulse-tube cryocoolers. The effective exposure time for each sky bin will be about 30 msec for a 3 years experiment life-time.

2. Scientific objectives

The major scientific objectives of IMBOSS are: - the observation of the baryon "missing" matter (WHIM); - the detection of X-ray features in the prompt emission of GRBs; - the study of the Galactic soft X-ray emission produced by thermal (and non-thermal) components of the Interstellar Medium (ISM). As for the Galactic emission, we point out that the structure of the hot gas is complex and high spectral resolution observations from the ROSAT and earlier all-sky survey have proven insufficient to disentangle it. High spectral resolution measurements promise to be a powerful tool in completing this task, because a substantial fraction of the emission is in characteristic lines of partially-ionized metals in the gas. We present in more details the potential capability of IMBOSS (and, more generally, of the microcalorimeters) in the observation of X-ray emission from WHIM and GRBs.

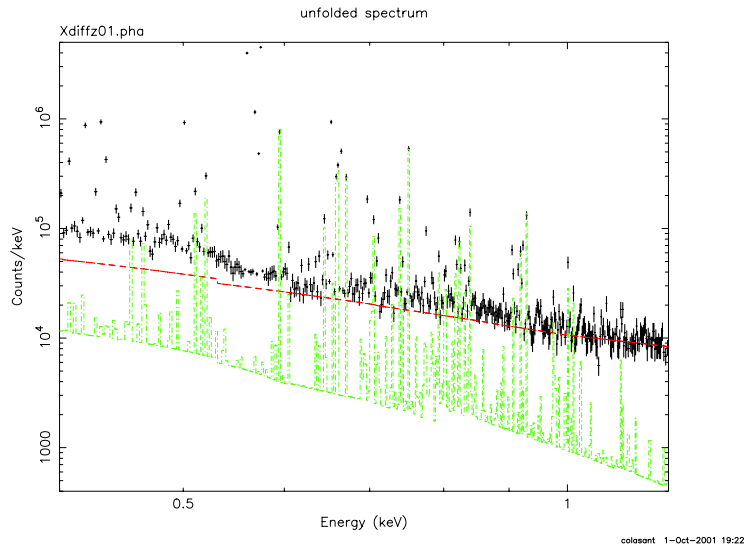


Fig. 1. Figure 1: Simulated spectrum for the WHIM and main emission lines. BLACK DATA POINT: simulated counts/keV; RED LINE: extragalactic component from discrete sources; GREEN LINE: soft X emission produced by WHIM.

At high redshifts ($z > 2$), the majority of baryons resides in the diffuse, photoionized intergalactic medium (IGM), detectable through absorption lines in the spectra of distant quasar. At lower redshift, the cosmic baryonic density is smaller compared to that seen at high z and expectations from nucleosynthesis. Hydrodynamic simulations of currently favored structure formation models predict that approximately 30%-40% of all baryons, in the present day universe, reside in a warm-hot intergalactic medium (WHIM) (Croft et al.). The WHIM lies in relatively smooth filamentary structures between galaxy and galaxy clusters with temperatures in the range $10^5 < T < 10^7$ K. It comprises gas shock-heated by accretion onto non equilibrium filamentary large-scale structure, with possibly a small energy contribution from non gravitational process such as supernova energy deposition. Simulations show that much of the radiation from the IGM is in the form of soft X-ray, with a mean intensity of 2.3×10^{-12} erg s $^{-1}$ cm $^{-2}$ deg $^{-2}$. About 35% the WHIM is responsible for the 18% of the flux incoming from the IGM. The IGM spectrum is a typical hot plasma emission (at temperature of few keV), with a large number of emission lines from elements such as O, Fe, Ne, N, Si, C and a metallicity limited to a maximum of $0.3 Z_{\odot}$ (Churazov et al.). Since the bulk of the radiation is emitted at redshift of 0.1 to 2, using microcalorimeters with a high spectral resolution, we shall be able to discriminate these lines from those of local emission by the shift of the emission line energy. Starting from the model of diffuse (galactic and extragalactic) soft X-ray emission, we have simulated the spectrum observed by a microcalorimeter, assuming a FOV of 10° , an integration time of 30 ksec and assuming that all the WHIM is located at $z=0.1$ (figure 1).

3. GRB prompt emission: iron features and absorption due to ionized circumstellar medium

Iron absorption and emission features have been detected so far in 5 GRBs (Piro et al., 1; Piro et al., 2). The observation of iron emission lines and absorption edges is an important tool to understand the origin of GRBs and the nature of their progenitors and to investigate the physical and kinematical state of the medium surrounding a GRB. Furthermore, X-ray line measurements allow to measure directly the redshift of the GRB, a capability that is particularly important for those classes of GRBs where optical counterparts have yet to be found. With its large field of view, IMBOSS will be able to detect about 14 GRB/year. For the brightest events, we expect to have enough statistic to perform a high resolution spectroscopy of the prompt emission. By a high resolution spectroscopy, we shall be able to discriminate the nature of the emission lines by the determination of their width σ_L . A narrow line could be produced from a medium at rest in the space: therefore it should be associated to stellar-forming regions. Broad lines are index of moving medium, probably pre-ejected from the supernova explosion of a massive star. The estimated line sensitivity of the detector will allow us to observe narrow lines with an equivalent width (EW) of 300 eV in 15 GRBs and broad lines, with an EW similar to that observed so far, in about 7 GRBs. The spectral capability of IMBOSS in detecting iron features is shown in figure 2.

The spectral range and the high resolution of IMBOSS will also enable us to study the absorption in the GRB spectrum due to circumburst medium. This issue is particularly important to clarify the proposed association of GRBs and Giant Molecular Clouds in star-forming regions. If GRBs are indeed embedded in a gas, we would expect that

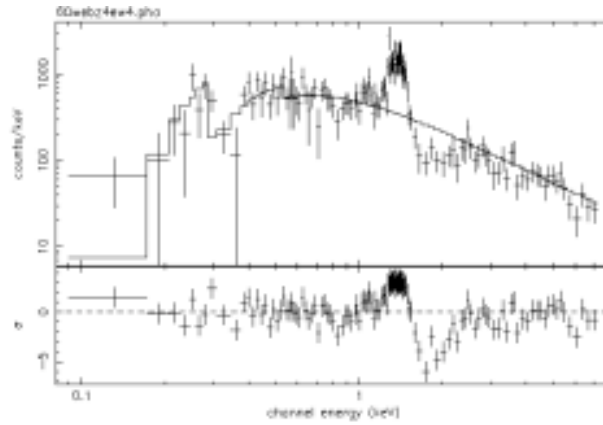


Fig. 2. Figure 2: Simulated spectrum of a GRB at redshift $z=4$. Three different iron features are superimposed to the simple power-law emission: a narrow emission line at 6.4 keV, with an E.W.=0.3 keV and $\sigma_L=0$ eV; a broad emission line at 6.9 keV, with an E.W.=4 keV and $\sigma_L=400$ eV; an absorption edge at 7.1 keV with an optical depth of 1.5 (all quantities referred to the restframe).

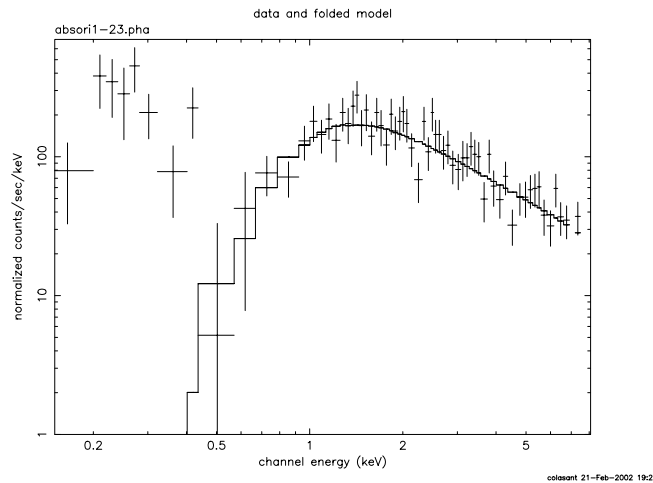


Fig. 3. Figure 3: Simulated spectrum of GRB prompt emission at redshift $z=1$, with an absorption due to hot highly ionized medium. The continuous line shows the best fit model with a power-law (for the GRB emission) and an absorption due to cold non-ionized medium. We assumed a medium temperature of 30000 K, a ionization parameter of 300 and a density $N_H = 10^{23} \text{ cm}^{-2}$. The presence of a ionized absorber is clearly visible by the excess emission below 0.5 keV, where the gas is transparent to X-ray, and by the presence of the OVII edge.

a significant fraction of this gas is ionized by GRB photons. In a ionized medium, we expect to observe, for high N_h (10^{23} cm^{-2}), deep edges from metal like oxygen. By the presence of this features, we can discriminate between hot ionized and cool medium. To focus this capability, we have simulated a spectrum assuming the presence of hot ionized circumburst medium and then we fitted it with a cool medium absorption to show the difference, as it can be seen in figure 3.

At high redshift ($z>3$), the edges fall out the detector energy windows, while, at low density ($N_h < 10^{22} \text{ cm}^{-2}$), their are not quite deep; so, in these cases, we could not discriminate between hot ionized and cool medium.

References

- Croft et al., astro-ph/0010345
 Churazov et al., 2001, Mont. Not. R. Astron. Soc. 323, 93
 Piro et al., 1999, ApJ 514, L73
 Piro et al., 2000, Science 290, 889



The mass temperature relation for clusters of galaxies

A. Del Popolo^{1,2}

¹ Dipartimento di Matematica, Università Statale di Bergamo, Piazza Rosate, 2 - I 24129 Bergamo, ITALY

² Feza Gürsey Institute, P.O. Box 6 Çengelköy, Istanbul, Turkey

Abstract. A recent observational finding, namely the existence of a break in the M-T relation, inferred from the resolved temperature profile of X-ray clusters observed by ASCA, shows how improved X-ray observations are crucial to understand the variety of physical processes in clusters of galaxies. Moreover, it seems likely that our best structure formation measurements of Ω_m will rely on medium-redshift measurements of the X-ray temperature function (XTF), and it is essential to make sure that our interpretation of cluster temperature functions is correct. To this aim, I re-derive the mass-temperature relation and its time evolution for clusters of galaxies in different cosmologies by means of two different models. The first one is a modification and improvement of a model by Del Popolo & Gambera (1999), namely based upon a modification of the top-hat model in order to take account of angular momentum acquisition by protostructures and of an external pressure term in the virial theorem. The second one is based on the merging-halo formalism of Lacey & Cole (1993). The final result is that, in both models, the M-T relation is as usual, $M \propto T^{3/2}$, at the high mass end, and $M \propto T^\gamma$, with a value of $\gamma > 3/2$ depending on the chosen cosmology. The evolution of the M-T relation, for a given M_{vir} , is more modest both in flat and open universes in comparison to previous estimate found in literature, even more modest than what found by V2000. Moreover the time evolution is more rapid in models with $L = 0$ than in models in which the angular momentum acquisition by protostructures is taken into account ($L \neq 0$). The effect of a non-zero cosmological constant is that of slightly increasing the evolution of the M-T relation with respect to open models with $L \neq 0$. The evolution is more rapid for larger values (in absolute value) of the spectral index, n .

The mass-temperature relation, obtained using the quoted models, is also compared with the data by Finoguenov, Reiprich & Bohringer (2001) (hereafter FRB). The comparison shows that the FRB data are best fitted by a low density Λ CDM model.

1. Introduction

In the past decade, observations of clusters of galaxies (e.g, ROSAT, ASCA) have shown the existence of a tight correlation between the total gravitating mass of clusters, M_{tot} , their X-ray luminosity (L_X), and temperature (T_X) of the intra-cluster medium (ICM) (David et al. 1993; Markevitch 1998; Horner, Mushotzky & Sharf 1999 (hereafter HMS)). Numerical simulations (Evrard, Metzler & Navarro 1996; Eke, Navarro & Frenk 1997; Mathiesen & Evrard 2001) and theoretical studies have motivated the existence of such kind of relations, whose comparison can provide strong constraints on the prevailing cosmological models.

Theoretical analyses suggest a self-similar relation, $M_{\text{tot}} \propto T_X^\alpha$ ¹ confirmed by the results of N-body simulations (Evrard, Metzler & Navarro 1996; Eke et al. 1998). The proportionality coefficient of the law has been usually fixed by using numerical simulations to calibrate it (Evrard et al. 1996; Thomas et al. 2001; but see Afshordi & Cen (2001) (hereafter AC) for a theoretical treatment).

A notheworthy drawback of the standard top-hat model has been stressed by Voit & Donahue (1998) (hereafter V98) and Voit (2000) (hereafter V2000). Using the merging-halo formalism of Lacey & Cole (1993), which accounts for the fact that massive clusters accrete matter quasi-continuously, they showed that the M-T relation evolves, with time, more modestly than what expected in previous models and this evolution is even more modest in open universes.

Moreover, recent studies have shown that the self-similarity in the M-T relation seems to break at some keV (Nevalainen, Markevitch & Forman (hereafter NMF); Xu, Jin & Wu 2001). By means of ASCA data, using a small

¹ $\alpha = 3/2$, almost unrelated to the settings of the cosmological parameters

sample of 9 clusters (6 at 4 keV and 3 at ~ 1 keV), NMF has shown that $M_{\text{tot}} \propto T_X^{1.79 \pm 0.14}$ for the whole sample, and $M_{\text{tot}} \propto T_X^{3/2}$ excluding the low-temperature clusters. Xu, Jin & Wu (2001) has found $M_{\text{tot}} \propto T_X^{1.60 \pm 0.04}$ (using the β model), and $M_{\text{tot}} \propto T_X^{1.81 \pm 0.14}$ by means of the Navarro, Frenk & White (1995) profile. FRB have investigated the T-M relation in the low-mass end finding that $M \propto T^2$, and $M \propto T^{3/2}$ at the high mass end. This behavior has been attributed to the effect of the formation redshift (FRB) (but see Mathiesen 2001 for a different point of view), or to cooling processes (Muanwong et al. 2001) and heating (Bialek, Evrard & Mohr 2000). AC has shown that non-sphericity introduces an asymmetric, mass dependent, scatter for the M-T relation altering its slope at the low mass end ($T \sim 3$ keV).

In this paper, I derive the mass-temperature relation, and its time evolution, for clusters of galaxies, in different cosmologies by means of two different models: the first one is a modification and improvement of a model by Del Popolo & Gambera (1999), based upon a modification of the top-hat model in order to take account of angular momentum acquisition by protostructures and of an external pressure term in the virial theorem. The second one is an improvement of a model proposed by V2000.

The plan of the paper is the following: in section (2) I describe the top-hat modified model (hereafter THM) and in section (3) the modified V2000 model (hereafter VM). Section (4) describes the results and section (5) is devoted to conclusions.

2. Review of the Top-Hat model

In the following, I'll use Del Popolo & Gambera (1999) in order to get the M-T relation. The model is fundamentally a modification of the top-hat model in order to take account of angular momentum acquisition by protostructures and uses a modified version of the virial theorem in order to include a surface pressure term (V2000, AC). This correction is due to the fact that at the virial radius r_{vir} the density is non-zero and this requires a surface pressure term to be included in the virial theorem (Carlberg, Yee & Ellingson 1997) (the existence of this confining pressure is usually not accounted for in the top-hat collapse model).

The equation governing the collapse of a density perturbation taking account angular momentum acquisition by protostructures can be obtained using a model due to Peebles (Peebles 1993) (see also Del Popolo & Gambera 1998, 1999) and is given by:

$$\frac{dv_r}{dt} = \frac{L^2(r)}{M^2 r^3} - g(r) = \frac{L^2(r)}{M^2 r^3} - \frac{GM}{r^2} \quad (1)$$

Assuming a non-zero cosmological constant Eq. (1) becomes:

$$\frac{dv_r}{dt} = -\frac{GM}{r^2} + \frac{L^2(r)}{M^2 r^3} + \frac{\Lambda}{3} r \quad (2)$$

(Peebles 1993; Bartlett & Silk 1993; Lahav 1991; Del Popolo & Gambera 1998, 1999). Integrating Eq. (2) we have:

$$\frac{1}{2} \left(\frac{dr}{dt} \right)^2 = \frac{GM}{r} + \int \frac{L^2}{M^2 r^3} dr + \frac{\Lambda}{6} r^2 + \epsilon \quad (3)$$

where the value of the specific binding energy of the shell, ϵ , can be obtained using the condition for turn-around, $\frac{dr}{dt} = 0$.

The CDM spectrum used in this paper is that of Bardeen et al. (1986) normalized to reproduce the observed abundance of rich cluster of galaxies (e.g., Bahcal & Fan 1998) Filtering the quoted spectrum on clusters scales, $R_f = 3h^{-1} Mpc$, we obtained the total angular momentum acquired during expansion, as described in Del Popolo & Gambera (1998, 1999) (more hints on the model and some of the model limits can be found in Del Popolo, Ercan & Gambera (2001)).

The temperature-mass relation can be obtained using energy conservation, using Eq. (3) and the virial theorem modified to take account of a surface pressure term. Assuming that:

$$\langle K \rangle + \langle E \rangle = 3P_{\text{ext}}V \quad (4)$$

(AC), (the meaning of $\langle \rangle$ is the time-average of the quantity considered) where P_{ext} is the pressure of the outer boundary of virialized region and V is the volume, and by using the same assumption of AC, namely:

$$3P_{\text{ext}}V = -\nu U \quad (5)$$

where ν is a coefficient and U is the total potential, I finally obtain:

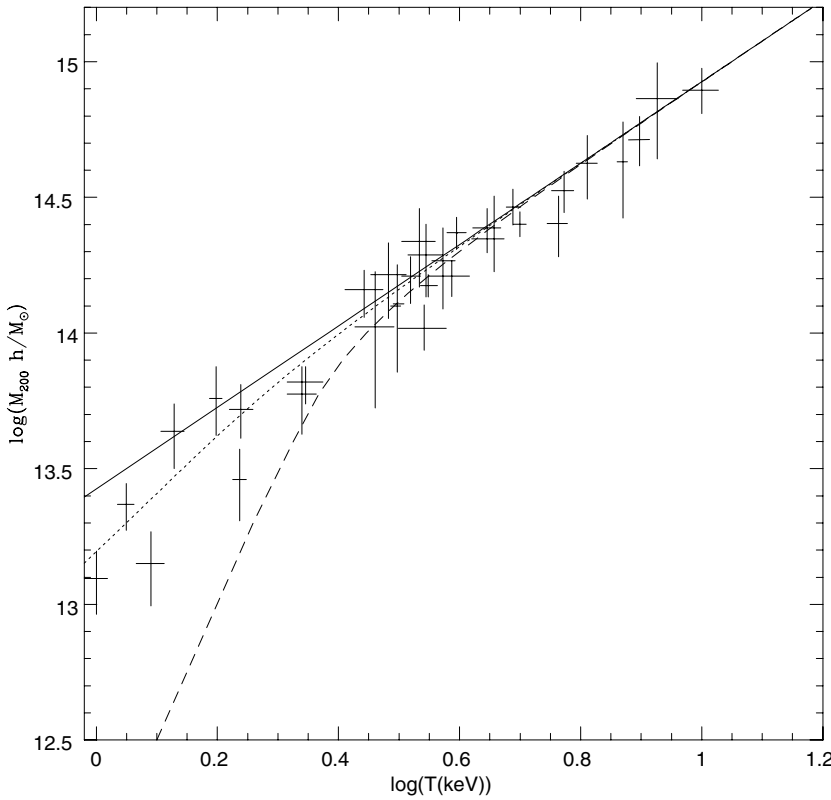


Fig. 1. M-T relation predicted by the modified top-hat model. The solid line is the prediction of Eq. (6), for $\Omega_\Lambda = 0$, $\Omega_0 = 1$, shifted downwards, similarly to AC, to fit the FRB observational data in the massive end. The dotted and dashed line represents the prediction of the same equation for $L \neq 0$, $\Omega_\Lambda = 0$, $\Omega_0 = 1$ and $L \neq 0$, $\Omega_\Lambda = 0$ and $\Omega_0 = 0.3$, respectively.

$$kT = 1.58(\nu + 1) \frac{\mu}{\beta} \frac{1}{\psi \xi} \Omega_0^{\frac{1}{3}} \left(\frac{M}{10^{15} M_\odot h^{-1}} \right)^{\frac{2}{3}} (1 + z_{ta}) \left[1 + \left(\frac{2^{10}}{3^2} \pi^{\frac{2}{3}} \right) \psi \xi \rho_{b,ta}^{\frac{2}{3}} \frac{1}{H^2 \Omega_0 M^{\frac{8}{3}} (1 + z_{ta})} \int_0^{r_{eff}} \frac{L^2}{r^3} dr - \frac{2}{3} \frac{\Lambda}{\Omega_0 H_0^2 (1 + z_{ta})^3} (\psi \xi)^3 \right] \text{keV} \quad (6)$$

where z_{ta} is the redshift at turn-around, ξ is a parameter given by $\xi = r_{ta}/x_1$, r_{ta} being the radius of the turn-around epoch, while x_1 is defined by the relation $M = 4\pi\rho_b x_1^3/3$, $\psi = r_{eff}/r_{ta}$, $\Omega_0 = \frac{8\pi G \rho_b}{3H_0^2}$ and $\Omega_\Lambda = \frac{\Lambda}{3H_0^2} = 1 - \Omega_0$.

The previous result reduces to the standard one of late-formation approximation (see Eq. 8 of V2000) for $\nu = L = \Lambda = 0$.

The value of r_{eff} , or the ratio $\psi = r_{eff}/r_{ta}$ is obtained, similarly to Lahav et al (1991) and is given by the cubic equation:

$$1 - \nu + (\xi\psi)^3 [\eta\nu + 2\eta] - \psi (2 + \eta\xi^3) - \frac{27}{32} \frac{\xi^9 \psi}{\rho_{ta}^3 \pi^3 G r_{ta}^8} \left(\nu \int_0^{r_{eff}} \frac{L^2}{r^3} dr + \int_0^{r_{ta}} \frac{L^2}{r^3} dr \right) = 0 \quad (7)$$

where

$$\eta = \frac{\Lambda}{4\pi G \rho_{ta}} = \frac{\Lambda r_{ta}^3}{3GM} = \frac{2\Omega_\Lambda}{\Omega_0} \left(\frac{\rho_{ta}}{\rho_{ta,b}} \right)^{-1} (1 + z_{ta})^{-3} \quad (8)$$

The previous equation reduces to the standard result $\frac{r_{eff}}{r_{ta}} = \frac{r_{vir}}{r_{ta}} = 1/2$, for $\Lambda = L = \nu = 0$, $\Omega_0 = 1$.

The derivation of the previous relation is fundamentally based on the approximation of cluster formation with the evolution of a spherical top-hat density perturbation (Peebles 1993) and on the additional assumption that each cluster observed at a redshift z has just reached the moment of virialization. This last assumption is currently known

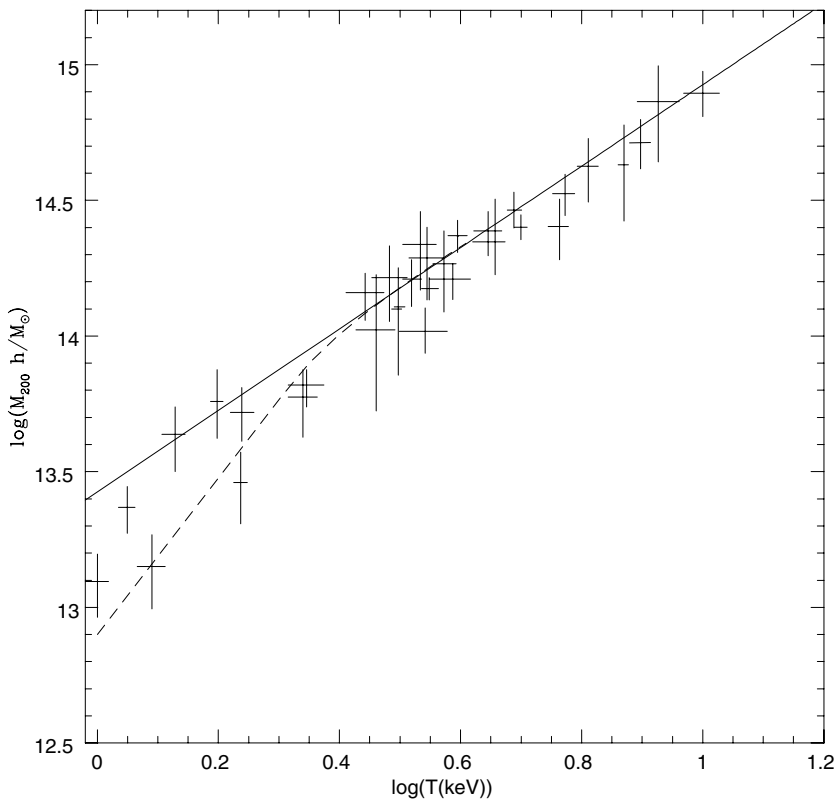


Fig. 2. M-T relation predicted by the modified top-hat model. As Fig. 1 but now $\Omega_\Lambda \neq 0$. The solid line is equivalent to the solid one in Fig. 1. The dashed line represents the case of a flat universe with $L \neq 0$, $\Lambda \neq 0$, ($\Omega_0 = 0.3$, $\Omega_\Lambda = 0.7$).

as the late-formation approximation, which is a good one in a critical $\Omega_0 = 1$, because for this value of Ω massive clusters develop rapidly at all redshifts and the moment of virialization is always close to that of observation. As shown by V2000, to obtain the proper normalization and time evolution of the M-T relation, one has to account:

- a) for the continuous accretion of mass of clusters;
- b) for the non-zero density at r_{vir} , requiring a change in the virial theorem by including a surface pressure term.

The M-T relation derived by means of a model of continuous accretion, as that of V2000, differs from the late-formation model in both normalization and time-dependent behavior. A comparison of the normalization predicted by the late-formation model with that predicted by simulations of Evrard, Metzler & Navarro (1996) shows that when $\Omega_0 = 1$ this normalization is only 4% below the empirical value, but it lies 20% below it for $\Omega_0 = 0.2$. In the case of V2000 model and for a power-law spectrum, a comparison with the same simulations show that the temperature normalization of the $n = -2$ case deviates by less than 10% over the range $0.2 < \Omega_0 < 1$ and by $\simeq 18\%$ in the case $n = -1$ (V2000). For the purpose of studying cluster evolution, the change in the M-T relation with z is more important than its normalization: although the differences in evolution of the M-T relation are of the order of 10% (V98), when it is introduced in the Press-Schechter model, they are amplified by the exponential term in the Press-Schechter formula.

In the next section, I'll extend the V2000 model to take account of tidal interaction between clusters and the evolution of the M-T relation, comparing the results with the those of the top-hat model.

3. Revisiting the continuous formation model

The late-formation approximation is a good one for many purposes, but a better one can be obtained in the low- Ω limit. As can be found in the literature, there are several ways of improving the quoted model (Kitayama & Suto 1996; Viana & Liddle 1996; V98, V2000). In the V98, V2000 approach, the top-hat cluster formation model is substituted by a model of cluster formation from spherically symmetric perturbations with negative radial density gradients. The fact that clusters form gradually, and not instantaneously, is taken into account in the merging-halo formalism of

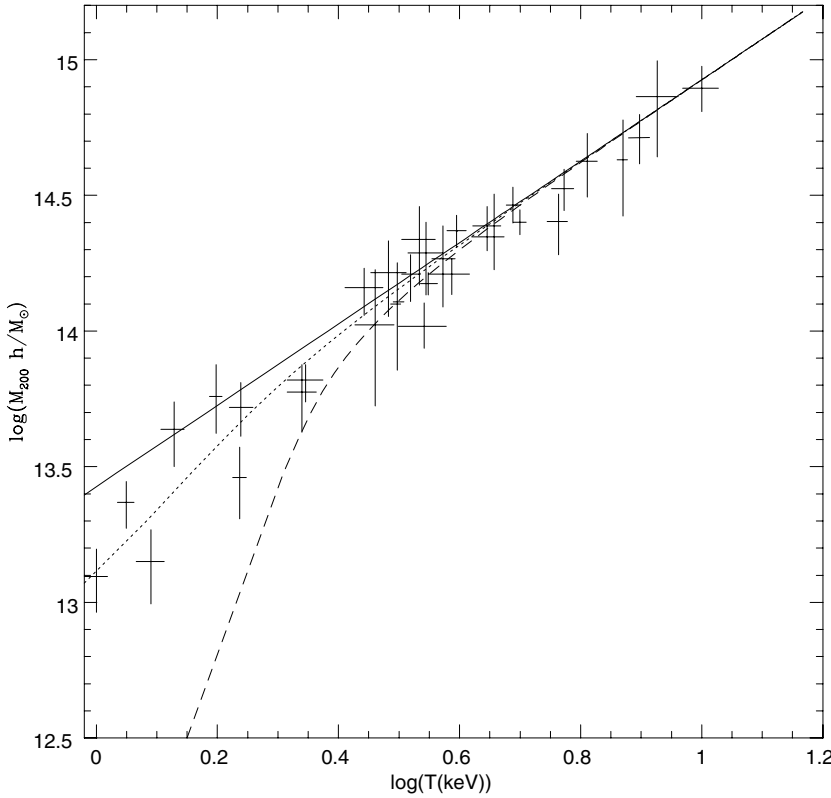


Fig. 3. M-T relation predicted by the modified cluster continuous-formation model. The solid line is the prediction of the quoted model, for $\Omega_\Lambda = 0$, $\Omega_0 = 1$, shifted downwards, similarly to AC, to fit the FRB observational data in the massive end. The dotted and dashed line represents the prediction of the same model for $L \neq 0$, $\Omega_\Lambda = 0$, $\Omega_0 = 1$ and $L \neq 0$, $\Omega_\Lambda = 0$ and $\Omega_0 = 0.3$, respectively.

Lacey & Cole (1993). As shown by V2000, the mass grows like $M \propto \omega^{-3/(n+3)}$ (Lacey & Cole 1993; V98; V2000). The virial energy of the cluster, $-E$, can be calculated by integrating the specific energy ϵ , $E = -\int \epsilon dM$. The cluster temperature can be obtained remembering that it is proportional to $\frac{E}{M}$. Integrating Eq.(3), I get:

$$t = \int \frac{dr}{\sqrt{2 \left[\epsilon + \frac{GM}{r} + \int_{r_i}^r \frac{L^2}{M^2 r^3} dr + \frac{\Lambda}{6} r^2 \right]}} \quad (9)$$

A particular shell will collapse if:

$$\epsilon + \frac{GM}{r_0} + \int_{r_i}^{r_0} \frac{L^2}{M^2 r^3} dr + \frac{\Lambda}{6} r_0^2 = 0 \quad (10)$$

(see V2000), and the shell reaches its maximum radius (turn-around radius, r_{ta}) at a time:

$$t_{\text{ta}} = \int_0^{r_0} \frac{dr}{\sqrt{2 \left[\epsilon + \frac{GM}{r} + \int_{r_i}^r \frac{L^2}{M^2 r^3} dr + \frac{\Lambda}{6} r^2 \right]}} \quad (11)$$

An approximate relation for $\epsilon(t)$, in an Einstein-de Sitter Universe is given by:

$$\epsilon = -\frac{1}{2} \left(\frac{2\pi G}{t_\Omega} \right)^{\frac{2}{3}} M^{2/3} \left[\left(\frac{M}{M_o} \right)^{-\frac{5}{3m}} - 1 \right] \left[1 + \frac{F}{M^{\frac{8}{3}}} \frac{1}{\left(\frac{M}{M_o} \right)^{-\frac{5}{3m}} - 1} \right] \quad (12)$$

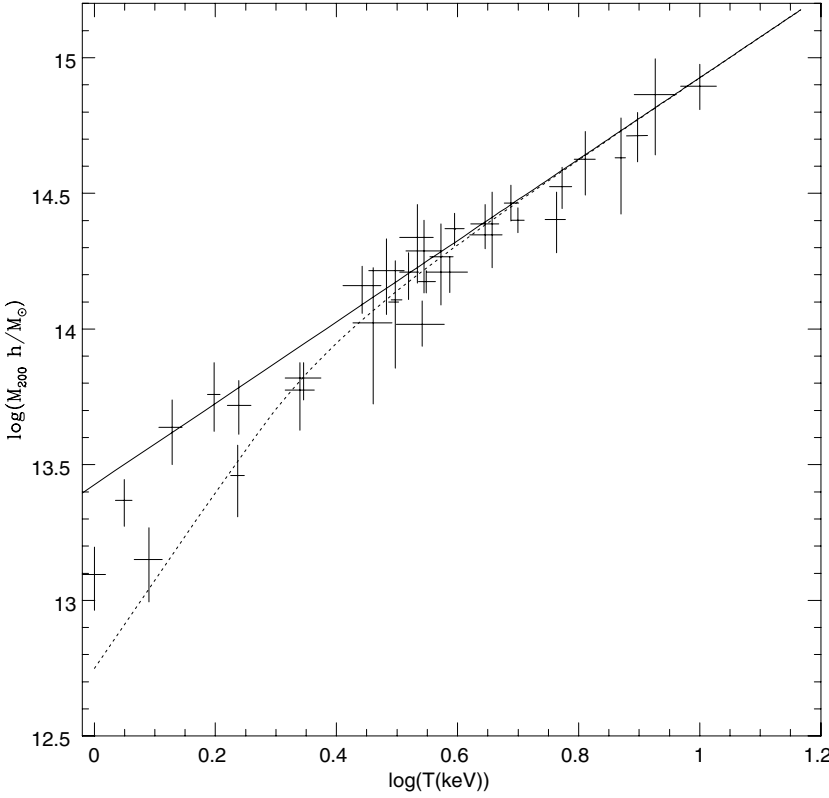


Fig. 4. M-T relation predicted by the modified cluster continuous-formation model. The solid line is the prediction of the quoted model, for $\Omega_\Lambda = 0$, $\Omega_0 = 1$, shifted downwards, similarly to AC, to fit the FRB observational data in the massive end. The dotted line represents the prediction of the same model for $L \neq 0$, $\Lambda \neq 0$, ($\Omega_\Lambda = 0.7$ and $\Omega_0 = 0.3$).

where

$$F = \frac{2^{7/3} \pi^{2/3} \xi \rho_b^{2/3}}{3^{2/3} H^2 \Omega} \int_0^r \frac{L^2 dr}{r^3} \quad (13)$$

Integrating with respect to mass, and dividing again by M , I get:

$$\frac{E}{M} = -\frac{\int \epsilon dM}{M} = \frac{3m}{10(m-1)} \left(\frac{2\pi G}{t_\Omega} \right)^{\frac{2}{3}} M^{\frac{2}{3}} \left[\frac{1}{m} + \left(\frac{t_\Omega}{t} \right)^{\frac{2}{3}} + \frac{K(m, x)}{M^{8/3}} \right] \quad (14)$$

$$\text{where } t_\Omega = \frac{\pi \Omega_0}{H_0(1-\Omega_0-\Omega_\Lambda)^{\frac{3}{2}}},$$

$$K(m, x) = (m-1) Fx \text{LerchPhi}(x, 1, 3m/5 + 1) - (m-1) F \text{LerchPhi}(x, 1, 3m/5) \quad (15)$$

where the *LerchPhi* function is defined as follows:

$$\text{LerchPhi}(z, a, v) = \sum_{n=0}^{\infty} \frac{z^n}{(v+n)^a} \quad (16)$$

If $K = 0$, Eq. (14) reduces to Eq. (10) of V2000. As stressed by V2000, some factors give rise to an higher value of E/M with respect the case of the late-formation value. The $m/(m-1)$ value which accounts for the effect of early infall. The $1/m$ value in the square bracket of Eq. (14) which accounts for the cessation of cluster formation when $t \gg t_\Omega$. Finally in Eq. (14) a new term is present, which comes from the tidal interaction. In order to obtain an expression for

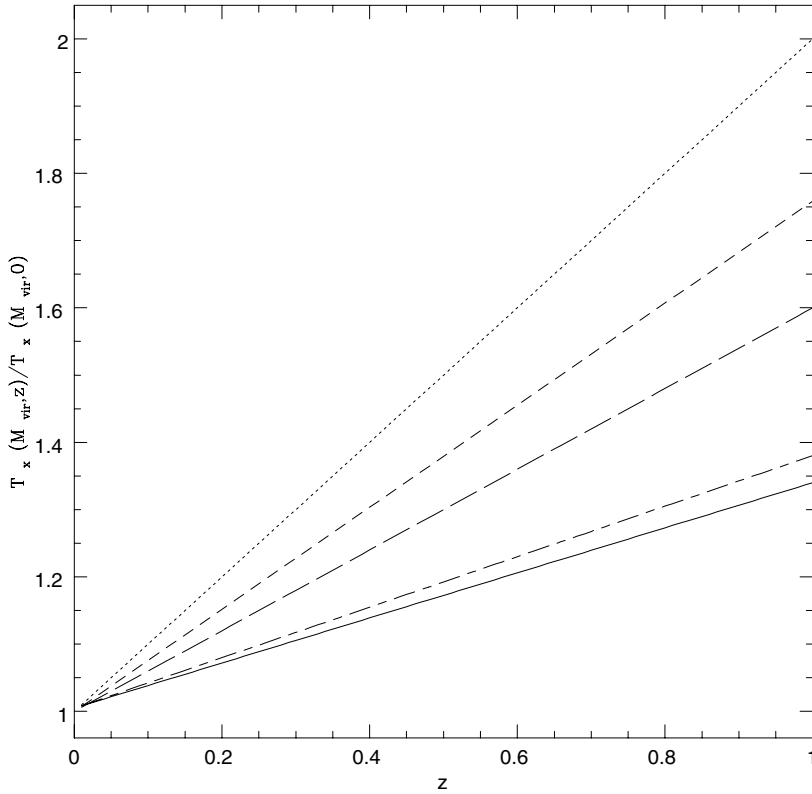


Fig. 5. Temperature evolution predicted by the top-hat M-T relation. The dotted line represents the prediction for $\Omega_0 = 1$ and $L = 0$ which coincides with the “classical” prediction, $T_X \propto (1+z)$. The short-dashed line represents the case $\Omega_0 = 0.2$ and $L = 0$, coinciding with the late formation model described in V2000 (Eq. 8). The long-dashed line represents $\Omega_0 = 1$ and $L \neq 0$. Finally, the short-long-dashed line represents the case $L \neq 0$, $\Lambda \neq 0$ ($\Omega_0 = 0.2$, $\Omega_\Lambda = 0.8$) and the solid line the case $L \neq 0$, $\Lambda = 0$, $\Omega_0 = 0.2$.

the kinetic energy, starting from E/M , I use the virial theorem with the surface pressure term correction as in V2000 and I finally get:

$$kT = \frac{2}{5} a \frac{\mu m_p}{2\beta} \frac{m}{m-1} \left(\frac{2\pi G}{t_\Omega} \right)^{\frac{2}{3}} M^{\frac{2}{3}} \left[\frac{1}{m} + \left(\frac{t_\Omega}{t} \right)^{\frac{2}{3}} + \frac{K(m,x)}{M_0^{8/3}} \right] \quad (17)$$

where $a = \frac{\bar{p}}{2\rho(r_{\text{vir}}) - \bar{p}}$ is the ratio between kinetic and total energy (V2000). Using the relation $\Delta_{\text{vir}} = \frac{8\pi^2}{Ht^2}$ (see V2000), and in the early-time limit: ($t \ll t_\Omega$), Eq. (17), reduces to:

$$kT = \frac{2}{5} \frac{m}{m-1} a \frac{\mu m_p}{2\beta} G M^{\frac{2}{3}} \left(\frac{4\pi}{3} \rho_b \Delta_{\text{vir}} \right)^{1/3} \quad (18)$$

which, in the case $n \sim -2$, $a \sim 2$ is identical to the late-formation formula, described in V2000 (see their Eq. (8)). Normalizing Eq. (17) similarly to V2000, I get:

$$kT \simeq 8keV \left(\frac{M^{\frac{2}{3}}}{10^{15} h^{-1} M_\odot} \right) \frac{\left[\frac{1}{m} + \left(\frac{t_\Omega}{t} \right)^{\frac{2}{3}} + \frac{K(m,x)}{M^{8/3}} \right]}{\left[\frac{1}{m} + \left(\frac{t_\Omega}{t_0} \right)^{\frac{2}{3}} + \frac{K_0(m,x)}{M_0^{8/3}} \right]} \quad (19)$$

where $K_0(m,x)$ indicates that $K(m,x)$ must be calculated assuming $t = t_0$

Eq. (19) when compared to the result of V2000 (Eq. 17) shows an additional term, mass dependent. This means that, as in the case of the top-hat model, the M-T relation is no longer self-similar showing a break at the low mass end (see next section).

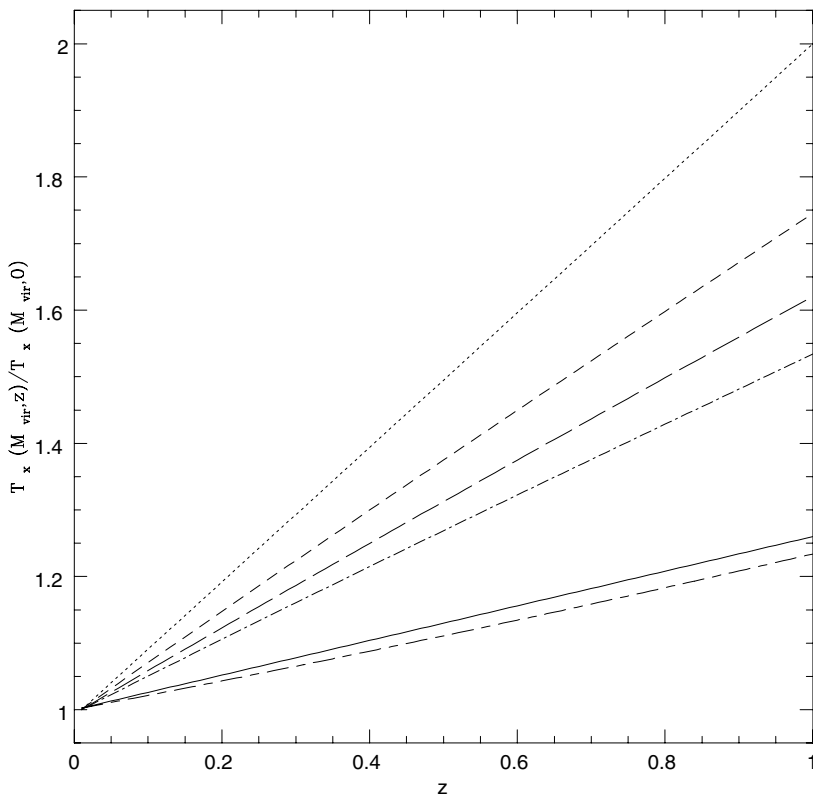


Fig. 6. Temperature evolution predicted by the modified cluster continuous-formation model in the case $\Omega_0 = 0.2$. The dotted line represents the “classical” prediction, $T_X \propto (1+z)$. The short-dashed line represents the late-formation approximation as expressed by Eq. (8) in V2000, namely $T_X \propto \Delta_{\text{vir}}^{1/3} \left[\frac{\Omega_0}{\Omega_0(z)} \right]^{1/3} (1+z)$. The long-dashed line and the dot-dashed one plot Eq. (17) for $L = 0$ and $n = -2$, $n = -1$, respectively. The solid line plot the same equation for $L \neq 0$ and $n = -1$. Finally the long-short dashed line represents Eq. 73 of AC.

4. Results

The results of the models described in the previous sections are plotted in Fig. 1-6.

Fig. 1 compares the M-T relation obtained by means of the THM model with the FRB data. The solid line is the prediction of Eq. (6), for $\Omega_\Lambda = 0$, $\Omega_0 = 1$, shifted downwards, similarly to AC, to fit the observational data in the massive end. The reason of the shift is due to the fact that X-ray mass estimates lead to normalizations about 50% higher than hydro-simulations, (while mass estimates from galaxy velocity dispersion is consistent with simulation results (HMS)). The dotted line represents the prediction of Eq. (6) for $L \neq 0$, $\Omega_\Lambda = 0$, $\Omega_0 = 1$. The plot shows a non-self-similar behavior. A break at $T_X \sim 3\text{keV}$ is evident and in this low mass range the power index $\alpha \sim 1.8$. It is interesting to note that the mass estimates using the observational β -model lead to a power index $1.7 < \alpha < 1.8$. Originally this behavior was interpreted as an artifact of the β -model (HMS), but the observation of a similar behavior for masses estimated from the resolved temperature profile (FRB) and confirmed by other studies (e.g., Xu, Jin & Wu (2001)), who found the break at $T_X = 3 - 4\text{keV}$. The quoted bent is interpreted in different ways (FRB; Mathiesen 2001; Xu, Jin & Wu 2001). In the model of this paper, the bent is entirely justified in terms of cluster tidal interaction with the neighboring ones, or in other terms it is strictly connected to the asphericity of clusters (see Del Popolo & Gambera 1999 for a discussion on the relation between angular momentum acquisition, asphericity and structure formation). Non-sphericity introduces an asymmetric bent, dependent on mass, in the M-T relation that gives rise to a different slope at the low mass end ($T \sim 3\text{keV}$): the lower the mass the larger the bent. A possible explanation for the reason of the origin of the bent is the following. The M-T relations found in this paper differ from previous models (e.g. V2000, AC), for the presence of a term depending on mass and angular momentum, L , originating from the gravitational interaction of the quadrupole moment of the protocluster with the tidal field of the matter of the

neighboring protostructures. This last term changes the dependence of the temperature on the mass, M , in the M-T relation.

Coming back to Fig. 1, the dashed line represents the prediction of Eq. (6) for $L \neq 0$, $\Omega_\Lambda = 0$ and $\Omega_0 = 0.3$. Fig. 1 shows that in an Einstein-de Sitter universe the scatter/bent is under-estimated, while in a Λ CDM model with $\Omega_0 = 0.3$ it is overestimated.

Fig. 2 represents the same calculation of the previous figure but now $\Omega_\Lambda \neq 0$. The solid line is equivalent to the solid one in Fig. 1. The dashed line represents the case $L \neq 0$, $\Lambda \neq 0$, ($\Omega_0 = 0.3$, $\Omega_\Lambda = 0.7$). It is evident that the effect of a non-zero cosmological constant is that of reducing the effect of L , and that the Λ CDM cosmology is in better agreement with the observed scatter.

The M-T relation predicted by the modified continuous formation model is plotted in Fig. 3 and Fig. 4. In Fig. 3, the solid line is the prediction of the quoted model, for $\Omega_\Lambda = 0$, $\Omega_0 = 1$, shifted downwards, similarly to AC and to the top-hat model (Fig. 1-2), to fit the FRB observational data in the massive end. The dotted and dashed line represents the prediction of the same model for $L \neq 0$, $\Omega_\Lambda = 0$, $\Omega_0 = 1$ and $L \neq 0$, $\Omega_\Lambda = 0$ and $\Omega_0 = 0.3$, respectively. In agreement with the predictions of the top-hat model, the M-T relation shows a break at the low mass end ($T \simeq 3\text{keV}$). The break is less “evident” in the case of a flat universe while much more evident in the case of an open one. A comparison with the FRB data shows, similarly to the top-hat model prediction, that in an Einstein-de Sitter universe the scatter/bent is under-estimated, while in a Λ CDM model with $\Omega_0 = 0.3$ it is overestimated. It is to be noted that the modified continuous formation model predicts a slightly larger scatter than the top-hat model.

Fig. 4 plots the M-T relation for the modified continuous formation model in a Λ CDM model. In this case, ϵ and then the M-T relation is calculated numerically by integrating and inverting Eq. (9). The solid line is the prediction for $\Omega_\Lambda = 0$, $\Omega_0 = 1$, shifted downwards, as previously described and motivated, while the dotted line represents the prediction of the same model for $L \neq 0$, $\Omega_\Lambda = 0.7$ and $\Omega_0 = 0.3$. The plot shows, similarly to the top-hat model, that the effect of a non-zero cosmological constant is that of reducing the effect of L , and that the Λ CDM cosmology is in a better agreement with the observed scatter. This last model predicts a slightly larger bent in the M-T relation when compared with the top-hat model.

A comparison between the Fig.1-2 and Fig. 3-4 shows that the prediction of the THM model and the VM model differs only for 1 – 2%. This little difference is possible because we have chosen the same normalization for the two models.

The study of the evolution of the M-T relation predicted by the modified top-hat model, for a fixed value of M_{vir} , is plotted in Fig. 5.

In this figure, the dotted line represents the prediction for $\Omega = 1$ and $L = 0$ which coincides with the “classical” prediction, $T_X \propto (1+z)$. The short-dashed line represents the case $\Omega_0 = 0.2$ and $L = 0$, which coincides with $T_X \propto \Delta_{\text{vir}}^{1/3} \left[\frac{\Omega_0}{\Omega_0(z)} \right]^{1/3} (1+z)$, given in V2000 (Eq. 8). As known, (see V98), decreasing Ω slows down the evolution. The long-dashed line represents $\Omega_0 = 1$ and $L \neq 0$. Comparing this result to the first one $\Omega_0 = 1$ and $L = 0$ shows that the effect of L in slowing down the evolution of T_X is larger than reducing Ω_0 of a noteworthy value (0.8, see short-dashed line). Finally, the short-long-dashed line represents the case $L \neq 0$, $\Lambda \neq 0$, $\Omega = 0.2$, $\Omega_\Lambda = 0.8$ and the solid line the case $L \neq 0$, $\Lambda = 0$, $\Omega_0 = 0.2$. As expected, reducing the value of Ω and taking account of tidal interaction of clusters ($L \neq 0$) produces a larger effect in the slowing down of evolution, while the effect of a non-zero cosmological constant has an opposite effect to that of L .

Fig. 6, is based upon the second model (modified continuous formation) and calculates the evolution for $\Omega_0 = 0.2$. The dotted line represents the “classical” prediction, $T_X \propto (1+z)$. This relation predicts the largest evolution for a given M_{vir} . The short-dashed line represents the late-formation approximation as expressed by Eq. (8) in V2000, namely $T_X \propto \Delta_{\text{vir}}^{1/3} \left[\frac{\Omega_0}{\Omega_0(z)} \right]^{1/3} (1+z)$. In this case, the temperature evolution is more modest than the previous one. The long-dashed line and the dot-dashed one, plot Eq. (17) for $L = 0$ and $n = -2$, $n = -1$, respectively. This last two lines show that, (see also V98), the continuous formation model produces an even more modest evolution of temperature with respect to the late-formation approximation. The solid line plot Eq. (17) for $L \neq 0$ and $n = -1$, while the long-short dashed line represents Eq. 73 of AC. The effect of the angular momentum is that of furtherly increase the slowing down effect of the temperature evolution. The low evolution of the M-T relation shown by the solid line is in agreement with Eq. 73 of AC.

A comparison between the Fig. 5 and Fig. 6 shows that the prediction, for what concerns the time evolution, of the THM model and the VM model differs $\leq 10\%$ (for $L \neq 0$, $\Lambda = 0$, $\Omega_0 = 0.2$).

5. Conclusions

In this paper, I used two different models in order to study the M-T relation and its time evolution. The main results of the paper can be summarized as follows:

- 1) the effect of angular momentum acquisition by protostructures is two fold:
 - a) The M-T relation is no longer self-similar: a break in the low mass end ($T \sim 3 - 4\text{keV}$) of the M-T relation is present. The behavior of the M-T relation is as usual, $M \propto T^{3/2}$, at the high mass end, and $M \propto T^\gamma$, with a value of $\gamma > 3/2$ in dependence of the chosen cosmology. Larger values of γ are related to open cosmologies, while ΛCDM cosmologies give results of the slope intermediate between the flat case and the open case. The FRB data are best fitted by a low density ΛCDM model.
 - 2) The evolution of the M-T relation is more rapid in models with $L = 0$. The effect of a non-zero cosmological constant is that of slightly increase the evolution of the M-T relation with respect open models with the same value of Ω_0 .
 - 3) The top-hat model gives comparable results to the continuous formation model, in the range of z and Ω_0 considered. For sake of precision, the top-hat model has a lower value of normalization. A comparison of the normalization predicted by the late-formation model with that predicted by simulations of (Evrard, Metzler & Navarro 1996) shows that when $\Omega_0 = 1$ this normalization is only 4% below the empirical value, but it lies 20% below it for $\Omega_0 = 0.2$. In the case of V2000 model and for a power-law spectrum, a comparison with the same simulations show that the temperature normalization of the $n = -2$ case deviates by less than 10% over the range $0.2 < \Omega_0 < 1$ and by $\simeq 18\%$ in the case $n = -1$ (V2000). Given the same value of normalization for both models, a comparison between the Fig.1-2 and Fig. 3-4 shows that the prediction of the THM model and the VM model differs only for 1 – 2%. A comparison between the Fig. 5 and Fig. 6 shows that the prediction, for what concerns the time evolution, of the THM model and the VM model differs $\leq 10\%$ (for $L \neq 0$, $\Lambda = 0$, $\Omega_0 = 0.2$).

References

- Afshordi N., Cen R., 2001, astro-ph/0105020
 Bahcal N.A., Fan X., 1998, ApJ 504, 1
 Bardeen J.M., Bond J.R., Kaiser N., Szalay A.S., 1986, ApJ 304, 15
 Bartlett, J.G., Silk, J., 1993, ApJ 407, L45
 Bialek J.J., Evrard A.E., Mohr J.J., 2001, ApJ 555, 597, (astro-ph/0010584)
 Carlberg R.G., Yee H.K.C., Ellingson E., 1997, ApJ 478, 462
 David L. P., Slyz A., Jones C., Forman W., Vrtilek S.D., 1993, ApJ, 412, 479
 Del Popolo A., Gambera M., 1998, A&A 337, 96
 Del Popolo A., Gambera M., 1999, A&A 344, 17
 Del Popolo A., Gambera M., 2000, A&A 357, 809
 Del Popolo, A., E. N. Ercan, Z. Q. Xia, 2001, AJ 122, 487
 Eke V.R., Cole S., Frenk C.S., 1996, MNRAS 282, 263
 Eke V.R., Navarro J.F., Frenk C.S., 1998, ApJ 469, 494
 Erdelyi A., Higher Transcendental Functions, Volume 1, chapter 1, section 11, McGraw Hill, New York, 1953.
 Evrard A.E., Metzler C.A., Navarro J.F., 1996, ApJ 469, 494
 Finoguenov A., Reiprich T.H., Böeringer H., 2001, A&A 368, 749
 Horner D.J., Mushotzky R.F., Scharf C.A., 1999, Apj 520, 78
 Kitayama T., Suto Y., 1996, ApJ 469, 480
 Lacey C., Cole S., 1993, MNRAS 262, 627
 Lahav O., Lilje P.B., Primack J. R., Rees M., MNRAS 1991, 251, 128
 Markevitch M., 1998, Apj 503, 77
 Mathiesen B.F., Evrard A.E., 2001, astro-ph/0004309 (ApJ, in press)
 Mathiesen B.F., 2001, MNRAS 326, 1, (astro-ph/0012117)
 Mohr J.J., Mathiesen B., Evrard A.E., 1999, ApJ 517, 627
 Muanwong O., Thomas P. A., Kay S. T., Pearce F. R., Couchman H. M. P., 2001, ApJ 552, 27, (astro-ph/0102048)
 Navarro J.F., Frenk C.S., White S.D.M., 1995, MNRAS 275, 720
 Nevalainen J., Markevitch M., Forman W., 2000, ApJ 532, 694
 Peebles, P.J.E., 1993, Principles of Physical Cosmology, Princeton University Press
 Thomas P.A., Muanwong O., Kay S.T., Liddle A.R., 2001, astro-ph/0112449
 Viana P.T.P, Liddle A.R., 1996 MNRAS 281, 323
 Voit C. M., Donahue M., 1998, ApJ 500, 111 (astro-ph/9804306)
 Voit C. M., 2000, ApJ 543, 113 (astro-ph/0006366)
 Xu H., Jing G., Wu X., 2001, ApJ 553, 78, (astro-ph/0101564)

Constellation-X Mirror Development: Lessons Learned Relevant to XEUS

R. Petre¹ and the Constellation-X SXT Team

Laboratory for High Energy Astrophysics, NASA/GSFC, Greenbelt, MD 20771 USA

Abstract. The X-ray mirror for Constellation-X has performance requirements and a design similar to that proposed for XEUS, incorporating multiply-nested, thin, segmented, accurately shaped reflectors. Technology development has been underway for several years, and the individual mirror components (mandrels, substrates, mounting approach) appear to meet the Constellation-X requirements. Construction of the first engineering unit incorporating the Constellation-X technical innovations is underway. Many of the lessons learned in the technology development to date are highly relevant to the XEUS mirror program. We review some of the relevant issues faced by Constellation-X, and discuss approaches we have taken to resolve them and how they might affect the XEUS program.



Constellation-X Mirror Development: Lessons Learned Relevant to XEUS

**R. Petre (NASA / GSFC)
and the Constellation-X SXT Team**

Con-X/XEUS: Slide: 1
11/28/2002 4:55 PM

Constellation-X



Abstract

The X-ray mirror for Constellation-X has performance requirements and a design similar to that proposed for XEUS, incorporating multiply-nested, thin, segmented, accurately shaped reflectors. Technology development has been underway for several years, and the individual mirror components (mandrels, substrates, mounting approach) appear to meet the Constellation-X requirements. Construction of the first engineering unit incorporating the Constellation-X technical innovations is underway. Many of the “lessons learned” in the technology development to date are highly relevant to the XEUS mirror program. We review some of the relevant issues faced by Constellation-X, and discuss approaches we have taken to resolve them and how they might affect the XEUS program.

Con-X/XEUS: Slide: 2
11/28/2002 4:55 PM

Constellation-X



Introduction

The XEUS mirror concept bears strong similarity to that of Constellation-X. The fundamental differences between the two mirrors are the substantially more ambitious size and performance goals set for XEUS. In the Table below we compare the Constellation-X and XEUS designs. Both mirrors use a multiply-nested, segmented, Wolter I design, with gold coated surfaces.

Given this strong similarity, the Constellation-X and XEUS mirror development programs face many common technology challenges and production and programmatic issues. The Constellation-X team has been addressing some of these technology challenges, and can offer some insight into what we have learned during our development phase.

Con-X/XEUS: Slide: 3
11/28/2002 4:55 PM

Constellation-X



Comparison between Constellation-X and XEUS

Constellation-X and XEUS Mirror Parameters

	Constellation-X	XEUS1 (2)
Diameter	1.6 m	4.07 m (9.90 m)
Focal Length	10 m	50 m
f/number	6	12.3 (5.05)
reflector length	20-50 cm	50 cm
reflector arc	60°, 30°.	22.5°, 11.25° (6.125°)
largest reflector surface area	0.16 m ²	0.22 (0.43) m ²
reflector thickness	0.4 mm	0.3 mm (< 0.3 mm)
Number of modules (petals)	18	32 (128)
Angular resolution	10" (5" goal)	5" (2" goal)
RMS microroughness	0.4 nm	0.5 nm
Substrate material	formed glass	electroformed Ni
Substrate density (g cm ⁻³)	2.4	7.9
Reflector material	gold	gold (+ multilayers)

Con-X/XEUS: Slide: 4
11/28/2002 4:55 PM

Constellation-X



Constellation-X Mirror Status

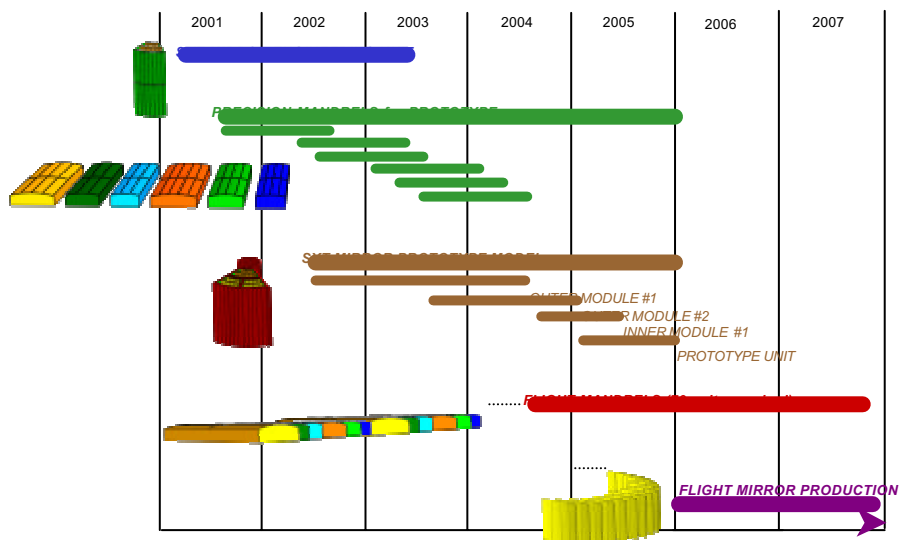
- Constellation-X in midst of an aggressive technology development program
 - Mission goal is to be ready for 2006-7 “new start”
 - X-ray mirror is identified as most critical technology development area
- Mirror development plan
 - Adjacent figure shows the mirror technology development roadmap
 - Four key development areas identified: substrates, mandrels, mounting and alignment, and metrology
 - Have adopted 3-stage, progressive approach: Engineering unit, prototype, flight unit
 - Currently, the first step toward the Engineering Unit, the first Optical Alignment Pathfinder (OAP-1), is nearing completion

Con-X/XEUS: Slide: 5
11/28/2002 4:55 PM

Constellation-X



SXT Technology Roadmap



Con-X/XEUS: Slide: 6
11/28/2002 4:55 PM

Constellation-X



SXT Development Approach

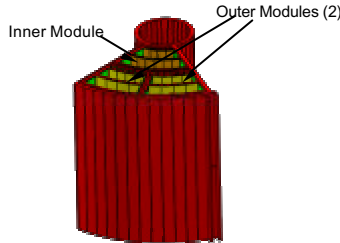
Engineering Unit



- Single inner module with
- 0.5 m dia. reflector pair (replicated from Zeiss precision mandrel)
 - Parabolic (P) and Hyperbolic (H) submodules
 - First modules to be aligned using etched silicon microcombs

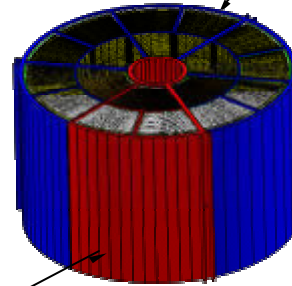
Con-X/XEUS: Slide: 7
11/28/2002 4:55 PM

Prototype Unit



- Flight Scale Assembly of
- 3 modules (2 outer and 1 inner)
 - Largest diameter same as for flight - 1.6 m
 - Each module has 3 to 9 reflector pairs
 - Demonstrates module to module alignment

Flight Unit



- Full flight Assembly
- 1.6 m outer diameter
 - 18 Small Modules
 - 70 to 170 reflector diameters

Constellation-X



Segmented X-ray Optic Development Process

	Optical Assembly Pathfinder			Prototype		
Configuration						
Module Type	Inner	Inner	Inner	Outer	Inner	Outer & Inner
Housing Material	Aluminum	Titanium	Composite	Composite	Composite	Composite
Focal Length	8.5m	8.5m	8.5m	10.0m	10.0m	10.0m
Optic Length (P&H)	2 x 20 cm	2 x 20 cm	2 x 20 cm	2 x 50 cm (TBR)	2 x 50 cm (TBR)	2 x 50 cm (TBR)
Nominal Optic Diameter(s)	50 cm	50 cm±	50 cm±	160 cm± 120 cm± 100 cm±	90 cm± (TBR) 70 cm± (TBR) 50 cm± (TBR)	160 cm± 40 cm± 120 cm± 70 cm± 100 cm± 50 cm±
Goals	Align 1 optical surface pair (P&H) to achieve <15 arcsec Evaluate alignment, optics assembly design & process, & optics metrology	Align up to 3 optical surface pairs (3P,3H) to achieve <15 arcsec. Evaluate alignment bar and mass production schemes Evaluate gravity sag	Higher fidelity unit which matched CTE between optics & housing Environmental and X-ray test	Flight-like configuration outer module Largest optical surfaces Environmental and X-ray test	Flight-like configuration inner module Environmental (TBR) and X-ray test	Demonstrate module to module alignment Environmental and X-ray test
Timeframe	Q4 of FY02	Q3 of FY03	Q1 of FY04	Q4 of FY05	Q3 of FY06	Q4 of FY06

Con-X/XEUS: Slide: 8
11/28/2002 4:55 PM

Constellation-X



Constellation-X Mirror “Lessons Learned”

Segmented vs. full shell mirrors

- Even for the substantially smaller diameter of Constellation-X, a segmented mirror approach is the only viable one
- Virtually impossible to fabricate 1.6 m diameter full-cylinder mandrels
- Even if mandrels were available, handling them would pose enormous difficulty
- Our experience has shown the extreme difficulty of making full shell mirrors with the required shell thickness that do not distort under their own weight.
- Although SXT team members have substantial experience building segmented mirrors (ASCA, Astro-E), the Constellation-X requirements have led to new approaches to almost all aspects of mirror production.



An Astro-E flight mirror, an example of a multiply nested, light weight, segmented mirror developed at GSFC



A 50-cm diameter electroformed Ni-alloy prototype for Constellation-X, produced at MSFC

Con-X/XEUS: Slide: 9
11/28/2002 4:55 PM

Constellation-X



Constellation-X Mirror “Lessons Learned”

Mandrel quality

- Accurately figured mandrels are essential
 - Rule of thumb from full shells is that rms figure of replica is twice that of mandrel (thus Constellation-X requires mandrels with ≈ 2 rms figure error)
 - Our experiments with small segments suggests it is possible to make replicas with figure errors approaching the mandrel figure
- Mandrel durability is a potentially serious issue
 - Metal (Ni-coated Al) mandrels show surface degradation after < 10 replications
 - Pyrex, fused silica and Zerodur mandrels show no degradation after many replications but can be more expensive to manufacture
 - Thin glass coatings on metal mandrels also seem to degrade after a few uses
- For glass forming, we can replace precise paraboloid and hyperboloid surfaces with lower cost conical mandrels because sagittal depth so small ($< 20 \mu\text{m}$ for the largest diameter reflectors)
 - Satisfactory replicas are obtained if forming mandrel figure error is $\approx 2 \mu\text{m}$
 - Precise reflector shape imparted into epoxy during replication

Con-X/XEUS: Slide: 10
11/28/2002 4:55 PM

Constellation-X



Constellation-X Mirror “Lessons Learned”

Reflector substrate material

- Hard to find good substrate material, even harder to make acceptable reflectors
- Surface figure of reflectors must be better than resolution goal - cannot rely on alignment to remove significant mid-frequency errors
- Several materials were considered
 - thermally formed glass was selected as most promising material
 - initial tests using thermally formed Be were also promising
 - silicon carbide is promising, but expensive and difficult to make segments from
 - electroformed Ni alloy, carbon fiber composite, and metallic foil were rejected
 - promising, stiff Ni alloys (6x pure nickel) for electroforming full shells were identified
 - stiffening rings were still needed to maintain circularity for complete shells
 - unable to electroform complete shells without significant axial distortion due to stress buildup
 - electroforming of undistorted segments was found to be extremely difficult
- Cannot expect that a surface formed from a preexisting substrate can maintain both figure and microsurface
- Our solution is a two-step process, a variant of that developed for Astri



Con-X/XEUS: Slide: 11
11/28/2002 4:55 PM

Constellation-X



Constellation-X Mirror “Lessons Learned”

Reflector production

- Rejected single process; need to make figure and surface separately
- Adopted approach is to impart overall figure via thermal forming, and optical surface via epoxy replication
- Reflectors are not perfect – edge effects must be accommodated in mounting
 - Roll-off on side edges; much can be removed by trimming
 - Distortions on ends due to epoxy-edge interaction during replication
 - Front and back edges are not necessarily an accurate radial reference
- Front and back edges cannot be cut precisely enough to use as axial reference
 - Use of inaccurate edge as reference can introduce significant tip error
 - Axis of each reflector must be aligned optically within housing, or alignment bars used to distort reflector to near nominal shape
 - Removal of tip errors via distortion is acceptable within the Con-X error budget, but possibly not the XEUS budget
- Forming process must be carefully controlled
 - Micron-sized dust particles produce ripples on surface that affect replica quality
 - Heating, cooling cycle affect reflector figure
- Important to make reflectors that can be handled nondestructively
 - This makes glass preferable over rolled or electroformed metal

Con-X/XEUS: Slide: 12
11/28/2002 4:55 PM

Constellation-X



Replication of segments off 50 cm Zeiss mandrel



Hand spraying of epoxy onto substrate



Insertion of sprayed substrate into vacuum attachment housing



Substrates in attachment housing



Attachment of substrates to mandrel under vacuum



Substrate attached to mandrel during curing



Removal of finished reflector

Con-X/XEUS: Slide: 13
11/28/2002 4:55 PM

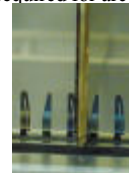
Constellation-X



Constellation-X Mirror "Lessons Learned"

Mounting and alignment

- Mounting and alignment scheme must accommodate imperfect reflectors
 - Contact points on reflector must conform to nominal surface; edges are not a good reference
- Essential to decouple mounting and alignment
 - A serious limitation of previous segmented mirrors
- Purely mechanical alignment won't work; alignment scheme must incorporate metrology
 - Mechanical run out error quickly exceeds the micron-level positioning tolerance required for arc second resolution
- Constellation-X is currently adopting a hybrid scheme
 - Reference reflector is located and aligned optically within housing
 - Subsequent reflectors indexed precisely to reference reflector radius using etched Si microstructures (provide 0.1 μm accuracy)
- As a fallback, we are prepared for need to align individual reflectors
- Manufacturing process must be designed around alignment scheme
 - Make accurate reflectors and design alignment scheme to avoid impossible tolerances
 - Can't locate radius of any reflector exactly ($< \text{few } \mu\text{m}$), but no need: need is to hold a reflector radius constant to micron accuracy
- In segmented mirrors, image distortions produced by rotation of reflector optical axis (tip errors) are as severe as those from incorrect slope (tilt)



Etched Si alignment structures

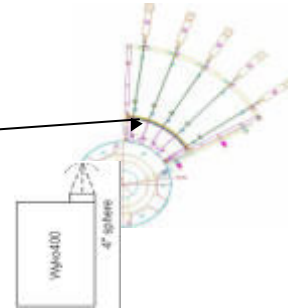
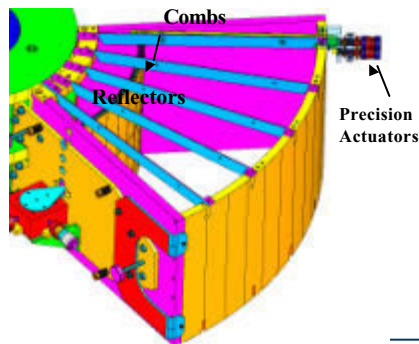
Con-X/XEUS: Slide: 14
11/28/2002 4:55 PM

Constellation-X



SXT Engineering Unit

- Alignment scheme incorporates 5 independent positioners, top and bottom, plus optional side positioners.
- Interferometer viewing through window in hub provides feedback on figure distortions.
- Centroid Detector Assembly (designed for AXAF mirrors) used to determine focal point and reflector distortions.



Constellation-X



Constellation-X Mirror “Lessons Learned”

Manufacturing issues

- Four Constellation-X mirrors must be assembled in < 4 years, at modest cost
 - Major industrial process design challenge - thousands of reflectors, dozens of segments, substantial parallel processing
- Mandrels represent a potential bottleneck
 - Few companies exist with expertise and equipment to manufacture mandrels
 - Even if we use multiple suppliers, mandrel production timescale is a problem
 - Each mandrel takes 6-8 months
 - Each mandrel costs ~\$500k
- One solution is to use one replication mandrel for every 3-5 radius reflectors
 - Real advantage of replication
 - Only poses a problem below resolution of a few arc seconds; optical formula does not change much for adjacent radius reflectors.

Constellation-X



The XEUUS View of Nearby Clusters of Galaxies

J. Schultz¹, J. Huovelin¹, O. Vilhu¹, P. Muhli¹, L. Alha¹, A. Luukanen², J. Pekola², H. Sipilä³, and S. Vajjärvi³

¹ Observatory, University of Helsinki, FI-00014, Finland (e-mail: Juho.Schultz@astro.helsinki.fi)

² Department of Physics, University of Jyväskylä, P.O.Box 35, FI-40351 Jyväskylä, Finland

³ Metorex International, P.O.Box 85, FI-02631 Espoo, Finland

Abstract. The high energy resolution of the TES and STJ spectrometers combined with the large effective area of XEUUS allow high-resolution spectroscopy of nearby clusters of galaxies. The emission line profiles of medium-Z elements should be a result of several effects, including thermal broadening, turbulence, and bulk velocity gradients due to cooling flows and/or cluster mergers. The feasibility of converting XEUUS spectro-imaging data to temperature and velocity maps is studied.

1. Introduction

The clusters of galaxies are the largest gravitationally bound objects in the Universe. Some clusters are seen as diffuse, roughly elliptical X-ray sources, as the hot and thin intracluster gas emits thermal bremsstrahlung in the X-ray band (Cavaliere & Fusco-Ferraro, 1976). As the gas feels the gravitation of dark matter, the density of dark matter can be estimated from X-ray observations (Markevitch & Vikhlin, 1997). However, the gas properties are also modified by cluster mergers, supernova ejecta from galaxies, and cooling flows. Cluster mergers mix the gas of two clusters, forming an irregular structure. Supernova ejecta increase the metallicity of the gas (Finoguenov et al., 2000). Therefore, metallicity gradients seen in clusters could provide some insight to the star formation history of the member galaxies. Sometimes the intracluster gas forms cooling flows (Fabian et al., 1991). For thermal bremsstrahlung, the volume emissivity is $\propto \rho^2 \sqrt{T}$ (see e.g. Rybicki & Lightman, 1979), so dense regions cool much faster. This leads to contraction and further increase in density, which in turn increases the cooling. This instability leads to the development of a cooling flow.

A typical timescale Δt of the changes in intracluster gas on a scale of ΔR can be estimated from $\Delta t \approx \Delta R/c_s$ where c_s is the speed of sound. For typical intracluster gas parameters, $c_s \approx 600 \text{ km s}^{-1}$, and $\Delta R \sim \text{Mpc}$, giving timescales of the order of 1 Gyr, a significant fraction of Hubble time. The properties of the intracluster gas can be considered as a logbook of activities within the cluster. X-ray observations with high spatial and spectral resolution can be used to read this logbook. After a brief overview of current instruments and fitting schemes, we present a data reduction and fitting scheme that would allow three-dimensional modeling of the intracluster gas.

2. Comparison of cryogenic and grating spectrometers

The grating spectrometers of XMM (RGS) and Chandra (LETG, HETG) have the highest spectral resolution currently available. However, grating spectrometers have two drawbacks when compared to cryogenic detectors. 1) The extra reflection from the grating decreases the effective area. 2) Energy resolution of diffuse source observations is degraded, as the energy of an event can not be uniquely calculated from its position. For example, the energy resolution of XMM RGS (at 1 keV) is $\frac{E}{\Delta E} \approx \frac{100}{\theta}$ for a diffuse source of θ arcmin.

The nearby clusters of galaxies have large angular extents and flat brightness profiles (compared to the PSF of modern X-ray telescopes). They often contain bright AGN that are seen as point sources. In grating spectrometers the spectra of the point sources and the hot cluster gas are mixed. Separating the point source spectra from the diffuse emission, and separating the spectra of the diffuse emission from different parts of the cluster should be done to analyze the cluster spectra.

The full spectral resolution of the XEUUS NFI $\frac{E}{\Delta E} \approx 500\text{--}1000$ at 1 keV can be achieved also for diffuse sources, as the resolution is intrinsic to the detector. The angular resolution will be about 5 arcseconds or better. Thus, the XEUUS NFI allows detailed spectro-imaging of interesting small-scale structures of nearby clusters.

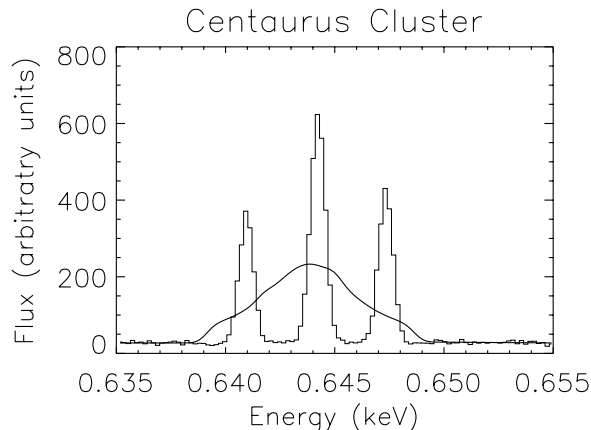


Fig. 1. A simulated line from the Centaurus Cluster. XEUS NFI (STJ), phase I mirror configuration and 5 ksec exposure. The line profile is a MEKAL simulation convolved with an inverse parabolic velocity profile ($v(r)_{rad} = A/(r^2 + Br + C)$). The thinner line presents three MEKAL simulations with different redshifts (0.01, 0.015 and 0.02), roughly corresponding to a structure that has been detected by ASCA (Dupke & Bregman, 2001) in the azimuthal direction. With XEUS NFI, radial velocity variations and turbulence of the order 600 km s^{-1} can be detected.

3. Current methods of cluster analysis

The X-ray spectrum of clusters is generally well-fitted with a thermal emission model, such as the MEKAL spectral model (see Kaastra 1992, Liedahl et al., 1995, Mewe et al., 1985, Mewe et al., 1986). The temperature and density maps of clusters are often derived either by fitting spectra from selected regions or converting measured hardness ratios to temperatures. The selection of the extraction regions is not a straightforward problem. Most common methods used are 1) Interesting features are detected by inspection, and regions corresponding to these are used (e.g. Markevitch et al., 2002); and 2) Adaptive binning (e.g. Johnstone et al., 2002). The field of view is divided automatically to regions. Region size is defined by having enough photons for spectral analysis, and a maximal angular resolution. The regions are usually rectangular.

Both methods have defects and good points. Selection by inspection may not detect all interesting features. Another defect is that is not easy to automate. The strong point is that the region shapes can be easily optimized. The weak point of adaptive binning is that rectangular extraction regions are not very physical, and variations in the spectra within the extraction regions are therefore probably more common than in other methods. However, the adaptive binning model can be easily automated and modified.

Temperature variations within the extraction region or along the line of sight have been detected in some cases. A sum of two or three thermal models can be used for the fitting, but the results are not always unique. It should be noted that the extraction regions are essentially columns with relatively large aspect ratios. Thus it is plausible to assume that in some cases the variations are along the line of sight, as the clusters are not two-dimensional structures. Three-dimensional modeling would allow modeling of variations along the line of sight. For high-resolution spectra, line positions and ratios can be used for deriving temperature distributions. Variations in metallicity may cause additional problems with these methods.

4. Suggestions for XEUS data analysis

The energy resolution of XEUS NFI allows line profile analysis of the brightest clusters of galaxies (see Fig. 1). The line profiles are broadened by turbulence and red- or blueshifted by bulk velocities. Thermal velocity of ions is of the order $v_{th} \approx \frac{c}{1000} \sqrt{T_{keV}/Z}$, where Z is the mass number. Therefore, thermal effects may be seen in the lines from medium- Z elements. The continuum and line ratio information can be used to estimate the temperature and density variations within the line of sight. This information can be used to construct turbulence and radial bulk velocity maps along the line of sight.

With multiple pointings, 3D maps of the intracluster gas properties can be derived. An example of 3D modeling is the elliptical shell model of Krawczynski (2002), in which the cluster is modeled as concentric elliptical shells. However, this model allows the parameters to vary only in the radial direction, and any asymmetries tend to reduce the goodness of the fits. Below, we present a 3D modeling scheme that can be considered as an expansion of adaptive

binning. Clusters are generally roughly elliptical in shape, but deviations from symmetry are often observed. The symmetry should be utilized as a regularization condition in the data analysis. As the deviations are often of physical origin, data analysis should not enforce symmetry too strictly.

The following is a data reduction scheme we have started implementing:

1. Divide the cluster to N_I lines of sight, and extract spectra from each of these. Bin the spectra so that only line intensities are fitted.
2. Divide each line of sight to N_J cells. Each cell has its own independent set of parameters, T_{ij}, ρ_{ij}, \dots (ij is the j th cell of the i th line of sight.)
3. Minimize $\chi^2 + \lambda F$ where F is a normalized regularization function and $\lambda \approx 0.001$ is a (Lagrangian) regularization coefficient.
4. Extract line profiles from the data.
5. Add a velocity distribution to the model, and repeat step 3 to fit the line profiles.

The selection of the regularization function is somewhat arbitrary, and several different functions should be tried for each case. Potential regularization functions are e.g. $\|\nabla^2(T, \rho, \dots)\|$ to avoid 'spiky' models, $\|\frac{\partial^2(T, \rho, \dots)}{\partial^2(\theta, \phi)}\|$ for spherical/elliptical symmetries and $\|(\rho - \rho_\beta)^2\|$ where ρ_β is the density of the appropriate β -model. An arbitrary linear combination of these functions could also be used. The results given with different regularization functions and λ values should be compared to find the optimal form of the function.

Acknowledgements. We thank Dr. Pasi Hakala for fruitful discussions. This research is a part of the consortium *High Energy Astrophysics and Space Astronomy* financed by the Academy of Finland and the Finnish Technology Agency TEKES within the framework of the Finnish space research programme ANTARES.

References

- Cavaliere A. & Fusco-Ferraro R., 1976, A&A 49, 137
 Dupke R.A. & Bregman J.N., 2001, ApJ 562, 266
 Fabian A.C., Nulsen P.E.J., Canizares, C.R., 1991, A&AR, Vol. 2, 191
 Finoguenov A., David L.P., Ponman T.J., 2000, ApJ 544, 188
 Johnstone R.M. et al., 2002, submitted to MNRAS (astro-ph/0202071)
 Kaastra J.S., 1992, An X-Ray Spectral Code for Optically Thin Plasmas (Internal SRON-Leiden Report, updated version 2.0)
 Krawczynski H., 2002, ApJL 569, 27
 Liedahl D.A., Osterheld A.L., & Goldstein, W.H. 1995, ApJL, 438, 115
 Markevitch M. & Vikhlinin A., 1997, ApJ 491, 467
 Markevitch M. et al., 2002, ApJ 567, L27
 Mewe R., Gronenschild E.H.B.M. & van den Oord G.H.J., 1985, A&AS, 62, 197
 Mewe R., Lemen J.R. & van den Oord G.H.J., 1986, A&AS, 65, 511
 Rybicki G.B. & Lightman A.P., 1979, 'Radiative processes in astrophysics', John Wiley



The physics of shocks in the proto-stellar environment: Herbig-Haro objects observed with XEUS

S. Sciortino¹, F. Favata², G. Micela¹, and A. Parmar²

¹ INAF - Oss. Astronomico di Palermo Giuseppe S. Vaiana, Piazza del Parlamento 1, 90134 Palermo, Italy

² ESA Astrophysics Mission Division, Research and Scientific Support Department, ESTEC,
Postbus 299, NL-2200, AG Noordwijk, The Netherlands

Abstract. We present the potential of XEUS for studying the X-ray emission of Herbig-Haro objects, namely of the shocks associated with jets from proto-stellar objects, recently detected for the first time with Chandra and XMM-Newton (cf. Pravdo et al. 2001, Favata et al. 2002a)

After discussing the additional evidence of such a phenomena based on the analysis of archival ROSAT data (Favata et al. 2002b) we show how for the first time with XEUS-1 and/or XEUS-2 it will be possible to study in detail the X-ray spectra of Herbig-Haro objects and determine the physical conditions and spatial structure of matter shocked by the protostellar jets, thus determining the influence of jet-induced X-ray emission on circumstellar environments in the star formation phase.

Simulations of spectra obtained under different assumptions about the physical conditions of the emitting plasma with current XEUS baseline detectors have been derived and have been presented. We show that even XEUS-1 will make possible to recognize the non-equilibrium condition of the shocked plasma and to recover the physical parameters of the emitting plasma.

Acknowledgements. We gratefully acknowledge the permission by the Springer Verlag to use their A&A L^AT_EX document class macro. This work has been supported by ASI and MIUR.

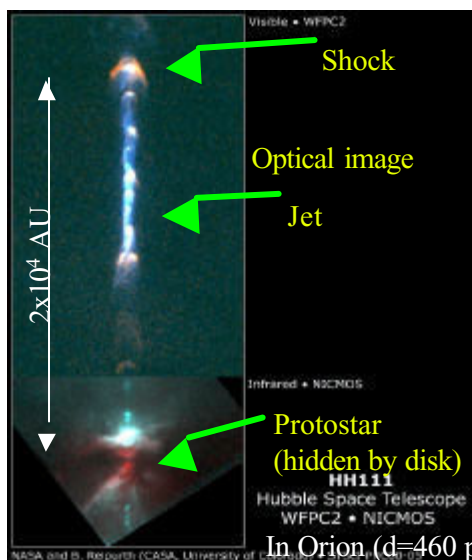
References

- Favata F., Fridlund C. V. M. , Micela G., Sciortino S., Kaas A. 2002a, A&A 386, 204
Favata F., Micela G., Sciortino S., Fridlund C. V. M. 2002b, in "New Visions of the X-ray Univers in the XMM-Newton and Chandra Era", F. Jansen et al. (eds), in press.
Pravdo S. H., Feigelson E. D., Garmire G., et al. 2001, Nature, 413, 798

The physics of shocks in the proto-stellar environment: Herbig-Haro objects observed with XEUS

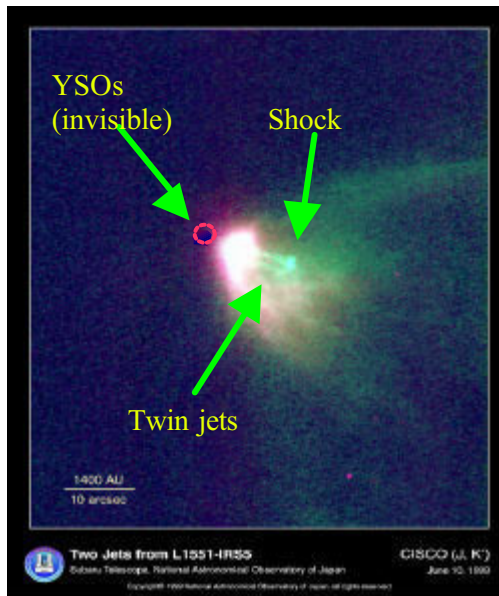
- ¥ S. Sciortino⁽¹⁾, F. Favata⁽²⁾, G. Micela⁽¹⁾, A. Parmar⁽²⁾
- ¥ ⁽¹⁾ INAF, Oss. Astronomico G.S. Vaiana, Palermo, Italy
- ¥ ⁽²⁾ European Space Agency, RSSD, Noordwijk, The Netherlands

What are Herbig-Haro (HH) objects?



- ¥ HH objects are small high-excitation nebulae
- ¥ Associated with outflows from Young Stellar Objects (YSO)
- ¥ Shocks (working surface) associated with jet hitting circumstellar medium as well as with internal shocks in jet
- ¥ UV and optical emission lines well known
- ¥ Not known as X-ray sources until XMM & *Chandra*

The HH 154 jets & shock



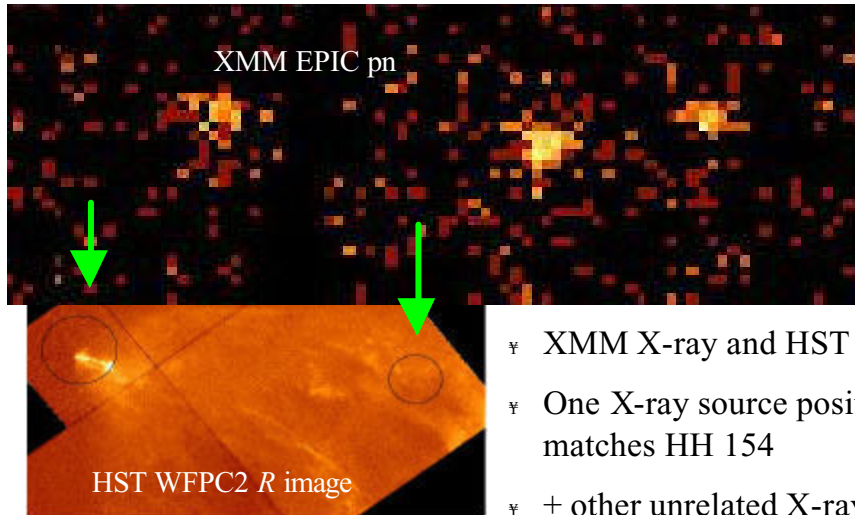
- ¥ Binary YSO (L1551 IRS5), highly obscured (150 mag)
- ¥ In Taurus SFR ($d = 140$ pc)
- ¥ Two high-excitation jets
- ¥ Shocked working surface (moderate obscuration, 7 mag)
- ¥ Also larger-scale molecular outflow (not relevant here)

The XMM observation of L1551

(cf. Favata et al. 2002, A&A, 386, 204)

- ¥ 50 ks observation of the L1551 star formation region.
- ¥ L1551 IRS5 & HH 154 well covered
- ¥ Good observation, low background
- ¥ An X-ray source positionally coincident with HH 154
- ¥ EPIC pn count rate 0.8 cts/ks

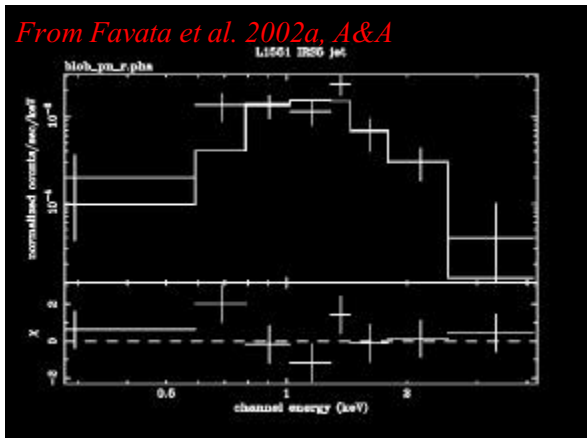
X-ray EPIC pn image of the L1551 IRS5 region



- ¥ XMM X-ray and HST optical images
- ¥ One X-ray source positionally matches HH 154
- ¥ + other unrelated X-ray sources

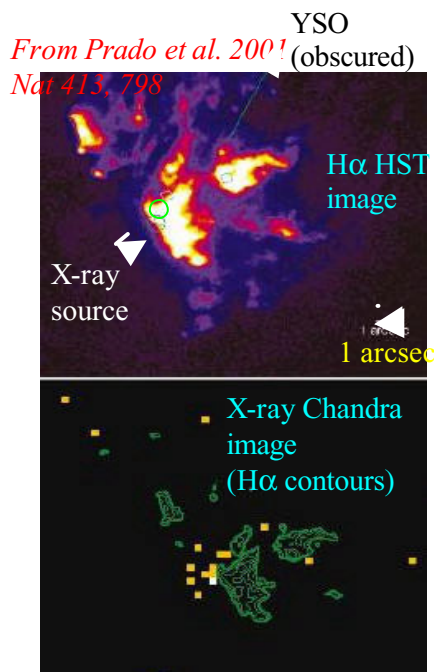
Dynamics of HH 154 shock

- ¥ Post-shock velocity $v_{ps} = 230$ km/s
- ¥ Ionization fraction $f \sim 1$
- ¥ Expected post-shock temperature
- ¥ $T_{ps} = 30v^2/(1+f)$, K ~ 0.6 MK (v in km/s)
- ¥ $n_{jet} = 500-10^4$ cm $^{-3}$ $M_{jet} = 1-2 \times 10^{-6} M_{sun}$
- ¥ $L_{kin} = 10^{41}-10^{42}$ erg/s $L_{H\alpha} = 5 \times 10^{28}$ erg/s
- ¥ **Shock size** $d \leq 10^{14}$ cm



The EPIC pn spectrum of the X-ray source associated with HH154

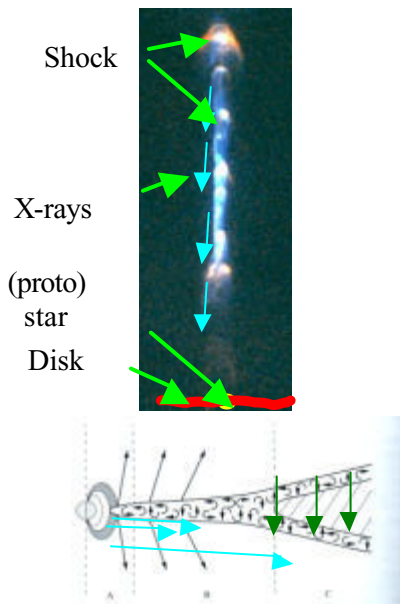
- ¥ Soft spectrum, well fit by absorbed thermal model
- ¥ $T \sim 4$ MK, $N_{\text{H}} = 7$ mag
- ¥ $EM = 10^{52} \text{ cm}^{-3}$, if $d=150$ pc $L_{\text{x}} = 3 \times 10^{29}$ erg/s



Chandra observation of X-ray emission from HH 2

- ¥ 21 ks Chandra pointing in Orion SFR ($d = 460$ pc)
- ¥ Weak soft X-ray source (11 photons, $E < 2$ keV) positionally coincident with HH 2
- ¥ $T \sim 1$ MK
- ¥ $L_{\text{x}} \sim 1-5 \times 10^{29}$ erg/s
- ¥ Physics of HH 2 similar to HH 154 (v, n)
- ¥ X-ray emission properties also similar to HH 154

Effects of HH X-ray emission on protostellar/protoplanetary environment



- ‡ L_x shock (10^{29} - 10^{31} erg/s) comparable to L_x YSO
- ‡ However, shock X-rays illuminate disk from above -> can reach outer, deeper parts of disk (and mimic effects of nearby high-mass stars)
- ‡ Ionization state of disk strongly influences e.g. viscosity, etc.
- ‡ Thus, X-ray emission from HH shocks likely to affect the conditions in the the protostellar and/or protoplanetary environment

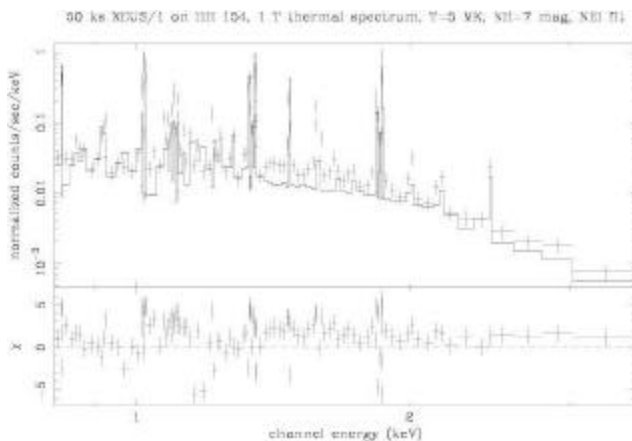
HH shocks: a new class of astrophysical soft X-ray sources

- ‡ 2 confirmed cases (HH 154 *XMM-Newton*, HH 2 *Chandra*)
- ‡ 2 strong candidates (HH 355F, HH 311) from ROSAT archival data (cf. Favata, Micela, Sciortino, Fridlund, in "New Visions of the X-ray Universe in the XMM Newton and Chandra Era", F. Jansen et al. eds, 2002, in press)
- ‡ $L_x = 10^{29}$ - 10^{31} erg/s (comparable range to YSO, T Tau)
- ‡ Likely to strongly influence protostellar and/or protoplanetary environment

Open issues and the role of XEUS

- ‡ Localization of emitting material through shock:
 - ‡ Requires spatial resolution (2-5" at least) & flux
 - ‡ Chandra can only study brightest ones
 - ‡ XEUS required for large majority of objects
- ‡ Physical conditions (CIE vs. NEI) and composition of plasma
 - ‡ Requires spectral resolution & photons
 - ‡ XMM can study brightest ones (none w/ RGS)
 - ‡ XEUS required for large majority of objects

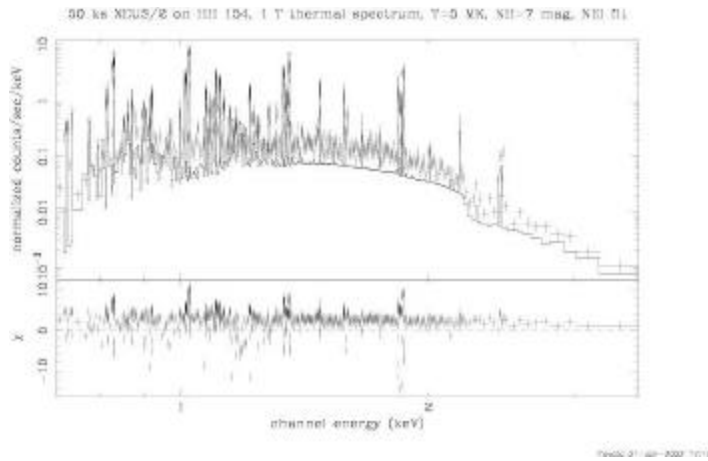
Simulations of XEUS-1 spectra of HH objects



Simulation of a spectrum obtained with the STJ + XEUS initial conf. in 50 ks on HH 154.

The simulated data assume a thermal equilibrium plasma, the fitted model is a non-equilibrium one. NEI condition easily recognized.

Simulations of XEUS-2 spectra of HH objects



Simulation of a spectrum obtained with the STJ + XEUS final configuration in 50 ks on HH 154.

The simulated data assume a thermal equilibrium plasma, the fitted model is a non-equilibrium one. Plasma in CEI and NEI can be easily recognized.

The shape of the K_α line as the evidence for the black hole existence

A.F. Zakharov¹ and S.V. Repin²

Institute of Theoretical and Experimental Physics, 25, B.Cheremushkinskaya st., Moscow, 117259, Russia;
Space Research Institute, 84/32, Profsoyuznaya st., Moscow, 117810, Russia

Abstract. Observations of Seyfert galaxies in X-ray region reveal the wide emissive lines in their spectra, which can arise in inner parts of accretion disks, where the effects of General Relativity (GR) must be counted. A spectrum of a solitary emission line of a hot spot in Kerr accretion disk is simulated, depending on the radial coordinate r and the angular momentum $a = J/M$ of a black hole, under the assumption of equatorial circular motion of a hot spot. It is shown that the characteristic two-peak line profile with the sharp edges arises at a large distance, (about $r \approx (3 - 10) r_g$). The inner regions emit the line, which is observed with one maximum and extremely wide red wing. High accuracy future spectral observations, being carried out, could detect the angular momentum a of the black hole.

The general status of black holes described in a number of papers (see, for example reviews by Zakharov (2000) and Liang (1998) and references therein). As it was emphasized in these reviews the most solid evidence for an existence of black holes comes from observations of some Seyfert galaxies because we need a strong gravitational field approximation to interpret these observational data, so probably we observe manifestations radiation processes from the vicinity of the black hole horizon (these regions are located inside the Schwarzschild black hole horizon, but outside the Kerr black hole horizon, thus we should conclude that we have manifestations of rotational black holes).

Recent observations of Seyfert galaxies in X-ray band (Fabian et al. (1995), Tanaka et al. (1995), Nandra et al. (1997a), Nandra (1997b), Malizia et al. (1997), Sambruna et al. (1998)) reveal the existence of wide iron K_α line (6.4 keV) in their spectra along with a number of other weaker lines (Ne X, Si XIII,XIV, S XIV-XVI, Ar XVII,XVIII, Ca XIX, etc.). The line width corresponds to the velocity of the matter motion of tens of thousands kilometers per second, reaching the maximum value $v \approx 80000 - 100000$ km/s (Tanaka et al. (1995)) for the galaxy MCG-6-30-15 and $v \approx 48000$ km/s (Weaver (1998)) for MCG-5-23-16. In some cases the line has characteristic two-peak profile (Tanaka et al. (1995), Yaqoob et al. (1997)) with a high "blue" maximum and the low "red" one and the long red wing, which gradually drops to the background level.

For individual objects, where the existence of the black holes is assumed, a strong variability of X-ray brightness was registered (Sulentic et al. (1998a)), as well as the rapid changes of the line profile (Yaqoob et al. (1997), NGC 7413) and the quasiperiodic oscillations (Paul et al. (1998), GRC 1915+105).

The large amount of observational data requires its comprehension, theoretical simulation and interpretation. The numerical simulations of the accretion disk spectrum under GR assumptions has been reported in the paper 1. In the paper by Cui et al. (1998) the observational manifestations of GR effects are considered in X-ray binaries. Different physical models of the origin of a wide emissive iron K_α line in the nuclei of Seyfert galaxies are analyzed in the papers by Sulentic et al. (1998b) and Fabian (2001).

The numerical approach, applied here based on the method, described earlier in papers by Zakharov (1993,1994,1995) and Zakharov and Repin (1999).

Many astrophysical processes, where the great energy release is observed, are assumed to be connected with the black holes. Because the main part of the astronomical objects, such as the stars and galaxies, possesses the proper rotation, then there are no doubts that the black holes, both stellar and supermassive, possess the intrinsic proper rotation too.

The stationary black holes are described by the Kerr metric:

$$ds^2 = -\frac{\Delta}{\rho^2} (dt - a \sin^2 \theta d\phi)^2 + \frac{\sin^2 \theta}{\rho^2} [(r^2 + a^2) d\phi - a dt]^2 + \frac{\rho^2}{\Delta} dr^2 + \rho^2 d\theta^2, \quad (1)$$

where $\rho^2 = r^2 + a^2 \cos^2 \theta$, $\Delta = r^2 - 2Mr + a^2$.

The equations geodesics can be simplified if we will use the complete set of the first integrals which were found by Carter (1968): $E = p_t$ is the particle energy at infinity, $L_z = p_\phi$ is z -component of its angular momentum, $m = p_i p^i$ is the particle mass and Q is the Carter's separation constant: $Q = p_\theta^2 + \cos^2 \theta [a^2 (m^2 - E^2) + L_z^2 / \sin^2 \theta]$. As shown by Zakharov (1991,1994) the equations of photon motion can be reduced to

$$\frac{dt'}{d\sigma} = -a (a \sin^2 \theta - \xi) + \frac{r^2 + a^2}{\Delta} (r^2 + a^2 - \xi a), \quad (2)$$

$$\frac{dr}{d\sigma} = r_1, \quad (3)$$

$$\frac{dr_1}{d\sigma} = 2r^3 + (a^2 - \xi^2 - \eta) r + (a - \xi) + \eta, \quad (4)$$

$$\frac{d\theta}{d\sigma} = \theta_1, \quad (5)$$

$$\frac{d\theta_1}{d\sigma} = \cos \theta \left(\frac{\xi^2}{\sin^3 \theta} - a^2 \sin \theta \right), \quad (6)$$

$$\frac{d\phi}{d\sigma} = - \left(a - \frac{\xi}{\sin^2 \theta} \right) + \frac{a}{\Delta} (r^2 + a^2 - \xi a), \quad (7)$$

where $\eta = Q/M^2 E^2$ and $\xi = L_z/ME$ are the Chandrasekhar's constants, which should be derived from the initial conditions in the disk plane; r and a are the appropriate dimensionless variables. The system (2)-(7) has also two integrals,

$$\epsilon_1 \equiv r_1^2 - r^4 - (a^2 - \xi^2 - \eta) r^2 - 2 [(a - \xi)^2 + \eta] r + a^2 \eta = 0, \quad (8)$$

$$\epsilon_2 \equiv \theta_1^2 - \eta - \cos^2 \theta \left(a^2 - \frac{\xi^2}{\sin^2 \theta} \right) = 0, \quad (9)$$

which can be used for the precision control.

We assume that the hot spot emits isotropically distributed quanta in the local frame. First, one should define the Chandrasekhar's constants for each quantum and then integrate the system (2)-(7) to either the infinity or the events horizon, depending on the constants values.

The trajectories classification, depending on the Chandrasekhar's constants can be found in the papers Zakharov (1986,1989). The details of simulation and initial conditions can be found in papers by Zakharov (1994) and Zakharov and Repin (1999).

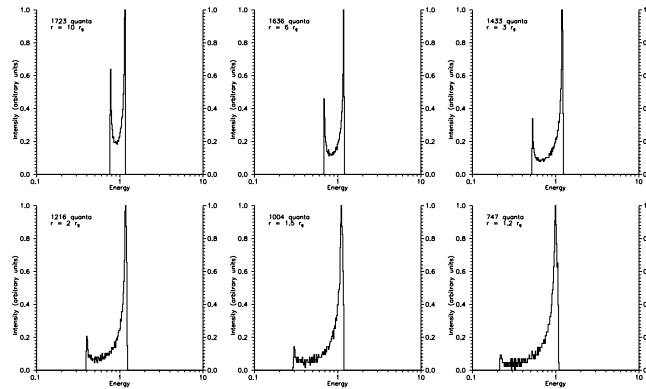


Fig. 1. Spectrum of a hot spot for $a = 0.9$, $\theta = 60^\circ$ and different values of the radial coordinate. The marginally stable orbit lays at $r = 1.16 r_g$.

The simulated spectrum of a hot spot for $a = 0.9$, $\theta = 60^\circ$ and different radius values is shown in Fig. 1. The proper quantum energy (in co-moving frame) is set to unity. The observer at infinity registers then the characteristic two-peak profile, where the “blue” peak is higher than the “red” one and the center is shifted to the left. Some spectrum juggling near its minimum is explained by pure statistical reasons and has no the physical nature.

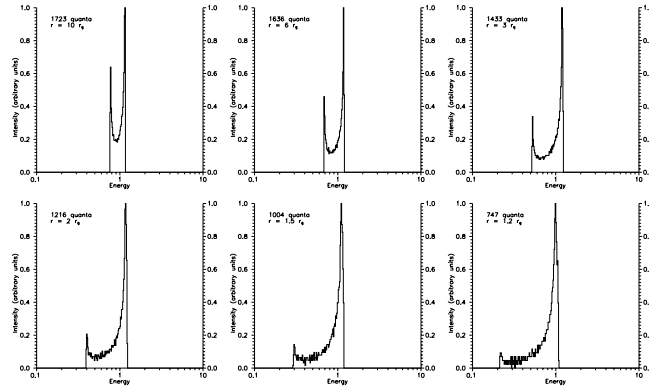


Fig. 2. Spectrum of a hot spot for $a = 0.9$, $r = 1.5 r_g$ and different θ angle values.

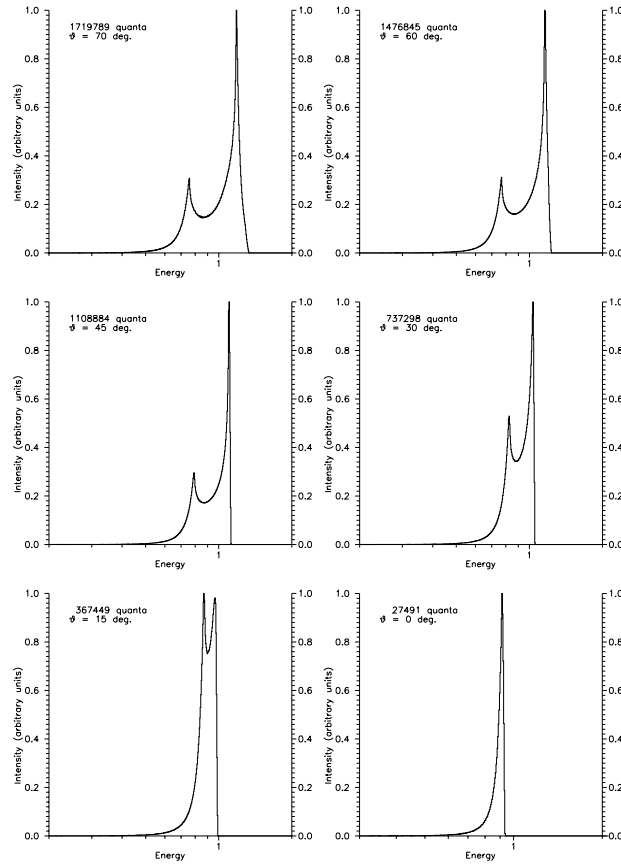


Fig. 3. The spectral line shape for different values of θ angle. The emitting region is the wide ring and its inner boundary is the last stable orbit (for rotational parameter $a = 0.9$ this r -value is equal to $r = 1.16 r_g$), its outer boundary corresponds to $r = 10 r_g$.

As far as the radius diminishes the spectrum is enhanced, i.e. increases the residual between the maximum and minimum quanta energy, registered by far observer. For example, for $a = 0.9$, $r = 1.2 r_g$ and $\theta = 60^\circ$, where r_g has its standard form $r_g = 2kM/c^2$, i.e. in the vicinity of the marginally stable orbit, the quanta, flown out to the distant observer, may differ 5 times in their energy. The red maximum decreases its height with diminishing the radius and at $r < 2 r_g$ becomes almost undistinguishable. It is interesting to note that the spectrum has very sharp edges, both red and blue. Thus, for $a = 0.9$, $r = 3 r_g$, $\theta = 60^\circ$ the distant observer has registered 1433 quanta of 20417

isotropically emitted; 127 of them ($\approx 9\%$) drop to the interval $1.184 < E < 1.202$ (blue maximum) and 43 quanta drop to $0.525 < E < 0.533$ (red maximum), whereas no one quantum has the energy $E < 0.518$ or $E > 1.236$.

A spectrum of a hot spot for $a = 0.9$, $r = 1.5 r_g$ and different θ values is shown on Fig. 2. The spectrum for $\theta = 60^\circ$ and the same a and r values is included in Fig. 1 and should be added to the current figure too. As it follows from the figure, the spectrum critically depends on the disk inclination angle. For large θ values, when the line of sight slips almost along the disk plane, the spectrum is strongly stretched, its red maximum is essentially absent, but the blue one appears narrow and very high. The red wing is strongly stretched because of the Doppler effect, so that the observer registers the quanta with 5 times energy difference. As far as the θ angle diminishes the spectrum grows narrow and changes the shape: its red maximum first appears and then gradually increases its height. At $\theta = 0^\circ$ both maxima merge to each other and the spectrum looks like the δ -function. It is evident because all the points of the emitting ring are equal in their conditions with respect to the observer. The frequency of registered quanta in that case is 2 time lower than the frequency of the emitted ones. A fall in frequency consists here in two effects, acting in the same direction: the transversal Doppler effect and the gravitational red shift.

The strong variability of Seyfert galaxies in X-ray does not contradict the assumption, that we observe the emission of the hot spots from the inner region of accretion disk, which can decay or grow dim, going towards a horizon as time passes. The spectrum dynamics is understood qualitatively by reference to Fig. 1, considered sequentially from top to bottom. It was considered the case of a wide accretion disk and it was shown that the shape of the spectral line retains its type with two peaks (see Fig.3, Zakharov and Repin (2002)). It is noted that the inner parts give the essential contribution into red wing of spectrum. The exact time characteristics of this process depend critically on the disk model and on the physical nature of a hot spot and are not discussed here.

The assumption can be checked out in long-term systematic X-ray observations with high time resolution of such Seyfert galaxies as NGC 1068, NCG 2110, MCG-6-30-15, NGC 4507, etc., where K_α line is sharply defined. The observations could confirm the existence of multiple spots, which motion and dynamics lead to X-ray variability in intensity and spectrum.

This work was supported in part by Russian Foundation for Basic Research (project N 00-02-16108).

References

- Bromley B.C., Chen K., Miller W.A., 1997, ApJ, 475, 57 .
 Carter B., 1968, Phys. Rev. D174, 1559.
 Cui W, Zhang S.N., Chen W., 1998, ApJ 492, L53.
 Fabian A.C., 2001, In "Relativistic Astrophysics" (Proceedings of the XXth Texas Symposium), ed. by J.C.Wheeler and H. Martel, (American Institute of Physics, AIP Conference Proceedings, vol. 586, New York, 2001) p. 643.
 Fabian A.C. et al., 1995, MNRAS 277, L11.
 Liang, E.P., 1998, Physics Reports 302, 69.
 Nandra K., et al., 1997a ApJ 476, 70.
 Nandra K., et al., 1997b ApJ 477, 602.
 Malizia A. et al., 1997 ApJSS 113, 311.
 Paul B., et al., 1998, ApJ 492, L63.
 Sambruna R.M., et al., 1998 ApJ 495, 749.
 Sulentic J.M., Marziani P., Calvani M., 1998a, ApJ 497, L65.
 Sulentic J.M., et al., 1998b, ApJ 501, 54.
 Tanaka Y., et al., 1995, Nature 375, 659.
 Weaver K.A., Krolik J.H., Pier E.A., 1998, ApJ 498, 213.
 Yaqoob T., et al., 1997 ApJ 490, L25.
 Zakharov A.F., 1986, ZhETPh 91, 3.
 Zakharov A.F., 1989, ZhETPh 95, 385.
 Zakharov A.F., 1991, AZh 35, 145.
 Zakharov A.F., 1993, Preprint MPA 755.
 Zakharov A.F., 1994, MNRAS 269, 283.
 Zakharov A.F., 1995, In "Annals for the 17th Texas Symposium on Relativistic Astrophysics", (The New York Academy of Sciences) 759, p. 550.
 Zakharov A.F., 2000, In "Fundamental problems of high energy physics and field theory" (Proceedings of the XXIII Workshop on High Energy Physics and Field Theory), ed. by I.V.Filimonova and V.A. Petrov, (Institute for High Energy Physics, Protvino) p. 169.
 Zakharov A.F., Repin S.V., 1999, AZh 76, 803.
 Zakharov A.F., Repin S.V., 2002, AZh 79, 400.

X-Ray Spectroscopy of Gamma-Ray Bursts: Present Results and Future Perspectives for XEUS

L. Piro

Istituto Astrofisica Spaziale e Fisica Cosmica, CNR, Via Fosso Cavaliere 100, 00133 Roma, Italy

Abstract. The detection of absorption and emission features in the X-ray spectra of GRB by BeppoSAX, Chandra ASCA and, more recently, by Newton-XMM, has opened new vistas, that go beyond the specific field of GRB. I will briefly review the results, summarize different models and describe the connection with massive progenitors in star-forming regions implied by these results. If GRBs are indeed associated with star formation, then it is likely that in a fraction of events the optical emission is heavily absorbed by dust. This scenario is one of the possible explanation for GHOSTs (GRB Hiding Optical Source/Transient a.k.a. "dark GRBs"), i.e. GRB that do show an X-ray afterglow but not an optical afterglow. Another intriguing possibility is that some of these events are located at very high redshift ($z > 5$), such that the optical photons are absorbed by Ly_α clouds. While there is evidence that a few of these events are located in host galaxies at $z < 5$, the origin of the majority of dark GRB, (about 50% of the whole population of long GRB) is still unclear. High- z GRB can also be hidden in another new class of GRB, the X-Ray rich GRB a.k.a. X-Ray Flashes. In these objects, about 30% of the population of long GRB, the bulk of the emission is observed in X-rays rather than in gamma rays, as it would be expected if $z > 10$. However, it is also possible that some of these events are intrinsically different from normal GRB. X-ray spectroscopy will play a key role in disentangling these new mysteries. But the most exciting perspective is on Cosmology. GRB are the brightest beacons in the Universe, producing copious emission of penetrating γ -ray and X-ray photons, that can pierce through dusty and obscured regions of star-forming galaxies in the early Universe. I will show how X-ray spectroscopy of GRB, as that provided by XEUS, will allow to probe star-formation sites and galaxies in the early Universe.

Acknowledgements: We gratefully acknowledge the permission by the Springer Verlag to use their A&A LATEX document class macro.

X-ray spectroscopy of GRB's: Present Results and Future Perspectives for XEUS

**Luigi Piro
IASF/CNR
Roma**

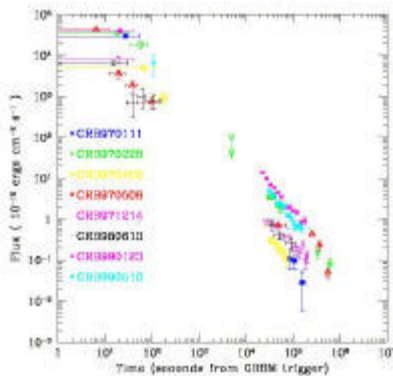
Summary

- X-ray afterglows
- Iron features and massive progenitors
- GHOSTS/dark GRBs and the link with star-formation
- X-Ray rich GRB's, high-z GRB's
- High resolution X-ray spectroscopy, XEUS & GRB's: probe of the Early Universe (see poster by Piro et al on **IMBOSS**)

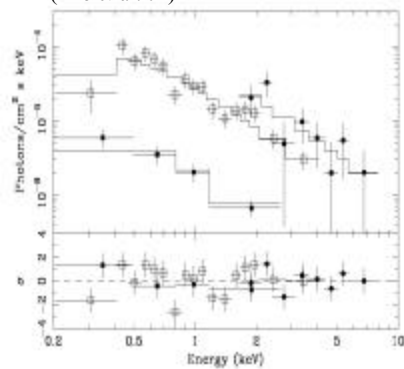
General properties of (X-Ray)

- $F \sim t^{-\delta} \nu^{-\alpha}$ afterglows
- $\delta_x = 1.1 - 1.9$ (average = 1.4); $\alpha_x \sim 1.0$

Temporal evolution of a collection of X-ray afterglows



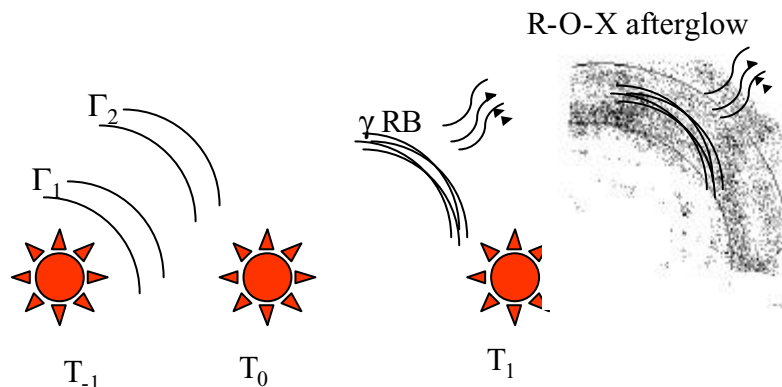
X-ray spectral evolution of GRB000926 by BSAX and Chandra (Piro et al. 01)



The fireball scenario



Observer

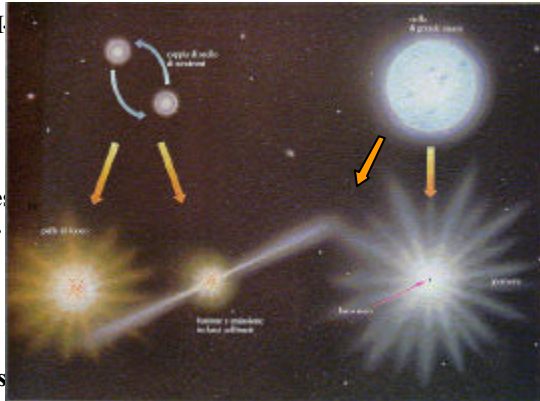


The progenitors of GRB

The nature of the progenitor can be inferred from the environment



- NS-NS (BH-NS & BH-WD) travel far from their formation sites before producing GRB's (Fryer et al 2000) => "clean environment": no lines
- Hypernovae/collapsar evolve much faster, going off in their formation site => "mass-rich environment" => lines



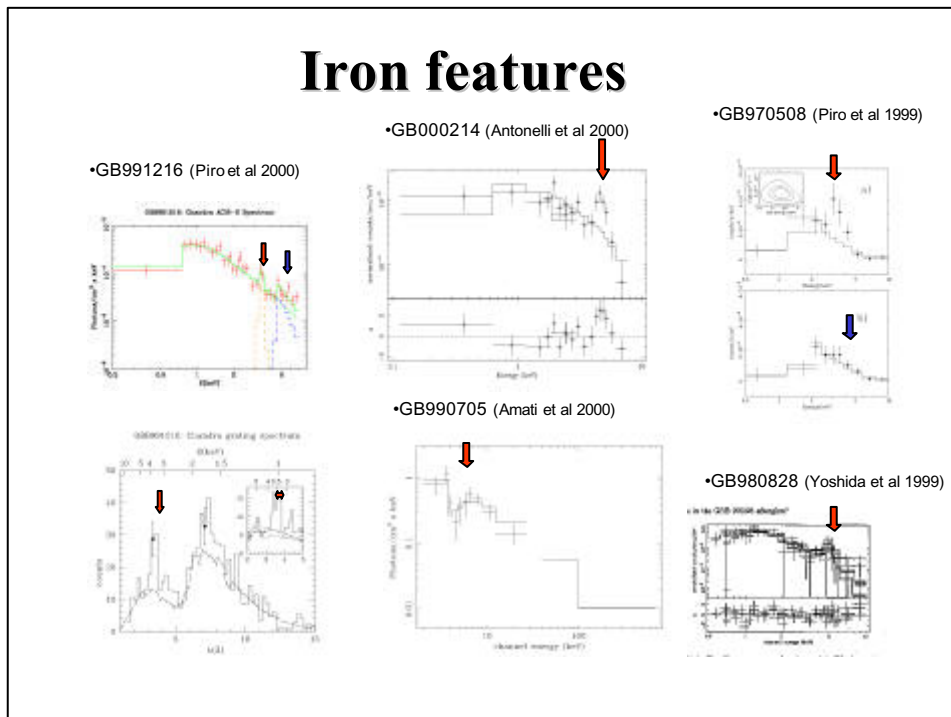
•  NS- NS merging

 Hypernova

X-ray Fe features

- Ubiquitous feature in several classes of X-ray sources
- Diagnostics of the environment nearby the central engine
- Independent and direct redshift determination

Iron features



Iron features in GRB's

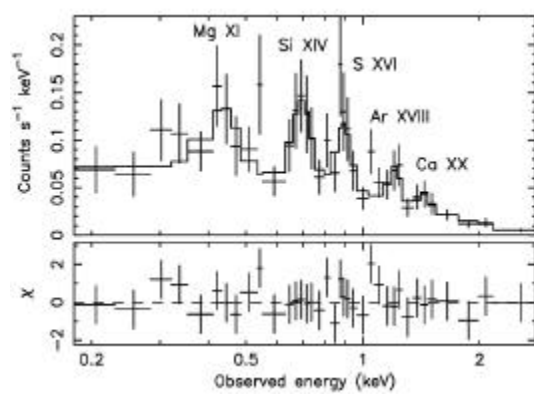
- **Energies consistent with that expected from the optical redshift (GB991216 Fe line and recombination edge observed at 3.4 keV and 4.5 keV corresponding exactly to the energy of the Fe line redshifted with $z=1.00\pm 0.02$; GB970508, $z=0.84$, GB970828, $z=0.9$). Note also that in GB990705 the predicted X-ray redshift is consistent with that found later by optical spectroscopy.**
- **The energy of Fe features in the afterglow indicate highly ionized atoms. This is consistent with a medium being ionized by a strongly variable radiation field (ionization vs recombination)**
- **The mass of Fe ($N_{\text{Fe}} = L_L t_{\text{rec}}$, where $t_{\text{rec}} = 30 T_7^{1/2} n_{10}^{-1}$ is the recombination time) ($M_{\text{Fe}} \approx 0.1 M_{\text{sun}}$) and high density and line width $\approx 0.1c$) indicates a SN explosion by a massive progenitor (e.g. Supernova model of Vietri and Stella). Alternatively the jet/bubble model of (Meszaros & Rees 2001) needs less iron but still requires a massive progenitor.**

Low-energy lines in GRB011211

Triggered and
localized by
BeppoSAX
GRBM+WFC

Follow-up by
Newton-XMM

Afterglow shows 3σ
evidence of low-
energy lines (ionized
Si, S,... : Reeves et al
02)



GRB localized and observed in X-rays

- As of Mar. 4, 2002 BeppoSAX has detected:

**30 X-ray afterglow candidates out of 34 GRB follow up
observations in X-rays**



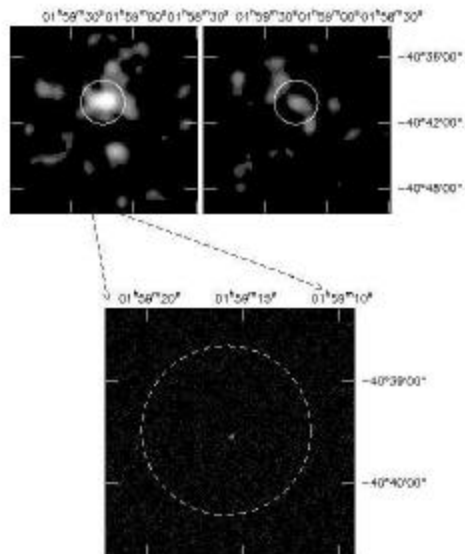
X-ray afterglows > 90%
Optical afterglows ~ 40% - 50%
Radio afterglows ~ 35% - 40%

GHOST's in the sky

- Grb Hiding Optical Source-Transient: GRB with X-ray but no O afterglow aka dark GRB
- Optical searches with same sensitivity & reaction times as in the cases with OT (Reichert, Ghisellini, Fruchter, Andersen,...)
- **OT heavily absorbed by star forming region ? Or located at $z > 5$ (such that intragalactic gas will absorb photons below Lyman limit)**
- How to disclose GHOST's:
 - arcsec X-ray or/and radio positioning
 - X-ray spectroscopy $\Rightarrow z$
 - IR observations

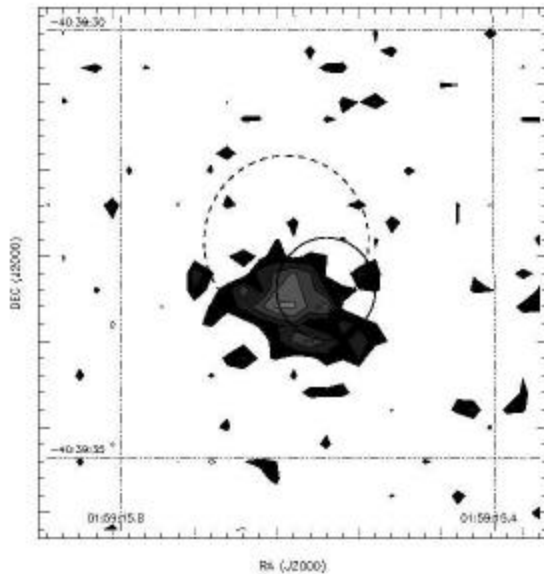
GRB000210: BeppoSAX & Chandra

- GRB localized by BeppoSAX. The brightest ever observed in γ -ray peak flux
- Simultaneous obs of the X-ray afterglow with Chandra.



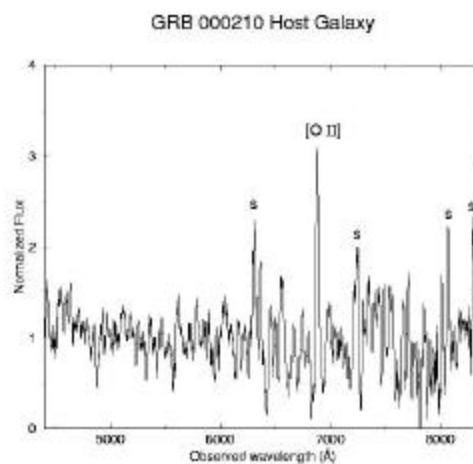
The host of GB000210?

- Obs at NOT, 1.54D, NTT, 2.2mESO starting 12 hrs after the GRB: no OT down to $R=23.5$
- A galaxy in the CXO error box
- VLA: radio transient
- (Piro, Frail, Gorosabel et al, 2002)



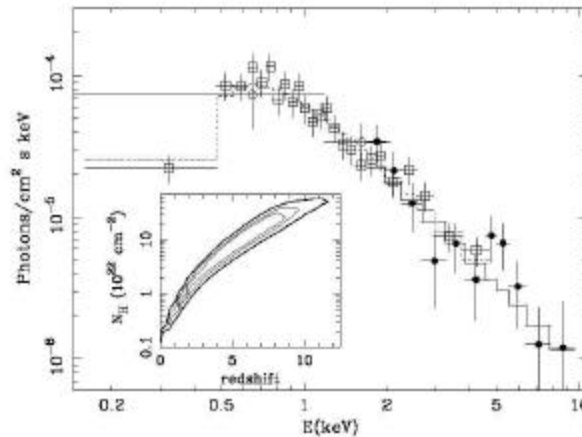
The redshift of the galaxy

- VLT spectrum and photometry (no B or V dropout) $z=0.85$
- The probability of a field galaxy with $R>23.5$ in the Chandra/radio ($1''$ error box) is 10^{-2}
- Another dark GRB associated with host galaxy at $z=0.96$ is GRB970828 (Djorgovski et al 01)



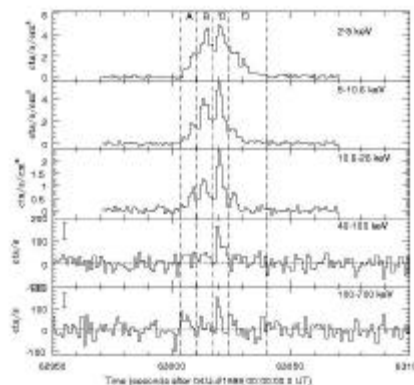
Dark GRB in star-forming GMC

- Significant absorption above the galactic in X-rays. At $z=0.85$ $N_{\text{H}}=(5 \text{ }_{\pm 1}) 10^{21} \text{ cm}^{-2}$
- Typical of a GMC
- Distribution of distances of optical afterglows vs host galaxy connects long GRB with star-formation sites and massive progenitors (Bloom et al 2002)



Other remaining mysteries

- **X-ray rich GRB/ X-Ray Flash: a new class discovered by BSAX: about 25% GRB's have very faint or absent gamma-ray emission (the bulk of the luminosity is in X-rays).**
- **GRB's in high dense medium (dirty fireball => smaller Lorentz factor (Dermer et al) or events at $z>5-10$? So far no OT found (a subclass of GHOST's).**



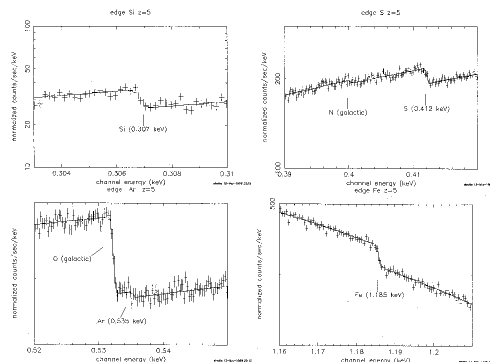
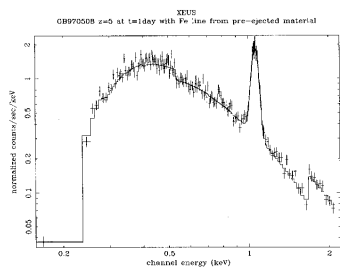
Feroci et al
2001, see also
Heise et al 2001

GRB: probes of star-formation in the far Universe

- The brightest ($L_{\text{iso}}=10^{53-54}$ erg/s, i.e. independent on the jet opening angle) and most distant sources in the Universe ($z=0.3-4.5$)
- They can be detected at farthest distances (in fact some of the constituents of mysterious classes of GRB can be high- z GRB)
- Associated with star-formation
- They can pinpoint obscured star-forming galaxies (X-rays and gamma-rays pierce through)

High resolution X-ray spectroscopy of GRB with XEUS

- The Fe line in a GRB like GB970508 but at $z=5$
- Study of the metallicity of the host galaxies of a GRB at $z=5$ through X-ray edges



XEUS' eye on GRB: a look into the early Universe

- **Deep into the GRB progenitor and its environment**
 - **Detailed X-ray spectral diagnostics of the nearby environment**
 - *Pre-ejected material of GRB at high z (>3)*
 - *reverberation mapping: history of the medium ejected by progenitor*
- **Far into the early Universe**
 - **Study of star forming regions at $z>3$**
 - *line features produced by the interaction of the GRB photons with environment*
 - *chemical and physical state of the medium by absorption features imprinted on the X-ray spectrum of GRB*
 - **Study of the medium in the parent galaxy**
 - *chemical and physical state of the medium by absorption features imprinted on the X-ray spectrum of GRB*
- **Probe the star forming regions in the early Universe (the first stars?) and the history of metal enrichment of distant galaxies**

General relativity from neutron stars and stellar-mass black holes

M. van der Klis¹

Astronomical Institute “Anton Pannekoek”, University of Amsterdam, Kruislaan 403, 1098 SJ Amsterdam, The Netherlands

Abstract. Millisecond X-ray time variability studies of accreting low-magnetic-field neutron stars and stellar-mass black holes probe the motion of matter in regions of strong gravity. For motion in this region, general relativity is no longer a small correction to the classical laws of motion, but instead dominates the dynamics. In the language of general relativity (GR): we are studying the motion in strongly curved spacetime. Such millisecond studies can therefore provide unique tests of gravitation theory in the strong-field regime. I discuss the prospects for mapping out space-time near accreting stellar-mass compact objects through millisecond timing with XEUS. The overwhelming consideration for timing sensitivity is collecting area: contrary to most applications, the signal to noise ratio for the aperiodic timing phenomena produced by the accretion flow increases *proportionally* with count rate rather than as the square root of it. With RXTE, using 0.6 m² collecting area, we have already been able to find several timing diagnostics of the strong field region. XEUS, by virtue of the sheer timing sensitivity provided by its order of magnitude larger area, in combination with the capabilities that this large area will provide to link timing and spectroscopy diagnostics of the strong-field region, shall be able to turn these *diagnostics* of GR into true *tests* of GR. Large-area missions such as XEUS provide simply enormous opportunities for probing strong-field gravity using millisecond timing. Clearly, it would be wise not to leave so much real estate in collecting area without a high-rate fast timing capability.

1. Introduction

The rationale for observing X-ray binaries in order to study gravitation is well known. In the inner few kilometers of the accretion flow onto a low-magnetic-field neutron star or stellar-mass black hole the accreting matter is moving under the influence of strong gravity. In this region, where the gravitational binding energy of a particle of mass m approaches its rest-mass energy: $GMm/r \sim mc^2$ or in other words, close to the Schwarzschild radius at $R_S = 2GM/c^2$, we are looking at the motion of matter in strongly curved spacetime. Classical physics is completely inadequate to describe the motion of matter here. Consequently, by studying this motion one learns about gravitation in the strong-field regime, a regime where general relativity has not yet been tested to any degree of confidence.

We currently have two diagnostics available to us in studying the accretion flows in the strong-field region: spectroscopy and timing¹ Of course, one wants to use both diagnostics and combine the information in order to obtain the best results. This talk concentrates on timing, the study of the time variability of the X-rays. For stellar-mass compact objects one needs to concentrate on the millisecond regime, because the main characteristic time scales in the strong-field region, such as the orbital time scale, are of that order: the Keplerian orbital frequency at the general-relativistic innermost stable circular orbit (at $3R_S$ or $r_{ISCO} = 8.9 \text{ km} \times (M/M_\odot)$) in a Schwarzschild geometry is $\nu_{ISCO} = 2192 \text{ Hz} \times (M/M_\odot)^{-1}$. I will discuss some examples of the strong synergy expected between timing and spectroscopy in probing the strong-field region in §5.

We have two main types of accreting systems at our disposal within which to study the accretion flow in the strong-field region: X-ray binaries and AGN. To a considerable degree the accretion flows in the inner regions of these two types of system are thought to be analogous, and again one wants to study both and describe the results in one coherent picture in order to obtain both the most precise and the broadest view. Both types of system have their observational and interpretative advantages. Those of the X-ray binaries include (i) that these systems are nearby and hence very bright, so that we can observe them with very good signal to noise, (ii) the fact that the presence of either

¹ Although plans are being discussed, it will nearly certainly take several decades before imaging these flows in X-rays becomes a practical possibility (White 2002).

a neutron star or a black hole at the center provides two distinct natural experiments that differ in only one important detail, the results of which we can compare and (iii) the short (millisecond) characteristic time scales, which make it feasible to observe millions of cycles of the variability, so that we can study the *parameters* of the stochastic process in the accretion flow that produces the variability rather than having to satisfy ourselves with one particular *realization* of it.

2. Neutron star spins

The first, and long-predicted, accretion-powered millisecond pulsar was finally discovered in 1998 in X-rays using the Rossi X-ray Timing Explorer (RXTE) (Wijnands and van der Klis 1998). The object SAX J1808.4–3658, shows 2.5 millisecond pulsations and can be inferred to have a 10^8 – 10^9 Gauss magnetic field strength, which implies that when placed in vacuum this object would turn on as a rotation-powered (radio) millisecond pulsar (Psaltis and Chakrabarty 1999). This discovery finally demonstrated that the millisecond spins inferred from spin-up theory and evolutionary considerations for the low-magnetic-field neutron stars in low-mass X-ray binaries (LMXBs) do indeed exist. It also showed that there is no fundamental reason why such low-field accreting pulsars would not be detected (i.e., the pulsations do not necessarily get smeared out of existence by scattering in a surrounding cloud of material, and even at this low field strength permanent hot spots do form as predicted). Since the XEUS meeting two more millisecond pulsars have been found with RXTE, with 2.3 and 5.4 millisecond spin periods and similar to SAX J1808.4–3658 and each other in several respects (Table 1). In particular, the population statistics now seem to point towards very low-mass companions, very compact systems, and very low current average accretion rates.

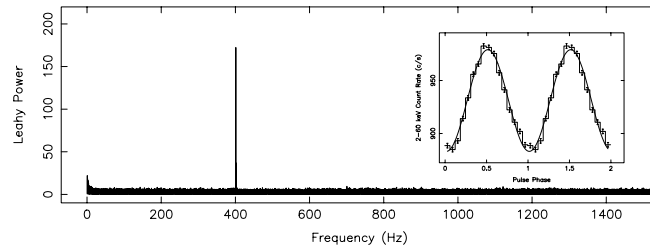


Fig. 1. The discovery power spectrum and pulse profile (inset) of the first accreting millisecond X-ray pulsar. Note the low harmonic content evident both from the absence of harmonics in the power spectrum and the near-sinusoidal pulse profile. (after Wijnands and van der Klis 1998)

We do not know the reason that millisecond pulsars have not been discovered in all neutron-star LMXBs. This may be because of lower pulse amplitudes, intrinsically, or, more excitingly, because these systems contain higher-mass, more compact neutron stars which smear out the pulsar beam more (through general relativistic gravitational bending of the radiation) than their less massive equivalents. The latter possibility would be in line with the low average accretion rates in the three newly discovered pulsating systems, although there seem to be other, similarly low current average accretion rate systems that do *not* pulse with the same strength. Another possibility is that these stars are spinning much faster, perhaps at sub-millisecond rates, so that orbital Doppler smearing dominates. Whatever the reason, after these discoveries it seems very likely that XEUS, with its order of magnitude better sensitivity than RXTE (Barret, this meeting), would detect many more millisecond pulsars and would allow to check on these exotic possibilities. The discovery of high-mass neutron stars, or sub-millisecond spins, would immediately put a very strong constraint on the equation of state of supranuclear density matter. The EoS will be further discussed by Miller at this meeting.

The burst oscillations, which are discussed in this meeting by Cole Miller, provide a nearly certain diagnostic of the neutron star spin in those LMXBs that show type 1 X-ray bursts. It has been suggested (Bildsten 1998) that based on the observed burst oscillation frequencies and their possible link with the kilohertz QPOs (§3), the neutron stars in all well-studied systems may spin at rates in a relatively narrow range, with a width of only a few 100 Hz, or perhaps even less, and that the reason for this might be gravitational radiation. In this description, gravitational radiation would be carrying angular momentum away from, as fast as the accretion disk is providing it to, the accreting neutron star, and all LMXBs would be bright, millisecond-periodic gravitational radiation sources (the brightest X-ray sources being the brightest in gravitational radiation as well, so Sco X-1 would then beat all other sources by an order of magnitude in gravitational radiation as well as X-ray flux). It would probably be necessary to keep track of the exact spin ephemeris of the sources to allow their detection with gravitational wave detectors, and a large area X-ray instrument would be

Table 1. Accreting millisecond pulsars.^a

Quantity	SAX J1808.4-3658	XTE J1751-305	XTE J0929-314
Discovery	15 Apr 1998	4 Apr 2002	7 May 2002
Pulse frequency(Hz)	401	435	185
Pulse period(ms)	2.49	2.30	5.40
Orbital period(min)	121	42.4	43.6
Projected orbital radius $a_x \sin i$ (light ms)	62.8	10.1	6.1
Mass function $f(M)$ ($10^{-6} M_\odot$)	37.8	1.26	0.27
Companion mass (M_\odot) ^b	> 0.04	> 0.014	> 0.008

^a Wijnands and van der Klis 1998, Chakrabarty and Morgan 1998, Psaltis and Chakrabarty 1999; Markwardt et al. 2002a,b; Remillard et al. 2002a, Galloway et al. 2002 ^b Assuming a $1.4 M_\odot$ neutron star.

required to do this. It only could do so if it was equipped with proper timing instrumentation able to deal with very bright objects, of the kind that Barret is describing at this meeting as a possible low-impact extension to the XEUS instrumentation.

3. The inner accretion flow

Quasi-periodic oscillations (QPOs) were discovered with RXTE in the X-ray flux of some 20 neutron-star LMXBs with frequencies varying up to more than 1300 Hz and quality factors up to $\sim 10^2$ (van der Klis 2000 for a review). Usually, two peaks are seen in the power spectra of the X-ray count-rate time series in the kHz domain. Because the accretion disk is a wonderful source of periodicities by virtue of its Keplerian motion at each radius, and because kHz frequencies are those expected from the inner emitting region of the accretion disk around a low-magnetic field neutron star, it seems natural to identify quasi-periodic variability at such a frequency with orbital motion at a preferred radius in the inner disk. The most straightforward preferred radius is that of the inner edge of the Keplerian disk which in many descriptions is expected to be quite sharp (e.g., Miller et al. 1998). Indeed, nearly all detailed models that have been put forward to explain kHz QPOs identify the frequency of one or the other of the two peaks as the Keplerian orbital frequency at the inner edge of the disk. This, of course, is a very important conclusion, as it means we are directly observing orbital motion in strong gravity.

As both kHz peaks, and indeed several lower-frequency phenomena as well, change in frequency together, apparently in the sense of an increase in frequency when the instantaneous accretion rate through the inner disk \dot{M}_d increases (see also van der Klis 2001), this then implies that the inner edge of the disk must move in when the frequency increases. The inner disk radius might vary between ~ 30 km for the lowest observed frequencies to less than 15 km for the highest frequencies (for a $1.4 M_\odot$ neutron star; note that the innermost stable circular orbit (ISCO) from general relativity is located at ~ 12.5 km for such an object). One immediate prediction is that there should be a maximum on the observed frequency. When the inner disk radius moves inward and the frequency increases, at some point the ISCO will be reached. The inner radius of the Keplerian disk can not become smaller than this, so the frequency increase would saturate (Miller et al. 1998). It is possible that such a saturation has already been seen (in 4U 1820–30, at a value implying an amazing $2.2 M_\odot$ neutron star, Zhang et al. 1998) but as noted by Zhang et al., this is uncertain. In any case, assuming general relativity, such a maximum on the kHz QPO frequency is a very strong prediction of the orbital interpretation, and with sufficient sensitivity we would expect to see this effect in most sources (currently, towards the highest frequencies the QPO amplitude drops with increasing frequency and the QPOs become too weak to detect before the location where the ISCO is expected is reached, §5).

Both in neutron stars and in black holes we now know of a whole set of variable-frequency phenomena whose frequencies vary together in correlation with \dot{M}_d , as described above for the kHz QPOs. Models for these phenomena tend to be in terms of orbital motion and vibrations at characteristic radii in the accretion disk that vary with accretion rate; a simple example is orbital motion at the inner edge of the Keplerian disk whose radius t_{in} depends on \dot{M}_d through the balance between gravitational, and radiative/magnetic stresses on the accreting material. In addition to these variable frequencies there are indications, again both in neutron stars and in black holes, for QPOs with approximately constant frequencies. These are very important, as their approximate independence of \dot{M}_d indicates they occur at frequencies set only by properties of the compact object, i.e., mass, angular momentum and perhaps magnetic field. This is suggestive of models relying heavily or exclusively on general relativity (see §4); a simple example would be the orbital frequency at the ISCO.

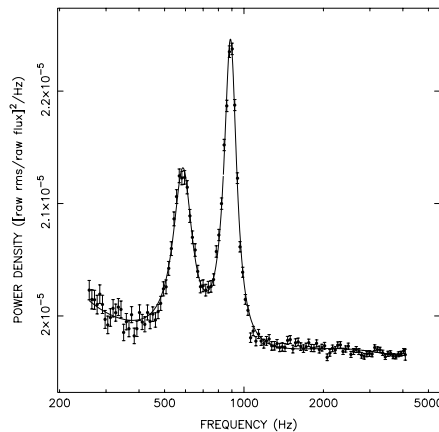


Fig. 2. Power spectrum of Sco X-1 exhibiting twin kHz QPO peaks (van der Klis et al. 1997)

For the highest-frequency QPOs in black hole systems it has been difficult to establish whether these are variable-frequency phenomena or not. It may be that the peaks in the power spectra move, but it seems more likely now that usually (but not always) we are looking at sets of harmonics whose relative strengths vary so as to simulate motion (Remillard et al. 2002b). The reason that such a simple property is so hard to determine is that these QPOs are weak and therefore quite erratically detected, often strongly energy dependent, and the sources in which they occur transient. The impression one gets is that there may be a whole spectrum of frequencies just below our current detection limit; the same may be true for the neutron star systems.

The issue of whether we are seeing the same phenomena in neutron star and black hole systems is a very important one, as a phenomenon occurring in both types of system can not rely on any property unique to either type: the presence or absence of a solid surface, a horizon, a non-aligned magnetic field, spinning surface hot spots or frame dragging as strong as around near-extremal Kerr black holes can then all be excluded as ingredients for their formation. This leaves essentially only phenomena in the accretion flow (most likely the disk although there are other possibilities, e.g., a jet) for their explanation. The similarities in the timing properties between neutron stars and black holes are sometimes quite striking (van der Klis 1994a,b). The strong correspondence between the properties of low-luminosity X-ray bursters and black holes in the low state (e.g. Inoue 1992, Olive et al. 1998, Belloni et al. 2002) certainly suggests to most experts that the same phenomena are seen. Somewhat more controversial but potentially very illuminating are identifications made based on frequency correlations between phenomena covering a wide range in Q and that strongly differ in observed frequency between neutron stars and black holes (Wijnands and van der Klis 1999, Psaltis et al. 1999).

4. Models and how to discriminate between them

By far the greatest effort in modeling the X-ray variability phenomena described in §3 has so far gone into finding ways to produce the correct frequencies. What are the frequencies that on first principles we might expect from the inner disk flow in the strong-field region?

First, it is important to recognize that in general relativity (GR), contrary to classical mechanics there are three frequencies associated with each orbit, leading to epicyclic motions superimposed on the usual orbital motion: (i) the usual azimuthal, Keplerian, orbital frequency ν_K and in addition, if the orbit is not circular, (ii) a radial frequency that because it is different from ν_K causes the pericenter of the orbit to precess (vide the Mercury perihelion precession, one of the classical weak-field tests of GR) and finally, if the plane of the orbit does not coincide with the equatorial plane of the central object's spin, (iii) a meridional (vertical) frequency causing the line of nodes of the orbit to precess, i.e., the orbital plane to “wobble”, a precession known as Lense-Thirring precession. These frequencies are exact predictions of GR expressible in closed form.

So, in principle, if there is a way to express these frequencies into X-ray modulations, a certain preferred radius in the inner disk can already produce three frequencies. Of course, an accretion disk is a hydrodynamical flow, so while the particles in that flow each individually might have exhibited those three frequencies in their test-particle orbits, collectively their motions will be more complex, and combination frequencies as well as additional ones due to hydrodynamics (such as pressure waves) may occur and interact with these three basic GR epicyclic ones (e.g., Psaltis and Norman 2000). Disk oscillation models (e.g. the diskoseismic models, Wagoner 1999) have been showing up these

various frequencies since well before the current complement of observed frequencies was found. Stella and Vietri (1998, 1999), and Cui et al (1998) proposed, for both neutron stars and black holes, identifications of observed frequencies with the basic GR orbital and epicyclic frequencies (see also Marković and Lamb 1998), and further disk oscillation calculations using different approximations were performed by for example Psaltis and Norman (2000, 2002). Models of this type are usually called relativistic precession models even when the actual motions are not the test-particle-orbit precessional ones. The models of Titarchuk et al. (1999), producing a multitude of frequencies, exemplify yet another approach to accretion flow oscillation modeling.

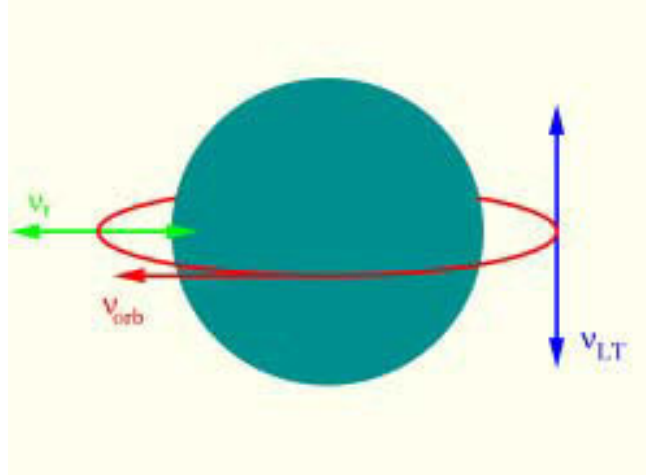


Fig. 3. Azimuthal, radial and meridional motion does not occur at the same frequency in general relativistic orbital motion, leading to epicyclic orbits.

Then, there is an entirely independent source of frequencies available to the inner flow in case the compact object is a neutron star: the neutron star spin. Beat frequency models (e.g., Miller et al, Campana, Cui) make use of this: in those models there is an interaction (mediated either by radiation or by the neutron star magnetic field) between the orbital frequency at the inner edge of the disk and the spin frequency of the star. This leads to interaction frequencies such as $\nu_B = \nu_K - \nu_s$, where ν_B is called the beat frequency and ν_s is the spin frequency. An approximate observed coincidence between the kHz QPO peak separation and the burst oscillation frequency in several neutron star systems is the strongest underpinning of models of this type. Of course, while relativistic precession models work for neutron stars as well as black holes, beat frequency models are applicable to neutron stars only.

Nearly all of the models discussed require particular preferred radii in the disk in order to single out particular frequencies, so in addition to these frequency models one needs “radius models”. *Variable radii* tend to be radii relying on disk physics and dependent on \dot{M}_d . Usually the inner radius of the Keplerian disk (within which the matter plunges in), set by magnetic or radiative stresses on the disk flow has been preferred, but one could also think of other disk physics radii, e.g., the radius of the inner radiation-pressure-dominated part of the disk. *Constant radii*, producing constant frequencies, tend to be those relying mostly on GR, e.g., the ISCO, which depends only on mass and angular momentum of the compact object. The diskoseismic models tend to produce approximately constant frequencies.

A particularly stimulating recent proposal is that made by Kluzniak and Abramowicz (2001), who suggest that it is GR itself that picks out the radii from the disk. Because the three GR orbital frequencies have different radius dependencies, there are particular radii, depending on mass and angular momentum of the central object only, at which two of these frequencies have simple integer ratios (2/3, 3/5). In their suggestion, at these radii in some of these cases a resonance occurs that amplifies those frequencies among the wide range present in the disk, and makes them observable. The observation of approximate 2/3 frequency ratios in the high-frequency QPOs in the black hole candidates GRO J1655–40 and XTE J1550–564 is suggestive of such an interpretation. This would mean that strong-field GR is exhibiting itself in pure form in these systems, picking out for us the frequencies preferred by gravitation theory from the multitude of frequencies in principle available from the hydrodynamical disk flow. As intermediate (non-integer) frequency ratios are in fact also observed, it may be that variable QPOs produced by some mechanism at a variable radius get enhanced in strength or coherence by resonances when that radius is close to the resonant radius. It may be worth exploring, as an alternative to existing beat-frequency models, to what extent interaction (by radiative or magnetic stresses) of the neutron star spin with the inner disk might be playing a role in similarly picking

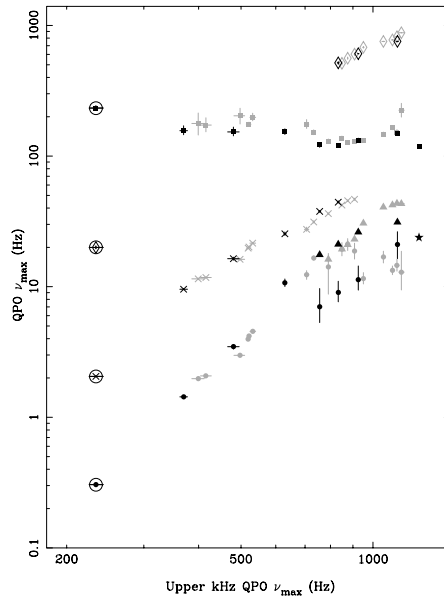


Fig. 4. Measurements of various characteristic frequencies in power spectra of 4U 1728–34 (gray) and 4U 0614+09 (black) plotted vs. one of them: the characteristic frequency of the upper kHz QPO. Note that most frequencies are variable and vary in correlation with each other, but that one seems to be approximately constant. After van Straaten et al. (2002).

out, rather than originating, sets of frequencies exhibiting commensurabilities with the spin frequency (see also Psaltis 2000).

Finally, identifying observed frequencies with frequencies expected from some mechanism at certain radii in the disk is not sufficient for a complete model: it is also necessary to specify how these frequencies get expressed in terms of a modulation of the X-ray count rate. For these “modulation models” self-luminous and/or occulting “blobs” in the accretion disk are sometimes postulated without a further physical description. Modulation of either the strength or the anisotropy of the accretion flow onto the compact object is a description that has been worked out in somewhat more detail in the Miller et al. (1998) “sonic point model” which is a beat-frequency model involving radiative truncation of the inner disk as well as a radiative spin-orbit interaction. The X-ray spectrum of nearly all QPOs is much harder than that of the average flux, which particularly in black hole systems seems difficult to reconcile with an origin in the accretion disk thought to produce a *soft* spectral component; perhaps one could get around this problem if the process in the disk modulates the production of seed photons for an upscattering process in a “corona” containing hot electrons. The fact that the photon energy dependence of the QPOs tends to be much larger in black hole than in neutron star systems certainly does suggest a relation with the X-ray spectral components, which in black hole systems are much more radically different than in neutron star ones.

How can observations discriminate between these various models? As it turns out, every physical frequency model predicts its own set of parasitic, weaker frequencies in addition to the strong ones it set out to explain in the first place (e.g., Miller et al. 1998). These predicted patterns of weaker frequencies provide a strong test of each model. Searches for such weaker power spectral features are very difficult because this is really work at the limit of the sensitivity of current instrumentation, and the distinct impression of the observers is that there is much that is hiding still, but a few successes have been accomplished: in three neutron star systems a lower side band has been detected to the lower-frequency one of the twin kHz peaks (Jonker et al. 2000) and in two or three black hole systems twin, instead of single, high-frequency QPOs have been detected (Strohmayer 2001, Miller et al. 2001, Remillard et al. 2002b). These detections have led to only one claim in each case of a theoretical explanation (Psaltis and Norman 2002, Kluzniak and Abramowicz 2001), an unusual situation that testifies to the discriminating power of such additional frequencies, but there are still too few frequencies detected for the full power of this method to be applied. With XEUS equipped with proper timing instrumentation nearly certainly the entire “fingerprint” of the underlying phenomenon would be mapped out as a spectrum of interrelated frequencies which would make such explanations, if successful, unassailable, as of course they should be in order to be accepted as true tests of GR in the strong-field regime. Modulation models can be constrained by combining timing and spectroscopic information; this will be discussed in §5 below.

5. XEUS and strong-field gravity

It is clear that with RXTE we have come a long way towards strong field gravity physics. We are seeing, and are able to study in some detail, variability at the dynamical time scale of the strong-field region in accreting low-magnetic field neutron stars as well as stellar-mass black holes and thus directly probing the matter flow in the strong-gravity region. The ISCO, the three orbital frequencies and the relativistic epicycles by necessity explicitly figure in our models now, and in fact most of the models can only work thanks to strong-field gravity effects (this is true for, e.g., the sonic point model, the relativistic precession and resonance models, the diskoseismic models). We may have seen direct evidence for the ISCO already, and in any case there are strong predictions for its observable effects on known observable phenomena. Observed approximately constant frequencies directly suggest phenomena that derive through GR from compact-object properties only. The relativistic precession and the relativistic resonance models are promising direct observational access to the three strong-field relativistic orbital frequencies, among which Lense-Thirring precession, which is a consequence of frame dragging.

With XEUS we shall be able to turn the *diagnostics* of GR that we have found with RXTE into true *tests* of GR. First, it will be very important to figure out the geometry underlying the signals that we are receiving. We should answer the question whether the conclusion that we are looking at orbital motion (which seems very likely) can be proven. We would like to determine if, as also seems very likely, we are indeed seeing some of the same phenomena in neutron stars and black holes, decide whether it is certain we are seeing constant-frequency phenomena (and if so if their frequencies are truly constant or just vary little), and we need to decide between the various frequency, radius and modulation models mentioned in §4.

The way in which we shall be able to make such progress with XEUS is by (i) the enormously increased timing sensitivity that will be attained thanks to XEUS's very large collecting area, and (ii) the ability that XEUS will have to combine millisecond timing information with sensitive high resolution spectroscopy.

With respect to **timing sensitivity** it is important to realize, that the signal-to-noise ratio (the "significance in σ 's") for measuring aperiodic timing phenomena such as QPOs is given by

$$S/N = \frac{1}{2} I r^2 \left(\frac{T}{\Delta\nu} \right)^{1/2}$$

where I is the count rate (assuming negligible background), T the integration time, and r the fractional rms and $\Delta\nu$ the power spectral width of the signal. This implies that S/N is *proportional* to count rate and hence, for a similar spectral response, to collecting area A , rather than to \sqrt{A} as is the usual case. Increasing the collecting area by a factor of ten implies that a 1σ effect changes into a 10σ effect (or that the same sensitivity can be attained in 1% of the time). For this reason alone XEUS provides an incredible opportunity for timing studies aimed at strong gravity physics in X-ray binaries, and we would be well advised to grab that opportunity.

The large sensitivity of XEUS will also open up an entirely new approach to millisecond timing studies, namely one where timing is combined with sensitive **spectroscopy**. Relativistically broadened Fe lines near 6.5 keV similar to those in AGNs (e.g., Fabian 2000) have long been suspected to exist in X-ray binaries as well (e.g., Zycki et al. 1999), and recent work with Chandra and XMM-Newton has confirmed that such lines can be detected in some neutron star and black hole binaries (Miller et al. 2002, Parmar et al. 2002); as is the case with AGNs, such lines are only detected in a subset of the candidate systems. These lines are broadened and distorted by ordinary Doppler shifts, Doppler beaming, transverse Doppler effect (time dilation) and gravitational redshift and diagnose the same strong-field region as millisecond timing. It was recently suggested that such broadened and distorted lines may also be seen at lower energies. With XEUS it will be possible to combine the spectroscopic and timing diagnostics to enormously improve the grip we have on what is going on in the inner disk. To zeroth order, the QPO frequency provides the orbital period, and the line profile the orbital velocity, so that we can solve for orbital radius r and central mass M . There are additional ways to determine these quantities, e.g.: M can also be determined from optical radial velocity measurements of the companion star, the gravitational redshift also depends only on M and r , the inner radius of the Keplerian disk can be constrained from the disk continuum emission. So, combining these measurements will provide strong tests of the models and shall certainly make it possible to prove (or disprove) that we are seeing orbital motion in the strong-field region.

Depending on details of instrumental implementation we shall be able to go further than that, if we can measure the line profile changes on short time scales, or equivalently the amplitude and phase differences between QPOs in several spectral bands within the line profile. The line widths are \sim keV, so moderate-resolution millisecond spectroscopy is sufficient to do this. Clearly, entirely different signals will be expected if the QPOs are caused by luminous blobs orbiting in the strong-field region (see also the talk by Miller at this meeting) and if they arise because the accretion

onto the neutron star surface is being modulated at the QPO frequency: such measurements will then be able to decide the emission geometry and constrain the modulation model.

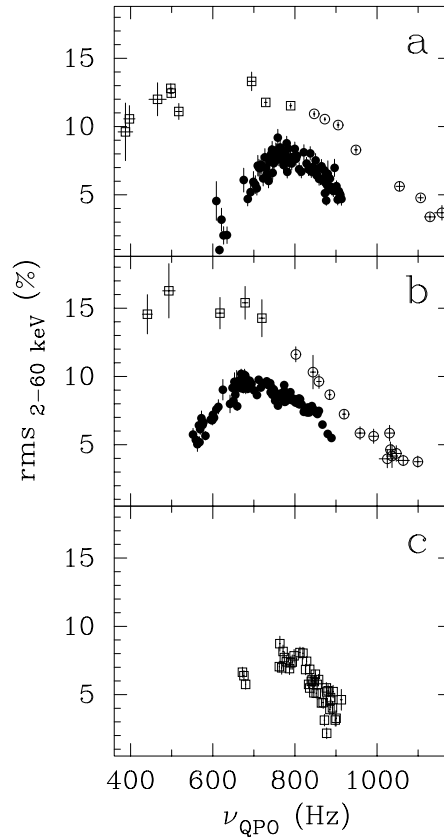


Fig. 5. The amplitude of the kHz QPOs as a function of their frequency for (a) 4U 1728–34, (b) 4U 1608–52, and (c) Aql X-1. For 4U 1728–34 and 4U 1608–52 the filled and open circles show the relation for the lower and the upper kHz QPO, respectively, and open squares indicate measurements with only a single QPO. The rms amplitudes are for the full PCA energy band. After Méndez et al. 2001.

Because of the enormously enhanced timing sensitivity, the frequency range over which certain QPOs are detected will be considerably widened. Current observations are still clearly limited by the fall-off of QPO amplitudes towards the extreme frequency. It is likely that this will make it possible to follow kHz QPOs up to the ISCO and consistently see the predicted frequency saturation there, at the same time proving orbital motion and providing a direct observation of a uniquely strong-field-GR effect; in relativistic precession models the two kHz peaks are predicted to coincide at the ISCO, so this will provide a strong test of the frequency model as well. The wider observable frequency range will also allow to test the different predictions of the various frequency models for the relations between the QPO frequencies (e.g., the quadratic dependence predicted for Lense-Thirring precession frequency or orbital frequency; the local maximum predicted in radial epicyclic frequency near the ISCO).

Measuring the patterns of weak related QPOs such as the full sideband patterns, and the weak harmonic patterns we are currently just able to glimpse in black holes will in a model-independent way test the neutron-star black-hole similarity, establish the reality of constant frequencies, and also, as already described in §4, provide conclusive tests of frequency models.

Finally, depending on the precise phenomenon, XEUS will make it possible to detect the QPOs either within one cycle ν^{-1} , or within its coherence time $\Delta\nu^{-1}$. This will open another plethora of possibilities, as this will allow to study them in the time domain. Then, it will for example be possible to perform wave form studies and quantitatively constrain compact object mass and angular momentum, orbital velocity and gravitational ray bending by modeling approaches such as described by Miller at this meeting. A nice recent example of the power of time domain studies that do not require any modeling is provided by the recent work by Wenfei Yu on the milliHertz nuclear-burning

oscillations in 4U 1636–53, which shows beautiful evidence for the nuclear X-ray flux pushing the inner disk out and lowering the kHz QPO frequency (Yu and van der Klis 2002).

Clearly, the opportunities provided by XEUS for doing strong gravity physics in X-ray binaries are simply tremendous.

References

- Belloni T., et al., 2002, astro-ph/0202213
Bildsten L., 1998, ApJ 501, L89
Chakrabarty D., Morgan E.H., 1998, Nature 394, 346
Cui W., Zhang S.N., Chen W., 1998, ApJ 492, L53
Fabian A.C., 2000, PASP 112, 1145
Galloway D.K., et al., 2002, IAUC 7900
Inoue H., 1992, ISAS RN 518
Jonker, P.G., 2000, ApJ 540, L29
Kluźniak W., Abramowicz M.A., 2001, astro-ph/0105057
Marković D., Lamb, F.K., 1998, ApJ 507, 316
Markwardt C.B., et al., 2002a, IAUC 7867
Markwardt C.B., et al., 2002b, IAUC 7870
Méndez M., et al., 2001, ApJ 561, 1016
Miller M.C., Lamb F.K., Psaltis D., 1998, ApJ 508, 791
Miller J.M., 2002, astro-ph/0202375
Miller J.M., et al., 2001, ApJ 563, 928
Olive J.F., et al., 1998, A&A 333, 942
Parmar A.N., 2002, astro-ph/0202452
Psaltis D., 2000, astro-ph/0012251
Psaltis D., Belloni T., van der Klis M., 1999, ApJ 520, L262
Psaltis D., Chakrabarty D., 1999, ApJ 521, 332
Psaltis D., Norman C., 2000, astro-ph/0001391
Psaltis D., Norman C., 2002, ApJ in prep.
Remillard R.A., et al., 2002a, IAUC 7893
Remillard R.A., et al., 2002b astro-ph/0202305
Stella L., Vietri M., 1998, ApJ 492, L59
Stella L., Vietri M., 1999, Phys. Rev. Lett. 82, 17
Strohmayer T., 2001, ApJ 552, L49
Titarchuk L., et al., 1999, ApJ 525, L129
Van der Klis M., 1994a, ApJ Supp. 92, 511
Van der Klis M., 1994b, A&A 283, 469
Van der Klis M., et al., 1997, ApJ 481, L97
Van der Klis M., 2000, Ann. Rev. Astr. Ap. 38, 717
Van der Klis M., 2001, ApJ 561, 943
Van Straaten S., et al., 2002, ApJ 568, 912
Wagoner R.V., 1999, Physics Reports 311, 259
White N.E., 2002, astro-ph/0202356
Wijnands R., van der Klis M., 1998, Nature 394, 344
Wijnands R., van der Klis M., 1999, ApJ 514, 939
Yu W., van der Klis M., 2002, ApJ 567, L67
Zhang W., Smale A.P., Strohmayer T.E., Swank J.H., 1998, ApJ 500, L171
Zycki P.T., Done C., Smith D.A., 1999, MNRAS 309, 561

In this workshop, the XEUS science case has been reviewed and was strongly endorsed by its participants as the next major leap in X-ray astrophysics in the post-CHANDRA/ XMM-NEWTON era. Moreover, several suggestions were offered at this occasion to further strengthen and enhance the scientific compellingness of the XEUS mission, either by tightening the existing requirement specifications of the current model payload, or by proposing explicit extensions to accommodate a specific science objective. As a reference framework for this rapporteur paper, I start from the XEUS key scientific objectives, i.e. four main themes, and the key observatory characteristics as they were formulated in the XEUS Mission Summary report (ref. sheet 1 and 2). The potential impact of the various contributions presented at this workshop on both the science case and on the required instrument capabilities are here globally analysed, obviously without attempting a priority assessment as yet.

- *Science themes*

In terms of the scientific relevance of XEUS for the study of the “local” universe, the importance of diagnostics and tests of General Relativity in the strong field limit, through linkage of fast timing and spectroscopy of compact objects, was strongly and repeatedly stressed. Therefore, this needs to be explicated in the identification of a fifth main theme in the key science objectives:

Theme 5: Tests of the General Theory of Relativity in the strong field limit.

- *Instrument requirements*

- A convincing case was made for pinning down the spatial resolution of the X-ray telescope at 2 arcseconds, driven by the alleged high surface density of objects at 10^{-18} ergs $\text{cm}^{-2}\text{sec}^{-2}$ ($\sim 10^5$ dg^{-2}).

- Desirability of enlarging the WFC field of view, arising from the potential rarity of high- z objects.

- Extension of the XEUS high-energy response in relation to resolving highly obscured AGN up to $z = 1$, detailed (imaging) spectroscopy of hard X-ray tails in compact binaries, SNRs, AGNs and clusters of galaxies to discriminate inverse Compton, synchrotron or non-thermal Bremsstrahlung emission processes.

- Adequate low energy response (down to 0.05 keV) for detection of red-shifted O-lines in early groups (clusters), the detection of the X-ray luminosity of star forming galaxies, the physical nature of the low-energy excess in local clusters and AGNs and the diagnostics of the multi-phase hot gas in interstellar media.

- Need for 1 eV energy resolution to uniquely resolve the absorption line complexes of the warm absorbers in AGNs and for dynamically sensitive absorption line spectroscopy of the IGM.

- Dedicated high-time-resolution focal plane sensing, aiming for sub-millisecond timing spectroscopy of compact sources, directed towards the key science of theme 5.

- Polarimetry: the throughput of XEUS is sufficiently large to allow sensitive polarimetry on a fairly large sample of bright sources.

In terms of development of the enabling technologies for XEUS the following observations can be made

- The XEUS Mirror Petal development is the top-priority for the next 2-3 years

- The development status of the focal plane imaging spectrometers is quite promising

XEUS Workshop at MPE

Rapporteur Talk, March 13, 2002

XEUS Key Science Objectives

- Theme 1: Origin and growth of the first massive black holes in the early Universe
- Theme 2: Formation of the first gravitationally bound, dark matter dominated systems, i.e. small groups of galaxies and their evolution
- Theme 3: Characterisation of the true intergalactic medium
- Theme 4: Evolution of metal synthesis to our epoch

Key Observatory Characteristics

- **Effective spectroscopic area $> 20 \text{ m}^2$ for photon energies $< 2 \text{ keV}$, resolution $< 2 \text{ eV}$**
 - **Significant detection of the most prominent X-ray emission lines O VII, Si XIII, Fe XXV against the (galactic) sky background**
- **Angular resolution between 2 and 5 arcsec**
 - **Minimise source confusion**
 - **Minimise photon background due to the galactic foreground X-ray emission**

Input relevant for theme 1/4, Issues

- Structure forms at $z=24 \rightarrow 300 M_{\odot}$ stellar mass $\rightarrow \text{SNR} \rightarrow 70 M_{\odot}$ BH, halo-accretion rate too small for rapid growth?
- Model scenario: start $10 M_{\odot}$ at $z=20 \rightarrow$ Eddington accretion rate leads to $10^8 M_{\odot}$ at $z=6$, but recent data show excess AGN-sources at low z , clustering in sheets, decline of space density beyond $z=4$: assumption of constant space density is challenged \rightarrow much lower statistics at high z
- HDF and DFS observations indicate that in the 0.5-2 keV band galaxies dominate for $F_x < 2 \cdot 10^{-17} \text{ cgs}$. CXO stacking analysis shows $(L_x)_g \sim 3-6 \cdot 10^{40} \text{ cgs}$ at $z=1$ and $(L_x)_g \sim 3 \cdot 10^{41} \text{ cgs}$ at $z=3$
- Cosmic X-ray Background: largest power in the 10-40 keV band \rightarrow issue of resolving highly obscured AGN

CONCL: XEUS has to deal with a mix of ULXs, star forming galaxies, (LL)AGNs and combi's with high surface density: $\sim 10^5 \text{ dg}^{-1}$ at 10^{-18} cgs

Theme 1/4: potential impact

- Strong incentive for spatial resolution of 2 arcsec (HEW)
- Potential rarity of high- z objects \rightarrow increase WFC-FOV for enhanced coverage
- Importance of star forming galaxies emphasises the importance of adequate low-energy response
- Enhance XEUS high-energy-response (e.g. $A_E \sim 3000 \text{ cm}^2$ in the 20-50 keV band) \rightarrow resolve highly-obscured AGNs of 10^{-15} cgs up to $z=1$, for $z > 1$ wavelength shifts into nominal range!
- Stress importance of correlation with the IR-diagnostics from future deep space observatories, e.g. ALMA, NGST

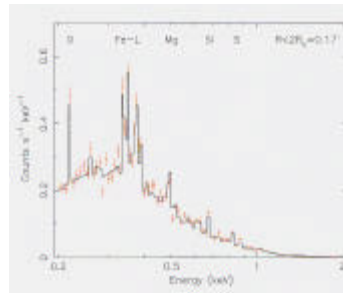
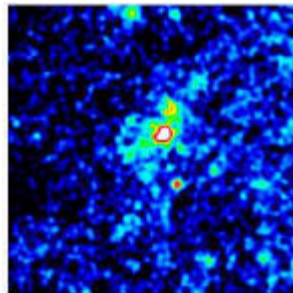
Input relevant to theme 2/4, Impact

XEUS is well tailored to the study of the formation and evolution of groups and clusters
 -Importance of the low-energy response (0.05-0.25 keV) for redshifted O-emission lines is stressed (see below)

Exposure 100 kilo-sec
 Angular resolution = 5''

Temperature = 1.5 keV
 Abundance = 0.3 solar

$Z=2$
 $L_X = 10^{36} \text{ Watt}$



Input relevant to theme 3/4, Impact

- Absorption line spectroscopy:
 - no longer speculative, detection of OVII and OVIII columns of 10^{16} cm^{-2} at $T \sim 1.5 \cdot 10^6 \text{ K}$
 - GRBs: most intense background light sources for diagnostics (highest intensity/sr). XEUS needs rapid response to Targets of Opportunity!
 - Simulations: XEUS1 \rightarrow line-EW of 0.3 keV, XEUS2 \rightarrow line-EW of 0.1 keV, measurement of dispersion velocities $< 2000 \text{ kms}^{-1}$. Need for 1 eV energy resolution
- Emission line spectroscopy:
 - Figure of merit is $\text{grasp} = A_E \cdot \Omega$ \rightarrow XEUS not suited due to extremely small value of the NFI $\cdot \Omega$

Scientific relevance of XEUS for study of the “local” Universe: AUXILIARY SCIENCE

- #Study of innermost orbits of binaries and AGN:
 - wide range of QPO frequencies
 - NS/BH similarities
 - waveform studies
 - diagnose General Relativity, TEST General Relativity
 - linkage between timing and spectroscopic properties
- # Hard X-ray tails in Clusters, SNRs (Inverse C, Synch, Non-T Brem)
- #Cold matter around binaries
- #Diagnostics of the hot ISM (gas phases, grains)
- #Relativistic disks(emission line profiles) and warm absorbers (absorption edges and lines) in AGN
- #Reverberation mapping (but: lack of correlation between relativistic Fe-K line and continuum not understood)
- #Physics of extended hot plasma sources (NEI, abundance, dynamics)

AUXILIARY SCIENCE: Impact

- Dedicated high-time-resolution FP-sensor (sub-millisecond regime), significance of “photon-limited” observations scale linearly with mirror collecting area
- High-energy sensitivity
- Bandwidth: accurate simultaneous measurement of the > 10 keV continuum and the low-energy excess (in particular for Cluster and AGN study)
- Strong incentive from absorption-line-spectroscopy for 1 eV resolution below 1 keV
- Polarimetry

Technology Issues 1

- **XEUS SYSTEM LEVEL STUDY: KICK-OFF APRIL 2002, DURATION 18 MONTHS(joined effort ESA D-Science/D-MSM).**
- **Mirror development aspects:**
 - plate manufacture
 - handling/fixing → integrated petal structure
 - metrology and alignment
- **Mirror technology aspects:**
 - Mass/Geometrical area (kgm^2): Ni not favoured !
 - Borofloat glass → slumped glass petal sheets → first results expected mid-2002
 - Ceramic SiC as alternative lightweight material
 - Multi-layer coated super-mirrors: advanced development in Japan, technological issue concerns the long term spectral stability of the multi-layer
 - Design for Metrology set-up with 1 arcsec accuracy, major issue concerns SPEED of X-ray quality test, assembly and alignment
- **→ XEUS MIRROR PETAL DEVELOPMENT TOP PRIORITY FOR THE NEXT 2-3 YEARS.**

Technology Issues 2

- **Focal plane sensors**
 - WFC: Active Pixel Array
 - NFI: Superconductive Tunneling Junction Array
 - NFI: Transition Edge Sensor Array
 - High-Energy: CdTe spectrometer Array
- **Technology readiness**
 - Good progress on all technologies:
 - WFC proven low-noise performance, NEC < 4 electrons
 - NFI single pixel performance closing in on requirement of 2 eV at 1 keV and 5eV at 8keV, e.g. TES single pixel resolution of 3.9 eV at 6 keV with 100 microsec response time, theoretically ~ 1 eV achievable
 - Array development now in progress: STJ → Ta/Al Droid configuration, Bismuth-TiAu-TES array with frequency-multiplexing read-out.
- → Development status of the enabling technologies for XEUS focal plane Imaging Spectrometers quite promising

List of participants (in alphabetical order)

=====

T. Abel	Penn State University, USA	tabel@astro.psu.edu
L. Angelini	GSFC USRA, USA	angelini@davide.gsfc.nasa.gov
O. Anthony	Network Computer College, Nigeria	dasukiservices@yahoo.com
M. Arnaud	Saclay	marnaud@discovery.saclay cea.fr
B. Aschenbach	MPE Garching, Germany	bra@mpe.mpg.de
S. Balogun	Eworld Training Center, Nigeria	Segsy2k@yahoo.co.uk
M. Barbera	INAF, Italy	barbera@astropa.unipa.it
X. Barcons	Instituto de Fisica de Cantabria, Spain	barcons@ifca.unican.es
D. Barret	CESR, France	Didier.Barret@cesr.fr
W. Becker	MPE Garching, Germany	web@mpe.mpg.de
M. Beijersbergen	cosine Research, The Netherlands	marco.beijersbergen@cosine.nl
J. Bleeker	SRON, The Netherlands	j.bleeker@sron.nl
H. Boehringer	MPE Garching, Germany	hxb@mpe.mpg.de
L. Boirin	ESTEC, ESA, The Netherlands	lboirin@rssd.esa.int
Th. Boller	MPE Garching, Germany	bol@xray.mpe.mpg.de
J. Bookbinder	SAO, USA	jbookbinder@cfa.harvard.edu
D. Breitschwerdt	MPE Garching, Germany	breitsch@mpe.mpg.de
U. Briel	MPE Garching, Germany	ugb@mpe.mpg.de
A. Brinkman	SRON, The Netherlands	A.Brinkman@sron.nl
M. Brusa	DipUniversita' di Bologna, Italy	brusa@bo.astro.it
H. Bräuninger	MPE Garching, Germany	hb@mpe.mpg.de
W. Burkert	MPE Garching, Germany	burkert@mpe.mpg.de
V. Burwitz	MPE Garching, Germany	burwitz@mpe.mpg.de
M. Cappi	TeSRE-CNR, Italy	mcappi@tesre.bo.cnr.it
F. Christensen	Danish Space Research Institute, Denmark	finn@dsri.dk
E. Churazov	MPA Garching, Germany	churazov@mpa-garching.mpg.de
O. Citterio	Brera Astronomical Observatory/INAF, Italy	pareschi@erate.mi.astro.it
A. Collura	IFCAI-CNR PALERMO, Italy	collura@oapa.astropa.unipa.it
A. Comastri	Osservatorio Astronomico di Bologna, Italy	comastri@bo.astro.it
E. Costa	CNR RomaIAS, Italy	costa@ias.rm.cnr.it
A. Del Popolo	Bergamo University, Italy	adelpopolo@alpha4.ct.astro.it
G. Di Cocco	IASF/CNR, Italy	dicocco@tesre.bo.cnr.it
T. Doehring	SCHOTT GLAS, Germany	Thorsten.Doehring@schott.com
U. Eichmann	Johann Wolfgang Goethe-Universität, Germany	eichmann@th.physik.uni-frankfurt.de
A. Fabian	Cambridge IoA, UK	acf@ast.cam.ac.uk
J. Feustel-Büechl	ESA, France	joerg.feustel-buechl@esa.int
M. Freyberg	MPE Garching, Germany	mjf@mpe.mpg.de
P. Friedrich	MPE Garching, Germany	pfriedrich@mpe.mpg.de
L. Gallo	MPE Garching, Germany	lgallo@mpe.mpg.de
L. Gastaldo	University and INFN of Genoa	loredana.gastaldo@inf.n.g.e.it
F. Gatti	Universiti & INFN of Genova, Italy	gatti@ge.infn.it
R. Genzel	MPE Garching, Germany	genzel@mpe.mpg.de
I. Georgantopoulos	National Observatory of Athens, Greece	ig@astro.noa.gr
M. Ghigo	Brera Astronomical Observatory/INAF, Italy	ghigo@erate.mi.astro.it
M. Giorgio	University Roma Tre, Italy	matt@fis.uniroma3.it
S. Grebenev	IKI, Russia	mykle@hea.iki.rssi.ru
R. Griffiths	Carnegie Mellon University, USA	riffith@astro.phys.cmu.edu
D. Grupe	MPE Garching, Germany	dgrupe@mpe.mpg.de
M. Guainazzi	XMM-Newton Science Operation Center, Spain	mguainaz@xmm.vilspa.esa.es
F. Haberl	MPE Garching, Germany	fwh@mpe.mpg.de
A. Hammesfahr	Astrium GmbH	axel.hammesfahr@astrium-space.com
M. Hanauske	Johann Wolfgang Goethe-Universität, Germany	hanauske@th.physik.uni-frankfurt.de
G. Hartner	MPE Garching, Germany	gih@mpe.mpg.de
G. Hasinger	MPE Garching, Germany	ghasinger@mpe.mpg.de
H. Hoervers	SRON, The Netherlands	H.F.C.Hoervers@sron.nl
S. Hofer	Kayser-Threde GmbH, Germany	SH@kayser-threde.de
R. Hudec	Astronomical Institute Ondrejov, Czech Rep.	rhudec@asu.cas.cz
A. Inneman	Centre of Advanced X-ray Technologie, Czech Rep.	adolf.inneman@reflex-co.cz
H. Inoue	ISAS, Japan	inoue@astro.isas.ac.jp
K. Iwasawa	University of Cambridge, UK	ki@ast.cam.ac.uk
M. Jonský	COMPAS, cons., Czech Rep.	compas@mail.drings.cz
J. Kaastra	SRON, The Netherlands	J.Kaastra@sron.nl
P. Kahabka	Sternwarte Universität Bonn, Germany	pkahabka@astro.uni-bonn.de
R. Keil	MPE Garching, Germany	rkeil@mpe.mpg.de
E. Kendziorra	University Tübingen, Germany	kendziorra@astro.uni-tuebingen.de
J. Kerp	Radioastronomisches Institut Bonn, Germany	jkerp@astro.uni-bonn.de
R. Kneissl	University of Cambridge, UK	rkneissl@mrao.cam.ac.uk
S. Komossa	MPE Garching, Germany	skomossa@mpe.mpg.de
S. Kraft	cosine research b.v.	S.Kraft@cosine.nl
S. Kulkarni	Caltech, USA	srk@astro.caltech.edu
P. Lechner	MPI Halbleiterlabor, Germany	peter.lechner@hll.mpg.de
I. Lehmann	MPE Garching, Germany	ile@xray.mpe.mpg.de
R. Lieu	Univ. of Alabama, USA	lieur@csparr.uah.edu
D. Lumb	Space Science Division, ESTEC	David.Lumb@rssd.esa.int
A. Luukanen	University of Jyväskylä, Finland	luukanen@phys.jyu.fi
R. Maiolino	Osservatorio Astrofisico di Arcetri, Italy	maiolino@arcetri.astro.it
G. Malaguti	IASF/CNR, Italy	malaguti@tesre.bo.cnr.it
N. Meidinger	MPE Garching, Germany	nom@mpe.mpg.de
M. Mendez	SRON, The Netherlands	M.Mendez@SRON.nl
A. Merloni	MPA Garching, Germany	am@MPA-Garching.MPG.DE
G. Micela	INAF-Osservatorio Astronomico di Palermo, Italy	giusi@oapa.astropa.unipa.it
C. Miller	University of Maryland, USA	miller@astro.umd.edu
K. Mitsuda	ISAS, Japan	mitsuda@astro.isas.ac.jp:wq
K. Nandra	NASA GSFC, USA	nandra@milkyway.gsfc.nasa.gov
D. Neumann	CEA/Saclay Service d'Astrophysique, France	ddon@cea.fr
F. Nicastro	Harvard-Smithsonian Center for Astrophysics, USA	fnicastro@cfa.harvard.edu
P. O'Brien	University of Leicester, UK	pto@star.le.ac.uk
Y. Ogasaka	Nagoya University, Japan	ogasaka@u.phys.nagoya-u.ac.jp
T. Okajima	Nagoya University	okajima@u.phys.nagoya-u.ac.jp
F. Paerels	Columbia University, USA	ts@astro.columbia.edu
M. Page	Mullard Space Science Lab, UCL, UK	mjp@mssl.ucl.ac.uk
G. Palumbo	Bologna Observatory, Italy	ggcpalumbo@bo.astro.it
F. Panessa	Universita' di Bologna, Italy	panessa@tesre.bo.cnr.it

G. Pareschi	Brera Astronomical Observatory/INAF, Italy	pareschi@merate.mi.astro.it
A. Parmar	ESTEC, The Netherlands	aparmar@rssd.esa.int
M. Pavlinsky	IKI, Russia	sergei@hea.iki.rssi.ru
D. Pergolesi	INFN, Italy	pergolesi@ge.infn.it
R. Petre	NASA GSFC, USA	rob@hatrack.gsfc.nasa.gov
F. Pfefferkorn	MPE Garching, Germany	pfefferk@mpe.mpg.de
E. Piconcelli	IASF/ITESRE, Italy	piconcel@tesre.bo.cnr.it
W. Pietsch	MPE Garching, Germany	wnp@mpe.mpg.de
L. Piro	IASF/CNR, Italy	piro@ias.rm.cnr.it
T. Ponman	University of Birmingham, UK	tjp@star.sr.bham.ac.uk
D. Porquet	CEA-Saclay, France	dporquet@cea.fr
P. Predehl	MPE Garching, Germany	prp@mpe.mpg.de
P. Ranalli	Universita' di Bologna, Italy	piero@anastasia.bo.astro.it
M. Razeti	University and INFN of Genoa	razeti@ge.infn.it
R. Rutledge	Caltech, USA	rutledge@tapir.caltech.edu
M. Schimmelpfennig	Germany	mshkg@aol.com
S. Schindler	Universitaet Innsbruck, Austria	sas@astro.livjm.ac.uk
E. Schmidt	Kayser-Threde GmbH, Germany	se@kayser-threde.de
J. Schultz	University of Helsinki, Finland	Juho.Schultz@astro.helsinki.fi
N. Schulz	MIT, USA	nss@space.mit.edu
S. Sciortino	INAF-Osservatorio Astronomico di Palermo, Italy	sciorti@oapa.astro.unipa.it
D. Southwood	ESA, FRANCE	David.Southwood@esa.int
H. Stoecker	Goethe Universitaet Frankfurt, Germany	stoecker@astro.uni-frankfurt.de
L. Strüder	MPE Garching, Germany	lts@hll.mpg.de
T. Stuffer	Kayser-Threde GmbH	su@kayser-threde.de
R. Sunyaev	MPA Garching, Germany	rsunyaev@mpa-garching.mpg.de
G. Tagliaferri	Osservatorio Astronomico di Brera, Italy	gtagliaf@merate.mi.astro.it
Y. Tanaka	MPE Garching, Germany	ytanaka@xray.mpe.mpg.de
J. Trümper	MPE Garching, Germany	jtrumper@mpe.mpg.de
H. Tsunemi	Osaka university, Japan	tsunemi@ess.sci.osaka-u.ac.jp
M. Turner	Leicester University, UK	mjlt@star.le.ac.uk
A. Valenzuela	MEDIA LARIO SRL, Italy	arnoldo.valenzuela@media-lario.it
D. Victor	Network Computer College, Nigeria	victorduruji@yahoo.com
G. Villa	IASF, Italy	gev@ifctr.mi.cnr.it
W. Voges	MPE Garching, Germany	whv@mpe.mpg.de
S. Volonte	ESA Head Office, The Netherlands	sergio.volonte@esa.int
J.-W. den Herder	SRON, The Netherlands	J.den.Herder@sron.nl
M. Watson	University of Leicester, UK	mgw@star.le.ac.uk
N. White	GSFC, USA	nwhite@lheapop.gsfc.nasa.gov
R. Willingale	University of Leicester, UK	rw@star.le.ac.uk
A. Zakharov	STATE SCIENTIFIC CENTER, Russia	Zakharov@vitep5.itep.ru
V. Zavlin	MPE Garching, Germany	zavlin@mpe.mpg.de
W. Zhang	NASA GSFC, USA	William.W.Zhang@gsfc.nasa.gov
J. Zicha	COMPAS, cons., Czech Rep.	compas@mail.drings.cz
D. Zschesche	Institut für Theor. Physik Frankfurt, Germany	ziesche@th.physik.uni-frankfurt.de
M. van der Klis	Amsterdam University, The Netherlands	michiel@astro.uva.nl

Author index

Abel T.	1
Angelini L., Snowden S., Loewenstein M., Mushotzky R.	243
Arnaud M.	39
Barcons X.	77
Barret D., Skinner G.K., Kendziorra E., Staubert R., Lechner P., Strüder L., Stella L., Miller C.	211
Boirin L., Parmar A.N.	247
Bleeker J.	363
Boller Th. Breitschwerdt D., Strüder L., Predehl P.	219
Breitschwerdt D., Freyberg M.J., Pietsch W.	251
Churazov E.	85
Citterio O., Ghigo M., Mazzoleni F., Pareschi G., Aschenbach B., Bräuninger H.	119
Comastri A., Ranalli P., Brusa M.	19
Costa E., Soffitta P., Di Persio G., Feroci M., Pacciani L., Rubini A., Bellazzini R., Brez A., Baldini L.	
Latronico L., Omodei N., Spandre G.	235
Del Popolo, A.	307
Fabian A.C.	207
Freyberg M.J., Breitschwerdt D.	255
Georgantopoulos I., Shanks T., Vallbe M., Zezas A., Ward M.J., Stewart G.C., Boyle B.J., Griffiths R.E.	35
Grupe D., Wills B.J.	259
Guainazzi M., Stanghellini C., Grandi P.	261
Hanaske M., Zschiesche D., Eichmann U., Satarov L.M., Mishustin I.N., Schaffner-Bielich J., Stöcker H., Greiner W.	277
Hasinger G.	7
Hudec R., Pína L., Inneman I., Brožek V., Chráska P., Neufuss K., Zentková M., Zentko A.	265
Hudec R., Pína L., Inneman, A.	271
Hoevers H., Verhoeve P.	127
Inoue H.	165
Kaastra J.S.	199
Kahabka P.	281
Kneissl R.	49
van der Klis M.	354
Komossa S., Hasinger G.	285
Lehmann I., Hasinger G., Mainier V.i and the Lockman Hole team	293
Lieu R.	227
Luukanen A., Huovelin J., Keinänen P., Kinnunen K., Nuottajärvi A., Pekola J., Schultz J., Vilhu O.	295
Miller M.C.	173
Nicastro F.	65
Brien P.O., Reeves J., Pounds K., Page K., Turner M.	191
Paerels F., Rasmussen A., Kahn S., Herder J.W., Vries C.	57
Page M.J., Stevens J.A., Carrera F.J.	299
Parmar A.N.	95
Piro L., Colasanti L., Costa E., Soffitta P., Gandolfi G., Feroci M., Pacciani L., De Pasquale M., De Rosa A., Gatti F., Pergolesi D., Razeti M., Ferrara A., Maiolino R., Mannucci F., Orio M., Ferrari A., Trussoni E., Fiore F., Stella L., Stratta G., McCammon D., Sanders T., Galeazzi M., Szymkowiak A., Porter S., Kelley R.	303
Piro L.	343
Petre R. and the Constellation-X SXT Team	317
Schulz N.S.	181
Schultz J., Huovelin J., Vilhu O., Muhli P., Alha L., Luukanen A., Pekola J., Sipilä H., Vaijärvi S.	327
Sciortino S., Favata F., Micela G., Parmar A.N.	331
Strüder L., Lechner P.	135
White N.E.	25S
Willingale R.	113